

Synthesis and Catalytic Application of P*S*iP- and P,N-Ligated Complexes of First-Row
Metals

by

Luke Murphy

Submitted in partial fulfillment of the requirements
for the degree of Doctor of Philosophy

at

Dalhousie University
Halifax, Nova Scotia
November 2018

© Copyright by Luke Murphy, 2018

Table of Contents

| | |
|---|-------------|
| List of Tables | v |
| List of Figures | vi |
| List of Schemes | xi |
| Abstract | xvi |
| List of Abbreviations and Symbols Used | xvii |
| Acknowledgements | xix |
| Chapter 1: Introduction | 1 |
| 1.1 Overview | 1 |
| 1.2 First-Row Transition Metal Catalysis..... | 4 |
| 1.3 Ligand Design for First-Row Transition Metals | 6 |
| 1.4 Pincer Complexes of First-Row Transition Metals | 15 |
| 1.4.1 Iron..... | 16 |
| 1.4.2 Cobalt..... | 22 |
| 1.4.3 Nickel..... | 28 |
| 1.5 First-Row Silyl Pincer Complexes | 32 |
| 1.6 P,N Ligation in Transition Metal Chemistry | 42 |
| 1.6.1 First-Row Metal Complexes of Monoanionic P,N Ligands | 43 |
| Chapter 2: Synthesis and Characterization of (Cy-PSiP)Fe Complexes and Application Toward Catalytic Olefin Hydrogenation | 51 |
| 2.1 Introduction | 51 |
| 2.2 Results and Discussion | 54 |
| 2.2.1 Synthesis and Reactivity of (Cy-PSiP)Fe(PMe ₃)Cl..... | 54 |
| 2.2.2 Reduction of (Cy-PSiP)Fe(PMe ₃)Cl..... | 61 |
| 2.2.3 Reactivity of (Cy-PSiP)Fe ^I and (Cy-PSiP)Fe ⁰ Complexes..... | 64 |
| 2.2.4 Rational Preparation of Fe ^{II} -hydride complexes | 69 |
| 2.2.5 Fe-Catalyzed Olefin Hydrogenation..... | 87 |
| 2.3 Summary and Conclusions | 93 |
| 2.4 Experimental..... | 95 |
| 2.4.1 General Considerations..... | 95 |
| 2.4.2 Synthetic Procedures and Characterization Data..... | 96 |
| 2.4.3 Crystallographic Solution and Refinement Details | 108 |

| | |
|--|------------|
| Chapter 3: Activation of Molecular Hydrogen and Oxygen by PSiP Complexes of Cobalt..... | 113 |
| 3.1 Introduction | 113 |
| 3.2 Results and Discussion | 114 |
| 3.2.1 Previous Work Involving Synthesis of Co ^{II} Halide Complexes of Cy-PSiP | 114 |
| 3.2.2 Reduction of (Cy-PSiP)Co ^{II} to (Cy-PSiP)Co ^I | 115 |
| 3.2.3 Investigation of Oxidative Addition Reactions at (Cy- PSiP)CoI and Alkene Hydrogenation catalysis. | 118 |
| 3.2.4 Reactivity of (Cy-PSiP)Co ^{II} Toward Molecular Oxygen | 129 |
| 3.3 Summary and Conclusions | 137 |
| 3.4 Experimental Section..... | 138 |
| 3.4.1 General Considerations..... | 138 |
| 3.4.2 Synthetic Procedures and Characterization Data..... | 139 |
| 3.4.3 Crystallographic Solution and Refinement Details | 145 |
| Chapter 4: Synthesis of (ⁱPr-PSiP^{Ind})M (M = Ni, Pd, Pt) Complexes and Catalytic CO₂ Reduction to the Formaldehyde Level..... | 147 |
| 4.1 Introduction | 147 |
| 4.2 Results and Discussion | 149 |
| 4.2.1 Synthesis of Group 10 Metal Chloride Complexes | 149 |
| 4.2.2 Metathesis Reactions of (ⁱ Pr-PSiP ^{Ind})NiCl | 152 |
| 4.2.3 Investigation of (ⁱ Pr-PSiP ^{Ind})M (M = Ni, Pd, Pt) Hydride Complexes | 156 |
| 4.2.4 Catalytic Hydroboration of CO ₂ to the Formaldehyde Level..... | 174 |
| 4.3 Summary and Conclusions | 182 |
| 4.4 Experimental..... | 184 |
| 4.4.1 General Considerations..... | 184 |
| 4.4.2 Synthetic Procedures and Characterization Data..... | 185 |
| 4.4.3 Crystallographic Solution and Refinement Details | 206 |
| Chapter 5: Fe and Co Complexes of a New Monoanionic P,N Ligand and Catalytic Hydrosilylation of Amides..... | 209 |
| 5.1 Introduction | 209 |
| 5.2 Results and Discussion | 211 |
| 5.2.1 Synthesis of a (P,N)H Proligand..... | 211 |

| | | |
|---|---|------------|
| 5.2.2 | Synthesis of (P,N)Fe and Co Halide Complexes..... | 214 |
| 5.2.3 | Synthesis and Reactivity of (P,N)Fe Amido Complexes | 218 |
| 5.2.4 | Synthesis of (P,N)Fe ^I Complexes..... | 223 |
| 5.2.5 | Synthesis of (P,N)Fe Alkyl Complexes..... | 227 |
| 5.2.6 | (P,N)Fe and Co-Catalyzed Reduction of Amides | 231 |
| 5.3 | Summary and Conclusions | 239 |
| 5.4 | Experimental..... | 241 |
| 5.4.1 | General Considerations..... | 241 |
| 5.4.2 | Synthetic Procedures and Characterization Data..... | 242 |
| 5.4.3 | Crystallographic Solution and Refinement Details | 254 |
| Chapter 6: Conclusions and Future Work | | 256 |
| 6.1 | Summary and Conclusions | 256 |
| 6.2 | Future Work..... | 260 |
| References | | 271 |
| Appendix A: Crystallographic Experimental Details..... | | 286 |
| Appendix B: Selected NMR Spectra of Reported Compounds | | 332 |
| Appendix C: Copyright Agreements..... | | 386 |

List of Tables

| | |
|---|-----|
| Table 2.2.1. Hydrogenation of 1-octene using 2-(N ₂) ₂ | 88 |
| Table 2.2.2. Hydrogenation of various substituted alkenes using 2-(N ₂) ₂ | 90 |
| Table 2.2.3. Hydrogenation of diphenylacetylene and various functionalized alkenes using 2-(N ₂) ₂ | 92 |
| Table 3.2.1. Alkene hydrogenation catalysis. | 129 |
| Table 4.2.1. Summary of relevant spectroscopic data for Group 10 metal hydride or η^2 -silane complexes prepared in this work. ^a | 173 |
| Table 4.2.2. Initial screening of CO ₂ hydroboration with HBPIn. ^a | 177 |
| Table 4.2.3. Hydroboration of CO ₂ with 4-NiH to the formaldehyde level. ^a | 179 |
| Table 5.2.1. Reduction of tertiary benzamides to tertiary benzylamines. | 234 |
| Table 5.2.2. Reduction of tertiary amides to tertiary amines. | 236 |
| Table 5.2.3. Reduction of secondary amides catalyzed by 5-2 using various reductants. | 238 |

List of Figures

| | |
|--|----|
| Figure 1.1.1. Common pincer ligand motifs encountered. D = central donor, most commonly nitrogen (neutral/anionic), carbon (anionic) or silicon (anionic). L = Neutral donor, most commonly an amine, imine, phosphine or carbene..... | 2 |
| Figure 1.1.2. Examples of commonly encountered bidentate ligand scaffolds. Neutral bis(phosphino)ferrocenes (left), monoanionic 1,3-diketimides or “NacNac” (center), dianionic catecholate (right)..... | 2 |
| Figure 1.1.3. Ligands employed in this work. Chemistry of Cy-PSiP (A) with Fe and Co described in Chapters 2 and 3, respectively. Chemistry of ⁱ Pr-PSiP ^{Ind} (B) with Ni described in Chapter 4. Chemistry of P ^{Cy} ,N ^{DiPP} (C) with Fe and Co described in Chapter 5..... | 4 |
| Figure 1.3.1. Structures of mono, bis and tris(phosphino)silyl pincer ligand precursors prepared by Stobart and co-workers. ¹⁹⁻²⁰ | 14 |
| Figure 1.4.1. General structure of (^R CNC)Fe(N ₂) ₂ (left). Conversions of selected alkenes to alkanes <i>via</i> hydrogenation catalyzed by (^{Mes} CNC)Fe(N ₂) ₂ | 22 |
| Figure 1.5.1. Structural diagram of the dimeric nickel complex featuring 5-coordinate silicon derived from (Ph-PSiP)NiCl and a hydride source. ⁷⁷ | 35 |
| Figure 1.6.1. Examples of other monoanionic P,N-based ligands designed to support metal catalysts for the oligomerization of ethylene. ^{86b, 86d, e} | 44 |
| Figure 2.1.1. Examples of existing Fe-based catalysts for the homogeneous hydrogenation of alkenes. | 52 |
| Figure 2.2.1. Crystallographically determined structure of 2-Br, with thermal ellipsoids shown at the 50% probability level. Hydrogen atoms have been omitted for clarity..... | 56 |
| Figure 2.2.2. Crystallographically determined structures of 2-Cl and 2-Me with thermal ellipsoids shown at the 50% probability level. Hydrogen atoms have been omitted for clarity. Only one of two crystallographically independent molecules of 2-Me is shown. | 57 |
| Figure 2.2.3. Crystallographically determined structures of 2-PMe ₃ and 2-(CO) ₂ with thermal ellipsoids shown at the 50% probability level. Hydrogen atoms and solvent molecules have been omitted for clarity. Only one of two crystallographically independent molecules of 2-PMe ₃ and 2-(CO) ₂ are shown. | 60 |

| | |
|--|----|
| Figure 2.2.4. Crystallographically determined structure of 2-Fe ^I with thermal ellipsoids shown at the 50% probability level. Hydrogen atoms have been omitted for clarity. Only one of two crystallographically independent molecules is shown..... | 63 |
| Figure 2.2.5. The crystallographically determined structure of 2-H(N ₂) shown with 50% displacement ellipsoids. Most hydrogen atoms have been omitted for clarity. The coordinated N ₂ is shown as blue spheres to indicate partial (12.5%) occupancy..... | 66 |
| Figure 2.2.6. Crystallographically determined structure of 2-H with thermal ellipsoids shown at the 50% probability level. Most hydrogen atoms have been omitted for clarity. | 70 |
| Figure 2.2.7. Crystallographically determined structure of 2-H ₃ with thermal ellipsoids shown at the 50% probability level. Most hydrogen atoms have been removed for clarity. Only one of two crystallographically independent molecules is shown. | 73 |
| Figure 2.2.8. Overlay of hydride region of low-temperature ¹ H NMR (300 MHz) spectra for 2-H ₃ between 193 – 300 K. Detailed NMR data (<i>vide infra</i>) was collected at 253 K..... | 76 |
| Figure 2.2.9. Overlay of hydride region of high-temperature ¹ H NMR spectra (500 MHz) between 300 – 353 K. First coalescence (of H2 and H3) occurs at <i>ca.</i> 343 K, second coalescence (of H1, H2 and H3) likely occurs above 353 K. | 76 |
| Figure 2.2.10. (A) Hydride region of ¹ H{ ³¹ P} spectrum for 2-H ₃ (253 K). (B) Hydride region of 1D TOCSY NMR spectrum for 2-H ₃ (253 K, 0.025 s mixing time, H3 irradiated). (C) Hydride region of 1D TOCSY NMR spectrum for 2-H ₃ (253 K, 0.05 s mixing time, H3 irradiated). (D) Hydride region of ¹ H NMR spectrum for 2-H ₃ (253 K). | 78 |
| Figure 2.2.11. (A) 1D NOESY spectrum for 2-H ₃ (253 K, 0.5 s mixing time, H1 and H2 irradiated). (B) 1D NOESY spectrum for 2-H ₃ (253 K, 0.5 s mixing time, H3 irradiated). (C) 1D NOESY spectrum for 2-H ₃ (300 K, 0.5 s mixing time, H3 irradiated). | 79 |
| Figure 2.2.12. Experimental (positive projections) and simulated (negative projections) spectra of the hydride resonances for 2-H ₃ . Top: 300 MHz, 253 K (toluene- <i>d</i> ₈). Bottom: 500 MHz, 268 K (toluene- <i>d</i> ₈). | 80 |
| Figure 2.2.13. Proposed bonding schemes for 2-H ₃ (most of the molecule has been omitted for clarity). (A) Silyl trihydride complex of Fe(IV), (B) η ² -silane complex between Si-H1 and Fe (bonding scenario proposed for 2-H ₃), (C) η ² -silane complex between Si-H1 and Fe with SISHA between Si and H2, (D) η ³ -silane complex between Si, H1, H2 and Fe. | 83 |

| | |
|--|-----|
| Figure 2.2.14. Crystallographically determined structures of 2-py(N ₂) and 2-(N ₂) ₂ with thermal ellipsoids shown at the 50% probability level. Most hydrogen atoms have been omitted for clarity..... | 86 |
| Figure 3.2.1. Crystallographically determined structure of 3-4 with thermal ellipsoids shown at the 50% probability level. Hydrogen atoms have been omitted for clarity..... | 117 |
| Figure 3.2.2. Some possible structural formulations for the species arising from treatment of (Cy-PSiP)CoN ₂ (PMe ₃) (3-3) with H ₂ | 121 |
| Figure 3.2.3. Examples of previously reported five-coordinate nonclassical Co ^I dihydrogen complexes..... | 121 |
| Figure 3.2.4. Partial (a) ¹ H and (b) ¹ H{ ³¹ P} NMR spectra (hydride region) of complex 3-5 in toluene- <i>d</i> ₈ (300 MHz, 25 °C), as well as (c) ¹ H and (d) ¹ H{ ³¹ P} NMR spectra (hydride region) of complex 3-5- <i>d</i> in toluene- <i>d</i> ₈ (300 MHz, 25 °C). | 122 |
| Figure 3.2.5. Partial variable temperature (a) ¹ H and (b) ¹ H{ ³¹ P} NMR spectra (hydride region) of complex 3-5 in toluene- <i>d</i> ₈ (300 MHz)..... | 124 |
| Figure 3.2.6. Partial ¹ H{ ³¹ P} NMR spectra (hydride region) of (a) complex 3-5- <i>d</i> formed upon addition of HD to 3-3 and (b) complex 3-5 formed upon addition of H ₂ to 3-3 in toluene- <i>d</i> ₈ (300 MHz, 80 °C). | 125 |
| Figure 3.2.7. Variable temperature ³¹ P{ ¹ H} NMR spectra of complex 3-5 in toluene- <i>d</i> ₈ (300 MHz)..... | 126 |
| Figure 3.2.8. Crystallographically determined structures for 3-6 (left) and 3-7 (right) with thermal ellipsoids drawn at the 50% probability level. Solvent molecules and hydrogen atoms have been omitted for clarity. Only one of the two crystallographically independent molecules of 3-7 is shown..... | 131 |
| Figure 3.2.9. Previously reported examples of PSiP and related NSiN ligand oxidation..... | 132 |
| Figure 3.2.10. ¹ H NMR spectra of (a) 3-7 and (b) 3-6 (benzene- <i>d</i> ₆ , 300 MHz)..... | 135 |
| Figure 4.2.1. Crystallographically determined structures of 4-PdCl (left) and 4-PtCl (right) with thermal ellipsoids shown at the 50% probability level. Hydrogen atoms have been omitted for clarity..... | 152 |
| Figure 4.2.2. ¹ H- ²⁹ Si HECADE spectra of (^{<i>i</i>} Pr-PSiP ^{<i>Ind</i>})H (top, blue) and 4-PdH (bottom, red). Opposite slopes in the crosspeak patterns indicate the corresponding coupling constant is of an opposite sign to the other..... | 159 |
| Figure 4.2.3. Variable temperature (top) ¹ H NMR (hydride region) and (bottom) ³¹ P{ ¹ H} NMR spectra of 4-NiH and 4-NiH* (toluene- <i>d</i> ₈). | 161 |

| | |
|--|-----|
| Figure 4.2.4. Variable temperature (top) ^1H NMR (hydride region) and (bottom) $^{31}\text{P}\{^1\text{H}\}$ NMR spectra of 4-NiH and 4-NiH* (methylcyclohexane- d_{12})..... | 163 |
| Figure 4.2.5. Crystallographically determined structures of 4-Ni·DMAP with thermal ellipsoids drawn at the 50% probability level. Solvent molecules and most hydrogen atoms have been omitted for clarity. Only one of the two crystallographically independent molecules of 4-Ni·DMAP is shown..... | 170 |
| Figure 4.2.6. Crystallographically determined structures of 4-Ni·PMe ₃ -B and 4-Pt·PMe ₃ with thermal ellipsoids drawn at the 50% probability level. Solvent molecules and most hydrogen atoms have been omitted for clarity..... | 172 |
| Figure 5.2.1. X-ray crystal structure for (P,N)H with thermal ellipsoids shown at the 50% probability level. Most hydrogen atoms have been omitted for clarity. Full refinement in progress. | 214 |
| Figure 5.2.2. Structural diagram (left) and X-ray crystal structure (right) of 5-3 obtained during the attempted synthesis of (P,N)CoN(SiMe ₃) ₂ following a modified version of the procedure described in Scheme 5.2.5. Most Cy and ⁱ Pr groups have been cropped for clarity. Thermal ellipsoids shown at the 50% probability level. Hydrogen atoms have been omitted for clarity. Full refinement in progress. | 220 |
| Figure 5.2.3. X-ray crystal structure of 5-4 with thermal ellipsoids shown at the 50% probability level. Hydrogen atoms have been omitted for clarity. Full refinement in progress..... | 222 |
| Figure 5.2.4. X-ray crystal structure of 5-5, with thermal ellipsoids drawn at the 50% probability level. Hydrogen atoms have been omitted for clarity. Full refinement in progress..... | 223 |
| Figure 5.2.5. X-ray crystal structure of 5-6 with thermal ellipsoids drawn at the 50% probability level. Hydrogen atoms have been removed for clarity. The data set was of poor quality, thus no metrical parameters for this structure are included. | 224 |
| Figure 5.2.6. X-ray crystal structure of 5-7 with thermal ellipsoids drawn at the 50% probability level. Hydrogen atoms have been omitted for clarity. Full refinement in progress. | 225 |
| Figure 5.2.7. Two perspectives of the naphthalene ligand in the X-ray crystal structure of 5-7 highlighting the distortion from planarity. The majority of the molecule has been omitted for clarity. | 226 |
| Figure 5.2.8. X-ray crystal structure of 5-8 with thermal ellipsoids drawn at the 50% probability level. Hydrogen atoms have been omitted for clarity..... | 228 |

Figure 5.2.9. Left, X-ray crystal structure of 5-9. Right, cropped X-ray crystal structure of 5-9 highlighting the square planar geometry around Co. Thermal ellipsoids drawn at the 50% probability level for both structures. All hydrogen atoms have been omitted for clarity. These structures represent a low quality data set and thus no metrical parameters are included.....230

List of Schemes

| | |
|--|----|
| Scheme 1.3.1. Mechanism for the hydrogenation of esters catalyzed by a (PNP)Fe-based catalyst featuring metal-ligand cooperativity in the form of ligand dearomatization/rearomatization..... | 9 |
| Scheme 1.3.2. (A) Cleavage of formic acid and dihydrogen by a PNP complex of iron. (B) Si-H bond cleavage of phenylsilane by a PCP complex of nickel. Note that the formal oxidation state of Fe and Ni in these examples has not changed during the bond-cleavage processes. | 11 |
| Scheme 1.3.3. Fe-catalyzed asymmetric transfer hydrogenation of ketones as reported by Morris and co-workers, note that the formal oxidation state of Fe remains +2 throughout the reaction..... | 12 |
| Scheme 1.3.4. Reversible reaction of a (PBP)Co complex with H ₂ , leading to addition of two equiv H ₂ across the Co-B bond. The dinitrogen adduct (left) was found to be an active precatalyst for hydrogenation of terminal olefins, the catalytic dehydrogenation of ammonia-boranes and the transfer hydrogenation of terminal olefins with ammonia-boranes. | 13 |
| Scheme 1.4.1. Catalytic pathway for CO ₂ hydrogenation by <i>trans</i> -[(^t Bu-PNP)Fe(H) ₂ (CO)]. ^{26b, 38} | 17 |
| Scheme 1.4.2. Hydrogenation of esters to alcohols by (ⁱ Pr-PNP)Fe(H)(HBH ₃)(CO). R ¹ and R ² = various alkyl and aryl substituents. ^{30a} | 18 |
| Scheme 1.4.3. Base and Lewis acid assisted (PNP)Fe catalyzed hydrogenation of CO ₂ to formate. ^{15a} | 19 |
| Scheme 1.4.4. H ₂ addition to (PNP)Fe(CO)H followed by CO ₂ insertion and subsequent disruption of the generated H-bonding interaction by Li ⁺ . P = ⁱ Pr ₂ P. ^{15a} | 19 |
| Scheme 1.4.5. Proposed mechanism for the hydrogenation of olefins catalyzed by (ⁱ PrPDI)Fe(N ₂) ₂ | 20 |
| Scheme 1.4.6. Reactivity of (ⁱ PrPDI)Fe(N ₂) ₂ toward diallyl ether and allyl ethyl ether leading to catalyst decomposition products. | 21 |
| Scheme 1.4.7. Reported mechanism for Co-catalyzed olefin isomerisation and hydroboration of <i>trans</i> -4-octene. Analogous mechanisms can be invoked for other internal alkene substrates. ^{49a} | 24 |
| Scheme 1.4.8. Hydrogenation of nitriles to primary amines catalyzed by (^t Bu-PNN)CoCl ₂ . R = various alkyl and aryl substituents. ⁴⁶ | 25 |

| | |
|--|----|
| Scheme 1.4.9. Structure of (^{Mes} CCC)Co(PPh ₃)(N ₂) precatalyst. While reduction of terminal alkenes is readily supported by this system, reduction of internal alkenes is sluggish and requires elevated reaction temperatures, as illustrated by the reduction of 4-vinylcyclohexene (inset) wherein the internal alkene is left intact..... | 26 |
| Scheme 1.4.10. Generation of the cationic Co ^{II} -alkyl hydrogenation precatalyst from reaction of the neutral Co ^{II} alkyl complex with H[BAR ^F ₄](Et ₂ O) ₂ . (BAR ^F ₄ = tetrakis(3,5-trifluoromethylphenyl)borate)..... | 27 |
| Scheme 1.4.11. General structure of asymmetric bis(imino)pyridyl Co ^I -methyl complex used for the asymmetric hydrogenation of olefins (left). General reaction scheme for asymmetric hydrogenation of selected olefins (right). R' = various alkyl. X = H, F, CF ₃ , NMe ₂ , OMe..... | 28 |
| Scheme 1.4.12. Catalytic cycle for the cyanomethylation of aldehydes catalyzed by (ⁱ Pr-POCOP)NiCH ₂ CN as proposed by Guan and co-workers. ⁶⁴ | 29 |
| Scheme 1.4.13. Hydroboration of CO ₂ to CH ₃ OBcat by catecholborane (HBcat), catalyzed by (^t Bu-POCOP)NiH. ^{69a} | 30 |
| Scheme 1.4.14. Proposed mechanism for Ni-catalyzed hydrosilylation of CO ₂ to the formaldehyde level (as a bis(silyl)acetal). | 31 |
| Scheme 1.5.1. Reversible rearrangement of (Cy-PSiP)NiMe involving Si-C bond cleavage steps. ^{25a} | 33 |
| Scheme 1.5.2. Synthesis of [Ph-PSi(μ -H)P]Ni(PPh ₃) reported by Iwasawa and co-workers. ⁷⁶ | 34 |
| Scheme 1.5.3. Proposed equilibrium for the observed dinitrogen-coordinated η^2 -(SiH) Ni complexes. ^{24c} | 37 |
| Scheme 1.5.4. Synthesis of a PSiP Co complex featuring an η^1 -(Si-H) interaction and subsequent reactivity with base (top) or upon standing in solution (bottom). ^{24d} | 38 |
| Scheme 1.5.5. Synthesis of (PSiP)Co(PMe ₃) ₂ and (PSiP)Fe(PMe ₃) ₂ H from the neutral ligand precursor (PSiP)H and M(Me) _n (PMe ₃) ₄ (M = Co, n = 1; M = Fe, n = 0). ^{73a} | 39 |
| Scheme 1.5.6. Synthesis of Fe and Co dinitrogen complexes of two variants of the Cy-PSiP ligand. ^{73b} | 41 |
| Scheme 1.6.1. Synthesis of some early examples of Ni complexes of monoanionic P ₃ N ligands as reported by Braunstein and co-workers. ^{83, 85} | 44 |
| Scheme 1.6.2. Synthesis of <i>N</i> -phosphinoamidinate complexes of Mn, Fe, Co and Ni..... | 45 |

| | |
|---|-----|
| Scheme 1.6.3. Synthesis of three-coordinate alkyl zinc complexes and a (P,N) ₂ Zn complex. | 48 |
| Scheme 1.6.4. Synthesis and structural variability of 4-coordinate Ni-methyl complexes supported by a monoanionic P,N ligand. | 49 |
| Scheme 2.2.1. Synthetic routes for the generation of 2-Br, 2-Me and 2-Cl, illustrating unexpected 1-electron chemistry leading to Fe ^I and Fe ^{III} complexes from an Fe ^{II} source. | 56 |
| Scheme 2.2.2. Synthetic routes for the preparation of 2-PMe ₃ , 2-py and 2-(CO) ₂ | 58 |
| Scheme 2.2.3. One- and two- electron reduction of 2-PMe ₃ to 2-Fe ^I and 2-Fe ⁰ , respectively. | 64 |
| Scheme 2.2.4. Synthetic route for the preparation of (Cy-PSiP)Fe(PMe ₃)(H)(N ₂) (2-H(N ₂)). | 67 |
| Scheme 2.2.5. Generation of hydride containing complexes on reaction of 2-Fe ⁰ with H ₂ gas and with H ₂ O vapour. | 69 |
| Scheme 2.2.6. Generation of 2-H and its conversion to (Cy-PSiP)FeH(PMe ₃)(N ₂), as well as reaction of either complex with H ₂ to generate the polyhydride complex, 2-H ₃ | 71 |
| Scheme 2.2.7. Synthesis of 2-py(N ₂) from 2-py and its conversion to 2-(N ₂) ₂ <i>via</i> formation of a pyridine-borane adduct. | 84 |
| Scheme 3.2.1. Synthesis of (Cy-PSiP)Co ^{II} -halide complexes. | 115 |
| Scheme 3.2.2. Synthesis of (Cy-PSiP)Co ^I species via Mg reduction of 3-2. | 116 |
| Scheme 3.2.3. Reactivity of 3-2 toward O ₂ and Me ₃ NO to generate Co ^{II} products resulting from both double- (3-6) and single- (3-7) Cy-PSiP ligand oxidation. | 130 |
| Scheme 4.1.1. Stepwise hydroboration of CO ₂ to boryl formate (A), bis(boryl)acetal (B), and methoxyborane (C) species, and lastly to methane (not yet reported). | 147 |
| Scheme 4.2.1. Synthetic route for the preparation of (ⁱ Pr-PSiP ^{Ind})H. | 149 |
| Scheme 4.2.2. Synthesis (left) and crystallographically determined structure (right) of 4-NiCl with thermal ellipsoids shown at the 50% probability level. Hydrogen atoms have been omitted for clarity. | 150 |
| Scheme 4.2.3. Synthetic routes for the preparation of 4-PdCl and 4-PtCl. | 151 |
| Scheme 4.2.4. Structure of ligand-rearranged (Cy-PSiP)Ni complex (left). Synthetic route for synthesis of ligand-rearranged (ⁱ Pr-PSiP ^{Ind})Ni complex, 4-Ni* (right). | 154 |
| Scheme 4.2.5. Synthetic route for the preparation of 4-Ni(C ₃ H ₅). | 155 |

| | |
|---|-----|
| Scheme 4.2.6. Synthetic routes for the preparation of 4-NiOTf and 4-NiNHDMP from 4-NiCl. | 156 |
| Scheme 4.2.7. Synthetic route for the preparation of 4-NiH, 4-PdH and 4-PtH. Structure shown is proposed solution-state structure at room temperature. | 157 |
| Scheme 4.2.8. Proposed interconversion of 4-NiH from a (μ -N ₂)-bridged dimer in the solid state, to a classical terminal silyl hydride in solution, to the η^2 -silane and dinitrogen adduct, 4-NiH*, at low temperature in solution. | 165 |
| Scheme 4.2.9. Synthesis of (ⁱ Pr-PSi ^H P ^{Ind})H. | 166 |
| Scheme 4.2.10. Synthetic routes for the successful preparations of 4-PdCl', 4-PtCl' and 4-PtH'. | 168 |
| Scheme 4.2.11. Generation of Ni and Pd formate complexes from the corresponding hydride complexes. The analogous reaction with Pt leads to formation of multiple unidentified products. | 175 |
| Scheme 4.2.12. Proposed mechanism for (POCOP)Ni or (PSiP)M (M = Ni, Pd) CO ₂ hydroboration with diverging pathways leading to generation of boryl formate (red), bis(boryl)acetal (blue) and methoxyborane (green). | 181 |
| Scheme 4.2.13. Methylene transfer reactions from (PinBO) ₂ CH ₂ | 182 |
| Scheme 5.1.1. General scheme for hydrosilylation of amides catalyzed by (P,N)Fe and (P,N)Co complexes prepared in this work. | 210 |
| Scheme 5.2.1. General synthetic routes attempted for the synthesis of (P ^{tBu} ,N ^{DiPP})H. Route A: Pd-catalyzed C-P cross-coupling reaction, ^{175b} followed by Pd-catalyzed C-N cross coupling. ^{175a} Route B: Pd-catalyzed C-N cross-coupling reaction, ^{92, 175a} followed by Pd-catalyzed C-P cross-coupling. ^{175b} Route C: Pd-catalyzed C-N cross coupling reaction, ^{92, 175a} followed by lithium-halogen exchange and quench with chlorophosphine and water. ⁹² | 212 |
| Scheme 5.2.2. Synthesis of (P,N)H. | 213 |
| Scheme 5.2.3. Synthesis of Fe and Co halide dimers 5-FeCl, 5-FeBr and 5-CoCl. | 215 |
| Scheme 5.2.4. Structures of enamidophosphinimine complexes of iron and measured magnetic moments in benzene- <i>d</i> ₆ as reported by Fryzuk and co-workers. | 216 |
| Scheme 5.2.5. Left: Synthetic procedure for the preparation of 5-1. Right: X-ray crystal structure of 5-1 with thermal ellipsoids shown at the 50% probability level. Hydrogen atoms have been omitted for clarity. | 217 |

| | |
|--|-----|
| Scheme 5.2.6. Left: Synthetic procedure for the preparation of 5-2. Right: X-ray crystal structure of 5-2 with thermal ellipsoids shown at the 50% probability level. Hydrogen atoms have been omitted for clarity. | 219 |
| Scheme 5.2.7. One proposed route for the reaction of 5-2 toward formic acid, ultimately yielding (P,N)H <i>via</i> formate and hydride complexes. | 221 |
| Scheme 5.2.8. Synthetic procedures for the preparation of 5-8 (A) and 5-9 (B). | 228 |
| Scheme 6.2.1. General variations in phosphine donor arms or fourth substituent on Si (R ⁷) may have an impact on the extent of SiH bonding, from silyl hydrides (left) to η^2 -SiH complexes (right). | 262 |
| Scheme 6.2.2. (A) Proposed synthesis of crown-ether stabilized 2-Fe ⁰ by performing reduction of 2-PMe ₃ with Na in the presence of, for example, 15-crown-5. (B) Proposed syntheses of pyridine analogues of 2-Fe ^I and 2-Fe ⁰ from 2-py. | 263 |
| Scheme 6.2.3. Proposed coordination of 5-hexen-2-one to 2-(N ₂) ₂ and proposed disruption of the Fe-O interaction by addition of an LiX salt. | 264 |
| Scheme 6.2.4. Structure of 3-3 and proposed synthesis of other (Cy-PSiP)Co ^I complexes which may be more active toward hydrogenation of alkenes than 3-3. | 265 |
| Scheme 6.2.5. Proposed syntheses of ^{<i>i</i>} Pr-PSiP ^{<i>Ind</i>} complexes of Fe (A) and Co (B) based on established syntheses of Cy-PSiP analogues. | 266 |
| Scheme 6.2.6. General proposed synthesis for two more variants of monoanionic P,N ligand, featuring 2,6-di- <i>t</i> -butylanilido or 2,6-diphenylanilido groups. | 267 |
| Scheme 6.2.7. Structure of complex 5-2 and some possible reactivity of primary amides under hydrosilylation conditions: dehydration to nitrile, hydrosilylation of amide to amine, hydrosilylation of nitrile to amine. | 269 |
| Scheme 6.2.8. Proposed synthesis of Mn complexes supported by PSiP pincer ligation. These routes are based on the synthesis of 2-PMe ₃ and 2-py for which the base used was BnMgCl, though other bases may be appropriate for the above reactions. | 270 |

Abstract

The study of PSiP pincer complexes of second- and third-row transition metals has led to the discovery of challenging bond activation chemistry as well as catalytic chemistry. While there now exists a considerable amount of literature regarding the behavior of PSiP complexes of the second- and third-row metals, comparatively little is known of the behavior of these ligands with the first-row metals. There has been a recent push toward the study of first-row transition metal chemistry in general, due to their high natural abundance and often lower toxicity when compared to their second- and third-row congeners. This document details progress toward the synthesis of a variety of novel Fe, Co and Ni complexes featuring PSiP ligation and application toward catalytic reduction of unsaturated substrates.

In terms of (PSiP)Fe chemistry, considerable progress has been made toward the synthesis of novel coordination complexes, in particular the synthesis of hydride complexes of Fe. Organometallic hydride complexes are often implicated as important catalytic intermediates, and in this case a bis(dinitrogen) adduct of an Fe hydride has been identified as a highly active catalyst for the hydrogenation of olefins. Co chemistry with the same ligand has unveiled intriguing examples of both H₂ and O₂ bond cleavage chemistry, and again has led to an example of an alkene hydrogenation catalyst.

A novel PSiP framework has been developed and applied toward chemistry of the group 10 transition metals, particularly nickel. In this regard, chemistry of complexes supported by this new ligand was found to be markedly different than that of similar complexes supported by the previous iteration of the ligand. In particular, a Ni hydride complex was successfully prepared and applied toward the selective reduction of CO₂ to the formaldehyde level *via* hydroboration.

Lastly, outside the realm of PSiP chemistry, a new monoanionic P,N-based ligand has been developed and its chemistry has been explored with respect to Fe and Co. Interesting coordination chemistry has been observed with this new ligand, and examples of reactive Fe and Co complexes have been obtained and applied toward the challenging reduction of tertiary amides to amines *via* catalytic hydrosilylation.

List of Abbreviations and Symbols Used

\AA = Angstrom

$^{\circ}$ = degree

δ = chemical shift

η = hapticity (contiguous donor atoms)

κ = hapticity (non-contiguous donor atoms)

λ = wavelength

μ_B = Bohr magneton

μ_{eff} = effective magnetic moment

9-BBN = 9-borabicyclo[3.3.1]nonane

Anal. Calcd. = analysis calculated

br = broad

cm^{-1} = wavenumber

COD = 1,5-cyclooctadiene

COSY = correlation spectroscopy

Cy = cyclohexyl

d = doublet

DBU = 1,8-diazabicycloundec-7-ene

DEPT = distortionless enhancement by polarization transfer

DiPP = 2,6-diisopropylphenyl

DFT = density functional theory

DMAP = 4-(*N,N*-dimethylamino)pyridine

dme = 1,2-dimethoxyethane

DPPF = 1,1'-diphenylphosphinoferrocene

DⁱPPF = 1,1'-diisopropylphosphinoferrocene

dt = doublet of triplets

ENDOR = electron nuclear double resonance

h = hour

HBCat = catecholborane

HBPIn = pinacolborane

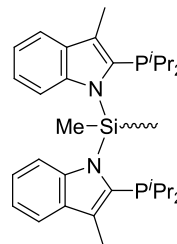
HECADE = heteronuclear couplings from ASSCI-domain experiments with E.COSY-type cross peaks)

HMBC = heteronuclear multiple bond correlation

HMQC = heteronuclear multiple quantum correlation

HSQC = heteronuclear single quantum correlation

Hz = Hertz



(ⁱPr-PSiP^{Ind}) =

m = multiplet

Mes = mesityl (2,4,6-trimethylphenyl)

min = minute

$^n J_{\text{XX}'}$ = *n* bond coupling constant between atom X and atom X'

K = Kelvin

kcal = kilocalorie

kJ = kilojoule

L = neutral donor

ORTEP = Oak Ridge thermal ellipsoid plot

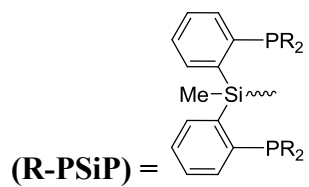
OTf = triflate (trifluoromethylsulfonate)

NHC = *N*-heterocyclic carbene

NOESY = nuclear Overhauser effect spectroscopy

ppm = parts per million

py = pyridine



SISHA = secondary interaction between a silicon and hydrogen atom

t = triplet

THF = tetrahydrofuran

TOCSY = total correlation spectroscopy

TOF = turnover frequency

TON = turnover number

wt% = weight percent

X = anionic donor

Acknowledgements

First I would like to thank my supervisor, Dr. Laura Turculet, for all her helpful advice, instruction and humour during the course of my studies, without which none of this work would be possible. Secondly I would also like to thank the other members of the Turculet group, past and present, for all their help and for maintaining a friendly and upbeat atmosphere in the lab. In addition I would like to specifically thank Adam Ruddy, Helia Hollenhorst and Dylan Hale for their contributions to Chapters 3, 4 and 5 of this document, respectively.

I would also like to thank the members of my supervisory committee, Drs. Jean Burnell, Alex Speed, Mark Stradiotto and Alison Thompson, for helpful discussions throughout my time at Dalhousie, as well as my external examiner Dr. Warren Piers for taking the time to evaluate my work.

Finally the Drs. Robert McDonald and Michael Ferguson of the University of Alberta must be acknowledged for all their hard work concerning X-ray data collection and solution refinement for the structures contained herein. Dr. Mike Lumsden of NMR-3 has also been an invaluable resource for questions concerning NMR data acquisition/interpretation.

Chapter 1: Introduction

1.1 Overview

The development of new transition metal complexes to facilitate challenging chemical transformations in an effective manner has become a fundamental aspect of organometallic chemistry.¹ The significance of this field is well-illustrated by the awarding of the 2001,² 2005³ and 2010⁴ Nobel Prizes in Chemistry for organometallic applications in asymmetric catalysis, olefin metathesis and Pd-catalyzed cross-coupling, respectively. Today, tremendous effort is still being focused on the discovery of novel organometallic catalytic transformations, motivated by such previous successes. At the heart of these efforts is the synthesis of new transition metal complexes and the study of their reactivity with a variety of substrate molecules.

Essential to the development of effective transition metal complexes for catalytic applications is not only the proper choice of transition metal, but also the selection of the coordination environment around the metal, *i.e.* the ancillary ligand(s). Ligand design has become an extensive field of chemistry in its own right, as it has been well-documented that the synergy between the ligand and metal in a given complex is vital to the function of any catalytic process. In the context of ligand design, the synthesis and exploration of ligands capable of binding in a multidentate fashion has drawn much focus. For example, tridentate ‘pincer’ ligand systems have the advantage of being highly tunable in terms of the donor atoms anchoring the ligand to the metal center, as well as the scaffolding connecting the various donor groups (Figure 1.1.1). The versatility made possible by using pincer ligands is not limited to tuning of electronic properties, but also extends to the steric features of the ligand-metal complex, which can be controlled by the choice of

substituents on the donor atoms. Such pincer ligands generally coordinate to the metal in a meridional fashion, such that the flanking donor groups are *trans*-disposed. However, flexibility in the ligand backbone can affect the coordination geometry, such that *cis*-disposed pincer donors are preferred.

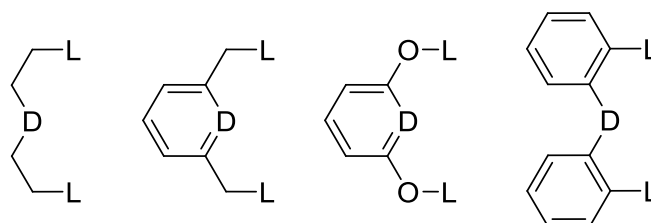


Figure 1.1.1. Common pincer ligand motifs encountered. D = central donor, most commonly nitrogen (neutral/anionic), carbon (anionic) or silicon (anionic). L = Neutral donor, most commonly an amine, imine, phosphine or carbene.

Considerable study has also gone into the development of *bidentate* ligands, which, as with the tridentate analogues, can be designed with a variety of combinations of neutral or anionic donor atoms anchored to some type of scaffold, which in turn may also be tuned with respect to steric and electronic features. Examples of neutral, monoanionic, and dianionic bidentate ligands have been employed for a variety of applications ranging from transition metal catalysis to stabilization of reactive species (Figure 1.1.2).

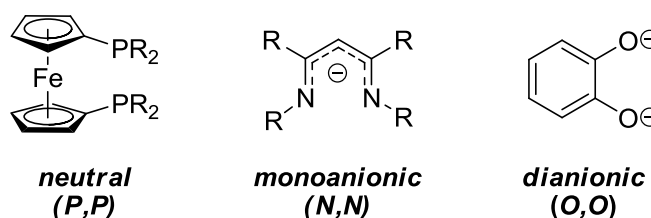


Figure 1.1.2. Examples of commonly encountered bidentate ligand scaffolds. Neutral bis(phosphino)ferrocenes (left), monoanionic 1,3-diketimidides or “NacNac” (center), dianionic catecholate (right).

Building on previous efforts in the Turculet group using silyl-based pincer transition metal complexes for the purposes of exploring bond activation chemistry and catalysis, the research described in Chapters 2, 3 and 4 of this document outlines efforts

to expand the chemistry of this versatile class of ligands to the first-row metals of groups 8, 9 and 10: iron, cobalt and nickel. Significant progress has been made in the investigation of (PSiP)Fe coordination chemistry and reactivity. A detailed study on the preparation of a variety of (PSiP)Fe hydride complexes has been carried out, and the application of such species in olefin hydrogenation catalysis has been outlined. In the course of these studies, a highly active Fe-based alkene hydrogenation catalyst was discovered. A study on the reactivity of (PSiP)Co complexes initially prepared by a former student, Adam Ruddy, has revealed interesting chemistry relating to the activation of H₂ and O₂, and a Co^I complex has also been shown to be a precatalyst for the hydrogenation of terminal olefins.

A third project details the use of a new bis(phosphinoindolyl) PSiP ligand (Figure 1.1.3B), initially developed by a fellow group member, Helia Hollenhorst, in group 10 transition metal chemistry. It was found that the new ligand allowed access to reactivity not observed in the parent PSiP system. Specifically, a highly active Ni-based catalyst was developed for the reduction of carbon dioxide, offering unprecedented selectivity toward reduction of CO₂ to a formaldehyde derivative.

Finally, a fourth project moves from tridentate PSiP ligands to the use of monoanionic, bidentate, P,N-based ligands in conjunction with iron and cobalt. In this regard a new monoanionic P,N ligand derivative (Figure 1.1.3C) has been synthesized and a variety of iron and cobalt complexes have been prepared in efforts to survey the coordination chemistry of metal complexes of this ligand class. In collaboration with a fellow group member, Dylan Hale, several Fe and Co complexes of this ligand have been

applied toward the challenging catalytic reduction of tertiary amides to amines using hydrosilanes as the reductant.

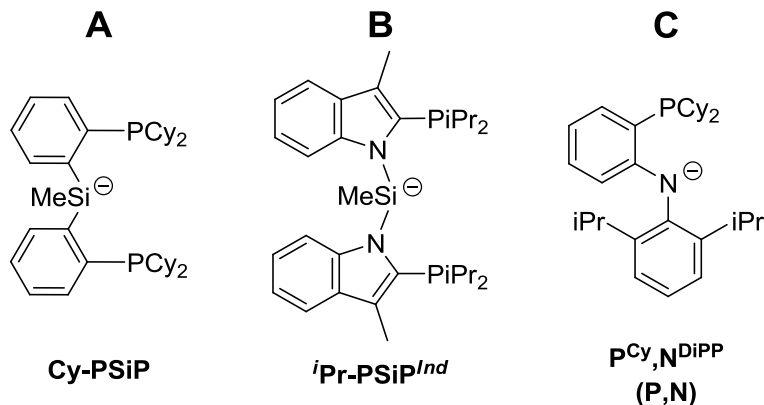


Figure 1.1.3. Ligands employed in this work. Chemistry of Cy-PSiP (A) with Fe and Co described in Chapters 2 and 3, respectively. Chemistry of $i\text{Pr-PSiP}^{\text{Ind}}$ (B) with Ni described in Chapter 4. Chemistry of $\text{PCy,N}^{\text{DiPP}}$ (C) with Fe and Co described in Chapter 5.

1.2 First-Row Transition Metal Catalysis

Some of the most effective transition metal-catalyzed transformations have been realized through the use of the so-called platinum-group metals, which include Ru, Rh, Ir, Pd and Pt. Common to all these metals, however, is a low natural abundance and prohibitively high cost. Many of these ‘noble’ metal complexes are also known to be quite toxic, thus the risk of catalyst-leaching in any pharmaceutical application, for example, becomes a serious concern.⁵ The high activity of noble metal-based catalysts is indeed their biggest asset, and thus far supersedes issues of cost and potential toxicity in many cases. However, the scarcity of these metals in nature is an issue that must eventually be addressed, and as a result the study of organometallic catalysts based on far more abundant, and often less toxic, first-row transition metals has been the subject of increasingly intense research for decades.⁶ The lower observed activity of many first-row transition metal complexes in catalytic applications is a serious limitation if they are to be

used in a large-scale application, an issue compounded by the often undesirable one-electron chemistry common to first-row metals. Notwithstanding these issues, transition metals found in the active sites of enzymes are almost exclusively from the first-row, underpinning their utility and importance in even the most fundamental biological reactions.⁷

The use of iron in catalytic applications is particularly attractive due in part to its 4.7 wt% abundance in the Earth's crust, the high accessibility of Fe salts and complexes, as well as the relatively low toxicity of many Fe compounds.⁸ In fact, simple salts of Fe^{II} and Fe^{III} have long been shown to participate in the catalysis of myriad classical organic transformations including substitutions, additions, eliminations, isomerizations, oxidations and reductions.⁶ Examples of noteworthy achievements in organometallic iron-based homogeneous catalysis are the CO₂ hydrogenation/formic acid dehydrogenation systems described by Ludwing, Laurenczy and Beller,⁹ with activities comparable to, or surpassing, state-of-the art precious metal catalysts in the dehydrogenation of formic acid. Cobalt is also an attractive candidate for catalysis for many of the same reasons as iron and cobalt complexes have found application in a number of impressive hydrogenation reactions, including the asymmetric hydrogenation of functionalized and unfunctionalized alkenes using chiral bis(phosphino)cobalt(II) complexes in high enantiomeric excess.¹⁰ There has also been considerable progress in the development of Ni-based organometallic catalysis, especially in terms of cross-coupling reactions. As a group 10 metal, like palladium or platinum, there are many examples of nickel undergoing the individual reaction steps attributed to most classical two-electron catalytic process (*e.g.* oxidative addition, transmetalation, reductive

elimination).¹¹ Though, as a wider range of oxidation states are more readily available to nickel than they are to palladium or platinum, mechanistic pathways can also be complicated and can lead to unexpected reactivity, as has been observed for iron and cobalt.¹¹

The exceptional reactivity organometallic catalysts based on iron, cobalt or nickel is largely owed to the choice of ancillary ligand selected to support the metal center. As outlined earlier, modular tridentate pincer ligands are powerful tools to fine-tune sterics and electronics, and, as a result, many of the most impressive catalytic transformations involving base metal complexes have been achieved in conjunction with some form of pincer ligand scaffold.

In this regard, in section 1.3 of this introductory chapter, a summary of ligand design strategies that have been utilized for the development of first-row metal catalysts will be described. Section 1.4 of this chapter highlights exceptional examples of transformations catalyzed by *first-row* transition metal complexes supported by tridentate pincer ligation, with a particular focus on the reduction of unsaturated substrates such as esters, aldehydes, ketones, nitriles, olefins and carbon dioxide. In section 1.5, a summary of the literature regarding the specific class of PSiP pincer complexes of Fe, Co and Ni will be provided. Finally, in section 1.6, a survey of noteworthy achievements stemming from the use of first-row metal complexes of monoanionic bidentate P,N-based ligands will be discussed.

1.3 Ligand Design for First-Row Transition Metals

As alluded to earlier, the tendency for first-row transition metals to readily participate in one-electron redox events can often lead to unexpected or undesirable

reactivity. The added complication of one-electron chemistry that comes with the first-row metals has led to the exploration of ligand design strategies specifically for this subset of the transition metals. Ligands that have found utility supporting the second- and third-row transition metals may also be adopted for the first-row metals in some cases, but may not be the optimum choice for promoting the desired transformation.

Second- and third-row transition metals are often better behaved with respect to the one-electron redox events that often plague the first-row metals, and instead tend to favor the fundamental two-electron steps traditionally invoked in most mechanisms for transition metal catalyzed transformations (*e.g.* oxidative additions and reductive eliminations). However, many of the ligands employed in conjunction with the second- and third-row metals for a particular application often act as ‘spectator’ ligands. These ligands, while obviously crucial to the reactivity of the overall catalyst system, generally only affect the resulting chemistry by influencing sterics or inductively influencing the electronics of the complex, the ligands themselves do not often become directly involved in the ensuing chemistry.

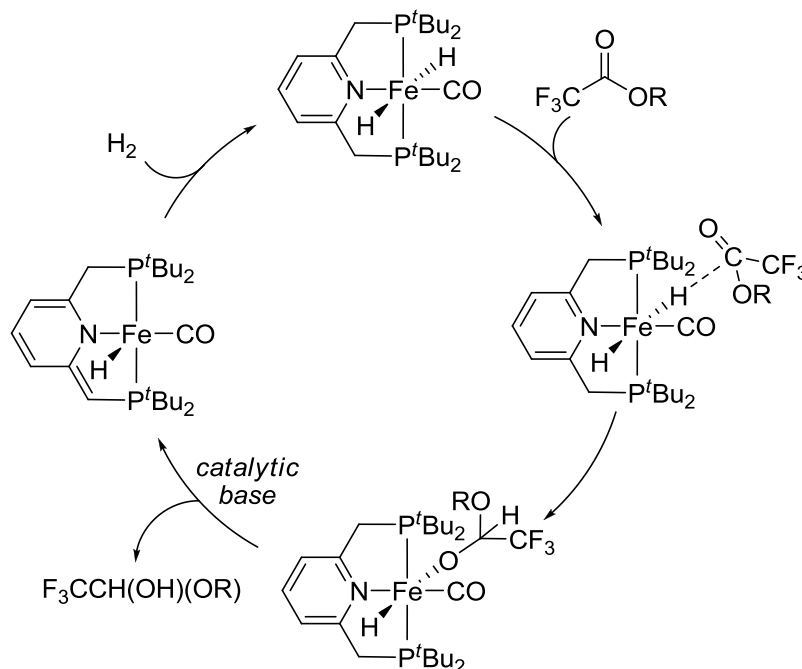
Ligands that do become directly involved in the chemistry occurring at the metal center are often termed ‘non-innocent’. There have been successes taking advantage of this phenomenon, with significant breakthroughs in this field using non-innocent ligands in conjunction with first-, second- and third-row transition metals. Examples of catalysis wherein the ligand acts in a cooperative nature with the metal center (termed metal-ligand cooperativity) have provided some of the most impressive results to date. Nature takes advantage of metal-ligand cooperativity in metalloenzymes, in which the metal-containing active sites are supported by a variety of, often amino acid-based,

functionalities which become directly involved in redox chemistry, proton transfers, and ligand associations and dissociations, vital to affect the particular enzymatic process.¹² Strategies involving metal-ligand cooperativity have also been proposed as a means to take advantage of the one-electron chemistry often exhibited by the first-row metals and achieve activities on par with second- and third-row metal catalysts.¹³

Metal-ligand cooperativity can be exhibited in a variety of manners, and the ligands which demonstrate this type of behavior can vary quite widely in their structure. One commonly encountered form of metal-ligand cooperativity comes from the use of redox-active ligands. As the name implies, redox-active ligands are capable of undergoing reduction or oxidation processes, often in place of the metal where such reactivity would typically be observed, particularly in the case of the first-row metals. In principle, in the presence of a redox-active ligand first-row metals can more easily support the classical two-electron processes exhibited by the more active noble metals. In a bond cleavage process this is achieved by the ligand supplying one or both of the electrons required to cleave the bond of the substrate molecule. In the former case, the second electron required would be supplied by the metal, accommodating a more favorable (for a first-row metal) one-electron oxidation, while in the latter case there would be no oxidation state change in the metal whatsoever. Commonly encountered examples of redox-active ligands are the bis(imino)pyridine ligands popularized by the Chirik group^{13a} (see section 1.4 for a discussion of Fe and Co hydrogenation catalysts using these ligands).

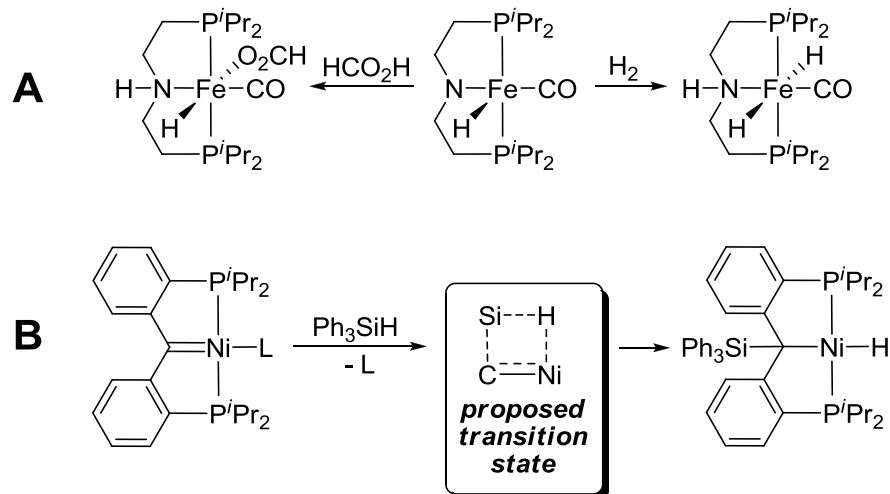
Proton transfer between a ligand bound in a transition metal complex and a substrate molecule is another commonly-encountered form of metal-ligand cooperation.

There are a broad number of complexes which can exhibit such reactivity with a variety of driving forces governing the reaction. For example, Milstein and co-workers¹⁴ have described PNP pincer-supported systems wherein rearomatization of a previously dearomatized ligand can encourage the transfer of a proton to the ligand *via* cleavage of a substrate E-H bond (the E portion of the molecule is typically added to the metal center). This type of metal-ligand cooperation has indeed been taken advantage of in base-metal catalysis, one example of which is the Fe-catalyzed hydrogenation of trifluoroacetate esters by bis(phosphino)pyridine-based pincer complexes (Scheme 1.3.1). In this example, the presence of catalytic base in solution results in deprotonation of a methylene linker present in the backbone of the PNP ligand, leading to an overall loss of aromaticity. Subsequent cleavage of H₂ restores this aromaticity through transfer of H⁺ to the previously deprotonated site, and H⁻ to the metal center.



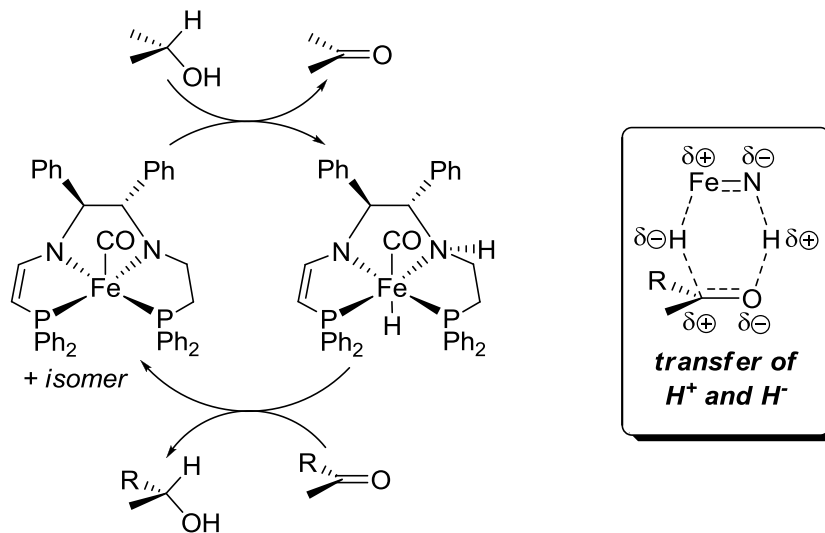
Scheme 1.3.1. Mechanism for the hydrogenation of esters catalyzed by a (PNP)Fe-based catalyst featuring metal-ligand cooperativity in the form of ligand dearomatization/rearomatization.

The driving force of restoration of aromaticity is not a prerequisite for this form of metal-ligand cooperativity. A sufficiently basic site in a ligand can serve as the proton acceptor in the cleavage of an E-H containing substrate, with the generated anion (E^-) typically coordinating to the metal center as with the above example. Bernskoetter and Hazari¹⁵ have demonstrated such a phenomenon with PNP-pincer complexes of iron (Scheme 1.3.2A). In one study, proton transfer from H_2 to the central amido ligand occurs with concomitant transfer of the generated hydride to the Fe center.^{15a} The same complex can also cleave the O-H bond of formic acid in an analogous fashion.^{15b} While these ligand-assisted processes were not proposed to be at play in the subsequent CO_2 hydrogenation/formic acid dehydrogenation catalysis outlined in the studies, they do serve as valuable examples of ligand-assisted bond cleavage by a first-row metal, with no change in the formal oxidation state of that metal. In another example, Piers and co-workers¹⁶ have demonstrated a ligand-assisted Si-H bond cleavage (Scheme 1.3.2B). Treatment of a (PCP)Ni complex with phenylsilane resulted in addition of the silane across the Ni carbene bond *via* a 4-centered transition state, consistent with metal-ligand cooperativity rather than an oxidative addition pathway. Once again, there is no change in the formal oxidation state of Ni from this reaction.



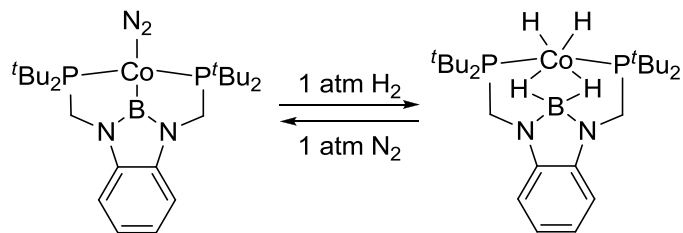
Scheme 1.3.2. (A) Cleavage of formic acid and dihydrogen by a PNP complex of iron. (B) Si-H bond cleavage of phenylsilane by a PCP complex of nickel. Note that the formal oxidation state of Fe and Ni in these examples has not changed during the bond-cleavage processes.

Metal-ligand cooperation involving such proton transfers has proven particularly fruitful in the context of transfer hydrogenation. One very notable example is the Fe-catalyzed asymmetric ketone transfer hydrogenation system described by Morris and co-workers.¹⁷ As with the above examples, a basic nitrogen atom in the ligand backbone is crucial to the observed activity. Isopropanol, serving as the source of ‘H₂’ undergoes O-H and C-H bond cleavage. The acidic O-H proton is transferred to the proximal amido nitrogen atom of the ligand, while the methine hydrogen is transferred to the Fe center (as a hydride), releasing an equivalent of acetone. The resulting metal complex then transfers this proton and hydride to a substrate ketone in a similar manner, furnishing the desired chiral alcohol and completing the catalytic cycle.



Scheme 1.3.3. Fe-catalyzed asymmetric transfer hydrogenation of ketones as reported by Morris and co-workers, note that the formal oxidation state of Fe remains +2 throughout the reaction.

Certain non-innocent ligands are also capable of facilitating transfer of hydrogen atoms from substrates as hydrides, rather than as protons as the previous examples highlighted. Often the ligand in question requires an electropositive atom (relative to hydrogen) to induce such a transfer. Peters and co-workers¹⁸ have demonstrated, for example, cleavage of H₂ by PBP pincer complexes of cobalt, as well as nickel. In one example,^{18a} treatment of a bis(phosphino)boryl cobalt complex with H₂ led to displacement of a coordinated N₂ ligand and addition of two equivs H₂ across the Co-B bond resulting in the generation of a dihydridoborato cobalt dihydride complex, a process which could be reversed by addition of N₂ (Scheme 1.3.4). In addition, this system was active for the hydrogenation of terminal olefins, the catalytic dehydrogenation of ammonia-boranes, and the transfer hydrogenation of terminal olefins with ammonia-boranes, results the authors attributed largely to the metal-ligand cooperation demonstrated by the Co-boryl complex.



Scheme 1.3.4. Reversible reaction of a (PBP)Co complex with H₂, leading to addition of two equiv H₂ across the Co-B bond. The dinitrogen adduct (left) was found to be an active precatalyst for hydrogenation of terminal olefins, the catalytic dehydrogenation of ammonia-boranes and the transfer hydrogenation of terminal olefins with ammonia-boranes.

Another electropositive atom (relative to hydrogen) often exploited in ligand design is silicon. Tridentate bis(phosphino)silyl pincer ligands were initially introduced in the late 1990s by Stobart and co-workers¹⁹ in a study mainly focused on the preparation of complexes featuring more rigid analogues of the already established bidentate “PSi”-type ligands (*i.e.* through replacement of an alkylene backbone with a more rigid 3-carbon benzyl backbone). It was noted that some bidentate PSi complexes could not offer the steric restraints required for meaningful selectivity toward bond reorganization in catalytic applications while conversely tetradentate P₃Si complexes were often too sterically restrictive, leading to shutdown in catalytic activity altogether. Therefore, it was hypothesized that *tridentate* PSiP ligands may offer an interesting balance between the two extremes. Structures of ligand precursors to each variety are depicted in Figure 1.3.1.²⁰

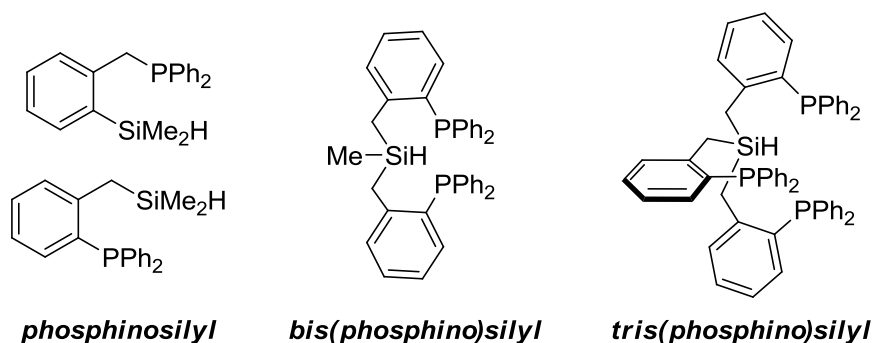


Figure 1.3.1. Structures of mono, bis and tris(phosphino)silyl pincer ligand precursors prepared by Stobart and co-workers.¹⁹⁻²⁰

Subsequently, in 2007 Peters and co-workers²¹ introduced a variant of tetradentate tris(phosphino)silyl ligands by removal the methylene linker present in those described by Stobart. Stobart's ligand systems incorporated aliphatic and benzylic ligand backbones, which were proposed to offer greater conformational flexibility but can also be envisaged to undergo unwanted β -hydride elimination processes involving the ligand backbone itself. Peters' P₃Si ligands have proven particularly robust, and have been studied extensively in a variety of contexts, including investigations into stoichiometric and catalytic reduction of N₂ by Fe complexes of such tris(phosphino)silyl ligands.²¹⁻²²

While the earliest examples of *tridentate* PSiP-pincer ligands were outlined by Stobart and co-workers,¹⁹⁻²⁰ very little development of these ligand systems ensued until the mid-2000s when Turculet and co-workers²³ incorporated *o*-phenylene linkers in place of the aliphatic and benzylic backbones, thus further rigidifying the ligand and eliminating β -hydrogens in the backbone altogether as with Peters' tetradentate analogues. As with Peters' PBP pincers described earlier, metal-ligand cooperativity may be envisaged for PSiP complexes in a somewhat similar manner, wherein transfer of hydrides from substrate molecules may result in a new M-H bond, a new Si-H bond, or in some cases a combination of the two (*e.g.* η^2 -(SiH) interactions). While unusual bonding

scenarios²³⁻²⁴ and M→Si/Si→M ligand migrations²⁵ involving PSiP complexes of the second- and third-row transition metals have been previously reported, their number are few, and even fewer examples with the first-row metals have been reported (see section 1.5 for a general discussion of the chemistry of PSiP complexes of the first-row metals). Furthermore, little effort has been made investigating whether these unusual binding scenarios and M→Si/Si→M ligand migrations can be taken advantage of in the context of a productive catalytic application, for example. Thus, the potential for PSiP ligands to act as non-innocent ligands and participate in metal-ligand cooperativity remains an unexplored avenue, especially with the first-row metals for which such behavior may be most desirable.

1.4 Pincer Complexes of First-Row Transition Metals

Despite the fact that first-row transition metal complexes can be far less catalytically active than their second- and third-row congeners, challenging and useful transformations have been achieved with such complexes, with or without the invocation of metal-ligand cooperativity. In the realm of pincer chemistry, complexes of iron, cobalt and nickel have been subject to intense investigation. Promising results have been obtained for these metals utilizing a variety of pincer ligand scaffolds. Thus far, the most commonly utilized pincer motifs for iron, cobalt and nickel chemistry are PNP- and PCP-based which include a variety of alterations to the backbone (*e.g.* POCOP-, PONOP-pincers) and substituents on the flanking atoms (*e.g.* isopropyl, phenyl). PNN- and CNC-based pincer complexes also feature prominently throughout this section. Highlights of a variety of *catalytic* reactions involving Fe-, Co- and Ni- pincer complexes will be outlined herein including the most prevalent examples of alkene hydrogenation catalysis

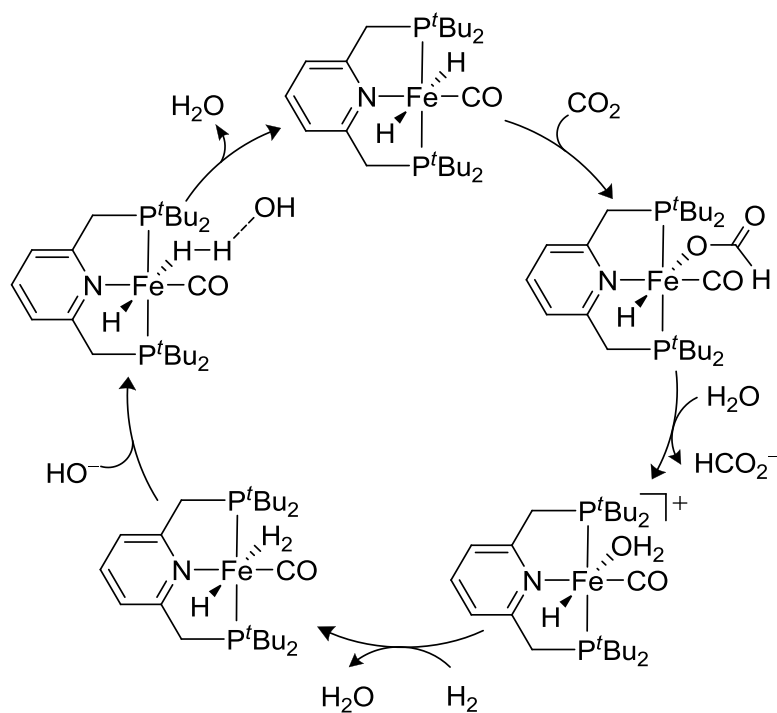
(prominent in Chapters 2 and 3 of this document), and catalytic CO₂ reduction (the focus of Chapter 4 of this document).

1.4.1 Iron

The application of Fe-pincer complexes in catalysis has focused largely on the reduction of unsaturated substrates. A variety of Fe-based pincer complexes have found application in, for example: the hydrogenation of carbon dioxide,^{15a, 26} alkynes,²⁷ ketones,²⁸ aldehydes,^{28c, 29} esters,^{14, 30} and nitriles;³¹ the hydrosilylation of alkenes³², ketones and aldehydes;³³ as well as the hydroboration of alkenes.³⁴ Furthermore, dehydrogenation using Fe-pincer complexes has been achieved for formic acid,^{15b, 35} methanol³⁶ and ammonia-borane.³⁷

Milstein and co-workers have utilized the bis(phosphino)pyridine ligand scaffold to great success for the catalytic hydrogenation of carbonyl-containing substrates. For example, a report from 2011 represents the first, and thus far one of only a handful of examples of Fe-catalyzed CO₂ hydrogenation.^{26b} At the time of publication, *trans*-[(^tBu-PNP)Fe(H)₂(CO)] (Scheme 1.4.1.), was found to be the most active Fe-based CO₂ hydrogenation catalyst, with a turnover number and turnover frequency of 788 and 156 h⁻¹ (39.4% yield of formate), respectively. Furthermore, these results were obtained in aqueous solution under relatively mild hydrogenation conditions (6-10 bar H₂, 80 °C). The authors invoked the possibility of a ligand-assisted step during hydrogenation, a hypothesis based on the known ligand ‘non-innocence’ of some pyridine-derived PNP ligands. In this context, the pyridine-based PNP backbone is dearomatized *via* deprotonation by hydroxide, and subsequently rearomatized through a proton migration from a dihydrogen ligand to regenerate the dihydride complex. DFT calculations later

provided by Yang and co-workers,³⁸ however, found that direct deprotonation of bound dihydrogen by hydroxide, is about 20 kcal mol⁻¹ more favorable than the ligand-assisted pathway (Scheme 1.4.1).

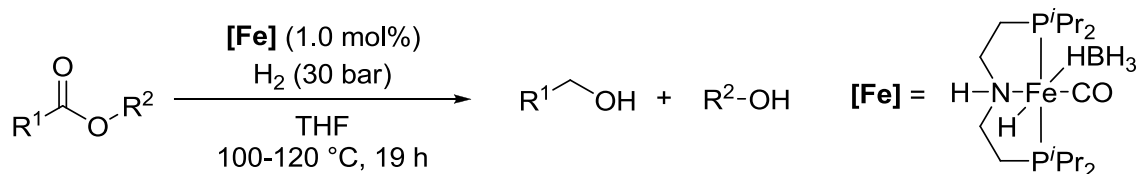


Scheme 1.4.1. Catalytic pathway for CO₂ hydrogenation by *trans*-[(^tBu-PNP)Fe(H)₂(CO)].^{26b, 38}

Using the same catalyst as that used for the CO₂ hydrogenation chemistry described above, Milstein reported on the base-assisted hydrogenation of esters to alcohols (described briefly in section 1.3).¹⁴ Prior to their work, no Fe-based catalyst for the direct hydrogenation of esters had been reported, though other less atom economical methods to achieve the same end with Fe catalysts were known (such as hydrosilylation followed by acidic or basic workup). Though their substrate scope was limited to trifluoroacetates, they were able to achieve yields in excess of 99% in many cases, with catalyst loadings of 1 mol% at a relatively low temperature (40 °C), though 25 bar H₂ was required. Based on reported yields, their catalyst system was most tolerant toward unsaturated or

fluorinated groups as the alkoxy portion of the ester, though it also performed well for the hydrogenation of aliphatic esters. Additionally, the reduction was selective for the ester functionality, while aromatic and olefinic portions of the substrate molecules remained intact.

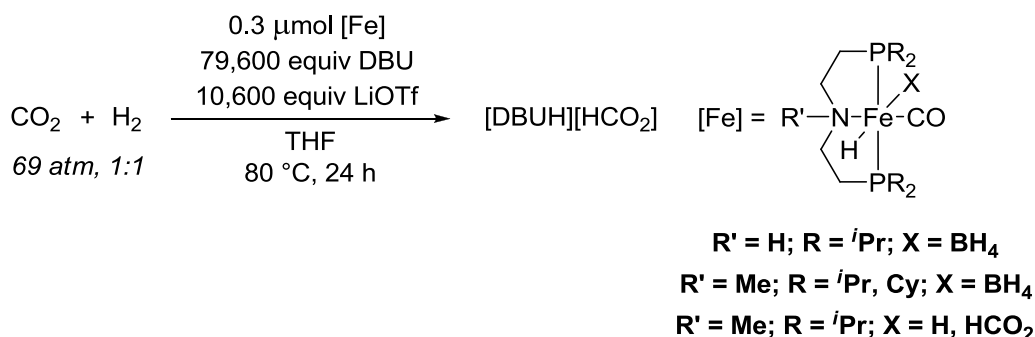
Shortly thereafter, Beller and co-workers^{30a} also reported a (PNP)Fe-based catalyst for ester hydrogenation, this time under base-free conditions (Scheme 1.4.2). While the reaction conditions for their system were harsher (typically 100-120 °C reaction temperatures and 30-50 bar H₂), the reported substrate scope was much more extensive, and not limited to trifluoroacetate esters. Alkyl, aromatic, and cyclic esters were all well-tolerated, and the retention of various functional groups (olefins, nitriles, halogens and heteroaromatics) throughout the hydrogenation process indicated good chemoselectivity as well.



Scheme 1.4.2. Hydrogenation of esters to alcohols by (*i*Pr-PNP)Fe(H)(HBH₃)(CO). R¹ and R² = various alkyl and aryl substituents.^{30a}

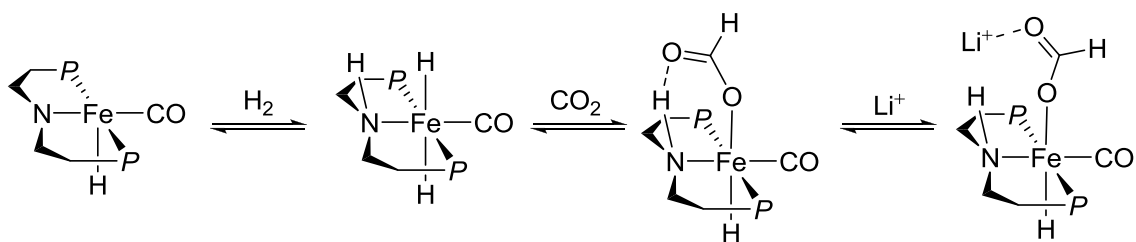
An improved system for the (PNP)Fe-catalyzed hydrogenation of CO₂ to formate (described briefly in section 1.3) was reported by Hazari and Bernskoetter^{15a} who reported turnover numbers of *ca.* 60,000 for the reaction. Like Milstein's system described earlier, excess base (in this case, 1,8-diazabicycloundec-7-ene, DBU) was necessary, and the highest turnover numbers were only obtained when using a vast excess of base (80,000 equivs), and excess Lewis acid additive (*e.g.* LiOTf). A higher pressure

was also required to achieve this result (69 atm of a 1:1 mixture of CO₂ : H₂) (Scheme 1.4.3).



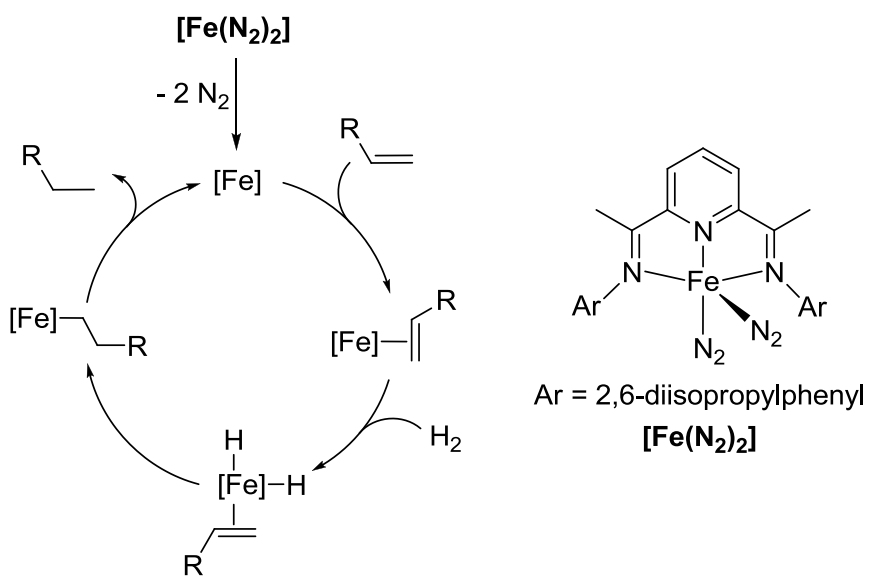
Scheme 1.4.3. Base and Lewis acid assisted (PNP)Fe catalyzed hydrogenation of CO₂ to formate.^{15a}

Like Milstein's system, the authors propose metal-ligand cooperation for the N-*H* version of their catalyst (R' = H in Scheme 1.4.3). The ability to interconvert between amido and amino variants of the PNP ligand was proposed to be vital to the high catalytic activity. The catalyst is also able to facilitate the reverse reaction, formic acid *dehydrogenation*, as formic acid can protonate the basic PNP amido, while the generated formate anion coordinates to the Fe center. A potential stabilizing hydrogen bonding interaction between the N-bound proton, and the carbonyl moiety of the bound formate was also invoked (Scheme 1.4.4).^{15b} Though this stabilizing interaction might actually serve to *hinder* the reverse reaction, CO₂ hydrogenation, evidence was provided that the H-bonding interaction could be disrupted by the presence of Li⁺ (Scheme 1.4.4).



Scheme 1.4.4. H₂ addition to (PNP)Fe(CO)H followed by CO₂ insertion and subsequent disruption of the generated H-bonding interaction by Li⁺. P = *i*Pr₂P.^{15a}

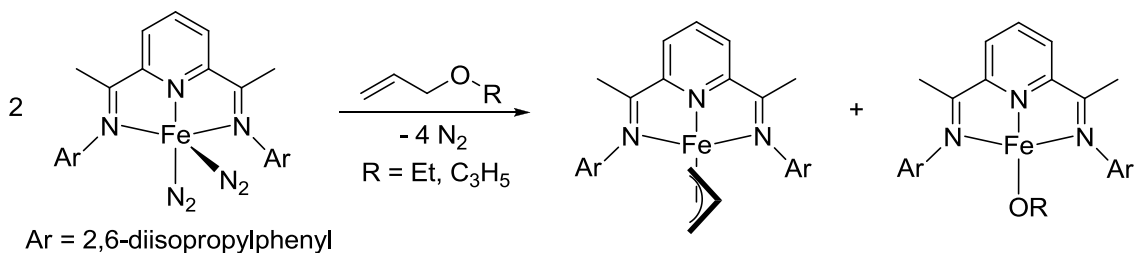
In 2004, Chirik and co-workers³⁹ developed an Fe-based olefin hydrogenation catalyst, (*iPr*PDI)Fe(N₂)₂, supported by a bis(imino)pyridinyl (NNN) scaffold (Scheme 1.4.5). The development of this catalyst marked an important step forward in the field of Fe-catalyzed olefin hydrogenation, as previously the only examples of such a transformation involved the use of Fe(CO)₅ as a catalyst at very high temperatures and pressures, or under photocatalytic conditions.⁴⁰ Around the same time Peters and co-workers⁴¹ reported olefin hydrogenation catalyzed by a tris(phosphino)borato-supported Fe complex under mild conditions (1-4 atm H₂, 23-50°C), albeit at higher (10 mol%) catalyst loadings.



Scheme 1.4.5. Proposed mechanism for the hydrogenation of olefins catalyzed by (*iPr*PDI)Fe(N₂)₂.

In Chirik's initial Fe system,³⁹ (*iPr*PDI)Fe(N₂)₂ was identified as a target due to its potential as a precursor to the 14-electron Fe(0) analogue (*iPr*PDI)Fe⁰. (*iPr*PDI)Fe(N₂)₂ represented the first Fe(0) bis(dinitrogen) complex reported at the time of publication, and was found to be active toward the catalytic hydrogenation of a variety of terminal, internal and *gem*-disubstituted olefins under very mild conditions and at low catalyst

loadings. However, trisubstituted olefins could not be hydrogenated under these conditions. In a subsequent report⁴² functional group tolerance in the catalytic system was investigated, with examples of amino, ether, ketone and ester functionalized alkenes undergoing hydrogenation of only the alkene moiety, under varying conditions (some requiring elevated temperatures or a higher catalyst loading). However, the authors also identified C-O bond cleavage of ethers and esters by the catalyst as a problematic side-reaction resulting in catalyst deactivation if substrate and catalyst were not kept frozen at liquid N₂ temperature until H₂ addition.⁴³ For example, treatment of (*i*^{Pr}PDI)Fe(N₂)₂ with diallyl ether led to the generation of both the corresponding allyl and allyloxy Fe^I complexes in a relative ratio of 1:1. While treatment with allyl ethyl ether gave the Fe^I-ethoxy and Fe^I-allyl complexes, again in about a 1:1 relative ratio (Scheme 1.4.6).



Scheme 1.4.6. Reactivity of (*i*^{Pr}PDI)Fe(N₂)₂ toward diallyl ether and allyl ethyl ether leading to catalyst decomposition products.

Investigations into ligand modifications of the existing scaffold led to replacing the flanking 2,6-diisopropylphenyl moieties with 2,6-dimethylphenyl groups, which increased the overall catalytic activity of the system. Conversely, exchanging the backbone methyl groups for phenyl substituents led to complexes more susceptible to THF or carbonyl coordination, resulting in overall diminished catalytic activity.⁴⁴ Finally, by moving away from the bis(imino)pyridine scaffold entirely, to a bis(NHC)pyridyl ligand (NHC = *N*-heterocyclic carbene), as depicted in Figure 1.4.1, the

Fe-catalyzed alkene hydrogenation could be expanded to a small scope of *trisubstituted* alkenes and one *tetrasubstituted* alkene (2,3-dimethyl-1*H*-indene).³² (^{Mes}CNC)Fe(N₂)₂, specifically was found to be more active than (^{*i*Pr}CNC)Fe(N₂)₂ and (^{Me}CNC)Fe(N₂)₂ for hydrogenation of tri- and tetrasubstituted alkenes at a 5 mol% catalyst loading (4 atm H₂, 23 °C, Figure 1.4.1), though (^{*i*Pr}CNC)Fe(N₂)₂ was the most active for an ester-functionalized trisubstituted alkene, which suggests possible catalyst deactivation *via* C-O bond cleavage or carbonyl coordination for the other catalysts.

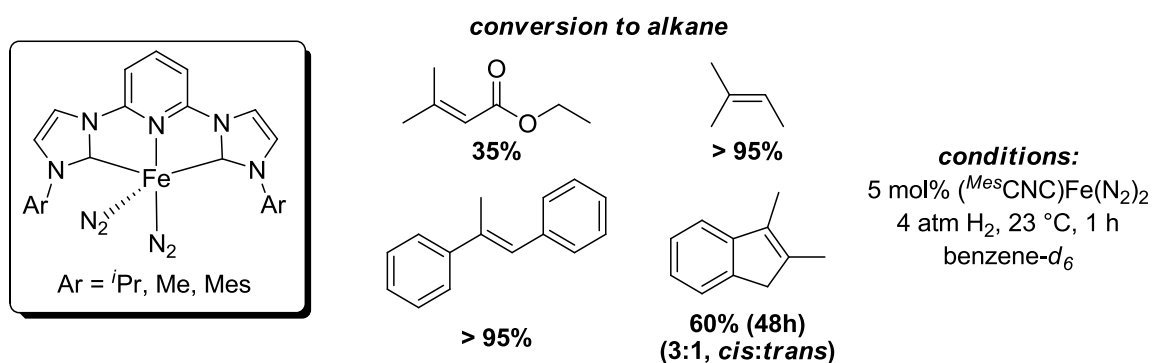


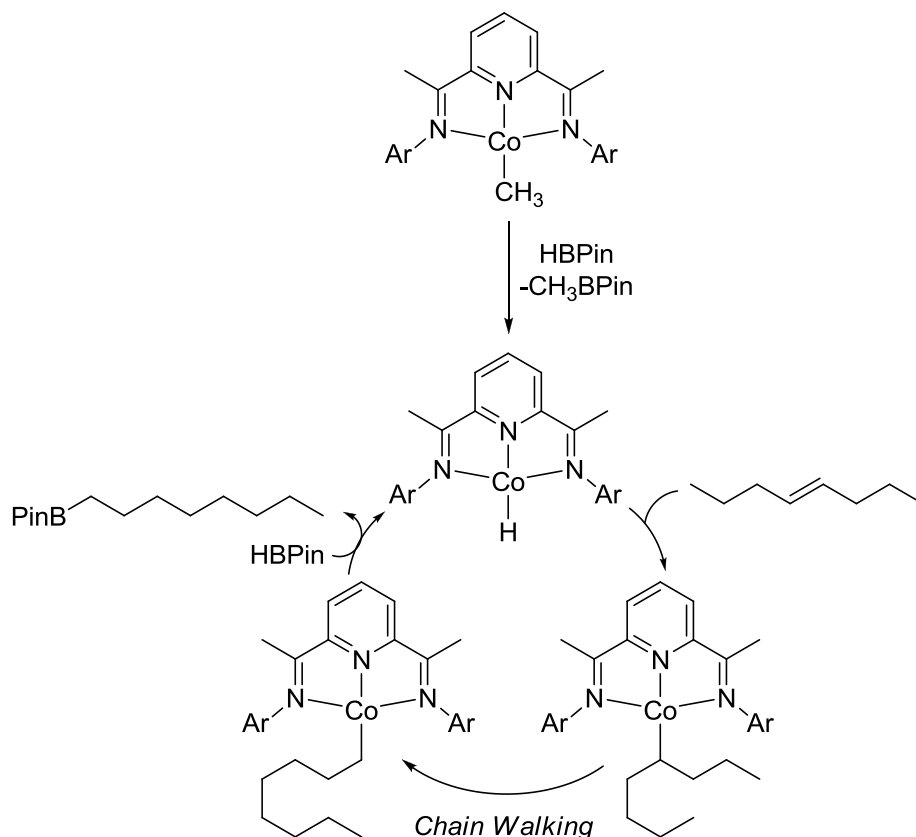
Figure 1.4.1. General structure of (^RCNC)Fe(N₂)₂ (left). Conversions of selected alkenes to alkanes *via* hydrogenation catalyzed by (^{Mes}CNC)Fe(N₂)₂.

1.4.2 Cobalt

The Chirik group has also made important contributions to the application of Co pincer complexes in catalysis, primarily through the use of bis(imino)pyridine (NNN) pincer ligands. In general, Co-catalyzed reactivity reported by the Chirik group and others include: the hydrogenation of alkenes⁴⁵ and nitriles;⁴⁶ the hydrosilylation of CO₂,⁴⁷ aldehydes and ketones;⁴⁸ the hydroboration of alkenes⁴⁹ and alkynes;⁵⁰ the borylation of heterocycles and arenes⁵¹ as well as the silylation of alkenes.⁵²

Chirik and co-workers^{49a} recently reported rare examples of Co-catalyzed alkene hydroboration, using Co^I-methyl complexes supported by bis(imino)pyridine pincer ligand scaffolds. The catalyst system described facilitates the isomerisation of internal

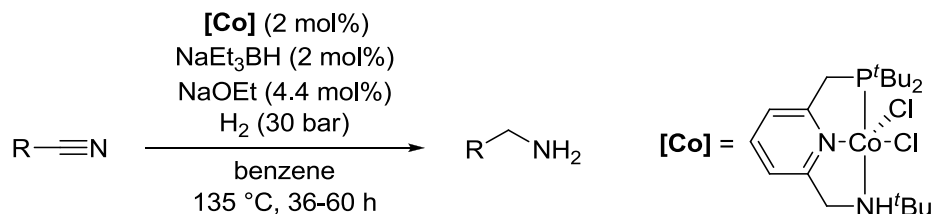
alkenes to the corresponding terminal alkene isomers, which are then hydroborated selectively to give *anti*-Markovnikov products (Scheme 1.4.7). Such reactivity and selectivity is highly desirable as one can envisage, for example, a mixture of alkene isomers of identical chain length all being isomerized and hydroborated to the same product with no need for any tedious separation steps. The catalysts studied were able to isomerize and hydroborate a variety of hindered and unhindered alkenes, including those involving migration through tertiary carbon centers to access terminal methyl-substituted products. Most examples proceeded to >98% conversion with temperatures up to 50 °C and catalyst loadings as low as 1 mol%. The activity towards hindered alkenes and the selectivity toward the terminal *anti*-Markovnikov products surpasses precious metal catalysts utilized for the same purpose.



Scheme 1.4.7. Reported mechanism for Co-catalyzed olefin isomerisation and hydroboration of *trans*-4-octene. Analogous mechanisms can be invoked for other internal alkene substrates.^{49a}

The hydrogenation of nitriles has been identified as an atom-economical route for the synthesis of primary amines. However, product selectivity is often poor and most existing catalysts are based on platinum group metals. Recently, Milstein⁴⁶ reported a PNN-based cobalt complex (Scheme 1.4.8) that is highly active for the selective reduction of nitriles to primary amines. The reaction conditions were optimized to include 2 mol% catalyst, 2 mol% NaEt₃BH, 4.4 mol% NaOEt and 30 bar H₂ at a reaction temperature of 135 °C. A wide substrate scope of mainly aromatic and heteroaromatic nitriles was demonstrated, with excellent conversion and high yield in most cases. More challenging benzylic and aliphatic nitriles were also tolerated, also giving good conversion and high yields, albeit over a longer reaction time. As the ligand is able to be

doubly-deprotonated (once at the neutral amine position, and once at the methylene portion of the same arm to give an overall monoanionic complex), the authors argue it is better equipped to facilitate the various protonation/deprotonation steps of the hydrogenation cycle. Although the identity of the active catalyst was not conclusively determined, a monoanionic Co^{I} hydride is presumed to be involved in the transformation.

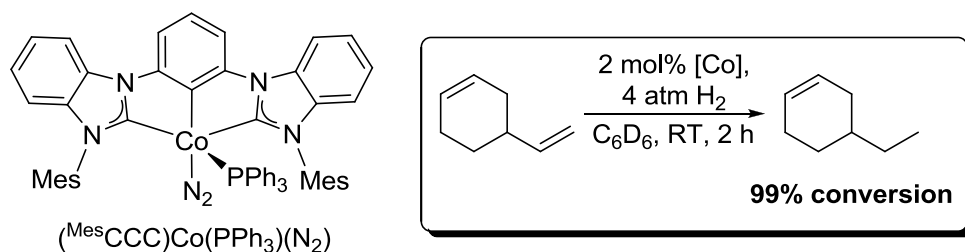


Scheme 1.4.8. Hydrogenation of nitriles to primary amines catalyzed by (t Bu-PNN)CoCl₂. R = various alkyl and aryl substituents.⁴⁶

As outlined in section 1.4.1., Chirik and co-workers have had success developing the field of Fe-catalyzed alkene hydrogenation, with their best results thus far coming from the use of bis(dinitrogen) complexes of the bis(NHC)pyridyl class of ligands, ($^R\text{CNC})\text{Fe}(\text{N}_2)_2$. Co^{I} -methyl complexes of this same ligand class have also been found to be effective catalysts for alkene hydrogenation, with the R = t Pr analogue outperforming the ($^{i\text{Pr}}\text{CNC})\text{Fe}(\text{N}_2)_2$ complex in a head-to-head study of a subset of di- and tri-substituted alkene substrates.^{45b} Tetramethylethylene was also hydrogenated (albeit at only 15% conversion over 24 h) in the Co system, while no conversion was observed in the Fe system under the same conditions.

Fout and co-workers⁵³ also used a bis(NHC) pincer for the application of alkene hydrogenation. Unlike Chirik's system described above, instead of pyridine, an anionic phenyl served as the central donor in an overall CCC-based pincer. Specifically, the authors found that the N_2 ligand ($^{Mes}\text{CCC})\text{Co}(\text{PR}_3)(\text{N}_2)$ (R = Me, Ph) could be reversibly displaced through treatment with H_2 gas, generating the $\sigma\text{-H}_2$ complexes

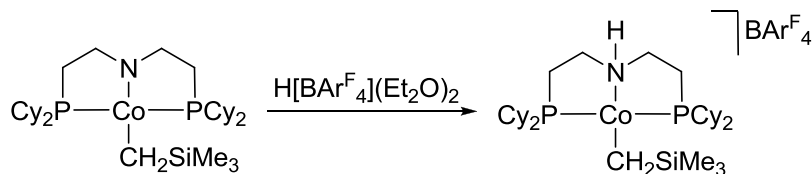
$(^{Mes}CCC)Co(PR_3)(H_2)$. The authors went on to demonstrate that the N_2 complex where $R = Ph$ (Scheme 1.4.9) was an active precatalyst for the hydrogenation of a variety of primarily terminal alkenes. They achieved room temperature activity at 4 atm H_2 using 2 mol% catalyst, affording > 99% conversion to the corresponding alkanes in most cases. However, internal alkenes proved less reactive, with reduction of cyclohexene requiring elevated temperature and a longer reaction time, and the reduction of 4-vinylcyclohexene leading to 4-ethylcyclohexene (rather than ethylcyclohexane) under their standard reaction conditions (Scheme 1.4.9).



Scheme 1.4.9. Structure of $(^{Mes}CCC)Co(PPh_3)(N_2)$ precatalyst. While reduction of terminal alkenes is readily supported by this system, reduction of internal alkenes is sluggish and requires elevated reaction temperatures, as illustrated by the reduction of 4-vinylcyclohexene (inset) wherein the internal alkene is left intact.

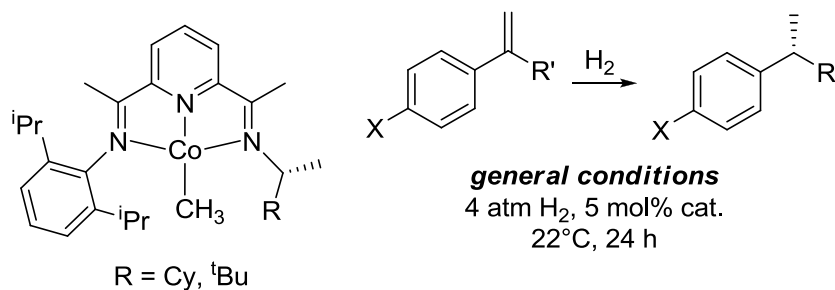
An example of a PNP-supported Co complex active for the hydrogenation of alkenes has also been reported by Hanson and co-workers.⁵⁴ The complex in question, a cationic Co^{II} -alkyl complex of the ligand bis[2-(dicyclohexylphosphino)ethyl]amine (Scheme 1.4.10) catalyzed the hydrogenation of a variety of mono and disubstituted alkenes ($\geq 99\%$ in most cases) under very mild conditions (2 mol% catalyst, 1 atm H_2 , 25 °C). Furthermore, hydrogenation of a variety of ketones, aldehydes and imines was also demonstrated, and the catalyst appeared to be largely unaffected by the presence of acidic protons (e.g. alcohol or carboxylic acid-containing substrates, H_2O). Interestingly no evidence for metal-ligand cooperativity was observed for the alkene hydrogenation

catalysis, mechanistic investigation indicated the hydrogenation reaction most likely proceeds through a $\text{Co}^{\text{I}}/\text{Co}^{\text{III}}$ redox cycle, with a Co-hydride complex being the active catalyst. In contrast, metal-ligand cooperativity *is* implicated in the hydrogenation of ketones, wherein a dramatic diminishment in catalytic activity was observed when using an *N*-methyl analogue of the Co catalyst.⁵⁵



Scheme 1.4.10. Generation of the cationic Co^{II} -alkyl hydrogenation precatalyst from reaction of the neutral Co^{II} alkyl complex with $\text{H}[\text{BARF}_4](\text{Et}_2\text{O})_2$. ($\text{BARF}_4 = \text{tetrakis}(3,5\text{-trifluoromethylphenyl})\text{borate}$)

Unlike Fe, in the case of Co, alkene hydrogenations have also been achieved asymmetrically using an NNN pincer ligand scaffold. In 2005, Budzelaar and co-workers⁵⁶ reported on the hydrogenation of a small scope of mono and disubstituted alkenes, catalyzed by bis(imino)pyridine complexes of Co^{I} . Building on these results, as well as a report by Bianchini and co-workers regarding the synthesis of 2-(alkylimino)-6-(arylimino)pyridyl ligands,⁵⁷ Chirik and co-workers^{45a} developed bis(imino)pyridine ligands wherein one ‘arm’ of the ligand features a chiral alkyl group, while the other features the classical aryl group. A Co^{I} -methyl complex of one such ligand, was found to be active for the enantioselective hydrogenation of a selection of prochiral disubstituted alkenes, giving high conversions to the corresponding alkanes, in very high enantiomeric excess in some cases (Scheme 1.4.11).



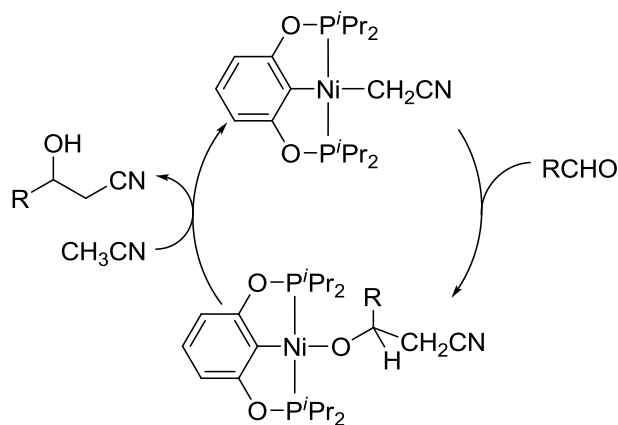
Scheme 1.4.11. General structure of asymmetric bis(imino)pyridyl Co^I-methyl complex used for the asymmetric hydrogenation of olefins (left). General reaction scheme for asymmetric hydrogenation of selected olefins (right). R' = various alkyl. X = H, F, CF₃, NMe₂, OMe.

1.4.3 Nickel

Unlike Fe and Co, many reports concerning Ni-pincer complexes are rooted in cross-coupling applications, likely due to the similarities nickel shares with its heavier congener, palladium. Carbon-sulfur,⁵⁸ Negishi,⁵⁹ Kumada,⁶⁰ Sonogashira,⁶¹ and Suzuki-Miyaura⁶² cross-coupling reactions have all been accomplished using nickel pincer complexes. Other catalytic processes reported include hydrogenation of phenylacetylene,⁶³ cyanomethylation of aldehydes,⁶⁴ fluorination of arenes,⁶⁵ hydrogen evolution,⁶⁶ hydrosilylation of CO₂,⁶⁷ aldehydes and ketones,⁶⁸ and reduction of CO₂ to the methanol level with borane.⁶⁹

Cyanomethylation of carbonyl substrates is a carbon-carbon bond forming reaction that ultimately leads to the production of β -hydroxynitriles but often requires the use of activated nitriles as substrates. Guan, and co-workers,⁶⁴ however, demonstrated cyanomethylation of aldehydes using acetonitrile, catalyzed by a nickel POCOP pincer complex, (ⁱPr-POCOP)NiCH₂CN (Scheme 1.4.12). Remarkably, this system was able to catalyze the coupling without the need for additional base, as is typically required for such transformations. Furthermore, TONs of up to 82,000 and TOFs of 1139 h⁻¹ were reported in one case where benchtop benzaldehyde and acetonitrile were employed,

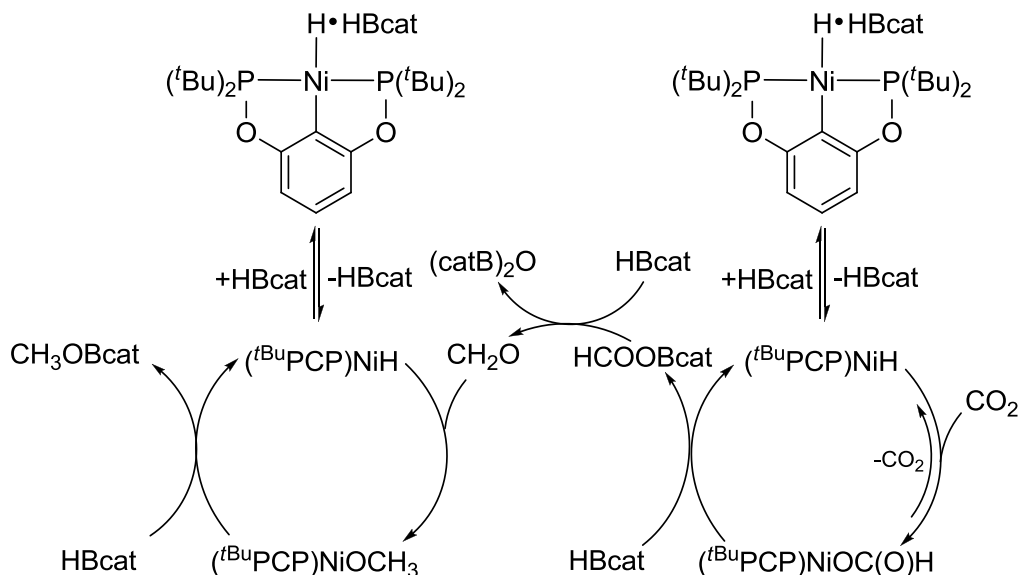
illustrating the robust nature of the pincer complex. In this particular case the catalyst loading could be decreased to 5 ppm (0.0005 mol%) without affecting catalytic performance. The scope was extended to a variety of alkyl and aryl aldehydes, as well as heterocyclic aldehydes, giving excellent yields over 2-72 h at room temperature. The *trans* influence of the pincer C-donor is proposed to play an important role in enhancing the nucleophilicity of the $(\text{NCCH}_2)^-$ anion, thereby facilitating attack on the substrate aldehyde. Relief of $d\pi$ - $p\pi$ repulsion between the nickel center and the oxygen of the generated alkoxide is the postulated to provide the thermodynamic driving force for the protonation of the alkoxynitrile by acetonitrile required for catalyst turnover (Scheme 1.4.12).



Scheme 1.4.12. Catalytic cycle for the cyanomethylation of aldehydes catalyzed by (*t*-Pr-POCOP)NiCH₂CN as proposed by Guan and co-workers.⁶⁴

Guan's group^{69a} has also demonstrated the efficient reduction of CO₂ to a methoxyboryl species catalyzed by a similar nickel POCOP pincer complex, (*t*-Bu-POCOP)NiH, *via* tandem hydroboration (Scheme 1.4.13). As is the case with many other metal hydride-catalyzed reductions of CO₂, the first step in this system is CO₂ insertion into the nickel hydride bond to generate the corresponding formate. An equivalent of borane (catecholborane, HBcat, in this case) regenerates the nickel hydride complex with

concomitant elimination of the formatoborate species HCO_2Bcat , which the authors propose is reduced to formaldehyde with a second equivalent of HBcat . The generated formaldehyde is then reduced by a third equivalent of HBcat in another cycle catalyzed by $(^t\text{Bu-POCOP})\text{NiH}$ to ultimately generate CH_3OBcat , which can then be hydrolyzed in air to afford methanol.

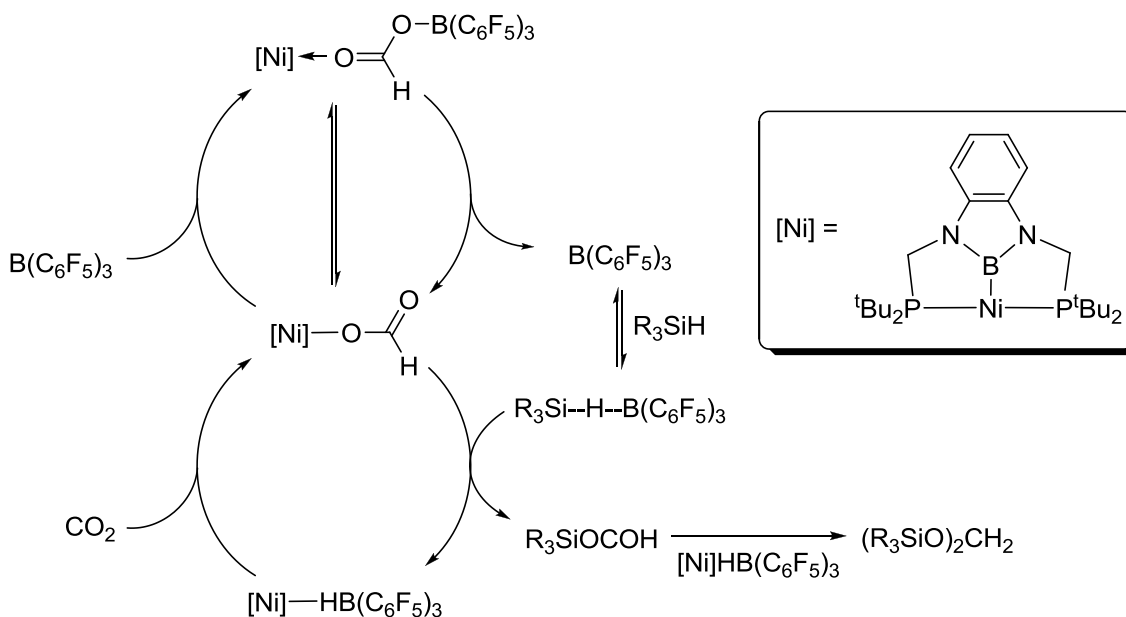


Scheme 1.4.13. Hydroboration of CO_2 to CH_3OBcat by catecholborane (HBcat), catalyzed by $(^t\text{Bu-POCOP})\text{NiH}$.^{69a}

The catalyst system described by Guan was able to achieve turnover frequencies of 495 h^{-1} at room temperature at a 0.2 mol% catalyst loading (relative to HBcat), with moderate (61%) yields of methanol after hydrolysis. At the time of publication this system was the most active for the reduction of CO_2 to the methoxide level, though recently a phosphine-borane frustrated Lewis pair (FLP) organocatalyst prepared by Fontaine⁷⁰ achieved the reduction of CO_2 to methanol with $\text{BH}_3\cdot\text{SMe}_2$, with TOFs over 737 h^{-1} .

López-Serrano and Rodríguez⁶⁷ described the hydrosilylation of CO_2 catalyzed by a bis(phosphino)boryl nickel complex. Most interesting about their system is the fact that

CO₂ was hydrogenated selectively to a bis(silyl)acetal, which represents an uncommon reduction of CO₂ to the formaldehyde level. Their catalyst system relies on the synthesis of a Ni formate complex, which when treated with one equiv B(C₆F₅)₃ generates a formatoborate species used for the actual catalysis, reminiscent of the Pd- and Pt-catalyzed reduction of CO₂ to methane reported by Turculet and co-workers previously.⁷¹ Conversion to the corresponding bis(silyl)acetals was selective (versus conversion to other potential reduction products such as methoxysilanes, or methane), but incomplete in most cases, and required extended reaction times at elevated temperatures. The authors' proposed mechanism is shown below in Scheme 1.4.14, wherein the role of the borane is to activate the silane reductant and support the formate and hydride complexes invoked throughout the catalytic cycle (as formatoborate and hydridoborate complexes, respectively).



Scheme 1.4.14. Proposed mechanism for Ni-catalyzed hydrosilylation of CO₂ to the formaldehyde level (as a bis(silyl)acetal).

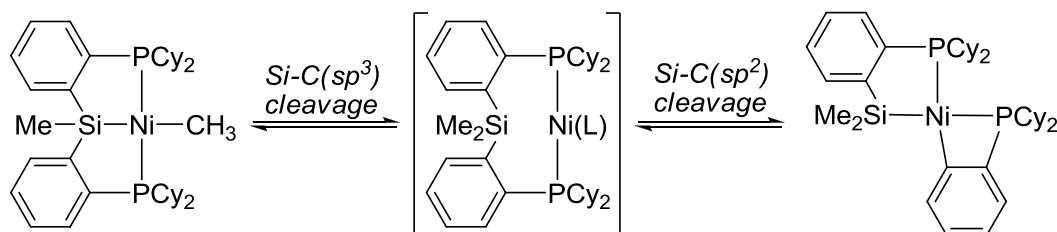
1.5 First-Row Silyl Pincer Complexes

The investigation of reactivity involving first-row pincer complexes has thus far been mainly focused on PCP- and PNP-based complexes. CNC- and NNN-based pincers have also received considerable attention, and each of these classes of pincer ligands has been strategically modified in various ways to affect the steric and/or electronic features at the metal center. The catalytic utility of pincer complexes that feature a central boryl donor has also been a recent topic of investigation.^{67, 72}

By comparison, the reactivity of silyl pincer complexes of first-row metals, especially iron and cobalt is largely unexplored. In fact, fewer than a dozen publications on the subject appear in the literature, and only a handful of these publications feature iron or cobalt,^{24d, 25b, 73} while the rest focus on nickel alone, or in conjunction with the other group 10 metals. The known trans-labilizing effect of such silyl ligands can promote coordinative unsaturation, while strong Si \rightarrow M σ -donation can, at the same time, tend to an electron-rich metal center. Together, these effects can often yield a complex poised for a challenging bond activation process, as has been observed in the past with C-H⁷⁴ and N-H⁷⁵ bond activations by the Turculet group.

The first PSiP pincer complexes of a first-row metal, nickel, were prepared by the Turculet group in 2009.^{25a} Previous work involving platinum PSiP complexes had led to the isolation of 16-electron (R-PSiP)Pt^{II} complexes featuring alkyl, aryl or silyl substituents *trans* to the Si donor of the pincer ligand (R-PSiP = κ^3 -(2-R₂PC₆H₄)₂SiMe, R = Ph, Cy). When attempting to prepare the analogous alkyl complexes of nickel and palladium a highly unusual ligand rearrangement was observed, involving, in the case of nickel, reversible Si-C(sp³) and Si-C(sp²) bond cleavage. As illustrated in Scheme 1.5.1,

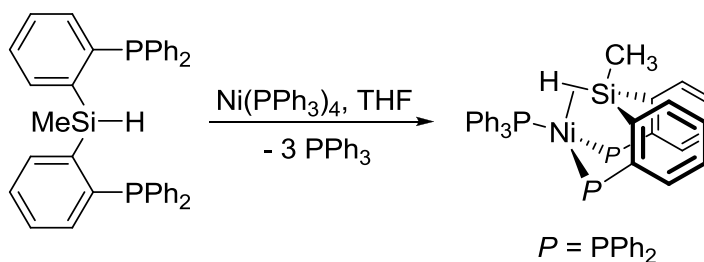
net Si-Me reductive elimination from the coordination sphere of nickel in (Cy-PSiP)NiMe is proposed to lead to a bis(phosphino)nickel(0) intermediate, which then undergoes Si-C(sp²) oxidative addition involving one of the bonds between silicon and the phenylene backbone of the ligand.



Scheme 1.5.1. Reversible rearrangement of (Cy-PSiP)NiMe involving Si-C bond cleavage steps.^{25a}

Iwasawa and co-workers⁷⁶ later investigated Ni, Pd and Pt complexes of the related Ph-PSiP ligand. Specifically, hydride complexes of the group 10 metals were targeted, however, in the cases of nickel(0) and palladium(0), η^2 -(SiH) complexes were obtained, as examples of ‘frozen intermediates’ of the desired Si-H oxidative addition (Scheme 1.5.2). ¹H and ²⁹Si NMR spectroscopy supported the notion that the complex remains in an η^2 -(SiH) form in solution. Coupling from the Si-H proton to both phosphorus atoms, as well as the methyl protons on silicon suggested a bonding interaction between Si and H was maintained, while simultaneously binding to the metal center. The J_{SiH} coupling constants of 110 Hz (Ni) and 97 Hz (Pd) also supported the η^2 -(SiH) formulation (*cf.* $^1J_{\text{SiH}} = 204$ Hz for the free ligand). Interestingly, the same reaction with a platinum precursor led to the desired oxidative addition product, (Ph-PSiP)Pt(PPh₃)H, with the hydride located *trans* to silicon in a trigonal bipyramidal geometry. No evidence of an η^2 -(SiH) complex was obtained in the case of platinum,

though evidence for an intermediate of the same formulation, but in square pyramidal geometry with the hydride *cis* to silicon, was obtained.



Scheme 1.5.2. Synthesis of $[Ph-PSi(\mu-H)P]Ni(PPh_3)$ reported by Iwasawa and co-workers.⁷⁶

Later, Nova and Hazari reported⁷⁷ that when attempting to prepare $(Ph-PSiP)MH$, $M = Ni, Pd$ (*i.e.* the targeted complexes of Iwasawa, without bound triphenylphosphine) from $(Ph-PSiP)MCl$ and $LiAlH_4$ or $LiEt_3BH$, highly unusual dimeric complexes featuring *five*-coordinate silicon, $(Ph-PSiP)_2M_2$, were obtained in 65% ($M = Ni$) and 45% ($M = Pd$) yield instead, with concomitant elimination of H_2 . The complexes crystallized in distorted square-pyramidal geometries at both Si atoms and both Ni/Pd atoms, with one long and one short Si-M contact each as part of an unsymmetrical 4 center-2 electron (4c-2e) bond (Figure 1.5.1). In solution, both complexes exhibited similar NMR spectra, with two resonances appearing in the ^{29}Si NMR spectra for each, indicating inequivalent silicon atoms. Instead of four signals in the ^{31}P NMR, however, two broad resonances were observed, which decoalesced into four signals at low temperature (-60 °C). The inequivalence, the authors argue, is likely due to slight orientation changes in the backbone and phenyl arms of the ligand.

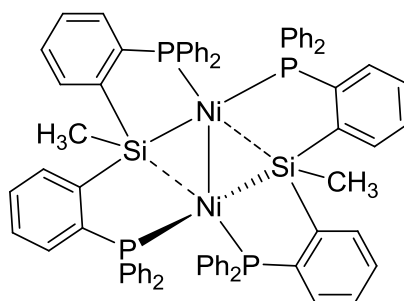


Figure 1.5.1. Structural diagram of the dimeric nickel complex featuring 5-coordinate silicon derived from (Ph-PSiP)NiCl and a hydride source.⁷⁷

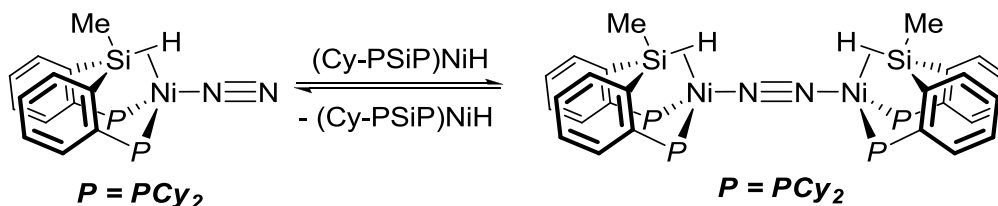
The above examples highlight the interesting observed behavior of this variety of PSiP ligands with group 10 metals, namely unusual reactivity and coordination modes of the ligand itself. There are very few examples, however, of productive reactivity of stable first-row PSiP complexes with substrate molecules. Building on their own work and the work by Iwasawa outlined above, Hazari and co-workers⁷⁸ illustrated through a variety of stoichiometric hydrogen evolving reactions that (Ph-PSiP)Ni(η^3 -cyclooctenyl) could possibly act as a synthetic equivalent of the thermally unstable (Ph-PSiP)NiH complex through a β -hydride elimination process. Their claim was bolstered by the fact that (Ph-PSiP)Ni(η^3 -cyclooctenyl) acted as a precatalyst for reactions typically catalyzed by hydride complexes, namely alkene isomerisation and CO₂ hydroboration, though product selectivity was quite poor in both cases.

The potential for CO₂ insertion into (PSiP)Ni hydrides, presumably a vital step for the above CO₂ hydroboration, has been investigated in a broad context by Hazari and Kemp.⁷⁹ In their study, the authors looked at a variety of new and previously reported⁷¹ PCP, PNP and PSiP complexes of nickel hydrides, as well as palladium hydrides, to study the effect of the central donor atom on the ease of CO₂ insertion into the metal hydride bond to generate the corresponding formates.

While CO₂ insertion into the metal hydride bonds of all the PCP and most of the PSiP complexes prepared was described as facile, no insertion into the metal hydride bonds of any of the studied PNP pincer ligand complexes was observed, supporting the notion that the stronger *trans* influence of the anionic donors helps to destabilize the metal hydride bond, facilitating CO₂ insertion. The η^2 -(SiH) complexes of nickel and palladium previously prepared by Iwasawa⁷⁶ were also tested for CO₂ insertion, though only the palladium analogue was able to insert CO₂, releasing triphenylphosphine, while the nickel remained unreactive. DFT calculations corroborated the observed trends in reactivity, and it was also found that CO₂ insertion into nickel hydride bonds *trans* to anionic carbon and especially silicon is energetically more favorable than the same reaction with palladium hydrides. Calculated transition states for all six scenarios (Ni or Pd as well as PNP, PCP or PSiP) indicate that the insertion step proceeds *via* a four-membered transition state involving the metal center, the hydride atom, and the carbon and an oxygen atom of CO₂.

While investigating the reactivity of these reported hydride complexes toward CO₂ insertion, Hazari, Kemp and co-workers⁷⁹ noted that the compound formulated as (Cy-PSiP)NiH was thermally unstable, though its corresponding formate complex could be isolated and was crystallographically characterized. More recently, Balcells, Hazari, *et al.*^{24c} uncovered an interesting situation where the presence of dinitrogen facilitates the isomerisation of (Cy-PSiP)NiH to an N₂-bridged dimer complex featuring η^2 -(SiH) interactions (Scheme 1.5.3). Support for the terminal silyl hydride form of (Cy-PSiP)NiH was provided in the form of an X-ray crystal structure, however, it was found that when crystallized under dinitrogen, the dimeric N₂-bridged complex was isolated instead and

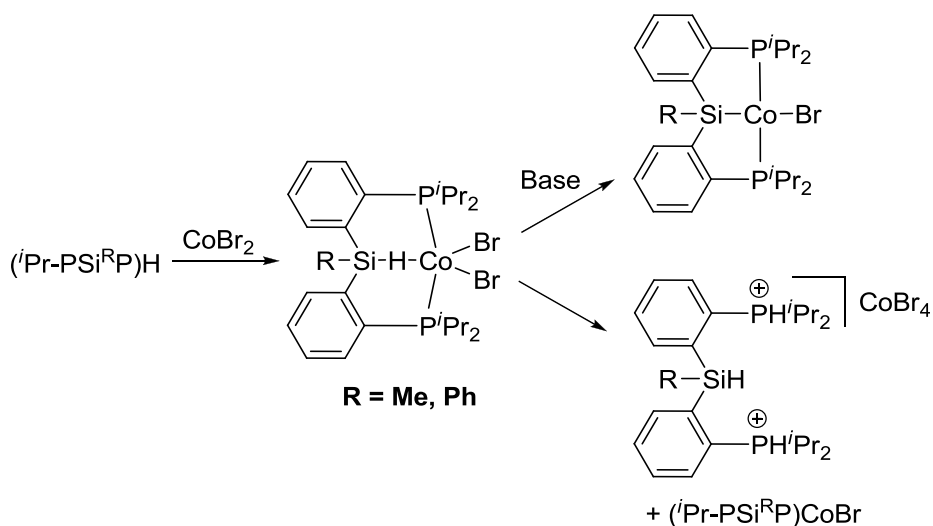
also crystallographically characterized. The authors argue that in an N_2 atmosphere, all three species are in equilibrium, with the relative concentrations of each species being dependent on N_2 concentration, as well as temperature.



Scheme 1.5.3. Proposed equilibrium for the observed dinitrogen-coordinated η^2 -(SiH) Ni complexes.^{24c}

As illustrated thus far, the chemistry of PSiP pincer complexes of first-row metals has focused almost exclusively on nickel. The success of the use of PSiP pincer ligands in conjunction with the heavier group 10 metals makes investigation of the analogous nickel complexes an obvious next step. Literature regarding iron and cobalt complexes of PSiP pincer ligands, however, has been lacking. The first report on the subject came from Sun and co-workers^{25b} who reported the synthesis of a number of PSiP pincer complexes of iron, cobalt and nickel. Treatment of the neutral (Ph-PSiP)H ligand with $M(\text{PPh}_3)_4$ led to the generation of complexes of the form $(\text{Ph-PSiP})M(\text{PMe}_3)_n\text{H}$ ($M = \text{Co}$, $n = 1$; $M = \text{Fe}$, $n = 2$). Other similar cobalt complexes were also isolated including $(\text{Ph-PSiP})\text{Co}(\text{PMe}_3)\text{Cl}$, $(\text{Ph-PSiP})\text{Co}(\text{PMe}_3)\text{HCl}$, $(\text{Ph-PSiP})\text{Co}(\text{PMe}_3)\text{HI}$ and $(\text{Ph-PSiP})\text{Co}(\text{PMe}_3)_2$, illustrating a range of possible (PSiP)Co complexes of various coordination number and oxidation states from cobalt Co^{I} to Co^{III} . The sole iron complex prepared, $(\text{Ph-PSiP})\text{Fe}(\text{PMe}_3)_2\text{H}$, was found to catalyze the hydrosilylation of a limited substrate scope of aldehydes and ketones. Hydrosilylation with triethoxysilane (1.5 equiv) proceeded over the course of 1-6 h in high yields with catalyst loadings of 1 mol%.

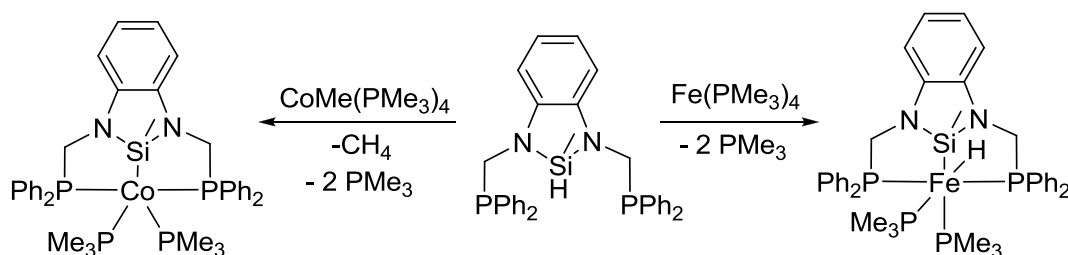
A unique example of an η^1 -(H-Si) interaction with a Co center was recently reported by Kim, Lee and co-workers.^{24d} Prior to synthesis of the compound in question the authors began by treating (*i*Pr-PSi^RP)H (R = Me, Ph) with CoBr₂ in the presence of triethylamine to afford (*i*Pr-PSi^RP)CoBr in good yield (Scheme 1.5.4). In the absence of base, a green colored intermediate was observed, which went on to form an unusual example of a doubly-protonated ligand (at both phosphorus atoms) with a CoBr₄²⁻ counter-ion. The green intermediate species was determined to be, formally, the CoBr₂ adduct of (Ph-PSiP)H, coordinated *via* both phosphorus atoms, as well as through an η^1 -(Si-H) interaction (Scheme 1.5.4). Such an η^1 -(Si-H) interaction can be thought of as a hydrogen atom bridging Si and Co in a 2-center-2-electron bond (versus a 3-center-2-electron bond for an η^2 -(SiH) interaction), a formulation supported by ENDOR and DFT data as the hydrogen atom could not be reliably located using X-ray diffraction techniques.



Scheme 1.5.4. Synthesis of a PSiP Co complex featuring an η^1 -(Si-H) interaction and subsequent reactivity with base (top) or upon standing in solution (bottom).^{24d}

Recently, Sun and co-workers^{73a} reported the preparation of Co- and Fe-complexes of another PSiP ligand variant featuring an *N*-heterocyclic silyl motif

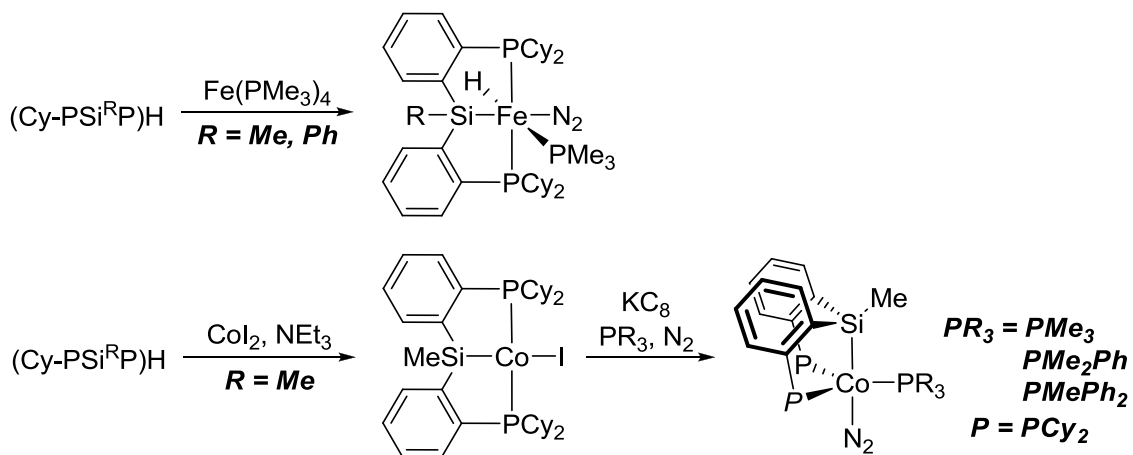
previously reported by Hill (Scheme 1.5.5).⁸⁰ Sun's work focused on the preparation of Fe and Co complexes and explored the catalytic activity of (PSiP)Co(PMe₃)HCl toward the Kumada cross-coupling of aryl halides with aryl Grignards. Reaction of the neutral silane ligand with Fe(PMe₃)₄ gave (PSiP)Fe(PMe₃)₂H, which in passing they found to be an ineffective hydrosilylation catalyst in contrast to (Ph-PSiP)Fe(PMe₃)₂H described earlier. They attribute the lack of activity to the electronegative nitrogen atoms bound to silicon, which render PMe₃ dissociation unfavorable, thereby preventing the generation of a vacant coordination site for the catalytic reaction. Reaction of the neutral ligand with CoMe(PMe₃)₄, gave (PSiP)Co(PMe₃)₂, which could be converted to either (PSiP)Co(PMe₃)I by reaction with MeI, or (PSiP)Co(PMe₃)HCl by reaction with HCl. The latter complex was found to be somewhat active for Kumada cross-coupling reactions. A variety of aryl chlorides, aryl dichlorides and aryl bromides were successfully coupled with aryl Grignards in moderate to good yield using 5 mol% catalyst at 40-50 °C.



Scheme 1.5.5. Synthesis of (PSiP)Co(PMe₃)₂ and (PSiP)Fe(PMe₃)₂H from the neutral ligand precursor (PSiP)H and M(Me)_n(PMe₃)₄ (M = Co, n = 1; M = Fe, n = 0).^{73a}

Finally, Iwasawa, Nishibayashi, and co-workers^{73b} expanded the scope of PSiP chemistry of Fe and Co by exploring reactivity with the Cy-PSiP ligand. In a route analogous to that employed by Sun and co-workers,^{25b} the authors treated two variants of the Cy-PSiP ligand with Fe(PMe₃)₄ (Scheme 1.5.6). One variant featured the traditional

SiMe moiety in the backbone, while the other was a SiPh derivative, Cy-PSi^{Ph}P. In contrast to the work by Sun and co-workers,^{25b} however, complexes of the type (Cy-PSi^RP)FeH(PMe₃)(N₂) (R = Me, Ph) were obtained, in low yields. Clearly the increased steric bulk, and/or donating ability, of the cyclohexyl variant of the ligand precludes coordination of the second equivalent of PMe₃ as observed for the diphenylphosphino variant, and instead dinitrogen occupies the coordination site *trans* to silicon. An analogous Co complex could not be prepared. However, by first preparing (Cy-PSiP)CoI and reducing with KC₈ in the presence of a phosphine under a nitrogen atmosphere, complexes of the type (Cy-PSiP)Co(PR₃)(N₂) (PR₃ = PMe₃, PMe₂Ph, PMePh₂) were prepared in low yields (Scheme 1.5.6). These dinitrogen complexes of Fe and Co were subsequently investigated as potential N₂ reduction catalysts, a study inspired by the use of tetradentate tris(phosphino)silyl pincer complexes developed by Peters and co-workers²² which have also exhibited activity toward catalytic N₂ reduction. Using their dinitrogen complexes of Fe and Co Iwasawa and co-workers pursued direct catalytic reduction of N₂ to ammonia by addition of KC₈ as reductant and [H(OEt₂)₂][B(C₆F₅)₄] as a proton source. While ammonia was generated using this route, only 1.2 equiv were detected relative to the amount of metal complex used. However, catalytic *silylation* of N₂ was met with some success. Under ambient conditions, and using Na as the reductant and Me₃SiCl as the silylating agent, less than 0.2 mol% Fe or Co catalyst was sufficient to yield 15-26 equivs N(SiMe₃)₃ in the case of the Fe catalysts, and 23-41 equivs N(SiMe₃)₃ in the case of the Co catalysts.



Scheme 1.5.6. Synthesis of Fe and Co dinitrogen complexes of two variants of the Cy-PSiP.^{73b}

The work described in Chapters 2, 3 and 4 of this document focuses on the synthesis, coordination chemistry, as well as catalytic applications, of novel Fe, Co and Ni complexes of PSiP-pincer ligands developed in the Turculet group. Challenges and successes associated with developing (Cy-PSiP)Fe complexes and exploring their reactivity with respect to E-H bond activation will be described in Chapter 2, including development of a catalyst active for the hydrogenation of alkenes, highly uncommon for Fe. Chemistry of existing (Cy-PSiP)Co complexes will be expanded upon in Chapter 3, including reactivity involving the cleavage of H₂ and O₂, as well as the catalytic hydrogenation of alkenes. This Co chemistry is an extension of work initially reported by Adam Ruddy, a former graduate student in the Turculet group.⁸¹ In Chapter 4, Ni complexes featuring the new ⁱPr-PSiP^{Ind} ligand scaffold will also be described, along with some Pd and Pt analogues for comparison. A detailed investigation into the structural and spectroscopic features of group 10 metal hydride complexes of this ligand will be described. In addition highly-selective Ni-catalyzed hydroboration of CO₂ to the formaldehyde level has been achieved using this new ligand.

1.6 P,N Ligation in Transition Metal Chemistry

In addition to the chemistry of tridentate ‘pincer’ ligands, there has been tremendous effort put into designing and developing novel *bidentate* ligand scaffolds. Just as with their tridentate analogues, the combinations of scaffolds and donor groups are endless, with some common examples being bis(phosphines), such as 1,1'-bis(diphenylphosphino)ferrocene (DPPF), a common ligand used in Pd-catalyzed cross-coupling reactions, and diamines such as the simple ethylenediamine. These bidentate ligands belong to a class known as homofunctional bidentate ligands, or simply homobidentate, wherein both donor groups are identical. When one of these donor groups is altered, even slightly, the ligand becomes known as heterofunctional bidentate, heterobidentate, or sometimes as a ‘hybrid’ ligand. While homobidentate ligands clearly have a demonstrated history of tremendous utility, the advantages heterobidentate ligands offer in terms of transition metal-based catalysis cannot be understated, and varies dramatically from case to case.

One such class of heterobidentate ligands are P,N-based ligands. As the shorthand implies, these ligands bind to the metal center through a P and an N atom, anchored to one another through some type of scaffold, which, as with the substituents on P or N, can vary quite dramatically. The combination of P and N donors in a single ligand offer the advantage of having both a soft and hard donor atom coordinating to a metal center, offering added stability throughout changes in metal oxidation state, very commonly invoked in transition metal-catalyzed reaction mechanisms *via* oxidative addition/reductive elimination steps. Furthermore, the π -accepting nature of phosphines can help stabilize a low oxidation state metal, while σ -donating N-ligands (and P-ligands)

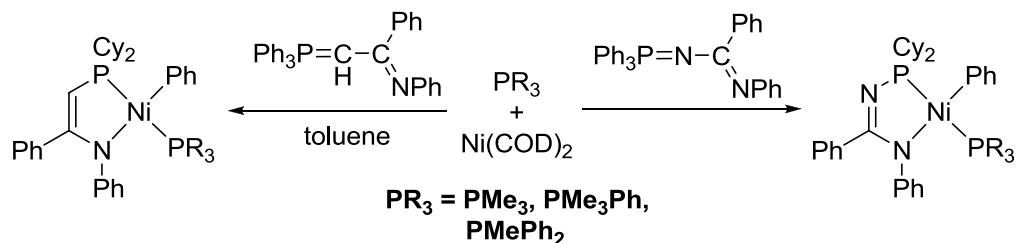
can increase electron density at the metal center.⁸² P,N ligands can be constructed to display redox non-innocence (described briefly in section 1.3), and in addition, substituents on each atom can be carefully chosen to tune both steric and electronic properties in attempts to ‘tailor-fit’ a ligand for a specific application.

A comprehensive review of the use of P,N ligands in transition metal-based catalysis is far beyond the scope this work, however, there do exist several reviews discussing this very topic.⁸² Instead, focus will be directed toward a specific class of P,N ligand: those that are monoanionic at nitrogen. Quite surprisingly, the chemistry of this class of ligand is remarkably underexplored when compared to their neutral analogues, especially when looking at complexes of these ligands with the first-row transition metals.

1.6.1 First-Row Metal Complexes of Monoanionic P,N Ligands

Some of the earliest examples of transition metal complexes of monoanionic P,N ligands were Ni complexes described by Braunstein and co-workers,⁸³ in the form of a diphenylphosphino ligand bridged to an arylamido group by a substituted ethylene linker. Notably these Ni complexes were derived from treatment of Ni(COD)₂ with an α -iminophosphorus ylide, wherein a formal P-Ph oxidative addition of the ylide to Ni generates the overall Ni^{II} complex (Scheme 1.6.1, left), Liang and co-workers⁸⁴ also reported similar chemistry with Ni. These and other related complexes were targeted for their potential as catalysts for the linear oligomerization of ethylene, though activity in this regard was found to be quite low.⁸³ In a subsequent study, Braunstein and co-workers modified their ligand precursor, using instead α -(*N*-phenylbenzylimino)azatriphenylphosphorane. The key difference between this ligand

precursor and that of the prior ligand precursor being the presence of a second N atom in the ligand backbone, in the place of the C atom bound to P. A similar synthetic route to the synthesis of the previous iteration of the P,N ligand gave analogous (P,N)NiPh(PR₃) complexes (Scheme 1.6.1, right), but once again the authors described activity toward ethylene oligomerization as ‘disappointing’.⁸⁵



Scheme 1.6.1. Synthesis of some early examples of Ni complexes of monoanionic P,N ligands as reported by Braunstein and co-workers.^{83, 85}

Other anionic P,N ligands have been prepared for the purposes of supporting metal catalyzed ethylene oligomerization and related reactions (Figure 1.6.1), but for the most part these ligands and related neutral analogues have not been used in conjunction with the first-row transition metals, most being involved in coordination to Pd or Ru.⁸⁶

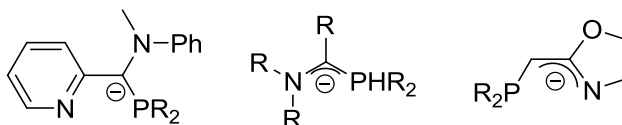
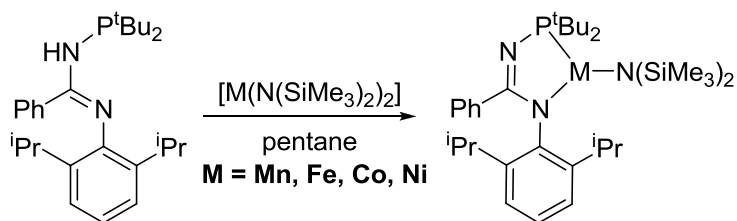


Figure 1.6.1. Examples of other monoanionic P,N-based ligands designed to support metal catalysts for the oligomerization of ethylene.^{86b, 86d, e}

Baker, Gordon and co-workers⁸⁷ developed a monoanionic P,N ligand, in addition to related P,P and N,N-type ligands, for the purposes of developing Fe-based catalysts for the dehydrogenation of ammonia-borane. The P,N ligand precursor, Cy₂PCH₂CH₂NHPh could be treated with FeCl₂ and 2 equiv KN(SiMe₃)₂ to generate the bis-ligated complex, [(P,N)₂Fe], which upon heating with ammonia borane facilitated the release of *ca.* 1.3 equiv H₂ (relative to ammonia borane added) on a first addition, and another 1.5 equiv H₂

on a second addition of ammonia borane. The authors conclude that while the motivation for tethering the bulky phosphino ligand to an amido ligand was to prevent ligand loss from the metal center, the resulting small N-Fe-P angle actually draws the groups closer to one another, while simultaneously increasing the distances of the P and N atoms of the second ligand from the Fe center, perhaps leading to an overall promotion of decomposition *via* loss of the second coordinating ligand.

More recently, Sydora, Stradiotto, Turculet and co-workers reported on the preparation of Mn, Fe, Co and Ni complexes of a mononanionic *N*-phosphinoamidinate ligand,⁸⁸ not unlike those mentioned above, previously described by Braunstein,⁸⁵ though prepared through a more modular synthetic route. Three-coordinate Mn, Fe, Co and Ni complexes of this class of ligand were readily accessible through treatment of the neutral ligand precursor with $\text{Fe}(\text{N}(\text{SiMe}_3)_2)_2$ or $\text{Co}(\text{N}(\text{SiMe}_3)_2)_2$ (Scheme 1.6.2). Notably the resulting Fe complex, $(\text{P,N})\text{Fe}(\text{N}(\text{SiMe}_3)_2)$ was found to be a highly active catalyst for the hydrosilylation of carbonyl compounds to alcohols. A wide scope of esters, aldehydes and ketones were successfully reduced to their corresponding alcohols under room temperature conditions, using < 1 mol% Fe, and only 1 equiv PhSiH_3 as the reductant relative to the substrate. The corresponding Co complex was found to be largely inactive under the same conditions.



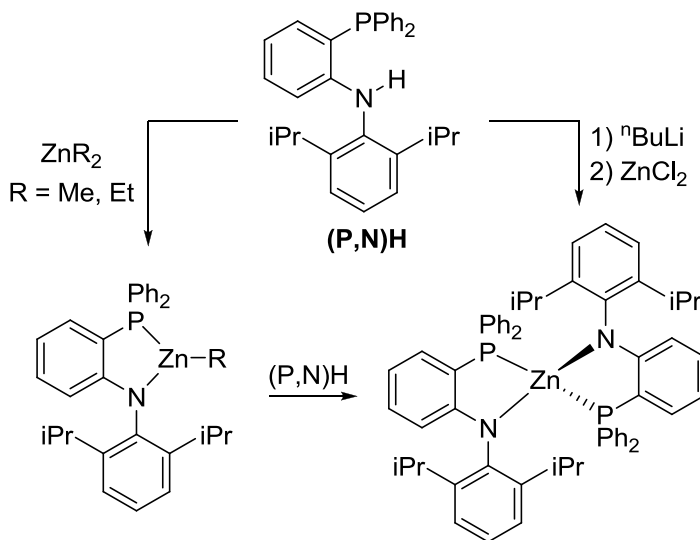
Scheme 1.6.2. Synthesis of *N*-phosphinoamidinate complexes of Mn, Fe, Co and Ni.

In subsequent study,⁸⁹ the same Co complex was found to be active for the catalytic isomerisation/hydroboration of alkenes (< 5 mol% catalyst, room temperature). A scope of terminal alkenes could be selectively hydroborated to give the *anti*-Markovnikov products, while linear internal alkenes such as *cis*- and *trans*-octene underwent isomerisation first, ultimately yielding the terminally hydroborated product selectively. Further investigation of this catalytic system was carried out through variation of substituents on the ligand scaffold, as well as the boranes used as reductants. In several cases diverging results were observed regarding which terminally reduced product was observed when using a 1,3,2-diazaboralane as the reductant rather than HBPIn.⁹⁰

Chemistry of the *N*-phosphinoamidinate class of ligands has also been recently expanded to include manganese.^{88b} Efforts were again directed toward the hydrosilylation of carbonyl compounds and, in the case of Mn, this also included reduction of a scope of tertiary amides to tertiary amines, a notoriously difficult transformation to achieve catalytically. A three-coordinate Mn^{II}-amido complex could be prepared using the same synthetic route as the analogous Fe and Co complexes (treatment of the neutral ligand precursor with [Mn(N(SiMe₃)₂)₂], Scheme 1.6.2), and under mild conditions (2-5 mol% catalyst, 25-75°C) a variety of tertiary amides were successfully reduced to their corresponding tertiary amines in high conversion (>90% in most cases). Aldehydes, esters and ketones could also be reduced under even milder conditions, illustrating utility for this Mn precatalyst across an unprecedented variety of substrates for a first-row transition-metal catalyst.

The last class of monoanionic P,N ligand to be discussed are derivatives of 2-phosphinoanilines, or diarylamido phosphines. Liang and co-workers⁹¹ demonstrated that

these ligands could be used to generate, and isolate, rare examples of monomeric, three-coordinate zinc complexes (Scheme 1.6.3). Even in the presence of coordinating solvents (Et₂O, THF), both the (P,N)ZnMe and (P,N)ZnEt complexes were isolated in their three-coordinate forms, and were later found to be active catalysts for the ring opening polymerization of ϵ -caprolactams.⁹² Attempts to prepare the corresponding chloride complex, (P,N)ZnCl, however, led instead to a bis-ligated Zn complex, wherein 2 equivs of the P,N ligand are coordinated to a single Zn center (Scheme 1.6.3).⁹¹ This bis-ligated complex could be rationally prepared by treatment of one of the alkyl complexes with a second equivalent of neutral ligand, (P,N)H, and illustrates a commonly encountered phenomenon with these ligands which may represent a deactivation pathway in an eventual catalytic process. Similar chemistry was soon uncovered for aluminum as well,⁹³ with examples of dialkylaluminum(III) and dichloroaluminum(III) complexes of the 2,6-dimethylanilido and 2,6-diisopropylanilido variants of the ligand being prepared and characterized. Unlike in the Zn chemistry, no evidence for the generation of bis-ligated complexes of Al was found.

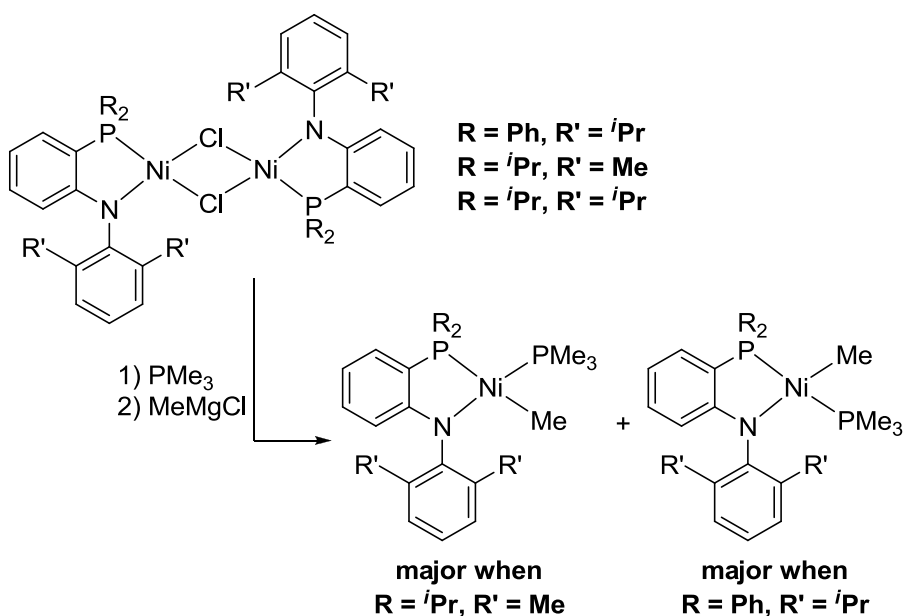


Scheme 1.6.3. Synthesis of three-coordinate alkyl zinc complexes and a $(P,N)_2Zn$ complex.

Expanding the chemistry of this class of ligand to Ni^{94} led initially to halide-bridged dimer complexes by treatment of the lithium salt of the ligand precursor with $NiCl_2(dme)$. This dimer complex was found to be a viable precursor to the synthesis of 4-coordinate alkyl complexes in the form of their PMe_3 adducts (Scheme 1.6.4), or as an η^3 -benzyl complex. *Cis*- and *trans*-isomers of the $NiMe$ complexes were observed, with the major isomer featuring Me coordinating in the position *trans* to the phosphino portion of the ligand, with PMe_3 *trans* to the anilido group. Conversely, only one isomer was observed for the corresponding $(P,N)NiCl(PMe_3)$ (PMe_3 *trans* to N) and $(P,N)NiPh(PMe_3)$ (PMe_3 *trans* to P) complexes.

Subsequent work⁹⁵ illustrated that varying the steric and electronic parameters of the P,N ligand had a dramatic effect on the relative ratio of such isomers. For example, in the case of $(P,N)NiMe(PMe_3)$ complexes, when the ligand bears both 2,6-diisopropylanilido and diphenylphosphino moieties, the major isomer features Me *cis* to the amido ligand. Conversely, when the ligand bears both 2,6-dimethylanilido and

diisopropylphosphino moieties, the major isomer features Me *trans* to the amido ligand (Scheme 1.6.4). In addition, when attempting to prepare a chloride dimer complex of the 2,6-dimethylanilido/diphenylphosphino variant of the ligand, a bis-ligated complex, (P,N)₂Ni, was isolated instead, reminiscent of the Zn chemistry described above, and illustrating the effect of decreasing steric bulk around the metal center (bulkier versions of the ligand supported the chloride dimer complexes). Finally, in terms of catalysis, the halide dimers served as viable precatalysts for the Kumada cross coupling of a small scope aryl halides with aryl and alkyl Grignards giving good selectivity and conversions under mild conditions (0.5 mol% catalyst, 60°C).



Scheme 1.6.4. Synthesis and structural variability of 4-coordinate Ni-methyl complexes supported by a monoanionic P,N ligand.

As the relatively small number of examples described in this section represent the majority of recent reports regarding first-row transition metal complexes of monoanionic P,N ligands, there is a clear opportunity to expand the chemistry of this versatile ligand class. Examples of exceptional catalytic activity have been reported in the case of the *N*-

phosphinoamidinate class of ligands, and interesting structural variability has been observed in the case of the diarylamido phosphine ligands used primarily by Liang. A better understanding of the behavior of metal-ligand complexes of this variety through the investigation of stoichiometric chemistry could lead to novel catalytic chemistry, or at the very least improvements on existing systems. The work described in Chapter 5 of this document, therefore, describes efforts to expand the chemistry of diarylamido phosphine ligands to iron and cobalt, of which thus far there are no examples reported in the literature. A new diarylamido phosphine ligand derivative was prepared and the ensuing complexes were applied toward the catalytic reduction of amides *via* hydrosilylation.

Chapter 2: Synthesis and Characterization of (Cy-PSiP)Fe Complexes and Application Toward Catalytic Olefin Hydrogenation

2.1 Introduction

As outlined in Chapter 1 of this document, pincer complexes of first-row transition metals have found application in a variety of bond activation and catalytic processes. In a few rare cases, the catalytic activity of such first-row pincer complexes rivals that of precious metal catalysts, which are widely considered to constitute the pinnacle of activity and reactivity in homogeneous organometallic catalysis. Despite such reports, first-row metal complexes of PSiP-pincer ligands are comparatively underexplored. In particular, the chemistry of (PSiP)Fe complexes is limited to two reports by Sun and co-workers,^{25b, 73a} and one from Iwasawa and co-workers.^{73b} The development of the chemistry first-row metal PSiP complexes could be advantageous, as such complexes may function as lower cost alternatives to the platinum group metal analogues that have been described by the Turculet group and others.^{23, 25a, 74-76, 96} Although the activity of first-row metal catalysts is often lower than that of precious-metal catalysts, the advantages of lower cost, increased availability, and often lower toxicity could surpass the potential issue of lower catalytic activity.

The hydrogenation of olefins, for example, is one of the most important and widely applied chemical transformations known. Olefin hydrogenation has application from the synthesis of fine chemicals, to the processing of petrochemicals, and is routinely employed on large scales.⁹⁷ Traditionally, olefin hydrogenation processes have been dominated by the use of transition metal-based compounds, most often of the Pt group, however, there has been recent success in the development of systems utilizing more

abundant and less costly first-row transition metal catalysts,⁹⁸ particularly cobalt.^{10, 18b, 40a, 45, 53-54, 56, 99} Well-defined examples of easily-accessible and easily-handled homogeneous catalysts with high activity and functional group tolerability still remain scarce, especially in the case of iron, which is an ideal metal to employ in catalysis,^{6, 8, 100} due primarily to its low cost and high abundance. In the latter portion of section 1.4.1 of this document, the most promising developments regarding homogeneous Fe-catalyzed olefin hydrogenation have been outlined in the form of Chirik's bis(imino)pyridinyl-^{39, 44a} and bis(NHC)pyridinyl-supported³² catalytic systems.

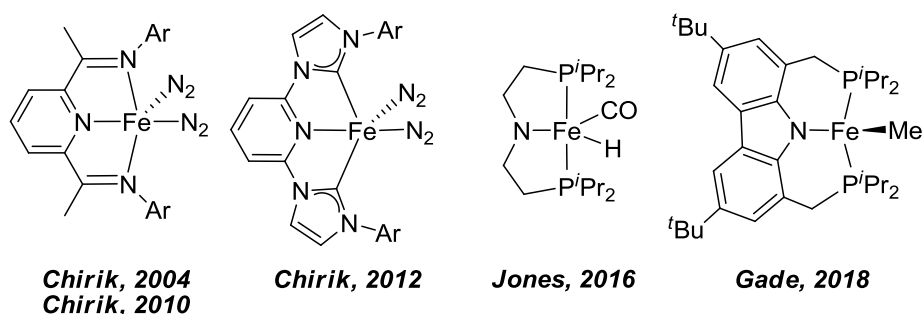


Figure 2.1.1. Examples of existing Fe-based catalysts for the homogeneous hydrogenation of alkenes.

The use of a bis(anthracene) metalate of iron, as well as other related iron-based complexes, for catalytic alkene hydrogenation were also recently explored, however, other than high conversions for a select number of terminal alkenes catalytic performance was quite poor for these systems.¹⁰¹ The hydrogenation of α,β -unsaturated carbonyl compounds by an Fe(II)/EDTA catalyst has also been reported.¹⁰² Monoanionic PNP pincer ligation has explored in the context of Fe-catalyzed alkene hydrogenation. Jones and co-workers¹⁰³ reported the hydrogenation of styrene derivatives using a (PNP)Fe(H)(CO) precatalyst (PNP = N(CH₂CH₂P'Pr₂)₂). While various styrenes, including substrates featuring ester and nitrile substitution on the arene ring, were

reduced with high conversion and selectivity, nonpolar aliphatic alkenes such as 1-hexene were not hydrogenated, even at increased temperature and pressure. Subsequently, Gade and co-workers¹⁰⁴ reported bis(phosphino)pyrrole (PNP)Fe(alkyl) complexes that functioned as precatalysts for alkene hydrogenation. Secondary aliphatic alkenes, such as 2-pentene and 2-hexene, were hydrogenated effectively, while trans-stilbene only reached 34% conversion after 72 h, and the tetrasubstituted alkene 2,3-dimethylbut-2-ene proved unreactive. Outside the realm of well-defined homogeneous Fe-based transition metal catalysts, several reports outline the *in situ* generation of putative Fe hydride clusters, or Fe nanoparticles in solution for alkene hydrogenation applications with varied rates of success.¹⁰⁵

While these examples illustrate headway has already been made in the field of Fe-catalyzed olefin hydrogenation, further effort is needed to develop effective catalysts that not only exhibit high activity and functional group tolerability, but are also easy to handle and not susceptible to decomposition in the presence of substrate.^{39, 43} Further investigation into the stoichiometric chemistry of ligand-supported Fe hydride complexes is also required as such Fe hydride complexes are expected to be vital intermediates in a catalytic cycle wherein coordination and subsequent insertion of the alkene into an Fe-H bond is likely a crucial fundamental synthetic step. In this regard, low-coordinate Fe-complexes supported by appropriate ancillary ligands are important synthetic targets they may promote the coordination of weakly donating or sterically congested alkenes, while at the same time satisfying important electronic requirements for the activation and eventual reduction of an unsaturated substrate.

In this chapter significant progress in the field of (Cy-PSiP)Fe chemistry is outlined. Reliable routes have been devised for the synthesis of the first known 5-coordinate (Cy-PSiP)Fe complexes, and evidence has also been obtained for a low-valent 4-coordinate complex, which appears unstable to 1-electron oxidation or reduction chemistry. Reduction to Fe^{I} and Fe^0 has been observed, and the resulting complexes have demonstrated activity toward the E-H bond cleavage of HBPIn, H_2 and H_2O . More importantly, (Cy-PSiP)Fe hydride chemistry has been explored in detail, including the synthesis of a unique η^2 -silane complex of an Fe^{II} dihydride, as well as a bis(dinitrogen) Fe^{II} hydride, which was found to be an isolable and easily-handled catalyst for the hydrogenation of a variety of alkenes, with examples of high conversion for substituted, unsubstituted and functionalized alkenes.

2.2 Results and Discussion

2.2.1 Synthesis and Reactivity of (Cy-PSiP)Fe(PMe₃)Cl

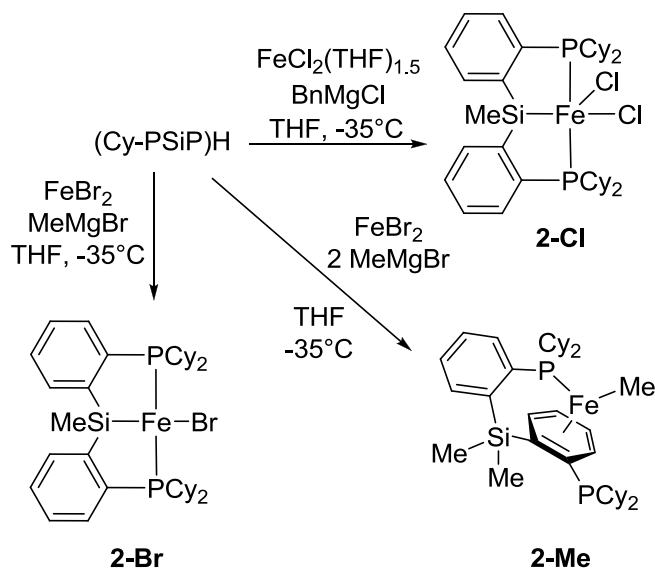
Previous work regarding the development of PSiP complexes of Fe reported by the Sun and Iwasawa groups have focused on the synthesis of saturated, 6-coordinate, 18-electron derivatives.^{25b, 73b} In efforts to uncover new and relevant reactivity toward substrate molecules featuring E-H bonds (*e.g.* hydrogen, silanes, boranes), four-coordinate Fe^{II} complexes of the form (R-PSiP)FeX (X = halide) were first targeted. While examples of Co analogues of this type have been successfully isolated and characterized,^{24d, 73b} to date, no evidence of the corresponding Fe complexes has been observed.

In an analogous fashion to the preparation of (Cy-PSiP)CoI,^{73b, 81} compounds of the form (Cy-PSiP)FeX (X = Cl, Br, I) were targeted through treatment of (Cy-PSiP)H with

an FeX_2 precursor and base. Such a halide complex could serve as a valuable synthon for a variety of other Fe^{II} complexes *via* simple salt metathesis routes, and also Fe^{I} complexes through one-electron reduction with, for example, an alkali or alkali earth metal. While many attempts were made to induce Si-H metalation by varying the iron starting material (FeCl_2 , $\text{FeCl}_2(\text{THF})_{1.5}$, FeBr_2 , $\text{FeBr}_2(\text{THF})_2$, FeI_2 , FeMes_2) or the base used for the dehydrohalogenation step (NEt_3 , MeMgBr , MesMgBr , BnMgCl), these attempts were mostly unsuccessful as the resulting products proved difficult to isolate in pure form. Furthermore, meaningful analysis of the reaction mixtures by NMR spectroscopy was hampered by the paramagnetic nature of the Fe species. In one case (Scheme 2.2.1) a minute amount of X-ray quality crystals of monomeric $(\text{Cy-PSiP})\text{FeBr}$ (**2-Br**) were successfully obtained, supporting at the very least the feasibility of complexes of the desired formulation. The solid state structure of **2-Br** features significantly distorted coordination geometry at the four coordinate Fe center that is intermediate between square planar and tetrahedral ($\text{Si-Fe-Br} = 146.08(03)^\circ$, $\text{P1-Fe-P2} = 134.64(4)^\circ$, $\tau_4 = 0.56$, $\tau'_4 = 0.52$),¹⁰⁶ with κ^3 -coordination of the PSiP ligand (Figure 2.2.1). However, complex **2-Br** could not be isolated reproducibly in appreciable quantities.

Related attempts to generate $(\text{Cy-PSiP})\text{FeCl}$ (Scheme 2.2.1) led to isolation of a small amount of $(\text{Cy-PSiP})\text{FeCl}_2$, **2-Cl**, identified by X-ray crystallographic analysis. The unexpected isolation of a putative Fe^{III} complex implies a concomitant reduction, perhaps through a disproportionation pathway (of $(\text{Cy-PSiP})\text{FeCl}$) wherein the reduced component quickly decomposes to Fe^0 and releases free ligand (free ligand observed by

$^{31}\text{P}\{^1\text{H}\}$ NMR spectroscopy, in addition to generation of a dark insoluble precipitate during the course of the reaction).



Scheme 2.2.1. Synthetic routes for the generation of **2-Br**, **2-Me** and **2-Cl**, illustrating unexpected 1-electron chemistry leading to Fe^{I} and Fe^{III} complexes from an Fe^{II} source.

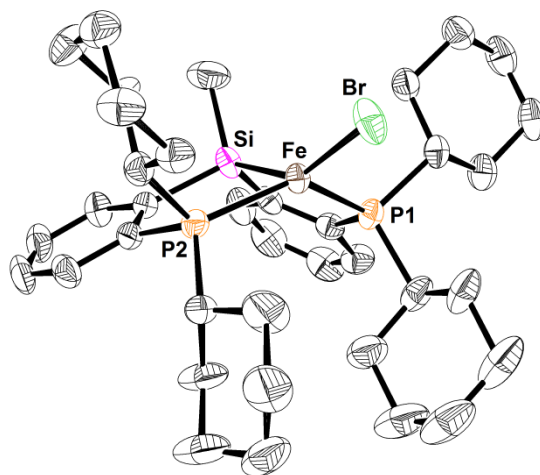


Figure 2.2.1. Crystallographically determined structure of **2-Br**, with thermal ellipsoids shown at the 50% probability level. Hydrogen atoms have been omitted for clarity. Selected interatomic distances (Å) and angles (°): Fe-Br 2.3688(6), Fe-P(1) 2.2965(9), Fe-P(2) 2.2970(9), Fe-Si 2.3440(10), Si-Fe-Br 146.08(3), P(1)-Fe-P(2) 134.64(4), P(1)-Fe-Br 105.96(3), P(2)-Fe-Br 110.21(3), Si-Fe-P(1) 82.19(3), Si-Fe-P(2) 82.81(3).

In a similar vein, in attempts to generate an alkyl derivative of (Cy-PSiP)FeBr, a second equiv of MeMgBr was included in the reaction. A small amount of crystals suitable for single crystal X-ray diffraction were isolated from the reaction mixture, revealing methylation both at Fe, and at Si, generating an (η^6 -arene)Fe^I-methyl complex, **2-Me**, a result of a 1-electron reduction process. While in all of these cases it must be emphasized that the obtained crystals and corresponding X-ray data likely only represent a small portion of the resultant product mixture, the observations nonetheless illustrate the propensity for undesired one-electron redox processes under the current reaction conditions, precluding reproducible isolation of a 4-coordinate Fe^{II} species.

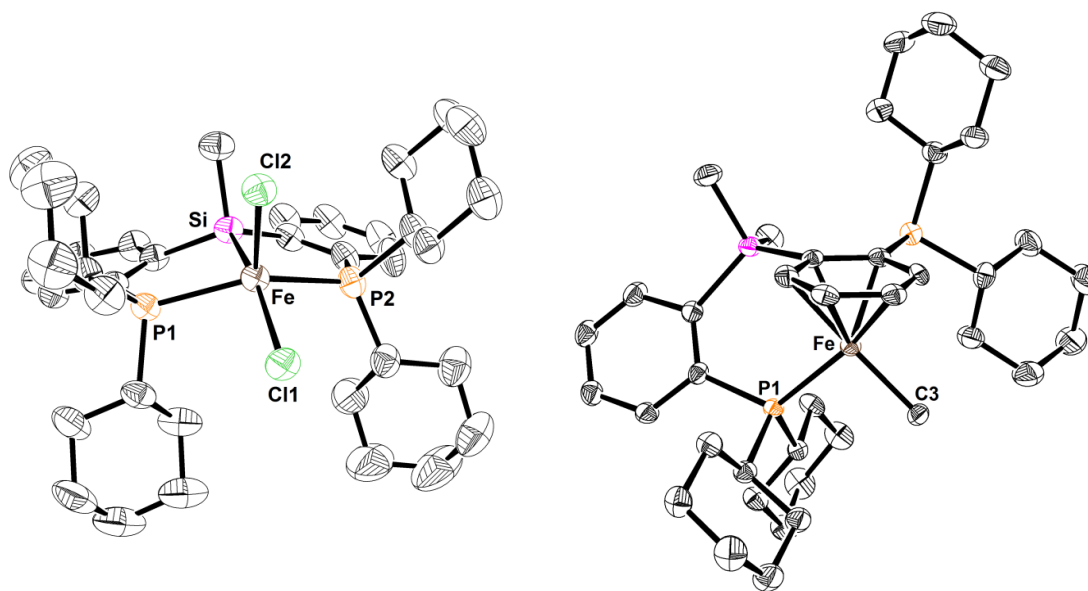
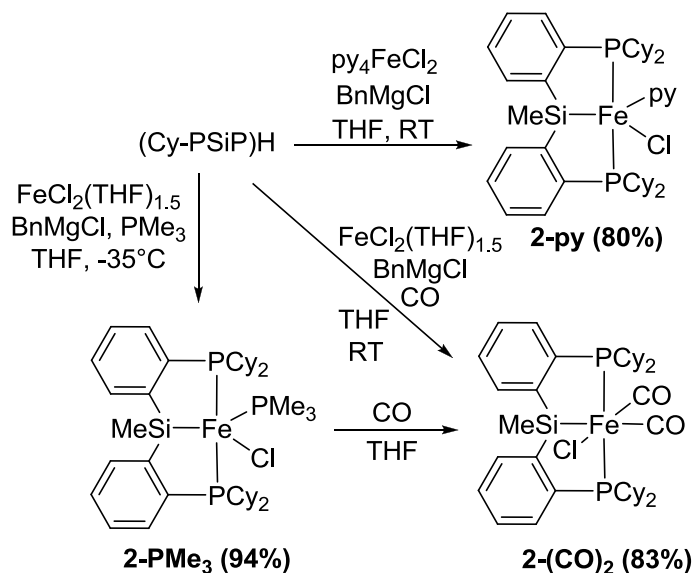


Figure 2.2.2. Crystallographically determined structures of **2-Cl** and **2-Me** with thermal ellipsoids shown at the 50% probability level. Hydrogen atoms have been omitted for clarity. Only one of two crystallographically independent molecules of **2-Me** is shown. Selected interatomic distances (Å) and angles (°) for **2-Cl**: Fe-Cl(1) 2.3121(6), Fe-Cl(2) 2.2657(6), Fe-P(1) 2.3870(6), Fe-P(2) 2.3866(7), Fe-Si 2.4187(6), P(1)-Fe-P(2) 142.75(2), Si-Fe-Cl(1) 157.11(2), Si-Fe-Cl(2) 101.45(2), Cl(1)-Fe-Cl(2) 101.43(2); for **2-Me**: Fe-P(1) 2.2500(10), Fe-C(3) 2.039(3), P(1)-Fe-C(3) 93.61(10)

As complexes of the type (Cy-PSiP)FeX (X = halide) proved challenging to isolate and displayed a tendency toward one-electron decomposition pathways,

stabilization of these reactive compounds with an additional L-donor ligand was pursued. The Sun^{25b} and Iwasawa^{73b} groups generated their (Cy-PSiP)M (M = Fe, Co, Ni) complexes through the use of the zero-valent M(PMe₃)₄ starting materials, and thus the resulting saturated compounds all feature one or two equivs PMe₃ bound to the metal center. With this in mind, we treated a stirring mixture of (Cy-PSiP)H, FeCl₂(THF)_{1.5} and PMe₃ with BnMgCl at -35°C, leading to generation of a transparent red solution (Scheme 2.2.2). After workup, (Cy-PSiP)Fe(PMe₃)Cl (**2-PMe₃**) was obtained as an analytically pure orange solid in 94% yield. Furthermore, use of CO in place of PMe₃ generated the corresponding bis(carbonyl) compound, **2-(CO)₂**, and use of py₄FeCl₂ in place of FeCl₂(THF)_{1.5} + PMe₃, led to the corresponding pyridine complex, **2-py**.



Scheme 2.2.2. Synthetic routes for the preparation of **2-PMe₃**, **2-py** and **2-(CO)₂**.

Solution magnetic moment measurements for **2-PMe₃** and **2-py** (benzene-*d*₆, 300 K) resulted in calculated μ_{eff} values of 3.0 μ_{B} ($S = 1$) and 2.9 μ_{B} ($S = 1$), respectively. X-ray quality crystals of **2-PMe₃** were obtained from a concentrated Et₂O solution at room temperature. The solid state structure of **2-PMe₃** (Figure 2.2.3) confirms the formulation

of this complex as a 16-electron PMe_3 adduct that features distorted trigonal bipyramidal coordination geometry at iron with κ^3 -coordination of the PSiP ligand. The pincer ligand phosphino donors and the PMe_3 ligand are bound in the equatorial plane, while Si and Cl take up the axial positions. The related diamagnetic five-coordinate Ru complex (Cy-PSiP)Ru(PMe_3)Cl adopts a slightly different geometry in the solid state, with one of the pincer ligand phosphino donors and the PMe_3 ligand bound in the axial positions of a similarly distorted trigonal bipyramidal structure.¹⁰⁷ Complex **2- PMe_3** is also closely related in structure to the tris(phosphino)silyl iron chloride complexes $(\text{Si}^{\text{R}}\text{P}_3)\text{FeCl}$ ($\text{Si}^{\text{R}}\text{P}_3 = [(2\text{-R}_2\text{PC}_6\text{H}_4)_3\text{Si}]^-$; R = Ph or ⁱPr) prepared by Peters and co-workers,²¹ which also feature slightly distorted trigonal bipyramidal geometry in the solid state and exhibit similar μ_{eff} values ($\mu_{\text{eff}} = 2.9 \mu_{\text{B}}$ and $3.3 \mu_{\text{B}}$ for R = Ph and ⁱPr, respectively).

Complexes **2- PMe_3** and **2-py** represent the first examples of stable 16-electron (PSiP)Fe complexes reported in the literature. While similarities exist between **2- PMe_3** and the related iron chloride complexes prepared by Peters and co-workers that feature tetradentate tris(phosphino)silyl ligation,²¹ the use of a tridentate ligand allows for the potential dissociation or displacement of PMe_3 from **2- PMe_3** (or pyridine from **2-py**) to more readily access a reactive low-coordinate iron species during the course of a reaction. For example, exposure of a THF solution of **2- PMe_3** to an atmosphere of CO led to displacement of the PMe_3 ligand and clean conversion to the diamagnetic 18-electron bis(carbonyl) complex (Cy-PSiP)Fe(CO)₂Cl (**2-(CO)₂**) which was isolated as a beige solid in 83% yield. Complex **2-(CO)₂** is diamagnetic and forms as a single C_s -symmetric isomer in solution, as indicated by the presence of a single ³¹P{¹H} NMR resonance at 86.2 ppm. The solid state structure of **2-(CO)₂** (Figure 2.2.3) and the presence of two

νCO IR stretches (1969, 1909 cm^{-1}), is consistent with the proposed formulation for this complex as a dicarbonyl species. The 6-coordinate complex features octahedral coordination geometry, with *mer*- κ^3 -coordination of the PSiP ligand.

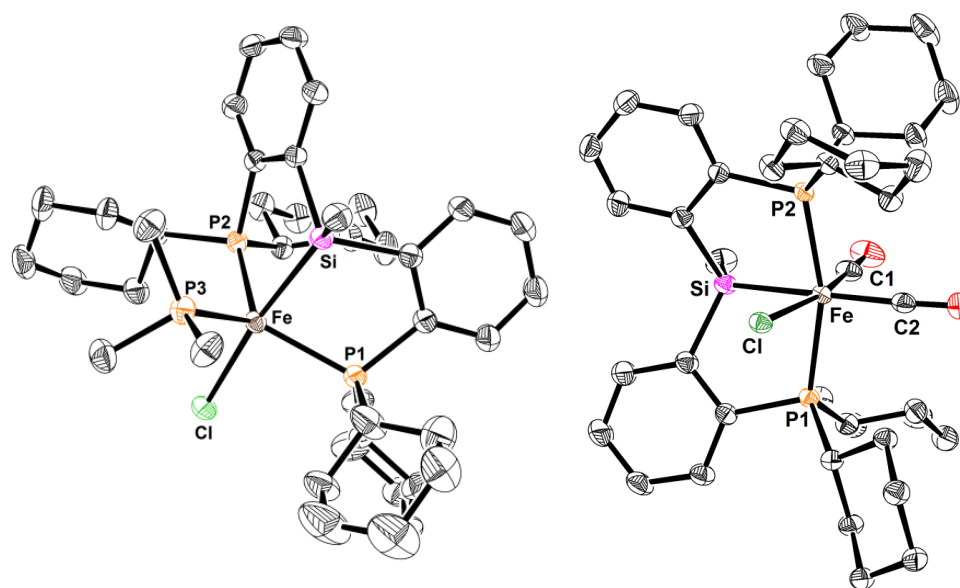


Figure 2.2.3. Crystallographically determined structures of **2-PMe₃** and **2-(CO)₂** with thermal ellipsoids shown at the 50% probability level. Hydrogen atoms and solvent molecules have been omitted for clarity. Only one of two crystallographically independent molecules of **2-PMe₃** and **2-(CO)₂** are shown. Selected interatomic distances (Å) and angles (°) for **2-PMe₃**: Fe-Cl 2.2731(6), Fe-Si 2.3436(6), Fe-P(1) 2.3224(6), Fe-P(2) 2.3346(6), Fe-P(3) 2.3113(6), Cl-Fe-Si 173.20(2), P(1)-Fe-P(2) 122.82(2), P(2)-Fe-P(3) 110.38(2), P(1)-Fe-P(3) 121.93(2); for **2-(CO)₂**: Fe-Cl 2.3435(4), Fe-P(1) 2.2786(4), Fe-P(2) 2.2761(4), Fe-Si 2.3284(5), Fe-C(1) 1.7228(17), Fe-C(2) 1.8203(16), C(1)-O(1) 1.159(2), C(2)-O(2) 1.145(2), Cl-Fe-Si 84.116(15), Cl-Fe-C(2) 101.71(5), C(1)-Fe-C(2) 90.46(8), Si-Fe-C(1) 83.77(6), P(1)-Fe-P(2) 162.500(17).

Salt metathesis reactions were pursued in attempts to replace the chloride ligand of **2-PMe₃** with ligands better suited to potential catalytic applications (*e.g.* hydrides, alkyls, amidos, alkoxys). Excluding the attempted generation of hydride complexes (which will be discussed in detail in section 2.2.4), reactions of **2-PMe₃** with reagents such as AgOTf, LiNH₂, LiNH(2,6-*i*Pr₂C₆H₃), LiCH₂SiMe₃, ^{*n*}BuLi, MeMgBr, BnMgCl, Me₂Zn, NaHCO₂ and NaOMe were attempted. Unfortunately, while in most cases a

reaction seemed to occur based on color change and/or formation of a precipitate, no identifiable products were obtained nor were any observed by NMR spectroscopy, presumably due to their paramagnetic nature. In the case of the targeted alkyl products, it is possible that any generation of an Fe-alkyl complex in this system could lead to ligand rearrangement processes as observed in the synthesis of **2-Me**. In fact ligand rearrangement processes involving (PSiP)M(alkyl) complexes occur rather frequently in the literature, with reported examples from the group 8, 9 and 10 transition metals,²⁵ though thus far none with iron or cobalt specifically. Generation of hydride compounds using both **2-PMe₃** and **2-py** as precursors was met with success (*vide infra*) though investigation of one-electron reduction chemistry was also pursued in further detail.

2.2.2 Reduction of (Cy-PSiP)Fe(PMe₃)Cl

In addition to the attempts at salt metathesis outlined earlier, single-electron reduction of **2-PMe₃** to an Fe^I complex was also pursued. Although the +1 oxidation state is not common for iron, there are several well-characterized examples of Fe^I complexes that have been previously reported, including related tris(phosphino)silyl species prepared by Peters and co-workers.²¹ Co^I complexes of the form (R-PSiP)Co(PMe₃)(N₂) have been synthesized^{73b} and applied toward N₂ reduction catalysis, and in a similar vein, Fe^{II} hydride complexes have also been generated by Iwasawa and co-workers in the same report, however, thus far there has been no well-defined examples of PSiP-supported Fe^I complexes reported in the literature. Such (Cy-PSiP)Fe^I complexes could be susceptible to oxidative addition reactions of E-H bonds (E = main group element), leading to Fe^{III} complexes of the type (Cy-PSiP)Fe(PMe₃)(E)(H). Thus, as a point of entry to this chemistry the analogous Fe complex to (Cy-PSiP)Co(PMe₃)(N₂) was targeted.^{73b} Toward

this end, a solution of **2-PMe₃** in THF was stirred with excess of magnesium overnight under a nitrogen atmosphere (Scheme 2.2.3), leading to the formation of the paramagnetic complex ($\mu_{\text{eff}} = 1.9 \mu_{\text{B}}$, $S = 1/2$) (Cy-PSiP)Fe(PMe₃)(N₂) (**2-Fe^I**), which was isolated as a yellow solid in 61% yield.

X-ray quality crystals of **2-Fe^I** were obtained from an Et₂O solution of **2-Fe^I** at -35 °C. As in the case of **2-PMe₃**, the solid state structure of **2-Fe^I** (Figure 2.2.4) features trigonal bipyramidal coordination geometry at the iron center, with κ^3 -coordination of the PSiP ligand. The pincer ligand phosphino donors and the PMe₃ ligand are bound in the equatorial plane, while Si and N₂ take up the axial positions. The structure of **2-Fe^I** is also similar to that of (Si^{*iPr*}P₃)Fe(N₂) reported by Peters and co-workers.²¹ The N-N bond distance of 1.119(2) Å in **2-Fe^I** is elongated relative to that of 1.065(5) Å observed for (Si^{*iPr*}P₃)Fe(N₂), which suggests increased electron backdonation from the iron center to the N₂ ligand (*cf.* N-N bond length of 1.0975 Å for free N₂). However, the ν_{NN} stretching frequency of 2011 cm⁻¹ observed for **2-Fe^I** is nearly identical to the value of 2008 cm⁻¹ obtained for (Si^{*iPr*}P₃)Fe(N₂), indicating minimal electronic differences between the two complexes (*cf.* $\nu_{\text{NN}} = 2331$ cm⁻¹ for free N₂). As such, the N₂ ligand in **2-Fe^I** is best described as weakly activated.¹⁰⁸

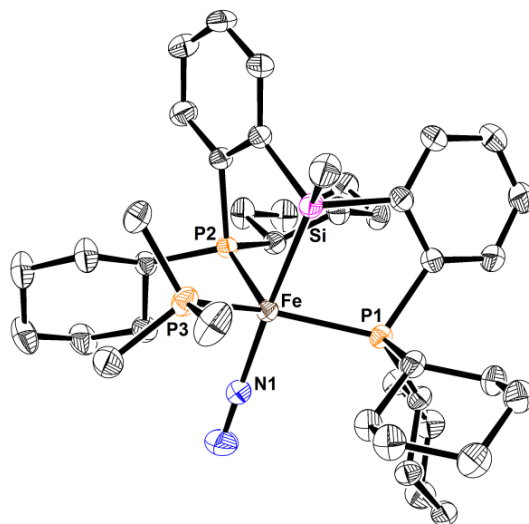
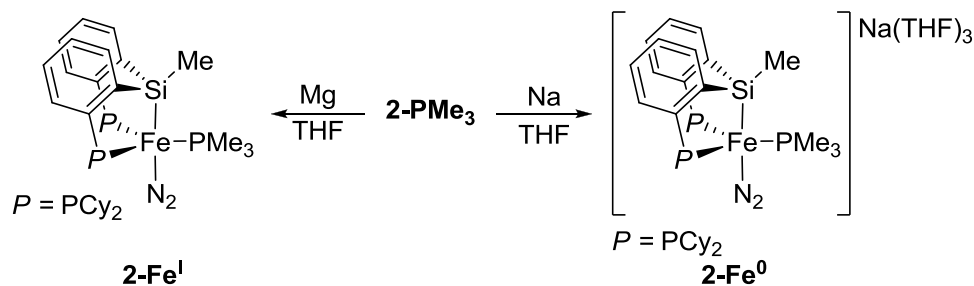


Figure 2.2.4. Crystallographically determined structure of **2-Fe^I** with thermal ellipsoids shown at the 50% probability level. Hydrogen atoms have been omitted for clarity. Only one of two crystallographically independent molecules is shown. Selected interatomic distances (Å) and angles (°): Fe-Si 2.3145(5), Fe-N(1) 1.8191(15), Fe-P(1) 2.2845(4), Fe-P(2) 2.2878(5), Fe-P(3) 2.2253(5), N(1)-N(2) 1.119(2), Si-Fe-N(1) 177.17(5), P(1)-Fe-P(2) 118.122(18), P(2)-Fe-P(3) 103.155(18), P(1)-Fe-P(3) 135.000(19).

The moderate yield of **2-Fe^I** obtained via the Mg reduction of **2-PMe₃** suggested the possibility of undesired side-reactions, or incomplete reaction, during this process. In an effort to address this possibility, the reduction was attempted with Na as the reducing agent to ensure complete reduction to the +1 oxidation state (Scheme 2.2.3). Interestingly, rather than the deep red solution formed in the case of the Mg reduction of **2-PMe₃**, a deep purple solution resulted from stirring a THF solution of **2-Fe^I** with excess sodium metal overnight under a nitrogen atmosphere. The ³¹P{¹H} NMR spectrum of the crude reaction mixture indicated the formation of a single *diamagnetic* product (**2-Fe⁰**, Scheme 2.2.3) featuring two resonances at 92.8 (d, 2 P, ²J_{PP} = 85 Hz) and 10.1 ppm (t, 1 P, ²J_{PP} = 85 Hz). The ¹H NMR spectrum of the crude mixture confirmed the presence of the Cy-PSiP ligand, an equiv of PMe₃, and approximately 3 equiv of THF. Based on these observations, **2-Fe⁰** was formulated as [(Cy-PSiP)Fe(PMe₃)(N₂)] [Na(THF)₃], an example

of an 18-electron, anionic, formally Fe^0 complex. The above formulation is based partly on a report by Peters and co-workers^{22b} who describe the formation of the related complex $[(\text{Si}^{iPr}\text{P}_3)\text{Fe}(\text{N}_2)][\text{Na}(\text{THF})_3]$ upon treatment of $(\text{Si}^{iPr}\text{P}_3)\text{Fe}(\text{N}_2)$ with sodium naphthalide. The $[\text{Na}(\text{THF})_3]^+$ counter-ion in the latter complex is coordinated to the distal nitrogen atom of the N_2 ligand.



Scheme 2.2.3. One- and two- electron reduction of $\mathbf{2-PMe}_3$ to $\mathbf{2-Fe^I}$ and $\mathbf{2-Fe^0}$, respectively.

The two Fe^0 complexes feature identical values for ν_{NN} as measured by IR spectroscopy (1891 cm^{-1}), indicative of considerable activation of the N_2 ligand. Unfortunately, $\mathbf{2-Fe^0}$ was found to be extremely sensitive to moisture and repeated attempts at crystallization and purification for combustion analysis have been unsuccessful. Attempts to silylate the terminal N atom of $\mathbf{2-Fe^0}$ by treatment with Me_3SiCl and $i\text{Pr}_3\text{SiCl}$ resulted in decomposition. Similarly, complexation of the Na^+ ion with crown ethers (*e.g.* dibenzo-15-crown-5), as was reported by Peters and co-workers,^{22b} has consistently led to decomposition.

2.2.3 Reactivity of $(\text{Cy-PSiP})\text{Fe}^I$ and $(\text{Cy-PSiP})\text{Fe}^0$ Complexes

Having successfully reduced $\mathbf{2-PMe}_3$ to both an Fe^I and an Fe^0 species, the reactivity of $\mathbf{2-Fe}^I$ was first probed with respect to oxidative addition E-H bonds (and PhI). Due to the difficulty associated with isolating $\mathbf{2-Fe}^I$ in pure form, this complex was

instead generated *in situ* in some cases by reduction of **2-PMe₃** with Mg in THF solution, and the reaction mixture was subsequently treated with the E-H-containing substrate (or PhI) in a one-pot fashion. For complex **2-Fe^I**, reactivity with PhI, PhNH₂, HBPin, PhC≡CH, PhSiH₃ and H₂, respectively, was probed in THF solution. While in most cases a reaction was observed (based on color change or formation of a precipitate) over the course of ca. 18 h at room temperature, most of these reactions led to the formation of paramagnetic product mixtures from which no pure material could be isolated. In the case of the reaction of **2-Fe^I** with HBPin in THF solvent, a mixture of red and green crystals was obtained by extraction into an Et₂O solution and slow evaporation of the solvent at -35 °C. While X-ray crystallographic analysis of the red crystals was not successful, the solid state structure of the green crystals was determined (Figure 2.2.5). The X-ray crystal structure of the green product revealed an iron hydride species formulated as (Cy-PSiP)Fe(PMe₃)(H)(N₂)_{0.125} (**2-H(N₂)**), whereby the N₂ ligand has an occupancy factor of 12.5%, indicating that the material represents a co-crystal of (Cy-PSiP)Fe(PMe₃)(H) (87.5%) and (Cy-PSiP)Fe(PMe₃)(H)(N₂)^{73b} (12.5%).

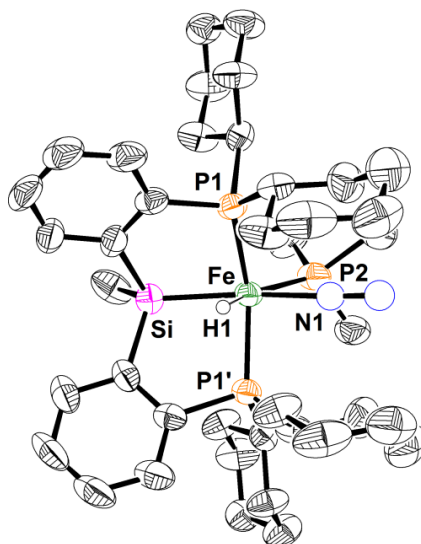
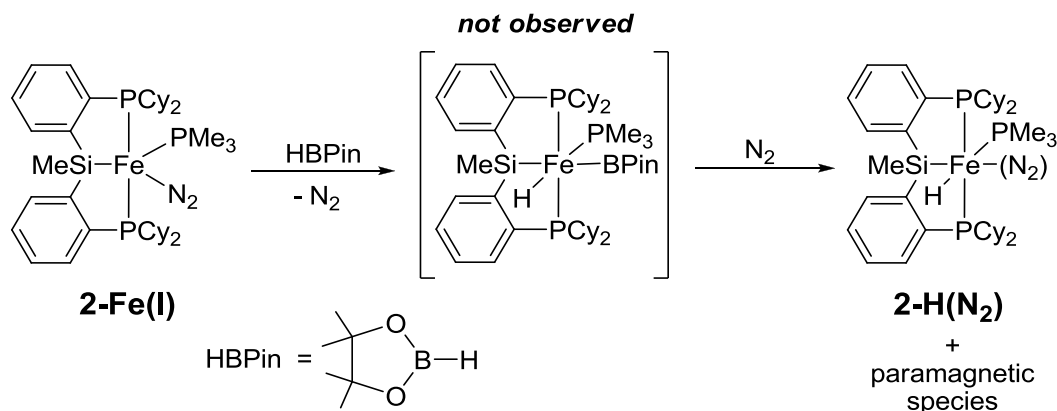


Figure 2.2.5. The crystallographically determined structure of **2-H(N₂)** shown with 50% displacement ellipsoids. Most hydrogen atoms have been omitted for clarity. The coordinated N₂ is shown as blue spheres to indicate partial (12.5%) occupancy. Selected interatomic distances (Å) and angles (°): Fe-Si 2.277(2), Fe-P(1) 2.2076(14), Fe-P(1)′ 2.2076(14), Fe-P(2) 2.209(3), Fe-H(1) 1.42(8), Fe-N(1) 2.05(5), N(1)-N(2) 1.12(7), P(1)-Fe-P(1)′ 147.24(9), P(2)-Fe-Si 126.25(10), P(2)-Fe-N(1) 74.0(14), N(1)-Fe-H(1) 85(3), Si-Fe-H(1) 75(3).

Like the fully-N₂ occupied analogue of **2-H(N₂)** reported by Iwasawa and co-workers,^{73b} the solid state structure of **2-H(N₂)** features octahedral geometry at the iron center with the hydride ligand coordinated *trans* to PMe₃. In this case, however, an empty coordination site is *trans* to Si that is partially occupied (12.5%) by N₂. The acute Si-Fe-H bond angle, 75(3)°, is reminiscent of other metal hydride complexes of the Cy-PSiP ligand, such as (Cy-PSiP)IrHCl and (Cy-PSiP)RhHCl, which also feature acute Si-M-H bond angles of 68.7(18)° and 65.8(12)°, respectively.⁷⁴ The short Si⋯H1 distance of *ca.* 2.34 Å is consistent with a potential interaction between Si and H1, as the distance is well within the sum of the Van der Waals radii of the two atoms (3.4 Å). However, this distance is relatively long by comparison with many η²-(SiH) complexes (Si⋯H distances in the range of 1.7 – 1.8 Å typically indicate σ-coordination),¹⁰⁹ and thus it cannot be definitively assigned as an example of σ-(SiH) coordination. The lack of the

expected BPin fragment in the structurally characterized product suggests that the hydrido boryl complex that is presumed to be an intermediate in the formation of **2-H(N₂)** (Scheme 2.2.4) is not stable, perhaps due to the steric strain that would be associated with a complex of the form (Cy-PSiP)Fe(PMe₃)(BPin)(H). While it is possible that the BPin fragment is lost by way of a bimolecular process involving B-B coupling to generate the PinB-BPin dimer (B₂Pin₂), no evidence of B₂Pin₂ was observed by ¹¹B NMR analysis of the reaction mixture, which only revealed an extremely broad resonance centered at -2.0 ppm. Thus it appears more likely that the BPin fragment is lost through a decomposition pathway, possibly involving unobserved (by NMR analysis), paramagnetic iron species. As a result, this reaction was not found to be reproducible.



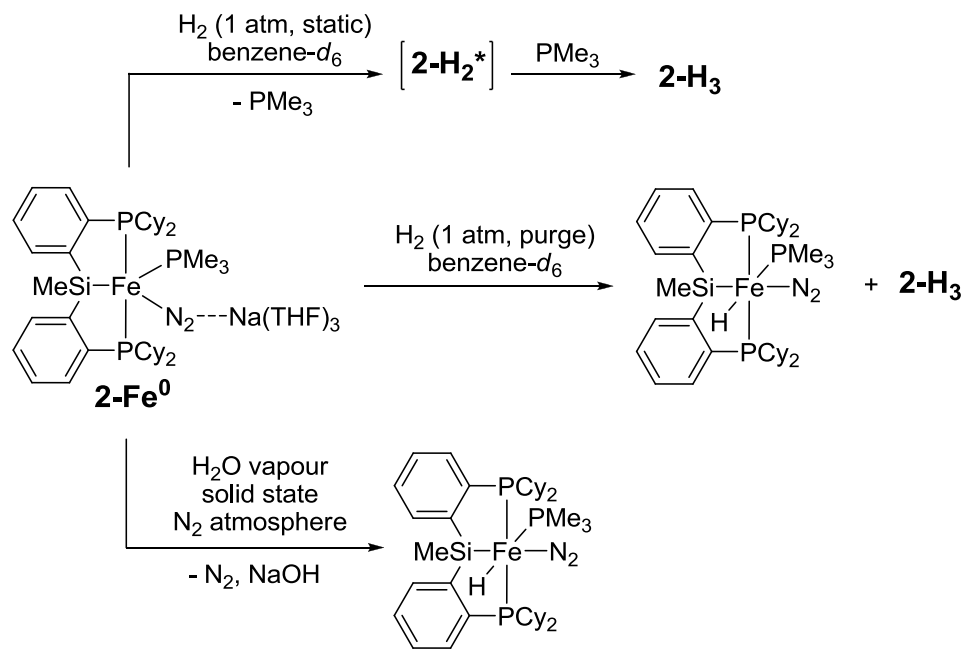
Scheme 2.2.4. Synthetic route for the preparation of (Cy-PSiP)Fe(PMe₃)(H)(N₂) (**2-H(N₂)**).

By comparison, upon treatment of **2-Fe⁰** with 1 atm of H₂ (Scheme 2.2.5), a rapid color change from purple to orange was observed over the course of 1-2 minutes. After approximately 1 h at room temperature, the ³¹P{¹H} NMR spectrum of the reaction mixture indicated the presence of (Cy-PSiP)H, free PMe₃, and a major product (**2-H₂***) giving rise to a singlet resonance at 105.3 ppm (*ca.* 2:1 ratio of **2-H₂*** to PMe₃, where **2-H₂*** and PMe₃ comprise 70% of the phosphorus-containing species, by ³¹P{¹H} NMR).

The ^1H NMR spectrum of this mixture features upfield shifted resonances at -8.45 ppm (broad) and -17.76 ppm (t, $J = 58$ Hz) that could be attributed to iron hydride species. The identity of **2-H₂*** remains unknown, as over time it appears to react with the free PMe_3 present in solution. Over the course of 12-18 h at room temperature, the $^{31}\text{P}\{^1\text{H}\}$ NMR resonance at 105.3 ppm diminishes drastically in intensity as does the resonance corresponding to free PMe_3 , while resonances corresponding to another new diamagnetic product (**2-H₃**) appear. This new product features $^{31}\text{P}\{^1\text{H}\}$ resonances centered at 100.8 ppm (d, $^2J_{\text{PP}} = 29$ Hz, 2 P) and 18.7 ppm (t, $^2J_{\text{PP}} = 30$ Hz, 1 P), indicating re-coordination of PMe_3 to the metal center. In addition, by ^1H NMR, broad multiplet patterns centered at -9.5 , -9.8 and -14.5 ppm appear, which all seem to be attributed to the single product, implying the presence of multiple hydride environments. The fate of the sodium ion (from **2-Fe⁰**) is unknown, as no precipitate was observed during the course of the reaction. When the reaction of **2-Fe⁰** with H_2 was carried out in the presence of BPh_3 (to trap any displaced PMe_3) a paramagnetic material that resisted crystallization attempts was produced, with concomitant generation of $\text{Me}_3\text{P}\cdot\text{BPh}_3$ (by $^{31}\text{P}\{^1\text{H}\}$ and ^{11}B NMR).

When the reaction of **2-Fe⁰** with H_2 was repeated under a purge of H_2 (Scheme 2.2.5), either at room temperature or at 40 °C, **2-H₃** was once again generated along with yet another new diamagnetic product (5:1 ratio for the room temperature reaction) giving rise to $^{31}\text{P}\{^1\text{H}\}$ NMR resonances at 84.2 (d, $^2J_{\text{PP}} = 17$ Hz) and 10.8 ppm (t, $^2J_{\text{PP}} = 18$ Hz) and a new hydride signal -14.85 ppm (dt, $^2J_{\text{HP}} = 24$ Hz, $^2J_{\text{HP}} = 69$ Hz), by ^1H NMR. Based on the nearly identical spectroscopic features of this new product to that of $(\text{Cy-PSiP})\text{FeH}(\text{PMe}_3)(\text{N}_2)$, reported by Iwasawa *et al.*,^{73b} this diamagnetic compound is assigned as such. Notably, this iron hydride complex is also generated as the major

product of a solid-state reaction of **2-Fe⁰** with water vapour carried out under an N₂ atmosphere, which presumably generates NaOH as a side product (Scheme 2.2.5), while in this case stoichiometry suggests NaH is generated as a by-product.



Scheme 2.2.5. Generation of hydride containing complexes on reaction of **2-Fe⁰** with H₂ gas and with H₂O vapour.

2.2.4 Rational Preparation of Fe^{II}-hydride Complexes

With the reaction of **2-Fe⁰** with dihydrogen and water leading to a variety of diamagnetic hydride complexes, identification of the remaining unknown compounds, particularly **2-H₃**, was pursued *via* their rational preparation. Thus, as an initial route to new Fe-hydride chemistry, **2-PMe₃** was treated with one equiv NaEt₃BH (Scheme 2.2.6). After workup, one major product, **2-H**, was initially isolated as a white solid, featuring, by ¹H NMR, a single hydride resonance centered at -18.53 ppm as a triplet of doublets (²J_{PH} = 64.2 Hz, ³J_{PH} = 24.0 Hz). These spectroscopic signatures are very similar to that of (Cy-PSiP)FeH(PMe₃)(N₂) reported by Iwasawa and co-workers,^{73b} and, in fact, this N₂ adduct is generally produced in small amounts along with **2-H**, and further conversion

from **2-H** to the N₂ adduct is also observed over time (ca. 30% conversion of **2-H** to (Cy-PSiP)FeH(PMe₃)(N₂) after 3 days in solution under an N₂ atmosphere, Scheme 2.2.6). Thus **2-H** is tentatively assigned as (Cy-PSiP)FeH(PMe₃), a five-coordinate analogue of Iwasawa's dinitrogen complex. X-ray quality crystals were obtained, and the solid state structure confirms the proposed formulation for this complex.

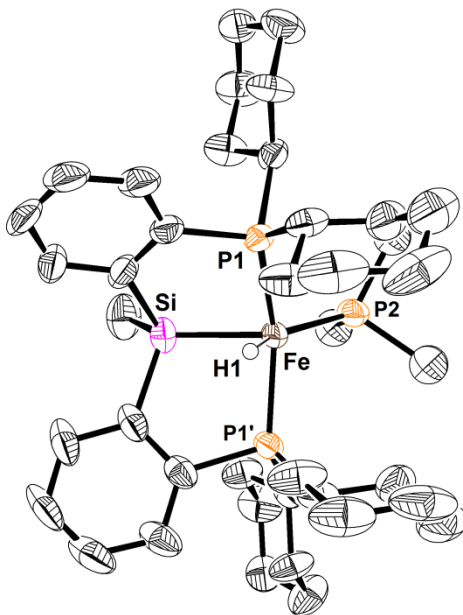
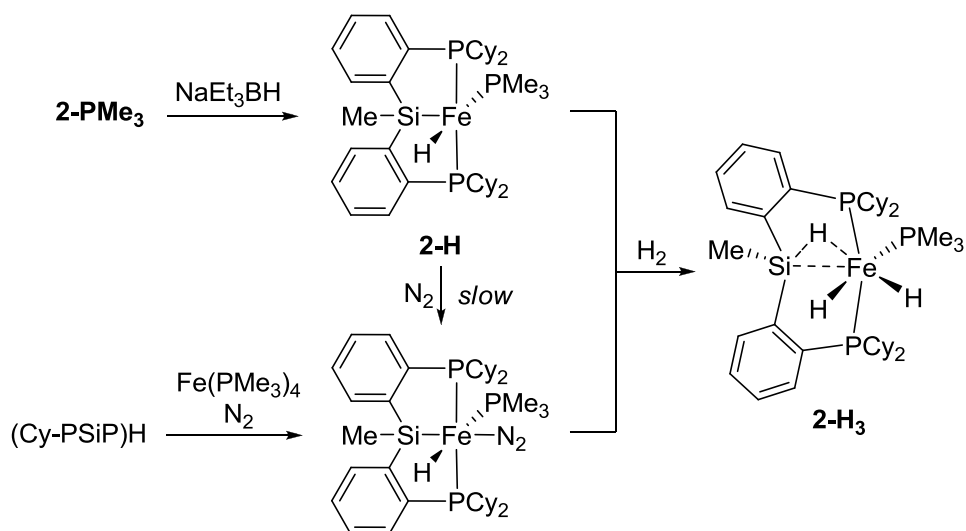


Figure 2.2.6. Crystallographically determined structure of **2-H** with thermal ellipsoids shown at the 50% probability level. Most hydrogen atoms have been omitted for clarity. Selected interatomic distances (Å) and angles (°): Fe-Si 2.2727(17), Fe-H(1) 1.43(6), Fe-P(1) 2.2081(10), Fe-P(2) 2.2044(18), Fe-P(1') 2.2080(10), Si-Fe-H(1) 75(2), P(1)-Fe-H(1) 73.54(6), P(1)-Fe-P(2), 104.61(3), P(1)'-Fe-P(2) 104.61(3), P(1)'-Fe-H 73.54(6).

Complex **2-H** features square pyramidal coordination geometry in the solid state, such that the silyl ligand donor occupies the axial position. The Si-Fe-H1 angle of *ca.* 75(2)° is acute and the Si···H1 distance of *ca.* 2.480 Å is less than the sum of the van der Waals radii for these atoms (3.4 Å). These metrical parameters are comparable to those measured for **2-H(N₂)** (*cf.* Si-Fe-H1 angle of 74.3° and Si···H1 = 2.336 Å for **2-H(N₂)**), and for (Cy-PSiP)FeH(PMe₃)(N₂) (Si-Fe-H angle of 83.2(15)°, Si···H1 not explicitly reported^{73b}). The solid state structure of the related complex (Cy-PSiP)Ru(PMe₃)H has

previously been reported, and features similar coordination geometry.¹⁰⁷ The J_{SiH} value of 19 Hz obtained for **2-H** falls outside the generally accepted range of values taken to indicate σ -(SiH) coordination (accepted values of J_{SiH} for σ -silane complexes range from ca. 40 - 70 Hz, however lower values are possible in some circumstances¹¹⁰). The downfield ^{29}Si chemical shift (77 ppm) as well as the value of ν_{FeH} (1815 cm^{-1}) lend support for the formulation of **2-H** as a classical silyl hydride complex. As these crystals were obtained under an N_2 atmosphere, the assignment of **2-H** as an N_2 -less analogue of $(\text{Cy-PSiP})\text{FeH}(\text{PMe}_3)(\text{N}_2)$ is not unreasonable, especially considering the spectroscopic similarities between the two samples. Thus it appears that when generated from **2-PMe₃**, coordination of dinitrogen to the resultant hydride is relatively slow, whereas when the hydride is accessed directly from reaction of $(\text{Cy-PSiP})\text{H}$ with $\text{Fe}(\text{PMe}_3)_4$, as per Iwasawa's synthetic route, only the dinitrogen coordinated analogue is obtained (Scheme 2.2.6). While some coordination of N_2 to **2-H** is observed, removal of dinitrogen through sequential freeze-pump-thaw cycles did not lead to regeneration of **2-H**.



Scheme 2.2.6. Generation of **2-H** and its conversion to $(\text{Cy-PSiP})\text{FeH}(\text{PMe}_3)(\text{N}_2)$, as well as reaction of either complex with H_2 to generate the polyhydride complex, **2-H₃**.

Interestingly, mixtures of **2-H** and (Cy-PSiP)FeH(PMe₃)(N₂) were found to react further upon standing in benzene solution (Scheme 2.2.6), generating **2-H₃**, the same multiple hydride-containing complex observed during the course of investigating the reactivity of **2-Fe⁰** toward H₂. Full conversion to this product was not observed directly from **2-H** or (Cy-PSiP)FeH(PMe₃)(N₂) (*ca.* 10% conversion to **2-H₃** over 3 days), and the conversion was accompanied by growth of signals in the -5 to -9 ppm region by ³¹P{¹H} NMR, perhaps indicative of demetalation of the Cy-PSiP ligand scaffold in some manner. Intrigued by a potential new route to this, as yet, unidentified product, a solution of a mixture of **2-H** and (Cy-PSiP)FeH(PMe₃)(N₂) was exposed to an atmosphere of H₂ gas to encourage formation of **2-H₃**. After a short period of heating at 65 °C, full and clean conversion to the desired product was achieved. X-ray quality crystals of the sample were obtained through slow evaporation of a benzene solution at room temperature, revealing **2-H₃** to be an η²-(SiH) complex of an Fe^{II} dihydride.

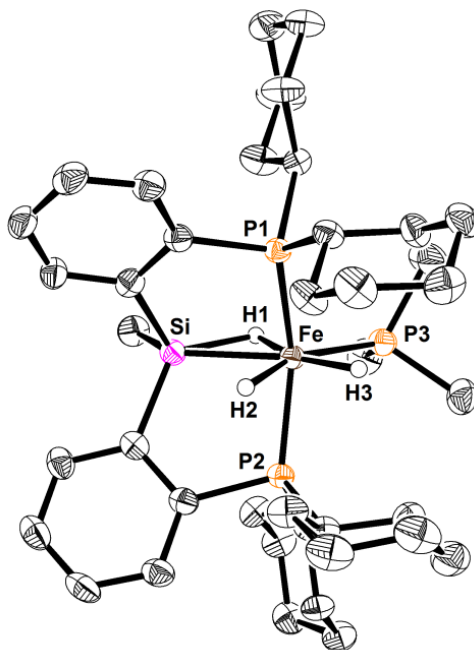


Figure 2.2.7. Crystallographically determined structure of **2-H₃** with thermal ellipsoids shown at the 50% probability level. Most hydrogen atoms have been removed for clarity. Only one of two crystallographically independent molecules is shown. Selected interatomic distances (Å) and angles (°): Fe-Si 2.2806(8), Fe-P(1) 2.2034(8), Fe-P(2) 2.1984(8), Fe-P(3) 2.2053(8), Fe-H(1) 1.49(4), Fe-H(2) 1.57(3), Fe-H(3) 1.54(4), Si-Fe-H(1) 50.7(14), P(3)-Fe-H(1) 78.7(14), P(3)-Fe-H(3) 77.8(14), H(2)-Fe-H(3) 83.9(19), Si-Fe-H(2) 69.6(13), P(1)-Fe-P(2) 147.56(3).

2-H₃ adopts distorted octahedral geometry in the solid state featuring *mer-κ³*-coordination of the PSiP ligand. The Fe-Si distance for **2-H₃** (2.2806(8) Å) is well within the expected range for an Fe-Si interaction (*cf.* Fe-Si distances of 2.2472(4) – 2.2844(4) Å for all (PSiP)Fe hydride complexes reported in this chapter). The Fe-H(1) distance of 1.49(4) Å is somewhat elongated relative to related hydride complexes (*cf.* Fe-H distances of 1.418(19) – 1.441(18) Å for all other (PSiP)Fe hydride complexes reported in this chapter), however, the Fe-H(2) and Fe-H(3) distances (1.57(3) Å and 1.54(4) Å, respectively) are also elongated in this complex. Most striking is the acute Si-Fe-H(1) angle of 50.7(14)°, indicative of significant distortion and a likely interaction between Si and H1 in the solid state. The measured distance of *ca.* 1.73 Å between Si-H1 is much

less than the sum of the van der Waals radii of the two atoms (3.4 Å), supporting an Si-H interaction in the solid state. The same can be said for Si-H2, with a measured distance of 2.34 Å, which, though significantly longer than the Si-H1 distance, is still less than sum of the van der Waals radii of the two nuclei. These metrical parameters support the formulation of **2-H₃** as an η^2 -(SiH) complex (through H1) of an Fe dihydride, with a potential secondary interaction between Si and H2 based on their proximity,¹⁰⁹ and the solution state spectroscopic data also lend support for this assignment (*vide infra*).

By ¹H NMR, each of H1, H2 and H3 (as labelled in Figure 2.2.7) exist in unique environments, as evidenced by three unique Fe-H ¹H NMR resonances, a complex multiplet centered at -9.7 ppm and two broad multiplet resonances centered at -9.4 and -14.6 ppm, which are assigned as H1, H2 and H3, respectively (detailed discussion of assignments to follow). At room temperature, selective 1D NOESY experiments (0.5 s mixing time, Figure 2.2.11C) indicate exchange between all three environments, consistent with the behavior upon addition of D₂ gas (*vide infra*). A ²⁹Si HMQC experiment was employed to assign H1 as the -9.7 ppm multiplet (¹J_{SiH} = 65 Hz). No correlation between ²⁹Si and either H2 or H3 was observed for any 2D ²⁹Si NMR experiment employed (¹H-²⁹Si HMQC, ¹H-²⁹Si HMBC). A recent review by Corey¹¹¹ outlines and tabulates spectroscopic data of a variety of metal-silyl and silane complexes, however, in general it was concluded that there is a considerable amount of ambiguity from complex to complex, and definitive assignment of a particular compound as, for example, η^1 -(Si-H-M), η^2 -(Si-H) or some other type of ‘non-classical’ interaction based on spectroscopic data is not a straightforward endeavour. Based on the value of 65 Hz for J_{SiH} and the ²⁹Si chemical shift (32.7 ppm) of **2-H₃**, the complex may appear to exhibit

‘non-classical’ behavior with respect to the Si-H-Fe interaction. However, the possibility that **2-H₃** exists as an Fe^{IV} silyl trihydride complex cannot be entirely ruled out, though this high oxidation state would be unusual for a *3d* metal. Furthermore, the lack of any measurable coupling between Si and H2 and H3 does not support this Fe^{IV} assignment, or indeed the presence of a significant Si-Fe interaction whatsoever.

Due to the extensive signal broadening at room temperature, variable temperature NMR experiments were carried out. Upon cooling (Figure 2.2.8), the signals in the hydride region of the ¹H spectrum gradually sharpened, with the best resolved coupling observed at a temperature of 253 K. Cooling further did not lead to further signal resolution and, while shimming quality worsened, in general, lineshape patterns remained consistent between 193 – 273 K. At higher temperatures (Figure 2.2.9), the broadened resonances begin to coalesce, with the signals corresponding to H2 and H3 coalescing at approximately 343 K. The signal for H1 also broadens significantly, though due to instrumental limitations complete coalescence of this signal could not be observed, though is anticipated to occur at a temperature higher than 353 K.

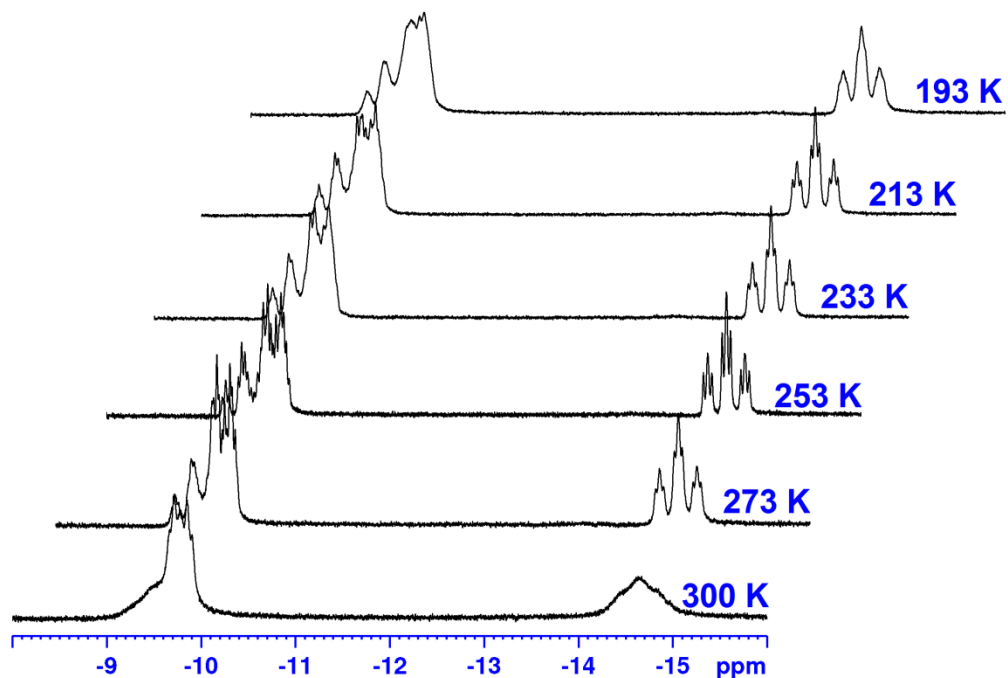


Figure 2.2.8. Overlay of hydride region of low-temperature ^1H NMR (300 MHz) spectra for 2-H_3 between 193 – 300 K. Detailed NMR data (*vide infra*) was collected at 253 K.

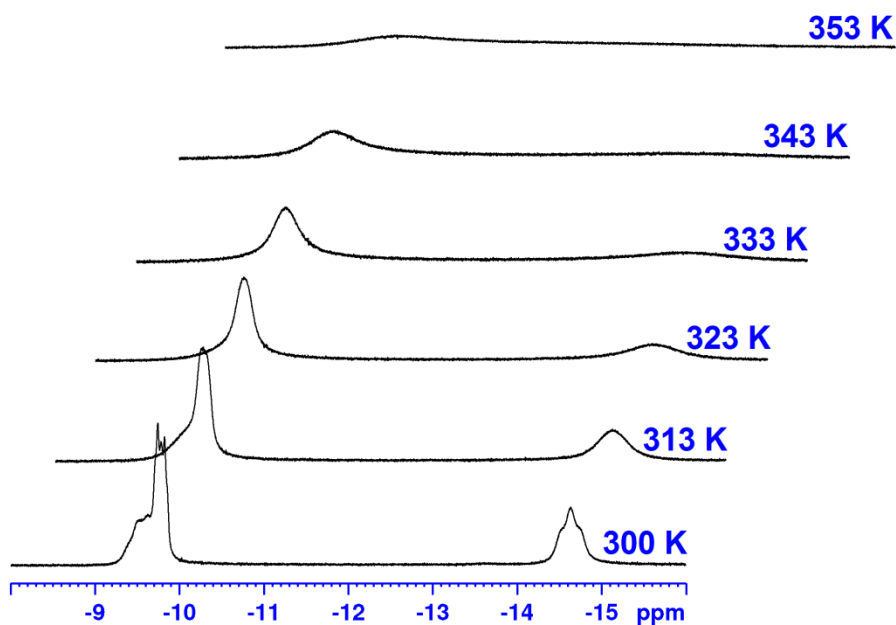


Figure 2.2.9. Overlay of hydride region of high-temperature ^1H NMR spectra (500 MHz) between 300 – 353 K. First coalescence (of H2 and H3) occurs at *ca.* 343 K, second coalescence (of H1, H2 and H3) likely occurs above 353 K.

Additional NMR experiments were carried out at 253 K where the best signal resolution was observed. 2D ^{29}Si NMR experiments revealed the same result as at room temperature, with Si coupling only to H1. A $^1\text{H}\{^{31}\text{P}\}$ experiment (Figure 2.2.10A) with the broadband decoupler centered at 59.8 ppm (*i.e.* the midpoint between both phosphorus resonances) allowed for approximate measurement of the $^2J_{\text{HH}}$ values for the three hydride signals, which were found to be on the order of approximately 8-11 Hz. Interestingly, no coupling was observed between H1 and H3, whose signals both appear as simple doublets in the $^1\text{H}\{^{31}\text{P}\}$ experiment, while the signal for H2 appears as an apparent triplet (overlapping doublet of doublets). This observation was corroborated with a ^1H - ^1H COSY experiment, where a cross peak was observed between the H2 and H3 signals, but not between the H1 and H3 signals.

Selective 1D TOCSY NMR experiments were also carried out with mixing times of 0.025 s and 0.050 s, with the signal for H3 being irradiated. For the longer mixing time experiment, responses were observed for both H1 and H2 signals (Figure 2.2.10C), while with a shorter mixing time only the signal for H2 responds (Figure 2.2.10B). This result implies that while there is indeed some through-bond coupling between H1 and H3, its magnitude is significantly smaller than that of J_{H1H2} , and is too small to be observed by traditional $^1\text{H}\{^{31}\text{P}\}$ or ^1H - ^1H COSY NMR experiments. A 1D TOCSY NMR experiment was also carried out, irradiating the overlapping signals of H1 and H2 with a 0.050 s mixing time (Figure 2.2.10B). Predictably, the H3 signal responds strongly, however, a significant response of the SiMe resonance was also observed. While it is unclear as to whether this is attributed to H1 or to H2, it does indicate that one or both of these atoms exhibits stronger coupling to the SiMe protons than does H3 (for which only a very small

SiMe response was observed for the same experiment), supporting the assignment of the -14.6 ppm multiplet as the hydride distal to Si, H3.

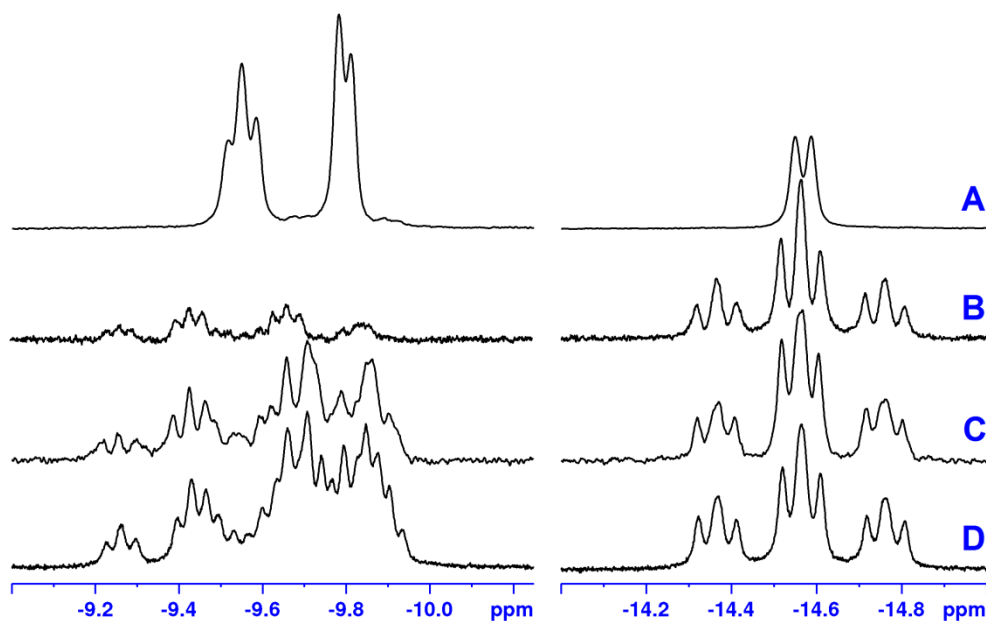


Figure 2.2.10. (A) Hydride region of $^1\text{H}\{^{31}\text{P}\}$ spectrum for **2-H₃** (253 K). (B) Hydride region of 1D TOCSY NMR spectrum for **2-H₃** (253 K, 0.025 s mixing time, H3 irradiated). (C) Hydride region of 1D TOCSY NMR spectrum for **2-H₃** (253 K, 0.05 s mixing time, H3 irradiated). (D) Hydride region of ^1H NMR spectrum for **2-H₃** (253 K).

Selective 1D NOESY experiments were also carried out at 253 K, irradiating either the overlapping H1 and H2 resonances (Figure 2.2.11A) or the resonance for H3 (Figure 2.2.11B). In the first case, significant responses are observed for both the SiMe signal (1.21 ppm), and the PMe₃ signal (1.34 ppm). No significant response from either SiMe nor PMe₃ is observed when H3 is irradiated. This may support the notion that the geometry observed in the solid state structure is retained somewhat in solution, with H3 located distal to Si, and on the opposite face of the molecule from SiMe.

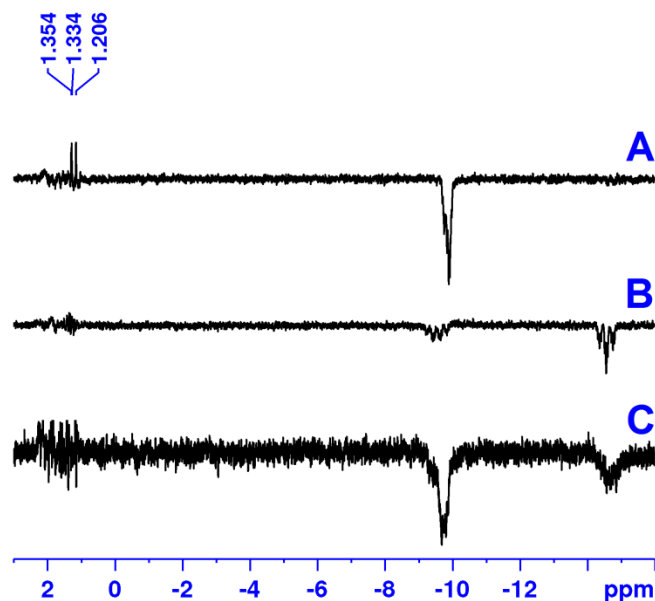


Figure 2.2.11. (A) 1D NOESY spectrum for **2-H₃** (253 K, 0.5 s mixing time, H1 and H2 irradiated). (B) 1D NOESY spectrum for **2-H₃** (253 K, 0.5 s mixing time, H3 irradiated). (C) 1D NOESY spectrum for **2-H₃** (300 K, 0.5 s mixing time, H3 irradiated).

Approximate values of ${}^2J_{\text{PH}}$ for H2 and H3 were extracted from the measured 1D TOCSY spectrum (Figure 2.2.10B) where the complex multiplet at -9.7 ppm corresponding to H1 has been eliminated from the spectrum. Coupling between the Cy-PSiP phosphorus nuclei and both H2 and H3 are quite similar (${}^2J_{\text{H2-PCy2}} \approx 50$ Hz, ${}^2J_{\text{H3-PCy2}} \approx 59$ Hz), implying a *cis*-relationship between these nuclei, consistent with the solid state structure. There is, however, a significant difference between values of ${}^2J_{\text{H-PMe3}}$ for these two hydrides, with ${}^2J_{\text{H2-PMe3}} \approx 71$ Hz, and ${}^2J_{\text{H3-PMe3}} \approx 12$ Hz. These values suggest a significant difference in the geometric relationship of H2 and H3 toward PMe₃, with H2 likely more *trans*-disposed to PMe₃ and H3 more *cis*-disposed, once again, this is consistent with the solid state structure. For H1, values of ${}^2J_{\text{PH}}$ were determined *via* a ${}^1\text{H}$ - ${}^{31}\text{P}$ HMBC experiment giving values of ${}^2J_{\text{H1-PCy2}} \approx 16$ Hz and ${}^2J_{\text{H1-PMe3}} \approx 41$ Hz, again implying a *cis*-relationship between these nuclei, consistent with the X-ray crystal structure. Iterative simulation of these experimentally determined values for **2-H₃**

revealed an ABXY₂Z spin system, where Y₂Z represents the phosphorus nuclei, X is the well-behaved H3 nucleus, and AB represent the H1 and H2 nuclei. Precise values of ²J_{HH} and ²J_{PH} (those reported in the experimental section) are derived from these calculations which were confirmed through comparison of simulated spectra using these parameters and experimental spectra collected at two magnetic field strengths (Figure 2.2.12).

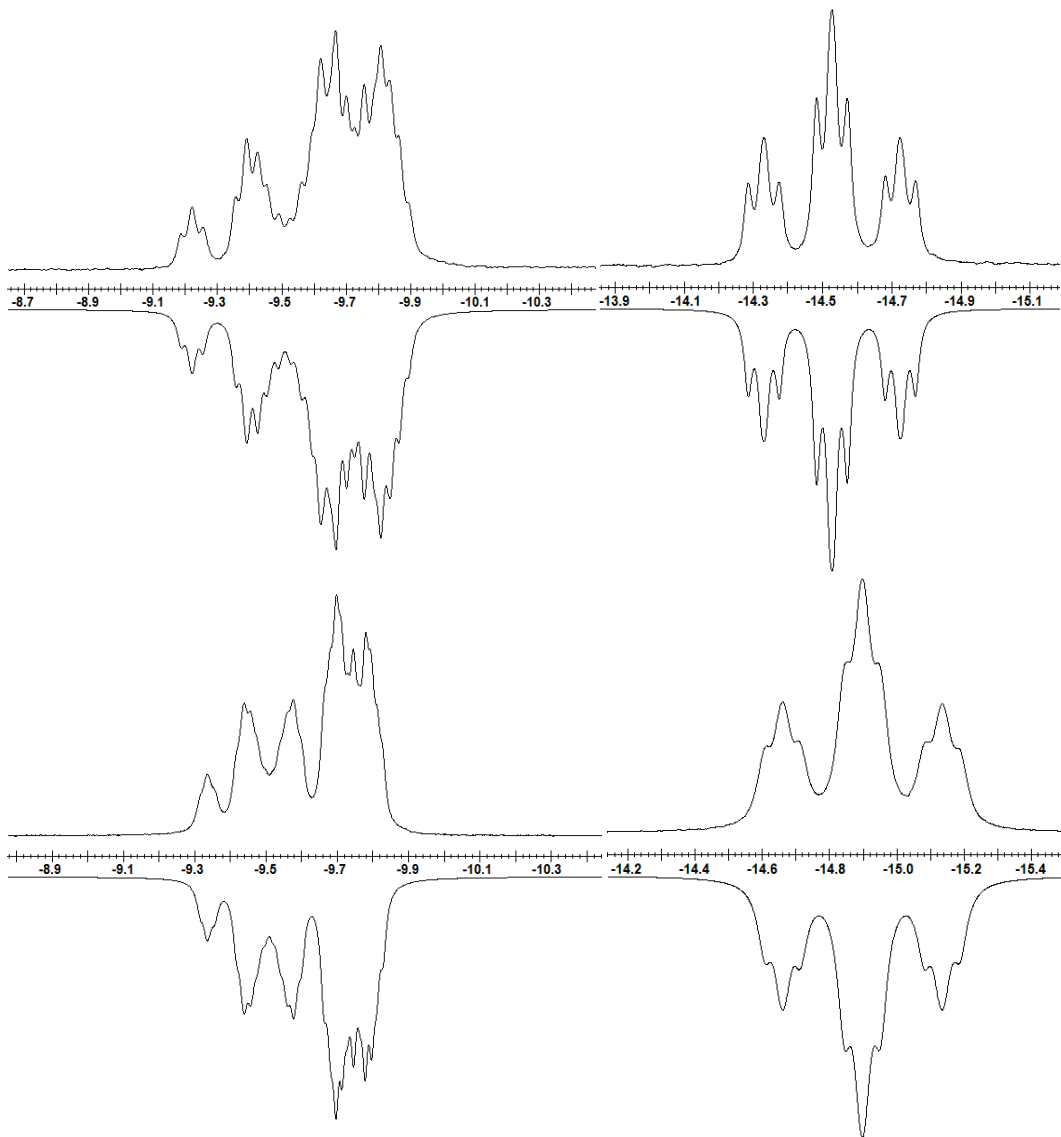


Figure 2.2.12. Experimental (positive projections) and simulated (negative projections) spectra of the hydride resonances for **2-H₃**. Top: 300 MHz, 253 K (toluene-*d*₈). Bottom: 500 MHz, 268 K (toluene-*d*₈).

Overall, the solution state structure of **2-H₃** does appear to be generally consistent with the solid state structure determined through X-ray crystallographic analysis. The presence of stronger Fe-H1 and Si-H1 interactions and a weaker Fe-Si interaction may offer an explanation for the lack of measurable Si coupling to H2 and H3. Sabo-Étienne¹⁰⁹ has previously described the importance of secondary interactions in silane complexes of ruthenium, and has noted that Si-H distances between 1.9 – 2.4 Å may indicate the presence of a ‘secondary interaction between a silicon and a hydrogen atom’ (SISHA). Thus, as the Si-H2 distance of 2.27 Å falls within this range, the presence of such an interaction (depicted in Figure 2.2.13C) cannot be discounted, though no through-bond coupling could be measured between Si and H2. Measurement of ν_{FeH} and ν_{SiH} values by infrared spectroscopy has been cited as a useful tool for the determination of the presence of a non-classical interaction, and for **2-H₃** values of 1925 cm⁻¹, 1871 cm⁻¹ and 1846 cm⁻¹ were obtained. Unfortunately as the hydride positions cannot be selectively deuterated (rapid exchange occurs as is observed with the reaction with D₂, *vide infra*), values of isotopically shifted IR stretches are of limited value. Sabo-Étienne¹⁰⁹ cites the presence of a ‘broad and intense IR band in the range 1650 – 1800 cm⁻¹’ as a good indicator of the presence of a σ -(SiH)-type interaction, however, none of the values for **2-H₃** lie within this range. The band at 1846 cm⁻¹ is indeed intense and very broad, and it certainly should be noted that Sabo-Étienne’s criteria is based on values obtained from Ru complexes, which could account for the discrepancy.

The related *Fe*-based comparison to **2-H₃** is perhaps that of Peters and co-workers,¹¹² [(PhBP^{*i*Pr}₃)Fe^{II}(H)(η^3 -H₂SiRR’)] (R = Me; R’ = Ph or Mes), which as the formula implies has been assigned as an η^3 -silane adduct by the authors (binding of the

silane through two H atoms, and Si, to the Fe center). A similar bonding scenario could be envisaged for **2-H₃**, and is depicted in Figure 2.2.13C, however there are some key differences between **2-H₃** and Peters' complex. In the case of **2-H₃** the Si-H-Fe interaction involves a tertiary silane and the metal coordination sphere does not feature a similar phosphino-borate component. The Si-H distances in Peters' complexes (1.464(1) Å and 1.552(2) Å) are both very reasonable for a significant Si-H interaction, while in **2-H₃** the Si-H₂ distance of *ca.* 2.27 Å is significantly elongated in comparison. Finally the authors indicate the ²⁹Si chemical shift of their complex is 162 ppm (for R' = Ph), dramatically downfield-shifted from that of the 32.7 ppm value measured for **2-H₃**. The authors also cite typical ²⁹Si chemical shift ranges of -28 to 55 ppm for η^2 -HSiR₃ metal complexes, and that the downfield shift to 162 ppm is likely reflective of the η^3 nature of their silane ligand. Unfortunately no IR data is reported for these complexes and thus no comparison can be made, however, it appears based on the other data provided that **2-H₃** cannot be reliably assigned as an η^3 -silane complex. Admittedly, the bonding scenario in **2-H₃** may change at high temperatures, however, no spectroscopic evidence could be obtained for this interaction due to significant signal broadening. At room temperature, and below, complex **2-H₃** is thus tentatively assigned as an η^2 -silane (as in Figure 2.2.13B). The closely related complex Fe(H)₂(H₂)(PEtPh₂)₃ has been unambiguously characterized as an Fe^{II}-dihydride dihydrogen adduct that features a similar *cis*-dihydride *mer*-tris(phosphine) coordination geometry to **2-H₃**,¹¹³ and is likely the most closely matched comparison to the present study.

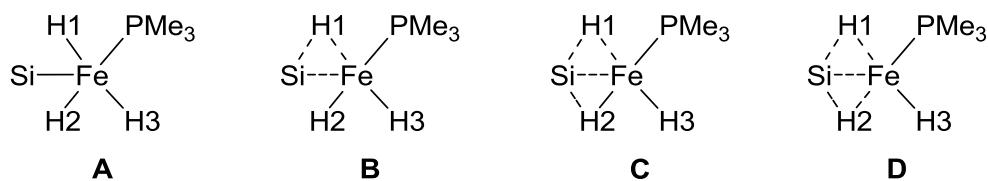
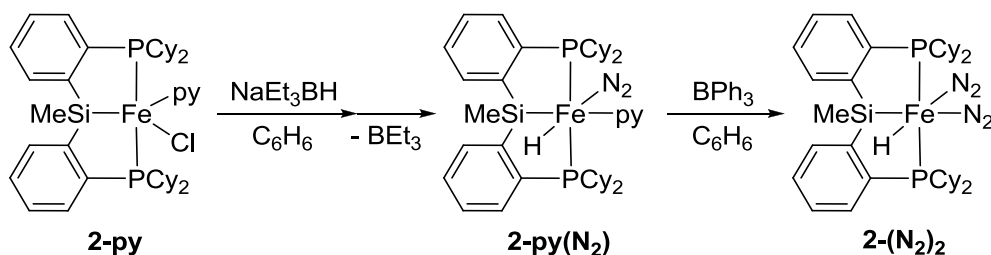


Figure 2.2.13. Proposed bonding schemes for **2-H₃** (most of the molecule has been omitted for clarity). (A) Silyl trihydride complex of Fe(IV), (B) η^2 -silane complex between Si-H1 and Fe (bonding scenario proposed for **2-H₃**), (C) η^2 -silane complex between Si-H1 and Fe with SISHA between Si and H2, (D) η^3 -silane complex between Si, H1, H2 and Fe.

Complex **2-H₃** is a remarkably stable compound, showing little to no evidence of thermal degradation upon extended periods of heating (days, 80 °C), and also appears to be at least moderately air and moisture stable. No reaction of **2-H₃** was observed upon addition of CO₂, furthermore, no alkene isomerisation was observed upon addition of 1-octene. Addition of BPh₃ to **2-H₃** did not lead to any apparent generation of Ph₃B·PMe₃, suggesting the PMe₃ in this complex is particularly strongly bound to the metal center when compared to that of (Cy-PSiP)FeH(PMe₃)(N₂), which does generate Ph₃B·PMe₃ on addition of BPh₃ (*vide infra*). **2-H₃** does undergo exchange with D₂, however, to generate **2-D₃**. This exchange is slow at room temperature (no ²H incorporation after 2 h at room temperature, by ¹H NMR) but can be accelerated with heating to 65 °C. From a mechanistic perspective, Sabo-Étienne and co-workers¹¹⁴ have shown that in the case of Ru(H)₂[(η^2 -HSiMe₂)CH₂CH₂(η^2 -H-SiMe₂)](PCy₃)₂, which features two classical dihydride ligands and two η^2 -(Si-H) interactions, facile exchange of all M-H occurs via a process involving equilibria between the parent structure and isomers that feature, in turn, one dihydrogen ligand, one η^2 -(Si-H) ligand, and a classical silyl group, or two dihydrogen ligands and two classical silyl groups. A similar process involving an intermediate that features a classical silyl group and a dihydrogen ligand can be invoked for hydride exchange in **2-H₃**.

In addition to reactivity of **2-PMe₃** toward hydride sources, similar chemistry was probed with **2-py** in anticipation that a more labile ligand, such as pyridine, could allow for access to lower valent iron hydride compounds reactive toward hydrogenation catalysis. Treatment of **2-py** with one equiv NaEt₃BH led to clean conversion to a single diamagnetic product, featuring a single resonance at 87.3 ppm by ³¹P{¹H} NMR. By ¹H NMR, a hydride resonance was observed at -16.31 ppm as a triplet (²J_{PH} = 58.5 Hz). Unexpectedly, however, upon workup partial conversion to a new diamagnetic hydride was observed, with a similar triplet hydride resonance centered at -15.35 ppm (²J_{PH} = 60.3 Hz). It was determined that the generation of a pyridine-triethylborane adduct was responsible for the unusual interconversion. Upon attempted workup, generated py·BEt₃ partially dissociates, allowing pyridine to re-coordinate to the Fe center, with BEt₃ being removed *in vacuo*. Addition of one equiv BPh₃ after the addition of NaEt₃BH was sufficient to trap pyridine permanently as a py·BPh₃ adduct. X-ray quality crystals (Figure 2.2.14) of both hydrides were obtained, revealing the pyridine-less complex to be (Cy-PSiP)FeH(N₂)₂ (**2-(N₂)₂**) and the pyridine-containing compound to be (Cy-PSiP)FeH(py)(N₂) (**2-py(N₂)**).



Scheme 2.2.7. Synthesis of **2-py(N₂)** from **2-py** and its conversion to **2-(N₂)₂** via formation of a pyridine-borane adduct.

Both **2-py(N₂)** and **2-(N₂)₂** feature distorted octahedral geometry at the Fe center with κ^3 -coordination of the ligand in a *mer* configuration. In each complex the hydride

ligand sits *cis* to Si, with acute Si-Fe-H(1) angles of 75.8(7)° and 78.8(7)° for **2-py(N₂)** and **2-(N₂)₂**, respectively. The Si-H(1) distances of *ca.* 2.35 Å and 2.44 Å (for **2-py(N₂)** and **2-(N₂)₂**, respectively) are both less than the sum of the van der Waals radii for the two atoms, and the measured values of J_{SiH} for the two complexes (67 Hz and 70 Hz, respectively) are somewhat high for typical values of ${}^2J_{\text{SiH}}$ for classical silyl hydrides, indicating the potential for non-classical interactions between H and Si in these complexes. Conversely, the ${}^{29}\text{Si}$ chemical shifts are downfield shifted, to 72.3 ppm and 69.0 ppm, respectively, which are more characteristic of a metal silyl complex rather than, for example, an η^2 -silane. Support for the assignment of these complexes as silyl hydrides is provided by infrared spectroscopy, where values of 1949 cm^{-1} and 2012 cm^{-1} for ν_{FeH} were measured for **2-py(N₂)** and **2-(N₂)₂**, respectively, neither of which are indicative of a non-classical Si-H interaction.¹⁰⁹

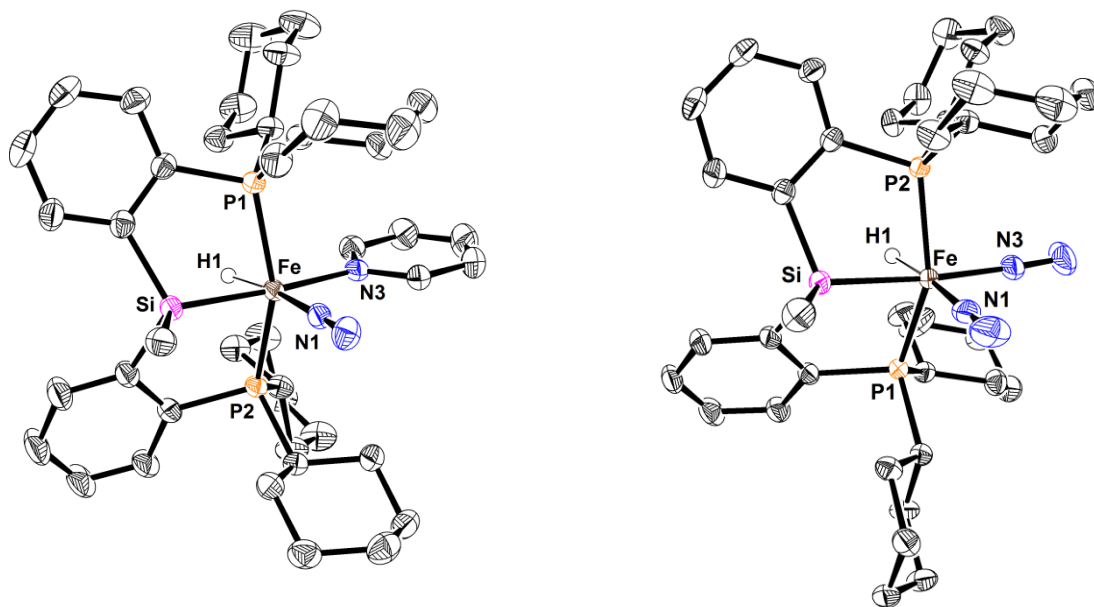


Figure 2.2.14. Crystallographically determined structures of **2-py(N₂)** and **2-(N₂)₂** with thermal ellipsoids shown at the 50% probability level. Most hydrogen atoms have been omitted for clarity. Selected interatomic distances (Å) and angles (°) for **2-py(N₂)**: Fe-H(1) 1.441(18), Fe-Si 2.2472(4), Fe-P(1) 2.2238(3), Fe-P(2) 2.2196(3), Fe-N(1) 1.7949(11), Fe-N(3) 2.0664(11), N(1)-N(2) 1.1228(16), Si-Fe-H(1) 75.8(7), N(3)-Fe-H(1) 95.7(7), N(1)-Fe-N(3) 95.55(5), Si-Fe-N(1) 92.92(3), P(1)-Fe-P(2) 156.068(14); for **2-(N₂)₂**: Fe-H(1) 1.418(19), Fe-Si 2.2844(4), Fe-P(1) 2.2268(3), Fe-P(2) 2.2147(3), Fe-N(1) 1.8368(12), Fe-N(3) 1.8654(12), N(1)-N(2) 1.1111(18), N(3)-N(4) 1.1065(18), Si-Fe-H(1) 78.8(7), N(3)-Fe-H(1) 96.6(7), N(1)-Fe-N(3) 91.97(6), Si-Fe-N(1) 92.61(4), P(1)-Fe-P(2) 149.831(13).

Both complexes feature an N₂ ligand in the position *trans* to the hydride, while in the presence of pyridine the N₂ *trans* to Si in **2-(N₂)₂** is displaced preferentially to generate **2-py(N₂)**. The N₂ ligand in **2-py(N₂)** is not anticipated to be highly activated based on measured metrical and spectroscopic parameters. The coordinated N₂ features a bond length of 1.1228(16) Å and a value of 2012 cm⁻¹ was measured for the ν_{NN} by IR spectroscopy indicating moderate activation of the N₂ ligand. Comparatively in **2-(N₂)₂**, the N₂ ligands are also not likely to be strongly bound, particularly the N₂ ligand *trans* to Si, which features a shorter bond length of 1.1065(18) Å compared to that of the N₂ *cis* to Si (1.1111(18) Å). By IR spectroscopy, N-N stretching frequencies of 2123 cm⁻¹ and

2063 cm^{-1} were measured, indicating one weakly and one moderately activated N_2 ligand. The propensity of **2-(N₂)₂** to recoordinate pyridine, as observed during its preparation, consistently leads to only one isomer of **2-py(N₂)** with preferential displacement of the N_2 ligand *trans* to Si, supporting the notion that this N_2 ligand is less tightly bound than the N_2 *cis* to Si. **2-(N₂)₂** can also be accessed from **2-PMe₃** through an analogous route, however, the instability of the $\text{PMe}_3\cdot\text{BPh}_3$ adduct generated consistently leads to formation of small amounts of **2-H**, **2-H₃** and $(\text{Cy-PSiP})\text{FeH}(\text{PMe}_3)(\text{N}_2)$, among other byproducts, precluding clean isolation of **2-(N₂)₂**.

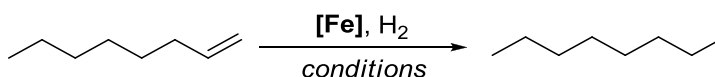
2-(N₂)₂ is a particularly intriguing complex as it can be thought of as a surrogate for the low-coordinate Fe hydride, $(\text{Cy-PSiP})\text{FeH}$, which does not appear to be an isolable complex under a nitrogen atmosphere. The N_2 ligands (again, particularly the ligand *trans* to Si) are anticipated to be displaced readily by a variety of incoming donors. With the proximal hydride ligand, **2-(N₂)₂** thus appears to be poised for coordination and subsequent insertion of an unsaturated substrate, thus it was decided to investigate the chemistry of **2-(N₂)₂** toward catalytic applications, in particular, reductions of unsaturated substrates, with hydrogenation reactions being identified as a primary target.

2.2.5 Fe-Catalyzed Olefin Hydrogenation

Very few examples of homogeneous Fe-catalyzed alkene hydrogenations have been described in the literature, and with two potentially labile N_2 ligands, similar to the design of many of Chirik's Fe-based olefin hydrogenation catalysts,^{39-40, 42} **2-(N₂)₂** is anticipated to be a highly active Fe hydride precatalyst. Thus, to survey the effectiveness of **2-(N₂)₂** as an alkene hydrogenation precatalyst, 1-octene was first investigated as a substrate. Using **2-(N₂)₂** at a 5 mol% catalyst loading, 1-octene was hydrogenated to *n*-octane in

98% conversion over 4 h (10 atm H₂, room temperature, Table 2.2.1, Entry 2). For 1-octene, the catalyst loading could be dropped to 0.5 mol% under the same conditions, affording 97% conversion to *n*-octane (Table 2.2.1, Entry 4). Under ambient conditions (1 atm H₂, room temperature), 5 mol% **2-(N₂)₂** was sufficient to afford *n*-octane in 99% conversion over 18 h (Table 2.2.1, Entry 5), a time which could be decreased to 4 h by running the reaction at 65 °C (Table 2.2.1, Entry 3).

Table 2.2.1. Hydrogenation of 1-octene using **2-(N₂)₂**.



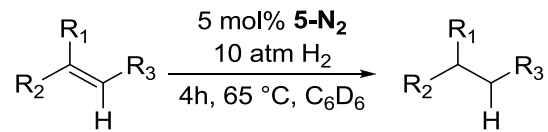
| entry | substrate | Fe (mol %) | time (h) | H ₂ pressure (atm) | temperature (°C) | conversion to alkane (%) |
|-------|-----------|------------|----------|-------------------------------|------------------|--------------------------|
| 1 | | 5 | 4 | 10 | 65 | 98 |
| 2 | | 5 | 4 | 10 | RT | 98 |
| 3 | | 5 | 4 | 1 | 65 | 97 |
| 4 | | 0.5 | 4 | 10 | 65 | 97 |
| 5 | | 5 | 18 | 1 | RT | 99 |

^aAll reactions were conducted in C₆D₆ using 0.0569 mmol 1-octene and a total reaction volume of 250 μL. Conversions are based on integration of diagnostic product signals relative to an internal standard (C₆H₃(OCH₃)₃), and are the average of two runs.

Encouraged by these initial results, the substrate scope was expanded to include a variety of substituted alkenes. For the substituted alkenes, moderately elevated temperature and pressure was required to afford high conversion, however, a wide variety of alkenes appeared to be active toward hydrogenation. Both *cis*- and *trans*-octene were hydrogenated quantitatively (Table 2.2.2, Entries 2 and 3), as was *cis*-stilbene (Table 2.2.2, Entry 6). For 4-vinylcyclohexene, at 65 °C, both the internal double bond, and the vinyl group were fully hydrogenated, yielding ethylcyclohexane in 94% conversion

(Table 2.2.2, Entry 5). When this substrate was hydrogenated at room temperature, the internal double bond was left intact, and 4-ethylcyclohexene was obtained selectively in 93% conversion (Table 2.2.2, Entry 4). A 1,1-disubstituted alkene, α -methylstyrene, was fully converted to cumene (Table 2.2.2, Entry 7), and the trisubstituted alkene, ethylenecyclohexane, was able to be hydrogenated to ethylcyclohexane in 97% conversion (Table 2.2.2, Entry 8).

As $(\text{Cy-PSiP})\text{FeH}(\text{PMe}_3)(\text{N}_2)_n$ ($n = 0, 1$) converts to **2-H₃** with the addition of hydrogen (*vide supra*), hydrogenation of *trans*-4-octene using **2-H₃** was also attempted for direct comparison with **2-(N₂)₂**. Under the typical hydrogenation conditions employed <5% conversion to *n*-octane was observed, thus it appears that the presence of PMe_3 dramatically inhibits catalytic activity, likely due to its strong binding to the metal center, preventing coordination of an incoming alkene substrate. Hydrogenation of 1-octene and *trans*-4-octene was also investigated using **2-Fe^I** as the catalyst under the same conditions. While some conversion to *n*-octane was indeed observed, conversions were very low (35% conversion of 1-octene, 17% conversion of *trans*-4-octene) in comparison to those of **2-(N₂)₂**.

Table 2.2.2. Hydrogenation of various substituted alkenes using **2-(N₂)₂**.

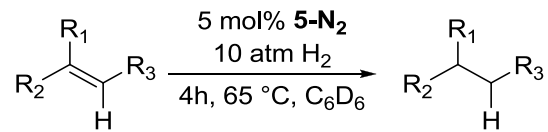
| entry | substrate | product | conversion (%) |
|-------|-----------|---------|-----------------|
| 1 | | | 98 |
| 2 | | | > 99 |
| 3 | | | > 99 |
| 4 | | | 93 ^b |
| 5 | | | 94 |
| 6 | | | > 99 |
| 7 | | | > 99 |
| 8 | | | 97 |

^aAll reactions were conducted in C₆D₆ using 0.0569 mmol substrate and a total reaction volume of 250 μL unless otherwise indicated. All reactions were performed at 65 °C, with 5 mol% catalyst, under 10 atm H₂ and for 4 h. Conversions are based on integration of diagnostic product signals relative to an internal standard (C₆H₃(OCH₃)₃), and are the average of two runs. ^bReaction performed at room temperature.

Functional group tolerance was also investigated in this system, and was found to be moderate. Ethyl crotonate was hydrogenated to ethyl butanoate in 80% conversion under the standard conditions (Table 2.2.3, Entry 2), while allyl butyl ether and allyl phenyl ether were hydrogenated in 96% and 98% conversions, respectively (Table 2.2.3, Entries 4 and 5). Notably for these C-O-containing substrates, no special precautions were required to prevent undesired C-O bond cleavage chemistry between substrate and catalyst.^{39, 43} All substrates could be combined with the catalyst at room temperature prior

to the addition of H₂. 5-hexen-2-one could only be hydrogenated in 11% conversion (Table 2.2.3, Entry 1), perhaps due to the substrate coordinating preferentially to the Fe-center over any incoming H₂, dramatically impeding catalytic activity. Hydrogenation of a terminal alkyne, phenylacetylene, was also attempted, however, a very complex mixture of products was obtained as observed by ¹H NMR spectroscopy, and while no unreacted phenylacetylene was observed (implying its catalytic consumption), the only products able to be identified were ethylbenzene (ca. 19% conversion), and 1,4-diphenylbutane (~14%). The generation of 1,4-diphenylbutane implies a homocoupling process, followed by a hydrogenation. Such a process could yield a variety of hydrogenated or partially hydrogenated derivatives, and may be attributable to the large product distribution obtained. A 1,2-disubstituted alkyne, diphenylacetylene, was better tolerated by the catalyst, and under standard conditions 36% conversion to bibenzyl was observed, with 42% conversion to *trans*-stilbene (Table 2.2.3, Entry 5). Increasing the temperature to 90 °C and the reaction time to 6 h, however, was sufficient to yield only bibenzyl in 92% conversion (Table 2.2.3, Entry 6).

Table 2.2.3. Hydrogenation of diphenylacetylene and various functionalized alkenes using **2-(N₂)₂**.



| entry | substrate | product | conversion (%) |
|-------|-----------|---------|-----------------|
| 1 | | | 11 |
| 2 | | | 80 |
| 3 | | | 96 |
| 4 | | | 98 |
| 5 | | | 42 ^b |
| 6 | | | 92 ^c |

^a All reactions were conducted in C₆D₆ using 0.0569 mmol substrate and a total reaction volume of 250 μL unless otherwise indicated. All reactions were performed at 65 °C, with 5 mol% catalyst, under 10 atm H₂ and for 4 h unless otherwise indicated. Conversions are based on integration of diagnostic product signals relative to an internal standard (C₆H₃(OCH₃)₃), and are the average of two runs. ^bAlso observed 36% conversion to bibenzyl, *cis*-stilbene not observed. ^cReaction performed in toluene-*d*₈, for 6 h, at 90°C.

It is clear that thus far, literature examples of Fe-catalyzed alkene hydrogenations illustrate that with increased catalytic activity can often come the additional issue of unwanted reactivity between substrate and catalyst. While for most substrates, mild heating and a pressure of H₂ is required to facilitate complete hydrogenation with **2-(N₂)₂**, with the exception of phenylacetylene, we observed no unwanted reactivity between substrate and catalyst, allowing for easy manipulation and reaction setup. Further efforts

to fine-tune the PSiP ligand scaffold may lead to increased activity toward hydrogenation and should be directed toward the goal of hydrogenation at ambient pressure.

2.3 Summary and Conclusions

Thus far, literature examples of iron complexes supported by phenylene-based PSiP pincer ligation have been limited to only two examples of coordinatively saturated 18-electron complexes of Fe^{II}, both of the form (R-PSiP)FeH(PMe₃)(N₂).^{25b, 73b} The results presented in this chapter document significant progress in expanding the Fe chemistry of this versatile class of ligands, providing examples of 14-, 15-, 16-, 17- and 18-electron Fe complexes across oxidation states from Fe⁰ to Fe^{III} in a wide range of geometries.

The 14-electron complex (Cy-PSiP)FeBr (**2-Br**) could not be isolated in appreciable amounts, perhaps due to its inherent instability toward one-electron reductions and oxidations (**2-Me** and **2-Cl** being Fe^I and Fe^{III} complexes isolated during attempted preparation of **2-Br** and related compounds). However, the low-coordinate compounds could be stabilized as the analogous 16-electron complexes, and **2-PMe₃** and **2-py** could be obtained far more reliably. Complex **2-PMe₃** in particular served as an excellent starting material for the preparation of other Fe complexes and the feasibility for the displacement of PMe₃ in **2-PMe₃** was demonstrated through reaction of this complex with CO, which afforded the corresponding bis(carbonyl) species **2-(CO)₂**.

The reduction chemistry of **2-PMe₃** was explored through treatment with reducing agents such as magnesium and sodium metal. Use of the milder reducing agent Mg led to the generation of the novel Fe^I-dinitrogen complex, **2-Fe^I**. The reactivity of **2-Fe^I** toward a variety of E-H (H-H, Si-H, B-H, C-H, N-H) bonds was investigated. Unfortunately, due

to the paramagnetic nature of the resulting products, little information regarding their formulation could be obtained in most cases. However, in the case of a reaction with HBP in a crystal structure of an Fe-hydride product (**2-H(N₂)**) was obtained, implying a B-H bond activation process. On the other hand, the reaction of **2-PMe₃** with sodium metal led to reduction of the Fe^{II} complex down to an anionic, formally Fe⁰ species, **2-Fe⁰**. **2-Fe⁰** exhibited reactivity toward H₂, to initially form a transient species resulting from displacement of PMe₃ from the Fe coordination sphere (**2-H₂***), which rapidly re-coordinated PMe₃ to generate a mixture of Fe^{II}-hydride complexes.

Reaction of **2-Fe⁰** with H₂O led to similar mixtures of hydride products, most of which could be rationally prepared through treatment **2-PMe₃** with various hydride sources, leading to **2-H**, the literature compound (Cy-PSiP)FeH(PMe₃)(N₂), and **2-H₃**. Complex **2-H₃** was identified as a unique example of an η²-(SiH) complex of an Fe dihydride and exhibited intriguing spectroscopy, which was investigated thoroughly through the use of a suite of 1D and 2D NMR experiments at high and low temperatures to elucidate the probable bonding situation in **2-H₃**.

Investigating the chemistry of **2-py** with hydride sources was very fruitful, leading to new routes for the preparation of the first (Cy-PSiP)Fe hydride complexes not featuring the strongly-coordinating PMe₃ ligand on the Fe center. **2-py(N₂)** could be converted to the corresponding bis(dinitrogen) complex **2-(N₂)₂**, which can be viewed as a surrogate for the low-coordinate complex (Cy-PSiP)FeH. Complex **2-(N₂)₂** was successfully employed as an effective precatalyst for the homogeneous hydrogenation of olefins and exhibited excellent activity toward a wide range of unsubstituted and

multiply-substituted alkenes. Esters and ethers were found to be well-tolerated by the catalyst, and hydrogenation of an alkyne was also demonstrated.

2.4 Experimental

2.4.1 General Considerations

All experiments were conducted under nitrogen in a glovebox or using standard Schlenk techniques. Tetrahydrofuran and diethyl ether were distilled from Na/benzophenone ketyl. Benzene, toluene, and pentane were first sparged with nitrogen and subsequently dried by passage through a double-column (one activated alumina column and one column packed with activated Q-5). All purified solvents were stored over 4 Å molecular sieves. Benzene-*d*₆ was degassed via three freeze-pump-thaw cycles and stored over 4 Å molecular sieves. The ligand precursor (Cy-PSiP)H⁷⁴ and FeCl₂(THF)_{1.5}¹¹⁵ were prepared by previously reported methods. All other reagents were purchased from commercial suppliers and used without further purification. Unless otherwise stated, ¹H, ¹³C, ¹¹B, ³¹P, and ²⁹Si characterization data were collected at 300K, with chemical shifts reported in parts per million downfield of SiMe₄ (for ¹H, ¹³C, and ²⁹Si), BF₃·OEt₂ (for ¹¹B), or 85% H₃PO₄ in D₂O (for ³¹P). ¹H and ¹³C NMR chemical shift assignments are based on data obtained from ¹³C{¹H}, ¹³C-DEPTQ, ¹H-¹H COSY, ¹H-¹³C HSQC, and ¹H-¹³C HMBC NMR experiments. ²⁹Si NMR assignments are based on ¹H-²⁹Si HMBC and ¹H-²⁹Si HMQC experiments. Solution magnetic moment measurements were determined by use of the Evans method.¹¹⁶ Infrared spectra were recorded as thin films between NaCl plates at a resolution of 4 cm⁻¹. X-ray data collection, solution, and refinement were carried out by Drs. Robert MacDonald and

Michael J. Ferguson at the University of Alberta X-ray Crystallography Laboratory, Edmonton, Alberta..

2.4.2 Synthetic Procedures and Characterization Data

(Cy-PSiP)FeBr (2-Br). A precooled (-35 °C) suspension of FeBr₂ (0.036 g, 0.17 mmol) in ca. 3 mL of THF was treated with (Cy-PSiP)H (0.10 g, 0.17 mmol). MeMgBr (0.057 mL, 3.0 M in THF, 0.17 mmol) was diluted to a total 1 mL volume in THF and was added dropwise to the reaction mixture. After stirring at room temperature for 2 h the reaction mixture was filtered through Celite. The volatile components of the filtrate were removed *in vacuo*. The remaining residue was extracted with ca. 10 mL of benzene and the extracts were filtered through Celite. The filtrate was collected and the volatile components were removed *in vacuo*. The remaining residue was extracted 4 times with 2 mL of pentane and subsequently dried under vacuum. The residue was then dissolved in ca. 2 mL Et₂O and the solvent was slowly evaporated at room temperature to afford a minute quantity of black needles of **1-Br** suitable for X-ray diffraction analysis.

(Cy-PSiP)FeCl₂ (2-Cl). To a suspension of FeCl₂ (0.049 g, 0.39 mmol) in ca. 7 mL THF was added (Cy-PSiP)H (0.23 g, 0.39 mmol). The mixture was cooled to -35 °C and BnMgCl (0.28 mL, 0.39 mmol) as a 1.4 M solution in THF was added dropwise to the stirring reaction mixture. The mixture was stirred for 18 h at room temperature and the volatiles were subsequently removed *in vacuo*. The resulting residue was triturated with 2 × 2 mL pentane and then extracted with ca. 10 mL benzene and filtered through Celite. The benzene was removed *in vacuo* leaving a red-purple solid which was triturated with 3 × 3 mL pentane and then washed with 3 × 5 mL pentane to yield **1-Cl** as a purple solid (0.10 g, 36% yield relative to FeCl₂). A minute quantity of crystals suitable for X-ray

crystallographic analysis were obtained by vapour diffusion of pentane into a concentrated 2:1 Et₂O : THF solution of **1-Cl** at room temperature. ¹H NMR (300 MHz, benzene-*d*₆): 15.27, 6.88, 6.26, 5.95, 5.23, 3.91, 2.82, 2.24, 2.00 – 0.50 (overlapping resonances), 0.23, -0.45, -0.81, -0.99, -4.19, -5.73, -14.72. μ_{eff} (benzene-*d*₆): 4.18 μ_{B} (S = 3/2).

[η^6 -C₆H₄(PCy₂)(κ^1 -SiMe₂C₆H₄PCy₂)]FeMe (2-Me). A mixture of (Cy-PSiP)H (0.075 g, 0.13 mmol) and FeBr₂ (0.027 g, 0.13 mmol) in ca. 5 mL of THF was cooled to -35 °C. MeMgBr (0.085 mL, 0.25 mmol) as a 3.0 M solution in THF was diluted to 2 mL in THF and added dropwise to the cold reaction mixture. The reaction mixture was stirred for 3 h at room temperature and subsequently filtered through a plug of Celite. Volatile components of the reaction mixture were removed *in vacuo* and the residue was washed with 3 × 2 mL pentane. The residue was recrystallized from Et₂O at room temperature yielding a minute quantity of green needles suitable for X-ray crystallographic analysis.

(Cy-PSiP)Fe(PMe₃)Cl (2-PMe₃). A solution of (Cy-PSiP)H (0.25 g, 0.42 mmol) in ca. 3 mL of THF was added to a suspension of FeCl₂(THF)_{1.5} (0.099 g, 0.42 mmol) in ca. 3 mL of THF. Neat PMe₃ (0.064 g, 0.85 mmol) was added to the resulting suspension. The reaction mixture was stirred at room temperature until all solids were dissolved to give a green solution (ca. 2-3 minutes). The reaction mixture was subsequently cooled to -35°C and BnMgCl (0.30 mL, 1.4 M in THF, 0.42 mmol) was added dropwise. The resulting red solution was stirred for 2 h at room temperature, at which point the volatile components were removed under vacuum. The resulting residue was extracted with ca. 5 mL benzene and filtered through Celite. The filtrate solution was evaporated to dryness

and the remaining residue was triturated with 3×5 mL of pentane to afford paramagnetic **2-PMe₃** (0.30 g, 94% yield) as a red-orange solid. Crystals of **2-PMe₃** suitable for X-ray diffraction analysis were obtained from a concentrated Et₂O solution at -35°C . μ_{eff} (benzene-*d*₆): $3.04 \mu_{\text{B}}$ ($S = 1$). ¹H NMR (benzene-*d*₆, 300 MHz) δ : 73.65, 62.73, 22.18, 6.56, 6.24, 5.29, 4.67, 3.90, $-0.40 - 2.10$ (overlapping resonances), -1.43 , -2.32 , -3.39 , -6.76 , -51.01 . Anal. Calcd. for C₄₀H₆₄P₃SiClFe: C, 63.44; H, 8.52. Found: C, 63.08; H, 8.74.

(Cy-PSiP)FeCl(py) (2-py). To a suspension of (pyridine)₄FeCl₂ (0.15 g, 0.34 mmol) in *ca.* 15 mL THF was added (Cy-PSiP)H (0.20 g, 0.34 mmol). The yellow suspension was stirred for 1 h at room temperature. BnMgCl (0.24 mL, 0.34 mmol) as a 1.4 M solution in THF was diluted to approximately 2 mL in THF and added dropwise to the stirring suspension at room temperature. A color change from bright yellow to dark red was observed, and the resulting mixture was stirred for 18 h at room temperature. The volatile components of the reaction mixture were removed *in vacuo* and the resulting residue was triturated with 3×3 mL pentane and extracted with *ca.* 10 mL benzene and filtered through Celite. The solvent was removed *in vacuo* and the residue triturated with 3×3 mL pentane and washed with 3×2 mL pentane to yield **2-py** as a red solid (0.21 g, 80% yield). μ_{eff} (benzene-*d*₆): $2.93 \mu_{\text{B}}$ ($S = 1$). ¹H NMR (benzene-*d*₆, 300 MHz) δ : 61.15, 42.00, 16.00, 15.97, 10.76, 8.75, 5.66, 5.15, 3.41, $2.50 - 0.40$ (overlapping resonances), -0.19 , -0.56 , -1.04 , -2.96 , -3.29 , -4.84 , -9.68 , -61.0 .

(Cy-PSiP)Fe(CO)₂Cl (2-(CO)₂). **Method 1:** A 250 mL resealable Schlenk flask equipped with a Teflon stopcock was charged with a solution of **2-PMe₃** (0.10 g, 0.13 mmol) in *ca.* 7 mL of THF. The solution was degassed via three freeze-pump-thaw cycles

and then placed under an atmosphere of CO. A color change from red-orange to light orange was observed in under 1 minute. After stirring for a further 10 minutes, the volatile components of the reaction mixture were removed *in vacuo*. The remaining residue was triturated with ca. 2 mL of pentane and subsequently washed with 3×2 mL of pentane to afford **2-(CO)₂** (0.081 g, 83% yield) as a beige solid. X-ray quality crystals of **2-(CO)₂** were grown from a concentrated Et₂O solution -35 °C. **Method 2:** A solution of Cy-PSiPH (0.250g, 0.423mmol) in ca. 10 mL THF was added to FeCl₂(THF)_{1.5} (0.099 g, 0.42 mmol) in a Teflon-sealed reaction vessel equipped with a stirbar. The mixture was degassed through three sequential freeze-pump-thaw cycles and then placed under an atmosphere of CO and cooled to 0 °C, BnMgCl (0.30 mL, 1.4 M THF, 0.42 mmol) was diluted to ca. 2 mL in THF and was added to the reaction mixture dropwise *via* syringe, under a flow of CO, resulting in a gradual color change to green-yellow. The reaction was stirred for 2 days at room temperature under ca. 1 atm CO. Volatile components of the reaction mixture were removed *in vacuo* and the resulting residue was triturated with 3×2 mL pentane and extracted with 5 mL benzene and filtered through Celite. Benzene was removed *in vacuo* and the residue was triturated with 3×2 mL pentane and washed with 3×1 mL cold Et₂O to yield **2·CO** as a beige solid (0.184 g, 59% yield). ¹H NMR (300 MHz, benzene-*d*₆): δ 8.13 (d, *J* = 7 Hz, 2 H, *H*_{arom}), 7.47 (m, 2 H, *H*_{arom}), 7.27 – 7.15 (overlapping resonances, 4 H, *H*_{arom}), 2.61 – 2.55 (overlapping resonances, 6 H, PCy), 2.20 – 1.95 (overlapping resonances, 8 H, PCy), 1.80 – 1.05 (overlapping resonances, 30 H, PCy), 0.95 (s, 3 H, SiMe). ¹³C{¹H} NMR (75.5 MHz, benzene-*d*₆): δ 218.1 (Fe-CO), 212.2 (Fe-CO), 156.6 (apparent t, *J* = 21 Hz, *C*_{arom}), 142.5 (apparent t, *J* = 24 Hz, *C*_{arom}), 133.7 (apparent t, *J* = 9 Hz, CH_{arom}), 131.0 (CH_{arom}), 129.4 (CH_{arom}), 127.6 (CH_{arom}), 42.8

(apparent t, $J = 9$ Hz, CH_{Cy}), 41.4 (apparent t, $J = 10$ Hz, CH_{Cy}), 33.6 ($\text{CH}_{2\text{Cy}}$). 29.9 ($\text{CH}_{2\text{Cy}}$), 29.0 – 28.8 (overlapping resonances, $\text{CH}_{2\text{Cy}}$), 28.2 ($\text{CH}_{2\text{Cy}}$), 27.7 ($\text{CH}_{2\text{Cy}}$), 27.3 ($\text{CH}_{2\text{Cy}}$), 26.6 ($\text{CH}_{2\text{Cy}}$), 26.3 ($\text{CH}_{2\text{Cy}}$), 9.2 (*SiMe*). $^{31}\text{P}\{^1\text{H}\}$ NMR (121.5 MHz, benzene- d_6): δ 86.2. ^{29}Si NMR (59.6 MHz, benzene- d_6): δ 64.3. IR (thin film, cm^{-1}): 1969 (s, νCO), 1909 (s, νCO). Anal. Calcd. for $\text{C}_{39}\text{H}_{55}\text{O}_2\text{P}_2\text{SiClFe}$: C, 63.37; H, 7.77. Found: C, 63.29; H, 7.87.

(Cy-PSiP)Fe(PMe₃)N₂ (2-Fe^I). Mg powder (0.027 g, 1.13 mmol) was added to a solution of **2-PMe₃** (0.085 g, 0.11 mmol) in ca. 5 mL THF. The resulting mixture was stirred for 18 h at room temperature and was subsequently filtered through Celite. The filtrate solution was evaporated to dryness *in vacuo* and the remaining residue was extracted with pentane (5 mL) and filtered through Celite. The filtrate was collected and the volatile components were removed *in vacuo*. The resulting red solid was washed with Et₂O (5 × 0.25 mL) and dried under vacuum to afford paramagnetic **2-Fe^I** (0.052 g, 61% yield) as a bright yellow solid. Crystals of **2-Fe^I** suitable for X-ray diffraction analysis were obtained from a concentrated Et₂O solution at –35 °C. μ_{eff} (benzene- d_6): 1.88 μ_{B} ($S = \frac{1}{2}$). ^1H NMR (300 MHz, benzene- d_6): δ 9.00, 8.20, 8.07, 7.66, 7.32, 7.22, 6.81, 5.68, 5.09, 4.41, 3.85, 3.27, 0.79 - 2.64 (overlapping resonances). IR (thin film, cm^{-1}): 2011 (s, νN_2). Anal. Calcd. for $\text{C}_{40}\text{H}_{64}\text{N}_2\text{P}_3\text{SiFe}$: C, 64.07, H, 8.60, N: 3.74. Found: C, 63.75; H, 8.83; N; 3.38.

[(Cy-PSiP)Fe(PMe₃)N₂][Na(THF)₃] (2-Fe⁰). A solution of **2-PMe₃** (0.13 g, 0.17 mmol) in ca. 10 mL of THF was treated with Na metal (0.040 g, 1.74 mmol). The reaction mixture was stirred at room temperature for 18 h during which time the red-orange solution darkened to a purple color. The volatile components of the reaction

mixture were removed *in vacuo* and the remaining dark purple residue was extracted with ca. 20 mL of pentane. The pentane extracts were collected and filtered through Celite. The pentane was removed *in vacuo* to afford **2-Fe⁰** as a dark purple solid (0.14 g, 87% yield). ¹H NMR (300 MHz, cyclohexane-*d*₁₂): δ 8.07 (d, *J* = 6.9 Hz, 2 H, *H*_{arom}), 7.20 (d, 2 H, *J* = 6.3 Hz, *H*_{arom}), 7.057.26 (m, 1 H, *H*_{arom}), 7.20 (apparent t, *J* = 7.20 Hz, 2 H, *H*_{arom}), 7.04 (apparent t, *J* = 6.6 Hz, 2 H, *H*_{arom}), 6.96 (apparent t, *J* = 6.6 Hz, 2 H, *H*_{arom}) 3.20 (m, 12 H, THF), 2.92 (m, 2 H, PCy), 2.53 (m, 2 H, PCy), 2.31 (m, 2 H, PCy), 2.13 – 1.97 (overlapping resonances, 8 H, PCy), 1.81 – 0.73 (overlapping resonances, 49 H, PCy + THF + PMe₃; the THF resonance was identified at 0.94 ppm, the PMe₃ resonance was identified as a doublet at 1.37 ppm (d, ²*J*_{PH} = 2.7 Hz, 9 H), 0.58 (s, 3 H, SiMe), 0.00 (m, 2 H, PCy). ¹³C{¹H} NMR (75.5 MHz, benzene-*d*₆): δ 148.4 (*C*_{arom}), 132.3 (t, *J* = 8.3, CH_{arom}), 128.5 (CH_{arom}), 126.1 (*C*_{arom}), 125.1 (CH_{arom}), 123.3 (CH_{arom}), 67.8 (THF), 43.4 (CH_{Cy}), 34.3 (CH_{Cy}), 30.1 (CH_{2Cy}), 29.5 (CH_{2Cy}), 28.5 – 25.5 (overlapping resonances, CH_{2Cy} + THF; the THF resonance was identified at 25.6 ppm), 24.2 (d, *J* = 12.1 Hz, PMe₃), 5.8 (SiMe). ³¹P{¹H} NMR (202.5 MHz, benzene-*d*₆): δ 92.8 (d, 2 H, P*SiP*, ²*J*_{PP} = 34 Hz), 10.1 (t, 1 H, PMe₃, ²*J*_{PP} = 32 Hz). ²⁹Si NMR (59.6 MHz, benzene-*d*₆): δ 62.7. IR (thin film, cm⁻¹): 1891 (s, νN₂).

(Cy-PSiP)Fe(PMe₃)H (2-H). To a solution of **2-PMe₃** (0.030 g, 0.040 mmol) in ca. 3 mL benzene was added NaEt₃BH (0.040 μL, 0.040 mmol) as a 1M solution in toluene *via* microsyringe. A color change from red to dark brown was observed and the resulting mixture was stirred for 18 h at room temperature. Volatile components of the reaction mixture were removed *in vacuo* and the residue was triturated with 3 × 1 mL pentane and extracted with 5 mL of a ca. 1:1 pentane : benzene mixture and filtered through a glass

microfiber filter. The filtrate was evaporated to dryness *in vacuo* and triturated with 3 × 1 mL pentane to afford **2-H** as a pale beige solid (0.021 g, 74% yield). As this complex was observed to gradually convert to both (Cy-PSiP)FeH(PMe₃)(N₂)^{73b} and **2-H₃** over time, no combustion analysis data could be obtained. ¹H NMR (500.1 MHz, benzene-*d*₆): δ 8.36 (d, *J* = 7.5 Hz, 2 H, *H*_{arom}), 7.01 (d, *J* = 8.0 Hz, 2 H, *H*_{arom}), 7.33 (t, *J* = 7.0 Hz, 2 H, *H*_{arom}), 7.23 (t, *J* = 7.5 Hz, 2 H, *H*_{arom}), 2.38 (m, 2 H, PCy), 2.16 (m, 4 H, PCy), 2.04 (m, 2 H, PCy), 1.05 – 1.90 (overlapping resonances, 45 H, PCy + PMe₃, the PMe₃ resonance was identified as a doublet (²*J*_{PH} = 5.5 Hz) at 1.49 ppm), 0.96 (s, 3 H, SiMe), -18.53 (td, ²*J*_{PH} = 64.0 Hz, ²*J*_{PH} = 24.0 Hz, 1 H, FeH). ¹³C{¹H} NMR (125.8 MHz, benzene-*d*₆): δ 160.5 (apparent t, *J* = 21 Hz, C_{arom}), 149.6 (m, C_{arom}), 132.0 (apparent t, *J* = 8 Hz, CH_{arom}), 128.5 (CH_{arom}), 128.4 (CH_{arom}), 127.0 (CH_{arom}), 42.5 (CH_{Cy}), 32.0 (CH_{Cy}), 29.9 (CH_{2Cy}), 29.6 (CH_{2Cy}), 29.1 (CH_{2Cy}), 28.8 (CH_{2Cy}), 28.6 – 26.6 (overlapping resonances, CH_{2Cy}), 24.3 (d, ¹*J*_{CP} = 16 Hz, PMe₃), 6.2 (SiMe). ³¹P{¹H} NMR (202.5 MHz, benzene-*d*₆): δ 90.0 (d, ²*J*_{PP} = 55 Hz, 2 P, PSiP), 3.6 (t, ²*J*_{PP} = 55 Hz, 1 P, PMe₃). ²⁹Si NMR (99.4 MHz, benzene-*d*₆): δ 77.4 (d, *J*_{SiH} = 19.5 Hz). IR (thin film, cm⁻¹): 1815 (m, νFeH).

(Cy-PSiP)FeH(PMe₃)(N₂)_{0.125} (2-H(N₂)). Mg powder (0.009 g, 0.33 mmol) was added to a solution of **2-PMe₃** (0.029 g, 0.033 mmol) in ca. 5 mL of THF. HBPIn (0.055 mL, 0.048 g, 0.33 mmol) was added dropwise to the reaction mixture. The resulting mixture was stirred at room temperature for 18 h, at which time the volatile components were removed *in vacuo*. The remaining residue was extracted with ca. 5 mL of Et₂O and the combined extracts were filtered through Celite. The filtrate solution was evaporated to dryness under vacuum and the remaining residue was triturated with 3 × 2 mL of

pentane and subsequently dried *in vacuo*. The residue was recrystallized from *ca.* 2 mL Et₂O at -35 °C to afford a minute quantity (*ca.* 5 mg) of green crystals of **2-H(N₂)**.

[Cy-PSi(μ -H)P]FeH₂(PMe₃) (2-H₃). To a solution of **2-PMe₃** (0.067 g, 0.089 mmol) in *ca.* 5 mL of benzene was added NaEt₃BH (0.089 mL, 0.089 mmol) as a 1 M solution in toluene *via* microsyringe. The resulting mixture was stirred for 2 h at room temperature and then evaporated to dryness *in vacuo*. The resulting residue was triturated with 3 \times 2 mL pentane and then redissolved in *ca.* 3 mL benzene and filtered through Celite. The filtrate was transferred to a 50 mL Teflon-sealed reaction vessel and subsequently degassed through sequential freeze-pump-thaw cycles and placed under an atmosphere of H₂ gas. The mixture was stirred for 18 h at 65 °C before volatile components of the reaction mixture were removed *in vacuo*. The residue was then triturated with 3 \times 2 mL pentane and then washed with 3 \times 1 mL pentane to yield **2-H₃** as a beige-yellow solid (0.052 g, 81% yield). X-ray quality crystals of **2-H₃** were grown from liquid-liquid diffusion of cold pentane into a concentrated solution of **2-H₃** in THF at room temperature. ¹H NMR (300 MHz, benzene-*d*₆; ABXY₂Z spin system, where Y₂Z = (RPCy₂)₂(PMe₃)); δ 8.22 (d, *J* = 6.9 Hz, 2 H, *H*_{arom}), 7.42 (d, *J* = 7.2 Hz, 2 H, *H*_{arom}), 7.26 (t, *J* = 7.2 Hz, 2 H, *H*_{arom}), 7.12 (t, *J* = 6.9 Hz, 2 H, *H*_{arom}), 2.53 (m, 2 H, PCy), 2.30 – 1.05 (overlapping resonances, 50 H, PCy + PMe₃ + SiMe; the PMe₃ resonance was identified as a doublet at 1.36 ppm (d, ²*J*_{PH} = 6.6 Hz, 9 H), the SiMe resonance was identified as a singlet at 1.13 ppm (s, 3 H)), 0.79 (m, 2 H, PCy), 0.42 (m, 2 H, PCy), A = -9.5 ppm (1H, FeH, ²*J*_{HH} = -9.18 Hz, ²*J*_{HH} = -11.63 Hz, ²*J*_{H-PCy₂} = 51.07 Hz, ²*J*_{H-PMe₃} = 70.40 Hz), B = -9.8 ppm (1H, SiHFe, ²*J*_{HH} = -9.18 Hz, ²*J*_{H-PCy₂} = 16.42 Hz, ²*J*_{H-PMe₃} = 41.07 Hz), X = -14.5 ppm (1H, FeH, ²*J*_{HH} = -11.63 Hz, ²*J*_{H-PCy₂} = 59.36 Hz, ²*J*_{H-PMe₃} =

15.31 Hz). $^{13}\text{C}\{\text{H}\}$ NMR (75.5 MHz, benzene- d_6): δ 160.1 (C_{arom}), 148.1 (C_{arom}), 131.8 (CH_{arom}), 127.7 (CH_{arom}), 127.3 (CH_{arom}), 125.8 (CH_{arom}), 39.0 (CH_{Cy}), 34.5 (apparent t, $J = 13.6$ Hz, CH_{Cy}), 29.6 ($\text{CH}_{2\text{Cy}}$), 29.1 ($\text{CH}_{2\text{Cy}}$), 28.4 – 27.3 (overlapping resonances, $\text{CH}_{2\text{Cy}}$), 26.7 ($\text{CH}_{2\text{Cy}}$), 9.13 (SiMe). $^{31}\text{P}\{\text{H}\}$ NMR (121.5 MHz, benzene- d_6): δ 100.8 (d, $^2J_{\text{PP}} = 29.2$ Hz, 2 P, P*SiP*), 18.7 (t, $^2J_{\text{PP}} = 29.2$ Hz, 1 P, P*Me*₃). ^{29}Si NMR (59.6 MHz, benzene- d_6): δ 32.7. IR (KBr pellet, cm^{-1}): 1925 (ν_{FeH}), 1871 (ν_{FeH}), 1846 (ν_{FeH}). Anal. Calcd. For $\text{C}_{40}\text{H}_{67}\text{P}_3\text{SiFe}$: C, 66.28; H, 9.32. Found: C, 65.94; H, 9.21.

(Cy-PSiP)FeH(py)(N₂) (2-py(N₂)). To a solution of **2-py** (0.037 g, 0.049 mmol) in *ca.* 3 mL of benzene was added NaEt₃BH (0.049 mL, 0.049 mmol) as a 1M solution in toluene *via* microsyringe. A gradual color change from dark red-orange to yellow-orange was observed and the mixture was stirred for 18 h at room temperature. Volatile components of the reaction mixture were removed *in vacuo* and the residue was triturated with 3 × 2 mL pentane. The residue was then extracted with *ca.* 3 mL benzene and filtered through Celite, combined with *ca.* 5 equiv pyridine (*ca.* 20 μL) and allowed to stir briefly (5 min) before all volatiles were removed *in vacuo*. The resulting solid was triturated with 3 × 2 mL pentane and washed with 3 × 0.5 mL cold pentane to afford a red solid mixture (0.024 g) of **2-py(N₂)** and **2-(N₂)₂**. Due to significant conversion of **2-py(N₂)** to **2-(N₂)₂** during workup, pure **2-py(N₂)** could not be isolated and thus no yield or combustion analysis data can be reported. A slight excess of pyridine was thus added to the mixture to minimize the amount of **2-(N₂)₂** for spectroscopic analysis. X-ray quality crystals of **2-py(N₂)** could be obtained from slow evaporation of an Et₂O solution of **2-py(N₂)** at room temperature (NMR analysis of these crystals again indicated a mixture of **2-py(N₂)** and **2-(N₂)₂**. ^1H NMR (300.1 MHz, benzene- d_6): δ 9.35 (broad, 1 H, H_{py}), 8.31

(d, $J = 7.2$ Hz, 2 H, H_{arom}), 8.14 (broad, 1 H, H_{py}), 7.75 (d, $J = 6.9$ Hz, 2 H, H_{arom}), 7.35 (apparent t, $J = 7.2$ Hz, 2 H, H_{arom}), 7.26 (apparent t, $J = 7.2$ Hz, 2 H, H_{arom}), 6.81 (broad, 1 H, H_{py}), 6.55 – 6.30 (overlapping resonances, 2 H, H_{py}), 2.62 (m, 2 H, PCy), 2.10 – 0.90 (overlapping resonances, 42 H, PCy), 0.75 (s, 3 H, SiMe), -15.34 (t, $^2J_{\text{PH}} = 60.6$ Hz, 1 H, FeH). $^{13}\text{C}\{\text{H}\}$ NMR (125.8 MHz, benzene- d_6): δ 162.2 (t, $J = 23.9$ Hz, C_{arom}), 159.8 (CH_{py}), 153.7 (CH_{py}), 147.1 (t, $J = 25.2$ Hz, C_{arom}), 133.4 (CH_{py}), 132.6 (t, $J = 8.8$ Hz, CH_{arom}), 129.0 (CH_{arom}), 128.9 (CH_{py}), 128.8 (CH_{arom}), 127.2 (CH_{arom}), 123.3 (CH_{py}), 40.4 (CH_{Cy}), 32.3 (CH_{Cy}), 29.9 (CH_2Cy), 29.4 (CH_2Cy), 29.2 (CH_2Cy), 28.9 (CH_2Cy), 28.4 – 28.1 (overlapping resonances, CH_2Cy), 28.0 (CH_2Cy), 27.7 (CH_2Cy), 27.5 (CH_2Cy), 27.3 (CH_2Cy), 6.2 (SiMe). $^{31}\text{P}\{\text{H}\}$ NMR (121.5 MHz, benzene- d_6): δ 80.2. ^{29}Si NMR (99.4 MHz, benzene- d_6): δ 72.3 ($^2J_{\text{SiH}} = 67.1$ Hz). IR (thin film, cm^{-1}): 2012 (νN_2), 1949 (νFeH).

(Cy-PSiP)FeH(N₂)₂ (2-(N₂)₂). To a solution of **2-py** (0.11 g, 0.14 mmol) in *ca.* 7 mL of benzene was added NaEt₃BH (0.14 mL, 0.14 mmol) as a 1M solution in toluene *via* microsyringe. A gradual color change from dark red-orange to yellow-orange was observed and the mixture was stirred for 18 h at room temperature. BPh₃ (0.034 g, 0.14 mmol) was then added to the reaction mixture as a solution in *ca.* 1 mL benzene) and the mixture was stirred for a further 2 h. Volatile components of the reaction mixture were removed *in vacuo* and the resulting residue was triturated with 3 × 3 mL pentane, then extracted with *ca.* 15 mL pentane and filtered through Celite. The filtrate was evaporated to dryness and subsequently washed with 3 × 1 mL pentane to yield **2-(N₂)₂** as a beige solid (0.051 g, 61% yield). X-ray quality crystals of **2-(N₂)₂** were obtained from slow evaporation of a concentrated 1:1 solution of pentane and Et₂O of **2-(N₂)₂** at room

temperature. ^1H NMR (500.1 MHz, benzene- d_6): δ 8.14 (d, $J = 7.5$ Hz, 2 H, H_{arom}), 7.58 (apparent d, $J = 7.5$ Hz, 2 H, H_{arom}), 7.30 (t, $J = 7.0$ Hz, 2 H, H_{arom}), 7.19 (t, $J = 7.5$ Hz, 2 H, H_{arom}), 2.49 (m, 2 H, PCy), 2.39 (m, 2 H, PCy), 2.23 (m, 2 H, PCy), 2.02 (m, 2 H, PCy), 1.91 (m, 2 H, PCy), 1.86 – 1.75 (overlapping resonances, 4 H, PCy), 1.70 (m, 2 H, PCy), 1.65 – 1.46 (overlapping resonances, 12 H, PCy), 1.44 – 1.04 (overlapping resonances, 16 H, PCy), 0.71 (s, 3 H, SiMe), -16.31 (t, $^2J_{\text{PH}} = 58.5$ Hz, 1 H, FeH). $^{13}\text{C}\{^1\text{H}\}$ NMR (125.8 MHz, benzene- d_6): δ 159.9 (apparent t, $J = 23.9$ Hz, C_{arom}), 145.1 (apparent t, $J = 26.4$ Hz, C_{arom}), 132.5 (apparent t, $J = 8.8$ Hz, CH_{arom}), 129.2 (CH_{arom}), 128.7 (CH_{arom}), 127.4 (CH_{arom}), 39.6 (apparent t, $J = 5.0$ Hz, CH_{Cy}), 38.6 (apparent t, $J = 10.1$ Hz, CH_{Cy}), 29.6 ($\text{CH}_{2\text{Cy}}$), 29.5 ($\text{CH}_{2\text{Cy}}$), 28.9 ($\text{CH}_{2\text{Cy}}$), 28.2 – 28.0 (overlapping resonances, $\text{CH}_{2\text{Cy}}$), 27.6 ($\text{CH}_{2\text{Cy}}$), 27.3 (apparent t, $J = 6.3$ Hz, $\text{CH}_{2\text{Cy}}$), 27.1 ($\text{CH}_{2\text{Cy}}$), 26.7 ($\text{CH}_{2\text{Cy}}$), 5.9 (SiMe). $^{31}\text{P}\{^1\text{H}\}$ NMR (202.5 MHz, benzene- d_6): δ 87.3. ^{29}Si NMR (99.4 MHz, benzene- d_6): δ 69.0 (d, $J_{\text{SiH}} = 70$ Hz). IR (thin film, cm^{-1}): 2123 (νN_2), 2063 (νN_2), 2012 (νFeH). Anal. Calcd. for $\text{C}_{37}\text{H}_{56}\text{N}_4\text{P}_2\text{SiFe}$: C, 63.24; H, 8.03; N, 7.97. Found: C, 62.91; H, 7.88; N, 7.80.

General Procedure for Catalytic Hydrogenation Experiments. All hydrogenations were performed on a 0.057 mmol substrate scale using a 250 μL total reaction volume. All substrates and catalysts were delivered *via* microsyringe as stock solutions in the indicated solvent (typically benzene- d_6). To a 1 dram vial containing pre-weighed internal standard (trimethoxybenzene) is added 0.057 mmol substrate (as a stock solution in benzene- d_6) and **2**-(N_2)₂ (as a stock solution in benzene- d_6). Additional benzene- d_6 was then added to bring the total reaction volume to 250 μL . The vial was then equipped with a stirbar and closed with a PTFE-sealed cap, with a needle inserted

through the seal to allow addition of H₂ gas. The vial was then transferred to a Parr reactor which was sealed and purged with H₂ gas and subsequently pressurized to 10 atm. The Parr reactor was heated to 65 °C in an oil bath for the duration of the reaction time. Afterward, the Parr reactor was removed from heat, allowed to cool, and depressurized of H₂. In the glovebox, the sample was transferred to an NMR tube for data acquisition. For calculation of NMR conversions, a chosen diagnostic product signal was integrated relative to that of the internal standard. An excessively long relaxation delay (60 seconds) was used to ensure accurate integration. All reactions were performed in duplicate and reported conversions are the average of both runs. The same procedure was followed for all hydrogenations at 10 atm, with variations in solvent, catalyst, or temperature as indicated. For hydrogenations at 1 atm (at room temperature or 65 °C), reactions were performed in 50 mL thick-walled reaction vessel equipped with a Teflon stopcock, from which headspace N₂ was removed *via* one freeze-pump-thaw cycle.

Procedure for Catalytic Hydrogenation of α -Methylstyrene. A 1 dram vial containing 1,3,5-trimethoxybenzene (9.7 mg) was charged with 0.057 mmol α -methylstyrene (82.7 μ L of a 0.69 M stock solution in benzene-*d*₆) and 2-(N₂)₂ (as 100 μ L of a 0.028 M stock solution in benzene-*d*₆). Benzene-*d*₆ (67.3 μ L) was then added to bring the total reaction volume to 250 μ L. The vial was then equipped with a stirbar and closed with a PTFE-sealed cap, with a needle inserted through the seal to allow for the introduction of H₂ gas. The vial was then transferred to a Parr reactor which was sealed and purged with H₂ and subsequently pressurized to 10 atm. The Parr reactor was heated at 65 °C in an oil bath for 4 h. Afterward, the Parr reactor was removed from heat, allowed to cool to room temperature, and depressurized of H₂. In the glovebox, the sample was transferred to an

NMR tube for data acquisition. 98.6% conversion to cumene (0.055 mmol) was calculated relative to the internal standard by ^1H NMR spectroscopy. This value represents one of two runs averaged to give the value reported in Table 2.2.2.

Procedure for Catalytic Hydrogenation of *cis*-Stilbene and Isolation of Bibenzyl. A 1 dram vial was charged with 0.020 g **2-(N₂)₂** (0.028 mmol) and 2.4 mL benzene. *cis*-Stilbene (102 μL , 0.57 mmol) was added *via* microsyringe. The vial was then equipped with a stirbar and closed with a PTFE-sealed cap with a needle inserted through the seal to allow for the introduction of H₂ gas. The vial was then transferred to a Parr reactor which was sealed and purged with H₂ and subsequently pressurized to 10 atm. The Parr reactor was heated at 65 °C in an oil bath for 4 h. Afterward, the Parr reactor was removed from heat, allowed to cool, and depressurized of H₂. In the glovebox, the sample was evaporated to dryness *in vacuo* and the residue was extracted with 3 mL pentane and filtered through a plug of silica gel. The filtrate solution was concentrated *in vacuo* and cooled to -35 °C. Bibenzyl was isolated as a white crystalline solid (0.095 g, 2 crops, 0.52 mmol by this method.

2.4.3 Crystallographic Solution and Refinement Details

Crystallographic data for each of **2-Br**, **2-Cl·(Et₂O)_{0.5}**, **2-Me**, **2-PMe₃**, **2-(CO)₂·(Et₂O)_{0.5}**, **2-Fe^I**, **2-H·(Et₂O)_{0.5}**, **2-H(N₂)·(Et₂O)_{0.75}**, **2-H₃·(C₅H₁₂)_{0.75}**, **2-py(N₂)·(Et₂O)₂** and **2-(N₂)₂** were obtained at 173(±2) K on either a Bruker D8/APEX II CCD diffractometer using Cu K α ($\lambda = 1.54178$ Å, microfocus source) radiation (for **2-Br**, **2-Me**, **2-PMe₃**, **2-(CO)₂·(Et₂O)_{0.5}**, **2-Fe^I**, **2-H·(Et₂O)_{0.5}**, **2-H(N₂)·(Et₂O)_{0.75}**, **2-H₃·(C₅H₁₂)_{0.75}**, **2-py(N₂)·(Et₂O)₂** and **2-(N₂)₂**) or a Bruker PLATFORM/APEX II CCD diffractometer using graphite-monochromated Mo K α ($\lambda = 0.71073$ Å) radiation (for **2-**

Cl·(Et₂O)_{0.5}), employing a sample that was mounted in inert oil and transferred to a cold gas stream on the diffractometer. Programs for diffractometer operation, data collection, and data reduction (including SAINT) were supplied by Bruker. Gaussian integration (face-indexed) was employed as the absorption correction method in each case. The structures of **2-Br**, **2-Me**, **2-PMe₃**, and **2-Fe^I** were solved by use of the Patterson search/structure expansion, while those of **2-Cl·(Et₂O)_{0.5}**, **2-(CO)₂·(Et₂O)_{0.5}**, **2-H·(Et₂O)_{0.5}**, **2-H(N₂)·(Et₂O)_{0.75}**, **2-H₃·(C₅H₁₂)_{0.75}**, **2-py(N₂)·(Et₂O)₂** and **2-(N₂)₂** were solved by use of intrinsic phasing methods. All structures were refined by use of full-matrix least-squares procedures (on F^2) with R_1 based on $F_o^2 \geq 2\sigma(F_o^2)$ and wR_2 based on $F_o^2 \geq -3\sigma(F_o^2)$.

For **2-Br** the crystal used for data collection was found to display non-merohedral twinning. Both components of the twin were indexed with the program *CELL_NOW* (Bruker AXS Inc., Madison, WI, 2004). The second twin component can be related to the first component by 3.8° rotation about the $[1 \ 1/5 \ -1/2]$ axis in real space and about the $[3/8 \ 1 \ -3/8]$ axis in reciprocal space. Integrated intensities for the reflections from the two components were written into a *SHELXL-2014* HKLF 5 reflection file with the data integration program *SAINTE* (version 8.34A), using all reflection data (exactly overlapped, partially overlapped and non-overlapped). The refined value of the twin fraction (*SHELXL-2014* BASF parameter) was 0.387(2).

For **2-Cl·(Et₂O)_{0.5}** attempts to refine peaks of residual electron density as disordered or partial-occupancy solvent diethyl ether oxygen or carbon atoms were unsuccessful. The data were corrected for disordered electron density through use of the SQUEEZE procedure as implemented in *PLATON*.¹¹⁷ A total solvent-accessible void

volume of 1576 Å³ with a total electron count of 155 (consistent with 4 molecules of solvent diethyl ether, or 0.5 molecules per formula unit of the iron complex molecule) was found in the unit cell.

For **2-Me** the crystal used for data collection was found to display non-merohedral twinning. Both components of the twin were indexed with the program *CELL_NOW* (Bruker AXS Inc., Madison, WI, 2004). The second twin component can be related to the first component by 180° rotation about the [1 1/4 3/4] axis in real space and about the [1 0 1] axis in reciprocal space. Integrated intensities for the reflections from the two components were written into a *SHELXL-2014* HKLF 5 reflection file with the data integration program *SAINTE* (version 8.34A), using all reflection data (exactly overlapped, partially overlapped and non-overlapped). The refined value of the twin fraction (*SHELXL-2014* BASF parameter) was 0.4740(12).

For **2-H·(Et₂O)_{0.5}** attempts to refine peaks of residual electron density as disordered or partial-occupancy solvent diethyl ether oxygen or carbon atoms were unsuccessful. The data were corrected for disordered electron density through use of the SQUEEZE procedure as implemented in *PLATON*.¹¹⁷ A total solvent-accessible void volume of 1146 Å³ with a total electron count of 221 (consistent with four molecules of solvent diethyl ether, or one-half solvent molecule per formula unit of the iron complex molecule) was found in the unit cell. The Flack parameter will refine to a value near zero if the structure is in the correct configuration and will refine to a value near one for the inverted configuration. The value observed herein (0.304(8)) is indicative of racemic twinning, and was accommodated during the refinement (using the *SHELXL-2014* TWIN

instruction.¹¹⁸ Primed atoms are related to unprimed atoms through the crystallographic mirror plane (x, y, z) upon which the atoms Fe, P2, Si and H1 are located.

For **2-H(N₂)·(Et₂O)_{0.75}** attempts to refine peaks of residual electron density as disordered or partial-occupancy solvent diethyl ether oxygen or carbon atoms were unsuccessful. The data were corrected for disordered electron density through use of the SQUEEZE procedure as implemented in *PLATON*.¹¹⁷ A total solvent-accessible void volume of 1150 Å³ with a total electron count of 258 (consistent with 6 molecules of solvent diethyl ether, or 0.75 molecules per formula unit of the iron complex molecule) was found in the unit cell. The data were tested for merohedral twinning using the TwinRotMat procedure as implemented in *PLATON*.¹¹⁹ The second twin component can be related to the first component by twofold rotation about the [1 1 0] axis (twin law [0 1 0 1 0 0 0 0 -1]). The refined value of the twin fraction (*SHELXL-2014* BASF parameter) was 0.453(10). The atoms comprising the coordinated N₂ ligand (N1 and N2) were refined isotropically with an occupancy factor of 0.125. Primed atoms are related to the unprimed atoms by the mirror plane parallel to [1 1 0].

For **2-H₃·(C₅H₁₂)_{0.75}** attempts to refine peaks of residual electron density as disordered or partial-occupancy solvent pentane carbon atoms were unsuccessful. The data were corrected for disordered electron density through use of the SQUEEZE procedure as implemented in *PLATON*.¹¹⁷ A total solvent-accessible void volume of 1200 Å³ with a total electron count of 254 (consistent with 6 molecules of solvent pentane, or 0.75 molecules per formula unit of the iron complex) was found in the unit cell. The data were tested for nonmerohedral twinning using the TwinRotMat procedure as implemented in *PLATON*.¹¹⁹ The second twin component can be related to the first

component by twofold rotation about the $[0\ 1\ -1]$ axis (twin law $[-1\ 0\ 0\ 0\ 0\ -1\ 0\ -1\ 0]$). Furthermore, the data also exhibited racemic (inversion) twinning. The refined value of the twin fractions (*SHELXL-2014* BASF parameter) were 0.128(2), 0.0386(2), and 0.155(2). The Flack parameter cannot be determined as twinning by inversion was present.

For **2-py(N₂)·(Et₂O)₂** attempts to refine peaks of residual electron density as disordered or partial-occupancy solvent diethyl ether oxygen or carbon atoms were unsuccessful. The data were corrected for disordered electron density through use of the SQUEEZE procedure as implemented in *PLATON*.¹¹⁷ A total solvent-accessible void volume of 1504 Å³ with a total electron count of 314 (consistent with 8 molecules of solvent diethyl ether, or 2 molecules per formula unit of the iron compound) was found in the unit cell.

With the exceptions noted above for **2-H(N₂)·(Et₂O)_{0.75}**, anisotropic displacement parameters were employed throughout for the non-hydrogen atoms. In the case of **2-H·(Et₂O)_{0.5}**, **2-H(N₂)·(Et₂O)_{0.75}**, **2-H₃·(C₅H₁₂)_{0.75}**, **2-(py)(N₂)·(Et₂O)₂** and **2-(N₂)₂**, the Fe-*H* (H1) (and H2 and H3 for **2-H₃·(C₅H₁₂)_{0.75}**) were located in the difference Fourier map and refined isotropically. All remaining hydrogen atoms were added at calculated positions and refined by use of a riding model employing isotropic displacement parameters based on the isotropic displacement parameter of the attached atom. Additional crystallographic information is provided in Appendix A.

Chapter 3: Activation of Molecular Hydrogen and Oxygen by PSiP Complexes of Cobalt

3.1 Introduction

As indicated in Chapters 1 and 2, over recent years there has been increasing interest in replacing platinum group metals with first-row transition metals in various reactivity applications due to their high abundance and significantly lower cost.^{6, 11, 100, 120} This has led to an increased interest in examining the reactivity properties of first-row metal complexes supported by PSiP ligation. In particular, building on prior investigations of Cy-PSiP Rh and Ir species,⁷⁴⁻⁷⁵ including aggressive bond activation reactivity exhibited by the latter, related (Cy-PSiP)Co complexes were targeted to study their reactivity towards small molecule substrates.

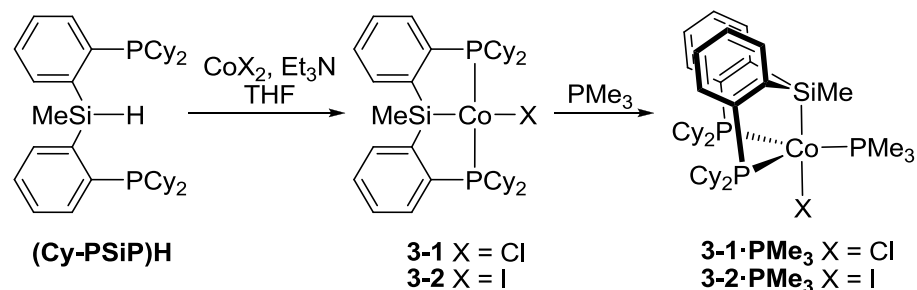
In this chapter the synthesis and characterization of low-coordinate (Cy-PSiP)Co^{II} halide complexes is described, as well as the reactivity of such species under reducing conditions aimed at accessing (Cy-PSiP)Co^I complexes. The ability of such (Cy-PSiP)Co^I species to undergo oxidative addition processes was evaluated, and evidence of H₂ activation was observed. In this regard, such Co^I species were found to be precatalysts for alkene hydrogenation. The reactivity of (Cy-PSiP)Co^{II} species towards O₂ and Me₃NO is also described, wherein the formation of a siloxo fragment by formal insertion of an oxygen atom into the Si-Co linkage is observed. In the course these investigations, two relevant publications pertaining to this work appeared. Kim, Lee and co-workers reported on the conversion of [ⁱPr-P(η^1 -SiH)P]CoBr₂ to (ⁱPr-PSiP)CoBr in the presence of base,^{24d} and Nishibayashi and co-workers reported on the synthesis of (Cy-PSiP)Co(PR₃)N₂ species and their activity in catalytic N₂ reduction.^{73b, 25b, 73a}

The results described in this chapter are a continuation of work initially done by a former graduate student in the Turculet group, Adam Ruddy.⁸¹ Adam Ruddy should be credited for all the work described in section 3.2.1, the synthesis and characterization of compound **3-3** (including other attempts at reducing compound **3-2**) and initial synthesis of compound **3-5**, as well as for investigating the chemistry of compound **3-3** toward I₂, iodobenzene and ammonia-borane (briefly mentioned in section 3.2.3).

3.2 Results and Discussion

3.2.1 Previous Work Involving Synthesis of Co^{II} Halide Complexes of Cy-PSiP

Previously,⁸¹ the synthesis of low-coordinate (Cy-PSiP)Co^{II} species was achieved by treatment of simple CoX₂ (X = halide) salts with the tertiary silane (Cy-PSiP)H in the presence of base (Scheme 3.2.1). In the case of CoCl₂, treatment with one equiv (Cy-PSiP)H and excess triethylamine in THF solution led to intractable mixtures from which pure material could not be isolated reliably. The use of CoI₂ under the same reaction conditions was found to be a much more reliable route for the preparation of the iodide analogue (Cy-PSiP)CoI (**3-2**), which could be reproducibly isolated in >90% yield via this route. Both complexes adopt distorted square-planar coordination geometry in the solid state, as determined by X-ray crystallographic analysis, with the halide ligand coordinated trans to the silyl group.

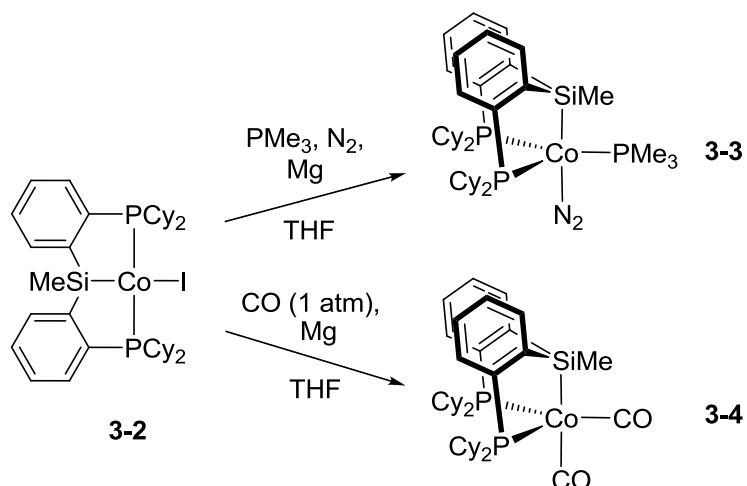


Scheme 3.2.1. Synthesis of (Cy-PSiP)Co^{II}-halide complexes.

Both complexes **3-1** and **3-2** were found to coordinate PMe₃ in a facile manner to generate the corresponding 17-electron adducts, **3-1·PMe₃** and **3-2·PMe₃** (Scheme 3.2.1). In the case of **3-1·PMe₃**, this complex was prepared via in situ generation of **3-1** and subsequent treatment with PMe₃. A yield of 27% was obtained for **3-1·PMe₃** prepared in this manner, despite the difficulty in isolating appreciable amounts of the precursor complex **3-1**. The iodide analogue **3-2·PMe₃** was isolated in 78% yield by treatment of isolated **3-2** with PMe₃. As was the case with their precursor complexes, both **3-1·PMe₃** and **3-2·PMe₃** were observed to be paramagnetic by NMR spectroscopy. An X-ray crystal structure of **3-1·PMe₃** revealed trigonal bipyramidal geometry with the chloride and silyl ligands lying in the apical positions, and the phosphine ligands occupying the equatorial plane.

3.2.2 Reduction of (Cy-PSiP)Co^{II} to (Cy-PSiP)Co^I

Several attempts were previously made⁸¹ to reduce complex **3-2** to a potential (Cy-PSiP)Co^I species. Reducing agents such as Na/Hg (0.5 and 1%), sodium naphthalide, and Mg were used with little success. In each case, **3-2** reacted with the reducing agent within minutes either at room temperature or -35 °C under a N₂ atmosphere to afford dark brown solutions. Despite multiple attempts to recrystallize/purify the crude products, no pure material was successfully isolated from these attempted reduction reactions.



Scheme 3.2.2. Synthesis of $(\text{Cy-PSiP})\text{Co}^{\text{I}}$ species via Mg reduction of **3-2**.

By comparison, treatment of **3-2**·PMe₃ with Mg powder at room temperature under a N₂ atmosphere led to formation of diamagnetic $(\text{Cy-PSiP})\text{Co}(\text{PMe}_3)(\text{N}_2)$ (**3-3**), which could be isolated in >90% yield as a red solid by use of this synthetic route (Scheme 3.2.2). Complex **3-3** was also independently synthesized by Nishibayashi and co-workers^{73b} via treatment of **3-2** with PMe₃ and KC₈ under a N₂ atmosphere, though in substantially lower yield. The coordination of N₂ to the Co center in **3-3** was corroborated by the use of IR spectroscopy, which revealed a characteristic N₂ stretching frequency of 2065 cm⁻¹. In a similar vein, treatment of **3-2** with CO (ca. 1 atm) and subsequently with Mg powder at room temperature under a CO atmosphere led to formation of the corresponding diamagnetic dicarbonyl complex, $(\text{Cy-PSiP})\text{Co}(\text{CO})_2$ (**3-4**, Scheme 3.2.2) in high yield.¹²¹ The X-ray crystal structure of **3-4** (Figure 3.2.1) indicates distorted trigonal bipyramidal geometry at Co, such that the phosphino donors and a CO ligand are coordinated in the equatorial positions (P(1)-Co-P(2) 124.60(2)°, P(1)-Co-C(2) 114.59(6)°, and P(2)-Co-C(2) 116.87(6)°) while Si and the second CO ligand are in the axial positions (Si-Co-C(1) 176.49(6)°). The presence of inequivalent CO ligands in **3-4** was confirmed by use of ¹³C{¹H} NMR spectroscopy, whereby each CO group gives rise

to a unique $^{13}\text{C}\{^1\text{H}\}$ NMR resonance at 207.3 and 220.8 ppm, respectively. In addition, two distinct CO stretches were observed in the infrared spectrum of **3-4** (1960 and 1909 cm^{-1}).

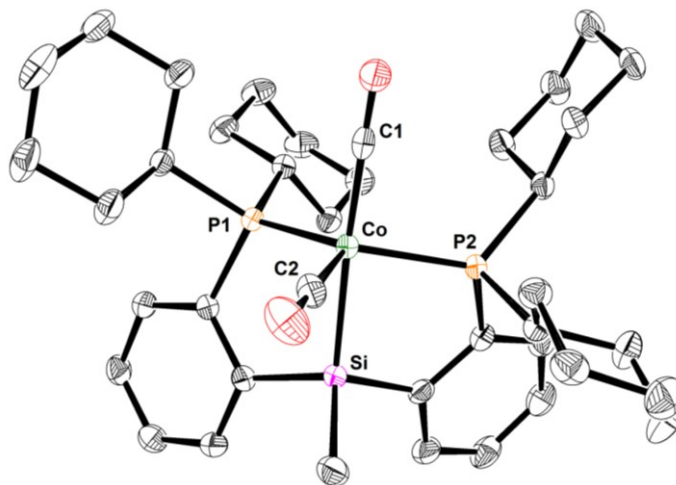


Figure 3.2.1. Crystallographically determined structure of **3-4** with thermal ellipsoids shown at the 50% probability level. Hydrogen atoms have been omitted for clarity. Selected interatomic distances (\AA) and angles ($^\circ$): Co-P(1) 2.2098(5), Co-P(2) 2.2098(5), Co-Si 2.3051(5), Co-C(1) 1.760(2), Co-C(2) 1.739(2), O(1)-C(1) 1.144(2), O(2)-C(2) 1.155(2), P(1)-Co-P(2) 124.60(2), P(1)-Co-C(2) 114.59(6), P(2)-Co-C(2) 116.87(6), Si-Co-C(1) 176.49(6), Si-Co-C(2) 84.09(7), C(1)-Co-C(2) 97.96(10).

Related PCP,¹²² POCOP,¹²³ PNCNP,¹²⁴ and PNP¹²⁵ dicarbonyl complexes of Co have been reported. While most such complexes that have been crystallographically characterized adopt square pyramidal coordination geometry with a CO ligand in the apical position, the solid state structure of **3-4** most closely resembles that of (Ph-PCP)Co(CO)₂ (Ph-PCP = 1,3-(Ph₂PCH₂)₂C₆H₃),¹²² which features a similar distorted trigonal bipyramidal geometry with a P-Co-P angle of 134.6(1) $^\circ$ (*cf.* 124.60(2) $^\circ$ for **3-4**). The CO stretching frequencies reported for the latter complex (1982 and 1929 cm^{-1}) are significantly higher than those noted for **3-4**, suggesting that there is increased back-bonding in **3-4** relative to (Ph-PCP)Co(CO)₂. By comparison, the CO stretching frequencies for **3-4** are closest in value to those reported by Kirchner¹²⁴ for

(PNCNP)Co(CO)₂, which gives rise to CO stretching bands at 1963 and 1906 cm⁻¹, as well as to those reported recently by Guan^{123b} for a series of (POCOP)Co(CO)₂ species (e.g. 1966 and 1912 cm⁻¹ for (1,3-(^tBu₂PO)₂C₆H₃)Co(CO)₂). Interestingly, while the related (PNP)Co(CO)₂ (PNP = (^tBu₂PCH₂SiMe₂)₂N⁻) complex has been observed in solution under 1 atm of CO and features significantly reduced CO stretching frequencies (1931 and 1840 cm⁻¹) relative to **3-4**, this complex readily dissociates CO and is in equilibrium with the isolable monocarbonyl adduct.^{125b} No evidence for facile dissociation of CO from **3-4** was observed.

3.2.3 Investigation of Oxidative Addition Reactions at (Cy-PSiP)CoI and Alkene Hydrogenation Catalysis.

Having successfully prepared isolable Co^I complexes supported by Cy-PSiP ligation, the ability of such complexes to undergo oxidative addition reactions was probed next. Treatment of **3-3** with I₂ (1 or 10 equiv) resulted in an exothermic reaction and the formation of a significant amount of brown precipitate. No clean Co-containing product could be isolated from these reaction mixtures. ³¹P{¹H} NMR analysis of the reaction mixtures indicated the presence of (Cy-PSiP)H in solution (-7.8 ppm). Alternatively, the reaction of **3-3** with iodobenzene (1 or 10 equiv) resulted in an immediate color change of the solution from orange to deep red. ¹H NMR analysis of these reaction mixtures indicated the disappearance of **3-3** as well as the formation of new unidentified, paramagnetic products. No ¹H NMR resonances that could be attributed to biphenyl were observed. Attempts to cleanly isolate the products of this reaction have not been successful thus far. The reaction of **3-4** with either I₂ or MeI also led to the formation of intractable mixtures containing unidentified paramagnetic species.

Next, attention was turned to the reaction of **3-3** with H₂. Treatment of a degassed benzene-*d*₆ solution of **3-3** with H₂ (ca. 1 atm) at room temperature resulted in a color change from orange to yellow-brown over the course of two minutes. Analysis of the reaction mixture by use of ³¹P{¹H} and ¹H NMR spectroscopy indicated the quantitative formation of a new diamagnetic species (**3-5**, Figure 3.2.2), which gives rise to two broad ³¹P{¹H} NMR resonances at 91.6 and 0.1 ppm corresponding to chemically equivalent Cy-PSiP phosphino groups and PMe₃, respectively. The ¹H NMR spectrum of **3-5** features a hydride resonance at -13.51 ppm (broad t, *J* = 38 Hz) that integrates to two hydrogen atoms (relative to the Cy-PSiP ligand backbone). The formation of complex **3-5** was also observed spectroscopically when **3-3** was reacted with 10 equiv H₃N·BH₃ in THF solution at room temperature. The dehydrogenation of H₃N·BH₃ does not appear to be catalytic, as only a small amount of dehydrogenated [BH₂NH₂]_n product (relative to unreacted H₃N·BH₃) was present after the reaction was complete, as determined by ¹¹B NMR analysis.¹²⁶ Complex **3-5** was found to be stable in solution at room temperature for multiple days when kept under an atmosphere of H₂. However, exposure of **3-5** to vacuum resulted in significant decomposition, which precluded the isolation of this complex. Furthermore, when a solution of **3-5** was simply exposed to an atmosphere of N₂, the slow regeneration of **3-3** was observed (by ³¹P{¹H} NMR) over the course of several days.

To a first approximation, complex **3-5** may be formulated as either a classical Co^{III} dihydride complex (Cy-PSiP)Co(PMe₃)(H)₂ or a Co^I dihydrogen complex (Cy-PSiP)Co(PMe₃)(H₂) (Figure 3.2.2). While dihydrogen complexes of first-row transition metals remain rare,¹²⁷ several well-characterized examples of Co^I-dihydrogen complexes

have been reported in recent years.^{53, 128} In this context, Peters and co-workers^{128b} have isolated closely related Co-dihydrogen complexes supported by tris-(*o*-diisopropylphosphinophenyl)silyl ligation ($\text{Si}^{iPr}\text{P}_3$) by treatment of a $\text{Co}^I\text{-N}_2$ adduct with H_2 (Figure 3.2.3). While $(\text{Si}^{iPr}\text{P}_3)\text{Co}(\text{H}_2)$ is thermally stable, allowing for X-ray crystallographic characterization of this complex, H_2 is displaced from the Co coordination sphere to re-form $(\text{Si}^{iPr}\text{P}_3)\text{Co}(\text{N}_2)$ upon exposure to a N_2 atmosphere. Similar reactivity was subsequently reported by Fout and co-workers,⁵³ who utilized the bis(carbene) pincer ligand bis(mesityl-benzimidazol-2-ylidene)phenyl (^{Mes}CCC) to prepare Co^I -dihydrogen complexes of the type $(^{Mes}\text{CCC})\text{Co}(\text{H}_2)(\text{PR}_3)$ ($\text{R} = \text{Me}, \text{Ph}$) by treatment of the corresponding $\text{Co}^I\text{-N}_2$ adducts with H_2 (Figure 3.2.3). As in the case of $(\text{Si}^{iPr}\text{P}_3)\text{Co}(\text{H}_2)$, $(^{Mes}\text{CCC})\text{Co}(\text{H}_2)(\text{PR}_3)$ is indefinitely stable under an H_2 atmosphere, but slowly converts to $(^{Mes}\text{CCC})\text{Co}(\text{N}_2)(\text{PR}_3)$ upon exposure to 1 atm of N_2 . By comparison, Caulton and co-workers have reported that treatment of the three-coordinate complex $[(^t\text{Bu}_2\text{PCH}_2\text{SiMe}_2)_2\text{N}]\text{Co}$ with ca. 4 atm of H_2 afforded partial conversion to the corresponding classical dihydride complex.¹²⁹

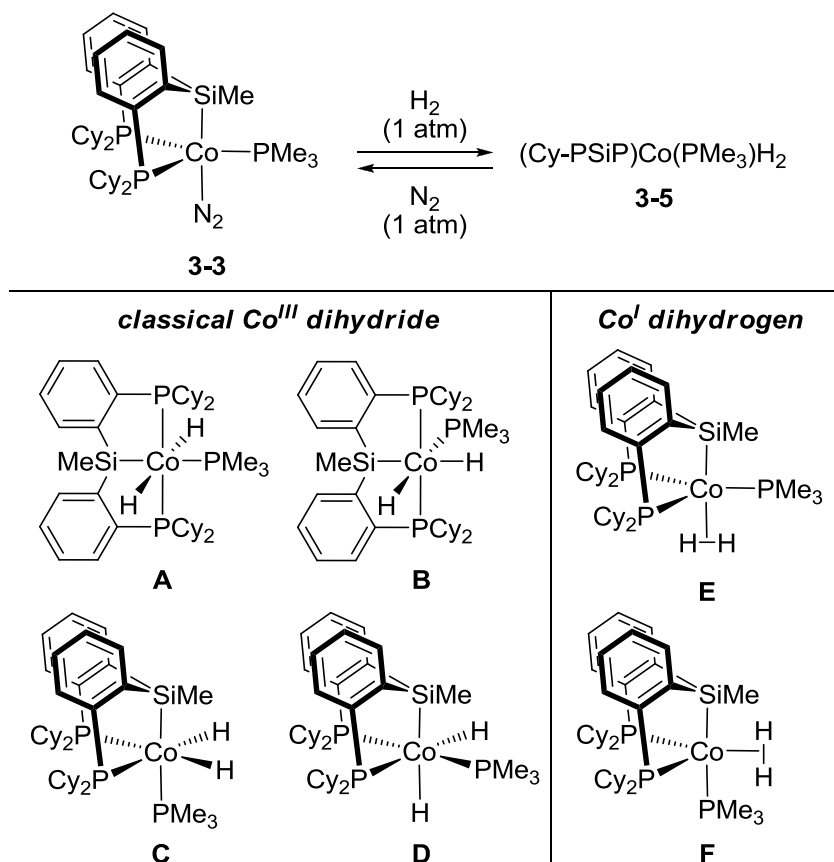


Figure 3.2.2. Some possible structural formulations for the species arising from treatment of (Cy-PSiP)CoN₂(PMe₃) (**3-3**) with H₂.

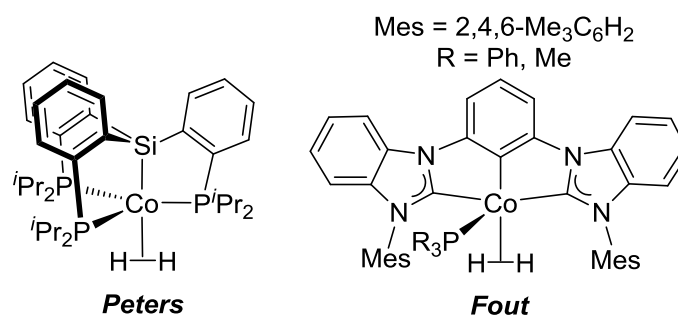


Figure 3.2.3. Examples of previously reported five-coordinate nonclassical Co^I dihydrogen complexes.

In the absence of neutron diffraction data, two NMR techniques that have traditionally been utilized for the characterization of nonclassical dihydrogen complexes are the measurement of ¹H relaxation rates ($T_{1(\text{min})}$) for the hydride resonance, and the measurement of ¹J_{HD} for the partially deuterated complex.^{127a, 130} In the case of the former

approach, while reduced values of $T_{1(\text{min})}$ (generally less than 35 ms) are typically associated with nonclassical H_2 complexes, it has been noted that T_1 relaxation can be significantly affected by metal nuclei that have a high gyromagnetic ratio, such as Co.¹³¹ Thus, low $T_{1(\text{min})}$ values are not necessarily indicative of nonclassical H_2 coordination in the case of Co. By comparison, the value of J_{HD} for a partially deuterated sample ($^1J_{\text{HD}}$ in the range of 15–35 Hz has been cited as typical for nonclassical H_2 complexes) can be more informative in such cases, and has been correlated to the H-H distance of the coordinated H_2 .^{130, 132} As such, in an effort to gain better understanding of the H_2 binding mode in **3-5**, complex **3-3** was treated with HD gas to afford the partially deuterated analogue **3-5-d**. While the resulting $^1\text{H}\{^{31}\text{P}\}$ NMR spectrum of **3-5-d** (toluene- d_8) does reveal changes in the appearance of the hydride resonance relative to **3-5**, these changes are not consistent with H-D coupling (Figure 3.2.4). Rather, it appears that two broad overlapping hydride resonances can now be found in the region of –13 to –14 ppm.

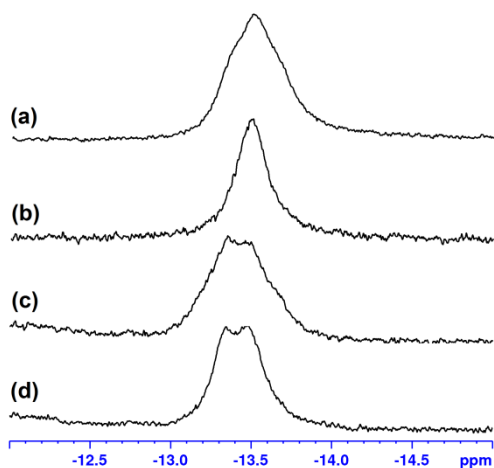


Figure 3.2.4. Partial (a) ^1H and (b) $^1\text{H}\{^{31}\text{P}\}$ NMR spectra (hydride region) of complex **3-5** in toluene- d_8 (300 MHz, 25 °C), as well as (c) ^1H and (d) $^1\text{H}\{^{31}\text{P}\}$ NMR spectra (hydride region) of complex **3-5-d** in toluene- d_8 (300 MHz, 25 °C).

The broad nature of the NMR resonances observed for **3-5-d** could in principle conceal a small H-D coupling. While such broadening may be partly attributed to the

quadrupolar nature of the Co nucleus, variable temperature NMR experiments were carried out for both **3-5** and **3-5-d** to determine if temperature dependent coalescence phenomena are implicated. Indeed, upon heating a sample of **3-5** in toluene-*d*₈ solution up to 80 °C under an H₂ atmosphere, the Co-H ¹H NMR resonance at -13.5 ppm sharpens considerably to reveal an apparent triplet of doublets (²J_{HP} = 18, 42 Hz, Figure 3.2.5a). The ¹H{³¹P} NMR spectrum of **3-5** at this temperature reveals a singlet at -13.5 ppm, confirming that H-H coupling is not observed (Figure 3.2.5b). No significant changes were observed in the ³¹P{¹H} NMR spectrum of **3-5** upon heating to 80 °C (Figure 3.2.7). By comparison, heating a sample of **3-5-d** in toluene-*d*₈ solution under an HD atmosphere did not result in comparable sharpening of the resonance centered at -13.5 ppm. However, the ¹H{³¹P} NMR spectrum of **3-5-d** at 70 °C reveals two singlet resonances at -13.7 and -13.5 ppm (Figure 3.2.6), which is proposed to correspond to a mixture of the isotopomers **3-5** and **3-5-d** that may form as a result of rapid H/D scrambling. Such H/D scrambling phenomena have been previously observed in the reaction of low valent Co species with HD or mixtures of H₂ and D₂.^{53, 128a-c, 131c}

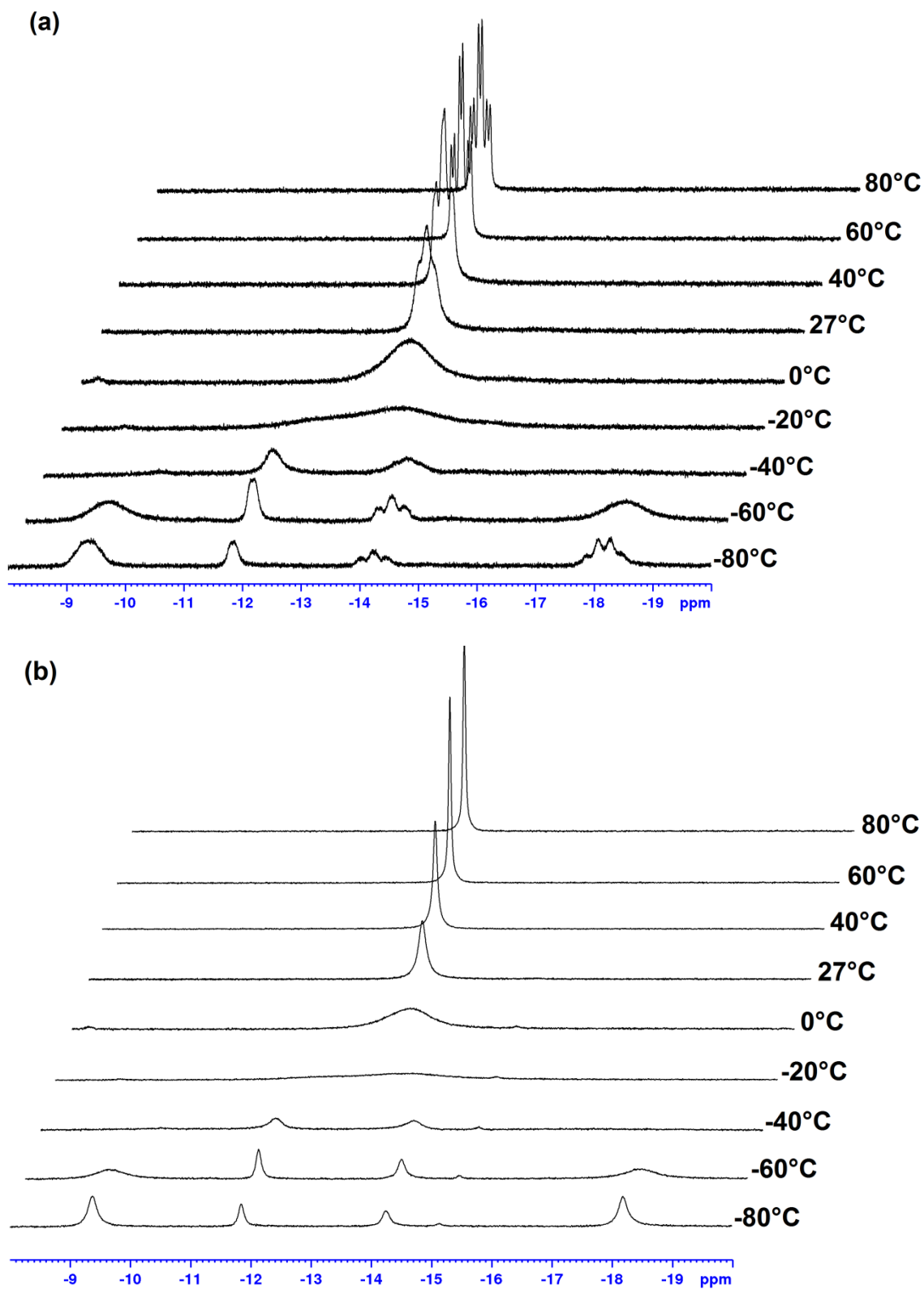


Figure 3.2.5. Partial variable temperature (a) ^1H and (b) $^1\text{H}\{^{31}\text{P}\}$ NMR spectra (hydride region) of complex **3-5** in toluene- d_8 (300 MHz).

The apparent absence of observable H-D coupling in the ^1H NMR spectrum of **3-5-d** suggests that **3-5** is likely better formulated as a classical Co^{III} dihydride complex. A number of structural formulations for such a six-coordinate dihydride species are possible (Figure 3.2.2, **A - D**).

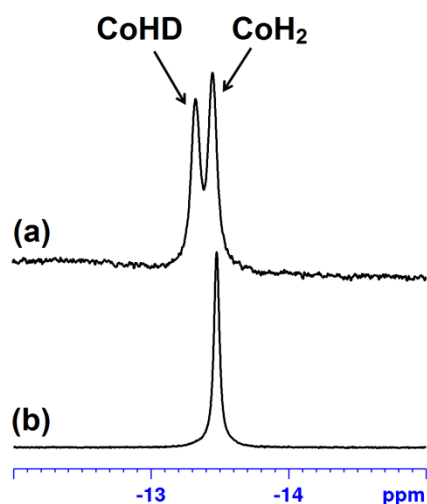


Figure 3.2.6. Partial $^1\text{H}\{^{31}\text{P}\}$ NMR spectra (hydride region) of (a) complex **3-5-d** formed upon addition of HD to **3-3** and (b) complex **3-5** formed upon addition of H_2 to **3-3** in toluene- d_8 (300 MHz, 80 $^\circ\text{C}$).

The NMR spectroscopic features observed for **3-5** at high temperature are not fully consistent with any of the static dihydride structures depicted in Figure 3.2.2, as structures **A - D** should each give rise to distinct Co-H environments. This is readily apparent for structures **B** and **D** where one hydride ligand is *trans* to Si, while the other is *trans* to P. For structure **A** the inequivalence arises from the relationship of each hydride to the SiMe group, which will lie *cis* to one hydride and *trans* to the other. While the Co-H ligands are chemically non-equivalent for **A**, **B** and **D**, in the case of a static structure **C** the hydride ligands are chemically equivalent but magnetically nonequivalent in the presence of phosphorus coupling. As a single resonance is observed in the ^1H NMR spectrum of complex **3-5** at ambient temperature, a rapid dynamic process that

interchanges Co-H environments can be invoked. Such site-exchange in six-coordinate metal dihydride complexes has been studied extensively, including the possibility of dihydrogen complexes as intermediates.^{131c, 133, 134} While such a process can involve dissociation of phosphine (either PMe_3 or a ligand arm), direct ^{31}P NMR evidence for such an intermediate in the range of -80 to 80 °C has not been observed (Figure 3.2.7).

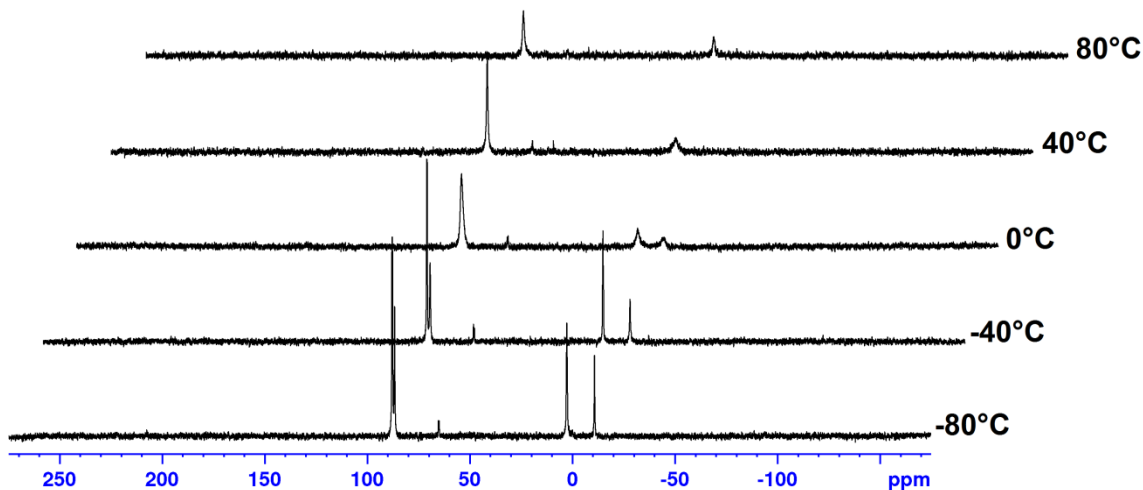


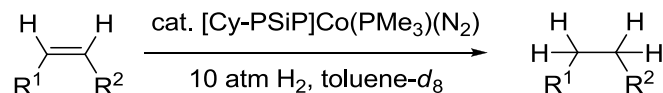
Figure 3.2.7. Variable temperature $^{31}\text{P}\{^1\text{H}\}$ NMR spectra of complex **3-5** in toluene- d_8 (300 MHz).

X-Ray crystallographic data has provided examples of the flexibility of κ^3 -(Cy-PSiP) coordination, with P-Co-P angles ranging from 124 - 160° (*vide supra*),⁸⁹ which suggests that both *fac*- and *mer*- κ^3 -(Cy-PSiP) coordination are feasible and non-dissociative mechanisms for exchange, such as the “trigonal twist” that has been invoked in some circumstances,^{133c, 135} can be accommodated. Upon cooling a sample of **3-5** in toluene- d_8 solution under an H_2 atmosphere, decoalescence is observed, such that four relatively broad, but distinct resonances (ca. 2:1:1:2 ratio) are found in the hydride region of the ^1H NMR spectrum at -80 °C (Figure 3.2.5). The $^{31}\text{P}\{^1\text{H}\}$ NMR spectrum of **5** at this temperature features resonances consistent with the presence of two (Cy-PSiP)Co(PMe₃)(H)₂ species in solution in a ca. 2:1 ratio, where each of these gives rise to

a single resonance corresponding to the Cy-PSiP phosphino donors (at 87.9 (br d, $^2J_{PP} = 23$ Hz) and 86.6 (br s) ppm, respectively, Figure 3.2.7). Thus it appears that two (Cy-PSiP)Co(PMe₃)(H)₂ species, each featuring inequivalent Co-H ligand environments, are present in solution at low temperature. These observations further support the argument that (Cy-PSiP)Co(PMe₃)(H)₂ exhibits complex dynamic behavior. Given the structural similarity between **3-5** and Peters' (Si^{*i*Pr}P₃)Co(H)₂, it is interesting that the latter complex coordinates H₂ in a σ -fashion, while the former appears to cleave the H-H bond. To some degree, this may reflect the increased donor ability of PMe₃ in **3-5** relative to the diisopropyl aryl phosphino donors of the Si^{*i*Pr}P₃ ligand.

Interestingly, (^{*Mes*}CCC)Co(N₂)(PPh₃) has been shown to be an effective pre-catalyst for alkene hydrogenation, including room temperature reactivity.⁵³ Mechanistic studies revealed that the dihydrogen complex (^{*Mes*}CCC)Co(H)₂(PPh₃) is the resting state of the active catalyst, which is proposed to cycle through Co^I/Co^{III} intermediates. Such examples of Co-catalyzed alkene hydrogenation catalysis involving metal-based redox processes are relatively rare.^{18b, 40a, 54-56, 99, 129b, 136} In an effort to assess the competency of **3-3** in alkene hydrogenation catalysis, the reduction of 1-octene with hydrogen gas was evaluated (Table 3.2.1, Entries 1 - 6). At a loading of 5 mol% **3-3**, no appreciable conversion to octane was observed (by ¹H NMR analysis relative to an internal standard of hexamethylbenzene) after 22 h at room temperature under 1 atm of H₂. Heating of the reaction mixture at 60 °C for 22 h afforded only minimal (28%) conversion to octane. Increasing the H₂ pressure to 10 atm resulted in 40% conversion after 4 h at room temperature, and 50% conversion to octane after 22 h at room temperature. By comparison, heating the reaction mixture at 60 °C for 4 h under 10 atm of H₂ afforded

95% conversion to octane. Reducing the loading of **3-3** to 2.5 mol% (Table 3.2.1, Entry 6) afforded comparable conversion (96%) after 4 h at 60 °C under 10 atm of H₂. Selectivity for alkene hydrogenation over ketone hydrogenation was demonstrated using 5-hexen-2-one, which led to 73% conversion to 2-hexanone with a 5 mol% catalyst loading (Entry 8). Lastly, under comparable reaction conditions, the hydrogenation of cyclohexene proved challenging, affording 27% conversion to cyclohexane after 4 h at 60 °C under 10 atm of H₂ (Entry 10). By comparison, the related complex (^{Mes}CCC)Co(N₂)(PPh₃) achieved >99% conversion of 1-octene to octane after 3 h at room temperature at a catalyst loading of 2 mol% under 4 atm of H₂, while >99% conversion of cyclohexene to cyclohexane was achieved after 22 h at 60 °C (2 mol% catalyst, 4 atm of H₂). These results indicate that while (^{Mes}CCC)Co(N₂)(PPh₃) is significantly more active for alkene hydrogenation catalysis, complex **3-3** is nonetheless a competent precatalyst for the hydrogenation of terminal alkenes under similar reaction conditions. As such, the (PSiP)Co system described herein represents a relatively rare example of Co-mediated alkene hydrogenation featuring redox-innocent ancillary ligation.

Table 3.2.1. Alkene hydrogenation catalysis.

| Entry | Substrate | Catalyst Loading (mol %) | Temperature (°C) | Time (h) | Conversion (%) ^a |
|----------------------|-----------------------|--------------------------|------------------|----------|-----------------------------|
| 1^d | 1-octene ^b | 5.0 | 25 | 22 | <5 |
| 2^d | 1-octene | 5.0 | 60 | 22 | 28 |
| 3 | 1-octene ^b | 5.0 | 25 | 4 | 40 |
| 4 | 1-octene ^b | 5.0 | 25 | 22 | 50 |
| 5 | 1-octene | 5.0 | 60 | 4 | 95 |
| 6 | 1-octene | 2.5 | 60 | 4 | 96 |
| 7 | 5-hexen-2-one | 2.5 | 60 | 4 | 46 ^c |
| 8 | 5-hexen-2-one | 5.0 | 60 | 4 | 73 ^c |
| 9 | cyclohexene | 2.5 | 60 | 4 | 21 |
| 10 | cyclohexene | 5.0 | 60 | 4 | 27 |

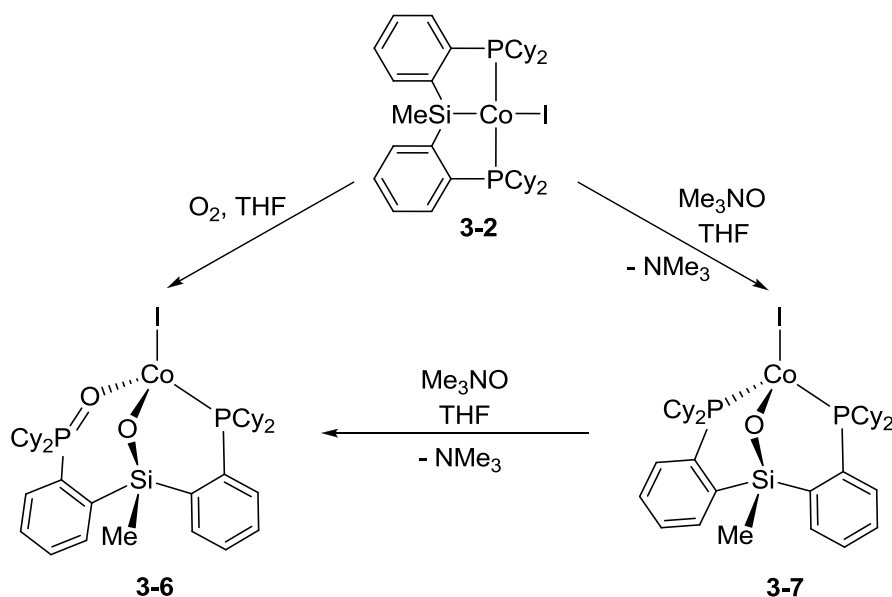
^aConversion was monitored by ¹H NMR integration relative to an internal standard (hexamethylbenzene for reactions in benzene-*d*₆ or trimethoxybenzene for reactions in toluene-*d*₈; average of two runs). ^bReaction was carried out in benzene-*d*₆. ^cSelective conversion to 2-hexanone. ^dReaction carried out under 1 atm H₂.

3.2.4 Reactivity of (Cy-PSiP)Co^{II} Toward Molecular Oxygen

In an effort to further probe the reactivity of (Cy-PSiP)Co species with small molecule substrates, the reaction of **3-2** with O₂ was also evaluated. Molecular oxygen is the most readily available and inexpensive oxidant, and has been investigated widely for application in catalytic oxidation reactions.¹³⁷ Cobalt complexes have been studied extensively in this regard.¹³⁸ The propensity of Co species to reversibly bind¹³⁹ and activate¹⁴⁰ O₂ has also been investigated. Studies involving the reactivity of bis(phosphino) pincer Co species with O₂ are limited to a report by Caulton^{125b} involving four-coordinate (PNP)CoX (X = Cl, I, N₃; PNP = (^tBu₂PCH₂SiMe₂)₂N⁻), which underwent rapid oxidation of both phosphino donors upon treatment with O₂,¹⁴¹ with no

discernible intermediate even at low temperature. The three-coordinate Co^{I} complex (PNP)Co reacted with O_2 at low temperature to afford a diamagnetic species presumed to be a (PNP)Co(O_2) complex that decomposed upon subsequent warming to generate intractable mixtures.^{129b}

Interestingly, it was found that bubbling of dry O_2 through a benzene solution of **3-2** at room temperature led to a rapid color change of the solution from red-orange to blue. A paramagnetic blue solid (**3-6**) was isolated in high yield from this reaction mixture (Scheme 3.2.3). The crystallographically determined solid state structure of **3-6** revealed the formal insertion of two oxygen atoms, one into the Si-Co bond, and the other into a P-Co bond to generate a Co^{II} -siloxo complex with coordinated phosphine, phosphine oxide and iodide ligands in a distorted tetrahedral geometry (Figure 3.2.8). The value of $4.16 \mu\text{B}$ was measured by the Evans method at room temperature for the solution-phase (benzene- d_6) magnetic moment of **3-6**, which is in the range of magnetic moments expected for high-spin Co^{II} in a tetrahedral geometry ($S = 3/2$).



Scheme 3.2.3. Reactivity of **3-2** toward O_2 and Me_3NO to generate Co^{II} products resulting from both double- (**3-6**) and single- (**3-7**) Cy-PSiP ligand oxidation.

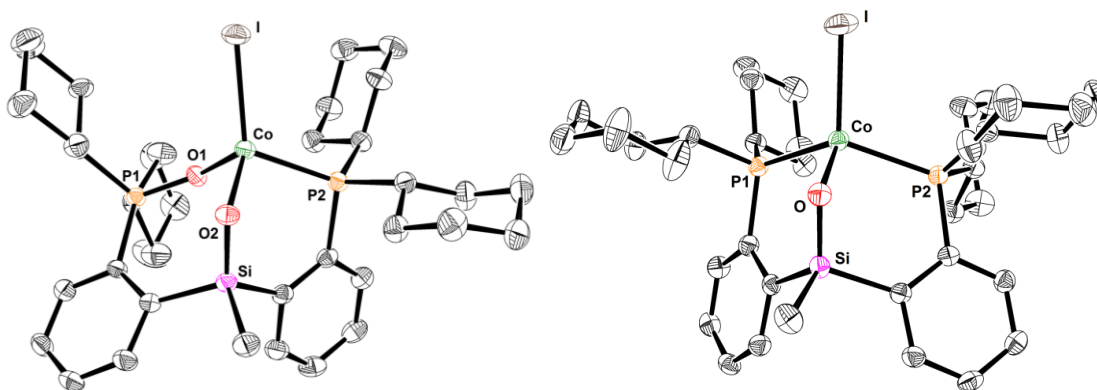


Figure 3.2.8. Crystallographically determined structures for **3-6** (left) and **3-7** (right) with thermal ellipsoids drawn at the 50% probability level. Solvent molecules and hydrogen atoms have been omitted for clarity. Only one of the two crystallographically independent molecules of **3-7** is shown. Selected interatomic distances (Å) and angles (°) for **3-6**: Co-I 2.5688(3), Co-P2 2.3573(6), Co-O1 1.9657(14), Co-O2 1.8805(13), P1-O1 1.5141(14), Si-O2 1.6018(15), I-Co-P2 116.630(17), I-Co-O1 116.07(4), I-Co-O2 122.80(4), P2-Co-O1 99.11(4), P2-Co-O2 99.75(5), O1-Co-O2 98.33(6), Co-O1-P1 139.48(9), Co-O2-Si 117.36(8). Selected interatomic distances (Å) and angles (°) for **3-7**: Co-I 2.5675(4), Co-P1 2.3591(7), Co-P2 2.3748(7), Co-O 1.8767(16), Si-O 1.6041(17), I-Co-P1 108.351(19), I-Co-P2 108.389(19), I-Co-O 123.99(5), P1-Co-P2 126.07(2), P1-Co-O 96.49(5), P2-Co-O 94.31(5), Co-O-Si 117.10(9).

A similar example of PSiP ligand oxidation has been reported for an (*i*-Pr-PSiP)Ni anilido complex.¹⁴² In this case, reaction with aerobic CO₂ led to the formation of multiple Ni species, including a dinuclear Ni^{II} μ -carbonato complex featuring oxidation at P and Si (Figure 3.2.9, **A**). Related reactivity involving oxidation at Si exclusively has also been reported (Figure 3.2.9, **B - F**). Milstein and co-workers¹⁴³ observed that exposure of a Pt^{II}-chloride precursor supported by a bis(diisopropylphosphino)silyl ligand featuring an Si-H unit to air in benzene solution over the course of a month afforded a Pt^{II}-metalosilanol species (Figure 3.2.9, **B**). This reactivity was accelerated by addition of an Ir catalyst that had previously been shown to facilitate the hydrolytic oxidation of organosilanes to silanols.¹⁴⁴ As well, Stobart and co-workers¹⁴⁵ have reported on the related reactivity of a bis(diphenylphosphinopropyl)silyl Ru^{II} complex under aerobic

conditions in refluxing benzene, which afforded a Ru species featuring the formal insertion of two oxygen atoms, one into the Si-Ru linkage and a second into a Si-Me linkage in the ligand backbone (Figure 3.2.9, **D**). It is noteworthy that these examples all involve exposure of silyl metal complexes to air, which also implicates water as a possible source of reactivity. In this regard, the metal catalyzed hydrolysis and alcoholysis of hydrosilanes is well-established,¹⁴⁶ and examples of similar oxidation at Si have been reported involving hydrolysis of PSiP-supported complexes in the absence of O₂ (Figure 3.2.9, **E - F**).^{145, 147} Lastly, an intriguing related example of oxidation at Si was reported by Puddephatt and co-workers¹⁴⁸ for a Pt^{II}-dimethyl complex supported by bis(2-pyridyl)-dimethylsilane (bps). Oxidation of (bps)PtMe₂ with oxygen/MeOH occurs with cleavage of a Me-Si bond to afford a Pt^{IV}-siloxy species (Figure 3.2.9, **C**).

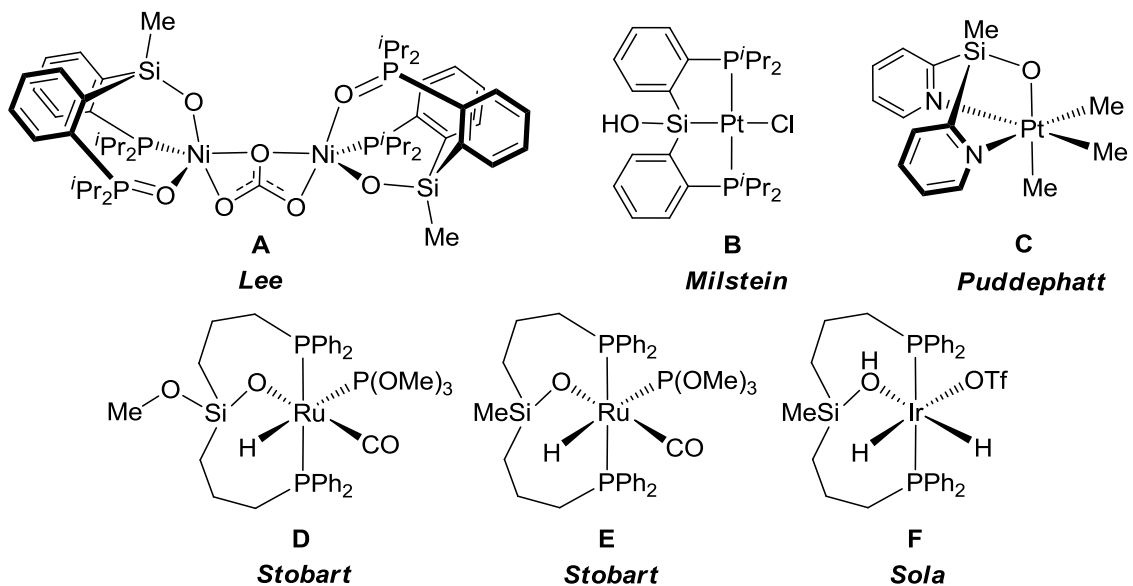


Figure 3.2.9. Previously reported examples of PSiP and related NSiN ligand oxidation.

While in most cases the mechanisms for the formation of these complexes are not fully known, in the case of the Ru example, the (biPSi)RuHL₂ (biPSi = (Ph₂PCH₂CH₂CH₂)₂SiMe) precursor is coordinatively saturated, and as such, the authors

suggest that reactivity with O₂ may occur via an outer-sphere electron transfer process to generate a cationic Ru^{III} species and O₂⁻; subsequent attack of superoxide on Si would lead to the Si-O linkages observed in the product **D** (Figure 3.2.9).¹⁴⁵ Interestingly, exposure of the siloxane species **E** to O₂ does not lead to the formation of **D**. In the case of the Ni example **A**, O₂ activation involving Ni^{II} is generally not well-established.¹⁴⁹ Moreover, the observation of multiple unidentified products in this reaction further complicates the mechanistic possibilities.¹⁴² By comparison, Puddephatt and co-workers¹⁴⁸ propose that the siloxane **C** (Figure 3.2.9) is formed by a pathway involving initial formation of a hydroperoxo Pt^{IV} cation with a methoxide anion, which reacts rapidly with a second molecule of (bps)PtMe₂ to form a cationic Pt^{IV}-hydroxo complex with a methoxide anion. Nucleophilic attack of the methoxide group at Si and methyl group transfer to Pt, followed by the displacement of the methoxy group from Si by the Pt-OH group affords the product **C** with elimination of methanol. This reactivity thus requires both O₂ and an alcohol.

By comparison with the aforementioned examples, the reaction of **3-2** with O₂ was conducted under anhydrous conditions. While the involvement of adventitious water in this transformation cannot be discounted, coordination of O₂ by Co^{II} species to form superoxo and μ -peroxo complexes is well-established,^{139, 150} which could implicate such species in the formation of **3-6**. Attempts to observe such an intermediate by treatment of **3-2** with O₂ at -78 °C in toluene-d₈ solution revealed exclusive formation of **3-6**, as indicated by ¹H NMR analysis of the reaction mixture in the range of -80 - 0 °C.

In an effort to shed further light on the transformation described above, the reactivity of **3-2** with the oxygen atom transfer agent Me₃NO was also investigated

(Scheme 3.2.3). It was found that treatment of **3-2** with one equiv Me₃NO in THF solution led to the formation of a new paramagnetic Co species (**3-7**). The ¹H NMR spectrum (benzene-*d*₆) of the isolated blue solid gave rise to paramagnetically shifted resonances that are distinct from those observed for **3-6** (Figure 3.2.10). The presence of roughly two times the number of resonances in the spectrum of **3-6** relative to that of **3-7** is in agreement with the asymmetric nature of complex **3-6** as observed in the solid state. The crystallographically determined solid state structure of **3-7** revealed the formal insertion of a single oxygen atom into the Si-Co bond, to afford a bis(phosphino)siloxy complex featuring a distorted tetrahedral geometry at the Co center (Scheme 3.2.3, Figure 3.2.8). The value of 4.14 μB was measured by the Evans method at room temperature for the solution-phase (benzene-*d*₆) magnetic moment of **3-7**, which is in the range of magnetic moments expected for high-spin Co^{II} in tetrahedral geometry (S = 3/2). Interestingly, while **3-7** does not appear to react further with O₂, treatment of **3-7** with a second equiv Me₃NO led to the clean formation of **3-6** via formal insertion of the second oxygen atom into a Co-P bond. Treatment of **3-6** with additional Me₃NO did not result in further reaction. The lack of reactivity of **3-7** toward O₂ is surprising and may indicate that both O atoms in **3-6** are provided by a single O₂ molecule in its reaction with **3-2**. A similar observation was made in related Ru chemistry reported by Stobart (*vide supra*).¹⁴⁵

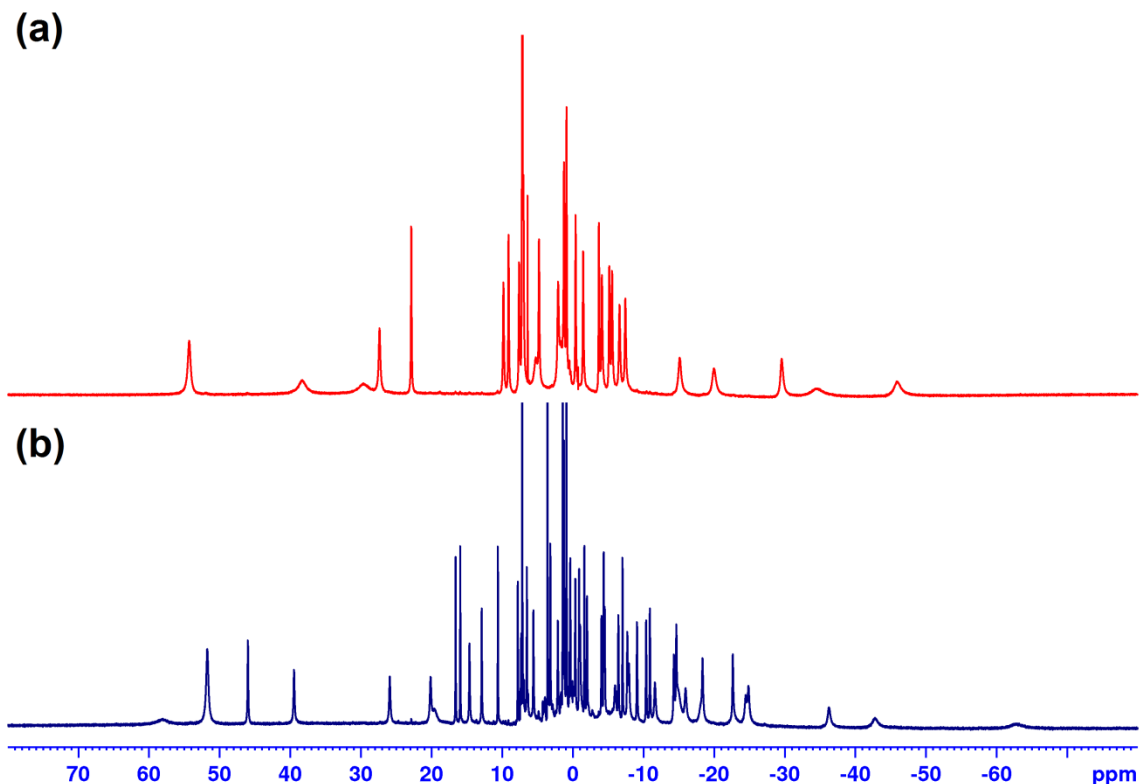


Figure 3.2.10. ^1H NMR spectra of (a) **3-7** and (b) **3-6** (benzene- d_6 , 300 MHz).

Related reactivity of (PNP)Co and (PCP)Ni species with oxygen atom transfer agents has been previously documented. Caulton and co-workers reported that treatment of (PNP)CoCl (PNP = $(^t\text{Bu}_2\text{PCH}_2\text{SiMe}_2)_2\text{N}^-$) with two equiv iodosobenzene, $\text{PhI}=\text{O}$, resulted in the oxidation of both phosphino donors to afford the $[\text{P}(\text{O})\text{NP}(\text{O})]\text{CoCl}$ product previously obtained from the reaction of (PNP)CoCl with O_2 .^{125b} The reaction of the three-coordinate Co^{I} complex (PNP)Co with one equiv $\text{PhI}=\text{O}$ resulted in the formation of three cobalt iodide species: (PNP)CoI (minor), $[\text{P}(\text{O})\text{NP}(\text{O})]\text{CoI}$ (minor), and $[\text{P}(\text{O})\text{NP}]\text{CoI}$ (major).^{129b} All three products feature oxidation at the metal to Co^{II} , and the latter two species feature either double or single insertion, respectively, of an oxygen atom into a Co-P linkage. While the mechanism by which the major product $[\text{P}(\text{O})\text{NP}]\text{CoI}$ is formed was not determined experimentally, the authors suggest a

possible pathway involving the generation of a transient (PNP)Co=O species that undergoes subsequent nucleophilic phosphine attack at the oxo functionality. Such an intramolecular process involving a late transition metal oxo complex has been reported by Milstein and co-workers for a [(PCN)Pt=O]⁺ species.¹⁵¹ In contrast, the putative Rh complex (PNP)Rh=O generated by the reaction of [(^tBu₂PCH₂SiMe₂)₂N]Rh with either amine-*N*-oxides, or N₂O, undergoes intramolecular C-H bond activation involving a P^tBu substituent to afford a cyclometalated hydroxy complex.¹⁵²

In the case of (PCP)Ni, Piers and co-workers¹⁵³ have recently reported on cationic Ni^{II} species that reacted with amine-*N*-oxide reagents to afford products resulting from formal oxygen atom insertion into either one or two of the Ni-P bonds. No experimental evidence in support of a Ni^{IV} oxo intermediate in these transformations could be obtained, and computational studies supported a mechanism involving coordination of amine-*N*-oxide to the Ni center and direct insertion of the oxygen atom into the Ni-P linkage in an apparently concerted manner. No evidence for C-O bond formation involving the PCP pincer ligands was reported.

In consideration of these related studies, the formation of **3-7** upon treatment of **3-2** with one equiv Me₃NO and its subsequent conversion to **3-6** may thus be postulated to occur via coordination of Me₃NO to Co and direct insertion of an oxygen atom from the bound *N*-oxide into Co-Si and Co-P linkages, respectively. Alternatively, one or both of these insertion steps may involve a transient, unobserved Co=O/Co-O' species.^{140a, 154} The formation of a strong Si-O bond is likely a thermodynamic driving force in this process.

3.3 Summary and Conclusions

The chemistry of Co^{II} halide complexes supported by Cy-PSiP ligation are detailed. Reduction of $(\text{Cy-PSiP})\text{Co}(\text{PMe}_3)\text{I}$ could be achieved under mild conditions using magnesium metal as the reducing agent to generate the Co^{I} dinitrogen complex $(\text{Cy-PSiP})\text{Co}(\text{PMe}_3)\text{N}_2$ in high yield. When this reaction was carried out under an atmosphere of CO, the corresponding dicarbonyl complex $(\text{Cy-PSiP})\text{Co}(\text{CO})_2$ was obtained. The CO stretching frequencies observed for this complex are comparable to those reported for related $(\text{PXCXP})\text{Co}(\text{CO})_2$ ($\text{X} = \text{O}, \text{N}$) species that feature dialkyl phosphinite and aminophosphine donors. While the one electron reduction of Co^{II} halide complexes proved facile, access to Co^{III} species supported by Cy-PSiP ligation was significantly more challenging. This is in contrast to observations by Sun and co-workers,^{25b, 73a} who have reported on readily isolable Co^{III} complexes supported by closely related diphenylphosphino PSiP derivatives.

Attempted oxidative addition reactions involving $(\text{Cy-PSiP})\text{Co}(\text{PMe}_3)\text{N}_2$ were generally unsuccessful, with the sole exception of H_2 , which reacted to afford the dihydride complex $(\text{Cy-PSiP})\text{Co}(\text{PMe}_3)(\text{H})_2$. The dihydride complex undergoes Co-H site exchange in solution and readily eliminates H_2 . Evidence for H/D scrambling was also observed when HD gas was used in place of H_2 . Exposure of the Co^{II} complex $(\text{Cy-PSiP})\text{CoI}$ to O_2 gas under anhydrous conditions led to rapid ligand oxidation at Si and P, with no evidence observed at low temperature for a Co^{III} superoxo or peroxo intermediate. Exclusive oxidation at Si to afford a Co^{II} -siloxo complex was observed upon treatment of $(\text{Cy-PSiP})\text{CoI}$ with one equiv Me_3NO . While this siloxo complex did not react further with O_2 , treatment with a second equiv of Me_3NO led to subsequent

oxidation involving one phosphino donor. This observation supports the notion that in the ligand oxidation reactivity observed with O₂, the O atoms incorporated at both Si and P are likely derived from the same O₂ molecule.

To some extent, the difficulty encountered in the attempts to access stable (Cy-PSiP)Co^{III} species mirrors observations made by Caulton and co-workers^{125b, 129b} in their investigation of (PNP)Co; this complex also proved challenging to oxidize despite the electron-rich PNP ligation. Caulton attributed these observations to the reducing power of the PNP ligand, and the need to balance the redox potential of cobalt versus the energy recouped in the formation of new Co-X bonds. It seems likely that similar arguments can be made in regard to the study described herein.

3.4 Experimental Section

3.4.1 General Considerations

All experiments were conducted under N₂ in a glovebox or using standard Schlenk techniques. Dry, oxygen-free solvents were used throughout. Tetrahydrofuran and diethyl ether were distilled from Na/benzophenone ketyl. Benzene, toluene, and pentane were first sparged with nitrogen and subsequently dried by passage through a double-column (one activated alumina column and one column packed with activated Q-5) solvent purification system. All purified solvents were stored over 4 Å molecular sieves. Deuterated solvents were degassed via three freeze-pump-thaw cycles and stored over 4 Å molecular sieves. The compound (2-Cy₂PC₆H₄)₂SiHMe was prepared according to literature procedure.⁷⁴ Compounds **3-1**, **3-2**, **3-1·PMe₃**, **3-2·PMe₃**, **3-3** and **3-5** were all prepared according to literature procedures.⁸¹ All other reagents were purchased from commercial sources and used without further purification. Unless otherwise stated, ¹H,

^{13}C , ^{31}P , and ^{29}Si characterization data were collected at room temperature, with chemical shifts reported in parts per million downfield of SiMe_4 (for ^1H , ^{13}C , and ^{29}Si), or 95% H_3PO_4 in D_2O (for ^{31}P). ^1H and ^{13}C NMR chemical shift assignments are based on data obtained from $^{13}\text{C}\{^1\text{H}\}$, ^{13}C -DEPTQ, ^1H - ^1H COSY, ^1H - ^{13}C HSQC, and ^1H - ^{13}C HMBC NMR experiments. ^{29}Si NMR assignments are based on ^1H - ^{29}Si HMBC experiments. Solution magnetic moments were determined by use of the Evans method.¹¹⁶ Infrared spectra were recorded at a resolution of 4 cm^{-1} .

3.4.2 Synthetic Procedures and Characterization Data

(Cy-PSiP)Co(PMe₃)(N₂) (3-3). Method 1: Magnesium powder (0.077g, 3.2 mmol) was added as a solid to a stirring solution of **3-2**·PMe₃ (0.27, 0.32 mmol) in ca. 10 mL THF at room temperature. The mixture was left to stir for 18 h, over which time a color change from red to brown to orange-red was observed. After 18 h the solvent was removed *in vacuo* and the residue was extracted with ca. 10 mL of benzene and filtered through Celite. The filtrate was dried *in vacuo* and the resulting orange material was washed with pentane ($2 \times 2\text{ mL}$) to afford **3-3** (0.22 g, 91%) as an orange solid. **Method 2:** A solution of **3-2** (0.63 g, 0.81 mmol) in ca. 10 mL of THF was treated with PMe₃ (0.062 g, 83 μL , 0.81 mmol), added *via* syringe. An immediate color change to deep red was observed and the reaction was allowed to stir for 1 h at room temperature. After 1 h, magnesium powder (0.20 g, 8.1 mmol) was added as a solid and the reaction mixture was stirred for 18 h, over which time a color change from deep red to brown to orange-red was observed. After 18 h, the solvent was removed *in vacuo* and the residue was extracted with ca. 15 mL of benzene. The benzene extract was filtered through Celite and the filtrate was dried under vacuum. The remaining residue was washed with pentane (2

× 2 mL) to afford **3-3** (0.59 g, 96%) as an orange solid. ^1H NMR (500 MHz, benzene- d_6): δ 7.72 (d, 2 H, $J = 7$ Hz, H_{arom}), 7.52 (apparent d, 2 H, $J = 7$ Hz, H_{arom}), 7.22 – 7.11 (overlapping resonances, 4 H, H_{arom}), 2.46 (m, 2 H, PCy), 2.24 (m, 2 H, PCy), 2.06-2.14 (overlapping resonances, 4 H, PCy), 0.64-1.85 (overlapping resonances, 48 H, PCy + PMe_3 (1.33 ppm, d, $^2J_{\text{PH}} = 6$ Hz) + SiMe (0.75 ppm)). $^{13}\text{C}\{^1\text{H}\}$ NMR (125.8 MHz, benzene- d_6): δ 160.3 (apparent d, $J = 62$ Hz, C_{arom}), 146.3 (apparent t, $J = 18$ Hz, C_{arom}), 132.5 (apparent t, $J = 11$ Hz, CH_{arom}), 129.2 (CH_{arom}), 128.9 (CH_{arom}), 127.2 (CH_{arom}), 41.1 (apparent t, $J = 24$ Hz, CH_{Cy}), 33.1 (apparent t, $J = 4$ Hz, CH_{Cy}), 30.3 (CH_2Cy), 29.9 (CH_2Cy), 29.6 (CH_2Cy), 28.8 – 28.9 (overlapping resonances, CH_2Cy), 28.3 (CH_2Cy), 27.3 (CH_2Cy), 26.4 (CH_2Cy), 23.5 (d, $^2J_{\text{PC}} = 19$ Hz, PMe_3), 8.1 (d, $J = 13$ Hz, SiMe). $^{31}\text{P}\{^1\text{H}\}$ NMR (202.5 MHz, benzene- d_6): δ 66.4 (d, 2 P, $^2J_{\text{PP}} = 83$ Hz, CyPSiP), -14.8 (t, 1 P, $^2J_{\text{PP}} = 83$ Hz, PMe_3). ^{29}Si NMR (99.4 MHz, benzene- d_6): δ 56.2. IR (Thin film, cm^{-1}): 2065 (s, N_2). Anal. Calcd. for $\text{C}_{40}\text{H}_{64}\text{CoN}_2\text{P}_3\text{Si}$: C, 63.81; H, 8.57, N, 3.72. Found: C, 63.47; H, 8.76; N, 3.55. The spectroscopic data obtained for **3-3** prepared by these routes is in agreement with that recently reported by Nishibayashi and co-workers.

(Cy-PSiP)Co(CO) $_2$ (3-4). A solution of **3-2** (0.13 g, 0.17 mmol) was dissolved in ca. 7 mL THF and transferred to a Teflon-sealed reaction vessel equipped with a stir bar. The solution was degassed via three sequential freeze-pump-thaw cycles and exposed to an atmosphere of CO gas. A color change from dark red to light orange-brown was observed. After ca. 10 minutes, volatile components of the reaction mixture were removed in vacuo and the remaining material was triturated with pentane (3×2 mL) to give a red-orange solid. The material was redissolved in ca. 10 mL THF, transferred to a Teflon-sealed reaction vessel and magnesium metal (0.038 g, 1.6 mmol) was added. The

solution was degassed once again and an atmosphere of CO gas was introduced. The reaction mixture was stirred for 14 h at room temperature during which time a color change to bright green was observed. The volatile components of the reaction mixture were removed in vacuo and the residue was extracted with ca. 5 mL benzene and filtered through Celite. The filtrate was dried under vacuum. The remaining material was triturated with 3×0.5 mL pentane and washed with 3×0.5 mL cold pentane to afford **3-4** (0.098 g, 82%) as a yellow solid. Crystals of **3-4** suitable for X-ray diffraction analysis were obtained from a concentrated Et₂O solution at -35 °C. ¹H NMR (500 MHz, benzene-*d*₆): δ 7.90 (d, 2 H, $J = 7$ Hz, H_{arom}), 7.45 (apparent d, 2 H, $J = 7$ Hz, H_{arom}), 7.25 (apparent t, 2 H, $J = 7$ Hz, H_{arom}), 7.14 (apparent t, 2 H, $J = 7$ Hz, H_{arom}), 2.29 – 2.13 (overlapping resonances, 6 H, PCy), 1.89 – 0.98 (overlapping resonances, 41 H, PCy + SiMe (1.07 ppm)). ¹³C{¹H} NMR (125.8 MHz, benzene-*d*₆): δ 220.8 (CO), 207.3 (CO), 157.9 (m, C_{arom}), 145.0 (m, C_{arom}), 132.6 (apparent t, $J = 13$ Hz, CH_{arom}), 129.8 (CH_{arom}), 128.4 (CH_{arom}), 128.1 (CH_{arom}), 41.9 (apparent t, $J = 15$ Hz, CH_{Cy}), 40.8 (apparent t, $J = 9$ Hz, CH_{Cy}), 29.6 ($\text{CH}_{2\text{Cy}}$), 29.5 ($\text{CH}_{2\text{Cy}}$), 29.4 ($\text{CH}_{2\text{Cy}}$), 28.4 ($\text{CH}_{2\text{Cy}}$), 27.8 – 27.7 (overlapping resonances, $\text{CH}_{2\text{Cy}}$), 27.6 (apparent t, $J = 5$ Hz, $\text{CH}_{2\text{Cy}}$), 27.4 (apparent t, $J = 6$ Hz, $\text{CH}_{2\text{Cy}}$), 26.8 ($\text{CH}_{2\text{Cy}}$), 26.7 ($\text{CH}_{2\text{Cy}}$), 8.0 (SiMe). ³¹P{¹H} NMR (202.5 MHz, benzene-*d*₆): δ 84.8. ²⁹Si NMR (99.4 MHz, benzene-*d*₆): δ 69.9. IR (Nujol mull, cm⁻¹): 1960 (s, CO), 1909 (s, CO). Anal. Calcd. for C₃₉H₅₅CoO₂P₂Si: C, 66.56; H, 7.87. Found: C, 65.16; H, 7.96.

(Cy-PSiP)Co(PMe₃)(H)₂ (3-5). Method 1: A degassed solution of **3-3** (0.010 g, 0.013 mmol) in ca. 0.7 mL of benzene-*d*₆ was exposed to 1 atm H₂ in a J. Young NMR tube. The solution changed color from orange to yellow-brown over the course of two

minutes. The sample was analyzed by use of $^{31}\text{P}\{^1\text{H}\}$ and ^1H NMR spectroscopy, which indicated quantitative conversion to **3-5**. **Method 2:** To a solution of **3-3** (0.096 g, 0.13 mmol) in ca. 5 mL THF was added $\text{H}_3\text{N}\cdot\text{BH}_3$ (0.061 g, 2.0 mmol) as a solid. A slow color change from orange to yellow-brown was observed and the reaction mixture was allowed to stir for 18 h at room temperature. After 18 h, an aliquot of the reaction mixture was analyzed by use of $^{31}\text{P}\{^1\text{H}\}$ NMR spectroscopy and the quantitative conversion of **3-3** to **3-5** was observed. ^1H NMR (300 MHz, benzene- d_6): δ 8.18 (d, 2 H, $J = 7$ Hz, Harom), 7.32 – 7.22 (overlapping resonances, 4 H, H_{arom}), 7.09 (m, 2 H, H_{arom}), 2.52 (m, 2 H, PCy), 2.20 - 1.09 (overlapping resonances, 50 H, PCy + PMe_3 (1.33 ppm, d, $^2J_{\text{HP}} = 6$ Hz) + SiMe (1.22 ppm)), 0.81 (m, 2 H, PCy), 0.50 (m, 2 H, PCy), -13.51 (broad t, 2 H, $J = 38$ Hz). $^{31}\text{P}\{^1\text{H}\}$ NMR (202.5 MHz, benzene- d_6): δ 91.6 (br s, 2 P, Cy-PSiP), 0.1 (br s, 1 P, PMe_3). ^{29}Si NMR (99.4 MHz, benzene- d_6): δ 54.7.

[Cy-PSi(O)P(O)]CoI (3-6). Method 1: A solution of **3-2** (0.045 g, 0.058 mmol) in ca. 5 mL benzene was treated with a solution of trimethylamine-*N*-oxide (0.0087 g, 0.12 mmol) in ca. 5 mL benzene leading to a color change from dark red to dark blue/purple. After stirring for 18 h at room temperature, the volatile components of the reaction mixture were removed *in vacuo* and the residue was triturated with 3×1 mL pentane. This material was washed with 3×0.5 mL pentane to afford **3-6** (0.036 g, 77%) as a blue solid. **Method 2:** A solution of **3-2** (0.048 g, 0.062 mmol) in ca. 5 mL benzene was transferred to a 250 mL Schlenk flask. Oxygen gas was then bubbled directly through the solution for 3 minutes at ambient temperature, during which time a color change from dark red to blue was observed. The solution was then sparged with N_2 for ca. 5 minutes to remove excess O_2 before the solvent was removed *in vacuo*. The residue

was triturated with 3×1 mL pentane and washed with 3×0.5 mL pentane to afford **3-6** (0.049 g, 97%) as a blue solid. Crystals of **3-6** suitable for X-ray diffraction analysis were obtained from a concentrated benzene solution at room temperature. $^1\text{H NMR}$ (300 MHz, benzene- d_6): δ 58.11, 51.75, 45.99, 39.46, 25.90, 20.14, 20.14, 19.47, 16.59, 15.93, 14.62, 12.89, 10.60, 7.78, 6.50, 5.57, 3.57, 3.17, 2.11, 1.43, 0.34, -0.37, -0.90, -1.04, -1.65, -2.02, -4.07, -4.38, -4.52, -6.01, -6.46, -7.05, -7.73, -7.96, -9.10, -10.39, -10.93, -11.64, -14.31, -14.67, -14.91, -15.98, -18.07, -18.38, -22.67, -24.50, -24.87, -36.29, -42.79, -62.71. μ_{eff} (benzene- d_6): $4.16 \mu_{\text{B}}$ ($S = 3/2$). Anal. Calcd for $\text{C}_{37}\text{H}_{55}\text{O}_2\text{P}_2\text{SiCoI}$: C, 55.02; H, 6.86. Found: C, 54.81; H, 7.08.

[Cy-PSi(O)P]CoI (3-7). A solution of **3-2** (0.18 g, 0.24 mmol) in ca. 5 mL THF was treated with a solution of trimethylamine-*N*-oxide (0.018 g, 0.24 mmol) in ca. 5 mL THF leading to a colour change from dark red to dark blue. After stirring for 1.5 h at room temperature, the volatile components of the reaction mixture were removed *in vacuo*. The residue was triturated with 3×1 mL pentane and washed with 3×0.5 mL pentane to yield **7** (0.18 g, 95%) as a blue solid. Crystals of **3-7** suitable for X-ray diffraction analysis were obtained from a concentrated Et_2O solution at -35 °C. $^1\text{H NMR}$ (300 MHz, benzene- d_6): δ 54.36, 38.37, 29.72, 27.41, 22.89, 9.82, 9.09, 4.78, 2.05 – 0.89 (overlapping resonances), -0.39, -1.48, -3.73, -4.14, -5.21, -5.57, -6.62, -7.45, -15.14, -20.02, -29.60, -34.74, -46.07. μ_{eff} (benzene- d_6): $4.14 \mu_{\text{B}}$ ($S = 3/2$). Anal. Calcd for $\text{C}_{37}\text{H}_{55}\text{OP}_2\text{SiCoI}$: C, 56.13; H, 7.00. Found: C, 55.80; H, 7.28.

General procedure for catalytic hydrogenation of alkenes. All room temperature reactions were performed in benzene- d_6 , while all catalytic runs at 60 °C were performed in toluene- d_8 . For each run the total reaction volume was kept a constant 750 μL . The

total amount of substrate used for each reaction was 0.13 mmol, while either 2.5 mg (2.5 mol% entries) or 5.0 mg (5.0 mol% entries) of catalyst was employed. All high pressure reactions were performed in a ParrTM high pressure apparatus under 10 atm H₂ gas in 1 dram vials equipped with a stirbar and a needle pierced through a PTFE-sealed cap. All room temperature reactions were performed in a J. Young NMR tube that was subjected to three freeze-pump-thaw cycles, and upon warming was charged with H₂ gas (1 atm) on a vacuum line. The catalytic reaction was monitored by use of ¹H and ¹³C{¹H} NMR spectroscopic techniques. Conversions (average of two runs) were determined on the basis of ¹H NMR integrations relative to an internal standard added prior to H₂ addition (hexamethylbenzene for reactions in benzene-*d*₆ or 1,3,5-trimethoxybenzene for reactions in toluene-*d*₈). In a typical catalysis run (Table 3.2.1, Entry 6) 2.5 mg (0.0033 mmol) of (Cy-PSiP)Co(PMe₃)(N₂) and 4.7 mg of internal standard (1,3,5-trimethoxybenzene, 0.039 mmol) were combined in a 1 dram vial. 1-Octene (0.13 mmol) was added as a stock solution in toluene-*d*₈, and additional toluene-*d*₈ was added to bring the total solution volume to 750 μL. The vial was equipped with a magnetic stirbar, closed with a PTFE-sealed cap, and a needle was pierced through the cap. The vial was placed in a ParrTM high pressure apparatus which was purged with H₂ gas and subsequently pressurized to 10 atm H₂ and heated to an internal temperature of 60 °C for 4 h. The reactor was allowed to cool to room temperature and depressurized. The contents of the vial were transferred to an NMR tube under an N₂ atmosphere. Conversion to *n*-octane was determined to be 96% based on ¹H NMR integration relative to the internal standard.

3.4.3 Crystallographic Solution and Refinement Details

Crystallographic data for each of **3-4**, **3-6**, and **3-7** were obtained at 173(\pm 2) K on a Bruker D8/APEX II CCD diffractometer using graphite-monochromated Mo K α (λ = 0.71073 Å; for **3-6**, and **3-7**) or Cu K α (λ = 1.54178 Å; for **3-4**) radiation, employing a sample that was mounted in inert oil and transferred to a cold gas stream on the diffractometer. Programs for diffractometer operation, data collection, and data reduction (including SAINT) were supplied by Bruker. Gaussian integration (face-indexed) was employed as the absorption correction method in each case. The structure of **3-4** was solved by intrinsic phasing, and those of **3-6** and **3-7** were solved by Patterson search/structure expansion. All structures were refined by use of full-matrix least-squares procedures (on F^2) with R_1 based on $F_o^2 \geq 2\sigma(F_o^2)$ and wR_2 based on $F_o^2 \geq -3\sigma(F_o^2)$. Anisotropic displacement parameters were employed throughout for all non-hydrogen atoms. An equivalent of toluene was located in the asymmetric unit for **3-1** and was refined in a satisfactory manner.

For **3-6**, 1.5 equiv benzene were located in the asymmetric unit. One disordered molecule of benzene was refined anisotropically over two positions (C11S-C16S and C21S-C26S), with an occupancy factor of 0.5 for each carbon atom in question. The remaining 0.5 equiv benzene (C31S-C36S) was refined anisotropically with an occupancy factor of 0.5 for each constituent carbon. Bond distances and 1,3-distances within the disordered solvent benzene molecules were restrained to idealized values of 1.39(1) Å and 2.40(1) Å, respectively, during refinement.

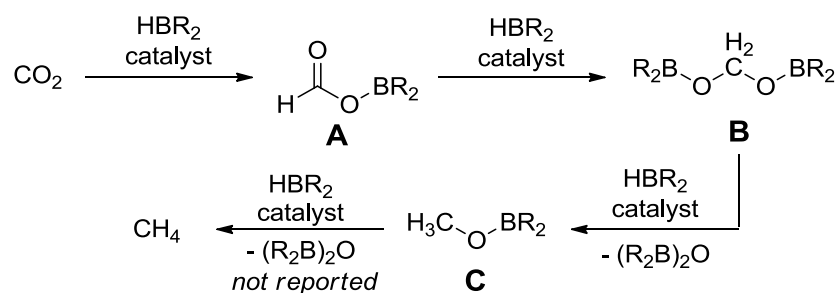
In the case of **3-7**, two independent molecules of [Cy-PSi(O)P]CoI (A and B) were located in the asymmetric unit; for convenience, only molecule A is discussed in the text.

All hydrogen atoms were added at calculated positions and refined by use of a riding model employing isotropic displacement parameters based on the isotropic displacement parameter of the attached atom. Additional crystallographic information is provided in Appendix A.

Chapter 4: Synthesis of (*i*Pr-PSiP^{Ind})M (M = Ni, Pd, Pt) Complexes and Catalytic CO₂ Reduction to the Formaldehyde Level

4.1 Introduction

Significant effort has been made in recent years to develop efficient methods of utilizing CO₂ as a C1-source for chemical synthesis.¹⁵⁵ Both transition metal and main group catalysts have been applied in this regard to achieve transformations such as the reduction of CO₂ to either formic acid, methanol, or methane, as well as coupling reactions involving alkenes and alkynes.¹⁵⁶ In this context, the hydroboration of CO₂ has received considerable attention and has been shown to be a versatile reaction that can yield a variety of products along the reduction pathway from CO₂ to methane (Scheme 4.1.1).^{69d, 157} In the majority of cases, the products of CO₂ hydroboration are boryl formate species (**A**, resulting from single reduction)^{78, 158} or methoxyborane species (**C**, resulting from triple reduction)^{69a, 70, 159} that can be hydrolyzed to yield formic acid or methanol, respectively. By comparison, *double* reduction to the corresponding bis(boryl)acetal (**B**)^{78, 160} is relatively rare, and full reduction to methane using hydroboranes has remained elusive to date.^{71, 161}



Scheme 4.1.1. Stepwise hydroboration of CO₂ to boryl formate (**A**), bis(boryl)acetal (**B**), and methoxyborane (**C**) species, and lastly to methane (not yet reported).

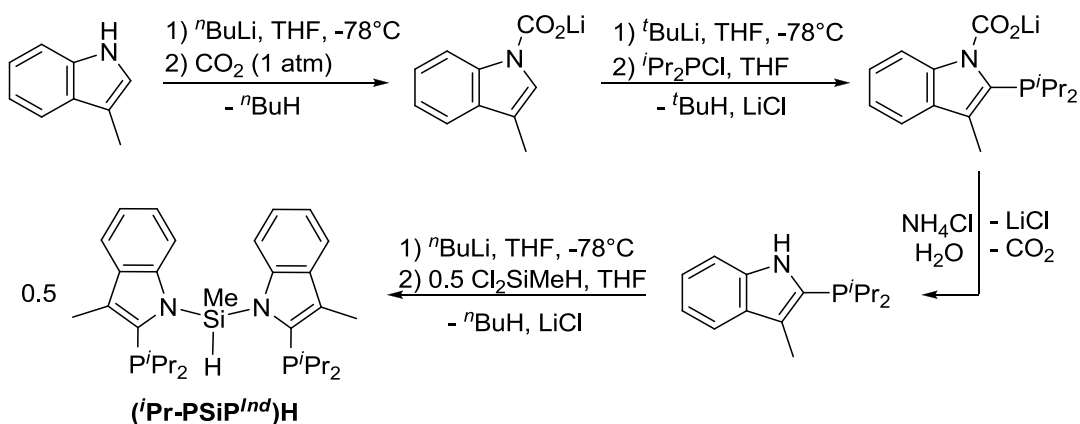
The selective formation of a bis(boryl)acetal product (Scheme 4.1.1B) by a *double* CO₂ reduction process is particularly intriguing, as it represents a reduction of CO₂ to the formaldehyde level. Formaldehyde has been identified as a ‘missing link’ in homogeneous CO₂ reduction catalysis that may serve as a useful C1 synthon for the formation of various E-C bonds (E = main group element).^{160b, 162} The first report of double hydroboration of CO₂ was disclosed by Bontemps, Sabo-Étienne and co-workers^{160a} in the course of investigations involving Ru-catalyzed CO₂ reduction with pinacolborane (HBPin). In a subsequent report,^{160d} the use of 9-BBN (9-borabicyclo[3.3.1]nonane) as reductant was also found to favored the formation of the corresponding bis(boryl)acetal. The *in situ* generated bis(boryl)acetal derived from 9-BBN was shown to be an effective methylene transfer reagent that could be utilized for the formation of C-N, C-O and C-C bonds, thereby providing new avenues for the utilization of CO₂ in synthesis.^{160d} Since these initial reports by Bontemps, Sabo-Étienne and co-workers, a handful of other CO₂ hydroboration studies have reported the generation of product mixtures containing bis(boryl)acetals, but these studies have not focused on optimizing the formation of this double reduction product.^{70, 78, 159c}

In this context, this chapter outlines the synthesis and characterization of a variety of Group 10 pincer complexes of a new bis(indolyl)phosphino-based P*Si*P ligand. Focus was put on the preparation of metal hydride derivatives, postulated as key species for CO₂ reduction catalysis. In particular a Ni complex of the new ligand was found to be highly active for the selective reduction of CO₂ to the formaldehyde level *via* hydroboration. Helia Hollenhorst should be credited for the initial synthesis of the bis(indolyl)phosphino-based ligand.

4.2 Results and Discussion

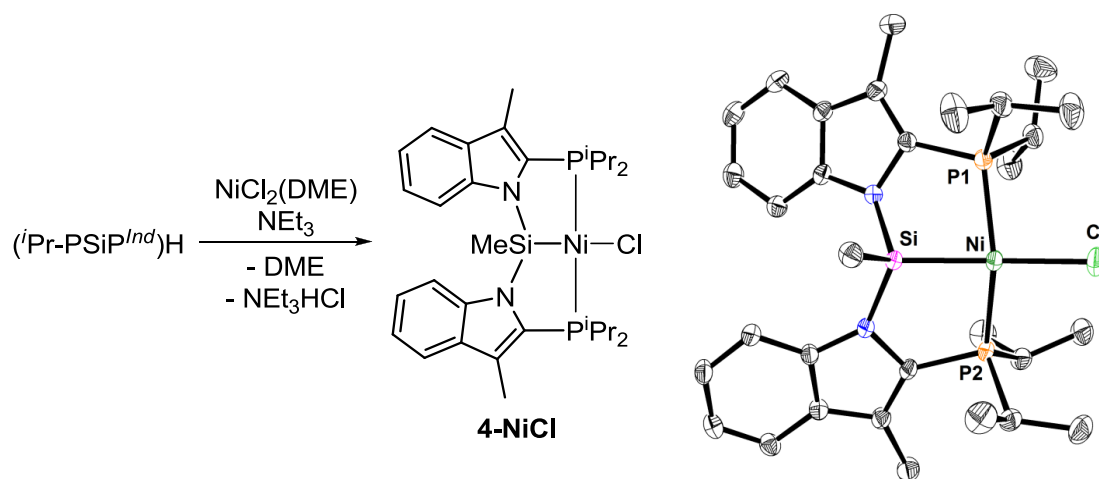
4.2.1 Synthesis of Group 10 Metal Chloride Complexes

Recently the new 3-methylindole derived PSiP ligand $i\text{Pr-PSiP}^{Ind}$ was developed in the Turculet group (Scheme 4.2.1).¹⁶³ The new ligand features an indolyne backbone, rather than the phenylene backbone of the (Cy-PSiP)H ligand (the ligand used in the chemistry described in Chapters 2 and 3 of this document). As ancillary ligand design is known to have a profound effect on the reactivity of the ensuing complexes, it was of interest to develop new first-row metal complexes supported by $i\text{Pr-PSiP}^{Ind}$ ligation in the hope of accessing new reactivity. The proposed increased electron-donating ability of the $i\text{Pr-PSiP}^{Ind}$ ligand (relative to Cy-PSiP) is anticipated lead to increased electron density at the metal center, which may translate into a greater propensity to undergo oxidative addition reactions. Like the phenylene-based PSiP ligands, $i\text{Pr-PSiP}^{Ind}$ is also tunable at phosphorus, though initial studies were focused on the isopropyl phosphino derivative. In keeping with the theme of first-row transition metal chemistry, nickel complexes of $i\text{Pr-PSiP}^{Ind}$ were targeted initially, with the ultimate goal of developing catalytic CO_2 reduction chemistry.



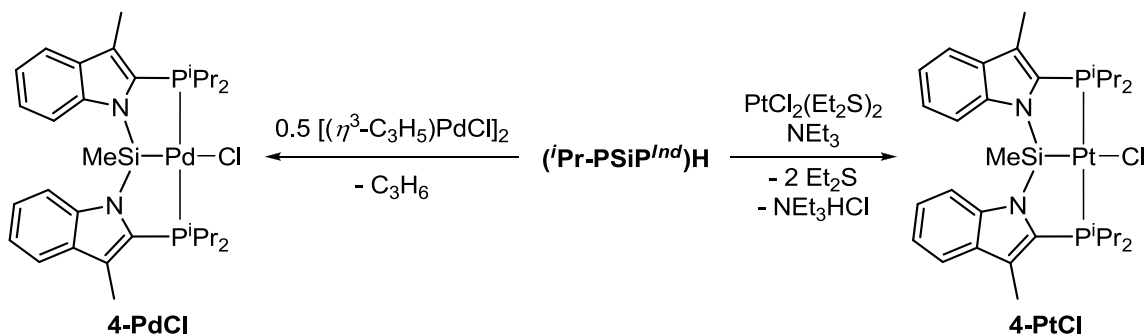
Scheme 4.2.1. Synthetic route for the preparation of $(i\text{Pr-PSiP}^{Ind})\text{H}$.

As with the Fe chemistry described in Chapter 2 of this document, the first target complexes for this work were simple Ni halide complexes of the type (*i*Pr-PSiP^{*Ind*})NiX. Such complexes are anticipated to serve as good starting points for the preparation of other (*i*Pr-PSiP^{*Ind*})Ni derivatives (*e.g.* hydrides) through salt metathesis routes. In this regard, treatment of (*i*Pr-PSiP^{*Ind*})H with one equiv of NiCl₂(DME) (DME = dimethoxyethane) and excess triethylamine led to the formation of diamagnetic (*i*Pr-PSiP^{*Ind*})NiCl (**4-NiCl**, Scheme 4.2.2), which was isolated as a yellow solid in 91% yield. The solid state structure of **4-NiCl** was determined by use of X-ray crystallographic techniques, revealing κ^3 -coordination of the PSiP ligand and distorted square planar geometry at the Ni center (Scheme 4.2.2). The structure of **4-NiCl** is similar to that previously reported for (Cy-PSiP)NiCl,^{25a} furthermore, the solution (benzene-*d*₆) NMR spectroscopic data obtained for **4-NiCl** is in full agreement with the structure observed in the solid state.



Scheme 4.2.2. Synthesis (left) and crystallographically determined structure (right) of **4-NiCl** with thermal ellipsoids shown at the 50% probability level. Hydrogen atoms have been omitted for clarity. Selected interatomic distances (Å) and angles (°): Ni-Cl 2.2170(5), Ni-P(1) 2.1938(5), Ni-P(2) 2.1824(5), Ni-Si 2.1850(5), Cl-Ni-P(1) 96.58(2), Cl-Ni-P(2) 98.55(2), Cl-Ni-Si 167.82(2), P(1)-Ni-P(2) 154.54(2), P(1)-Ni-Si 83.542(18), P(2)-Ni-Si 85.881(18).

While the focus of this document thus far has been on the development of new first-row transition metal chemistry of PSiP ligands, it is also informative to prepare analogues of the second- and third-row transition metals for the purposes of comparison. This is particularly true for the case of the newly developed $i\text{Pr-PSiP}^{Ind}$ ligand, as comparisons can not only be made between transition metals, but between this new ligand scaffold and the classical phenylene-based backbone utilized previously in Ni, Pd and Pt chemistry. Thus, the Pd and Pt analogues to **4-NiCl** were targeted *via* similar routes. Treatment of $(i\text{Pr-PSiP}^{Ind})\text{H}$ with one half equiv of $[(\eta^3\text{-C}_3\text{H}_5)\text{PdCl}]_2$ led to rapid generation of $(i\text{Pr-PSiP}^{Ind})\text{PdCl}$, **4-PdCl**, which could be isolated as a white solid in 88% yield. In the case of Pt, treatment of $(i\text{Pr-PSiP}^{Ind})\text{H}$ with $\text{PtCl}_2(\text{Et}_2\text{S})_2$ and excess triethylamine required an extended period of heating (4 days, 75 °C) to generate $(i\text{Pr-PSiP}^{Ind})\text{PtCl}$, **4-PtCl**, which could be isolated as an off-white solid in 84% yield.



Scheme 4.2.3. Synthetic routes for the preparation of **4-PdCl** and **4-PtCl**.

Solid state structures of both **4-PdCl** and **4-PtCl** were determined through X-ray crystallographic analysis (Figure 4.2.1), revealing very similar structures to that of **4-NiCl**. In both cases, the complexes feature κ^3 -coordination of the PSiP ligand in overall distorted square planar geometry about the metal center. Spectroscopically and crystallographically, these complexes are once again comparable to the related Group 10

metal chloride complexes of the bis(phenylene)phosphino-based PSiP ligand reported previously.^{25a}

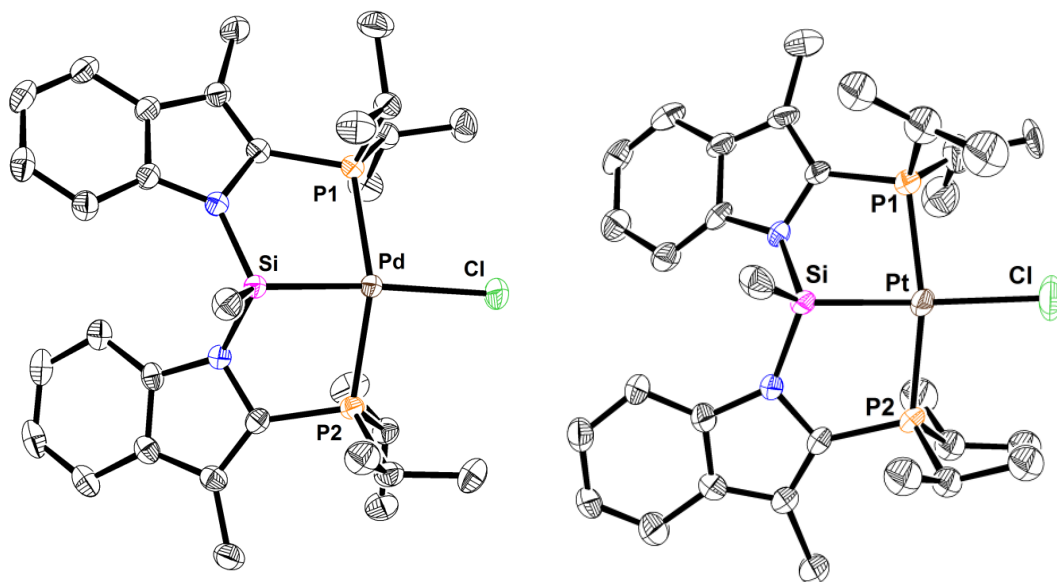
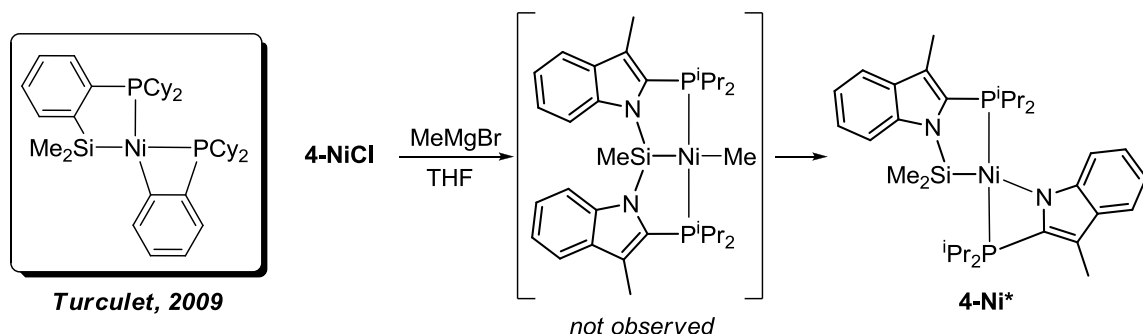


Figure 4.2.1. Crystallographically determined structures of **4-PdCl** (left) and **4-PtCl** (right) with thermal ellipsoids shown at the 50% probability level. Hydrogen atoms have been omitted for clarity. Selected interatomic distances (Å) and angles (°) for: **4-PdCl**, Pd-Cl 2.4255(5), Pd-P(1) 2.3156(4), Pd-P(2) 2.3216(4), Pd-Si 2.2483(5), Cl-Pd-P(1) 100.407(16), Cl-Pd-P(2) 95.083(16), Cl-Pd-Si 174.176(17), P(1)-Pd-P(2) 159.013(16), P(1)-Pd-Si 84.817(16), P(2)-Pd-Si 81.387(16); **4-PtCl**, Pt-Cl 2.432(3), Pt-P(1) 2.311(3), Pt-P(2) 2.283(3), Pt-Si 2.266(3), Cl-Pt-P(1) 94.76(12), Cl-Pt-P(2) 96.84(11), Cl-Pt-Si 175.29(13), P(1)-Pt-P(2) 159.88(10), P(1)-Pt-Si 83.67(9), P(2)-Pt-Si 85.95(9).

4.2.2 Metathesis Reactions of (*i*Pr-PSiP^{Ind})NiCl

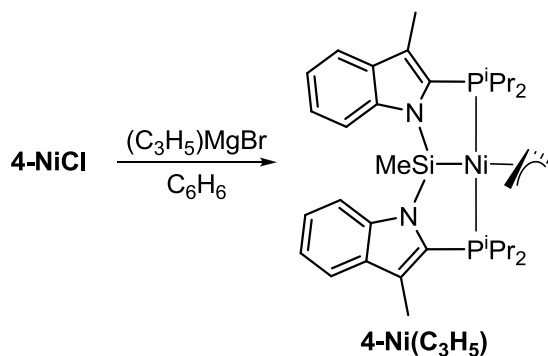
With a synthetically useful (*i*Pr-PSiP^{Ind})Ni^{II} precursor complex in hand, the chemistry of **4-NiCl** toward metathesis reactions in general was briefly investigated in efforts to elucidate the variety of complexes one might be able to access from this easily obtained starting material. In particular the reactivity of **4-NiCl** toward MeMgBr was identified as an intriguing reaction based on previously reported chemistry of the analogous Cy-PSiP ligand scaffold. It was reported that reaction of (Cy-PSiP)NiCl with MeMgBr led to generation of (Cy-PSiP)NiMe and a second complex resulting from

migration of Me to Si, and cleavage of a Si-C(sp²) bond to generate the broken-ligand complex shown in Scheme 4.2.4.^{25a} In efforts to determine whether the bis(indolylene)phosphino scaffold would be susceptible to such a rearrangement, **4-NiCl** was treated with one equiv MeMgBr. In contrast to the reaction of (Cy-PSiP)NiCl with MeMgBr, one major product was formed in this case, as observed by ³¹P{¹H} NMR spectroscopy, with resonances centered at 58.0 ppm and 5.3 ppm as doublets with ²J_{PP} = 185 Hz, indicative of inequivalent, *trans*-disposed, phosphines. By ¹H NMR, two indole-*Me* resonances (3 H each) were observed at 2.43 ppm and 2.29 ppm, as apparent doublets with *J* = 0.6 Hz and 1.2 Hz, respectively, consistent with the presence of inequivalent phosphorus environments. In addition, a strong resonance was observed at 0.83 ppm (6 H) as a broad doublet with *J* = 1.5 Hz. Overall, these observations are consistent with a similar Ni to Si migration of the installed methyl group, followed, in this case, by an Si-N bond cleavage to generate **4-Ni***, shown in Scheme 4.2.4. The spectroscopic features are largely similar to that as observed for the Cy-PSiP ligand, with the notable exception that in this case the product appears to feature *trans*-disposed phosphines, rather than *cis*-disposed. It is thus clear that the new bis(indolylene)phosphino scaffold does not preclude the previously observed ligand rearrangement process, but does have an effect on the ensuing geometry.



Scheme 4.2.4. Structure of ligand-rearranged (Cy-PSiP)Ni complex (left). Synthetic route for synthesis of ligand-rearranged (ⁱPr-PSiP^{Ind})Ni complex, **4-Ni*** (right).

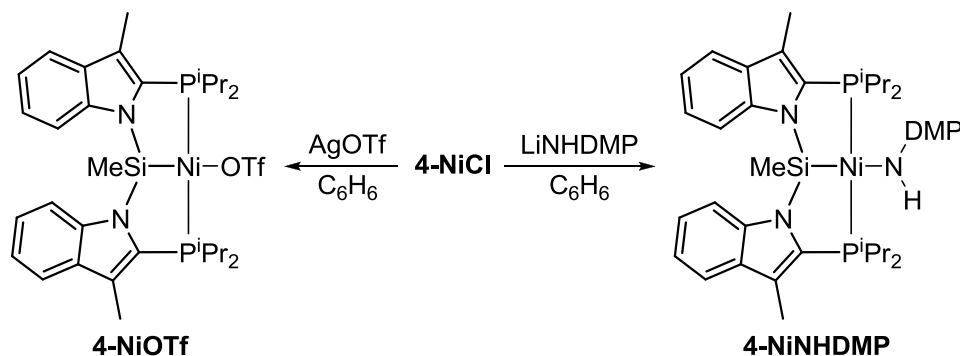
In addition to the attempted preparation of (ⁱPr-PSiP^{Ind})NiMe, the corresponding allyl complex was also targeted to determine whether it would be susceptible to a similar rearrangement process. Thus **4-NiCl** was treated with one equiv (C₃H₅)MgCl, leading to generation of (ⁱPr-PSiP^{Ind})Ni(η^3 -C₃H₅), **4-Ni(C₃H₅)**, which could be isolated as a yellow solid in 89% yield. By ³¹P{¹H} NMR spectroscopy **4-Ni(C₃H₅)** features an AB quartet splitting pattern, with resonances centered at 38.8 ppm and 32.6 ppm each exhibiting ²J_{PP} = 98 Hz, not unlike that of (Cy-PSiP)Ni(η^3 -C₃H₅) reported previously (53.3 ppm, 45.1 ppm, ²J_{PP} = 113 Hz). In addition, by ¹³C{¹H} NMR, three distinct resonances for the allyl carbon atoms were observed at 95.0, 48.4 and 42.6 ppm, again quite similar to those observed for (Cy-PSiP)Ni(η^3 -C₃H₅) (95.2, 49.5, 41.5 ppm), supporting the formulation of **4-Ni(C₃H₅)** as an η^3 -allyl complex. No evidence for any ligand rearrangement was observed during the preparation or isolation of this complex, as was also the case for (Cy-PSiP)Ni(η^3 -C₃H₅), perhaps due to the additional stabilization provided by the allyl ligand as a LX-type ligand, as opposed to the methyl (X-type) ligand.



Scheme 4.2.5. Synthetic route for the preparation of **4-Ni(C₃H₅)**.

Outside of the preparation of the corresponding Ni hydride complex (*vide infra*), synthesis of an amido complex, as well as a triflate complex, were also pursued *via* salt metathesis. Treatment of **4-NiCl** with one equiv of either lithium 2,6-dimethylanilide, or silver triflate, in benzene (Scheme 4.2.6) led to quantitative formation of the corresponding amido and triflate complexes, **4-NiNHDMP** and **4-NiOTf**, by $^{31}\text{P}\{^1\text{H}\}$ NMR. **4-NiNHDMP** was isolated as a red solid in 79% yield, while **4-NiOTf** could be isolated as an orange solid in 72% yield. Both complexes feature a single singlet resonance by $^{31}\text{P}\{^1\text{H}\}$ NMR, (27.1 ppm and 35.5 ppm, respectively) indicative of C_s symmetry in solution, as with the precursor, **4-NiCl**. In the case of **4-NiNHDMP**, by ^1H NMR two resonances for the methyl groups of the aniline ring were observed (at 3.61 and 2.27 ppm, respectively), suggesting restricted rotation of the anilide ligand, rendering the two methyl groups inequivalent. Additionally, the *NH* signal was observed as a singlet at 0.28 ppm, and confirmed through a ^1H - ^{15}N HMQC experiment where a cross peak between this signal and a ^{15}N resonance centered at -49.9 ppm was observed. Overall this initial survey into metathesis reactions of **4-NiCl** indicate that simple metathesis reactions are viable for the production of a variety of new 4-coordinate Ni complexes, however,

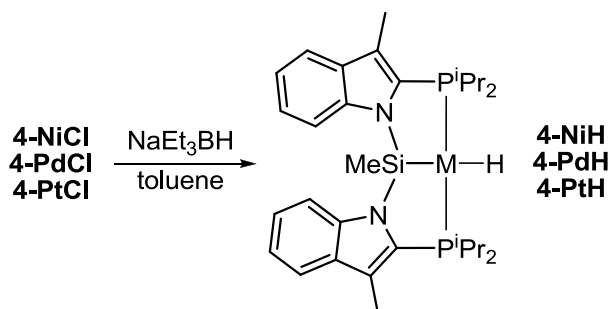
complications in the form of ligand rearrangement can arise when attempting to prepare the corresponding methyl complex.



Scheme 4.2.6. Synthetic routes for the preparation of **4-NiOTf** and **4-NiNHDMPP** from **4-NiCl**.

4.2.3 Investigation of (*i*Pr-PSiP^{Ind})M (M = Ni, Pd, Pt) Hydride Complexes

With the eventual goal of investigating catalytic CO₂ reduction chemistry, simple metal hydride complexes were identified as important targets as they are often invoked as important intermediates in a catalytic CO₂ reduction cycle, often in the initial stage of reaction wherein insertion of CO₂ into the metal-hydride bond to generate the corresponding formate precedes the actual reduction chemistry. With the success of the previously outlined metathesis reactions, it was rationalized that a similar route may prove viable for the synthesis of the corresponding Ni-, Pd- and Pt-hydride complexes. Thus, cold toluene solutions of each **4-NiCl**, **4-PdCl** and **4-PtCl** were treated with one equiv of NaEt₃BH, leading to rapid generation of the corresponding hydride complexes, **4-NiH**, **4-PdH** and **4-PtH** as observed by ³¹P{¹H} and ¹H NMR.



Scheme 4.2.7. Synthetic route for the preparation of **4-NiH**, **4-PdH** and **4-PtH**. Structure shown is proposed solution-state structure at room temperature.

The generation of all three hydride complexes proceeds quite smoothly, and in each case a single product is observed by $^{31}\text{P}\{^1\text{H}\}$ NMR as a sharp singlet centered at 65.6 ppm, 63.3 ppm and 61.2 ppm for **4-NiH**, **4-PdH** and **4-PtH**, respectively. **4-PdH** and **4-PtH** can be isolated as orange-yellow and tan solids in 86% and 76% yield, respectively. By ^1H NMR the hydride resonances for these complexes are shifted rather dramatically downfield from the typical hydride region (< 0 ppm). For **4-PdH** this shift is less dramatic, with the hydride signal appearing as triplet ($^2J_{\text{PH}} = 15$ Hz) at 0.15 ppm. For **4-PtH**, however, the hydride resonance appears as a triplet ($^2J_{\text{PH}} = 18$ Hz), with Pt satellites ($^1J_{\text{PtH}} = 900$ Hz) at 4.21 ppm. While these ^1H chemical shifts do seem unusual for metal hydride complexes, a trend has recently proposed for pincer-supported group 10 metal hydride complexes,^{24a} wherein the more *trans*-influencing the atom *trans* to the hydride ligand is, the further downfield will be the hydride chemical shift by ^1H NMR. In addition downfield shifts are also observed in these systems on moving from Ni, Pd to Pt, a trend that holds with the current series of complexes. Efforts to further elucidate the nature of the bonding scenario in **4-PdH** and **4-PtH** by collection of ^{29}Si NMR data further confound the situation. ^{29}Si NMR chemical shifts for the two complexes were found to be 60.1 ppm and 64.1 ppm, respectively, and more in line with the formulation

of these complexes as classical silyl metal hydride complexes than any sort of non-classical complex. Conversely, values of J_{SiH} , including the sign of the coupling constant, for **4-PdH** and **4-PtH** were measured to be -101 Hz and -67 Hz, respectively through use of a ^1H - ^{29}Si HECADe experiment (Figure 4.2.2). The magnitudes of these coupling constants, while lower than that for an uncoordinated silane (typical range of ca. 150-200 Hz;^{110b} cf. $^1J_{\text{SiH}} = 252$ Hz for (*i*Pr-PSiP^{Ind})H), are quite high when compared to usual values of $^2J_{\text{SiH}}$ for transition metal silyl hydride (typically ≤ 20 Hz).^{110b} Additionally, the magnitude of these J_{SiH} constants does not vary as a function of temperature (less than 2 Hz variation in the range of -80 - 60 °C), nor was any other evidence of temperature dependence observed in the ^1H , ^{29}Si , and $^{31}\text{P}\{^1\text{H}\}$ NMR features of **4-PdH** and **4-PtH** over this temperature range (toluene-*d*₈).

In terms of the signs of the coupling constants, one-bond Si-H coupling constants are known to be negative^{110b} (cf. $^1J_{\text{SiH}} = -252$ Hz for (*i*Pr-PSiP^{Ind})H), though, it is not immediately clear whether a $^2J_{\text{SiH}}$ for this class of compounds should be expected to be positive or negative. The measured $^2J_{\text{SiH}}$ between the Si*Me* protons and the Si atom itself in (*i*Pr-PSiP^{Ind})H (7 Hz), **4-PdH** and **4-PtH** (7 Hz each) were all found to be positive (Figure 4.2.2). Nikonov^{110a} has also noted that in the event of a non-classical interaction, the observed J_{SiH} is actually a combination of both $^1J_{\text{SiH}}$ and $^2J_{\text{SiH}}$ components, which, if of opposing signs, may lead to an unexpected overall value and thus skew the interpretation, and ultimately the assignment, of the complex. By analogy with related (Cy-PSiP)PdH and (Cy-PSiP)PtH complexes, which were found unequivocally to be classical silyl metal hydride complexes in the *solid* state *via* a neutron diffraction study,^{24a} **4-PdH** and **4-PtH** are assigned as such in the solid state. In solution, however,

the possibility for a non-classical interaction (*i.e.* as an η^2 -silane complex) cannot presently be ruled out.

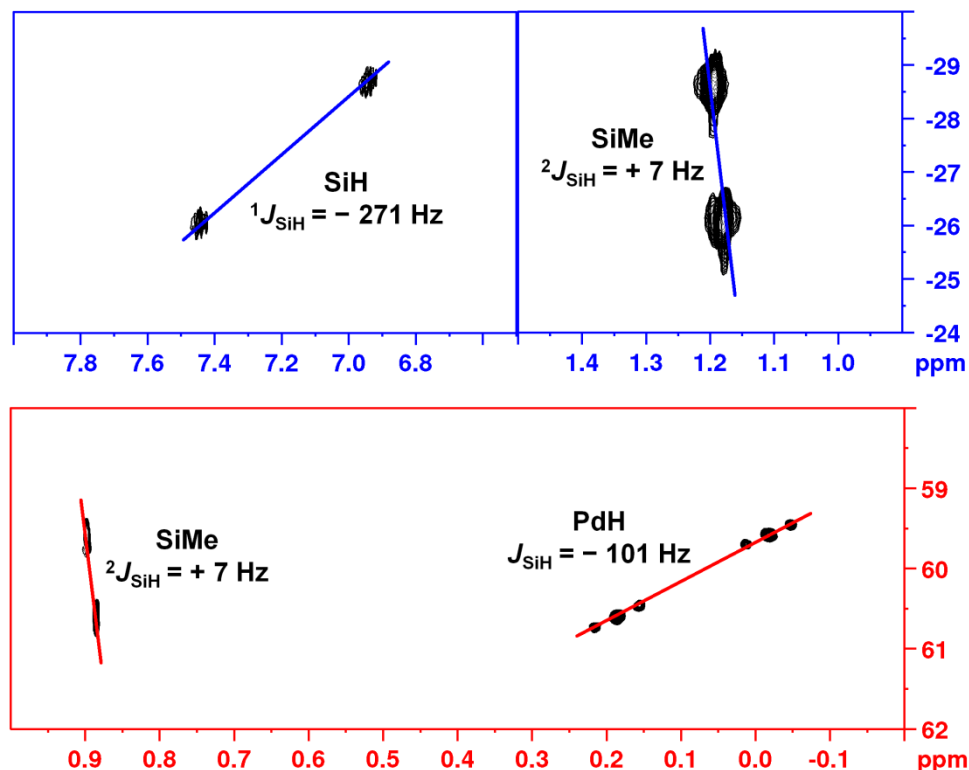


Figure 4.2.2. ^1H - ^{29}Si HECADE spectra of (*i*Pr-PSiP^{Ind})H (top, blue) and **4-PdH** (bottom, red). Opposite slopes in the crosspeak patterns indicate the corresponding coupling constant is of an opposite sign to the other.

In the case of **4-NiH**, a single product can be obtained quite easily from treatment of either **4-NiCl** or **4-NiOTf** with NaEt_3BH . Unlike the related complex (Cy-PSiP)NiH which is thermally sensitive,⁷⁹ **4-NiH** does not appear to decompose in solution at temperatures up to 80 °C, as indicated by ^1H and $^{31}\text{P}\{^1\text{H}\}$ NMR analysis. At room temperature by ^1H NMR, the hydride resonance appears as a broad singlet at -4.79 ppm. While the chemical shift itself is not unusual and follows the previously described trend of chemical shifts for pincer-ligated group 10 metal hydrides, the signal lacks the expected $^2J_{\text{PH}}$ coupling to the ligand phosphorus atoms. The broad nature of the signal

indicated the possibility for temperature dependent behavior, thus a variety of low temperature NMR experiments were carried out in efforts to elucidate the nature of the dynamic behavior of **4-NiH**.

At low temperature (213 K, toluene- d_8 , Figure 4.2.3) the hydride resonance at -4.79 ppm is resolved into an apparent triplet with ${}^2J_{\text{PH}} = 47$ Hz. Concurrent with these lineshape changes, low temperature NMR spectra (${}^1\text{H}$, ${}^{31}\text{P}\{^1\text{H}\}$, ${}^{29}\text{Si}$) for **4-NiH** also indicate the presence of a second (${}^i\text{Pr-PSiP}^{Ind}$)NiH species (**4-NiH***), which appears to interconvert with **4-NiH** depending on not only temperature but solvent as well. Complex **4-NiH*** gives rise to a ${}^{31}\text{P}\{^1\text{H}\}$ NMR resonance centered at 35.3 ppm and features a hydride ${}^1\text{H}$ NMR resonance at -2.55 ppm (${}^2J_{\text{PH}} = 38$ Hz; toluene- d_8). Below 233 K the ${}^{31}\text{P}\{^1\text{H}\}$ NMR resonance for **4-NiH*** begins to decoalesce, such that at 193 K it has decoalesced into two broad signals centered at 40.7 and 28.3 ppm, respectively (Figure 4.2.3). No such lineshape changes were observed for the ${}^{31}\text{P}\{^1\text{H}\}$ NMR resonance corresponding to **4-NiH**, which persists in solution over this temperature range, though relative ratios of **4-NiH** and **4-NiH*** do alter with temperature. Interestingly, while **4-NiH** gives rise to a ${}^{29}\text{Si}$ NMR resonance at 59.8 ppm, the ${}^{29}\text{Si}$ resonance for **4-NiH*** was observed at -10.5 ppm (193 K, toluene- d_8 , $J_{\text{SiH}} = 89$ Hz). Unfortunately, despite repeated efforts, the sign of the J_{SiH} constant observed for **4-NiH*** could not be determined, nor could the magnitude of J_{SiH} for **4-NiH**, including at low temperature.

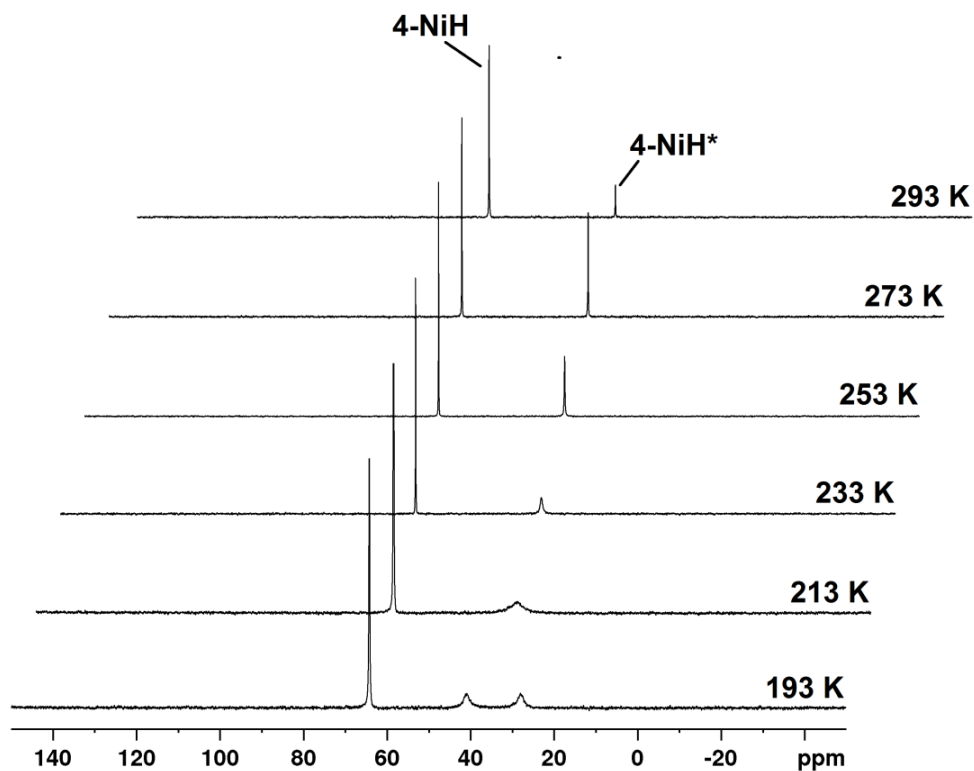
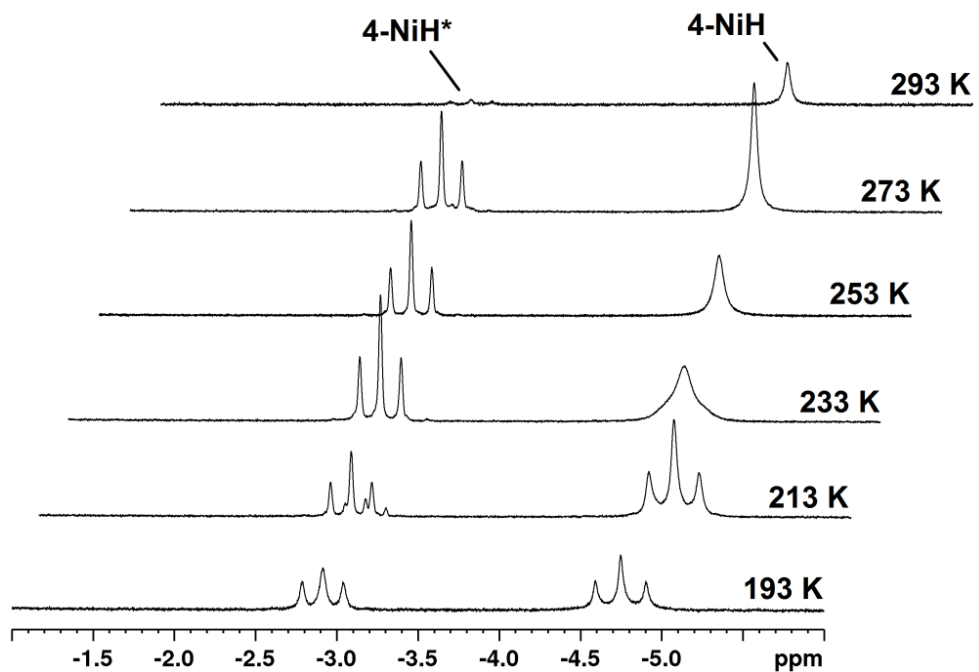


Figure 4.2.3. Variable temperature (top) ^1H NMR (hydride region) and (bottom) $^{31}\text{P}\{^1\text{H}\}$ NMR spectra of **4-NiH** and **4-NiH*** (toluene- d_8).

The relative ratio of **4-NiH** : **4-NiH*** appears to be both temperature and solvent dependent. As such, while the room temperature NMR spectra (^1H , $^{31}\text{P}\{^1\text{H}\}$, ^{29}Si) of **4-NiH** in benzene- d_6 show no evidence of a second hydride species in solution, a **4-NiH** : **4-NiH*** ratio of ca. 4:1 was observed for a room temperature toluene- d_8 solution (by ^1H and $^{31}\text{P}\{^1\text{H}\}$ NMR). When the temperature is decreased to 253 K, the amount of **4-NiH*** increases to afford a ca. 4:3 ratio of **4-NiH** : **4-NiH***, and a ratio of ca. 1:1 was observed at 193 K (Figure 4.2.3). Somewhat similar behavior was observed when low temperature NMR data was collected on a sample of **4-NiH** in methylcyclohexane- d_{14} solution (Figure 4.2.4). At 293 K a ratio of **4-NiH** : **4-NiH*** of ca. 7:1 was observed (^1H and $^{31}\text{P}\{^1\text{H}\}$ NMR). This ratio decreased dramatically to 1:1 at 273 K, and further decreased to 1:10 at 253 K. At 233 K essentially only **4-NiH*** is present in solution, and the $^{31}\text{P}\{^1\text{H}\}$ NMR signal for this complex is significantly broadened. At 193 K the $^{31}\text{P}\{^1\text{H}\}$ NMR resonance for **4-NiH*** has decoalesced to two broad signals centered at 39.8 and 28.0 ppm, respectively.

Finally, when a prepared solution of **4-NiH** in toluene- d_8 was degassed *via* sequential freeze-pump-thaw cycles, only negligible formation of **4-NiH*** was observed. When performing the low temperature NMR experiments, still only negligible amounts of **4-NiH*** was observed, which strongly implies conversion between **4-NiH** and **4-NiH*** involves coordination of N_2 gas from the reaction atmosphere, a reaction which appears to be more favorable in methylcyclohexane solvent than in toluene.

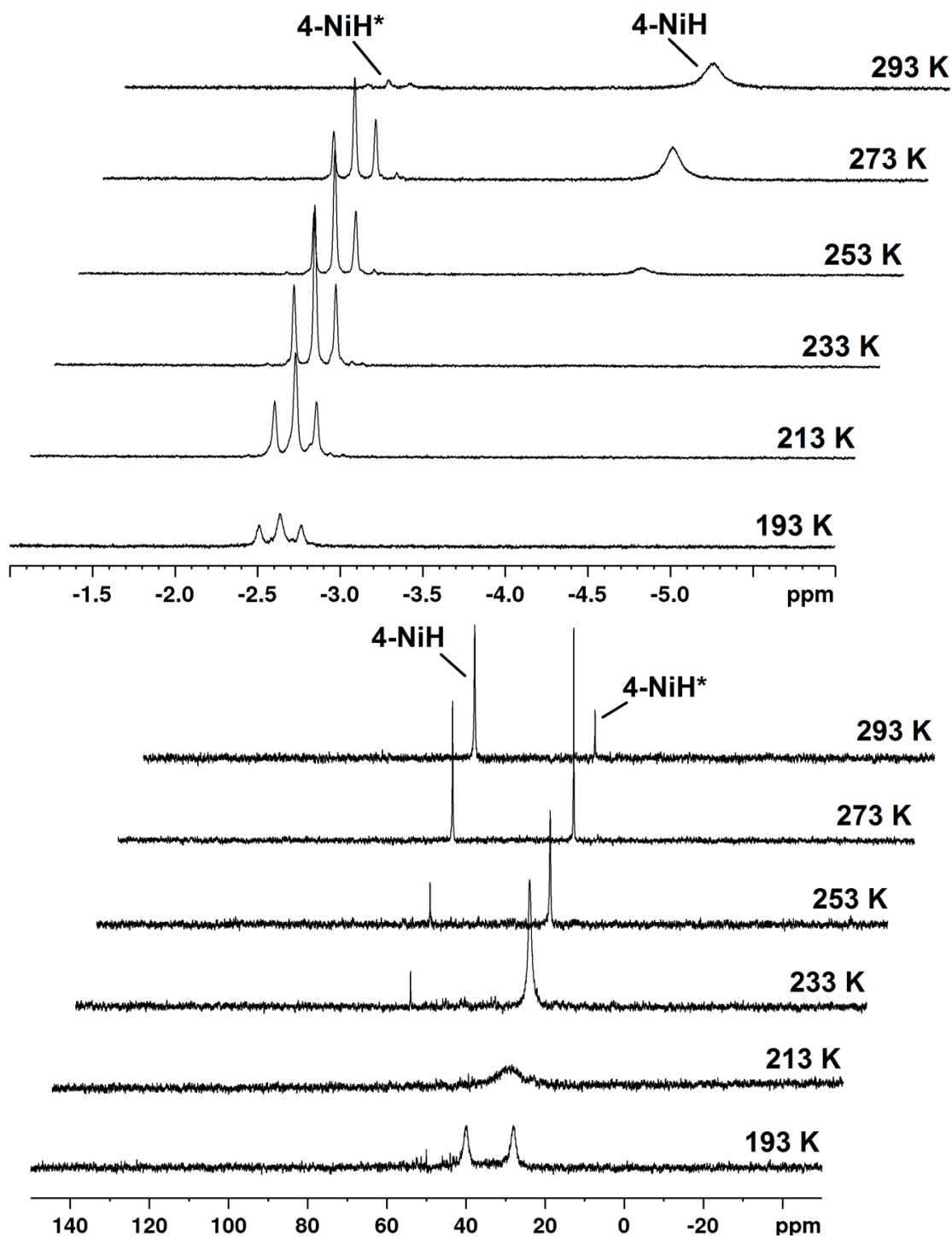
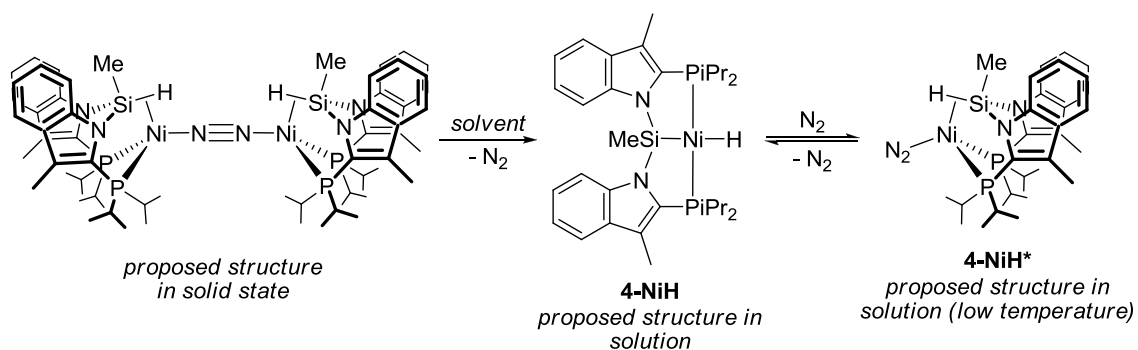


Figure 4.2.4. Variable temperature (top) ^1H NMR (hydride region) and (bottom) $^{31}\text{P}\{^1\text{H}\}$ NMR spectra of 4-NiH and 4-NiH* (methylcyclohexane- d_{12}).

In considering the formulation of 4-NiH, 4-PdH, and 4-PtH in solution, the NMR features observed (*vide supra*) suggest several possibilities along the continuum between

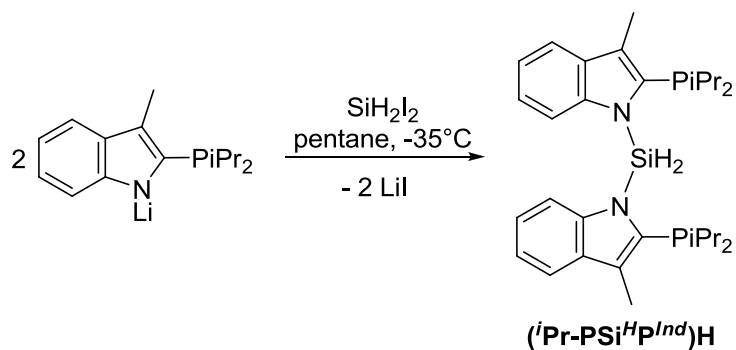
terminal metal hydride and η^2 -silane complexes, perhaps including scenarios where such species are in equilibrium. With respect to **4-NiH**, ^1H , $^{31}\text{P}\{^1\text{H}\}$ and ^{29}Si NMR data provide clear evidence for a temperature and solvent dependent equilibrium between two Ni hydride species in solution. Moreover, the Ni hydride species **4-NiH*** that appears to increase in concentration at low temperature involves the coordination of N_2 from the reaction atmosphere (*vide supra*) and gives rise to a significantly upfield-shifted ^{29}Si NMR resonance relative to **4-NiH**, **4-PdH**, and **4-PtH**.

On the basis of these data, **4-NiH** is tentatively assigned as a terminal Ni-H species formulated as $(^i\text{Pr-PSiP}^{Ind})\text{NiH}$ and **4-NiH*** as an N_2 -adduct involving η^2 -(SiH) coordination to the Ni center (Scheme 4.2.8). The interconversion between such structures in $(\text{Cy-PSiP})\text{NiH}(\text{L})$ ($\text{L} = \text{N}_2$ or CO) has been observed previously, and trends in ^{29}Si NMR data reported for such species are indeed consistent with our observations for **4-NiH** and **4-NiH***.^{24c} On the basis of the NMR data available for **4-NiH***, it cannot be definitively assigned as a monomeric species of the type $[\text{}^i\text{Pr-P}(\eta^2\text{-SiH})\text{P}^{Ind}]\text{Ni}(\text{N}_2)$ or a related N_2 -bridged dimer. However, in the solid state, the IR spectrum of the Ni hydride features a weak intensity band at 2075 cm^{-1} while the Raman spectrum features an intense band at 2073 cm^{-1} , assigned to coordinated N_2 . These data suggest that in the solid state the Ni hydride is likely best formulated as the N_2 -bridged dimer $\{[\text{}^i\text{Pr-P}(\eta^2\text{-SiH})\text{P}^{Ind}]\text{Ni}\}_2(\mu\text{-N}_2)$ (Scheme 4.2.8), which would be anticipated to feature a Raman-active N_2 ligand. This result is in agreement with the observations of Hazari and co-workers in regard to the formulation of the related N_2 adducts of $(\text{Cy-PSiP})\text{NiH}$.^{24c}



Scheme 4.2.8. Proposed interconversion of **4-NiH** from a ($\mu\text{-N}_2$)-bridged dimer in the solid state, to a classical terminal silyl hydride in solution, to the η^2 -silane and dinitrogen adduct, **4-NiH***, at low temperature in solution.

To further investigate the potential dynamic behavior of the hydride ligands in **4-NiH**, in addition to **4-PdH** and **4-PtH** *vis-à-vis* migration from metal to silicon, a variation of the ligand precursor, (*i*Pr-PSiP^{Ind})H, was targeted wherein the methyl group on Si is replaced by a second H atom, giving, overall, (*i*Pr-PSi^HP^{Ind})H. Once the corresponding hydride complexes of this new ligand derivative are prepared, exchange between the metal hydride and the silicon hydrogen atoms could be monitored through selective 1D NMR (NOESY) experiments, with the goal of illustrating, in a novel manner, the propensity for H to migrate between metal and silicon. This ligand variant can be accessed through treatment of the lithium salt of 2-(dipropan-2-ylphosphanyl)-3-methyl-1*H*-indole¹⁶⁴ with half an equiv of SiH₂I₂ in pentane at -35 °C (Scheme 4.2.9). The equivalent SiH₂ resonance appears as an apparent triplet ($J_{\text{PH}} = 9.6$ Hz) at 6.72 ppm, confirmed by the presence of a cross-peak at -57.5 ppm in a ¹H-²⁹Si HMQC experiment ($^1J_{\text{SiH}} = 249$ Hz). Unfortunately, the preparation of the corresponding chloride and hydride complexes was met with considerable difficulty especially in the case of Ni.

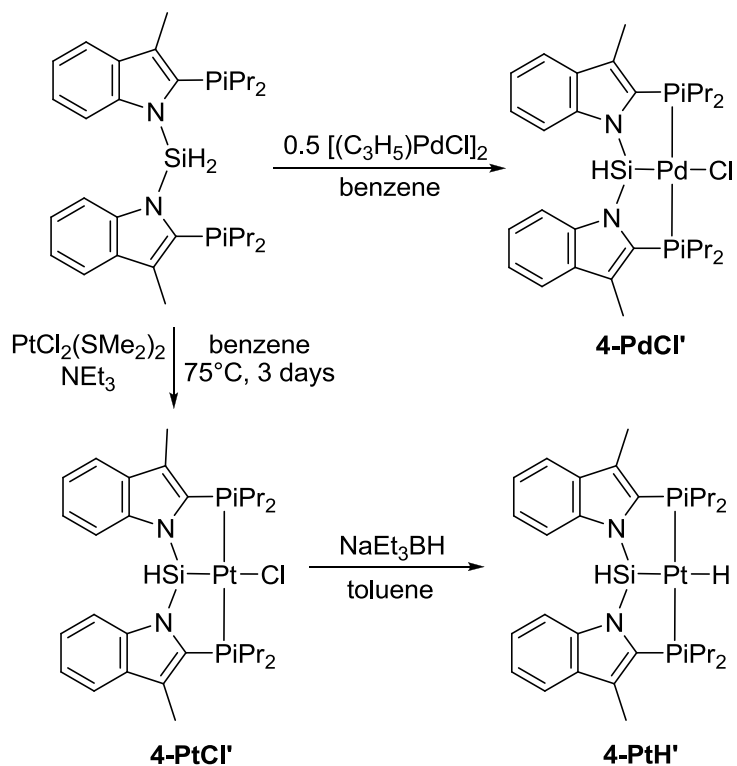


Scheme 4.2.9. Synthesis of (*i*Pr-PSi^HP^{Ind})H.

For Pt, treating PtCl₂(SMe₂)₂ with (*i*Pr-PSi^HP^{Ind})H in the presence of excess triethylamine led to the clean formation of (*i*Pr-PSi^HP^{Ind})PtCl, **4-PtCl'** after a period of heating in benzene solution (Scheme 4.2.10). **4-PtCl'** could be isolated in 89% yield as a white solid. The SiH resonance appears as a triplet with Pt satellites (³J_{PH} = 1.5 Hz, ²J_{PH} = 126 Hz), but otherwise the ¹H spectroscopic features of **4-PtCl'** are largely similar to those of **4-PtCl**. By ²⁹Si NMR, **4-PtCl'** features a relatively upfield-shifted resonance at 0.3 ppm (*cf.* 22.2 ppm for **4-PtCl**), and a characteristically large ¹J_{SiH} of 223 Hz, strongly implying no unusual bonding scenario for the SiH moiety in this particular complex. Similarly, for Pd, treatment of (*i*Pr-PSi^HP^{Ind})H with half an equiv of [(C₃H₅)PdCl]₂ (Scheme 4.2.10) led to generation of (*i*Pr-PSi^HP^{Ind})PdCl, **4-PdCl'**, isolated as an off-white solid in 59% yield. **4-PdCl'** features an SiH₂ resonance centered at 6.18 ppm as an apparent triplet (*J*_{PH} = 7.8 Hz), which couples to a ²⁹Si resonance at 17.4 ppm as determined by a ¹H-²⁹Si HMQC experiment (¹J_{SiH} = 229 Hz). Again these features are consistent with a classical Si-H bond, and thus both **4-PdCl'** and **4-PtCl'** can be considered direct analogues of **4-PdCl** and **4-PtCl**.

The corresponding Ni complex, **4-NiCl'** was not able to be prepared in a clean fashion. Multiple attempts using an analogous route to the synthesis of **4-NiCl** were

attempted under varying conditions, but in each case multiple product formation was observed by $^{31}\text{P}\{^1\text{H}\}$ and ^1H NMR spectroscopy. Attempts were also made to directly prepare the eventual target complex, **4-NiH'** by treating (*i*-Pr-PSi^{H*Ind*})H with Ni(COD)₂, however, as with the attempts at preparing **4-NiCl'** multiple product formation was observed with no evidence of the targeted hydride being formed in any amount. These results may imply the targeted compounds simply are not stable, perhaps through the loss of H₂ in the case of **4-NiH'** preparation, or HCl in the case of **4-NiCl'** preparation (particularly in the presence of excess triethylamine), however, in the absence of any conclusive data regarding generated complexes in these reactions, little can be said regarding the nature of these reactions. Similar attempts at generating **4-PdH'** by treatment of **4-PdCl'** with NaEt₃BH were met with failure. Multiple product formation was observed in each case, again implying perhaps the targeted complex is unstable toward H₂ elimination or some other decomposition process.



Scheme 4.2.10. Synthetic routes for the successful preparations of **4-PdCl'**, **4-PtCl'** and **4-PtH'**.

The corresponding Pt hydride complex, **4-PtH'** was found to be easily accessible, however, through simple treatment of **4-PtCl'** with $NaEt_3BH$ in toluene (Scheme 4.2.10). At room temperature, by 1H NMR spectroscopy both the SiH and PtH resonances are unique and well separated, with the SiH resonance centered at 7.37 ppm as a doublet ($^3J_{HH} = 6.0$ Hz) with Pt satellites ($^2J_{PtH} = 81.5$ Hz). The PtH resonance, meanwhile appears as a triplet of doublets, with Pt satellites, centered at 3.90 ppm ($^3J_{HH} = 6.0$ Hz, $^2J_{PtH} = 17.5$ Hz, $^1J_{PtH} = 564.2$ Hz). **4-PtH'** has a ^{29}Si chemical shift of 35.1 ppm, and the 1H - ^{29}Si HMQC spectrum features two distinct cross-peaks for the SiH ($^1J_{SiH} = 206$ Hz) and the PtH ($^2J_{SiH} = 70$ Hz). Overall these spectroscopic data support the formulation of **4-PtH'** as a direct analogue of **4-PtH** with no evidence of any additional interaction between Pt and the SiH . Furthermore, selective 1D NOESY experiments were carried

out, with the PtH resonance irradiated at temperatures from 300 – 353 K (mixing times of 0.5 s and 1.0 s), but no evidence for any chemical exchange was observed for the PtH and SiH in any experiment, small responses of the isopropyl methyl signals were observed in all experiments, consistent with some amount of through-space interaction between the PtH and these methyl groups. For the Pt complexes, therefore, it seems likely that the Pt hydrides exist as simple terminal hydride complexes with little tendency toward non-classical SiH interactions.

To investigate further the influence of an added donor ligand (*i.e.* other than dinitrogen) on **4-NiH**, the synthesis of complexes of the type (*i*Pr-PSiP^{*Ind*})NiH(L) (L = DMAP, PMe₃), **4-Ni·DMAP**, **4-Ni·PMe₃** was pursued. Complexes **4-Ni·DMAP** and **4-Ni·PMe₃** were both readily prepared by treatment of **4-NiH** with 1 equiv of DMAP or PMe₃, and could be isolated as yellow and off-white solids in 98% and 70% yields, respectively. In the case of **4-Ni·DMAP**, the NMR spectroscopic data obtained (*e.g.* upfield ²⁹Si chemical shift of -24.1 ppm, *J*_{SiH} = -69 Hz) are very similar to that of **4-NiH*** and thus support the formulation of this complex as [*i*Pr-P(η^2 -SiH)P^{*Ind*}]Ni(DMAP) in solution, rather than a DMAP adduct of a classical metal hydride, (*i*Pr-PSiP^{*Ind*})NiH(DMAP). Crystals of **4-Ni·DMAP** were obtained through low temperature evaporation of a concentrated Et₂O solution, and the resulting structure determined X-ray crystallographic analysis was also found to be in agreement with this assignment of **4-Ni·DMAP** as an η^2 -silane complex.

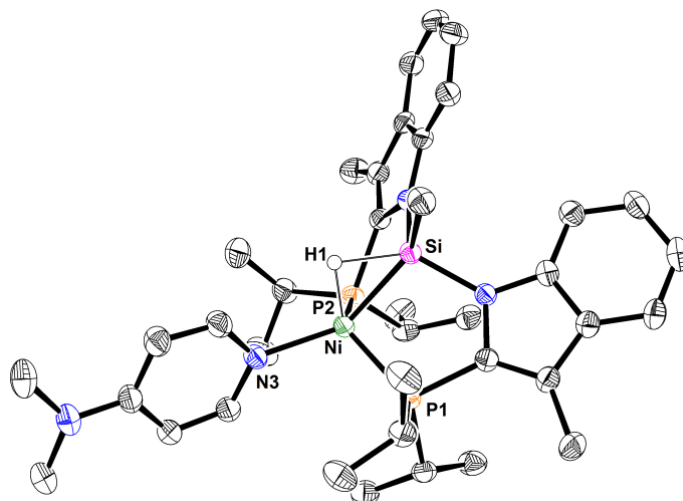


Figure 4.2.5. Crystallographically determined structures of **4-Ni·DMAP** with thermal ellipsoids drawn at the 50% probability level. Solvent molecules and most hydrogen atoms have been omitted for clarity. Only one of the two crystallographically independent molecules of **4-Ni·DMAP** is shown. Selected interatomic distances (Å) and angles (°): Ni-H(1) 1.50(3), Ni-P(1) 2.1816(7), Ni-P(2) 2.2245(8), Ni-Si 2.1745(8), Ni-N(3) 2.040(2), P(1)-Ni-P(2) 118.44(3), P(1)-Ni-Si 89.98(3), P(1)-Ni-N(3) 106.67(7), P(2)-Ni-Si 88.42(3), P(2)-Ni-N(3) 112.97(7), Si-Ni-H(1) 48.3(12), Si-Ni-N(3) 139.99(7), N(3)-Ni-H(1) 93.7(12)

By comparison, in the case of **4-Ni·PMe₃**, NMR analysis is consistent with the existence of two Ni hydride species in solution in a ca. 2 : 1 ratio (**4-Ni·PMe₃-A** = major, **4-Ni·PMe₃-B** = minor). While the ²⁹Si chemical shift of 6.3 ppm ($J_{\text{SiH}} = -82$ Hz) for **4-Ni·PMe₃-A** is relatively upfield, the minor constituent **4-Ni·PMe₃-B** gives rise to a ²⁹Si NMR resonance at 65.7 ppm ($J_{\text{SiH}} = -81$ Hz), which is more closely aligned with NMR data obtained for **4-NiH**. Complexes **4-Ni·PMe₃-A** and **4-Ni·PMe₃-B** both exhibit equivalent phosphorus environments associated with the *i*Pr-PSiP^{Ind} ligand, which is consistent with C₅-symmetric structures in solution. However the substantial difference in ²J_{PP} values for these two complexes (²J_{PP} for **4-Ni·PMe₃-A** = 6 Hz ; for **4-Ni·PMe₃-B** = 111 Hz) suggests that the orientation of the PMe₃ ligand relative to the *i*Pr-PSiP^{Ind} phosphino donors is considerably different in each case. The ²⁹Si and ³¹P{¹H} NMR data

for **4-Ni·PMe₃-A** is consistent with data previously reported for the related complexes [Ph-P(η^2 -SiH)P]Ni(PR₃) (R = Ph, Me; Ph-PSiP = κ^3 -(2-Ph₂PC₆H₄)₂SiMe)^{25b, 76} that were found to exhibit similarly upfield-shifted ²⁹Si NMR resonances, large values of J_{SiH} , and small values of $^2J_{\text{PP}}$. By comparison, NMR data for **4-Ni·PMe₃-B** is similar to that reported for the trigonal bipyramidal complex (Ph-PSiP)PtH(PPh₃) that features a terminal hydride ligand coordinated *trans* to Si.⁷⁶

On the basis of these data, we assign **4-Ni·PMe₃-A** as a PMe₃ adduct featuring η^2 -SiH coordination to the metal center, while **4-Ni·PMe₃-B** is assigned as a complex of the type (^{*i*}Pr-PSiP^{*Ind*})NiH(PMe₃) with a terminal hydride ligand coordinated *trans* to Si. Thus it appears the mixture of **4-Ni·PMe₃-A** and **4-Ni·PMe₃-B** generated upon treatment of **4-NiH** with PMe₃ represents a unique example of the Si-H oxidative addition product (**4-Ni·PMe₃-B**), and the η^2 -SiH complex associated with “arrested oxidative addition” (**4-Ni·PMe₃-A**) existing simultaneously in solution as an isomeric mixture. No conclusive evidence for a temperature dependent equilibrium involving **4-Ni·PMe₃-A** and **4-Ni·PMe₃-B** was obtained by ¹H and ³¹P{¹H} NMR analysis (193 – 353 K), although broadening of NMR features was observed at low temperature and slight changes in the ratio of **4-Ni·PMe₃-A** : **4-Ni·PMe₃-B** were noted at elevated temperatures. In addition, no evidence for chemical exchange was obtained by selective excitation of the NiH resonances *via* NOESY experiments (0.5 s and 1 s mixing times; 353 K).

While **4-Ni·PMe₃-A** and **4-Ni·PMe₃-B** could not be separated on a preparative scale, a sample of X-ray quality crystals obtained from the mixture of the two complexes revealed a five-coordinate complex featuring approximate trigonal bipyramidal coordination geometry at Ni (sum of angles around equatorial plane = 359.98 °) with Si

and a terminal hydride ligand (H1) in the axial positions, which is consistent with the formulation of **4-Ni·PMe₃-B** (Figure 4.2.6).

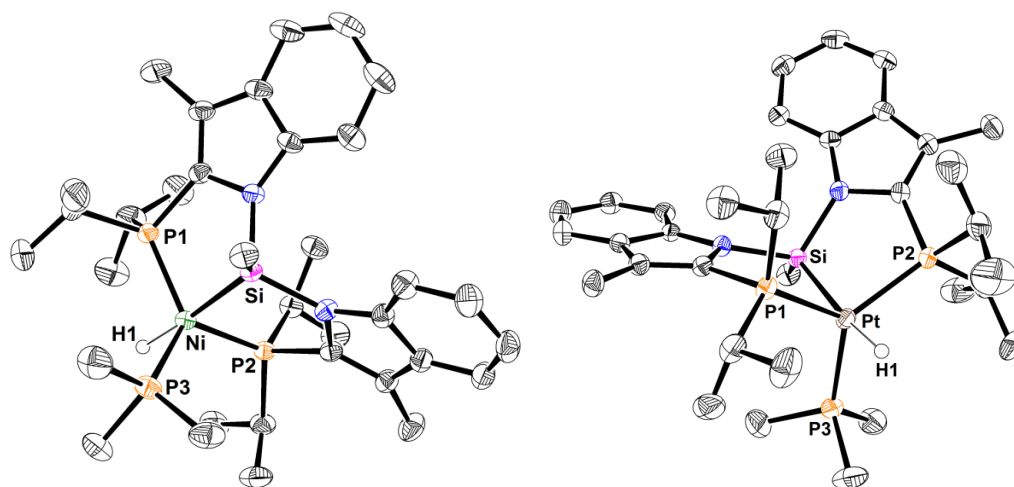


Figure 4.2.6. Crystallographically determined structures of **4-Ni·PMe₃-B** and **4-Pt·PMe₃** with thermal ellipsoids drawn at the 50% probability level. Solvent molecules and most hydrogen atoms have been omitted for clarity. Selected interatomic distances (Å) and angles (°): for **4-Ni·PMe₃-B** Ni-H(1) 1.49(3), Ni-P(1) 2.1611(5), Ni-P(2) 2.1794(5), Ni-P(3) 2.1727(5), Ni-Si 2.2057(5), Si-Ni-H(1) 175.6(10), P(1)-Ni-P(2) 119.10(2), P(1)-Ni-P(3) 126.58(2), P(2)-Ni-P(3) 114.30(2); for **4-Pt·PMe₃** Pt-H(1) 1.53(3), Pt-P(1) 2.3048(6), Pt-P(2) 2.2963(6), Pt-P(3) 2.3126(7), Pt-Si 2.3319(6), Si-Pt-H(1) 170.2(13), P(1)-Pt-P(2) 120.63(2), P(1)-Pt-P(3) 116.28(2), P(2)-Pt-P(3) 123.03(2).

The analogous Pt complex to **4-Ni·PMe₃-B** could also be prepared readily through addition of one equiv PMe₃ to **4-PtH**, giving **4-Pt·PMe₃** in 97% yield as an off-white solid after workup. Unlike the Ni-analogue, no evidence for any portion of **4-Pt·PMe₃** existing as anything but the terminal silyl hydride complex has been obtained. By ³¹P{¹H} NMR spectroscopy a single product is observed with resonances centered at 34.1 ppm (d with Pt satellites, ²J_{PP} = 149 Hz, ¹J_{PtP} = 2754 Hz) and -64.8 ppm (t with Pt satellites, ²J_{PP} = 149 Hz, ¹J_{PtP} = 2944 Hz). By ¹H NMR meanwhile, the hydride resonance appears at -10.7 ppm as a broad resonance with Pt satellites (¹J_{PtH} = 645 Hz, J_{SiH} = 69 Hz). The solid state structure of **4-Pt·PMe₃** is largely comparable to that of **4-Ni·PMe₃-**

B, with approximate trigonal bipyramidal geometry (sum of angles around equatorial plane = 359.94 °), where Si and the hydride ligand sit in the axial positions.

Overall, it is evident that a substantial amount of structural variability is possible for (*i*Pr-PSiP^{Ind})NiH(L) complexes, where terminal hydride as well as complexes involving η^2 -SiH coordination are both accessible, and may even co-exist, in ratios dependent on factors such as the nature of L (*e.g.* N₂, DMAP, PMe₃), as well as solvent and temperature. Furthermore, in comparing the NMR features of such bis(phosphino)silyl Group 10 hydride complexes (Table 4.2.1), the available data suggests that such species generally feature relatively large, negative J_{SiH} values that can be associated with *both* η^2 -SiH interactions and *trans*-Si-M-H coordination. Indeed, the NMR data obtained appear to suggest that in this specific family of complexes the ²⁹Si chemical shift may be a better predictor of the extent of Si-H interaction, such that complexes that feature an η^2 -SiH interaction involving the *i*Pr-PSiP^{Ind} ligand also give rise to relatively upfield-shifted ²⁹Si NMR resonances (Table 4.2.1).

Table 4.2.1. Summary of relevant spectroscopic data for Group 10 metal hydride or η^2 -silane complexes prepared in this work.^a

| Compound | ¹ H NMR M-H (ppm) | ²⁹ Si NMR (ppm) | J_{SiH} (Hz) |
|--------------------------|------------------------------------|-------------------------------|--------------------------|
| 4-NiH | - 4.79 | 59.8 | n/a |
| 4-NiH* | - 2.92 ^b | - 10.5 ^b | 89 ^{b,c} |
| 4-PdH | 0.15 | 60.1 | - 101 |
| 4-PtH | 4.23 | 64.1 | - 67 |
| 4-Ni·DMAP | - 3.50 | - 24.1 | - 69 |
| 4-Ni·PMe ₃ -A | - 5.44 | 6.3 | - 82 |
| 4-Ni·PMe ₃ -B | - 10.18 | 65.7 | - 81 |
| 4-Pt·PMe ₃ | - 10.74 | 38.5 | 67 ^c |

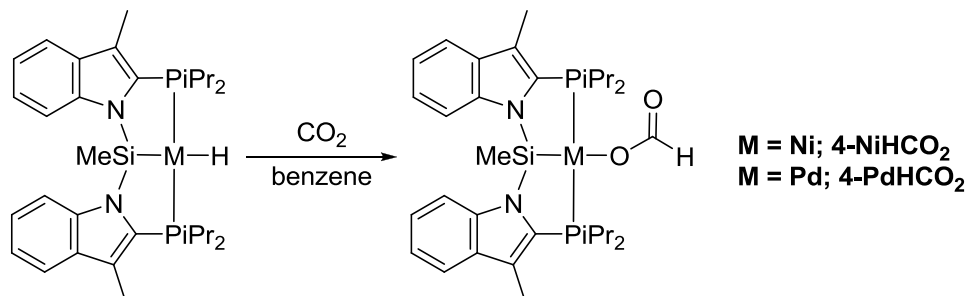
^a benzene-*d*₆, RT; ^b toluene-*d*₈, 193 K; ^c the sign of J_{SiH} could not be determined.

4.2.4 Catalytic Hydroboration of CO₂ to the Formaldehyde Level

The insertion of CO₂ into a metal-hydride bond to generate a formate species is commonly proposed as the first step of catalytic cycles for CO₂ reduction. As such, in an effort to probe the potential for **4-NiH** (or **4-PdH** and **4-PtH**) to act as a catalyst for the reduction of CO₂, a benzene-*d*₆ solution of **4-NiH** was exposed to an atmosphere of CO₂ (Scheme 4.2.11). Rapid (*ca.* 5 min, room temperature) and quantitative conversion to a new single product was observed by ³¹P{¹H} NMR spectroscopy as a singlet resonance centered at 34.6 ppm, consistent with the formation of a C_s-symmetric complex. By ¹H NMR, the loss of the NiH resonance at -4.79 ppm was observed, along with the appearance of a characteristic singlet resonance centered at 8.71 ppm, implying the insertion of CO₂ into the Ni-H bond to generate the desired formate complex. A ¹H-¹³C HSQC experiment revealed a cross-peak at 168.8 ppm correlating to the resonance at 8.71 ppm, again supporting the formation of the formate complex (*i*Pr-PSiP^{*Ind*})Ni(HCO₂), **4-NiHCO₂**. In addition, these data are in agreement with those reported for the related Ni formate complex (Cy-PSiP)Ni(HCO₂).⁷⁹ Despite repeated attempts, **4-NiHCO₂** could not be isolated in solid form and appears to decompose upon attempted isolation.

In the case of Pd, treatment of **4-PdH** with CO₂ (*ca.* 1 atm, benzene-*d*₆, Scheme 4.2.11) also appears to generate a formate complex (**4-PdHCO₂**) as the major product, however, this reaction was not as clean as in the case of Ni and **4-PdHCO₂** could not be successfully isolated. ¹H NMR analysis of the reaction mixture indicates that **4-PdHCO₂** gives rise to a formate resonance at 9.26 ppm, while by ³¹P{¹H} NMR a singlet resonance centered at 39.0 ppm implies the generation of a C_s-symmetric product as with **4-NiHCO₂**. Attempts to generate an analogous Pt formate species by treatment of **4-PtH**

with CO₂ led to the formation of multiple unidentified products from which no pure material could be isolated. By comparison, the related Ni and Pd formate complexes (Cy-PSiP)M(HCO₂) have previously been found to be isolable,^{71, 79} while the Pt derivative can be generated under a CO₂ atmosphere and readily eliminates CO₂ to reform the parent Pt hydride complex.⁷¹



Scheme 4.2.11. Generation of Ni and Pd formate complexes from the corresponding hydride complexes. The analogous reaction with Pt leads to formation of multiple unidentified products.

Three possible approaches to the catalytic reduction of CO₂ with **4-NiHCO₂** were envisioned: hydrogenation,¹⁶⁵ hydrosilylation,⁷¹ or hydroboration.^{69a, 160} Attempts at stoichiometric hydrogenation or hydrosilylation of **4-NiHCO₂** have thus far proven unsuccessful. By comparison, treatment of a benzene-*d*₆ solution of **4-NiHCO₂** with 2 equiv of pinacolborane (HBPin) and CO₂ (ca. 1 atm) led to the generation of PinBOMe and (PinB)₂O (ca. 1:1 ratio by ¹H NMR) after 25 minutes at room temperature, as evidenced by ¹¹B NMR resonances at 22.7 and 21.9 ppm, respectively.^{160a} The formation of these products indicates that hydroboration of CO₂ to the methanol level has occurred (hydrolysis of PinBOMe readily affords methanol). The ¹H NMR spectrum of the reaction mixture corroborates these observations (¹H NMR resonances for CH₃OBPin: 3.51 ppm (s, 3 H, CH₃OBPin), 1.04 (s, 12 H, CH₃OBPin), for (PinB)₂O: 1.02 ppm (s, 12 H)), but interestingly a singlet at 5.50 ppm was also observed (ca. 6-10% relative to

CH₃OBPin). The latter resonance correlates well with the chemical shift attributed to the methylene protons of (PinBO)₂CH₂, an intermediate recently implicated in CO₂ hydroboration.^{160a, 160d} This bis(boryl)acetal represents a rare reduction of CO₂ to the *formaldehyde* level. Formaldehyde is considered the ‘missing link’ in homogeneous CO₂ reduction catalysis, as very few examples of reduction to, or even mere detection of, formaldehyde during the homogeneous reduction of CO₂ have been noted, and those only recently.^{71, 160b, 166} It is worth noting explicitly that the (PSiP)Pd and Pt-catalyzed hydrosilylation of CO₂ to methane generates a bis(*silyl*)acetal intermediate during the course of the reaction which, in the presence of catalytic amounts of B(C₆F₅)₃, is further reduced to methane. Notably, this bis(*silyl*) acetal can be *exclusively* generated in the absence of the additional Lewis acid.⁷¹ Interestingly, Sabo-Étienne and co-workers have demonstrated that (PinBO)₂CH₂ can function as a source of the CH₂ moiety in synthetic applications.^{160d}

In efforts to determine whether the reduction of CO₂ could be carried out catalytically, an initial catalytic screen was carried out in benzene solution at room temperature, using 1 atm of CO₂ with HBPIn as the reductant. To begin, the catalytic performance of **4-NiH**, **4-PdH**, and **4-PtH**, respectively, were assessed at a 0.2 mol% loading. After a 1 h reaction time, NMR analysis of the reaction mixtures indicated negligible formation of products resulting from CO₂ hydroboration in the case of **4-PtH** (Table 4.2.2, Entry 3), unsurprising considering the unproductive reactivity of this complex toward CO₂. For **4-PdH**, 39% conversion to PinB(CO₂H) was observed, with minimal formation of other hydroboration products (Table 4.2.2, Entry 2). By comparison, for **4-NiH** highly selective (84%) formation of the corresponding

bis(boryl)acetal was observed (Table 4.2.2, Entry 1), as indicated by a characteristic ^1H NMR resonance at 5.51 ppm corresponding to the methylene protons of the acetal.^{160a} In an effort to establish the necessity of **4-NiH** for this reactivity, control experiments utilizing **4-NiCl** as the Ni source were carried out under identical conditions with no CO_2 reduction products observed spectroscopically after 1 h (Table 4.2.2, Entry 4). Similarly, NaEt_3BH alone was not effective as a catalyst (Table 4.2.2, Entry 5).

Table 4.2.2. Initial screening of CO_2 hydroboration with HBPIn.^a

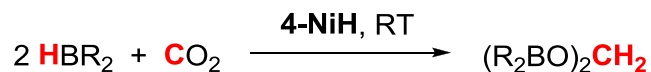
$\text{CO}_2 \xrightarrow[\text{catalyst}]{\text{HBPIn}}$ **boryl formate** $\xrightarrow[\text{catalyst}]{\text{HBPIn}}$ **bis(boryl)acetal** $\xrightarrow[\text{catalyst}]{\text{HBPIn}}$ **methoxyborane** + $(\text{PinB})_2\text{O}$

| Entry | Catalyst | Conversion to boryl formate | Conversion to bis(boryl)acetal | Conversion to methoxyborane |
|----------|---------------------------|-----------------------------|--------------------------------|-----------------------------|
| 1 | 4-NiH | < 5% | 84% (1.8 mmol) ^b | < 5% |
| 2 | 4-PdH | 39% (1.6 mmol) | 6% | < 5% |
| 3 | 4-PtH | < 5% | < 5% | < 5% |
| 4 | 4-NiCl | 0 | 0 | 0 |
| 5 | NaEt₃BH | 0 | 0 | 0 |

^a Reaction conditions: benzene-*d*₆, 4.2 mmol HBPIn, [HBPIn] = 4.8 M, 1 atm CO_2 , 0.2 mol% M (M = Ni, Pd, Pt) or NaEt_3BH vs. HBPIn, RT, 1 h. Conversions on the basis of ^1H NMR integration using C_6Me_6 as an internal standard (average of two runs). ^b TON = 420 based on mol B-H reacted per mol of Ni.

Intrigued by the selectivity of **4-NiH** for the reduction of CO_2 to the formaldehyde level further experiments were conducted to optimize this reactivity (Table 4.2.3). It was first established that under the initial screening conditions, increasing the reaction time to 4 h led to 97% conversion of HBPIn to the targeted acetal (Table 4.2.3, Entry 1). This represents the highest selectivity reported to date for hydroboration to the formaldehyde level with negligible overreduction to the methoxyborane (ca. 1% by ^1H NMR analysis

after 4 h).¹⁰ By comparison, in the only previous example of selective CO₂ double hydroboration (with 9-BBN), a yield of 85% bis(boryl)acetal and 8% methoxyborane was obtained at full 9-BBN conversion by use of Fe(H)₂(DMPE)₂ as the precatalyst.^{160d} Decreasing the catalyst loading by a factor of 10 led to a dramatic drop-off in reactivity (Table 4.2.3, Entry 2). The effect of concentration on the catalytic performance of **4-NiH** was evaluated by performing reactions at lower concentrations of HBPIn. Once again it was found that the conversion to the bis(boryl)acetal product decreased significantly (Table 4.2.3, Entries 4 and 5). The reactivity of alternative boranes was also examined and it was determined that HBCat and 9-BBN each provided negligible conversion to any products arising from CO₂ hydroboration (Table 4.2.3, Entries 6 and 7). Lastly, the effect of varying the solvent was examined by performing the catalytic reaction in THF-*d*₈ and cyclohexane-*d*₁₂ solution and found that while the use THF resulted in decreased formation of the bis(boryl)acetal product, the use of cyclohexane resulted in 92% conversion to the bis(boryl)acetal in 1 h at room temperature (Table 4.2.3, Entries 8 and 9).

Table 4.2.3. Hydroboration of CO₂ with 4-NiH to the formaldehyde level.^a

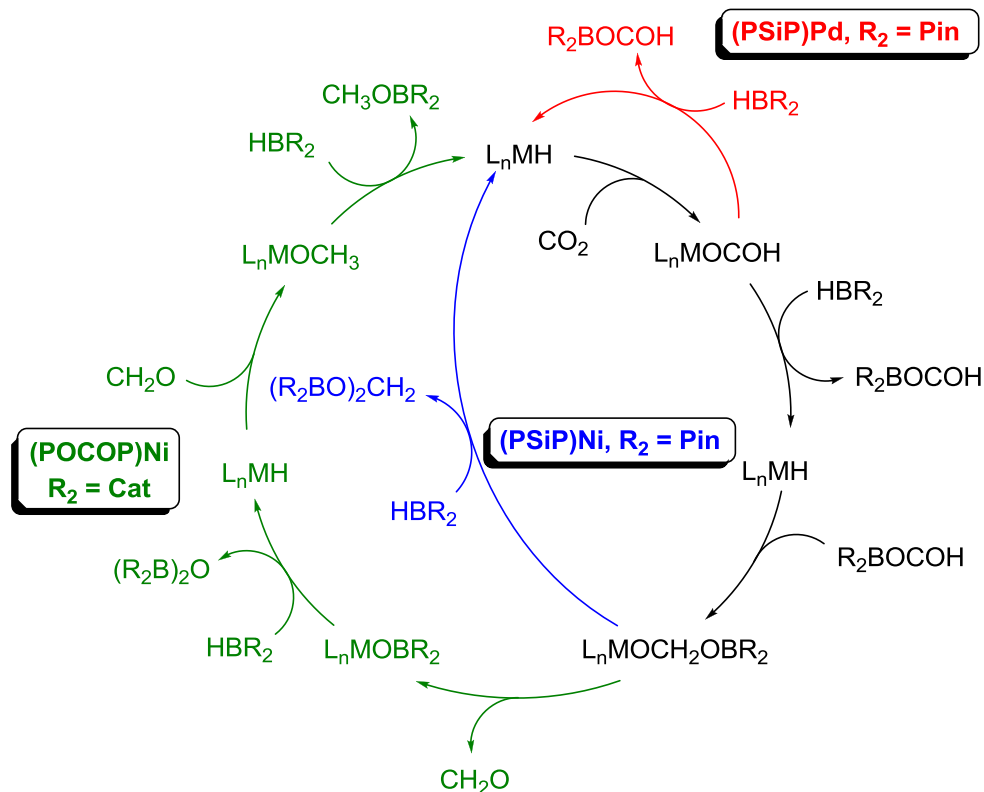
| Entry | mol% Ni | HBR ₂ | [HBR ₂] (mol/L) | Solvent | Time (h) | Conversion to bis(boryl)acetal |
|-------|---------|------------------|-----------------------------|--------------------------------|----------|--------------------------------|
| 1 | 0.2 | HBPIn | 4.8 | C ₆ D ₆ | 4 | 97% ^b |
| 2 | 0.02 | HBPIn | 4.8 | C ₆ D ₆ | 1 | <5% |
| 3 | 0.2 | HBPIn | 4.8 | C ₆ D ₆ | 1 | 84% |
| 4 | 0.2 | HBPIn | 0.96 | C ₆ D ₆ | 1 | 21% |
| 5 | 0.2 | HBPIn | 0.096 | C ₆ D ₆ | 1 | <5% |
| 6 | 0.2 | HBCat | 4.8 | C ₆ D ₆ | 1 | <5% |
| 7 | 0.2 | 9-BBN | 0.96 | C ₆ D ₆ | 1 | <5% |
| 8 | 0.2 | HBPIn | 4.8 | THF- <i>d</i> ₈ | 1 | 30% |
| 9 | 0.2 | HBPIn | 4.8 | C ₆ D ₁₂ | 1 | 92% |

^a 1 atm CO₂. Conversions on the basis of ¹H NMR integration using C₆Me₆ as an internal standard (average of two runs). Throughout, no indication of boryl formate and minimal (≤5%) conversion to methoxyborane were observed. ^b TON = 487 based on mol B-H reacted per mol of Ni; 71% isolated yield.

Having optimized reaction conditions for the formation of the HBPIn-derived bis(boryl)acetal, (PinBO)₂CH₂, it was also found that this compound could be readily isolated as an analytically pure, moisture-sensitive solid in 71% yield, which may facilitate its utility as a synthon for subsequent chemical manipulation. Samples of (PinBO)₂CH₂ stored under a nitrogen atmosphere proved stable in the solid state for several days. While (PinBO)₂CH₂ rapidly hydrolyzes to generate formaldehyde upon exposure to water, in benzene-*d*₆ solution under an inert atmosphere 64% of the acetal was found to persist after 96 h at room temperature (by ¹H NMR integration relative to ferrocene internal standard).

The mechanism of this CO₂ hydroboration likely follows a pathway similar to those proposed by Guan and co-workers^{69a} and Sabo-Étienne and co-workers (Scheme 4.2.12).^{160c} Insertion of CO₂ into the Ni-H bond of **4-NiH** to generate the corresponding

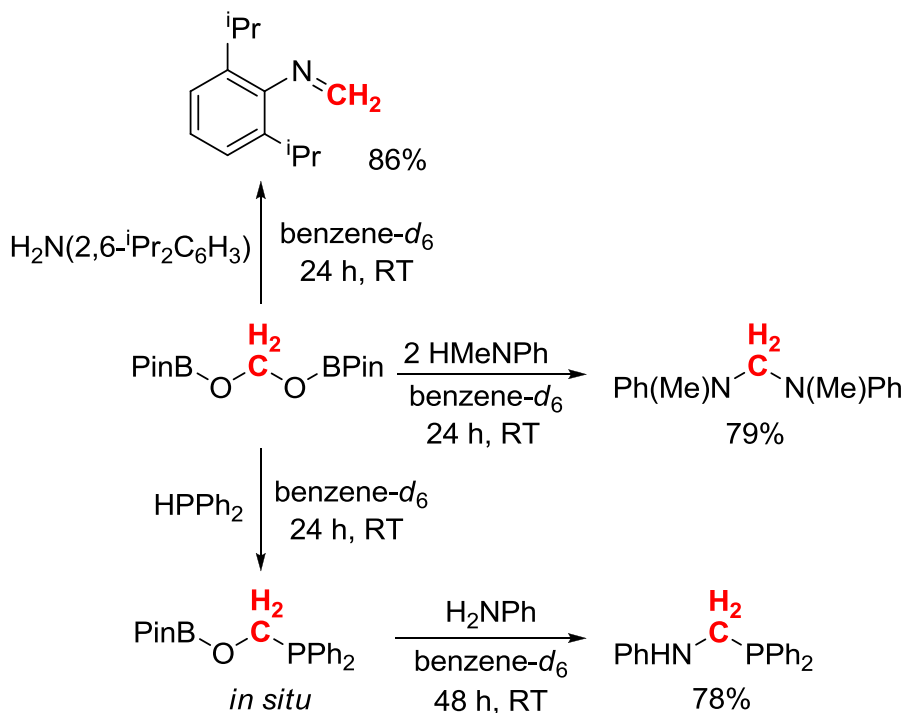
formate is followed by net addition of one equiv HBPin across the C=O bond giving a complex of the form (*i*Pr-PSiP^{Ind})Ni(OCH₂OBPin). This complex could then undergo dissociation of [OCH₂OBPin]⁻ followed by oxidative addition of HBPin and subsequent loss of (PinBO)₂CH₂, or may undergo σ -bond metathesis directly with an equiv of HBPin to give the same product and regenerate **4-NiH** (blue pathway in Scheme 4.2.12). In the case of **4-PdH** the insertion of CO₂ into the Pd-H bond is perhaps simply followed by a σ -bond metathesis reaction with HBPin to generate the boryl formate directly (red pathway in Scheme 4.2.12). In the case of full reduction to methoxyborane, Guan and co-workers^{69a} propose same initial sequence of steps leading to a (POCOP)Ni(OCH₂OBCat) complex, however, they then propose extrusion of formaldehyde followed by σ -bond metathesis with HBCat to regenerate (POCOP)NiH and (CatB)₂O. Insertion of the previously generated formaldehyde into the Ni-H bond then gives a Ni-OCH₃ complex, which can then undergo σ -bond metathesis with HBCat to regenerate (POCOP)NiH and the methoxyborane product (green pathway in Scheme 4.2.12). Attempts were to generate and identify (*i*Pr-PSiP^{Ind})Ni(OCH₂OBPin) as an intermediate were unsuccessful, thus further study to aid in elucidation of the mechanism is required.



Scheme 4.2.12. Proposed mechanism for (POCOP)Ni or (PSiP)M (M = Ni, Pd) CO₂ hydroboration with diverging pathways leading to generation of boryl formate (red), bis(boryl)acetal (blue) and methoxyborane (green).

Bontemps, Sabo-Etienne and co-workers^{160d} have previously reported that *in situ* generated bis(boryl)acetal derived from the hydroboration of CO₂ with 9-BBN is an effective source of formaldehyde that can undergo subsequent reactivity with substrates such as anilines, amines, alcohols and ylides to form C-N, C-O, and C-C bonds. Intrigued by this reactivity, we sought to study the reactivity of isolated (PinBO)₂CH₂ in this regard. Indeed, similar methylene transfer reactivity was observed for the reaction of (PinBO)₂CH₂ with anilines (Scheme 4.2.13), such that treatment with H₂N(2,6-ⁱPr₂C₆H₃) led to formation of CH₂=N(2,6-ⁱPr₂C₆H₃) (86% conversion by ¹H NMR after 24 h at RT), while treatment with HN(Me)Ph led to the formation of [Ph(Me)N]₂CH₂ (79% conversion after 24 h at RT). Net methylene transfer to phosphorus was also observed upon

treatment of $(\text{PinBO})_2\text{CH}_2$ with HPPH_2 . While the latter reaction leads exclusively to the generation of a monophosphine intermediate assigned as $\text{PinBOCH}_2\text{PPh}_2$, treatment of this species (generated *in situ*) with H_2NPh led to the formation of $\text{Ph}(\text{H})\text{NCH}_2\text{PPh}_2$ (78% based on $(\text{PinBO})_2\text{CH}_2$). This reactivity confirms the utility of $(\text{PinBO})_2\text{CH}_2$ as an effective methylene transfer reagent.



Scheme 4.2.13. Methylene transfer reactions from $(\text{PinBO})_2\text{CH}_2$.

4.3 Summary and Conclusions

In summary, a new PSiP ligand featuring an indolyene backbone was developed and utilized for the synthesis of Group 10 pincer complexes. Nickel, palladium, and platinum chloride complexes (**4-NiCl**, **4-PdCl** and **4-PtCl**) supported by this ligand were readily prepared and characterized. In the case of Ni, salt metathesis routes proved viable for the synthesis of allyl (**4-Ni(C₃H₅)**), anilido (**4-NiNHDMP**) and triflate (**4-NiOTf**)

complexes, however, a ligand rearrangement process involving Si-N bond cleavage was observed when attempting to prepare the corresponding NiMe complex.

Corresponding group 10 metal hydride complexes of the *i*Pr-PSiP^{Ind} ligand (**4-NiH**, **4-PdH**, **4-PtH**) were also found to be readily isolable. Solution NMR and single crystal X-ray data revealed that a significant amount of structural variability is possible for such complexes, particularly in the case of Ni, where terminal hydride (**4-NiH·PMe₃-B**) as well as complexes involving η^2 -SiH coordination (**4-NiH***, **4-NiH·PMe₃-A**, **4-NiH·DMAP**) are both accessible, and may even co-exist, in ratios dependent on factors such as the nature of additional co-ligands, including N₂ from the reaction atmosphere, as well as solvent and temperature. Attempts were made to observe potential migration of H between metal and Si through the preparation of hydride complexes of a derivative of *i*Pr-PSiP^{Ind} featuring an SiH bond. Only the Pt hydride complex (**4-PtH'**) was found to be isolable in this case, and no evidence for chemical exchange between SiH and PtH could be obtained.

While both the Ni and Pd hydride complexes of *i*Pr-PSiP^{Ind} were shown to be capable of CO₂ insertion affording formate complexes, these formate complexes were not isolable. However, both hydride species were active for catalytic hydroboration of CO₂ with HBPin, displaying divergent selectivity. Thus, the Pd catalyst (**4-PdH**) exhibited moderate activity in the hydroboration of CO₂ to the formate level, whereas the analogous Ni species (**4-NiH**) exhibited unprecedented selectivity for hydroboration to the formaldehyde level. We further demonstrated that the HBPin-derived bis(boryl)acetal product could be successfully isolated and utilized as a source of methylene for the formation of C-N and C-P bonds.

4.4 Experimental

4.4.1 General Considerations

All experiments were conducted under nitrogen in a glovebox and/or using standard Schlenk techniques. Tetrahydrofuran and diethyl ether were distilled from Na/benzophenone ketyl. Benzene, toluene, and pentane were first sparged with nitrogen and subsequently dried by passage through a double-column (one activated alumina column and one column packed with activated Q-5) solvent purification system. All purified solvents were stored over 4 Å molecular sieves. Benzene-*d*₆, toluene-*d*₈, methylcyclohexane-*d*₁₄ and tetrahydrofuran-*d*₈ were degassed via three freeze-pump-thaw cycles and stored over 4 Å molecular sieves. The compound diisopropyl(3-methyl-2-indolyl)-phosphine was prepared according to a literature procedure.¹⁶⁴ All other reagents were purchased from commercial suppliers and used without further purification. Unless otherwise stated, ¹H, ¹³C, ¹¹B, ³¹P, and ²⁹Si characterization data were collected at 300K, with chemical shifts reported in parts per million downfield of SiMe₄ (for ¹H, ¹³C, and ²⁹Si), BF₃·OEt₂ (for ¹¹B), or 85% H₃PO₄ in D₂O (for ³¹P). ¹H and ¹³C NMR chemical shift assignments are based on data obtained from ¹³C{¹H}, ¹³C-DEPTQ, ¹H-¹H COSY, ¹H-¹³C HSQC, and ¹H-¹³C HMBC NMR experiments. ²⁹Si NMR assignments are based on ¹H-²⁹Si HMBC, ¹H-²⁹Si HMQC and ¹H-²⁹Si HECADE¹⁶⁷ experiments. The 2D ¹H-²⁹Si HECADE data was acquired using a value for the one-bond ¹H-²⁹Si coupling of 180 Hz and a TOCSY mixing time of 60 msec; in order to ensure adequate digital resolution in F2 for the measurement of coupling constants, the acquisition time was adjusted to 1.14 s resulting in a digital resolution of 0.88 Hz/point. In experiments involving the reactivity of the acetal, (PinBO)₂CH₂, a 60 s relaxation delay was used when determining reaction

yields by NMR integration relative to a ferrocene internal standard. Infrared spectra were recorded as thin films between NaCl plates at a resolution of 4 cm⁻¹. X-ray data collection, solution, and refinement were carried out by Drs. Robert MacDonald and Michael J. Ferguson at the University of Alberta X-ray Crystallography Laboratory, Edmonton, Alberta.

4.4.2 Synthetic Procedures and Characterization Data

(ⁱPr-PSiP^{Ind})H. A pre-cooled (-78 °C) solution of diisopropyl(3-methyl-2-indolyl)phosphine (4.00 g, 16.2 mmol) in THF (*ca.* 100 mL) was treated with ⁿBuLi (1.6 M in hexanes, 10.1 mL, 16.2 mmol), added dropwise over the course of 10 min. The resulting reaction mixture was stirred for 20 min at -78 °C, then allowed to warm to room temperature over the course of 1 h. The reaction mixture was once again cooled to -78 °C and neat Cl₂SiHMe (0.84 mL, 8.10 mmol) was added by syringe. The mixture was allowed to warm to room temperature over the course of 18 h with stirring, during which time a white precipitate was observed. The volatile components of the reaction mixture were subsequently removed under vacuum and benzene (*ca.* 60 mL) was added to the remaining residue. The resulting slurry was filtered through Celite. The filtrate solution was collected and the volatile components were removed *in vacuo*. The remaining residue was triturated with pentane (4 × 3 mL) and subsequently washed with pentane (3 × 4 mL) to afford (ⁱPr-PSiP^{Ind})H (3.21 g, 74% yield) as an off-white solid. ¹H NMR (500 MHz, benzene-*d*₆): δ 7.56 (apparent d, 4 H, *J* = 8 Hz, *H*_{arom}), 7.25 – 7.09 (5 H, SiH + *H*_{arom}; the SiH resonance was identified at 7.19 ppm by the use of ¹H-²⁹Si correlation spectroscopy), 2.27 (s, 6 H, Indole-*Me*), 2.22 (m, 4 H, PCHMe₂), 1.19 (m, 3 H, SiMe), 1.04 (dd, 6 H, ³*J*_{HH} = 7 Hz, ³*J*_{HP} = 16 Hz, PCHMe₂), 0.98 (dd, 6 H, ³*J*_{HH} = 7 Hz,

$^3J_{\text{HP}} = 17$ Hz, PCHMe_2), 0.77 (dd, 6 H, $^3J_{\text{HH}} = 7$ Hz, $^3J_{\text{HP}} = 13$ Hz, PCHMe_2), 0.67 (dd, 6 H, $^3J_{\text{HH}} = 7$ Hz, $^3J_{\text{HP}} = 14$ Hz, PCHMe_2). $^{13}\text{C}\{^1\text{H}\}$ NMR (126 MHz, benzene- d_6): δ 143.3 (C_{arom}), 136.1 (C_{arom}), 133.4 (C_{arom}), 123.2 (CH_{arom}), 120.5 (CH_{arom}), 118.9 (CH_{arom}), 115.5 (CH_{arom}), 25.9 (apparent d, $J = 9$ Hz, PCHMe_2), 25.2 (apparent d, $J = 9$ Hz, PCHMe_2), 22.1 - 21.4 (overlapping resonances, PCHMe_2), 11.1 (Indole-*Me*), 4.5 (Si*Me*). $^{31}\text{P}\{^1\text{H}\}$ NMR (202 MHz, benzene- d_6): δ -8.5. ^{29}Si NMR (100 MHz, benzene- d_6): δ -27.3 ($^1J_{\text{SiH}} = -271$ Hz). Anal. Calcd for $\text{C}_{31}\text{H}_{46}\text{N}_2\text{P}_2\text{Si}$: C, 69.37; H, 8.64; N, 5.22. Found: C, 69.47; H, 8.89; N, 5.25.

(*i*Pr-PSi^HP^{Ind})H. The lithium salt of 2-(dipropylphosphanyl)-3-methyl-1*H*-indole (0.10 g, 0.41 mmol), prepared *via* treatment of 2-(dipropylphosphanyl)-3-methyl-1*H*-indole with 1 equiv ^{*n*}BuLi, was dissolved in ca. 5 mL pentane and cooled to -35 °C. Simultaneously, a solution of SiH_2I_2 (20.5 μL , 0.41 mmol) was prepared in 5 mL pentane and also cooled to -35 °C. The pentane solution of the lithium salt was added dropwise with mixing to the solution of SiH_2I_2 leading to immediate precipitation of a white solid material. The mixture was allowed to react for 18 h at room temperature after which point the mixture was filtered through Celite. The residue was extracted with 2 x 10 mL pentane and filtered through Celite. All extracts were combined and concentrated *in vacuo* to yield a white solid. The solid was washed with 2×0.5 mL pentane and evaporated to dryness *in vacuo* to give pure (*i*Pr-PSi^HP^{Ind})H (0.064 g, 60% yield) as a white solid. ^1H NMR (300 MHz, benzene- d_6): δ 7.90 (apparent d, 2 H, $J = 7.2$ Hz, H_{arom}), 7.56 (m, 2 H, H_{arom}), 7.22 (m, 4 H, H_{arom}), 6.72 (t, $^3J_{\text{SiH}} = 9.9$ Hz, 2 H, SiH_2), 2.24 (s, 6 H, Indole-*Me*), 2.16 (m, 4 H, PCHMe_2), 0.95 (d, $^3J_{\text{HH}} = 6.9$ Hz, 6 H, PCHMe_2), 0.99 (d, $^3J_{\text{HH}} = 6.9$ Hz, 6 H, PCHMe_2), 0.64 (d, $^3J_{\text{HH}} = 6.9$ Hz, 6 H, PCHMe_2), 0.60 (d, $^3J_{\text{HH}} = 6.9$ Hz, 6

H, PCHMe_2). $^{13}\text{C}\{^1\text{H}\}$ NMR (75.5 MHz, benzene- d_6): δ 143.0 (d, $J = 9.8$ Hz, C_{arom}), 135.1 (d, $J = 11.3$ Hz, C_{arom}), 133.5 (C_{arom}), 123.2 (C_{arom}), 123.0 (CH_{arom}), 120.8 (CH_{arom}), 118.6 (CH_{arom}), 116.1 (d, $J = 6.8$ Hz, CH_{arom}), 25.2 (d, $J_{\text{CP}} = 9.1$ Hz, PCHMe_2), 21.8 (PCHMe_2), 21.5 (PCHMe_2), 21.0 (PCHMe_2), 20.9 (PCHMe_2), 10.9 (Indole-Me). $^{31}\text{P}\{^1\text{H}\}$ NMR (121.5 MHz, benzene- d_6): δ -8.2. ^{29}Si NMR (99.4 MHz, benzene- d_6): δ -57.5 ($^1J_{\text{SiH}} = 249$ Hz). Anal. Calcd for $\text{C}_{30}\text{H}_{44}\text{N}_2\text{P}_2\text{Si}$: C, 68.93; H, 8.48; N, 5.36. Found: C, 68.54; H, 8.35; N, 5.73.

($^i\text{Pr-PSiP}^{\text{Ind}}$)NiCl (4-NiCl). A room-temperature solution of ($^i\text{Pr-PSiP}^{\text{Ind}}$)H (0.40 g, 0.75 mmol) in benzene (ca. 3 mL) was added to a suspension of $\text{NiCl}_2(\text{DME})$ (0.16 g, 0.75 mmol) in benzene (ca. 3 mL). Neat NEt_3 (1.05 mL, 7.5 mmol) was added, and the resulting mixture was stirred for 16 h at room temperature. The reaction mixture was subsequently filtered through Celite. The filtrate solution was collected, and the volatile components were removed under vacuum. The remaining residue was triturated with pentane (3×5 mL) and then washed with pentane (ca. 1 mL) and dried under vacuum to afford **4-NiCl** (0.43 g, 91% yield) as an orange-yellow solid. ^1H NMR (300 MHz, benzene- d_6): δ 7.64 (m, 2 H, H_{arom}), 7.57 (m, 2 H, H_{arom}), 7.21–7.15 (4 H, H_{arom}), 2.95 (m, 2 H, PCHMe_2), 2.72 (m, 2 H, PCHMe_2), 2.24 (s, 6 H, Indole-Me), 1.48 (m, 12 H, PCHMe_2), 1.18–1.04 (12 H, PCHMe_2), 0.54 (s, 3 H, SiMe). $^{13}\text{C}\{^1\text{H}\}$ NMR (75.5 MHz, benzene- d_6): δ 141.6 (apparent t, $J = 6$ Hz, C_{arom}), 138.0 (C_{arom}), 133.2 (apparent t, $J = 27$ Hz, C_{arom}), 123.8 (CH_{arom}), 121.6 (CH_{arom}), 120.9 (C_{arom}), 120.4 (CH_{arom}), 117.5 (CH_{arom}), 28.7 (apparent t, $J = 12$ Hz, PCHMe_2), 27.5 (apparent t, $J = 13$ Hz, PCHMe_2), 20.8 (apparent d, $J = 12$ Hz, CHMe_2), 20.3 (apparent d, $J = 11$ Hz, CHMe_2), 12.2 (Indole-Me), 6.4 (SiMe). $^{31}\text{P}\{^1\text{H}\}$ NMR (121.5 MHz, benzene- d_6): δ 36.0. ^{29}Si NMR (59.6 MHz,

benzene-*d*₆): δ 43.8. Anal. Calcd for C₃₁H₄₅ClN₂P₂NiSi: C, 59.11; H, 7.20; N, 4.45. Found: C, 59.58; H, 7.19; N, 4.12. Although these results in % C are outside the range viewed as establishing analytical purity, they are provided to illustrate the best values obtained to date. Crystals of **4-NiCl** suitable for X-ray diffraction analysis were obtained from a concentrated Et₂O solution at -35 °C.

(ⁱPr-PSiP^{Ind})PdCl (4-PdCl). A solution of [(η^3 -C₃H₅)PdCl]₂ (0.085 g, 0.23 mmol) in benzene (ca. 5 mL) was added to a solution of (ⁱPr-PSiP^{Ind})H (0.25 g, 0.47 mmol) in benzene (ca. 5 mL). The reaction mixture was stirred at room temperature for 20 min. The volatile components of the reaction mixture were subsequently removed under vacuum. The remaining residue was triturated with 3 × 2 mL of pentane and then washed with pentane (ca. 1 mL) and dried under vacuum to afford **4-PdCl** (0.31 g, 88% yield) as a white solid. Despite prolonged exposure to vacuum, **4-PdCl** as prepared above was found to routinely retain pentane (\leq 1 equiv). ¹H NMR (300 MHz, benzene-*d*₆): δ 7.62–7.56 (4 H, *H*_{arom}), 7.25–7.11 (4 H, *H*_{arom}), 3.18 (m, 2 H, PCHMe₂), 2.63 (m, 2 H, PCHMe₂), 2.22 (s, 6 H, Indole-Me), 1.56 (m, 6 H, PCHMe₂), 1.42 (m, 6 H, PCHMe₂), 1.09 (m, 6 H, PCHMe₂), 0.96 (m, 6 H, PCHMe₂), 0.54 (s, 3 H, SiMe). ¹³C{¹H} NMR (75.5 MHz, benzene-*d*₆): δ 141.3 (apparent t, *J* = 7 Hz, C_{arom}), 137.4 (C_{arom}), 132.3 (apparent t, *J* = 25 Hz, C_{arom}), 123.4 (CH_{arom}), 121.6 (C_{arom}), 121.2 (CH_{arom}), 119.9 (CH_{arom}), 117.2 (CH_{arom}), 28.7 (apparent t, *J* = 13 Hz, PCHMe₂), 26.7 (apparent t, *J* = 13 Hz, PCHMe₂), 20.4–19.5 (overlapping resonances, PCHMe₂), 11.5 (Indole-Me), 7.0 (SiMe). ³¹P{¹H} NMR (121.5 MHz, benzene-*d*₆): δ 38.5. ²⁹Si NMR (59.6 MHz, benzene-*d*₆): δ 41.8. Anal. Calcd for C₃₁H₄₅ClN₂P₂PdSi·C₅H₁₂ (2-Pd·C₅H₁₂): C, 57.67; H, 7.66; N, 3.74. Found: C, 58.00; H, 7.02; N, 3.58. Although these results in % H are outside the

range viewed as establishing analytical purity, they are provided to illustrate the best values obtained to date. Crystals of **4-PdCl** suitable for X-ray diffraction analysis were grown from a concentrated Et₂O solution at -35 °C.

(ⁱPr-PSi^HP^{Ind})PdCl (4-PdCl). A solution of (ⁱPr-PSi^HP^{Ind})H (0.020 g, 0.038 mmol) in ca. 1 mL of benzene was added to dry [(C₃H₅)PdCl]₂ (0.007 g, 0.019 mmol) to give a dark yellow solution. After approximately 2 h the volatiles were removed *in vacuo* and the residue was washed with 3 × 1.5 mL pentane to afford **4-PdCl** as an off-white solid (0.015 g, 59% yield). ¹H NMR (300 MHz, benzene-*d*₆): δ 7.53 (apparent d, *J* = 8.1 Hz, 2 H, *H*_{arom}), 7.44 (apparent d, *J* = 8.1 Hz, 2 H, *H*_{arom}), 7.16 (m, 2 H, *H*_{arom}), 7.06 (m, 2 H, *H*_{arom}), 6.18 (t, ³*J*_{PH} = 7.8 Hz, 1 H, SiH), 3.17 (m, 2 H, PCHMe₂), 2.57 (m, 2 H, PCHMe₂), 2.19 (s, 6 H, indole-Me), 1.51 (m, 6 H, PCHMe₂), 1.44 (m, 6 H, PCHMe₂), 1.13 (m, 6 H, PCHMe₂), 0.95 (m, 6 H, PCHMe₂). ¹³C{¹H} NMR (75.5 MHz, benzene-*d*₆): δ 142.4 (t, *J* = 6.8 Hz, C_{arom}), 136.8 (C_{arom}), 132.0 (t, *J* = 25.7 Hz, C_{arom}), 123.9 (CH_{arom}), 122.0 (C_{arom}), 121.4 (CH_{arom}), 119.9 (CH_{arom}), 115.9 (CH_{arom}), 28.0 (t, *J* = 12.8 Hz, PCHMe₂), 26.7 (t, *J* = 13.6 Hz, PCHMe₂), 20.2 (PCHMe₂), 20.0 (PCHMe₂), 19.7 (PCHMe₂), 19.4 (PCHMe₂), 11.5 (indole-Me). ³¹P{¹H} NMR (121.5 MHz, benzene-*d*₆): δ 41.2. ²⁹Si NMR (59.6 MHz, benzene-*d*₆): δ 17.4 (d, ¹*J*_{SiH} = 229.1 Hz). Anal. Calcd for C₃₀H₄₃N₂P₂PdSiCl: C, 54.30; H, 6.53; N, 4.22. Found: C, 53.98; H, 6.43; N, 4.17.

(ⁱPr-PSiP^{Ind})PtCl (4-PtCl). A solution of 1 (0.25 g, 0.47 mmol) in benzene (ca. 5 mL) was added to a solution of (Et₂S)₂PtCl₂ (0.21 g, 0.47 mmol) in benzene (ca. 5 mL). Neat NEt₃ (0.65 mL, 4.7 mmol) was added to the reaction mixture. The solution was subsequently heated at 75 °C with stirring for 4 days, during which time a color change to bright yellow was observed. The reaction mixture was subsequently cooled to room

temperature and was filtered through Celite. The filtrate solution was collected, and the volatile components were removed under vacuum. The remaining residue was washed with pentane (2×3 mL) and dried under vacuum to afford **4-PtCl** (0.33 g, 84% yield) as an off-white solid. Despite prolonged exposure to vacuum, **4-PtCl** as prepared above was found to routinely retain pentane (≤ 1 equiv). ^1H NMR (300 MHz, benzene- d_6): δ 7.80 (m, 2 H, H_{arom}), 7.58 (m, 2 H, H_{arom}), 7.24–7.18 (4 H, H_{arom}), 3.45 (m, 2 H, PCHMe_2), 2.84 (m, 2 H, PCHMe_2), 2.24 (s, 6 H, Indole-Me), 1.53 (m, 6 H, PCHMe_2), 1.41 (m, 6 H, PCHMe_2), 1.12 (m, 6 H, PCHMe_2), 0.94 (m, 6 H, PCHMe_2), 0.53 (s with Pt satellites, 3 H, $^3J_{\text{PtH}} = 22$ Hz, SiMe). $^{13}\text{C}\{^1\text{H}\}$ NMR (75.5 MHz, benzene- d_6): δ 141.2 (C_{arom}), 137.4 (C_{arom}), 132.3 (apparent t, $J = 31$ Hz, C_{arom}), 123.4 (CH_{arom}), 121.4 (C_{arom}), 121.1 (CH_{arom}), 120.1 (CH_{arom}), 117.3 (CH_{arom}), 28.0 (apparent t, $J = 16$ Hz, PCHMe_2), 27.0 (apparent t, $J = 16$ Hz, PCHMe_2), 20.1–19.2 (overlapping resonances, PCHMe_2), 11.4 (Indole-Me), 5.2 (SiMe). $^{31}\text{P}\{^1\text{H}\}$ NMR (121.5 MHz, benzene- d_6): δ 42.0 (s with Pt satellites, $^1J_{\text{PtP}} = 2719$ Hz). ^{29}Si NMR (59.6 MHz, benzene- d_6): δ 22.2 (s with Pt satellites, $^1J_{\text{SiPt}} = 1506$ Hz). Anal. Calcd for $\text{C}_{31}\text{H}_{45}\text{ClN}_2\text{P}_2\text{PtSi}\cdot\text{C}_5\text{H}_{12}$ (2-Pt· C_5H_{12}): C, 51.57; H, 6.85; N, 3.34. Found: C, 52.37; H, 6.60; N, 3.29. Although these results in % C are outside the range viewed as establishing analytical purity, they are provided to illustrate the best values obtained to date. Crystals of **4-PtCl** suitable for X-ray diffraction analysis were obtained from a concentrated Et_2O solution at -35 °C.

($^i\text{Pr-PSi}^{\text{H}}\text{P}^{\text{Ind}}$)PtCl (4-PtCl). A solution of ($^i\text{Pr-PSi}^{\text{H}}\text{P}^{\text{Ind}}$)H (0.064 g, 0.12 mmol) in ca. 5 mL of benzene was added to a solution of $(\text{Et}_2\text{S})_2\text{PtCl}_2$ (0.055 g, 0.12 mmol) in ca. 5 mL of benzene. Neat NEt_3 (0.124 g, 1.22 mmol) was added dropwise to the reaction mixture. The solution was subsequently heated at 75 °C with stirring for two days. The

reaction mixture was filtered through Celite. The filtrate solution was evaporated to dryness under vacuum and the remaining solid was washed with pentane (3 × 2 mL) to afford **4-PtCl'** (0.082 g, 89% yield) as a white solid. ¹H NMR (300 MHz, benzene-*d*₆): δ 7.64 (m, 2 H, *H*_{arom}), 7.55 (m, 2 H, *H*_{arom}), 7.16 (overlapping resonances, 4 H, *H*_{arom}), 5.99 (t with Pt satellites, ³*J*_{PH} = 1.5 Hz, ²*J*_{PtH} = 63.0 Hz, 1H, SiH), 3.43 (m, 2 H, PCHMe₂), 2.80 (m, 2 H, PCHMe₂), 2.21 (s, 6 H, indole-Me), 1.47 (m, 12 H, PCHMe₂), 1.15 (m, 6 H, PCHMe₂), 0.94 (m, 6 H, PCHMe₂). ¹³C{¹H} NMR (125.8 MHz, benzene-*d*₆): δ 142.2 (*C*_{arom}), 136.8 (*C*_{arom}), 132.1 (apparent t, *J* = 24 Hz, *C*_{arom}), 123.8 (CH_{arom}), 121.8 (*C*_{arom}), 121.2 (CH_{arom}), 120.1 (CH_{arom}), 116.2 (CH_{arom}), 27.5 (apparent t, *J* = 19 Hz, PCHMe₂), 27.2 (apparent t, *J* = 18 Hz, PCHMe₂), 20.1 (PCHMe₂), 19.6 (PCHMe₂), 19.4 (PCHMe₂), 19.2 (PCHMe₂), 11.6 (indole-Me). ³¹P{¹H} NMR (202.5 MHz, benzene-*d*₆): δ 43.9 (s with Pt satellites, ¹*J*_{PtP} = 2674 Hz). ²⁹Si NMR (99.4 MHz, benzene-*d*₆): δ 0.3 (d with Pt satellites, ¹*J*_{SiH} = 223 Hz, ¹*J*_{SiPt} = 1510 Hz). Anal. Calcd for C₃₀H₄₃ClN₂P₂PtSi: C, 47.90; H, 5.76; N, 3.72. Found: C, 47.85; H, 5.71; N, 3.56.

(*i*-Pr-PSi^HP^{Ind})PtH (**4-PtH'**). A solution of **4-PtCl'** (0.041 g, 0.055 mmol) in ca. 5 mL toluene was cooled to -35 °C and 55 μL of cold NaEt₃BH solution (0.055 mmol, 1 M, toluene) was added dropwise. The mixture was allowed to warm to room temperature and after 18 h a formation of a white precipitate was observed. The volatile components of the reaction mixture were removed *in vacuo* and the resultant residue was extracted with ca. 10 mL pentane and filtered through Celite to give a bright yellow solution. The pentane was removed *in vacuo* to yield **4-PtH'** as a bright yellow solid (0.0285 g, 73% yield). ¹H NMR (500 MHz, toluene-*d*₈): δ 7.98 (d, *J* = 8.5 Hz, 2 H, *H*_{arom}), 7.53 (d, *J* = 7.5 Hz, 2 H, *H*_{arom}), 7.37 (d with Pt satellites, ³*J*_{HH} = 6.0 Hz, ²*J*_{PtH} = 81.5 Hz, 1 H, SiH), 7.20

(apparent t, $J = 7.0$ Hz, 2 H, H_{arom}), 7.14 (apparent t, $J = 7.5$ Hz, 2 H, H_{arom}), 3.90 (td with Pt satellites, $^2J_{\text{PH}} = 17.5$ Hz, $^3J_{\text{HH}} = 6.0$ Hz, $^1J_{\text{PH}} = 940.2$ Hz, 1 H, PtH), 2.63 (m, 2 H, PCHMe₂), 2.38 (m, 2 H, PCHMe₂), 2.31 (s, 6 H, indole-Me), 1.34 (m, 6 H, PCHMe₂), 1.18 (m, 6 H, PCHMe₂), 0.88 (m, 12 H, PCHMe₂). ¹³C{¹H} NMR (125.8 MHz, toluene-*d*₈): δ 142.2 (apparent t, $J = 5.0$ Hz, C_{arom}), 136.9 (C_{arom}), 136.5 (apparent t, $J = 31.4$ Hz, C_{arom}), 123.3 (CH_{arom}), 120.3 (CH_{arom}), 119.8 (CH_{arom}), 119.1 (C_{arom}), 115.8 (CH_{arom}), 29.1 (apparent t, $J = 16.3$ Hz, PCHMe₂), 25.4 (apparent t, $J = 17.6$ Hz), 22.8 (PCHMe₂), 19.9 – 19.8 (overlapping resonances, PCHMe₂), 19.2 (apparent t, $J = 16.3$ Hz, PCHMe₂), 11.1 (indole-Me). ³¹P{¹H} NMR (202.5 MHz, toluene-*d*₈): δ 62.5 (s with Pt satellites, $^1J_{\text{PPt}} = 2674$ Hz). ²⁹Si NMR (99.4 MHz, toluene-*d*₈): δ 35.1 (dd with Pt satellites, $^1J_{\text{SiH}} = 206$ Hz, $^2J_{\text{SiH}} = 70$ Hz, $^1J_{\text{PtSi}} = 1892$ Hz).

(ⁱPr-PSiP^{Ind})Ni(η^3 -C₃H₅) (4-Ni(C₃H₅)). To a solution of 4-NiCl (0.030 g, 0.046 mmol) in *ca.* 3-5 mL benzene was added (C₃H₅)MgCl dropwise (23 μ L, 0.046 mmol, 2.0M THF). After approximately 30 minutes at room temperature, the volatile components of the reaction mixture were removed *in vacuo* and the residue was triturated with 3 \times 1 mL pentane. The residue was then extracted with *ca.* 5 mL pentane and filtered through Celite. The pentane was removed *in vacuo* to afford 4-Ni(C₃H₅) as a bright yellow solid in 89% yield. ¹H NMR (300.1 MHz, benzene-*d*₆): δ 8.27 (apparent d, $J = 8.4$ Hz, 1H, H_{arom}), 8.18 (apparent d, $J = 8.1$ Hz, 1H, H_{arom}), 7.65 (apparent d, $J = 7.5$ Hz, 1H, H_{arom}), 7.56 (apparent d, $J = 7.5$ Hz, 1H, H_{arom}), 7.40 (apparent t, $J = 7.8$ Hz, 1H, H_{arom}), 7.27 (apparent t, $J = 7.4$ Hz, 1H, H_{arom}), 7.22 – 7.08 (overlapping resonances, 2 H, H_{arom}), 4.68 (m, 1 H, CH₂CH=CH₂), 3.02 (m, 1 H, CH₂CH=CH₂), 2.97 – 2.78 (overlapping resonances, 2 H, CH₂CH=CH₂ + CH(CH₃)₂), 2.70 (m, 1 H, CH₂CH=CH₂),

2.48 (m, 1 H, $\text{CH}(\text{CH}_3)_2$), 2.33 (s, 3 H, indole-*Me*), 2.31 (s, 3 H, indole-*Me*), 2.24 – 1.98 (overlapping resonances, 3 H, $\text{CH}_2\text{CH}=\text{CH}_2 + \text{CH}(\text{CH}_3)_2$), 1.22 (s, 3 H, Si*Me*), 1.15 – 0.98 (overlapping resonances, 9 H, $\text{CH}(\text{CH}_3)_2$), 0.93 – 0.72 (overlapping resonances, 12 H, $\text{CH}(\text{CH}_3)_2$), 0.26 (m, 3 H, $\text{CH}(\text{CH}_3)_2$). $^{13}\text{C}\{^1\text{H}\}$ NMR (75.5 MHz, benzene- d_6): δ 142.2 (apparent d, $J = 8.3$ Hz, C_{arom}), 141.1 (apparent d, $J = 12.8$ Hz, C_{arom}), 138.2 (apparent d, $J = 40.7$ Hz, C_{arom}), 136.4 (apparent d, $J = 5.3$ Hz, C_{arom}), 136.1 – 135.4 (overlapping resonances, C_{arom}), 123.2 (CH_{arom}), 123.1 (CH_{arom}), 120.1 (CH_{arom}), 119.9 (CH_{arom}), 119.7 (CH_{arom}), 119.6 (CH_{arom}), 119.2 (C_{arom}), 117.6 (C_{arom}), 115.3 (CH_{arom}), 114.7 (CH_{arom}), 95.0 ($\text{CH}_2\text{CH}=\text{CH}_2$), 48.4 (apparent d, $J = 15.1$ Hz, $\text{CH}_2\text{CH}=\text{CH}_2$), 42.6 ($\text{CH}_2\text{CH}=\text{CH}_2$), 30.7 – 29.9 (overlapping resonances, $\text{CH}(\text{CH}_3)_2$), 27.0 (apparent d, $J = 16.6$ Hz, $\text{CH}(\text{CH}_3)_2$), 25.3 (apparent dd, $J = 6.8$ Hz, $J = 14.3$ Hz, $\text{CH}(\text{CH}_3)_2$), 21.0 (apparent d, $J = 9.8$ Hz, $\text{CH}(\text{CH}_3)_2$), 20.0 – 19.6 (overlapping resonances, $\text{CH}(\text{CH}_3)_2$), 17.8 (apparent d, $J = 9.8$ Hz, $\text{CH}(\text{CH}_3)_2$), 11.4 (indole-*Me*), 11.3 (indole-*Me*), 8.2 (Si*Me*). $^{31}\text{P}\{^1\text{H}\}$ NMR (121.5 MHz, benzene- d_6): δ AB quartet, 38.8 (apparent d, $^2J_{\text{PP}} = 98.4$ Hz), 32.6 (apparent d, $^2J_{\text{PP}} = 97.2$ Hz). ^{29}Si NMR (59.6 MHz, benzene- d_6): δ 53.4.

(i -Pr-PSiP^{Ind})NiNHDMP (4-NiNHDMP). A solution of **4-NiCl** (0.075 g, 0.12 mmol) in ca. 7 mL benzene was added quickly to a stirring suspension of LiNHDMP (0.015 g, 0.12 mmol) in ca. 5 mL benzene. The mixture darkened to a brown color upon addition. The reaction mixture was stirred for 18 h at room temperature and was subsequently filtered through a glass microfiber filter. The filtrate was evaporated to dryness under vacuum and the remaining residue was triturated with pentane (3 \times 5 mL) and washed with pentane (2 \times 1 mL) and dried *in vacuo* to afford **4-NiNHDMP** (0.067 g, 79% yield) as a red solid. ^1H NMR (500 MHz, benzene- d_6): δ 7.64 (d, 2 H, $J = 8.0$ Hz,

H_{arom}), 7.59 (d, 2 H, $J = 7.5$ Hz, H_{arom}), 7.28 (d, 1 H, $J = 7.5$ Hz, H_{arom}), 7.21 – 7.14 (overlapping resonances, 5 H, H_{arom}), 6.52 (t, 1 H, $J = 7.5$ Hz, H_{arom}), 3.61 (s, 3 H, ArMe), 2.62 (m, 2 H, PCHMe₂), 2.52 (m, 2 H, PCHMe₂), 2.27 (s, 3 H, ArMe), 2.24 (s, 6 H, indole-Me), 1.19 (m, 6 H, PCHMe₂), 1.08 (m, 6 H, PCHMe₂), 1.00 (m, 12 H, PCHMe₂), 0.57 (s, 3 H, SiMe), 0.28 (s, 1 H, NH). ¹³C{¹H} NMR (125.8 MHz, benzene-*d*₆): δ 159.6 (CN_{arom}-DMP), 141.2 (C_{arom}), 137.3 (C_{arom}), 133.3 (t, $J = 26.4$ Hz, C_{arom}), 129.7 (CH_{arom}-DMP), 128.5 (CH_{arom}-DMP), 123.2 (C_{arom}-DMP), 123.2 (CH_{arom}), 120.9 (CH_{arom}), 119.7 (t, $J = 1.3$ Hz, C_{arom}), 119.7 (CH_{arom}), 117.4 (C_{arom}-DMP), 116.8 (CH_{arom}), 108.7 (CH_{arom}-DMP), 27.2 (t, $J = 11.0$ Hz, PCHMe₂), 26.2 (t, $J = 11.3$ Hz, PCHMe₂), 22.8 (ArMe), 20.1 (ArMe), 20.1 (PCHMe₂), 19.3 (PCHMe₂), 19.1 (PCHMe₂), 18.1 (PCHMe₂), 11.5 (indole-Me), 5.7 (SiMe). ³¹P{¹H} NMR (202.5 MHz, benzene-*d*₆): δ 27.1. ¹⁵N NMR (50.7 MHz, benzene-*d*₆): δ -49.9. ²⁹Si NMR (99.4 MHz, benzene-*d*₆): δ 44.2.

(ⁱPr-PSiP^{Ind})NiOTf (4-NiOTf). To a solution of 4-NiCl (0.33 g, 0.52 mmol) in ca. 5 mL benzene was added AgOTf (0.14 g, 0.52 mmol) as a solution in ca. 2 mL benzene, dropwise with stirring. The reaction mixture was stirred for 18 h at room temperature during which time a colorless precipitate was formed in the orange reaction mixture. The mixture was subsequently filtered through Celite and the solvent was removed *in vacuo*. The resulting residue was washed with pentane (3 × 2 mL) to afford 4-NiOTf (0.28 g, 72% yield) as an orange solid. ¹H NMR (500 MHz, benzene-*d*₆): δ 7.52 (d, 2 H, $J = 7.5$ Hz, H_{arom}), 7.43 (d, 2 H, $J = 8.0$ Hz, H_{arom}), 7.17 – 7.07 (overlapping resonances, 4 H, H_{arom}), 2.90 (m, 2 H, PCHMe₂), 2.69 (m, 2 H, PCHMe₂), 2.16 (s, 6 H, indole-Me), 1.41 – 1.30 (m, 12 H, PCHMe₂), 1.09 (m, 6 H, PCHMe₂), 1.01 (m, 12 H, PCHMe₂), 0.66 (s, 3 H, SiMe). ¹³C{¹H} NMR (125.8 MHz, benzene-*d*₆): δ 140.7 (t, $J = 5.4$ Hz, C_{arom}), 136.7

(C_{arom}), 129.6 (t, $J = 28.8$ Hz, C_{arom}), 128.2 (q, $^1J_{CF} = 30.2$ Hz, CF₃), 123.7 (CH_{arom}), 121.9 (C_{arom}), 121.4 (CH_{arom}), 119.9 (CH_{arom}), 116.4 (CH_{arom}), 26.6 (t, $J = 11.5$ Hz, PCHMe₂), 26.3 (t, $J = 11.5$ Hz, PCHMe₂), 21.0 (PCHMe₂), 19.9 (PCHMe₂), 19.2 (PCHMe₂), 19.0 (PCHMe₂), 11.7 (indole-Me), 6.6 (SiMe). $^{19}\text{F}\{^1\text{H}\}$ NMR (470.6 MHz, benzene-*d*₆): $\delta -76.8$. $^{31}\text{P}\{^1\text{H}\}$ NMR (202.5 MHz, benzene-*d*₆): $\delta 35.5$. ^{29}Si NMR (99.4 MHz, benzene-*d*₆): $\delta 36.3$.

(^{*i*}Pr-PSiP^{*Ind*})NiH (4-NiH). A cold (−35 °C) solution of **4-NiH** (0.10 g, 0.16 mmol) in toluene (ca. 5 mL) was treated with NaEt₃BH (1.0 M in toluene, 0.16 mL, 0.16 mmol), which was added in a dropwise manner via pipet. The resulting yellow solution was warmed to room temperature over the course of 2 h with stirring. The volatile components of the reaction mixture were subsequently removed under vacuum. The remaining residue was triturated with 3 × 2 mL of pentane and then extracted with pentane (ca. 10 mL). The combined extracts were filtered through Celite, and the clear yellow filtrate solution was collected. The filtrate was evaporated to dryness *in vacuo*, and the remaining residue was subsequently washed with cold (−35 °C) pentane (3 × 0.5 mL) and dried under vacuum to afford a yellow solid, which is formulated as the N₂-bridged dimer $\{[{}^i\text{Pr-P}(\eta^2\text{-SiH})\text{P}^{\text{Ind}}]\text{Ni}\}_2(\mu\text{-N}_2)$ (0.068 g, 70% yield) on the basis of IR and Raman analysis. Raman data for isolated $\{[{}^i\text{Pr-P}(\eta^2\text{-SiH})\text{P}^{\text{Ind}}]\text{Ni}\}_2(\mu\text{-N}_2)$ (solid state, cm^{−1}): 2073 (s). IR (thin film, cm^{−1}): 2075 (w). Repeated attempts to obtain satisfactory elemental analysis for isolated $\{[{}^i\text{Pr-P}(\eta^2\text{-SiH})\text{P}^{\text{Ind}}]\text{Ni}\}_2(\mu\text{-N}_2)$ were unsuccessful. As discussed in the text (*vide supra*), upon dissolution in benzene $\{[{}^i\text{Pr-P}(\eta^2\text{-SiH})\text{P}^{\text{Ind}}]\text{Ni}\}_2(\mu\text{-N}_2)$ generates **4-NiH** quantitatively (by NMR analysis). NMR data for **4-NiH**: ^1H NMR (300 MHz, benzene-*d*₆) δ 8.13 (apparent d, 2 H, H_{arom}), 7.63 (m, 2 H,

H_{arom}), 7.28–7.18 (4H, H_{arom}), 2.59 (m, 2 H, PCHMe_2), 2.39 (m, 2 H, PCHMe_2), 2.33 (s, 6 H, Indole-Me), 1.36–1.19 (12 H, PCHMe_2), 1.01 (m, 6 H, PCHMe_2), 0.90 (s, 3 H, SiMe), 0.87–0.77 (6 H, PCHMe_2), –4.79 (br s, 1 H, NiH); ^1H NMR (300 MHz, –60 °C, toluene- d_8) δ –4.91 (br t, $^2J_{\text{PH}} = 47$ Hz, 1 H, NiH); $^{13}\text{C}\{^1\text{H}\}$ NMR (125.8 MHz, benzene- d_6) δ 141.4 (apparent t, $J = 6$ Hz, C_{arom}), 138.0 (apparent t, $J = 26$ Hz, C_{arom}), 137.3 (C_{arom}), 123.0 (CH_{arom}), 120.2 (CH_{arom}), 119.7 (CH_{arom}), 118.0 (C_{arom}), 116.2 (CH_{arom}), 29.0 (apparent t, $J = 14$ Hz, PCHMe_2), 25.5 (apparent t, $J = 16$ Hz, PCHMe_2), 21.6 (PCHMe_2), 20.9 (PCHMe_2), 19.3 (PCHMe_2), 19.1 (PCHMe_2), 11.2 (Indole-Me), 5.6 (SiMe); $^{31}\text{P}\{^1\text{H}\}$ NMR (121.5 MHz, benzene- d_6) δ 65.6; ^{29}Si NMR (99.4 MHz, benzene- d_6) δ 59.8. Despite repeated efforts, the value of J_{SiH} for **4-NiH** was not able to be measured. The reversible coordination of N_2 to **4-NiH** in solution is both temperature and solvent dependent, such that formation of the N_2 adduct **4-NiH*** can be observed at low temperature. Selected NMR data for **4-NiH***: ^1H NMR (300 MHz, 0 °C, toluene- d_8) δ –2.92 (t, $^2J_{\text{PH}} = 38$ Hz, 1 H, NiH), a 3:2 ratio of **4-NiH** to **4-NiH*** was observed; ^1H NMR (300 MHz, –40 °C, methylcyclohexane- d_{14}) δ –2.58 (t, $^2J_{\text{PH}} = 38$ Hz, 1 H, NiH), near-quantitative formation of **4-NiH*** was observed: $^{31}\text{P}\{^1\text{H}\}$ NMR (121.5 MHz, 0 °C, toluene- d_8) δ 35.2 (s); $^{31}\text{P}\{^1\text{H}\}$ NMR (121.5 MHz, –80 °C, toluene- d_8) δ 40.7 (br s, 1 P), 27.9 (br s, 1 P); ^{29}Si NMR (99.4 MHz, –80 °C, toluene- d_8) δ –10.5 ($|J_{\text{SiH}}| = 89$ Hz). Despite repeated efforts, the sign of J_{SiH} for **4-NiH*** was not able to be measured.

(ⁱPr-PSiP^{Ind})PdH (4-PdH). A cold (–35 °C) solution of **4-PdCl** (0.11 g, 0.16 mmol) in toluene (*ca.* 10 mL) was treated with NaEt_3BH (1.0 M in toluene, 0.16 mL, 0.16 mmol), which was added in a dropwise manner *via* pipette. The resulting solution was allowed to warm to room temperature over the course of 18 h with stirring. The

volatile components of the reaction mixture were subsequently removed under vacuum and the remaining residue was triturated with 3×1 mL of pentane. The residue was then extracted with pentane (*ca.* 10 mL) and the combined extracts were filtered through Celite. The filtrate solution was evaporated to dryness *in vacuo* and the remaining residue was washed with cold pentane (3×0.5 mL) and dried under vacuum to afford **4-PdH** (0.086 g, 86% yield) as an orange-yellow solid. ^1H NMR (300 MHz, benzene-*d*₆): 8.06 (m, 2 H, H_{arom}), 7.63 (m, 2 H, H_{arom}), 7.28 - 7.17 (4 H, H_{arom}), 2.58 (m, 2 H, PCHMe_2), 2.40 (m, 2 H, PCHMe_2), 2.31 (s, 6 H, Indole-*Me*), 1.43 (m, 6 H, PCHMe_2), 1.26 (m, 6 H, PCHMe_2), 1.00 – 0.77 (15 H, PCHMe_2 + *SiMe*; the *SiMe* resonance was identified at 0.92 ppm by correlation spectroscopy), 0.15 (br t, $^2J_{\text{PH}} = 15$ Hz, 1 H, PdH). $^{13}\text{C}\{^1\text{H}\}$ NMR (75.5 MHz, benzene-*d*₆): δ 141.5 (apparent t, $J = 7$ Hz, C_{arom}), 137.7 (apparent t, $J = 26$ Hz, C_{arom}), 137.4 (C_{arom}), 123.0 (CH_{arom}), 120.4 (CH_{arom}), 119.7 (CH_{arom}), 119.0 (C_{arom}), 116.7 (CH_{arom}), 28.6 (apparent t, $J = 14$ Hz, PCHMe_2), 26.2 (apparent t, $J = 14$ Hz, PCHMe_2), 22.3 (PCHMe_2), 20.8 (PCHMe_2), 19.9 - 19.4 (overlapping resonances, PCHMe_2), 19.6 (PCHMe_2), 11.2 (Indole-*Me*), 7.0 (*SiMe*). $^{31}\text{P}\{^1\text{H}\}$ NMR (121.5 MHz, benzene-*d*₆): δ 63.3. ^{29}Si NMR (99.4 MHz, benzene-*d*₆): δ 60.1 ($J_{\text{SiH}} = -101$ Hz). Anal. Calcd for $\text{C}_{31}\text{H}_{46}\text{N}_2\text{P}_2\text{PdSi}$: C, 57.89; H, 7.21; N, 4.36. Found: C, 57.52; H, 7.31; N, 4.03.

(*i*-Pr-PSiP^{*Ind*})PtH (4-PtH). A cold (-35 °C) solution of **4-PtCl** (0.11 g, 0.14 mmol) in toluene (*ca.* 10 mL) was treated with NaEt_3BH (1.0 M in toluene, 0.14 mL, 0.14 mmol), which was added in a dropwise manner *via* pipette. The resulting solution was allowed to warm to room temperature over the course of 18 h with stirring. The volatile components of the reaction mixture were subsequently removed under vacuum and the remaining residue was triturated with 3×1 mL of pentane. The residue was then

extracted with pentane (*ca.* 10 mL) and the combined extracts were filtered through Celite. The filtrate solution was evaporated to dryness *in vacuo* and the remaining residue was washed with cold pentane (3 × 0.5 mL) and dried under vacuum to afford **4-PtH**·C₅H₁₂ (0.086 g, 76% yield) as a tan solid. Despite prolonged exposure to vacuum, **4-PtH** as prepared above was found to routinely retain pentane (≤ 1 equiv). ¹H NMR (300 MHz, benzene-*d*₆): δ 8.17 (apparent d, *J* = 8 Hz, 2 H, *H*_{arom}), 7.63 (m, 2 H, *H*_{arom}), 7.31 - 7.19 (4 H, *H*_{arom}), 4.21 (t with Pt satellites, ²*J*_{PH} = 18 Hz, ¹*J*_{PtH} = 900 Hz, 1 H, PtH), 2.64 (m, 2 H, PCHMe₂), 2.46 (m, 2 H, PCHMe₂), 2.31 (s, 6 H, Indole-Me), 1.41 (m, 6 H, PCHMe₂), 1.20 (m, 6 H, PCHMe₂), 0.97 – 0.78 (15 H, PCHMe₂ + SiMe; the SiMe resonance was identified at 0.94 ppm by correlation spectroscopy). ¹³C{¹H} NMR (75.5 MHz, benzene-*d*₆): δ 141.0 (apparent t, *J* = 6 Hz, *C*_{arom}), 137.5 (*C*_{arom}), 136.7 (*C*_{arom}), 122.9 (CH_{arom}), 120.1 (CH_{arom}), 119.8 (CH_{arom}), 118.6 (*C*_{arom}), 116.6 (CH_{arom}), 29.3 (apparent t, *J* = 16 Hz, PCHMe₂), 25.9 (apparent t, *J* = 18 Hz, PCHMe₂), 22.2 (PCHMe₂), 20.4 - 18.8 (overlapping resonances, PCHMe₂), 11.0 (Indole-Me), 7.2 (s with Pt satellites, ²*J*_{PtC} = 60 Hz, SiMe). ³¹P{¹H} NMR (202.5 MHz, benzene-*d*₆): δ 61.2 (s with Pt satellites, ¹*J*_{PtP} = 2692 Hz). ²⁹Si NMR (59.6 MHz, benzene-*d*₆): δ 64.1 (¹*J*_{SiPt} = 968 Hz, *J*_{SiH} = -67 Hz). Anal. Calcd for C₃₁H₄₆N₂P₂PtSi·C₅H₁₂ (**4-PtH**·C₅H₁₂): C, 53.78; H, 7.27; N, 3.48. Found: C, 53.32; H, 7.13; N, 3.52.

[ⁱPr-P(η^2 -SiH)P^{Ind}]Ni(DMAP) (4-NiH·DMAP). A solution of {[ⁱPr-P(η^2 -SiH)P^{Ind}]Ni}₂(μ -N₂) (0.048 g, 0.039 mmol) in benzene (*ca.* 5 mL) was treated with DMAP (0.009 g, 0.078 mmol) to produce a clear yellow solution. The reaction mixture was allowed to stand at room temperature for 14 h. The volatile components of the reaction mixture were subsequently removed under vacuum and the remaining residue

was washed with 2×1 mL of cold (-35 °C) pentane and dried *in vacuo* to afford **4-NiH·DMAP** (0.055 g, 98% yield) as a bright yellow solid. ^1H NMR (500 MHz, benzene- d_6): δ 8.71 (d, $J = 7$ Hz, 2 H, H_{arom}), 8.23 (d, $J = 9$ Hz, 2 H, H_{arom}), 7.68 (d, $J = 8$ Hz, 2 H, H_{arom}), 7.28 (t, $J = 8$ Hz, 2 H, H_{arom}), 7.21 (t, $J = 8$ Hz, 2 H, H_{arom}), 5.75 (d, $J = 7$ Hz, 2 H, H_{arom}), 2.76 (m, 2 H, PCHMe_2), 2.65 (m, 2 H, PCHMe_2), 2.51 (s, 6 H, Indole-Me), 2.03 (s, 6 H, NMe_2), 1.35 (d, $^3J_{\text{HH}} = 2$ Hz, 3 H, SiMe), 1.22 – 1.09 (24 H, PCHMe_2), -3.50 (t, $^2J_{\text{PH}} = 40$ Hz, 1 H, Si-H-Ni). $^{13}\text{C}\{^1\text{H}\}$ NMR (125.8 MHz, benzene- d_6): δ 156.0 (CH_{arom}), 152.8 (C_{arom}), 141.1 (apparent t, $J = 6$ Hz, C_{arom}), 138.2 (apparent t, $J = 21$ Hz, C_{arom}), 135.8 (C_{arom}), 122.3 (CH_{arom}), 119.4 (CH_{arom}), 119.1 (CH_{arom}), 116.1 (C_{arom}), 115.2 (CH_{arom}), 106.2 (CH_{arom}), 38.1 (NMe_2), 29.7 (apparent t, $J = 13$ Hz, PCHMe_2), 27.9 (apparent t, $J = 6$ Hz, PCHMe_2), 21.1 (apparent t, $J = 6$ Hz, PCHMe_2), 20.6 (PCHMe_2), 20.4 (PCHMe_2), 20.1 (apparent t, $J = 5$ Hz, PCHMe_2), 11.5 (Indole-Me), 10.5 (SiMe). $^{31}\text{P}\{^1\text{H}\}$ NMR (202.5 MHz, benzene- d_6): δ 28.6. ^{29}Si NMR (99.4 MHz, benzene- d_6): δ -24.1 (d, $^1J_{\text{SiH}} = -69$ Hz). Anal. Calcd for $\text{C}_{38}\text{H}_{56}\text{N}_4\text{P}_2\text{NiSi}$: C, 63.60; H, 7.87; N, 7.81. Found: C, 63.35; H, 7.81; N, 7.57. X-ray quality crystals of **4-NiH·DMAP** were obtained from a concentrated Et_2O solution at -35 °C.

$[\text{}^i\text{Pr-P}(\eta^2\text{-SiH})\text{P}^{\text{Ind}}]\text{Ni}(\text{PMe}_3)$ (**4-NiH·PMe₃-A**) + $[\text{}^i\text{Pr-PSiP}^{\text{Ind}}]\text{NiH}(\text{PMe}_3)$ (**4-NiH·PMe₃-B**). A room temperature solution of $\{[\text{}^i\text{Pr-P}(\eta^2\text{-SiH})\text{P}^{\text{Ind}}]\text{Ni}\}_2(\mu\text{-N}_2)$ (0.038 g, 0.031 mmol) in benzene (*ca.* 5 mL) was treated with PMe_3 (0.024 g, 0.31 mmol), which was added dropwise by syringe. After standing for 2 h at room temperature the reaction mixture was evaporated to dryness under vacuum and the remaining residue was triturated with 3×2 mL pentane. The residue was subsequently washed with pentane (3×2 mL) to afford a *ca.* 2 : 1 mixture (by ^1H and $^{31}\text{P}\{^1\text{H}\}$ NMR) of isomers **4-NiH·PMe₃-**

A and **4-NiH·PMe₃-B** as an off-white solid (0.029 g, 70% overall yield based on Ni). NMR data for **4-NiH·PMe₃-A**: ¹H NMR (500 MHz, benzene-*d*₆): δ 8.22 (d, *J* = 8.5 Hz, 2 H, *H*_{arom}), 7.59 (d, *J* = 8.0 Hz, 2 H, *H*_{arom}), 7.26 – 7.14 (overlapping resonances, 4 H, *H*_{arom}), 2.62 (m, 2 H, PCHMe₂), 2.38 (s, 6 H, indole-*Me*), 2.24 (m, 2 H, PCHMe₂), 1.48 (s, 3 H, SiMe), 1.22 – 0.92 (overlapping resonances, 27 H, PCHMe₂ + PMe₃; the PMe₃ resonance was identified at 1.05 ppm (d, ²*J*_{PH} = 6.5 Hz) by correlation spectroscopy), 0.69 (m, 6 H, PCHMe₂), -5.44 (td, ²*J*_{PH} = 36.5 Hz, ²*J*_{PH} = 21.5 Hz, 1 H, NiH). ¹³C{¹H} NMR (125.8 MHz, benzene-*d*₆): δ 141.5 (*C*_{arom}), 136.5 (*C*_{arom}), 136.1 (*C*_{arom}), 122.7 (*CH*_{arom}), 119.6 (*CH*_{arom}), 119.3 (*CH*_{arom}), 117.3 (*C*_{arom}), 114.9 (*CH*_{arom}), 28.2 (apparent t, *J* = 12.6 Hz), 25.2 (apparent t, *J* = 8.8 Hz), 24.3 (m, PMe₃), 21.0 – 18.8 (overlapping resonances, PCHMe₂), 11.7 (indole-*Me*), 9.9 (SiMe). ³¹P{¹H} NMR (202.5 MHz, benzene-*d*₆): δ 42.2 (d, ²*J*_{PP} = 6 Hz, 2 P, PiPr₂), -23.0 (t, ²*J*_{PP} = 6 Hz, 1 P, PMe₃). ²⁹Si NMR (99.4 MHz, benzene-*d*₆): δ 6.2 (*J*_{SiH} = 83 Hz). NMR data for **4-NiH·PMe₃-B**: ¹H NMR (500 MHz, benzene-*d*₆): δ 8.25 (d, *J* = 8.5 Hz, 2 H, *H*_{arom}), 7.63 (d, *J* = 7.5 Hz, 2 H, *H*_{arom}), 7.32 – 7.14 (overlapping resonances, 4 H, *H*_{arom}), 2.56 (m, 4 H, PCHMe₂), 2.40 (s, 6 H, indole-*Me*), 1.30 – 0.93 (overlapping resonances, 36 H, PCHMe₂ + SiMe + PMe₃; the SiMe resonance was identified at 1.25 ppm by correlation spectroscopy; the PMe₃ resonance was identified at 1.16 ppm (d, ²*J*_{PH} = 5.0 Hz) by correlation spectroscopy), -10.18 (dt, ²*J*_{PH} = 48.5 Hz, ²*J*_{PH} = 37.5 Hz, 1 H, NiH). ¹³C{¹H} NMR (125.8 MHz, benzene-*d*₆): δ 141.5 (*C*_{arom}), 140.0 (*C*_{arom}), 136.9 (*C*_{arom}), 122.8 (*CH*_{arom}), 119.8 (*CH*_{arom}), 119.6 (*CH*_{arom}), 116.8 (*C*_{arom}), 115.0 (*CH*_{arom}), 27.4 (apparent t, *J* = 15.1 Hz, 2 C, PCHMe₂), 24.5 (m, PMe₃), 21.0 – 18.8 (overlapping resonances, PCHMe₂), 11.6 (indole-*Me*), 7.52 (d, *J* = 6.3 Hz, SiMe). ³¹P{¹H} NMR (202.5 MHz, benzene-*d*₆): δ 56.8 (d, ²*J*_{PP}

= 111 Hz, 2 P, *PiPr*₂), -19.2 (t, ²*J*_{PP} = 111 Hz, 1 P, *PMe*₃). ²⁹Si NMR (99.4 MHz, benzene-*d*₆): δ 65.8 (*J*_{SiH} = 81 Hz). Anal. Calcd for C₃₄H₅₅N₂P₃NiSi: C, 60.81; H, 8.26; N, 4.17. Found: C, 60.56; H, 8.12; N, 4.01. X-ray quality crystals of **4-NiH·PMe₃-B** were obtained from a concentrated Et₂O solution at -35 °C.

(^{*i*}Pr-PSiP^{*Ind*})PtH(PMe₃) (**4-PtH·PMe₃**). To a solution of **4-PtH** (0.020 g, 0.027 mmol) in *ca.* 2-3 mL benzene was added *PMe*₃ dropwise (5 μL, 0.046 mmol). After 2-3 h stirring at room temperature, volatile components of the reaction mixture were removed *in vacuo* and the resulting residue was triturated with 3 × 1 mL pentane yielding 0.021 g **4-PtH·PMe₃** as an off-white solid (0.027 mmol, 97% yield). ¹H NMR (500.1 MHz, benzene-*d*₆): δ 8.26 (apparent d, *J* = 8.0 Hz, 2 H, *H*_{arom}), 7.60 (apparent d, *J* = 8.0 Hz, 2 H, *H*_{arom}), 7.29 (apparent t, *J* = 7.5 Hz, 2 H, *H*_{arom}), 7.18 (apparent t, *J* = 7.5 Hz, 2 H, *H*_{arom}), 2.38 (s, 6 H, indole-*Me*), 2.33 (m, 2 H, CH(CH₃)₂), 2.24 (m, 2 H, CH(CH₃)₂), 1.35 (s, 3 H, Si*Me*), 1.30 (broad d, ²*J*_{PH} = 5.5 Hz, 9 H, *PMe*₃), 1.11 (m, 6 H, CH(CH₃)₂), 0.88 (overlapping resonances, 12 H, CH(CH₃)₂), 0.79 (m, 6 H, CH(CH₃)₂), -10.74 (broad s with Pt satellites, ¹*J*_{PtH} = 643 Hz, 1 H, PtH). ¹³C{¹H} NMR (125.8 MHz, benzene-*d*₆): δ 141.2 (apparent t, *J* = 6.1 Hz, *C*_{arom}), 139.7 (apparent t, *J* = 25.1 Hz, *C*_{arom}), 137.5 (*C*_{arom}), 122.8 (CH_{arom}), 119.9 (CH_{arom}), 119.7 (CH_{arom}), 116.4 (*C*_{arom}), 115.3 (CH_{arom}), 29.4 (m, CH(CH₃)₂), 28.6 (m, CH(CH₃)₂), 27.1 (m, *PMe*₃), 21.1 (apparent t, *J* = 5.4 Hz, CH(CH₃)₂), 20.9 (apparent t, *J* = 3.9 Hz, CH(CH₃)₂), 19.5 – 19.3 (overlapping resonances, CH(CH₃)₂), 11.4 (indole-*Me*), 8.2 (Si*Me*). ³¹P{¹H} NMR (202.5 MHz, benzene-*d*₆): δ 34.1 (d with Pt satellites, ²*J*_{PP} = 148 Hz, ¹*J*_{PtP} = 2749 Hz, 2 P, *PiPr*₂), -64.8 (t with Pt satellites, ²*J*_{PP} = 146 Hz, ¹*J*_{PtP} = 2948 Hz, 1 P, *PMe*₃). ²⁹Si NMR (59.6 MHz, benzene-*d*₆): δ 38.5 (²*J*_{SiH} = 67 Hz, ¹*J*_{PtSi} = 837 Hz).

(ⁱPr-PSiP^{Ind})Ni(HCO₂) (4-NiHCO₂). A room temperature solution of {[ⁱPr-P(η^2 -SiH)P^{Ind}]Ni}₂(μ -N₂) (0.012 g, 0.010 mmol) in benzene-*d*₆ (ca. 1 mL) was transferred to a J-Young NMR tube and degassed via three freeze-pump-thaw cycles. CO₂ (ca. 1 atm) was introduced to the tube at ambient temperature. After 10 minutes at room temperature, NMR analysis of the reaction mixture indicated the quantitative formation of **4-NiHCO₂**. ¹H NMR (300 MHz, benzene-*d*₆): δ 8.71 (s, 1 H, HCO₂), 7.62 (apparent d, *J* = 7 Hz, 2 H, H_{arom}), 7.55 (apparent d, *J* = 7 Hz, H_{arom}), 7.17 – 7.11 (4 H, H_{arom}), 2.76 (m, 2 H, PCHMe₂), 2.56 (m, 2 H, PCHMe₂), 2.23 (s, 6 H, Indole-Me), 1.38 – 1.27 (12 H, PCHMe₂), 1.19 – 1.08 (12 H, PCHMe₂), 0.67 (s, 3 H, SiMe). ¹³C{¹H} NMR (75.5 MHz, benzene-*d*₆): δ 168.8 (HCO₂), 140.9 (apparent t, *J* = 6 Hz, C_{arom}), 137.0 (C_{arom}), 131.9 (apparent t, *J* = 28 Hz, C_{arom}), 123.2 (CH_{arom}), 121.0 (CH_{arom}), 120.4 (C_{arom}), 119.7 (CH_{arom}), 116.7 (CH_{arom}), 27.3 (apparent t, *J* = 12 Hz, PCHMe₂), 26.3 (apparent t, *J* = 11 Hz, PCHMe₂), 19.5 - 19.1 (overlapping resonances, PCHMe₂), 11.4 (Indole-Me), 5.2 (SiMe). ³¹P{¹H} NMR (121.5 MHz, benzene-*d*₆): δ 34.6. ²⁹Si NMR (99.4 MHz, benzene-*d*₆): δ 42.2.

(ⁱPr-PSiP^{Ind})Pd(HCO₂) (4-PdHCO₂). A room temperature solution of **4-PdHCO₂** (0.015 g, 0.023 mmol) in benzene-*d*₆ (ca. 1 mL) was transferred to a J-Young NMR tube and degassed via three freeze-pump-thaw cycles. CO₂ (ca. 1 atm) was introduced to the tube at ambient temperature. After 10 minutes at room temperature, NMR analysis of the reaction mixture indicated the formation of **4-PdHCO₂** as the major product. Selected NMR data for **4-PdHCO₂**: ¹H NMR (300 MHz, benzene-*d*₆) δ 9.26 (s, 1 H, HCO₂), 2.20 (s, 6 H, Indole-Me), 0.65 (s, 3 H, SiMe); ³¹P{¹H} NMR (121.5 MHz, benzene-*d*₆) δ 39.0.

General Conditions for Catalytic Hydroboration of CO₂. For all catalytic runs using HBPIn or HBCat, the total reaction volume was kept a constant 872 μL (combined volume of borane and solvent). Unless otherwise stated, reactions were performed at room temperature for 1 h. If any precipitate was observed over the course of the reaction, excess deuterio solvent was added immediately prior to NMR data acquisition, to ensure that all reaction components were solubilized. For the more dilute reactions, the amounts of catalyst and HBPIn were decreased, and the volume difference was made up with added benzene-*d*₆. Due to solubility issues, catalytic runs involving 9-BBN were performed at a concentration of 0.96 M in 9-BBN monomer. In a typical catalysis run (Table 4.2.2, Entry 1), 0.005 g (0.0041 mmol) of $\{[{}^i\text{Pr-P}(\eta^2\text{-SiH})\text{P}^{\text{Ind}}]\text{Ni}\}_2(\mu\text{-N}_2)$ (delivered as a 100 μL aliquot of a 0.041 M stock solution of $\{[{}^i\text{Pr-P}(\eta^2\text{-SiH})\text{P}^{\text{Ind}}]\text{Ni}\}_2(\mu\text{-N}_2)$ in benzene-*d*₆) was added to 0.0054 g of C₆Me₆ (the internal standard) in a 1 dram vial. Benzene-*d*₆ (162 μL) and HBPIn (610 μL , 4.20 mmol) were added to the reaction mixture, and the combined mixture was subsequently transferred to a 250 mL Teflon-sealed reaction vessel. The solution was degassed *via* three freeze-pump-thaw cycles, and subsequently exposed to *ca.* 1 atm of CO₂ for 3 min at ambient temperature, after which the reaction vessel was sealed. The reaction mixture was stirred for 1 h at room temperature, during which time a precipitate (subsequently identified as (PinBO)₂CH₂) separated from solution. Benzene-*d*₆ (*ca.* 1 mL) was added to the reaction vessel to dissolve all reaction components, and the conversion to (PinBO)₂CH₂ was determined to be 84% (average of two runs) on the basis of ¹H NMR spectroscopic analysis relative to the internal standard.

Synthesis and Isolation of (PinBO)₂CH₂. In a typical optimized catalysis run (Table 4.2.3, Entry 1), 0.005 g (0.0041 mmol) of $\{[{}^i\text{Pr-P}(\eta^2\text{-SiH})\text{P}^{\text{Ind}}]\text{Ni}\}_2(\mu\text{-N}_2)$ (delivered as a 100 μL aliquot of a 0.041 M stock solution of $\{[{}^i\text{Pr-P}(\eta^2\text{-SiH})\text{P}^{\text{Ind}}]\text{Ni}\}_2(\mu\text{-N}_2)$ in benzene-*d*₆) was added to 0.0054 g of C₆Me₆ (the internal standard) in a 1 dram vial. Benzene-*d*₆ (162 μL) and HBPin (610 μL , 4.20 mmol) were added to the reaction mixture, and the combined mixture was subsequently transferred to a 250 mL Teflon-sealed reaction vessel. The solution was degassed *via* three freeze-pump-thaw cycles, and subsequently exposed to *ca.* 1 atm of CO₂ for 3 min at ambient temperature, after which the reaction vessel was sealed. The reaction mixture was stirred for 4 h at room temperature, during which time a precipitate separated from solution. Benzene-*d*₆ (*ca.* 1 mL) was added to the reaction vessel to dissolve all reaction components, and the conversion to (PinBO)₂CH₂ was determined to be 96% (this represents one of the two runs averaged to obtain 97% conversion to (PinBO)₂CH₂ as shown in Table 4.2.3, Entry 1) on the basis of ¹H NMR spectroscopic analysis relative to the internal standard. The volatile components of the reaction mixture were removed *in vacuo* and the remaining white residue consisting of (PinBO)₂CH₂ was washed with 3 × 1 mL of cold (−35 °C) pentane and dried under vacuum, thus affording an initial crop of (PinBO)₂CH₂. The pentane washes were combined, from which additional (PinBO)₂CH₂ was collected by crystallization at −35 °C. Compound (PinBO)₂CH₂ was isolated as a white solid in 71% combined yield (0.45 g, 1.50 mmol). ¹H NMR (500 MHz, benzene-*d*₆): δ 5.51 (s, 2 H, CH₂), 1.01 (s, 24 H, CH₃). ¹¹B NMR (160.5 MHz, benzene-*d*₆): δ 22.8. ¹³C{¹H} NMR (125.8 MHz, benzene-*d*₆): δ 85.7 (CH₂), 82.9 (CMe₂), 24.6 (CMe₂). Anal. Calcd for C₁₃H₂₆B₂O₆: C, 52.05; H, 8.74. Found: C, 51.87; H, 8.60.

Generation of $\text{CH}_2=\text{N}(2,6\text{-}^i\text{Pr}_2\text{C}_6\text{H}_3)$. $(\text{PinBO})_2\text{CH}_2$ (0.032 g, 0.11 mmol) and ferrocene (0.034 g, 0.18 mmol) were dissolved in benzene- d_6 (750 μL) and neat $\text{H}_2\text{N}(2,6\text{-}^i\text{Pr}_2\text{C}_6\text{H}_3)$ (20 μL , 0.11 mmol) was added *via* syringe to the solution. The reaction mixture was subsequently transferred to an NMR tube. After standing for 24 h at room temperature, 86% conversion to $2,6\text{-}^i\text{Pr}_2\text{C}_6\text{H}_3\text{NCH}_2$ was observed, as determined by ^1H NMR integration relative to the ferrocene internal standard. ^1H NMR (300 MHz, benzene- d_6) δ : 7.25 (d, 1 H, $^2J_{\text{HH}} = 18$ Hz, CH_2), 7.09 – 7.01 (overlapping resonances, 3 H, H_{arom}), 6.85 (d, 1 H, $^2J_{\text{HH}} = 18$ Hz, CH_2), 2.96 (sept, 2 H, $^3J_{\text{HH}} = 7$ Hz, CHMe_2), 1.11 (d, 6 H, $^3J_{\text{HH}} = 7$ Hz, CHMe_2). These NMR data are consistent with those reported previously.^{160d}

Generation of $[\text{Ph}(\text{Me})\text{N}]_2\text{CH}_2$. $(\text{PinBO})_2\text{CH}_2$ (0.026 g, 0.087 mmol) and ferrocene (0.017 g, 0.091 mmol) were dissolved in benzene- d_6 (750 μL) and neat HMeNPh (19 μL , 0.18 mmol) was added *via* syringe to the solution. The reaction mixture was subsequently transferred to an NMR tube. After standing for 24 h at room temperature, 79% conversion to $[\text{Ph}(\text{Me})\text{N}]_2\text{CH}_2$ was observed, as determined by ^1H NMR integration relative to the ferrocene internal standard. ^1H NMR (500 MHz, benzene- d_6) δ : 7.18 (m, 4 H, H_{arom}), 6.79 (apparent t, 2 H, $J = 8$ Hz, H_{arom}), 6.68 (d, 4 H, $J = 8$ Hz, H_{arom}), 4.33 (s, 2 H, CH_2), 2.48 (s, 6 H, NMe). These NMR data are consistent with those reported previously.^{160d}

Generation of $\text{PinBOCH}_2\text{PPh}_2$ and $\text{Ph}(\text{H})\text{NCH}_2\text{PPh}_2$. $(\text{PinBO})_2\text{CH}_2$ (0.026 g, 0.087 mmol) and ferrocene (0.022 g, 0.12 mmol) were dissolved in benzene- d_6 (750 μL) and neat HPPH_2 (15 μL , 0.086 mmol) was added *via* syringe to the solution. The reaction mixture was subsequently transferred to an NMR tube. After standing for 24 h at room

temperature, 82% conversion to PinBOCH₂PPh₂ was observed, as determined by ¹H NMR integration relative to the ferrocene internal standard. Neat H₂NPh (20 μL, 0.22 mmol) was subsequently added to the reaction mixture. The resulting solution was allowed to stand at room temperature for 48 h to obtain PhNHCH₂PPh₂ in 78% yield relative to initial (PinBO)₂CH₂ (> 95% conversion relative to PinBOCH₂PPh₂), as determined by ¹H NMR integration relative to the ferrocene internal standard. NMR data for PinBOCH₂PPh₂: ¹H NMR (500 MHz, benzene-*d*₆) δ 7.56 – 7.52 (m, 4 H, *H*_{arom}), 7.09 – 7.02 (overlapping resonances, 6 H, *H*_{arom}), 4.74 (d, 2 H, ²*J*_{PH} = 7 Hz, CH₂), 0.96 (s, 12 H, CH₃). ¹¹B NMR (160.5 MHz, benzene-*d*₆): δ 22.7; ¹³C{¹H} NMR (125.8 MHz, benzene-*d*₆) δ 136.8 (d, *J* = 13 Hz, C_{arom}), 133.9 (d, *J* = 19 Hz, CH_{arom}), 128.8 (CH_{arom}), 128.7 (d, *J* = 6 Hz, CH_{arom}), 82.8 (CMe₂), 65.4 (d, ¹*J*_{PC} = 13 Hz, CH₂), 24.6 (CMe₂); ³¹P{¹H} NMR (202.5 MHz, benzene-*d*₆) δ -11.7. NMR data for PhNHCH₂PPh₂: ¹H NMR (300 MHz, benzene-*d*₆) δ 7.39 (m, 4 H, *H*_{arom}), 7.15 – 7.01 (overlapping resonances, 8 H, *H*_{arom}), 6.74 (apparent t, 1 H, *J* = 8 Hz, *H*_{arom}), 6.41 (d, 2 H, *J* = 8 Hz, *H*_{arom}), 3.61 (m, 2 H, CH₂), 3.48 (broad s, 1 H, NH), 1.01 (s, 12 H, CMe₂); ³¹P{¹H} NMR (121.5 MHz, benzene-*d*₆) δ -19.3. The NMR data for Ph(H)NCH₂PPh₂ are consistent with those reported previously.¹⁶⁸

4.4.3 Crystallographic Solution and Refinement Details

Crystallographic data for each of **4-NiCl·Et₂O**, **4-PdCl**, **4-PtCl·Et₂O**, **4-NiH·DMAP·(Et₂O)_{0.75}**, **4-NiH·PMe₃·B·PhMe** and **4-PtH·PMe₃** were obtained at 173(±2) K on either a Bruker D8/APEX II CCD diffractometer using CuKα (λ = 1.54178 Å, microfocus source) radiation (for **4-NiCl·Et₂O** and **4-NiH·PMe₃·B·PhMe**) or a Bruker PLATFORM/APEX II CCD diffractometer using graphite-monochromated Mo

$K\alpha$ ($\lambda = 0.71073 \text{ \AA}$) radiation (for **4-PdCl**, **4-PtCl·Et₂O**, **4-NiH·DMAP·(Et₂O)_{0.75}** and **4-PtH·PMe₃**), employing a sample that was mounted in inert oil and transferred to a cold gas stream on the diffractometer. Programs for diffractometer operation, data collection, and data reduction (including SAINT) were supplied by Bruker. Gaussian integration (face-indexed) was employed as the absorption correction method in each case. The structures of **4-NiCl·Et₂O**, **4-PdCl** and **4-PtCl·Et₂O** were solved by use of the Patterson search/structure expansion, while those of **4-NiH·DMAP·(Et₂O)_{0.75}**, **4-NiH·PMe₃-B·PhMe** and **4-PtH·PMe₃** were solved by use of intrinsic phasing methods. All structures were refined by use of full-matrix least-squares procedures (on F^2) with R_1 based on $F_o^2 \geq 2\sigma(F_o^2)$ and wR_2 based on $F_o^2 \geq -3\sigma(F_o^2)$.

For **4-PtCl·Et₂O** the crystal used for data collection was found to display non-merohedral twinning. Both components of the twin were indexed with the program *CELL_NOW* (Bruker AXS Inc., Madison, WI, 2004). The second twin component can be related to the first component by 180° rotation about the [0 1 0] axis in both real space and reciprocal space. Integrated intensities for the reflections from the two components were written into a *SHELXL-2014* HKLF 5 reflection file with the data integration program *SAINTE* (version 8.34A), using all reflection data (exactly overlapped, partially overlapped and non-overlapped). The refined value of the twin fraction (*SHELXL-2014* BASF parameter) was 0.3(5). The following pairs of distances were constrained to be equal (within 0.01 Å) during refinement: $d(\text{P1-C31A}) = d(\text{P1-C31B})$; $d(\text{P2-C44A}) = d(\text{P2-C44B})$. The following constraints were applied to distances within the disordered solvent diethyl ether molecule: $d(\text{O1SA-C1SA}) = d(\text{O1SA-C3SA}) = d(\text{O1SB-C1SB}) = d(\text{O1SB-C3SB}) = 1.45(1) \text{ \AA}$; $d(\text{C1SA-C2SA}) = d(\text{C3SA-C4SA}) = d(\text{C1SB-C2SB}) =$

$d(\text{C3SB}-\text{C4SB}) = 1.52(1) \text{ \AA}$; $d(\text{O1SA}\dots\text{C2SA}) = d(\text{O1SA}\dots\text{C4SA}) = d(\text{O1SB}\dots\text{C2SB}) = d(\text{O1SB}\dots\text{C4SB}) = 2.42(1) \text{ \AA}$; $d(\text{C1SA}\dots\text{C3SA}) = d(\text{C1SB}\dots\text{C3SB}) = 2.35(1) \text{ \AA}$.

For **4-NiH·DMAP·(Et₂O)_{0.75}** the crystal used for data collection was found to display non-merohedral twinning. Both components of the twin were indexed with the program *CELL_NOW* (Bruker AXS Inc., Madison, WI, 2004). The second twin component can be related to the first component by 180° rotation about the [0.205 0 1] axis in real space and about the [0 0 1] axis in reciprocal space. Integrated intensities for the reflections from the two components were written into a *SHELXL-2014* HKLF 5 reflection file with the data integration program *SAINTE* (version 8.34A), using all reflection data (exactly overlapped, partially overlapped and non-overlapped). The refined value of the twin fraction (*SHELXL-2014* BASF parameter) was 0.1137(4). The partially-occupied and inversion-disordered solvent diethylether molecule (O2S, C5S, C6S, C7S, C8S) was restrained to have the same approximate geometry as the well-behaved one by use of the *SHELXL SAME* instruction.

Anisotropic displacement parameters were employed throughout for the non-hydrogen atoms. In the case of **4-NiH·DMAP·(Et₂O)_{0.75}**, **4-NiH·PMe₃-B·PhMe** and **4-PtH·PMe₃**, the Ni-*H* (H1), and Pt-*H* (H1) were located in the difference Fourier map and refined isotropically. All remaining hydrogen atoms were added at calculated positions and refined by use of a riding model employing isotropic displacement parameters based on the isotropic displacement parameter of the attached atom. Additional crystallographic information is provided in Appendix A.

Chapter 5: Fe and Co Complexes of a New Monoanionic P,N Ligand and Catalytic Hydrosilylation of Amides

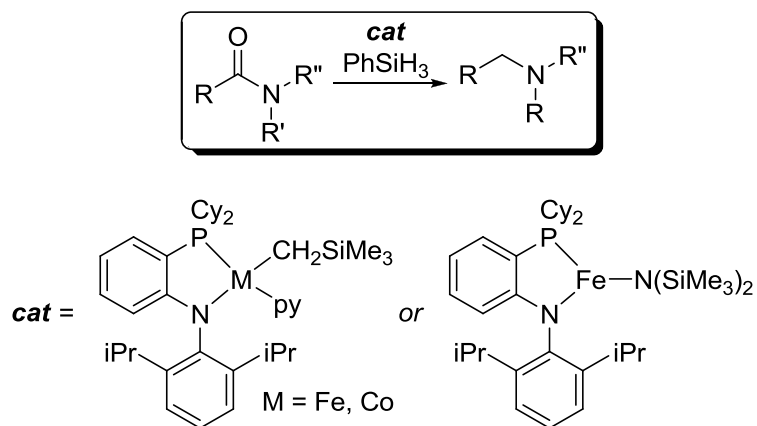
5.1 Introduction

The synthesis of amines from amides is a fundamental transformation in chemistry typically achieved through the use of reactive alkali metal hydrides or boron hydrides. Examples of amide hydrosilylation to amines catalyzed by second- and third-row transition metals have been reported in the literature, but comparatively few examples using the cheaper and more abundant first-row metals have been achieved.¹⁶⁹ One of the earliest examples comes from Beller and co-workers who reported the hydrosilylation of a broad scope of tertiary amides catalyzed by $\text{Fe}_3(\text{CO})_{12}$ in 2-10 mol% catalyst loadings.¹⁶⁹ Since that time amide reductions catalyzed by Mn,^{88b, 170} Ni¹⁷¹, Cu¹⁷² and Zn¹⁷³ have also featured prominently in the literature, in addition to other Fe-catalyzed examples,¹⁷⁴ though the number of reports describing this transformation are still very few in number compared to more facile reductions of, for example, aldehydes and ketones. Additionally, most of these reports still involve use of high catalyst loadings and high temperatures over long reaction times.

As described in section 1.6 of this document, despite the rich chemistry of P,N ligands used in conjunction with various transition metals, the specific class of *monoanionic* P,N ligands has received considerably less attention, particularly with the first-row transition metals, examples of which are limited to a handful of reports. Some of the most promising of these examples come from the use of *N*-phosphinoamidinate ligands, which have been found to support low-coordinate complexes of Mn, Fe and Co.^{88a, b, 89-90} These complexes have been found to be active toward the catalytic reduction

of unsaturated substrates, such as the hydroboration of alkenes,⁸⁹⁻⁹⁰ the hydrosilylation of ketones and aldehydes,^{88a} and, most relevantly to the work described in this chapter, the challenging hydrosilylation of tertiary amides to tertiary amines.^{88b}

Although diarylamido phosphines are a structurally simple class of monoanionic P,N ligands, outside a few reports of Ni and Zn chemistry, their coordination chemistry is relatively unexplored and there are no examples of this specific class of ligands being used in conjunction with Fe or Co. In this chapter, a new diarylamido phosphine derivative is reported and complexes of Fe and Co with this ligand are described. In addition, in collaboration with a fellow group member, Dylan Hale, a study on the use of two Fe-based and one Co-based complex as catalysts for the hydrosilylation of tertiary and secondary amides has been carried out (Scheme 5.1.1).



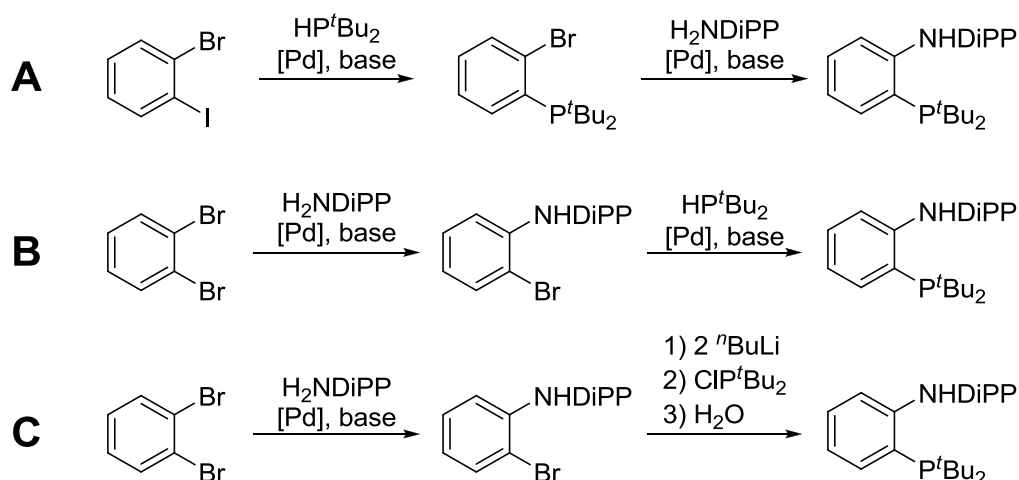
Scheme 5.1.1. General scheme for hydrosilylation of amides catalyzed by (P,N)Fe and (P,N)Co complexes prepared in this work.

As stated above, the study of catalytic amide hydrosilylation was done in collaboration with Dylan Hale, who should be credited for the entirety of the amide reduction catalysis scope and isolation of amines presented in section 5.2.6.

5.2 Results and Discussion

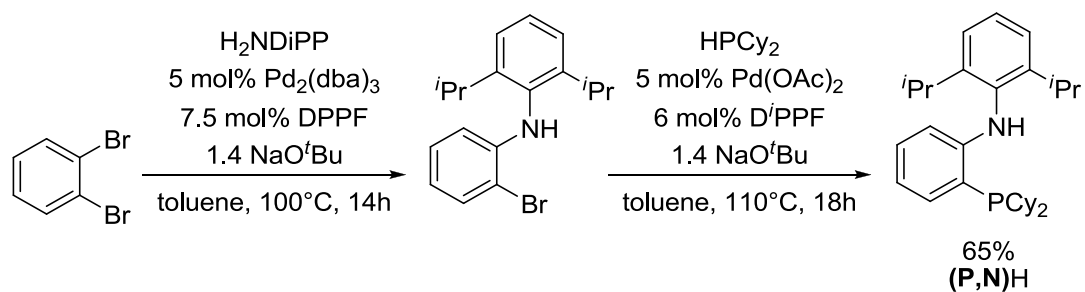
5.2.1 Synthesis of a (P,N)H Proligand

At the onset of the project, it was noted that some of the diarylamido phosphine ligands employed by Liang and co-workers led to the generation of stable and often unreactive bis-ligated species in the cases of Ni and Zn, a result likely attributed to insufficient steric crowding around the metal center.^{91, 95} In order to circumvent collapse to these undesired reaction products, a phenylene-bridged P,N ligand was targeted featuring increased steric bulk on one or both ends of the ligand relative to those of Liang's ligands. In this regard, the first target was (P^{*t*Bu},N^{*DiPP*})H, a proligand featuring a di-*t*-butylphosphino moiety in addition to a 2,6-diisopropylphenyl group on the nitrogen end of the ligand. A variety of methods could be envisaged for the synthesis of this ligand, involving Pd cross-coupling reactions and/or lithiation/metathesis routes.^{92, 175} Unfortunately, in all cases outlined in Scheme 5.2.1, while the first step of the reaction typically proceeded without issue, the second step either afforded no reaction, or gave complicated mixtures of products from which no desired product could be isolated. While revisiting this chemistry may be worthwhile, it does appear under these literature conditions that the combination of di-*t*-butylphosphino and 2,6-diisopropylanilido groups on a single ligand with only a phenylene spacer may not be readily accessible.



Scheme 5.2.1. General synthetic routes attempted for the synthesis of $(P^{tBu}, N^{DiPP})H$. Route **A**: Pd-catalyzed C-P cross-coupling reaction,^{175b} followed by Pd-catalyzed C-N cross coupling.^{175a} Route **B**: Pd-catalyzed C-N cross-coupling reaction,^{92, 175a} followed by Pd-catalyzed C-P cross-coupling.^{175b} Route **C**: Pd-catalyzed C-N cross coupling reaction,^{92, 175a} followed by lithium-halogen exchange and quench with chlorophosphine and water.⁹²

Attempts were instead redirected to the synthesis of $(P^{Cy}, N^{DiPP})H$, which was anticipated to be somewhat less bulky than the di-*t*-butylphosphino analogue described above. While Liang has already prepared the similar $(P^{iPr}, N^{DiPP})H$ ligand,⁹² as mentioned above, the generation of bis-ligated complexes of the form $(P,N)_2M$, particularly on tetrahedral Zn centers was problematic.⁹¹⁻⁹² Thus, while Cy and *i*Pr substituents are not anticipated to impart vastly different steric constraints on a metal center, the overall larger PCy₂ donor may be sufficiently bulky to preclude coordination of a second equivalent of ligand on a single metal center. Fortunately, unlike $(P^{tBu}, N^{DiPP})H$, $(P^{Cy}, N^{DiPP})H$ (hereafter referred to simply as **(P,N)H**) is readily accessible through an analogous route to that depicted in Scheme 5.2.1B (Scheme 5.2.2).¹⁷⁵



Scheme 5.2.2. Synthesis of (P,N)H.

(P,N)H can be isolated as a beige solid and is soluble in a wide range of organic solvents. Single crystals suitable for X-ray diffraction were isolated (Figure 5.2.1), which, in conjunction with solution state NMR spectroscopic data confirmed the desired formulation and connectivity of the ligand precursor. (P,N)H can also be readily deprotonated using $^n\text{BuLi}$ to afford the corresponding lithium salt, (P,N)Li as a bright yellow solid. (P,N)Li is a particularly useful form of the ligand precursor, as upon treatment with metal halide starting materials, the ligand can be metalated *via* a simple salt metathesis pathway. Alternatively, (P,N)H itself may be employed and metalated *via* an *in situ* deprotonation pathway with an appropriate base.

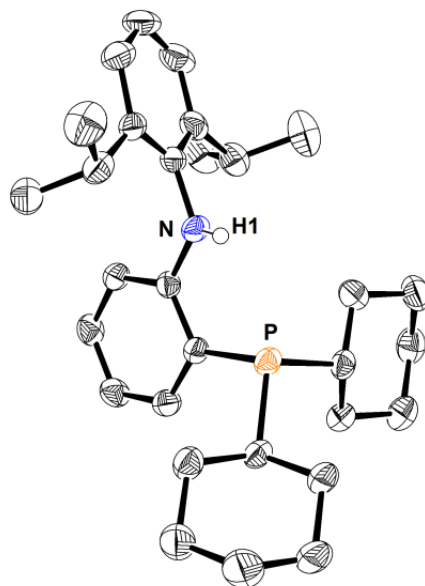
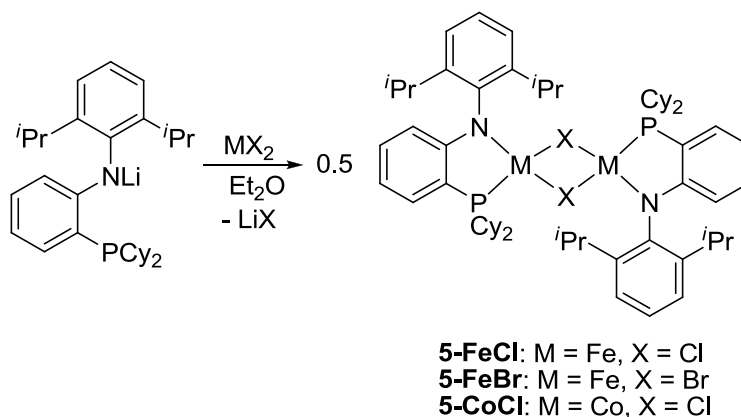


Figure 5.2.1. X-ray crystal structure for **(P,N)H** with thermal ellipsoids shown at the 50% probability level. Most hydrogen atoms have been omitted for clarity. Full refinement in progress.

5.2.2 Synthesis of **(P,N)Fe** and **Co Halide Complexes**

In an effort to further develop first-row transition metal chemistry supported by new ancillary ligands, focus was first directed toward the synthesis of Fe and Co complexes of the newly prepared P,N ligand. Considering the accessibility of Fe and Co halide starting materials, and the potential utility of the resulting **(P,N)M** halide complexes as precatalysts or precursors to more reactive compounds, investigating the reactivity of **(P,N)H** or **(P,N)Li** toward FeX_2 and CoX_2 starting materials was identified as an important starting point for this project. With the ultimate goal of coordinating the P,N ligand in its anionic form, it was rationalized that exploring reactivity as its lithium salt would be the most sensible route to accessing the desired halide complexes. Treating suspensions of either FeCl_2 , FeBr_2 or CoCl_2 in Et_2O with an Et_2O solution of **(P,N)Li** led to rapid reaction, yielding orange-red solutions in the case of Fe, and a dark purple solution in the case of Co. Upon workup, orange solids in the case of Fe (**5-FeCl** and **5-**

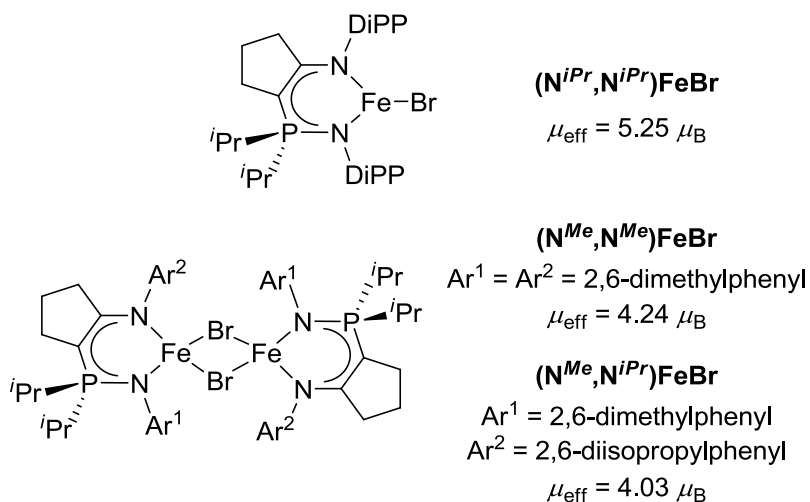
FeBr) and a dark blue solid in the case of Co (**5-CoCl**) were isolated. Upon measuring ^1H NMR spectra for all three complexes, broad resonances within the range of 70 to -50 ppm were observed, and no signal at all could be observed by $^{31}\text{P}\{^1\text{H}\}$ NMR, indicative of paramagnetic complexes. Unfortunately, crystals of these complexes suitable for X-ray diffraction analysis have remained elusive, thus far. Liang and co-workers have previously reported⁹⁴ that treatment of $(\text{P}^{iPr}, \text{N}^{DiPP})\text{Li}$ with $\text{NiCl}_2(\text{dme})$ led to the formation of the dinuclear complex $[(\text{P}^{iPr}, \text{N}^{DiPP})\text{NiCl}]_2$ which features bridging chloride ligands and square planar coordination geometry at Ni. On the basis of this, we tentatively assign **5-FeCl**, **5-FeBr** and **5-CoCl** as related dinuclear complexes featuring bridging halides (Scheme 5.2.3).



Scheme 5.2.3. Synthesis of Fe and Co halide dimers **5-FeCl**, **5-FeBr** and **5-CoCl**.

Solution magnetic moments were measured for the three dimer complexes using the Evans method (benzene- d_6 , 300 K), yielding values of $\mu_{\text{eff}} = 4.0 \mu_{\text{B}}$ (**5-FeCl**), $3.9 \mu_{\text{B}}$ (**5-FeBr**) and $3.0 \mu_{\text{B}}$ (**5-CoCl**). These values are lower than what would typically be expected for high-spin, tetrahedral d^6 (Fe) and d^7 (Co) complexes, however, this observation can be rationalized on the basis of anti-ferromagnetic coupling between metal centers *via* the bridging halides¹⁷⁶ if the complexes remain in their dimeric form in

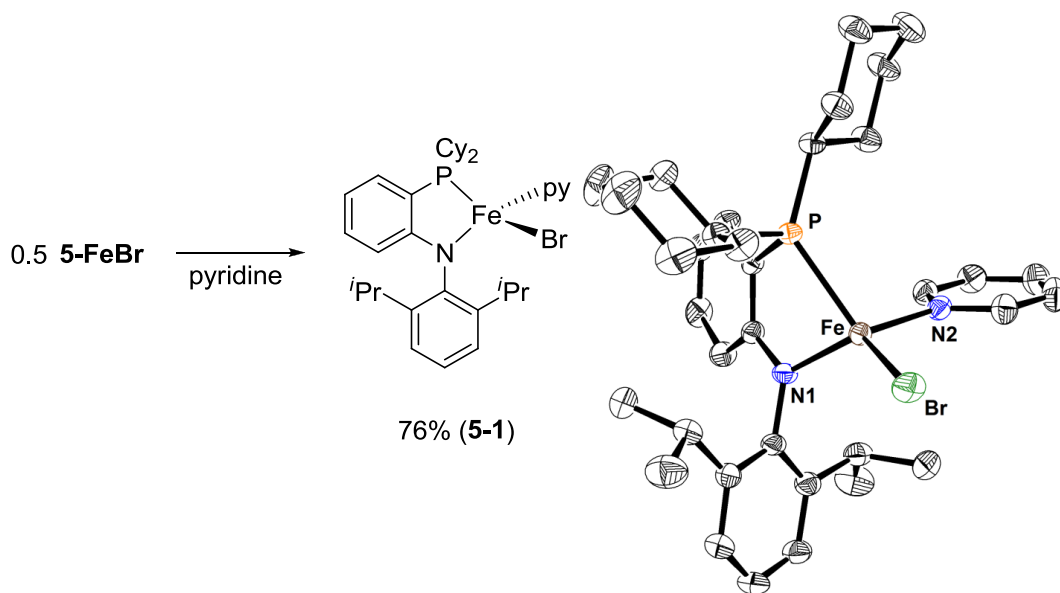
benzene- d_6 solution. Fryzuk and co-workers¹⁷⁶ noted similar observations in the course of their investigations into enamidophosphinimine complexes of iron. Much like the current system, it was found that treatment of an alkali metal salt of their ligand precursors with an FeX_2 source led to the generation of dinuclear halide-bridged complexes in some cases, and mononuclear complexes in others, dependent primarily on the size of the substituents on the ligand backbone (Scheme 5.2.4). The authors observed expected μ_{eff} values, determined by the Evans method, for the mononuclear species ($\mu_{\text{eff}} = 5.25 \mu_{\text{B}}$ for $(\text{N}^{iPr}, \text{N}^{iPr})\text{FeBr}$, benzene- d_6), while lower magnetic moment values were measured for the dinuclear complexes ($\mu_{\text{eff}} = 4.24 \mu_{\text{B}}$ and $4.03 \mu_{\text{B}}$ for $[(\text{N}^{Me}, \text{N}^{Me})\text{FeBr}]_2$ and $[(\text{N}^{iPr}, \text{N}^{Me})\text{FeBr}]_2$, respectively, benzene- d_6).



Scheme 5.2.4. Structures of enamidophosphinimine complexes of iron and measured magnetic moments in benzene- d_6 as reported by Fryzuk and co-workers.

The solubility of **5-FeCl**, **5-FeBr**, **5-CoCl** in hydrocarbon solvent (pentane, benzene) was observed to be quite low, while they dissolve readily in ethereal solvents such as THF. This can perhaps be attributed to coordination of THF to the metal center, resulting in cleavage of the dimer to generate two equivalents of metal halide monomer with coordinated THF, though this has not been directly confirmed. Indirect evidence

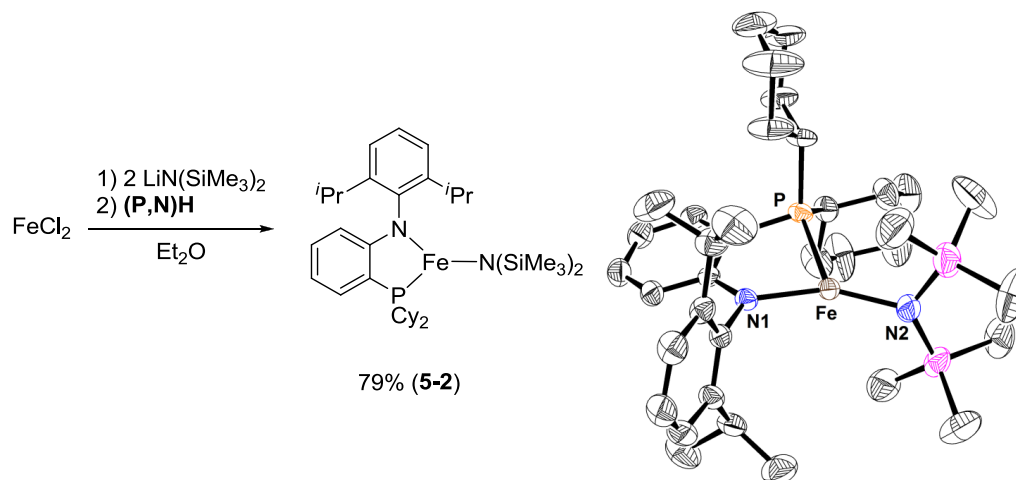
that, at the very least, for the dinuclear formulation of **5-FeBr** comes from the observation that treatment of **5-FeBr** with pyridine (in which **5-FeBr** is soluble) led to clean generation of monomeric (P,N)FeBr(py), **5-1**, as a red-orange solid (Scheme 5.2.5). As in the case of **5-FeBr**, **5-1** is paramagnetic, with $\mu_{\text{eff}} = 5.2 \mu_{\text{B}}$, which, unlike the dimer complexes is fully consistent with the $S = 2$ ground state expected for a high-spin, tetrahedral, d^6 iron complex. The paramagnetic nature of **5-1** limits the utility of NMR spectroscopic data, however, X-ray quality crystals of this complex were successfully isolated, which, in conjunction with combustion analysis data, strongly supports the proposed formulation of **5-1**. As this complex can be obtained analytically pure from the reaction of **5-FeBr** with pyridine, this is also support for the formulation of **5-FeBr** as the bromide bridged complex.



Scheme 5.2.5. Left: Synthetic procedure for the preparation of **5-1**. Right: X-ray crystal structure of **5-1** with thermal ellipsoids shown at the 50% probability level. Hydrogen atoms have been omitted for clarity. Selected interatomic distances (Å) and angles (°): Fe-Br 2.3755(3), Fe-P 2.4024(5), Fe-N(1) 1.9523(15), Fe-N(2) 2.1215(16), N(1)-Fe-Br 121.67(5), N(2)-Fe-Br 108.97(5), N(2)-Fe-P 102.76(5), N(1)-Fe-P 83.33(5).

5.2.3 Synthesis and Reactivity of (P,N)Fe Amido Complexes

Amido complexes have previously been identified as highly active precatalysts in related (P,N)Fe chemistry for the hydrosilylation of carbonyl substrates.^{88a} Thus a desirable target for this work was an Fe amido complex. While treatment of a THF solution of **5-FeCl** or **5-FeBr** (as well as **5-CoCl**) with an alkali metal amido reagent is likely a viable synthetic route, it was found to be much more straightforward to the Fe^{II} amido starting material Fe(N(SiMe₃)₂)₂ *in situ* from the reaction of FeBr₂ with two equiv LiN(SiMe₃)₂, and treat this with one equiv of (P,N)H. Such a route eliminates a synthetic step, as well as the isolation of the poorly soluble halide dimer **5-FeX** (X = Cl or Br) prior to reaction with LiN(SiMe₃)₂. Following this synthetic protocol, the desired amido complex, (P,N)FeN(SiMe₃)₂ (**5-2**), can indeed be generated and isolated as a bright yellow-orange solid in 79% yield. X-ray quality crystals of **5-2** were obtained, confirming the anticipated connectivity and 3-coordinate nature of the bulky amido complex (Scheme 5.2.6).



Scheme 5.2.6. Left: Synthetic procedure for the preparation of **5-2**. Right: X-ray crystal structure of **5-2** with thermal ellipsoids shown at the 50% probability level. Hydrogen atoms have been omitted for clarity. Selected interatomic distances (Å) and angles (°): Fe-P 2.4425(7), Fe-N(1) 1.9409(19), Fe-N(2) 1.904(2), P-Fe-N(1) 84.90(6), N(1)-Fe-N(2) 153.09(9), P-Fe-N(2) 122.01(7).

Complex **5-2** is an example of a three-coordinate, formally 12-electron Fe^{II} complex, likely stabilized by the steric crowding provided by the P,N ligand and the bulky bis(trimethylsilyl)amido group. The complex adopts a trigonal planar geometry (sum of angles around Fe = 360°), with comparable Fe-N1 and Fe-N2 distances of 1.9409(19) and 1.904(2) Å, respectively. Both N1 and N2 are planar, with the sum of the angles surrounding N1 of 359.72°, and 359.50° for N2. As such the possibility of N → Fe π -bonding cannot be discounted. Similar structural features around Fe were observed for the previously reported *N*-phosphinoamidinate analogue of **5-2**.^{88a} Not surprisingly, **5-2**, is paramagnetic as observed by ¹H NMR spectroscopy. Solution magnetic moment data (Evans method, benzene-*d*₆, 300 K) gives a μ_{eff} value of 4.9 μ_{B} , consistent with an S = 2 ground state, as was also determined for the *N*-phosphinoamidinate analogue of **5-2**.^{88a}

Attempts were made to generate the corresponding Co analogue of **5-2** using a similar synthetic route to that outlined in Scheme 5.2.6. However, no clean product was

able to be obtained from such reaction mixtures. In one a minute sample of crystals of a decomposition product (**5-3**) resulting from reaction with either adventitious O₂ or H₂O were obtained. The solid state structure of **5-3** (Figure 5.2.2) features two Co centers and two ligand equivalents. In one portion of the molecule, oxidation at phosphorus, presumably by O₂ or H₂O, has produced a phosphine oxide resulting in κ^2 -N,O-coordination of the ligand to Co1 (as labelled in Figure 5.2.2). The second equivalent of ligand has undergone a P-C activation process leading to a μ -phosphido moiety between the Co1 and Co2 centers. Finally the anilido arene substituent of one ligand equivalent is coordinating in an η^6 -manner to the Co2 center. While **5-3** itself is not anticipated to be a useful compound, and no attempts have been made to regenerate it, it does serve to demonstrate a possible reaction that may arise in the course of this chemistry.

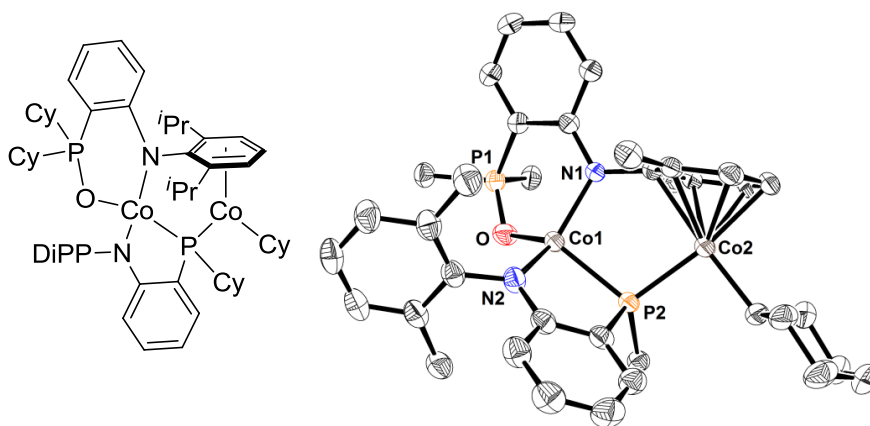
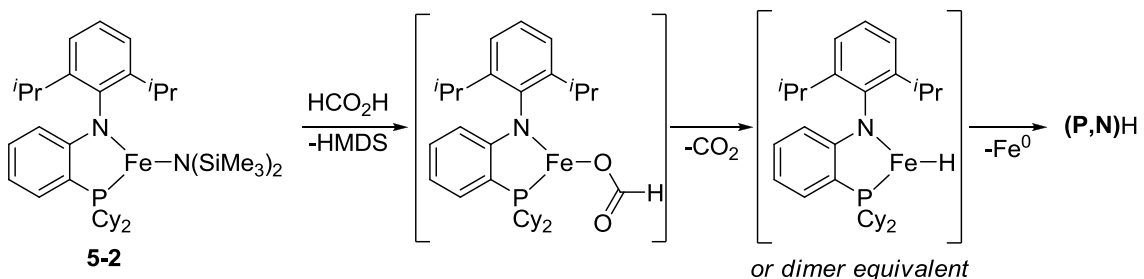


Figure 5.2.2. Structural diagram (left) and X-ray crystal structure (right) of **5-3** obtained during the attempted synthesis of (P,N)CoN(SiMe₃)₂ following a modified version of the procedure described in Scheme 5.2.6. Most Cy and ⁱPr groups have been cropped for clarity. Thermal ellipsoids shown at the 50% probability level. Hydrogen atoms have been omitted for clarity. Full refinement in progress.

Complex **5-2** is anticipated to be very reactive owing to its coordinatively unsaturated nature, and may serve as a useful synthon for the synthesis of a variety of (P,N)FeX complexes *via* a protonolysis route. In this regard, the reaction of **5-2** with one

equiv formic acid was attempted in the hope of accessing a formate complex, which could represent a viable starting point for the investigation of CO₂ reduction chemistry. While a fairly clean reaction of **5-2** with formic acid was observed, the resulting product (as observed by ³¹P{¹H} NMR spectroscopy) was not the desired (P,N)Fe(HCO₂) complex, but in fact the ligand precursor itself (P,N)H. It is possible that the acid-base reaction may have occurred at the anilido donor rather than the FeN(SiMe₃)₂ site. Alternatively, protonolysis of the FeN(SiMe₃)₂ may indeed occur, but this may be followed by rapid expulsion of CO₂, leading to a transient Fe hydride complex that undergoes N-H reductive elimination to give the neutral ligand (Scheme 5.2.7). In fact a variety of routes have been undertaken in attempts to synthesize an iron hydride complex of this P,N ligand, but thus far none have been successful, perhaps pointing to the instability of such a complex toward possible reductive elimination processes.



Scheme 5.2.7. One proposed route for the reaction of **5-2** toward formic acid, ultimately yielding (P,N)H *via* formate and hydride complexes.

Alternatively, the reaction of **5-2** with *ca.* 1.3 equiv aniline did not generate (P,N)H, on the basis of ³¹P NMR analysis. Single crystals suitable for X-ray diffraction were obtained from the crude reaction mixture. While the desired deprotonation step does indeed appear to have occurred according to the resulting structure, the corresponding product was found to be a *trinuclear* Fe anilido complex, **5-4** wherein two equivalents of the targeted (P,N)FeNHPPh are bridged by an Fe(NHPPh)₂ moiety (Figure

5.2.3). Attempts were made to reproduce this result by reaction of three equivs FeBr_2 with six equivs LiNHPH and then two equivs $(\text{P,N})\text{H}$, in a manner similar to that described in Scheme 5.2.6, however, thus far the synthesis of this trinuclear complex has not been found to be reliable, nor has the targeted mononuclear anilido complex been successfully isolated.

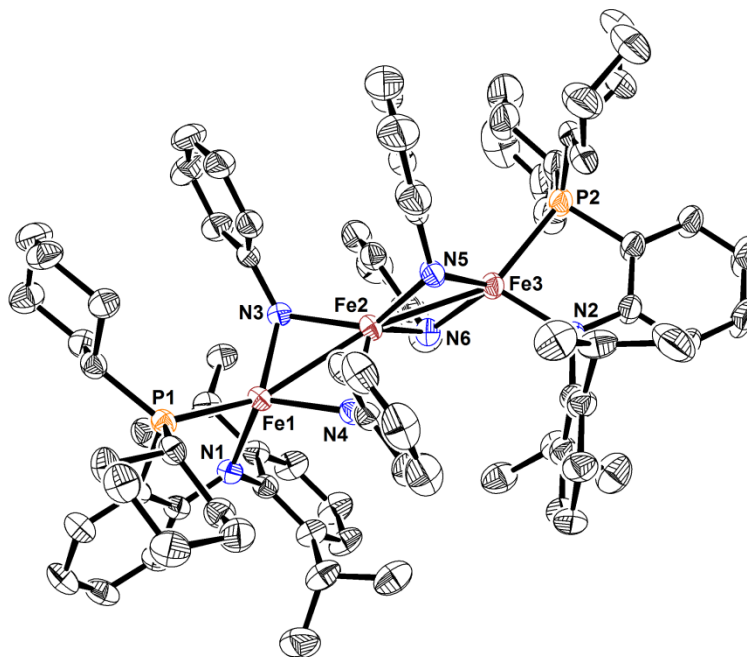


Figure 5.2.3. X-ray crystal structure of **5-4** with thermal ellipsoids shown at the 50% probability level. Hydrogen atoms have been omitted for clarity. Full refinement in progress.

Unlike the unusual reactivity observed with aniline, treatment of **5-2** with an equivalent of phenol proceeded in a much more predictable manner, giving the corresponding phenoxide complex (**5-5**) with concomitant formation of HMDS. Complex **5-5** could be isolated in 89% yield. Single crystal X-ray diffraction confirmed the formulation of the resulting product as a phenoxy-bridged Fe^{II} dinuclear complex featuring distorted tetrahedral coordination geometry at each Fe center (Figure 5.2.4).

Solution magnetic moment data was collected for **5-5**, giving a value of $\mu_{\text{eff}} = 5.4 \mu_{\text{B}}$. The value of μ_{eff} for **5-5** is consistent with an $S = 2$ ground state, for the tetrahedral complex.

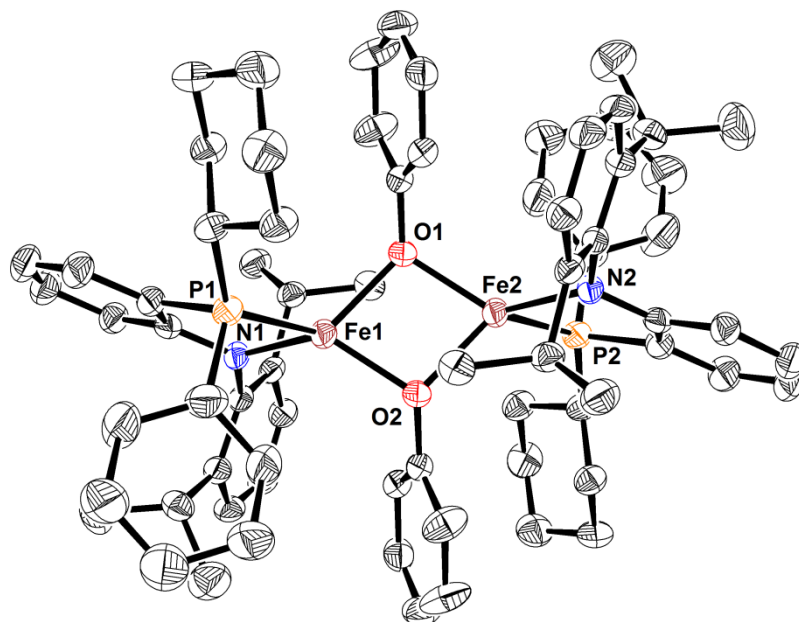


Figure 5.2.4. X-ray crystal structure of **5-5**, with thermal ellipsoids drawn at the 50% probability level. Hydrogen atoms have been omitted for clarity. Full refinement in progress.

5.2.4 Synthesis of (P,N)Fe^I Complexes

In addition to the synthesis of various (P,N)Fe^{II} complexes, attempts were also made to prepare (P,N)Fe^I complexes *via* the 1-electron reduction of (P,N)Fe halide precursors, such as the dimer complexes described earlier in section 5.2.2. As the Fe^{IV} oxidation state is quite uncommon, oxidative addition reactions to an Fe^{II} center are not expected to be favorable. However, oxidative addition to an Fe^I center, leading to a product in the +3 oxidation state can be considered a much more likely transformation if the Fe^I precursor can be prepared in a reliable manner. To this end, reduction of **5-FeCl** was pursued by treating a THF solution of **5-FeCl** with two equivs sodium naphthalide (one equiv per Fe center). Benzene was also added to the reaction mixture (*ca.* 2-3 equiv)

in efforts to either stabilize the resulting Fe^{I} species as an arene complex, or to potentially induce a C-H oxidative addition reaction of benzene at the Fe^{I} center. A color change from red-orange to a deep red color was observed over the course of an hour at room temperature, which persisted after stirring overnight prior to workup. A bright orange solid was isolated from the reaction mixture which was crystallized from a THF/pentane mixture. The resulting crystals were sufficient to obtain an X-ray structure of the product, however, the quality of the dataset was found to be poor and thus was not fully-refined. Nevertheless, the data obtained does appear to indicate the generation of an η^6 -benzene complex of Fe^{I} , as depicted in Figure 5.2.5.

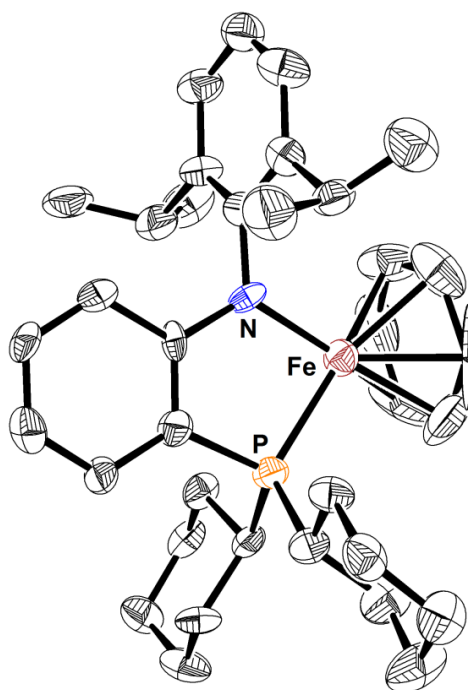


Figure 5.2.5. X-ray crystal structure of **5-6** with thermal ellipsoids drawn at the 50% probability level. Hydrogen atoms have been removed for clarity. The data set was of poor quality, thus no metrical parameters for this structure are included.

Repeated attempts have been made to produce higher quality crystals of this reduction product, and while the reaction itself does appear to be reproducible in the

sense that a bright orange solid can be isolated in each case, crystallization of this reduction product has proven challenging and thus far the dataset represented by the structure shown in Figure 5.2.5 remains the only means of reliably identifying this reduction product. While attempting to reproduce the synthesis of **5-6**, the reduction of **5-FeBr** with sodium naphthalide (as opposed to **5-FeCl**) was also investigated. Thus the reduction of **5-FeBr** was performed under analogous conditions to that of **5-FeCl** described above, and similar color changes were observed during the course of the reaction. A dark red solution was ultimately obtained (from a red-orange starting material) and an orange solid was isolated from the reaction mixture. Crystallization of this solid was attempted, and in this case crystals were obtained which allowed for the collection of a high quality dataset. In this case, however, rather than an η^6 -benzene complex, the product appears to be an Fe complex of sodium naphthalide itself, wherein the naphthalide ligand is coordinated to the Fe center in an η^4 -fashion, as depicted in Figure 5.2.6.

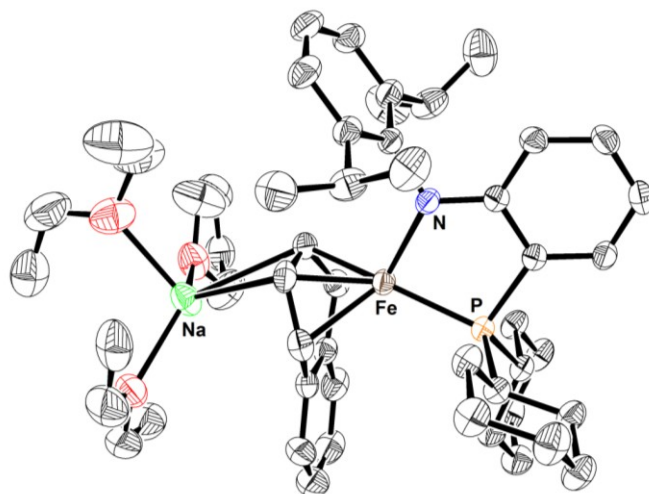


Figure 5.2.6. X-ray crystal structure of **5-7** with thermal ellipsoids drawn at the 50% probability level. Hydrogen atoms have been omitted for clarity. Full refinement in progress.

Based on the X-ray structure of **5-7**, the compound appears to be an example of a formally anionic Fe-naphthalene complex with a solvated sodium counter-ion. Upon examination of the measured distances between the C atoms of the naphthalene ligand and the Fe center, the naphthalene seems to be coordinating in an η^4 -fashion (Fe-C = 2.031 – 2.185 Å for four closest Fe-C contacts, Fe-C = 2.759, 2.770 Å for next two closest contacts) to the Fe center. The opposite face of the naphthalene ligand is coordinated in an η^2 fashion to a Na⁺ counter-ion (Na-C = 2.740, 2.785 Å for two closest contacts, Na-C = 3.165 – 3.231 Å for next four closest contacts). The Na⁺ is solvated by two equivs diethyl ether and one equiv THF in the crystal structure. The naphthalene ligand itself is distorted from planarity in the ring involved in the coordination to Fe and Na (Figure 5.2.7), such that the ring is bent at a 26.25° - 28.03° angle about the C50-C53 axis (dihedral angles of C51-C52-C53-C54 and C52-C51-C50-C59, respectively).

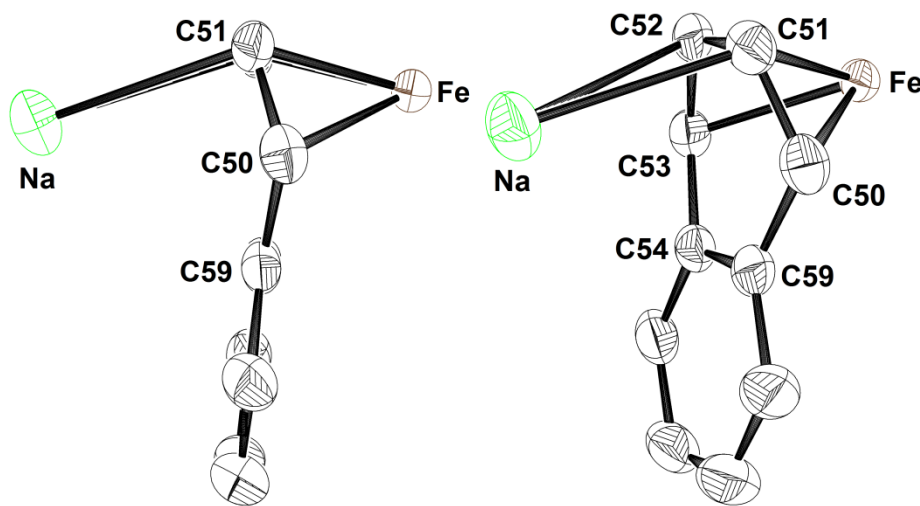


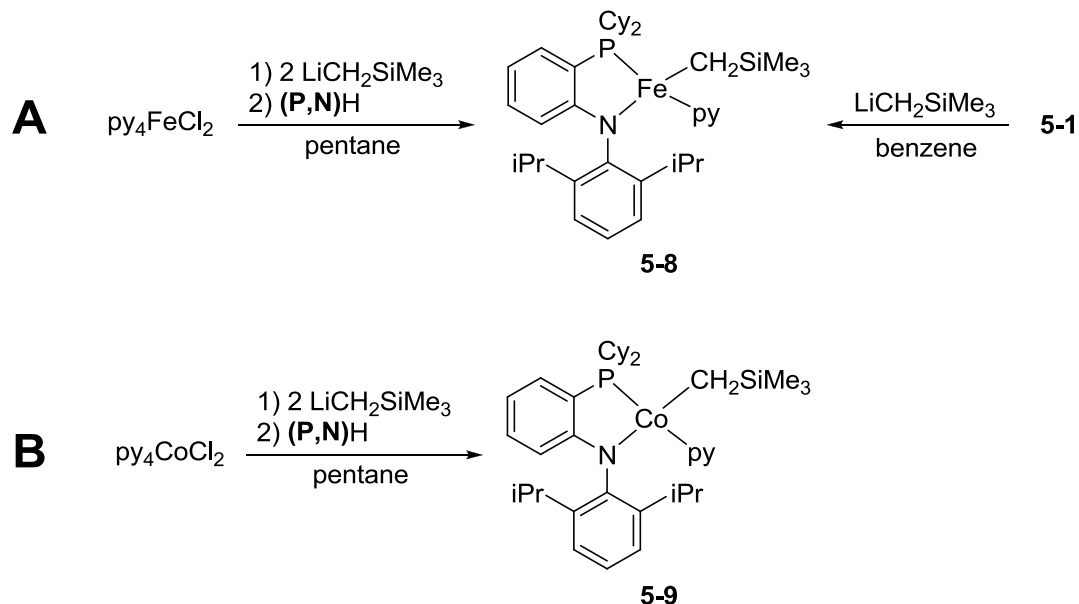
Figure 5.2.7. Two perspectives of the naphthalene ligand in the X-ray crystal structure of **5-7** highlighting the distortion from planarity. The majority of the molecule has been omitted for clarity.

Examples of formally anionic naphthalene complexes of Fe are quite uncommon, but not unprecedented. The closest analogue to **5-7** is likely [K(18-crown-6){Cp*Fe(η^4 -

C₁₀H₈}] reported by Wolf and co-workers in 2010.¹⁷⁷ This complex is similarly accessed through the 1-electron reduction of an Fe^{II} halide precursor (Cp*FeCl) with potassium naphthalide. The resulting complex features an analogous η^4 -bound naphthalene ligand with Fe-C distances of 1.975 – 2.076 Å for the 4 coordinating C atoms. The naphthalene is also similarly bent like that of **5-7**, though to an angle 35.1° (*cf.* 26.25° - 28.03° for **5-7**). The counter-ion in this case, a crown ether-encapsulated K⁺ ion, is coordinated to the opposite face of the naphthalene, but on the second ring of the ligand rather than the same ring coordinated to the Fe (as in **5-7**). The authors argue that, computationally and spectroscopically,^{177b} the Fe center appears to be in the +2 oxidation state, implying a dianionic naphthalene ligand, consistent with the bent nature of the naphthalene ring. While such a scenario can easily be envisaged for **5-7**, it has evaded reproduction and thus no additional data outside the X-ray structure has been obtained. Any assignments regarding the Fe oxidation state would therefore be speculative at this point.

5.2.5 Synthesis of (P,N)Fe Alkyl Complexes

To explore the feasibility of generating P,N-supported Fe alkyl complexes, **5-1** was chosen as a suitable precursor for the treatment with alkyl lithium reagents. Reaction of **5-1** with one equiv LiCH₂SiMe₃ in benzene solution (Scheme 5.2.8A) led to a color change from a bright red to a dark red solution along with precipitation of LiBr. After workup, **5-8** was isolated from the reaction mixture as an analytically pure red solid in 89% yield. X-ray quality crystals were obtained from slow evaporation of an Et₂O solution revealing **5-8** to be the desired Fe^{II} alkyl, (P,N)Fe(py)CH₂SiMe₃. Compound **5-8** could also be prepared by *in situ* generation of py₄Fe(CH₂SiMe₃)₂ (*via* reaction of py₄FeCl₂ with 2 equiv LiCH₂SiMe₃) and treatment with (P,N)H (Scheme 5.2.8A).



Scheme 5.2.8. Synthetic procedures for the preparation of **5-8** (A) and **5-9** (B).

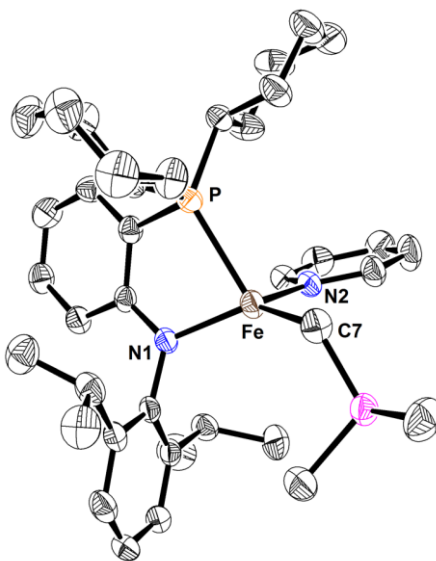


Figure 5.2.8. X-ray crystal structure of **5-8** with thermal ellipsoids drawn at the 50% probability level. Hydrogen atoms have been omitted for clarity. Selected interatomic distances (Å) and angles (°): Fe-P 2.4239(9), Fe-N(1) 2.007(2), Fe-N(2) 2.160(2), Fe-C(7) 2.045(3), P-Fe-N(1) 82.86(7), N(1)-Fe-C(7) 135.05(11), N(2)-Fe-C(7) 110.06(11), P-Fe-N(2) 97.92(6).

Compound **5-8** is paramagnetic and solution magnetic moment measurements (Evans method, benzene- d_6 , 300 K) gave a value of $\mu_{\text{eff}} = 5.2 \mu_{\text{B}}$, consistent with an $S = 2$ ground state, as is expected for a high-spin d^6 metal center in tetrahedral geometry. The

crystal structure of **5-8** confirms the expected tetrahedral geometry. In the X-ray structure of **5-8** the three aromatic rings lie approximately orthogonal to one another, with the CH₂SiMe₃ group pointed toward the opposite face of the molecule from the PCy₂ groups. The Fe-C(7) distance of 2.045(3) Å is typical for other FeCH₂SiMe₃ complexes reported in the literature.^{81, 178}

The analogous Co complex to **5-8** was also targeted using a similar route. Thus py₄Co(CH₂SiMe₃)₂ (generated *in situ* from the reaction of py₄CoCl₂ with 2 equiv LiCH₂SiMe₃) was treated with one equiv (**P,N**)H in pentane (Scheme 5.2.8B), leading to a gradual color change from dark green/brown to dark red along with precipitation of LiCl. After workup (**P,N**)Co(py)CH₂SiMe₃, **5-9**, was isolated in 82% yield as an analytically pure dark red solid. Unlike **5-8**, solution magnetic moment measurements for **5-9** gave a value of μ_{eff} of 2.3 μ_{B} , consistent with an S = 1/2 ground state. Assuming a d⁷-configuration for **5-9**, an S = 1/2 ground state is not likely to correspond with tetrahedral Co^{II}. Instead, the solution magnetic moment measurements are more in line with a square planar geometry around Co. While a high quality X-ray structure of **5-9** has not yet been obtained, a low quality data set for **5-9** supports the expected square planar geometry around Co.

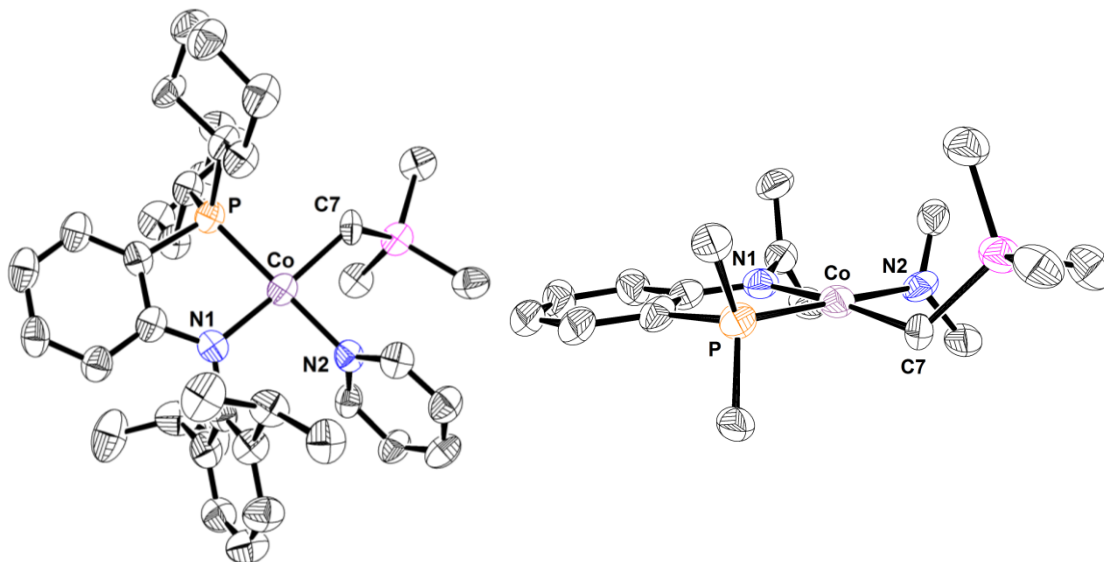


Figure 5.2.9. Left, X-ray crystal structure of **5-9**. Right, cropped X-ray crystal structure of **5-9** highlighting the square planar geometry around Co. Thermal ellipsoids drawn at the 50% probability level for both structures. All hydrogen atoms have been omitted for clarity. These structures represent a low quality data set and thus no metrical parameters are included.

Complex **5-8** and **5-9** are among only a few reported Fe and Co alkyl complexes supported by a P,N ligand. Some closely related examples are Co^{II}- and Co^{III}-methyl complexes of 2-(diphenylphosphino)anilido ligands that have been reported by Klein and co-workers.¹⁷⁹ Neither of these complexes, however, are 4-coordinate, with the Co^{II} complex being five-coordinate, trigonal bipyramidal (two PMe₃ co-ligands). The Co^{III} complex, meanwhile, is described as an octahedral Co-dimethyl complex, wherein both methyl ligands are situated trans to the P,N ligand, and the apical positions are occupied by PMe₃ ligands. Though the authors note that upon attempts at crystallization of this complex only the Co^{II}-methyl complex is obtained, implying loss of Me by some pathway. In the case of Fe, an analogous *N*-phosphinoamidinate complex to **5-8** has been previously documented and crystallographically characterized,⁸¹ however, this complex could not be isolated in pure form.

The ease in preparation and isolation of alkyl complexes **5-8** and **5-9** makes them attractive as potential precursors to other compounds or as precatalysts in their own right. The alkyl group may undergo protonation in the presence of an acidic substrate, as has already been demonstrated for the amido complex, **5-2**, allowing access to new Fe or Co complexes, or giving way to a reactive low-coordinate species. For this reason, these complexes, in addition to complex **5-2**, were subsequently investigated for their activity as catalysts for the reduction of amides.

5.2.6 (P,N)Fe and Co-Catalyzed Reduction of Amides

Having surveyed readily accessible stoichiometric chemistry of P,N complexes of Fe and Co, the utility of a subset of these complexes in a catalytic setting was next investigated. The catalytic reduction of tertiary amides *via* hydrosilylation was chosen for this purpose. Traditionally, tertiary amides are reduced to their corresponding amines under harsh conditions using reagents such as LiAlH₄. However, the utility of first-row transition metal catalysis in this regard has been a topic of recent inquiry, with a handful of examples in which such reactivity has been achieved.^{9b, 88b, 169, 171-174, 175b, 180}

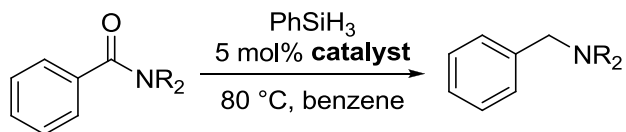
One of the best examples of a well-defined first-row metal catalyst active for the hydrosilylation of amides is a recently reported (*N*-phosphinoamidinate)manganese complex from Sydora, Stradiotto, Turculet and co-workers.^{88b} A three-coordinate amido complex of this P,N ligand was found to be an active precatalyst for the hydrosilylation of a variety of tertiary amides under very mild conditions (25 °C over 18 h, or 75 °C over 1 h in most cases). Room temperature reactivity could be achieved at the cost of a longer reaction time, while a slight increase in catalyst loading (5 mol%) and temperature (75 °C) could decrease reaction times from 18 h to 1 h in most cases. A broad substrate scope

of amides was reported, with > 90% conversions to the corresponding tertiary amines in most cases. While Fe-based catalysts have been targeted, most examples thus far have required high temperatures and long reaction time to achieve catalytic turnover.

In an effort to develop an effective Fe-based catalyst for amide reduction, complex **5-2** was selected for screening due to its similarity to the successful Mn-based catalyst described above. In addition, complex **5-8** and its Co analogue, **5-9** were also screened for their catalytic activity. It was previously proposed by Beller¹⁶⁹ that the active catalyst in such an amide hydrosilylation mechanism is likely to be some sort of metal hydride or silyl complex. Thus in the case of the Mn-chemistry described earlier, the amido complex is likely activated in some manner to generate the active, perhaps silyl- or hydride-based, catalyst. Complex **5-2** may be expected to be activated in a similar manner, while the alkyl complexes **5-8** and **5-9** can be envisaged to act as sources of hydrides or silyls after protonation of the alkyl ligand and its loss as the neutral alkane in the presence of excess PhSiH₃.

To survey the effectiveness of **5-2**, **5-8** and **5-9** as catalysts for the hydrosilylation of amides, a head-to-head study of the three complexes was performed. Each catalyst was employed in a 5 mol% loading relative to tertiary amide, and the reductions were all performed with one equiv PhSiH₃ in benzene solution at 80 °C to offer direct comparisons between the three precatalysts. The results of these reactions are summarized in Table 5.2.1 and Table 5.2.2. In general, the best-behaved substrates are unsubstituted benzamides, the results of which are summarized specifically in Table 5.2.1. It is immediately apparent that both Fe-based catalysts outperform the Co-based catalyst, **5-9**. Based on conversions and reaction times, amides with primary alkyl

substituents (*e.g.* methyl, benzyl) on N are most easily reduced to their corresponding amines (Table 5.2.1, Entries 1-4), presumably due to steric effects. In the case of the morpholine derivative (Table 5.2.1, Entry 6), longer reaction times were required but full conversion could still be achieved in 18-23 h for the Fe-based catalysts. For the Co-based catalyst, full conversion was observed only for the piperidine derivative (Table 5.2.1, Entry 3), while conversions for all other benzamides ranged from 60-75%. Between the two Fe catalysts, little difference in activity between the two can be ascertained based on conversions and reaction time for this subset of the substrate scope. The largest discrepancy comes from the reduction of *N,N*-diisopropylbenzamide (Table 5.2.1, Entry 5), which is clearly the most challenging substrate for all three catalysts. 24 h reaction times were required for all three catalysts, yet only **5-2** gave high conversion. The Fe-alkyl (**5-8**) catalyst afforded only 75% conversion over 24 h, while the Co-alkyl (**5-9**) afforded 60% conversion in the same timeframe. In the case of the reduction of *N,N*-dibenzylbenzamide (Table 5.2.1, Entry 2), the catalyst loading could be dropped to 1 mol% in the case of **5-2**, still giving > 99% conversion in 1 h. Additionally, this substrate could be reduced in > 99% conversion using PMHS (polymethylhydrosiloxane) (2 mol% catalyst, 80 °C), previously described as a more economical and greener alternative to PhSiH₃.¹⁶⁹

Table 5.2.1. Reduction of tertiary benzamides to tertiary benzylamines.

| Entry | Amide | 5-2 | | 5-8 | | 5-9 | |
|-------|-------|---------------------------|----------|-----------|----------|-----------|----------|
| | | Conv. (%) | Time (h) | Conv. (%) | Time (h) | Conv. (%) | Time (h) |
| 1 | | > 99 (57) ^a | 1 | > 99 | 1 | 75 | 1 |
| 2 | | > 99 (74) ^b | 1 | > 99 | 1 | 60 | 1 |
| 3 | | > 99 (81) | 1 | > 99 | 1 | > 99 | 1 |
| 4 | | > 99 (71) | 1 | 95 | 1 | 70 | 1 |
| 5 | | 95 (88) | 24 | 75 | 24 | 60 | 24 |
| 6 | | > 99 (78) | 23 | > 99 | 18 | 65 | 4 |

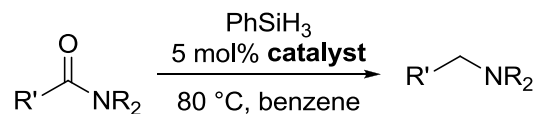
All reactions were conducted using 5 mol% catalyst. Reactions were conducted in benzene on a 0.2 mmol scale of substrate at 80 °C for the specified reaction time. Conversions were determined by gas chromatography against an internal standard (dodecane). Bracketed numbers are isolated yields. ^aLow isolated yield due in part to volatility of reduction product. ^bReaction using either 1 mol% or 5 mol% catalyst gave > 99% conversion, isolated yield is from 1 mol% catalyst reaction. Reaction using 5 equiv PMHS in place of PhSiH₃ and a 2 mol% catalyst loading gave > 99% conversion.

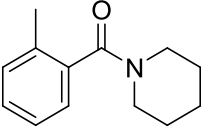
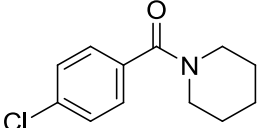
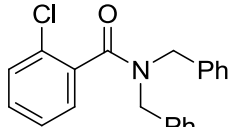
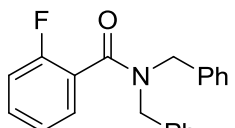
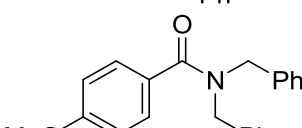
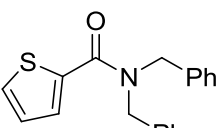
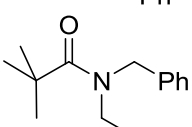
Expanding the substrate scope to include substituted benzamides, a thiophene-based amide and a *tert*-butyl amide (Table 5.2.2) further illustrates the superior activity of 5-2 toward amide hydrosilylation relative to the metal alkyls 5-8 and 5-9. The presence of

an *ortho*-methyl substituent on the arene ring does not appear to impact catalytic turnover for **5-2** and **5-8**, however, in the case of Co (**5-9**) a dramatic decrease in activity (> 99% conversion to 60% conversion) is observed (Table 5.2.2, Entry 1). The presence of electron donating or withdrawing groups on the arene ring does appear to have some impact on activity, but not when in the *para* position. Only marginal differences in conversion are observed between *para*-chloro (Table 5.2.2, Entry 2) and *para*-methoxy (Table 5.2.2, Entry 5) substituted benzamides relative to their unsubstituted analogues, for all three catalysts, though it should be noted reaction times increased from 1 to 4 h in all cases. The presence of an *ortho*-fluoro group, however, decreases activity quite noticeably for all three catalysts (Table 5.2.2, Entry 4), as reaction times increased from 1 to 24 h to achieve similar conversions for **5-2** and **5-9**, while that of **5-8** was only 60% (versus > 99% for the unsubstituted analogue). An *ortho*-chloro substituent (Table 5.2.2, Entry 3) also dramatically decreased catalytic activity for all three precatalysts, such that only 15% and 25% conversion were observed for **5-8** and **5-9** after 4 h. Precatalyst **5-2** afforded 65% conversion 4 h for this substrate, however, this is a significant drop from the > 99% conversion over 1 h for the unsubstituted analogue, for which the catalyst loading could also be decreased to 1% with no loss in conversion (Table 5.2.1, Entry 2). The disparity between the results for the *ortho*-chloro and *para*-chloro derivatives may suggest that steric effects play a more important role than electronics in terms of influencing overall catalytic activity. The Fe-based catalysts can also tolerate a thiophene-based amide quite well (Table 5.2.2, Entry 6), with higher conversions achieved for the amido-based catalyst (**5-2**) albeit over a slightly longer reaction time.

The Co-based catalyst (**5-9**), however, only gave 25% conversion over 4 h. Similar observations were noted for the *tert*-butyl amide (Table 5.2.2, Entry 7).

Table 5.2.2. Reduction of tertiary amides to tertiary amines.

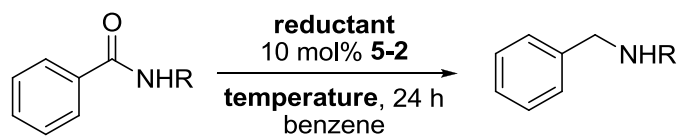


| Entry | Amide | 5-2 | | 5-8 | | 5-9 | |
|-------|---|-----------|----------|-----------|----------|-----------|----------|
| | | Conv. (%) | Time (h) | Conv. (%) | Time (h) | Conv. (%) | Time (h) |
| 1 |  | > 99 (81) | 1 | > 99 | 1 | 60 | 1 |
| 2 |  | > 90 (84) | 4 | 95 | 4 | > 99 | 4 |
| 3 |  | 65 | 4 | 15 | 4 | 25 | 4 |
| 4 |  | > 99 (76) | 24 | 60 | 24 | 40 | 24 |
| 5 |  | 95 (60) | 4 | 95 | 4 | 70 | 4 |
| 6 |  | 90 (92) | 6 | 80 | 1 | 25 | 4 |
| 7 |  | 90 (84) | 4 | 70 | 4 | 30 | 1 |

All reactions were conducted using 5 mol% catalyst. Reactions were conducted in benzene on a 0.2 mmol scale of substrate at 80 °C for the specified reaction time. Conversions were determined by gas chromatography against an internal standard (dodecane).

With the Fe-amido precatalyst (**5-2**) generally outperforming the alkyl-based precatalysts (**5-8** and **5-9**), this complex was chosen for further investigation toward the reduction of *secondary* amides *via* hydrosilylation. While catalytic reduction of tertiary amides is already rare, catalytic reduction of *secondary* amides to secondary amines has been reported even less commonly, even when including reports of second- or third-row transition metal-based catalysts.^{170-172, 173b, 181} The reductions of *N*-methylbenzamide and *N*-benzylbenzamide with PhSiH₃ catalyzed by **5-2** were attempted, increasing reaction temperatures to 110 °C, reaction times to 24 h and doubling the catalyst loading to 10 mol%. Highlighting the difficulty this transformation poses, only 65% conversion to the secondary amine was observed for *N*-methylbenzamide (Table 5.2.3, Entry 1) and 30% conversion for *N*-benzylbenzamide (Table 5.2.3, Entry 2). Using HBPin as the reductant in place of PhSiH₃ for *N*-benzylbenzamide led to 65% conversion to the secondary amine, at a lowered reaction temperature of 80 °C (Table 5.2.3, Entry 3). These results represent a proof-of-concept for the Fe-catalyzed reduction of secondary amides using a P,N-supported Fe precatalyst. Further optimization of reaction conditions and optimization of the structure of the catalyst itself may provide improved reactivity.

Table 5.2.3. Reduction of secondary amides catalyzed by **5-2** using various reductants.



| Entry | Amide | Reductant | Temperature (°C) | Conv. (%) |
|-------|-------|---------------------------------|------------------|-----------|
| 1 | | PhSiH ₃ (1 equiv) | 110 | 65 |
| 2 | | PhSiH ₃ (1 equiv) | 110 | 30 |
| 3 | | HBPi _n (2 equiv) | 80 | 65 |

All reactions were conducted using 10 mol% catalyst unless otherwise specified. Reactions were conducted in benzene on a 0.2 mmol scale of substrate at the specified temperature for 24 h unless otherwise indicated. Conversions were determined by gas chromatography against an internal standard (dodecane).

While the activity of the Co-based catalyst **5-9** is poor in comparison to the Fe-based catalysts, the activity of **5-2**, in particular, toward the catalytic hydrosilylation of amides is competitive with the best reported Fe-based catalysts for this transformation.^{169,}

^{174a-d} Direct comparison of this catalyst with others reported, however, is not straightforward, as there are many parameters to consider and each system brings its own sets of advantages and disadvantages. The substrate scope presented in this work is comparable in size to that of many of the best Fe-catalyzed examples in the literature.^{174b-}

^d From a catalyst loading perspective, use of 5 mol%, or even as high as 10 mol%, Fe is quite typical for this transformation.^{169, 174a, 174c} Examples of systems employing 1 mol% or less of Fe for amide reductions are uncommon. One report from Adolfsson and co-workers^{174b} used 1 mol% Fe(OAc)₂ in conjunction with an *in situ* generated *N*-

heterocyclic carbene and a LiCl additive. While conversion amounts from amide to amine were comparable to the present study, primary, secondary and aliphatic amides were not tolerated, and notably only primary alkyl substituents on *N* were reported in their substrate scope. Nagashima and co-workers^{174d} report use of 0.5 mol% Fe in the form of a heptanuclear Fe carbonyl cluster. Again, conversions were comparable to the present study, and one example of reduction of a secondary amide was provided, but their system relied on the use of a more costly silane (than PhSiH₃, for example), 1,2-bis(dimethylsilyl)benzene (BDSB). Furthermore only primary alkyl substituents on *N* were reported in their scope.

In terms of reaction conditions (*e.g.* temperature, reaction time), 100 °C reaction temperatures are used quite commonly for Fe-catalyzed amide reductions, while reaction times can vary more widely from 30 min on the lower end (1 example^{174d}) to more typical 5-24 h reaction times depending on the substrate. In this regard, the activity of **5-2** is highly competitive to that of the best examples in the literature, as 1-4 h reaction times are required for all but the most difficult substrates. The 80 °C reaction temperatures used in this study are lower than most reported Fe-catalyzed examples. Nagashima and co-workers^{174c} reported ambient temperature amide reductions catalyzed by Fe(CO)₅ or Fe₃(CO)₅, but this was only in conjunction with a 400 W high-pressure mercury lamp (9 h reaction time, 10 mol% catalyst).

5.3 Summary and Conclusions

The synthesis and characterization of a monoanionic P,N-based ligand has been described and an initial survey into its coordination chemistry with Fe and Co has been performed. Halide-bridged dinuclear complexes **5-FeCl**, **5-FeBr** and **5-CoCl** can be

accessed through treatment of simple MX_2 ($\text{M} = \text{Fe}, \text{Co}$; $\text{X} = \text{Cl}, \text{Br}$) salts with $(\text{P},\text{N})\text{Li}$, though these dinuclear complexes are poorly soluble in hydrocarbon solvents. In coordinating solvents, however, these halide-bridged dimers appear to dissolve readily, suggesting potential dissociation to the mononuclear complex in solution. In this regard an example of a monomeric Fe bromide complex has been characterized in the form of its pyridine adduct, **5-1**.

Attempts to reduce $(\text{P},\text{N})\text{Fe}^{\text{II}}$ complexes to corresponding Fe^{I} species by treatment with sodium naphthalide have been met with limited success. Crystallographic evidence for an Fe^{I} arene complex, **5-6**, has been obtained. However, under similar reaction conditions a sodium naphthalide complex of $(\text{P},\text{N})\text{Fe}$ (**5-7**) has also been obtained. Both of these complexes have proven challenging to isolate on a preparative scale. Metathesis reactions of Fe^{II} precursors were more successful, and a three-coordinate Fe^{II} amido (**5-2**), and four-coordinate Fe^{II} (**5-8**) and Co^{II} alkyl (**5-9**) complexes were prepared in high yield. Complex **5-2** was found to be particularly reactive toward protic reagents, and in one case a phenoxy-bridged dimer complex was obtained through reaction of **5-2** with phenol.

Lastly, **5-2**, **5-8** and **5-9** were employed as precatalysts for the reduction of tertiary amides to amines *via* hydrosilylation. In general, the Fe-based catalysts outperformed the Co catalyst under analogous reaction conditions. Between the two Fe-based catalysts, the Fe amido complex (**5-2**) appeared to be the most active toward hydrosilylation of tertiary amides. High conversions were achieved for a fairly broad scope of tertiary amides under moderate reaction conditions compared to literature precedents (5 mol% catalyst loading, 80 °C reaction temperatures). Some evidence for

the hydrosilylation of *secondary* amides was also observed, though, in general further optimization of the catalyst as well as the reaction conditions are required.

5.4 Experimental

5.4.1 General Considerations

All experiments were conducted under nitrogen in a glovebox or using standard Schlenk techniques. Tetrahydrofuran and diethyl ether were distilled from Na/benzophenone ketyl. Benzene, toluene, and pentane were first sparged with nitrogen and subsequently dried by passage through a double-column (one activated alumina column and one column packed with activated Q-5) solvent purification system. All purified solvents were stored over 4 Å molecular sieves. Benzene-*d*₆ was degassed via three freeze-pump-thaw cycles and stored over 4 Å molecular sieves. *N*-(2-bromophenyl)-2,6-diisopropylaniline was prepared by previously reported methods.^{175a} All other reagents were purchased from commercial suppliers and used without further purification. Unless otherwise stated, ¹H, ¹³C, ¹¹B, ¹⁵N and ³¹P characterization data were collected at 300K with chemical shifts reported in parts per million downfield of SiMe₄ (for ¹H and ¹³C), BF₃·OEt₂ (for ¹¹B), or 85% H₃PO₄ in D₂O (for ³¹P). ¹H and ¹³C NMR chemical shift assignments are based on data obtained from ¹³C{¹H}, ¹³C-DEPTQ, ¹H-¹H COSY, ¹H-¹³C HSQC, and ¹H-¹³C HMBC NMR experiments. Solution magnetic moments were determined using the Evans method.¹¹⁶ Infrared spectra were recorded as thin films between NaCl plates at a resolution of 4 cm⁻¹. X-ray data collection, solution, and refinement were carried out by Drs. Robert MacDonald and Michael J. Ferguson at the University of Alberta X-ray Crystallography Laboratory, Edmonton, Alberta.

5.4.2 Synthetic Procedures and Characterization Data

***N*-(2-dicyclohexylphosphino)-2,6-diisopropylamine ((P,N)H).** Following a modified literature procedure,^{175b} Pd(OAc)₂ (0.19 g, 0.85 mmol) and 1,1'-diphenylphosphinoferrocene (0.42 g, 1.0 mmol) were combined with 10 mL toluene in a 250 mL reaction vessel adapted with a Teflon stopcock. The reaction mixture was stirred for 5 min at room temperature. Afterward, NaO^tBu (2.28 g, 23.7 mmol) and HPCy₂ (3.71 mL, 16.9 mmol) were added to the reaction mixture. *N*-(2-bromophenyl)-2,6-diisopropylamine (5.62 g, 0.017 mol, prepared according to literature procedures^{175a}) was also added to the reaction mixture and toluene was added to bring the total reaction volume to approximately 40 mL. The mixture was stirred at 110 °C for 18 h, after which time the volatile components were removed *in vacuo* and the resulting residue was triturated with 3 × 10 mL pentane. The residue was extracted with 50 mL of a ca. 1 : 20 mixture of Et₂O in hexanes and filtered through a Celite and silica gel plug to yield a dark red filtrate. The solvent was removed *in vacuo*, and the residue triturated with 3 × 5 mL pentane before being extracted with ca. 30 mL hexanes and filtered once again through a plug of Celite and silica gel. The filtrate was concentrated *in vacuo* and cooled to -35 °C yielding (P,N)H as a beige crystalline material which was washed with 3 × 1 mL cold pentane. Additional (P,N)H could be isolated through serial crystallization from hexanes and washing the resulting crystals with cold pentane yielding 4.94 g (P,N)H overall as a beige solid (11.0 mmol, 65% yield). Single crystals suitable for X-ray diffraction were isolated from a pentane solution of (P,N)H at room temperature. ¹H NMR (500 MHz, benzene-*d*₆): δ 7.34 – 7.19 (overlapping resonances, 3 H, *H*_{arom,DiPP} + 1 H, *NH*, + 1 H, *H*_{arom}), 6.97 (apparent t, 1 H, *J*_{HH} = 7.5 Hz, *H*_{arom}), 6.69 (apparent t, 1 H, *J*_{HH} = 7.5 Hz), 6.32 (dd, 1 H,

$J_{\text{HH}} = 7.5 \text{ Hz}$, $J_{\text{HH}} = 4.0 \text{ Hz}$), 3.40 (septet, 2 H, $^3J_{\text{HH}} = 7.0 \text{ Hz}$, CHMe_2), 2.00 (m, 4 H, PCy), 1.77 (m, 4 H, PCy), 1.65 (m, 2H, PCy), 1.58 (m, 2H, PCy), 1.45 – 1.16 (overlapping resonances, 10 H), 1.23 (d, 6 H, $^3J_{\text{HH}} = 7.0 \text{ Hz}$, CHMe_2), 1.15 (d, 6 H, $^3J_{\text{HH}} = 7.0 \text{ Hz}$, CHMe_2). $^{13}\text{C}\{^1\text{H}\}$ NMR (125.8 MHz, benzene- d_6): δ 154.3 (d, $^1J_{\text{PC}} = 20.1 \text{ Hz}$, C_{arom}), 147.9 (2C, C_{arom}), 136.9 (C_{arom}), 133.5 (CH_{arom}), 130.6 (CH_{arom}), 127.6 (CH_{arom}), 124.2 (2C, CH_{arom}), 117.4 (CH_{arom}), 116.1 (d, $^2J_{\text{PC}} = 13.8 \text{ Hz}$, C_{arom}), 111.6 (CH_{arom}). $^{31}\text{P}\{^1\text{H}\}$ NMR (202.5 MHz, benzene- d_6): δ -27.2. Anal. Calcd for $\text{C}_{30}\text{H}_{44}\text{N}_1\text{P}_1$: C, 80.13; H, 9.86; N, 3.12. Found: C, 80.08; H, 10.12; N, 3.10.

[(P,N)FeCl]₂ (5-FeCl). To a stirring suspension of FeCl_2 (0.028 g, 0.22 mmol) in *ca.* 5 mL Et_2O was added, dropwise, a solution of the lithium salt of (P,N)H (0.10 g, 0.22 mmol), generated through the 1 : 1 reaction of (P,N)H with $^n\text{BuLi}$, as a solution in 5 mL Et_2O . The mixture was stirred for 18 h at room temperature during which time a color change from pale yellow to dark orange was observed. The volatile components of the reaction mixture were removed *in vacuo* and the residue was triturated with $3 \times 2 \text{ mL}$ pentane and then extracted with 5 mL of a *ca.* 50 : 50 mixture of benzene and pentane and filtered through Celite. The solvent was removed *in vacuo* and the residue was washed with $3 \times 1 \text{ mL}$ pentane to yield **5-FeCl** as an orange solid in 86.1% yield (0.102 g, 0.0947 mmol dimer). μ_{eff} (benzene- d_6): 4.0 μ_{B} . ^1H NMR (300 MHz, benzene- d_6): δ 46.51, 45.83, 41.68, 13.01, 3.17, 1.21, 1.16, 0.10, -1.14, -1.59, -2.23, -3.29, -5.28, -6.03, -9.60, -14.67, -24.28, -32.34, -34.03.

[(P,N)FeBr]₂ (5-FeBr). To a stirring suspension of FeBr_2 (0.047 g, 0.22 mmol) in *ca.* 5 mL Et_2O was added, dropwise, a solution of the lithium salt of (P,N)H (0.10 g, 0.22 mmol), generated through the 1 : 1 reaction of (P,N)H with $^n\text{BuLi}$, as a solution in 5 mL

Et₂O. The mixture was stirred for 18 h at room temperature during which time a color change from pale yellow to dark orange was observed. The volatile components of the reaction mixture were removed *in vacuo* and the residue was triturated with 3 × 2 mL pentane and then extracted with 5 mL of a *ca.* 50 : 50 mixture of benzene and pentane and filtered through Celite. The solvent was removed *in vacuo* and the residue was washed with 3 × 1 mL pentane to yield **5-FeBr** as an orange solid in 86% yield (0.11 g, 0.095 mmol dimer). μ_{eff} (benzene-*d*₆): 3.9 μ_{B} . ¹H NMR (300 MHz, benzene-*d*₆): δ 64.74, 47.36, 46.47, 44.75, 43.93, 40.34, 13.97, 13.46, 6.77, 5.81, 3.32, 2.80, -0.45, -0.97, -1.54, -2.07, -2.19, -5.34, -5.92, -7.04, -7.61, -12.04, -12.84, -14.61, -17.21, -22.87, -25.66, -30.13, -37.24, -39.19, -44.08.

[(P,N)CoCl]₂ (5-CoCl). To a stirring suspension of CoCl₂ (0.029 g, 0.22 mmol) in *ca.* 5 mL Et₂O was added, dropwise, a solution of the lithium salt of **(P,N)H** (0.10 g, 0.22 mmol), generated through the 1 : 1 reaction of **(P,N)H** with ⁿBuLi, as a solution in 5 mL Et₂O. The mixture was stirred for 18 h at room temperature during which time a color change from pale blue to dark blue-purple was observed. The volatile components of the reaction mixture were removed *in vacuo* and the residue was triturated with 3 × 2 mL pentane and then extracted with 5 mL benzene and filtered through Celite. The solvent was removed *in vacuo* and the residue was washed with 3 × 1 mL pentane to yield **5-CoCl** as a blue solid in 85% yield (0.20 g, 0.19 mmol dimer). μ_{eff} (benzene-*d*₆): 3.0 μ_{B} . ¹H NMR (300 MHz, benzene-*d*₆): δ 67.76, 42.96, 35.19, 34.34, 21.68, 14.32, 1.20, 0.87, -7.85, -9.00, -9.24, -11.43, -14.70, -16.97, -26.55, -34.80, -35.64, -36.25, -40.46.

(P,N)FeBr(py) (5-1). Solid **5-FeBr** (0.059 g, 0.051 mmol) is dissolved in *ca.* 3 mL neat pyridine leading to immediate dissolution and formation of a deep red solution

which was stirred for approximately 3 h at room temperature. Excess pyridine was removed *in vacuo* and the residue was triturated with 3×2 mL pentane and washed with 3×1 mL cold pentane to yield **5-1** as a bright red solid in 76% yield (0.051 g, 0.077 mmol). X-ray quality crystals of **5-1** were grown from Et₂O solution of **5-1** at -35 °C. μ_{eff} (benzene-*d*₆): 5.2 μ_{B} (S = 2). ¹H NMR (300 MHz, benzene-*d*₆): δ 54.27, 43.12, 39.22, 31.84, 9.40, 5.77, 5.15, 3.38, 1.23, 0.87, -0.16 , -0.44 , -2.27 , -4.01 , -21.76 , -42.40 , -42.67 . Anal. Calcd. for C₃₅H₄₈N₂PBrFe: C, 63.36; H, 7.29; N, 4.22. Found: C, 63.04; H, 7.36; N, 4.07.

(P,N)FeN(SiMe₃)₂ (5-2). To a suspension of FeBr₂ (0.14 g, 0.67 mmol) in *ca.* 5 mL Et₂O is added, dropwise, a solution of LiN(SiMe₃)₂ (0.22 g, 1.33 mmol) in *ca.* 5 mL Et₂O. The resulting mixture was then stirred for 30 min at room temperature after which point **(P,N)H** (0.30 g, 0.67 mmol) as a solution in *ca.* 5 mL Et₂O was added dropwise to the stirring reaction mixture. A color change to cloudy yellow-orange was observed as the mixture was stirred for 2 h at room temperature. Et₂O and HMDS were removed *in vacuo* and the resulting residue was extracted with *ca.* 3-5 mL benzene and filtered through Celite. The benzene was removed *in vacuo* and the resulting orange-yellow solid was washed with 3×0.5 mL cold pentane to afford **5-2** as a yellow solid in 79% yield (0.35 g, 0.53 mmol). X-ray quality crystals were grown from slow a concentrated pentane solution at -35 °C. μ_{eff} (benzene-*d*₆): 5.2 μ_{B} (S = 2). ¹H NMR (300 MHz, benzene-*d*₆): 80.24, 64.86, 32.51, 31.44, 29.17, -11.87 , -12.73 , -15.12 , -15.60 , -19.68 , -20.45 , -32.86 , -41.63 , -43.96 , -47.34 , -75.87 , -80.65 . Anal. Calcd. for C₃₆H₆₁N₂PSi₂Fe: C, 65.03; H, 9.25; N, 4.21. Found: C, 64.79; H, 9.21; N, 4.18.

(P(O),N)Co-(P,N)CoCy (5-3). To a suspension of CoCl_2 (0.009 g, 0.067 mmol) in *ca.* 5 mL Et_2O was added $\text{LiN}(\text{SiMe}_3)_2$ (0.022 g, 0.13 mmol), dropwise as a solution in 3 mL Et_2O . A gradual color change to blue-green was observed and after *ca.* 20 min **(P,N)H** (0.030 g, 0.067 mmol) was added dropwise as a solution in 3 mL Et_2O . After stirring for 2 h at room temperature the resulting suspension was filtered through Celite to give a light purple solution. The filtrate was concentrated *in vacuo* and a minute quantity of **5-3** was obtained as a green crystalline solid from the Et_2O solution at $-35\text{ }^\circ\text{C}$.

[(P,N)Fe(NHPh)]₂Fe(NHPh)₂ (5-4). To a solution of **5-2** (0.028 g, 0.043 mmol) in *ca.* 5 mL Et_2O was added neat aniline (5.0 μL , 0.052 μL , 0.055 mmol) *via* microsyringe. The reaction mixture was stirred for 18 h at room temperature and the volatile components of the reaction mixture were then removed *in vacuo*. Pentane (0.5 – 1.0 mL) was added to the resulting oil and a small quantity of **5-4** was obtained as an orange crystalline solid from this solution at room temperature.

[(P,N)Fe(OPh)]₂ (5-5). To a solution of **5-2** (0.10 g, 0.15 mmol) in *ca.* 5 mL Et_2O was added, dropwise, a solution of phenol (0.014 g, 0.15 mmol) in *ca.* 5 mL Et_2O . The reaction mixture was stirred for 18 h at room temperature during which time a bright orange precipitate was formed. The volatile components of the reaction mixture were removed *in vacuo* and the resulting residue was triturated with 3×1 mL pentane and washed with 2×0.5 mL pentane to yield **5-5** as a bright orange powder in 89% yield (0.079 g, 0.066 mmol dimer). X-ray quality crystals were grown from an Et_2O solution of **5-5** at room temperature. μ_{eff} (benzene-*d*₆): 5.4 μ_{B} (S = 2). ¹H NMR (300 MHz, benzene-*d*₆): δ 59.88, 52.88, 38.67, 21.11, 20.80, 18.50, 16.09, 6.28, 4.23, 3.88, 2.55, 0.76, -0.48 ,

-3.19, -6.75, -9.57, -14.31, -22.84, -24.07, -32.02, -36.86, -77.22. Anal. Calcd. for $C_{72}H_{96}N_2O_2P_2Fe_2$: C, 72.35; H, 8.10; N, 2.34. Found: C, 72.08; H, 8.14; N, 2.20.

(P,N)Fe(C₆H₆) (5-6). To a solution of 6.2 mg naphthalene (0.048 mmol) in 3 mL THF was added Na metal (5.5 mg, 0.241 mmol). The mixture was stirred for 2.5 h at room temperature giving a dark green solution. In a separate vial, 26 mg (0.024 mmol) **5-FeCl** was dissolved in *ca.* 3 mL THF. One drop of benzene was added to the reaction mixture, and the freshly prepared Na naphthalide solution was added dropwise to the reaction mixture after filtration through Celite. The mixture was stirred for 18 h at room temperature, during which time a color change to deep red was observed. The volatile components of the reaction mixture were removed *in vacuo* and the residue was extracted with 5 mL benzene and filtered through Celite. Benzene was removed *in vacuo* and the residue was triturated with 3 × 2 mL pentane and washed with 2 × 0.5 mL pentane to give a bright orange solid. The solid was crystallized from diffusion of pentane into a concentrated THF solution of the solid at -35 °C yielding a small amount (*ca.* 5 mg) of **5-8** as a dark orange crystalline solid.

(P,N)Fe(C₈H₁₀)[Na(OEt)₂(THF)] (5-7). To a solution of 22 mg naphthalene (0.17 mmol) in 5 mL THF was added Na metal (20 mg, 0.86 mmol). The mixture was stirred for 2.5 h at room temperature giving a dark green solution. In a separate vial, 100 mg (0.086 mmol) **5-FeBr** was dissolved in *ca.* 5 mL THF. Two drops of benzene were added to the reaction mixture, and the freshly prepared Na naphthalide solution was added dropwise to the reaction mixture after filtration through Celite. The mixture was stirred for 18 h at room temperature during which time a color change to deep red was observed. The volatile components of the reaction mixture were removed *in vacuo* and the residue

was extracted with 5 mL benzene and filtered through Celite. Benzene was removed *in vacuo* and the residue was triturated with 3 × 2 mL pentane and washed with 2 × 0.5 mL pentane to give a bright orange solid. The solid was crystallized from slow evaporation of an Et₂O solution of the solid at –35 °C yielding a small amount (*ca.* 10 mg) of **5-8** as orange needles.

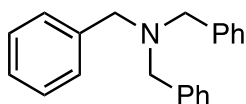
(P,N)Fe(py)CH₂SiMe₃ (5-8). A suspension of py₄FeCl₂ (0.049 g, 0.11 mmol) in *ca.* 5 mL Et₂O was cooled to –35 °C. A solution of LiCH₂SiMe₃ (0.021 g, 0.224 mmol) in *ca.* 5 mL Et₂O was added dropwise to the stirring suspension. A color change from bright yellow to dark red was observed over the course of 1-2 minutes. After *ca.* 15 minutes of stirring at room temperature, the reaction mixture was again cooled to –35 °C and a solution of **(P,N)H** (0.050 g, 0.112 mmol) in *ca.* 5 mL Et₂O was added dropwise to the stirring mixture. The resulting reaction mixture was stirred at room temperature for 18 h, during which time the color lightened to a bright red. The volatile components of the reaction mixture were removed *in vacuo* and the residue was triturated with 3 × 2 mL pentane and then extracted with *ca.* 5 mL benzene and filtered through Celite. The solvent was removed *in vacuo* and the resulting residue was triturated with 3 × 2 mL pentane and washed with 3 × 0.5 mL cold pentane to yield **5-8** as a bright red solid in 90% yield (0.067 g, 0.10 mmol). X-ray quality crystals were obtained from an Et₂O solution of **5-8** at –35 °C. μ_{eff} (benzene-*d*₆): 5.2 μ_{B} (S = 2). ¹H NMR (300 MHz, benzene-*d*₆): δ 49.88, 37.72, 30.47, 28.60, 20.69, 20.03, 9.24, 3.91, 2.00, –1.02, –3.24, –9.22, –31.35, –38.38. Anal. Calcd. for C₃₉H₅₉N₂PSiFe: C, 69.83; H, 8.87; N, 4.18. Found: C, 69.61; H, 8.95; N, 4.46.

(P,N)Co(py)CH₂SiMe₃ (5-9). A suspension of py₄CoCl₂ (0.30 g, 0.67 mmol) in *ca.* 7 mL pentane was cooled to –35 °C. A solution of LiCH₂SiMe₃ (0.13 g, 1.35 mmol) in *ca.* 5 mL pentane was added dropwise to the stirring suspension. A color change from blue to dark red-brown was observed during the addition. After *ca.* 15 minutes of stirring at room temperature, the reaction mixture was again cooled to –35 °C and a solution of **(P,N)H** (0.30 g, 0.67 mmol) in *ca.* 7 mL pentane was added dropwise to the stirring mixture. The reaction mixture was stirred at room temperature for 18 h, after which point the volatile components removed *in vacuo*. The resulting red residue was triturated with 3 × 2 mL pentane and then extracted with *ca.* 10 mL benzene and filtered through Celite. The solvent was removed *in vacuo* and the resulting residue was triturated with 3 × 2 mL pentane and washed with 3 × 2 mL cold pentane to yield **5-9** as a red solid in 82% yield (0.37 g, 0.55 mmol). X-ray quality crystals were obtained from an Et₂O solution of **5-9** at –35°C. μ_{eff} (benzene-*d*₆): 2.3 μ_{B} (S = ½). ¹H NMR (300 MHz, benzene-*d*₆): δ 30.30, 25.71, 14.59, 13.60, 11.43, 7.40, 5.30, 2.91, 1.94, 0.61, 0.28, –3.45, –6.53, –30.68. Anal. Calcd. for C₃₉H₅₉N₂PSiCo: C, 69.51; H, 8.82; N, 4.16. Found: C, 69.22; H, 8.64; N, 4.10.

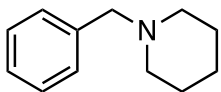
General Procedure for the Reduction of Amide Substrates. Amide (0.2 mmol) and reductant (one of PhSiH₃ (0.2 mmol), PMHS (1 mmol) or HBPin (0.4 mmol)) were combined in an oven-dried 1 dram vial equipped with a magnetic stirbar. The precatalyst (**5-2**, **5-8** or **5-9**) was then added as a stock solution (64 mM) in benzene (313 μ L for 10 mol% runs, 156 μ L for 5 mol% runs, 62 μ L for 2 mol% runs, 31 μ L for 1 mol% runs), as well as an additional 300 μ L of benzene. The vial was sealed with a PTFE-lined cap, removed from the glovebox, and heated to 80 °C or 110 °C for the specified reaction time. The reaction mixture was then exposed to air, diluted with 1 mL of

dichloromethane, and filtered through a Celite plug. The mixture obtained was then analyzed by gas chromatography against a dodecane internal standard to measure conversion of the amide to the amine.

General Procedure for the Isolation of Tertiary Amines. Amide reductions were conducted on either a 0.4 mmol or 0.6 mmol scale for the purpose of isolation. An oven-dried 1 dram vial equipped with a magnetic stirbar was charged with 0.4 mmol (or 0.6 mmol) amide and 0.4 mmol (or 0.6 mmol). Complex **5-2** was then added as 312 μL (or 468 μL) of a 64 mM benzene stock solution, as was an additional 600 μL (or 900 μL) of benzene. The vial was sealed with a PTFE-lined cap, removed from the glovebox, and heated at 80 $^{\circ}\text{C}$ for the specified reaction time. The reaction mixture was then exposed to air and the volatile components were removed under vacuum. The crude residue was purified by flash column chromatography using either silica gel or neutral alumina as the stationary phase. The combined fractions were concentrated under reduced pressure to afford the corresponding amine.

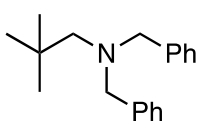


Tribenzylamine. Silica gel column chromatography [ethyl acetate : hexanes (1 : 4)], 74% yield (0.13 g, 0.44 mmol), solid. ^1H NMR (300.1 MHz, CDCl_3): δ 7.44 – 7.42 (overlapping resonances, 6 H, H_{arom}), 7.36 – 7.31 (m, overlapping resonances, 6 H, H_{arom}), 7.27 – 7.22 (overlapping resonances, 3 H, H_{arom}), 3.59 (s, 6 H, CH_2). $^{13}\text{C}\{^1\text{H}\}$ NMR (75.5 MHz, CDCl_3): δ 139.9 (C_{arom}), 128.9 (CH_{arom}), 128.4 (CH_{arom}), 127.1 (CH_{arom}), 58.1 (CH_2).



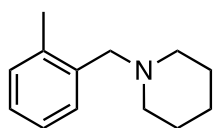
Benzylpiperidine. Neutral alumina column chromatography [ethyl acetate: hexanes (1 : 10)], 81% yield (0.09 g, 0.46 mmol), liquid. ^1H NMR (300.1 MHz, CDCl_3): δ 7.25 – 7.14 (m, overlapping resonances, 5 H, H_{arom}), 3.41

(s, 2 H, CH_2), 2.32 (m, 4 H, CH_2), 1.52 (m, 4 H, CH_2), 1.38 (m, 2 H, CH_2). $^{13}C\{^1H\}$ NMR (75.5 MHz, $CDCl_3$): δ 138.8 (C_{arom}), 129.3 (CH_{arom}), 129.2 (CH_{arom}), 126.9 (CH_{arom}), 64.0 (Ph- CH_2), 54.6 (CH_2), 26.1 (CH_2), 24.5 (CH_2).



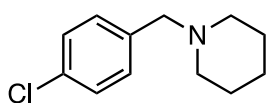
Dibenzyl(2,2-dimethylpropyl)amine. Silica gel column chromatography [ethyl acetate : hexanes (3 : 20)], 84% yield (0.09 g,

0.34 mmol), liquid. 1H NMR (500.0 MHz, $CDCl_3$): δ 7.47 (m, 4 H, H_{arom}), 7.40 (m, 4 H, H_{arom}), 7.32 (m, 2 H, H_{arom}), 3.69 (s, 4 H, CH_2), 2.43 (s, 2 H, CH_2), 0.90 (s, 9 H, CH_3). $^{13}C\{^1H\}$ NMR (125.8 MHz, $CDCl_3$): δ 140.4 (C_{arom}), 129.3 (CH_{arom}), 128.2 (CH_{arom}), 126.9 (CH_{arom}), 66.0 (CH_2), 60.9 (Ph- CH_2), 33.2 ($C(CH_3)_3$), 28.6 (CH_3).



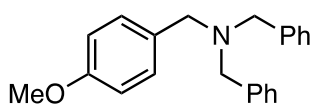
(2-Tolylbenzyl)piperidine. Neutral alumina column chromatography

[ethyl acetate : hexanes (1 : 20)], 73% yield (0.08 g, 0.44 mmol), liquid. 1H NMR (500.0 MHz, $CDCl_3$): δ 7.40 – 7.25 (overlapping resonances, 4 H, H_{arom}), 3.52 (s, 2 H, CH_2), 2.54 – 2.46 (overlapping resonances, 7 H, $CH_2 + CH_3$), 1.67 (m, 4 H, CH_2), 1.56 (m, 2 H, CH_2). $^{13}C\{^1H\}$ NMR (125.8 MHz, $CDCl_3$): δ 137.5 (C_{arom}), 137.3 (C_{arom}), 130.2 (CH_{arom}), 129.8 (CH_{arom}), 126.8 (CH_{arom}), 125.5 (CH_{arom}), 61.7 (Ar- CH_2), 54.8 (CH_2), 26.3 (CH_2), 24.7 (CH_2), 19.4 (CH_3).

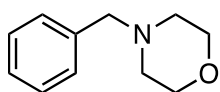


(4-Chlorobenzyl)piperidine. Neutral alumina column chromatography [ethyl acetate : hexanes (1 : 10)], 99% yield (0.08

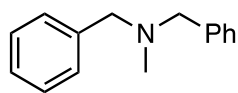
g, 0.4 mmol), liquid. 1H NMR (500.0 MHz, $CDCl_3$): δ 7.29 – 7.24 (overlapping resonances, 4 H, H_{arom}), 3.54 (s, 2 H, CH_2), 2.35 (broad s, 4 H, CH_2), 1.57 (m, 4 H, 2 CH_2), 1.44 (m, 2 H, CH_2). $^{13}C\{^1H\}$ NMR (125.8 MHz, $CDCl_3$): δ 137.5 (C_{arom}), 132.3 (C_{arom}), 130.5 (CH_{arom}), 128.3 (CH_{arom}), 63.2 (CH_2), 54.6 (CH_2), 26.1 (CH_2), 24.4 (CH_2).



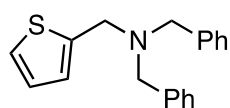
***N,N*-Dibenzyl-1-(4-methoxyphenyl)methanamine.** Silica gel column chromatography [ethyl acetate : hexanes (3 : 20)], 60% yield (0.08 g, 0.24 mmol), liquid. ^1H NMR (300.1 MHz, CDCl_3): δ 7.49 – 7.47 (m, overlapping resonances, 4 H, H_{arom}), 7.41 – 7.36 (overlapping resonances, 6 H, H_{arom}), 7.32 – 7.28 (overlapping resonances, 2 H, H_{arom}), 6.95 – 6.92 (overlapping resonances, 2 H, H_{arom}), 3.85 (s, 3 H, CH_3), 3.63 (s, 4 H, CH_2), 3.58 (s, 2 H, CH_2). $^{13}\text{C}\{^1\text{H}\}$ NMR (75.5 MHz, CDCl_3): δ 159.2 (C_{arom}), 140.4 (CH_{arom}), 132.2 (C_{arom}), 130.5 (CH_{arom}), 129.4 (CH_{arom}), 128.8 (CH_{arom}), 127.4 (CH_{arom}), 114.2 (CH_{arom}), 58.4 (CH_3), 57.8 (CH_2), 55.8 (CH_2).



***N*-Benzylmorpholine.** Neutral alumina column chromatography [ethyl acetate : hexanes (1 : 10)], 78% yield (0.08 g, 0.47 mmol), liquid. ^1H NMR (500.0 MHz, CDCl_3): δ 7.38 – 7.28 (overlapping resonances, 5 H, H_{arom}), 3.75 (m, 4 H, CH_2), 3.54 (s, 2 H, CH_2), 2.49 (m, 4 H, CH_2). $^{13}\text{C}\{^1\text{H}\}$ NMR (125.8 MHz, CDCl_3): δ 137.9 (C_{arom}), 129.3 (CH_{arom}), 128.4 (CH_{arom}), 127.2 (CH_{arom}), 67.4 (CH_2), 63.6 (Ph- CH_2), 53.7 (CH_2).

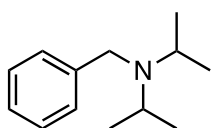


***N*-methyldibenzylamine.** Silica gel column chromatography [ethyl acetate : hexanes (1 : 4)], 71% yield (0.09 g, 0.43 mmol), solid. ^1H NMR (500.0 MHz, CDCl_3): δ 7.27 – 7.26 (overlapping resonances, 4 H, H_{arom}), 7.23 – 7.20 (overlapping resonances, 4 H, H_{arom}), 7.15 – 7.12 (overlapping resonances, 2 H, H_{arom}), 3.42 (s, 4 H, CH_2), 2.09 (s, 3 H, CH_3). $^{13}\text{C}\{^1\text{H}\}$ NMR (125.8 MHz, CDCl_3): δ 139.5 (C_{arom}), 129.0 (CH_{arom}), 128.3 (CH_{arom}), 127.0 (CH_{arom}), 62.0 (CH_2), 42.4 (CH_3).

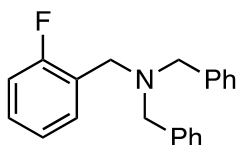


***N,N*-dibenzyl-2-thiophenemethanamine.** Neutral alumina column chromatography [ethyl acetate : hexanes (1 : 50)], 92% yield (0.11 g,

0.37 mmol), white solid. ^1H NMR (500.0 MHz, CDCl_3): δ 7.31 – 7.30 (m, 4 H, H_{arom}), 7.21 – 7.18 (m, 4 H, H_{arom}), 7.12 – 7.09 (overlapping resonances, 3 H, H_{arom}), 6.82 – 6.78 (overlapping resonances, 2 H, H_{arom}), 3.65 (s, 2 H, CH_2), 3.49 (s, 4 H, CH_2). $^{13}\text{C}\{^1\text{H}\}$ NMR (125.8 MHz, CDCl_3): δ 143.2 (C_{arom}), 139.3 (C_{arom}), 128.7 (CH_{arom}), 128.2 (CH_{arom}), 126.9 (CH_{arom}), 126.3 (CH_{arom}), 125.4 (CH_{arom}), 124.5 (CH_{arom}), 57.5 (CH_2), 52.1 (CH_2).



***N,N*-diisopropylbenzylamine.** Silica gel column chromatography [ethyl acetate : hexanes (17 : 100)], 88% yield (0.09 g, 0.47 mmol), liquid. ^1H NMR (300.1 MHz, CDCl_3): δ 7.43 – 7.40 (overlapping resonances, 2 H, H_{arom}), 7.34 – 7.29 (overlapping resonances, 2 H, H_{arom}), 7.22 (m, 1 H, H_{arom}), 3.68 (s, 2 H, CH_2), 3.06 (sept, 2 H, $^3J_{\text{HH}} = 6.6$ Hz, $\text{CH}(\text{CH}_3)_2$), 1.06 (d, 12 H, $^3J_{\text{HH}} = 6.6$ Hz, $\text{CH}(\text{CH}_3)_2$). $^{13}\text{C}\{^1\text{H}\}$ NMR (75.5 MHz, CDCl_3): δ 143.4 (C_{arom}), 128.1 (CH_{arom}), 127.9 (CH_{arom}), 126.2 (CH_{arom}), 49.0 (CH_2), 47.9 ($\text{CH}(\text{CH}_3)_2$), 20.9 ($\text{CH}(\text{CH}_3)_2$).



***N,N*-dibenzyl-1-(2-fluorophenyl)methanamine.** Silica gel column chromatography [ethyl acetate : hexanes (1 : 10)], 76% yield, (0.09 g, 0.3 mmol), solid. ^1H NMR (500.0 MHz, CDCl_3): δ 7.52 (m, 1 H, H_{arom}), 7.39 – 7.37 (overlapping resonances, 4 H, H_{arom}), 7.30 – 7.27 (overlapping resonances, 4 H, H_{arom}), 7.21 – 7.07 (overlapping resonances, 5 H, H_{arom}), 6.97 (1 H, H_{arom}), 3.62 (s, 2 H, CH_2), 3.56 (s, 4 H, CH_2). $^{13}\text{C}\{^1\text{H}\}$ NMR (125.8 MHz, CDCl_3): δ 161.5 (d, C_{arom} , $^1J_{\text{CF}} = 245$ Hz), 139.7 (CH_{arom}), 131.1 (d, CH_{arom} , $J_{\text{CF}} = 4.4$ Hz), 128.8 (CH_{arom}), 128.5 (d, CH_{arom} , $J_{\text{CF}} = 8.4$ Hz), 128.4 (CH_{arom}), 127.0 (CH_{arom}), 126.4 (d, C_{arom} , $J_{\text{CF}} = 14.1$ Hz), 124.1 (d, CH_{arom} , $J_{\text{CF}} = 3.3$ Hz), 115.3 (d, CH_{arom} , $J_{\text{CF}} = 22.2$ Hz), 58.2 (CH_2), 50.3 (CH_2). $^{19}\text{F}\{^1\text{H}\}$ NMR (470.5 MHz, CDCl_3): δ -118.2 (s).

5.4.3 Crystallographic Solution and Refinement Details

Crystallographic data for each of **5-1**, **5-2** and **5-8** were obtained at 173(±2) K on either a Bruker D8/APEX II CCD diffractometer using CuK α ($\lambda = 1.54178$ Å, microfocus source) radiation (for **5-1** and **5-2**) or a Bruker PLATFORM/APEX II CCD diffractometer using graphite-monochromated Mo K α ($\lambda = 0.71073$ Å) radiation (for **5-8**), employing a sample that was mounted in inert oil and transferred to a cold gas stream on the diffractometer. Programs for diffractometer operation, data collection, and data reduction (including SAINT) were supplied by Bruker. Gaussian integration (face-indexed) was employed as the absorption correction method in each case. The structures of **5-2** and **5-8** were solved by use of the Patterson search/structure expansion, while that of **5-1** was solved by use of intrinsic phasing methods. All three structures were refined by use of full-matrix least-squares procedures (on F^2) with R_1 based on $F_o^2 \geq 2\sigma(F_o^2)$ and wR_2 based on $F_o^2 \geq -3\sigma(F_o^2)$.

For **5-2** Corresponding distances within the conformers of the disordered cyclohexyl group were constrained to be equal (within 0.03 Å) during refinement: $d(\text{C11A-C12A}) = d(\text{C11B-C12B})$; $d(\text{C11A-C16A}) = d(\text{C11B-C16B})$; $d(\text{C12A-C13A}) = d(\text{C12B-C13B})$; $d(\text{C13A-C14A}) = d(\text{C13B-C14B})$; $d(\text{C14A-C15A}) = d(\text{C14B-C15B})$; $d(\text{C15A-C16A}) = d(\text{C15B-C16B})$; $d(\text{C11A}\cdots\text{C13A}) = d(\text{C11B}\cdots\text{C13B})$; $d(\text{C11A}\cdots\text{C15A}) = d(\text{C11B}\cdots\text{C15B})$; $d(\text{C12A}\cdots\text{C14A}) = d(\text{C12B}\cdots\text{C14B})$; $d(\text{C12A}\cdots\text{C16A}) = d(\text{C12B}\cdots\text{C16B})$; $d(\text{C13A}\cdots\text{C15A}) = d(\text{C13B}\cdots\text{C15B})$; $d(\text{C14A}\cdots\text{C16A}) = d(\text{C14B}\cdots\text{C16B})$.

Anisotropic displacement parameters were employed throughout for the non-hydrogen atoms. Additional crystallographic details for **5-1**, **5-2** and **5-8** can be found in Appendix A

Chapter 6: Conclusions and Future Work

6.1 Summary and Conclusions

As detailed in Chapter 1 of this document, there has been a tremendous push toward the discovery of cost-effective 3d-transition metal catalysts as alternatives to the second- and third-row metal catalysts that are ubiquitous in chemical synthesis. Exceptional examples of Fe-, Co- and Ni-based catalysts have been reported, most of which benefit from judicious choice of ancillary ligand(s) to impart the necessary steric and electronic characterization on the metal center in order to facilitate a given transformation. The use of bis(phosphino)silyl pincer ligands in conjunction with first-row transition metals has thus far been largely limited to complexes of Ni, with few examples of Fe- and Co-based PSiP complexes reported.

In Chapter 2, significant progress in developing the chemistry of PSiP complexes of Fe has been described. Initial targets of this study were 4-coordinate, 14-electron complexes of Fe in the form of Fe halides or Fe alkyls. While crystallographic evidence for the 4-coordinate Fe bromide complex **2-Br** has been provided, this complex has proven difficult to obtain on a preparative scale. Complex **2-Br** and similar low coordinate PSiP Fe species may be highly susceptible to redox chemistry, as examples of compounds of both Fe^{III} (**2-Cl**) and Fe^I (**2-Me**) have been obtained during efforts to prepare 4-coordinate Fe-chloride and Fe-methyl complexes, respectively. Stabilization of these reactive low-coordinate complexes with an additional L donor ligand was far more successful, and the first examples of 5-coordinate (PSiP)Fe complexes were obtained as PMe₃ (**2-PMe₃**) and pyridine (**2-py**) adducts. Similarly, an 18-electron di(carbonyl) complex (**2-(CO)₂**) could also be reproducibly prepared.

The reactivity of **2-PMe₃** toward 1-electron reduction was investigated, and the corresponding Fe^I-dinitrogen complex (**2-Fe^I**) could be isolated by treatment with Mg⁰. Reaction of **2-PMe₃** with Na⁰ led to formation of a highly sensitive Fe⁰ complex **2-Fe⁰**. The latter complex was found to react with a variety of protic reagents, to form diamagnetic hydride species. Attempts to prepare such hydride complexes provided a unique example of a 5-coordinate (PSiP)Fe-hydride (**2-H**), as well as a highly unusual η^2 -(SiH) adduct of an Fe-dihydride (**2-H₂**), which was characterized both crystallographically and in solution.

Finally, replacing PMe₃ as a stabilizing ligand with pyridine allowed for the isolation of a bis(dinitrogen) adduct of an Fe hydride (**2-(N₂)₂**). This complex was found to be highly effective for the catalytic hydrogenation of alkenes, including mono, di and trisubstituted substrates, a disubstituted alkyne, as well as alkenes featuring ester and ether functionalities.

In Chapter 3 of this document, the chemistry of (PSiP)Co complexes was examined in further detail. Reduction Co^{II} halide complexes of Cy-PSiP was readily achieved, allowing for the isolation of two Co^I complexes depending on the identity of an added L donor to the reaction mixture. Complex **3-3** was prepared by reducing (Cy-PSiP)CoI with Mg metal in the presence of PMe₃, while **3-4** could be prepared from the reduction of (Cy-PSiP)CoI with Mg metal under a CO atmosphere.

While one electron reduction of Co^{II} halide complexes proved straightforward, attempts to prepare Co^{III} species supported by Cy-PSiP ligation were considerably more challenging. Oxidative addition reactions involving **3-3** were mostly unsuccessful. However, when **3-3** was treated with H₂, the dihydride complex **3-5** was generated.

Complex **3-5** could not be isolated as it was observed to readily eliminate H₂ when not kept under an H₂ atmosphere. Both hydride positions appeared to exchange readily in solution and the complex appeared to be highly dynamic, as evidenced by variable temperature NMR spectroscopy. Complex **3-5** was also found to be a viable precatalyst for the hydrogenation of terminal alkenes.

The reactivity of O₂ toward (Cy-PSiP)CoI was investigated, and it was observed that exposure of this complex to O₂ led to rapid oxidation of the ligand at both Si and P, generating compound **3-6**. Reaction of (Cy-PSiP)CoI with Me₃NO, meanwhile, afforded a Co^{II}-siloxy complex, **3-7**. While this siloxy complex did not react further with O₂, treatment with a second equiv of Me₃NO led to subsequent oxidation involving one phosphino donor to generate **3-6**. This observation supports the notion that the O atoms incorporated at both Si and P are derived from the same O₂ molecule.

In Chapter 4, group 10 transition metal chemistry of a new bis(indolylphosphino)silyl pincer ligand (*i*Pr-PSiP^{Ind}) was investigated, with a particular emphasis on Ni chemistry. Four-coordinate Ni (**4-NiCl**), Pd (**4-PdCl**), and Pt (**4-PtCl**) chloride complexes were prepared readily, each of which could be converted to their corresponding hydride complexes (**4-NiH**, **4-PdH**, and **4-PtH**) by treatment with NaEt₃BH. Complex **4-NiCl** was also shown to be a viable precursor to a number of other Ni^{II} complexes *via* simple salt metathesis reactions, such that Ni allyl (**4-Ni(C₃H₅)**), Ni anilido (**4-NiNHDMP**) and Ni triflate (**4-NiOTf**) complexes were all prepared in high yields.

The chemistry of group 10 metal hydride complexes supported by *i*Pr-PSiP^{Ind} was investigated in further detail with respect to the potential for interactions between Si and

H in the prepared complexes. To this end, a derivative of the *i*Pr-PSiP^{Ind} ligand, featuring an SiH moiety in the backbone in place of the SiMe group was prepared. While Pd and Pt chloride complexes (**4-PdCl'** and **4-PtCl'**) of this ligand derivative were readily prepared, the corresponding Ni complex could not be isolated. NMR investigation of the Pt hydride complex of the SiH-variant of the ligand (**4-PtH'**) revealed no evidence for chemical exchange between the SiH and PtH on the NMR timescale.

The Ni hydride complex of the parent *i*Pr-PSiP^{Ind} ligand (**4-NiH**) displayed unusual spectroscopic features, and an NMR study of this complex revealed a temperature and solvent dependent equilibrium involving an apparent terminal Ni^{II} hydride and a Ni⁰ complex featuring N₂ coordination and an η²-(SiH) interaction (**4-NiH***). Analogous DMAP- and PMe₃-supported η²-(SiH) complexes (**4-NiH·DMAP** and **4-NiH·PMe₃-B**) were also prepared and fully characterized. The PMe₃ case represents a unique example of both the η²-(SiH) Ni⁰ complex and the classical Ni^{II} silyl hydride complex (**4-NiH·PMe₃-A**) co-existing in solution.

While both **4-NiH** and **4-PdH** were found to be reactive toward CO₂ insertion, to generate the corresponding formate complexes **4-NiHCO₂** and **4-PdHCO₂**, only the Ni complex reacted in a quantitative manner. Hydroboration of CO₂ catalyzed by **4-NiH** was investigated, and under optimized conditions selective reduction of CO₂ to the formaldehyde level was achieved. The isolated bis(boryl)acetal could then be used as a surrogate for formaldehyde in a variety of condensation reactions to prepare several examples of CH₂-containing compounds, wherein the CH₂ moiety is derived from CO₂.

Lastly, in Chapter 5 of this document, focus was turned from tridentate PSiP ligands to *bidentate* monanionic P,N ligands in the context of Fe and Co chemistry. A

new monoanionic P,N-based ligand derivative was prepared, and its coordination chemistry with Fe and Co was investigated. Simple halide complexes of Fe^{II} and Co^{II} supported by such P,N ligation are proposed to adopt a dinuclear structure, and three such complexes (**5-FeCl**, **5-FeBr** and **5-CoCl**) have been prepared. A four-coordinate monomeric Fe^{II} bromide complex (**5-1**) was also prepared through treatment of the corresponding dimer **5-FeBr** with pyridine.

Reduction of the dinuclear Fe^{II} dimer complexes to corresponding Fe^I species has been marginally successful, with crystallographic evidence for an Fe^I arene complex (**5-6**) and a sodium naphthalide complex (**5-7**) obtained. In the case of **5-7** the oxidation state of Fe thus far remains somewhat ambiguous. Fe^{II} amido (**5-2**), and four-coordinate Fe^{II} (**5-8**) and Co^{II} alkyl (**5-9**) complexes could be prepared far more readily, as could a phenoxy-bridged dinuclear complex (**5-5**).

Complexes **5-2**, **5-8** and **5-9** were found to be active precatalysts for the hydrosilylation of tertiary amides. The Fe-based catalysts appeared to be more effective than the Co-based catalyst, with the 3-coordinate Fe amido complex **5-2** apparently exhibiting the highest reactivity. High conversions were achieved for a fairly broad scope of tertiary amides under moderate reaction conditions and evidence for the hydrosilylation of *secondary* amides was also observed.

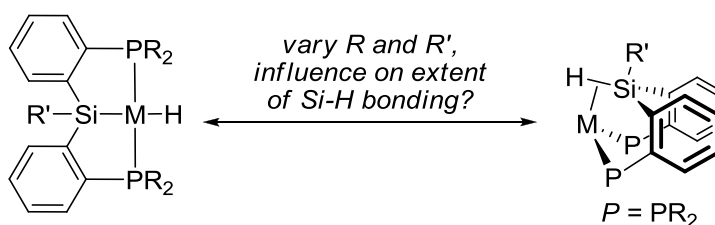
6.2 Future Work

The chemistry of Fe and Co complexes supported by PSiP pincer ligation is still very much in its infancy, however, the results presented herein highlight the potential for the discovery of new bond-activation and catalytic chemistry facilitated by such complexes. In addition, unusual behavior of PSiP metal complexes in terms of

interconversion between classical silyl hydride complexes and η^2 -SiH complexes may represent a new avenue for reactivity *via* metal-ligand cooperativity.

A better understanding of the factors that influence interconversion between silyl hydride and η^2 -SiH complexes (Scheme 6.2.1) may aid in the development of systems that take advantage of this interconversion in a productive manner. In Chapter 4, temperature, solvent as well as presence of an additional L donor ligand in solution, were all demonstrated to have a clear impact on such an interconversion for Ni complexes of the i Pr-PSiP^{Ind} ligand. Another factor to investigate in such a context would be the structure of the ligand itself. While the anionic silyl donor is key in this regard, the ligand backbone, as well as the flanking donor groups could be altered strategically, in order to study the effects such changes have on the formation of η^2 -SiH complexes. Most straightforward would be to systematically vary the phosphine donors (Scheme 6.2.1). The ligand synthesis is quite versatile, meaning a variety of (R-PSiP)H ligand precursors could be prepared quite readily (literature examples already include Ph-PSiP, Cy-PSiP, i Pr-PSiP). In the specific case of Ph-PSiP, the effects of electron-withdrawing or electron-donating groups on the aromatic rings could be systematically investigated by preparing, for example, various metal hydride complexes of these ligands and observing any trends in key spectroscopic features commonly found in the corresponding ^1H NMR, ^{29}Si NMR and IR spectra. The ligands can be modified more dramatically, for example, by exchanging *P* donors with *N* or *O* donors, or even by looking at bidentate or tetradentate analogues, all of which will likely have a dramatic impact on the observed chemistry. An often overlooked portion of the ligand to vary is the identity of the fourth substituent on Si. In the majority of cases, this fourth substituent is a methyl group, though examples of

SiPh ,^{73b} SiF ,¹⁸² SiCl ,¹⁸³ SiH^{96c} and SiOH^{143} ligand precursors have been prepared as well. In most of these cases, however, the substituent was modified in hopes that it would become directly involved in the chemistry at Si (e.g. Si-F or Si-Cl bond activation in the cases of SiF and SiCl derivatives or dehydrogenation to generate a metasilanone in the case of the SiOH derivative). Again, a more systematic approach to substitution in this position may offer important insights regarding the behavior of the resulting metal hydride complexes in particular (Scheme 6.2.1).

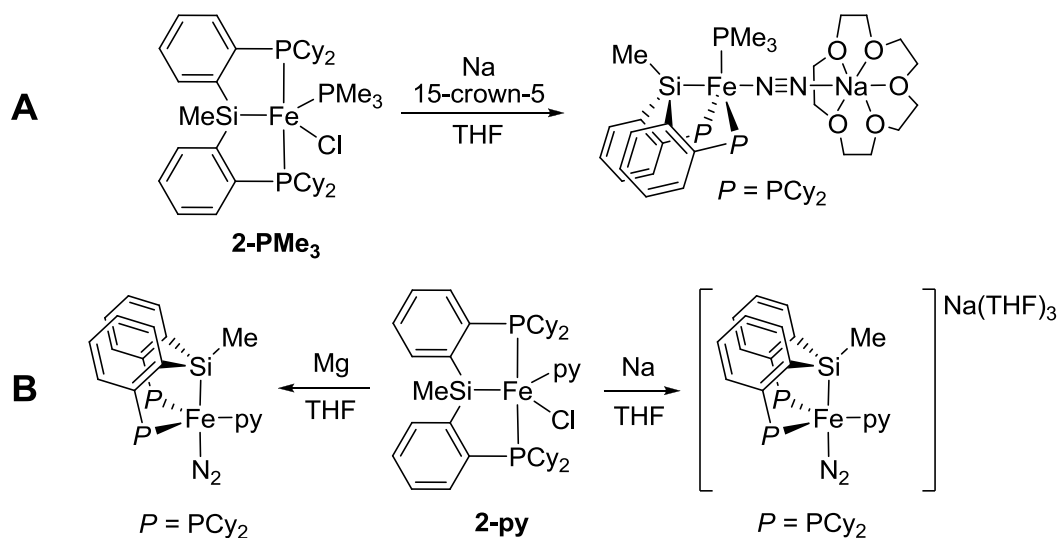


Scheme 6.2.1. General variations in phosphine donor arms or fourth substituent on Si (R') may have an impact on the extent of SiH bonding, from silyl hydrides (left) to η^2 -SiH complexes (right).

In Chapter 2, a wide range of Fe complexes supported by P SiP pincer ligation were reported. In particular, routes to Fe^{I} and Fe^0 complexes were outlined which displayed reactivity toward substrates featuring E-H bonds. In general, the Fe^0 complex **2-Fe⁰** was highly sensitive and could not be isolated in pure form. Attempts to encapsulate the THF-solvated Na^+ counter-ion with a crown ether were unsuccessful, but performing the synthesis of **2-Fe⁰** in the *presence* of the crown ether may prove to be a viable route to accessing a more stable version of this complex (Scheme 6.2.2A).

It was also shown in Chapter 2 that while **2-(N₂)₂** was highly active toward the hydrogenation of alkenes, the presence of PMe_3 had a dramatic impact on the reactivity, and no hydrogenation of even 1-octene was observed when **2-H₃** was used in place of the bis(dinitrogen) complex. In a similar vein, while the Fe^{I} complex, **2-Fe^I** appeared to

display limited reactivity toward oxidative addition, this may have been due to the presence of strongly-coordinating PMe_3 on the metal center. Thus it would be pertinent to investigate the chemistry of related complexes that do not feature PMe_3 . A viable starting point in this context would be to perform the reduction of **2-py** in an analogous fashion to that of **2- PMe_3** with the hope of accessing a more reactive Fe^{I} complex of the form $(\text{Cy-PSiP})\text{Fe}(\text{py})(\text{N}_2)$ (Scheme 6.2.2B). Reduction with Na metal may also lead to an Fe^0 analogue, however, as the PMe_3 complex **2- Fe^0** is already extremely reactive, a pyridine analogue may be even more difficult to handle (Scheme 6.2.2B).

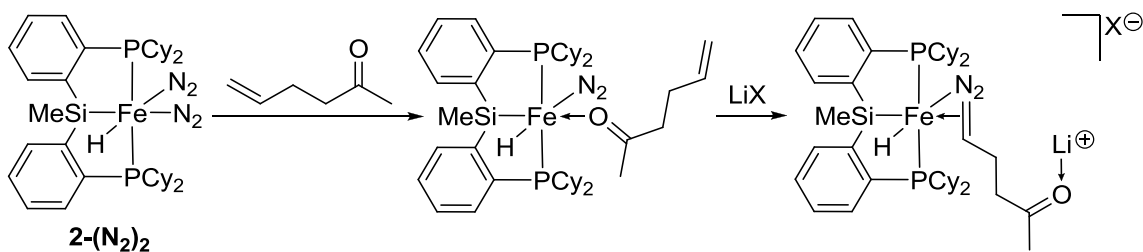


Scheme 6.2.2. (A) Proposed synthesis of crown-ether stabilized **2- Fe^0** by performing reduction of **2- PMe_3** with Na in the presence of, for example, 15-crown-5. (B) Proposed syntheses of pyridine analogues of **2- Fe^{I}** and **2- Fe^0** from **2-py**.

The activity of **2- $(\text{N}_2)_2$** toward the catalytic hydrogenation of alkenes described in Chapter 2 is competitive with the best Fe-based examples published in the literature to date, however, there is certainly room for improvement in this system. The poor activity toward the reduction of 5-hexen-2-one to 2-hexanone was proposed to be a result of competitive coordination of the ketone moiety to the metal center over H_2 , precluding the eventual reduction of the alkene portion substrate. While increasing steric bulk at the

metal center may prevent coordination of the ketone over a smaller molecule (H_2), it may also diminish overall catalytic activity, as was observed in the presence of PMe_3 , as the alkene portion of the molecule still presumably needs to coordinate to the metal center to enter the catalytic cycle.

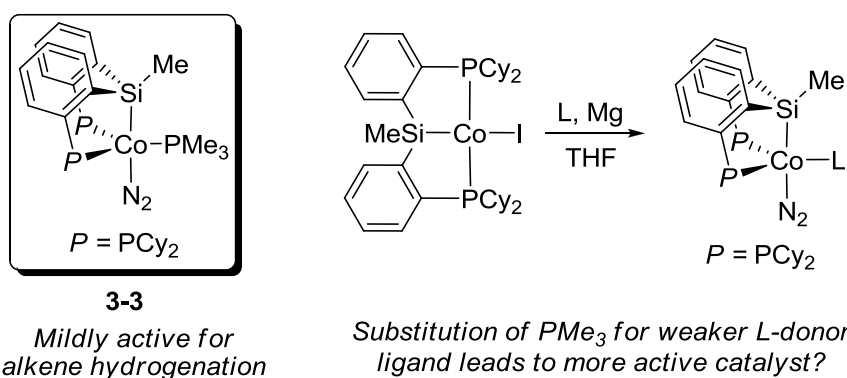
It follows that a selective disruption of carbonyl coordination to the metal center would be preferential to disrupting bonding of *all* potential ligands to the metal center, *via* an increase in steric bulk of the ligand for example. It has been previously proposed that the use of Lewis acid additives, such as Li^+ salts, can disrupt hydrogen bonding in metal formate complexes through the formation of Li-O interactions.^{15a} While the specific bonding scenario of ketones to **2-(N₂)₂** under catalytic hydrogenation conditions is currently unknown, it is possible the presence of Li^+ in solution may weaken any potential ketone-metal interaction by formation of an $\text{Li}^+\text{-O}$ interaction. The choice of counter-ion for Li^+ would need to be made judiciously, but should presumably be quite non-coordinating, as to prevent formation of perhaps less-reactive anionic Fe^{II} complexes.



Scheme 6.2.3. Proposed coordination of 5-hexen-2-one to **2-(N₂)₂** and proposed disruption of the Fe-O interaction by addition of an LiX salt.

The Co-based complex, **3-3**, was also found to be an active precatalyst for the hydrogenation of a small scope of alkenes. Thus far the role of **3-5** in the hydrogenation of alkenes is unknown, additional insight regarding this role, and the mechanism of the

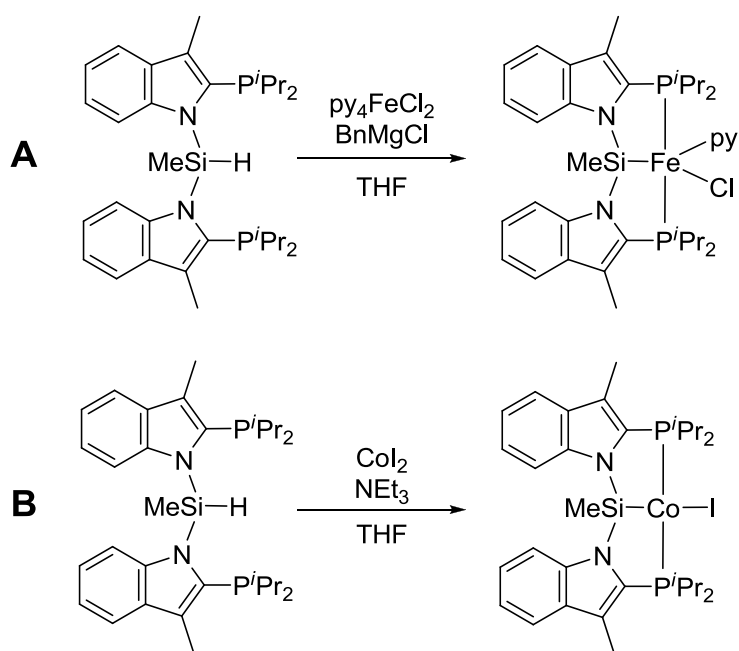
hydrogenation in general, could be obtained through a computational study. Notably, **3-3** was able to hydrogenate 5-hexen-2-one to 2-hexanone in about 73% conversion under similar conditions to that of **2-(N₂)₂**. While otherwise, the catalytic activity of **3-3** was found to be significantly reduced by comparison with **2-(N₂)₂**, it is important to note that **3-3** features PMe₃ bound to the Co center. With the dramatic increase in catalytic activity in the Fe system on moving from a PMe₃ complex to an N₂ complex, it follows that a similar strategy may be employed to design a Co-based catalyst much more active than **3-3**, and perhaps more functional-group tolerant than **2-(N₂)₂**. As **3-3** can be generated from the reduction of (Cy-PSiP)CoI with Mg in the presence of PMe₃, similar reductions could be carried out with other less-coordinating L donor ligands in place of PMe₃ (e.g. pyridine, acetonitrile, xylyl isocyanide). Hydrosilylation of unsaturated substrates using such Fe or Co complexes may also be an interesting avenue to explore, as would the introduction of chiral functionality in the PSiP ligand to investigate the potential for enantioselective reductions whether *via* hydrogenation, hydrosilylation or another route.



Scheme 6.2.4. Structure of **3-3** and proposed synthesis of other (Cy-PSiP)Co^I complexes which may be more active toward hydrogenation of alkenes than **3-3**.

Only Ni, Pd and Pt chemistry of the new ⁱPr-PSiP^{Ind} ligand has been described in Chapter 4 of this document, thus a natural step for future work involving this ligand

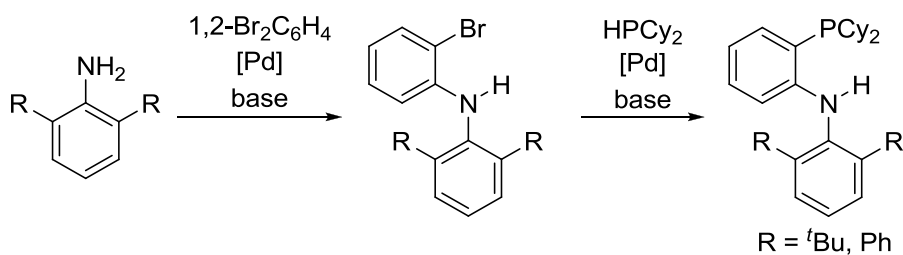
would be expanding this chemistry to other late transition metals. Of particular interest would be the group 8 and 9 first-row transition metals, Fe and Co, for which complexes of the Cy-PSiP variant of the ligand have been described in Chapters 2 and 3 of this document. Catalytic chemistry (selective CO₂ hydroboration to the formaldehyde level) unsupported by the Cy-PSiP variant of the ligand was accessible through preparation of analogous *i*Pr-PSiP^{Ind} complexes, thus a such ligand change may benefit (or of course may hinder) the alkene hydrogenation catalysis described in Chapters 2 and 3.



Scheme 6.2.5. Proposed syntheses of *i*Pr-PSiP^{Ind} complexes of Fe (A) and Co (B) based on established syntheses of Cy-PSiP analogues.

In Chapter 5 of this document, Fe and Co complexes of a new monoanionic P,N ligand were described, as were their application toward the hydrosilylation of amides to amines. As with the proposed ligand alterations to the PSiP ligand described above, it is entirely likely that optimization of steric and electronic properties of the P,N ligand will have a profound impact on the resulting catalytic activity in this context. Decreasing the steric bulk of the ligand can be detrimental, however, as was shown by Liang and co-

workers, wherein smaller variants of the P,N ligand tended to lead to the generation of bis-ligated metal complexes, particularly in the case of Zn.⁹¹ Conversely, increasing the steric bulk imparted by the ligand was met with considerable difficulty, specifically in the attempted synthesis of a di-*t*-butylphosphino variant of the P,N ligand. Increasing steric bulk on the *N* end of the ligand may prove more feasible, however, with some examples including incorporation of a 2,6-di-*t*-butylanilido group, or a *m*-terphenylamido (2,6-diphenylanilido) group (Scheme 6.2.6).

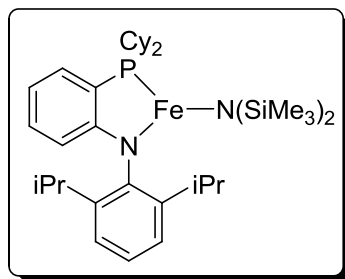


Scheme 6.2.6. General proposed synthesis for two more variants of monoanionic P,N ligand, featuring 2,6-di-*t*-butylanilido or 2,6-diphenylanilido groups.

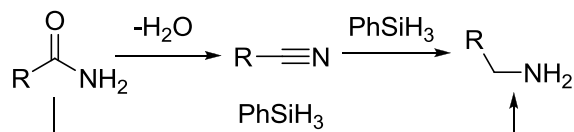
Overall, the catalytic reduction of amides is a particularly challenging reaction, however, complexes such as **5-2**, **5-8** and **5-9** may also be very active for the catalytic hydrosilylation of other carbonyl containing substrates, such as aldehydes, ketones and esters. While a number of systems describing such a reduction have already been reported, including those involving P,N-ligation,^{88a, b} there is always room for improvement, especially in the reduction of more challenging amides. Further examination of substitution on the benzene ring in the benzamide substrates could offer additional insight into the steric and electronic effects of substituents in that portion of the molecule. Additional investigation of alkyl amides and a wider range of *N*-substitution (*e.g.* with phenyl groups on *N*, or tertiary alkyl groups on *N*) would also provide useful scope for this transformation. In examining the literature, a higher degree of substitution

on the alkyl groups directly attached to *N* (e.g. isopropyl vs. methyl or benzyl) seems to have a dramatic impact on catalytic activity, as it does in the current study. Beller and co-workers,¹⁶⁹ for-example, report only 59% yield of benzyl(diisopropyl)amine from *N,N*-diisopropylbenzamide, and 50% yield of benzyl(diphenyl)amine from *N,N*-diphenylbenzamide (compared to 80-100% yields for most other substrates). Most other studies of this reactivity^{174b-d} do not typically include such substrates, focusing instead on primary alkyl substitution at *N*.

The Fe-catalyzed reduction of secondary amides continues to be a formidable challenge, as is evident by the results shown in Table 5.2.3. Few examples of secondary amide reductions catalyzed by Fe complexes appear in the literature, with only one or two such examples reported in each study.^{169, 174a, 174d} Beller and co-workers^{174e} have shown that under hydrosilylation conditions, primary amides tend to dehydrate to the corresponding nitrile, and the authors were able to devise a dual-catalyst system to facilitate this dehydration, as well a subsequent reduction of the produced nitrile to the primary amine (Scheme 6.2.7). The reactivity of Fe and Co complexes of the P,N ligand described in Chapter 5 toward primary amides remains to be examined, and may prove to be a fruitful avenue to explore. The catalytic reduction of nitriles, whether *via* the use of hydrosilanes or some other reductant (e.g. boranes, hydrogen), may also prove interesting in this context.



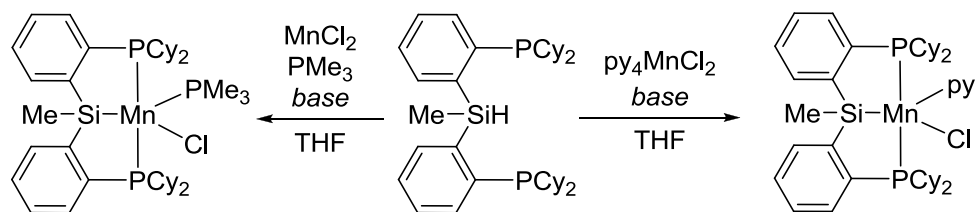
5-2



Will **5-2** and/or related complexes catalyze any of these transformations?

Scheme 6.2.7. Structure of complex **5-2** and some possible reactivity of primary amides under hydrosilylation conditions: dehydration to nitrile, hydrosilylation of amide to amine, hydrosilylation of nitrile to amine.

Chapters 2 through 5 of this document detail investigations into the chemistry of PSiP and P,N complexes of first-row transition metals of group 8, 9 and 10 (Fe, Co and Ni). Particularly in the case of PSiP pincer ligation, it would be very interesting to extend this chemistry to group 7 through the preparation of PSiP complexes of manganese. It is surprising to note that thus far there have been no (PSiP)Mn complexes reported in the literature. Si-H oxidative addition to Mn has been demonstrated,¹⁸⁴ and there have even been examples of η^2 -(SiH)¹⁸⁵ and silylene¹⁸⁶ complexes of Mn described, thus chemistry of Si with Mn has already been established. The wide range of oxidation states readily available to Mn, in addition to demonstrated success in Mn-based catalysis in conjunction with other ligand systems (*e.g.* P,N-based systems^{88b}), may lead to altogether new chemistry unsupported by the group 8, 9 and 10 transition metals. Preparation of PSiP complexes of Mn may be as simple as adapting established routes for the synthesis of, for example, **2-PMe₃** and **2-py** (Scheme 6.2.8), as both MnCl₂ and py₄MnCl₂ are readily accessible starting materials.



Scheme 6.2.8. Proposed synthesis of Mn complexes supported by PSiP pincer ligation. These routes are based on the synthesis of **2-PMe₃** and **2-py** for which the base used was BnMgCl, though other bases may be appropriate for the above reactions.

References

- [1] Hartwig, J. F. *Organotransition Metal Chemistry: From Bonding to Catalysis*, University Science Books: Sausalito, CA: **2010**.
- [2] (a) Knowles, W. S. *Angew. Chem. Int. Ed.* **2002**, *41*, 1998-2007; (b) Noyori, R. *Angew. Chem. Int. Ed.* **2002**, *41*, 2008-2022; (c) Sharpless, K. B. *Angew. Chem. Int. Ed.* **2002**, 2024-2032.
- [3] (a) Chauvin, Y. *Angew. Chem. Int. Ed.* **2006**, *45*, 3741-3747; (b) Grubbs, R. H. *Angew. Chem. Int. Ed.* **2006**, *45*, 3760-3765; (c) Schrock, R. R. *Angew. Chem. Int. Ed.* **2006**, *45*, 3748-3759.
- [4] Wu, X. F.; Anbarasan, P.; Neumann, H.; Beller, M. *Angew. Chem. Int. Ed.* **2010**, *49*, 9047-9050.
- [5] Davies, I. W.; Matty, L.; Hughes, D. L.; Reider, P. J. *J. Am. Chem. Soc.* **2001**, *123*, 10139-10140.
- [6] Bauer, I.; Knolker, H. J. *Chem. Rev.* **2015**, *115*, 3170-3387.
- [7] (a) Cammack, R. *Nature* **1999**, *397*, 214-215; (b) Manchanda, R.; Brudvig, G. W.; Crabtree, R. H. *Coord. Chem. Rev.* **1995**, *144*, 1-38.
- [8] Enthaler, S.; Junge, K.; Beller, M. *Angew. Chem. Int. Ed.* **2008**, *47*, 3317-3321.
- [9] (a) Federsel, C.; Boddien, A.; Jackstell, R.; Jennerjahn, R.; Dyson, P. J.; Scopelliti, R.; Laurenczy, G.; Beller, M. *Angew. Chem. Int. Ed.* **2010**, *49*, 9777-9780; (b) Boddien, A.; Mellmann, D.; Gärtner, F.; Jackstell, R.; Junge, H.; Dyson, P. J.; Laurenczy, G.; Ludwig, R.; Beller, M. *Science* **2011**, *333*, 1733-1736.
- [10] Friedfeld, M. R.; Shevlin, M.; Hoyt, J. M.; Krska, S. W.; Tudge, M. T.; Chirik, P. J. *Science* **2013**, *342*, 1076-1080.
- [11] Tasker, S. Z.; Standley, E. A.; Jamison, T. F. *Nature* **2014**, *509*, 299-309.
- [12] van der Vlugt, J. I. *Eur. J. Inorg. Chem.* **2012**, *2012*, 363-375.
- [13] (a) Chirik, P. J.; Wieghardt, K. *Science* **2010**, *327*, 794-796; (b) Dzik, W. I.; van der Vlugt, J. I.; Reek, J. N.; de Bruin, B. *Angew. Chem. Int. Ed.* **2011**, *50*, 3356-3358.
- [14] Zell, T.; Ben-David, Y.; Milstein, D. *Angew. Chem. Int. Ed.* **2014**, *53*, 4685-4689.

- [15] (a) Zhang, Y.; MacIntosh, A. D.; Wong, J. L.; Bielinski, E. A.; Williard, P. G.; Mercado, B. Q.; Hazari, N.; Bernskoetter, W. H. *Chem. Sci.* **2015**, *6*, 4291-4299; (b) Bielinski, E. A.; Lagaditis, P. O.; Zhang, Y.; Mercado, B. Q.; Würtele, C.; Bernskoetter, W. H.; Hazari, N.; Schneider, S. *J. Am. Chem. Soc.* **2014**, *136*, 10234-10237.
- [16] LaPierre, E. A.; Piers, W. E.; Spasyuk, D. M.; Bi, D. W. *Chem. Commun.* **2016**, *52*, 1361-1364.
- [17] Zuo, W.; Lough, A. J.; Li, Y. F.; Morris, R. H. *Science* **2013**, *342*, 1080-1083.
- [18] (a) Lin, T. P.; Peters, J. C. *J. Am. Chem. Soc.* **2013**, *135*, 15310-15313; (b) Lin, T. P.; Peters, J. C. *J. Am. Chem. Soc.* **2014**, *136*, 13672-13683.
- [19] Gossage, R. A.; McLennan, G. D.; Stobart, S. R. *Inorg. Chem.* **1996**, *35*, 1729-1732.
- [20] Brost, R. D.; Bruce, G. C.; Joslin, F. L.; Stobart, S. R. *Organometallics* **1997**, *16*, 5669-5680.
- [21] Mankad, N. P.; Whited, M. T.; Peters, J. C. *Angew. Chem. Int. Ed.* **2007**, *119*, 5870-5873.
- [22] (a) Whited, M. T.; Mankad, N. P.; Lee, Y.; Oblad, P. F.; Peters, J. C. *Inorg. Chem.* **2009**, *48*, 2507-2517; (b) Lee, Y.; Mankad, N. P.; Peters, H. M. *Nat. Chem.* **2010**, *2*, 558-565.
- [23] MacInnis, M. C.; MacLean, D. F.; Lundgren, R. J.; McDonald, R.; Turculet, L. *Organometallics* **2007**, *26*, 6522-6525.
- [24] (a) Suh, H. W.; Balcells, D.; Edwards, A. J.; Guard, L. M.; Hazari, N.; Mader, E. A.; Mercado, B. Q.; Repisky, M. *Inorg. Chem.* **2015**, *54*, 11411-11422; (b) Mitton, S. J.; McDonald, R.; Turculet, L. *Organometallics* **2009**, *28*, 5122-5136; (c) Charboneau, D. J.; Balcells, D.; Hazari, N.; Lant, H. M. C.; Mayer, J. M.; Melvin, P. R.; Mercado, B. Q.; Morris, W. D.; Repisky, M.; Suh, H.-W. *Organometallics* **2016**, *35*, 3154-3162; (d) Kim, J.; Kim, Y.; Sinha, I.; Park, K.; Kim, S. H.; Lee, Y. *Chem. Commun.* **2016**, *52*, 9367-9370.
- [25] (a) Mitton, S. J.; McDonald, R.; Turculet, L. *Angew. Chem. Int. Ed.* **2009**, *48*, 8568-8571; (b) Wu, S.; Li, X.; Xiong, Z.; Xu, W.; Lu, Y.; Sun, H. *Organometallics* **2013**, *32*, 3227-3237; (c) Takaya, J.; Iwasawa, N. *Organometallics* **2009**, *28*, 6636-6638; (d) Suh, H.-W.; Guard, L. M.; Hazari, N. *Chem. Sci.* **2014**, *5*, 3859-3872; (e) Kameo, H.; Ishii, S.; Nakazawa, H. *Dalton Trans.* **2013**, *42*, 4663; (f) Bernal, M. J.; Torres, O.; Martin, M.; Sola, E. *J. Am. Chem. Soc.* **2013**, *135*, 19008-19015.

- [26] (a) Rivada-Wheelaghan, O.; Dauth, A.; Leitus, G.; Diskin-Posner, Y.; Milstein, D. *Inorg. Chem.* **2015**, *54*, 4526-4538; (b) Langer, R.; Diskin-Posner, Y.; Leitus, G.; Shimon, L. J.; Ben-David, Y.; Milstein, D. *Angew. Chem. Int. Ed.* **2011**, *50*, 9948-9952.
- [27] Srimani, D.; Diskin-Posner, Y.; Ben-David, Y.; Milstein, D. *Angew. Chem. Int. Ed.* **2013**, *52*, 14131-14134.
- [28] (a) Langer, R.; Leitus, G.; Ben-David, Y.; Milstein, D. *Angew. Chem. Int. Ed.* **2011**, *50*, 2120-2124; (b) Bauer, G.; Kirchner, K. A. *Angew. Chem. Int. Ed.* **2011**, *50*, 5798-5800; (c) Gorgas, N.; Stöger, B.; Veiros, L. F.; Pittenauer, E.; Allmaier, G.; Kirchner, K. *Organometallics* **2014**, *33*, 6905-6914; (d) Chakraborty, S.; Lagaditis, P. O.; Förster, M.; Bielinski, E. A.; Hazari, N.; Holthausen, M. C.; Jones, W. D.; Schneider, S. *ACS Catal.* **2014**, *4*, 3994-4003; (e) Bonitatibus, P. J., Jr.; Chakraborty, S.; Doherty, M. D.; Siclován, O.; Jones, W. D.; Soloveichik, G. L. *Proc. Nat. Acad. Sci. USA* **2015**, *112*, 1687-1692.
- [29] Zell, T.; Ben-David, Y.; Milstein, D. *Catal. Sci. Tech.* **2015**, *5*, 822-826.
- [30] (a) Werkmeister, S.; Junge, K.; Wendt, B.; Alberico, E.; Jiao, H.; Baumann, W.; Junge, H.; Gallou, F.; Beller, M. *Angew. Chem. Int. Ed.* **2014**, *53*, 8722-8726; (b) Chakraborty, S.; Dai, H.; Bhattacharya, P.; Fairweather, N. T.; Gibson, M. S.; Krause, J. A.; Guan, H. *J. Am. Chem. Soc.* **2014**, *136*, 7869-7872.
- [31] Chakraborty, S.; Leitus, G.; Milstein, D. *Chem. Commun.* **2015**, *52*, 1812-1815.
- [32] Yu, R. P.; Darmon, J. M.; Hoyt, J. M.; Margulieux, G. W.; Turner, Z. R.; Chirik, P. J. *ACS Catal.* **2012**, *2*, 1760-1764.
- [33] (a) Tondreau, A. M.; Lobkovsky, E.; Chirik, P. J. *Org. Lett.* **2008**, *10*, 2789-2792; (b) Bhattacharya, P.; Krause, J. A.; Guan, H. *Organometallics* **2011**, *30*, 4720-4729; (c) Zhao, H.; Sun, H.; Li, X. *Organometallics* **2014**, *33*, 3535-3539; (d) Huang, S.; Zhao, H.; Li, X.; Wang, L.; Sun, H. *RSC Adv.* **2015**, *5*, 15660-15667.
- [34] Obligacion, J. V.; Chirik, P. J. *Org. Lett.* **2013**, *15*, 2680-2683.
- [35] Zell, T.; Butschke, B.; Ben-David, Y.; Milstein, D. *Chem. Eur. J.* **2013**, *19*, 8068-8072.
- [36] Alberico, E.; Sponholz, P.; Cordes, C.; Nielsen, M.; Drexler, H. J.; Baumann, W.; Junge, H.; Beller, M. *Angew. Chem. Int. Ed.* **2013**, *52*, 14162-14166.
- [37] Bhattacharya, P.; Krause, J. A.; Guan, H. *J. Am. Chem. Soc.* **2014**, *136*, 11153-11161.
- [38] Yang, X. *ACS Catal.* **2011**, *1*, 849-854.

- [39] Bart, S. C.; Lobkovsky, E.; Chirik, P. J. *J. Am. Chem. Soc.* **2004**, *126*, 13794-13807.
- [40] (a) Chirik, P. J. *Acc. Chem. Res.* **2015**, *48*, 1687-1695; (b) Frankel, E. N.; Emken, E. A.; Peters, H. M.; Davison, V. L.; Butterfield, R. O. *J. Org. Chem.* **1964**, *29*, 3292-3297; (c) Schroeder, M. A.; Wrighton, M. S. *J. Am. Chem. Soc.* **1976**, *98*, 551-558.
- [41] Daida, E. J.; Peters, J. C. *Inorg. Chem.* **2004**, *43*, 7474-7495.
- [42] Trovitch, R. J.; Lobkovsky, E.; Bill, E.; Chirik, P. J. *Organometallics* **2008**, *27*, 1470-1478.
- [43] Trovitch, R. J.; Lobkovsky, E.; Bouwkamp, M. W.; Chirik, P. J. *Organometallics* **2008**, *27*, 6264-6278.
- [44] (a) Russell, S. K.; Darmon, J. M.; Lobkovsky, E.; Chirik, P. J. *Inorg. Chem.* **2010**, *49*, 2782-2792; (b) Hojilla Atienza, C. C.; Tondreau, A. M.; Weller, K. J.; Lewis, K. M.; Cruse, R. W.; Nye, S. A.; Boyer, J. L.; Delis, J. G. P.; Chirik, P. J. *ACS Catal.* **2012**, *2*, 2169-2172.
- [45] (a) Monfette, S.; Turner, Z. R.; Semproni, S. P.; Chirik, P. J. *J. Am. Chem. Soc.* **2012**, *134*, 4561-4654; (b) Yu, R. P.; Darmon, J. M.; Milsman, C.; Margulieux, G. W.; Stieber, S. C.; DeBeer, S.; Chirik, P. J. *J. Am. Chem. Soc.* **2013**, *135*, 13168-13184.
- [46] Mukherjee, A.; Srimani, D.; Chakraborty, S.; Ben-David, Y.; Milstein, D. *J. Am. Chem. Soc.* **2015**, *137*, 8888-8891.
- [47] Scheuermann, M. L.; Semproni, S. P.; Pappas, I.; Chirik, P. J. *Inorg. Chem.* **2014**, *53*, 9463-9465.
- [48] Zhou, H.; Sun, H.; Zhang, S.; Li, X. *Organometallics* **2015**, *34*, 1479-1486.
- [49] (a) Obligacion, J. V.; Chirik, P. J. *J. Am. Chem. Soc.* **2013**, *135*, 19107-19110; (b) Zhang, L.; Zuo, Z.; Leng, X.; Huang, Z. *Angew. Chem. Int. Ed.* **2014**, *53*, 2696-2700.
- [50] Obligacion, J. V.; Neely, J. M.; Yazdani, A. N.; Pappas, I.; Chirik, P. J. *J. Am. Chem. Soc.* **2015**, *137*, 5855-5858.
- [51] (a) Obligacion, J. V.; Semproni, S. P.; Chirik, P. J. *J. Am. Chem. Soc.* **2014**, *136*, 4133-4136; (b) Schaefer, B. A.; Margulieux, G. W.; Small, B. L.; Chirik, P. J. *Organometallics* **2015**, *34*, 1307-1320.
- [52] Atienza, C. C.; Diao, T.; Weller, K. J.; Nye, S. A.; Lewis, K. M.; Delis, J. G.; Boyer, J. L.; Roy, A. K.; Chirik, P. J. *J. Am. Chem. Soc.* **2014**, *136*, 12108-12118.

- [53] Tokmic, K.; Markus, C. R.; Zhu, L.; Fout, A. R. *J. Am. Chem. Soc.* **2016**, *138*, 11907-11913.
- [54] Zhang, G. Q.; Scott, B. L.; Hanson, S. K. *Angew. Chem. Int. Ed.* **2012**, *51*, 12102-12106.
- [55] Zhang, G. Q.; Vasudevan, K. V.; Scott, B. L.; Hanson, S. K. *J. Am. Chem. Soc.* **2013**, *135*, 8668-8681.
- [56] Knijnenburg, Q.; Horton, A. D.; van der Heijden, H.; Kooistra, T. M.; Hetterscheid, D. G. H.; Smits, J. M. M.; de Bruin, B.; Budzelaar, P. H. M.; Gal, A. W. *J. Mol. Cat.* **2005**, *232*, 151-159.
- [57] Bianchini, C.; Mantovani, G.; Meli, A.; Migliacci, F.; Zanobini, F.; Laschi, F.; Sommazzi, A. *Eur. J. Inorg. Chem.* **2003**, 1620-1631.
- [58] (a) Zhang, J.; Medley, C. M.; Krause, J. A.; Guan, H. *Organometallics* **2010**, *29*, 6393-6401; (b) Wellala, N. P.; Guan, H. *Org. Biomol. Chem.* **2015**, *13*, 10802-10807.
- [59] Wang, Z.-X.; Wang, L. *Org. Lett.* **2007**, *9*, 4335-4338.
- [60] (a) Sun, K.; Wang, L.; Wang, Z.-X. *Organometallics* **2008**, *27*, 5649-5656; (b) Wang, Z.-X.; Wang, L. *Chem. Commun.* **2007**, *23*, 2423-2425; (c) Sun, Y.; Li, X.; Sun, H. *Dalton Trans.* **2014**, *43*, 9410; (d) Zhang, Y.; Song, G.; Ma, G.; Zhao, J.; Pan, C.-L.; Li, X. *Organometallics* **2009**, *28*, 3233-3238; (e) Sun, Y.; Li, X.; Sun, H. *Inorg. Chim. Act.* **2014**, *415*, 95-97.
- [61] Gallego, D.; Bruck, A.; Irran, E.; Meier, F.; Kaupp, M.; Driess, M.; Hartwig, J. F. *J. Am. Chem. Soc.* **2013**, *135*, 15617-15626.
- [62] (a) Tu, T.; Mao, H.; Herbert, C.; Xu, M.; Dotz, K. H. *Chem. Commun.* **2010**, *46*, 7796-7798; (b) Xu, M.; Li, X.; Sun, Z.; Tu, T. *Chem. Commun.* **2013**, *49*, 11539-11541.
- [63] Wilson, G. L.; Abraha, M.; Krause, J. A.; Guan, H. *Dalton Trans.* **2015**, *44*, 12128-12136.
- [64] Chakraborty, S.; Patel, Y. J.; Krause, J. A.; Guan, H. *Angew. Chem. Int. Ed.* **2013**, *52*, 7523-7526.
- [65] Vabre, B.; Petiot, P.; Declercq, R.; Zargarian, D. *Organometallics* **2014**, *33*, 5173-5184.
- [66] (a) Ramakrishnan, S.; Chakraborty, S.; Brennessel, W. W.; Chidsey, C. E. D.; Jones, W. D. *Chem. Sci.* **2016**, *7*, 117-127; (b) Luca, O. R.; Blakemore, J. D.; Konezny, S. J.; Praetorius, J. M.; Schmeier, T. J.; Hunsinger, G. B.; Batista, V. S.; Brudvig, G. W.; Hazari, N.; Crabtree, R. H. *Inorg. Chem.* **2012**, *51*, 8704-8709.

- [67] Rios, P.; Curado, N.; López-Serrano, J.; Rodríguez, A. *Chem. Commun.* **2015**, *52*, 2114-2117.
- [68] (a) Chakraborty, S.; Krause, J. A.; Guan, H. *Organometallics* **2009**, *28*, 582-586; (b) Kundu, S.; Brennessel, W. W.; Jones, W. D. *Inorg. Chem.* **2011**, *50*, 9443-9453.
- [69] (a) Chakraborty, S.; Zhang, J.; Krause, J. A.; Guan, H. *J. Am. Chem. Soc.* **2010**, *132*, 8872-8873; (b) Huang, F.; Zhang, C.; Jiang, J.; Wang, Z. X.; Guan, H. *Inorg. Chem.* **2011**, *50*, 3816-3825; (c) Chakraborty, S.; Patel, Y. J.; Krause, J. A.; Guan, H. *Polyhedron* **2012**, *32*, 30-34; (d) Chakraborty, S.; Zhang, J.; Patel, Y. J.; Krause, J. A.; Guan, H. *Inorg. Chem.* **2013**, *52*, 37-47.
- [70] Courtemanche, M. A.; Legare, M. A.; Maron, L.; Fontaine, F. G. *J. Am. Chem. Soc.* **2013**, *135*, 9326-9329.
- [71] Mitton, S. J.; Turculet, L. *Chem. Eur. J.* **2012**, *18*, 15258-15262.
- [72] El-Zaria, M. E.; Aarii, H.; Nakamura, H. *Inorg. Chem.* **2011**, *50*, 4149-4161.
- [73] (a) Xiong, Z.; Li, X.; Zhang, S.; Shi, Y.; Sun, H. *Organometallics* **2016**, *35*, 357-363; (b) Imayoshi, R.; Nakajima, K.; Takaya, J.; Iwasawa, N.; Nishibayashi, Y. *Eur. J. Inorg. Chem.* **2017**, *32*, 3769-3778.
- [74] MacLean, D. F.; McDonald, R.; Ferguson, M. J.; Caddell, A. J.; Turculet, L. *Chem. Commun.* **2008**, 5146-5148.
- [75] Morgan, E.; MacLean, D. F.; McDonald, R.; Turculet, L. *J. Am. Chem. Soc.* **2009**, *131*, 14234-14236.
- [76] Takaya, J.; Iwasawa, N. *Dalton Trans.* **2011**, *40*, 8814-8821.
- [77] Nova, A.; Suh, H.-W.; Schmeier, T. J.; Guard, L. M.; Eisenstein, O.; Hazari, N.; Maseras, F. *Angew. Chem. Int. Ed.* **2014**, *53*, 1103-1108.
- [78] Suh, H.-W.; Guard, L. M.; Hazari, N. *Polyhedron* **2014**, *84*, 37-43.
- [79] Suh, H.-W.; Schmeier, T. J.; Hazari, N.; Kemp, R. A.; Takase, M. K. *Organometallics* **2012**, *31*, 8225-8236.
- [80] Dixon, L. S. H.; Hill, A. F.; Sinha, A.; Ward, J. S. *Organometallics* **2014**, *33*, 653-658.
- [81] Ruddy, A. J. *PhD Thesis, Dalhousie University, Halifax, NS, Canada*, **2014**.

- [82] (a) Guiry, P. J.; Saunders, C. P. *Adv. Synth. Catal.* **2004**, *346*, 497-537; (b) Braunstein, P. *Chem. Rev.* **2006**, *106*, 134-159; (c) Liang, L. C. *Coord. Chem. Rev.* **2006**, *250*, 1152-1177; (d) Kostas, I. D. *Curr. Org. Synth.* **2008**, *5*, 227-249; (e) Zhang, W. H.; Chien, S. W.; Hor, T. S. A. *Coord. Chem. Rev.* **2011**, *255*, 1991-2024; (f) Carroll, M. P.; Guiry, P. J. *Chem. Soc. Rev.* **2014**, *43*, 819-833.
- [83] Braunstein, P.; Pietsch, J.; Chauvin, Y.; Mercier, S.; Saussine, L.; DeCian, A.; Fischer, J. *J. Chem. Soc., Dalton Trans.* **1996**, 3571-3574.
- [84] Lee, P. Y.; Liang, L. C. *Inorg. Chem.* **2008**, *47*, 749-758.
- [85] Braunstein, P.; Pietsch, J.; Chauvin, Y.; DeCian, A.; Fischer, J. *J. Organomet. Chem.* **1999**, *582*, 371-377.
- [86] (a) Braunstein, P.; Naud, F. *Angew. Chem. Int. Ed.* **2001**, *40*, 680-699; (b) Braunstein, P.; Naud, F.; Rettig, S. J. *New J. Chem.* **2001**, *25*, 32-39; (c) Speiser, F.; Braunstein, P.; Saussine, L. *Acc. Chem. Res.* **2005**, *38*, 784-793; (d) Braunstein, P.; Naud, F.; Graiff, C.; Tiripicchio, A. *Chem. Commun.* **2000**, *11*, 897-898; (e) Lapointe, A.; Guram, A.; Powers, T. S.; Jandeleit, B.; Boussie, T.; Lund, C. Substituted aminomethylphosphines, compositions and coordination complexes of same, their synthesis and processes using same. US6177528, January 23, 2001.
- [87] Baker, R. T.; Gordon, J. C.; Hamilton, C. W.; Henson, N. J.; Lin, P. H.; Maguire, S.; Murugesu, M.; Scott, B. L.; Smythe, N. C. *J. Am. Chem. Soc.* **2012**, *134*, 5598-5609.
- [88] (a) Ruddy, A. J.; Kelly, C. M.; Crawford, S. M.; Wheaton, C. A.; Sydora, O. L.; Small, B. L.; Stradiotto, M.; Turculet, L. *Organometallics* **2013**, *32*, 5581-5588; (b) Kelly, C. M.; McDonald, R.; Sydora, O. L.; Stradiotto, M.; Turculet, L. *Angew. Chem. Int. Ed.* **2017**, *56*, 15901-15904; (c) Macaulay, C. M.; Gustafson, S. J.; Fuller, J. T.; Kwon, D.-H.; Ogawa, T.; Ferguson, M. J.; McDonald, R.; Lumsden, M. D.; Bischof, S. M.; Sydora, O. L.; Ess, D. H.; Stradiotto, M.; Turculet, L. *ACS Catal.* **2018**, *8*, 9907-9925.
- [89] Ruddy, A. J.; Sydora, O. L.; Small, B. L.; Stradiotto, M.; Turculet, L. *Chem. Eur. J.* **2014**, *20*, 13918-13922.
- [90] Ogawa, T.; Ruddy, A. J.; Sydora, O. L.; Stradiotto, M.; Turculet, L. *Organometallics* **2016**, *36*, 417-423.
- [91] Liang, L.-C.; Lee, W.-Y.; Hung, C.-H. *Inorg. Chem.* **2003**, *42*, 5471-5473.
- [92] Liang, L. C.; Lee, W. Y.; Tsai, T. L.; Hsu, Y. L.; Lee, T. Y. *Dalton Trans.* **2010**, *39*, 8748-8758.
- [93] Liang, L.-C.; Huang, M.-H.; Hung, C.-H. *Inorg. Chem.* **2004**, *43*, 2166-2174.

- [94] Liang, L.-C.; Lee, W.-Y.; Yin, C.-C. *Organometallics* **2004**, *23*, 3538-3547.
- [95] Chen, M.-T.; Lee, W.-Y.; Tsai, T.-L.; Liang, L.-C. *Organometallics* **2014**, *33*, 5852-5862.
- [96] (a) MacInnis, M. C.; McDonald, R.; Ferguson, M. J.; Tobisch, S.; Turculet, L. *J. Am. Chem. Soc.* **2011**, *133*, 13622-13633; (b) Takaya, J.; Iwasawa, N. *J. Am. Chem. Soc.* **2008**, *130*, 15254-15255; (c) Whited, M. T.; Deetz, A. M.; Boerma, J. W.; DeRossa, D. E.; Janzen, D. E. *Organometallics* **2014**, *33*, 5070-5073.
- [97] (a) Handbook of Homogeneous Hydrogenation (Eds.: Wiley-VCH, Weinheim, **2007**); (b) Blaser, H. U.; Malan, C.; Pugin, B.; Spindler, F.; Steiner, H.; Studer, M. *Adv. Synth. Catal.* **2003**, *345*, 103-151.
- [98] (a) Chirik, P., In *Catalysis Without Precious Metals*, Bullock, R. M., Ed. Wiley-VCH: Weinheim, 2010; pp 83-110; (b) Junge, K.; Schroder, K.; Beller, M. *Chem. Commun.* **2011**, *47*, 4849-4859; (c) Le Bailly, B. A. F.; Thomas, S. P. *RSC Adv.* **2011**, *1*, 1435-1445.
- [99] Friedfeld, M. R.; Margulieux, G. W.; Schaefer, B. A.; Chirik, P. J. *J. Am. Chem. Soc.* **2014**, *136*, 13178-13181.
- [100] Fürstner, A. *ACS Cent. Sci.* **2016**, *2*, 778-789.
- [101] Buschelberger, P.; Gartner, D.; Reyes-Rodriguez, E.; Kreyenschmidt, F.; Koszinowski, K.; Jacobi von Wangelin, A.; Wolf, R. *Chem. Eur. J.* **2017**, *23*, 3139-3151.
- [102] Bhor, M. D.; Pandra, A. G.; Jagtap, S. R.; Bhanage, B. M. *Catal. Lett.* **2008**, *124*, 157-164.
- [103] Xu, R.; Chakraborty, S.; Bellows, S. M.; Yuan, H.; Cundari, T. R.; Jones, W. D. *ACS Catal.* **2016**, *6*, 2127-2135.
- [104] Ott, J. C.; Blasius, C. K.; Wadepohl, H.; Gade, L. H. *Inorg. Chem.* **2018**, *57*, 3183-3191.
- [105] (a) Gieshoff, T. N.; Chakraborty, U.; Villa, M.; Jacobi von Wangelin, A. *Angew. Chem. Int. Ed.* **2017**, *129*, 3639-3643; (b) Gieshoff, T. N.; Villa, M.; Welther, A.; Plois, M.; Chakraborty, U.; Wolf, R.; Jacobi von Wangelin, A. *Green Chem.* **2015**, *17*, 1408-1413.
- [106] (a) Yang, L.; Powell, D. R.; Houser, R. P. *Dalton Trans.* **2007**, 955-964; (b) Okuniewski, A.; Rosiak, D.; Chojnacki, J.; Becker, B. *Polyhedron* **2015**, *90*, 47-57.
- [107] MacInnis, M. C.; Ruddy, A. J.; McDonald, R.; Ferguson, M. J.; Turculet, L. *Dalton Trans.* **2016**, *119*, 5870-5873.

- [108] Fryzuk, M. D.; Johnson, S. A. *Coord. Chem. Rev.* **2000**, *200*, 379-409.
- [109] Lachaize, S.; Sabo-Etienne, S. *Eur. J. Inorg. Chem.* **2006**, *2006*, 2115-2127.
- [110] (a) Nikonov, G. I. *Adv. Organomet. Chem.* **2005**, *53*, 217-309; (b) Corey, J. Y. *Chem. Rev.* **2011**, *111*, 863-1071.
- [111] Corey, J. Y. *Chem. Rev.* **2016**, *116*, 11291-11435.
- [112] Thomas, C. M.; Peters, J. C. *Angew. Chem. Int. Ed.* **2006**, *45*, 776-780.
- [113] (a) Aresta, M.; Giannoccaro, P.; Rossi, M.; Saco, A. *Inorg. Chim. Act.* **1971**, *5*, 115-118; (b) Crabtree, R. H.; Hamilton, D. G. *J. Am. Chem. Soc.* **1986**, *108*, 3124-3125; (c) Vandersluys, L.; Eckert, J.; Eisenstein, O.; Hall, J. H.; Huffman, J. C.; Jackson, S. A.; Koetzle, T. F.; Kubas, G. J.; Vergamini, P. J.; Caulton, K. G. *J. Am. Chem. Soc.* **1990**, *112*, 4831-4841.
- [114] Atheaux, I.; Delpech, F.; Donnadiou, B.; Sabo-Étienne, S.; Chaudret, B.; Hussein, K.; Barthelat, J. C.; Braun, T.; Duckett, S. B.; Perutz, R. N. *Organometallics* **2002**, *21*, 5347-5357.
- [115] Kern, R. J. *J. Inorg. Nucl. Chem.* **1962**, *24*, 1105-1109.
- [116] Bain, G. A.; Berry, J. F. *J. Chem. Ed.* **2008**, *85*, 532-536.
- [117] Spek, A. L. *Acta Cryst.* **2015**, *C71*, 9-18.
- [118] Sheldrick, G. M. *Acta Cryst.* **2015**, *C71*, 3-8.
- [119] (a) Spek, A. L. *Acta Cryst.* **1990**, *A46*, C34; (b) Spek, A. L. *J. Appl. Cryst.* **2003**, *36*, 7-13.
- [120] (a) Chirik, P.; Morris, R. *Acc. Chem. Res.* **2015**, *48*, 2495; (b) Bullock, R. M. *Science* **2013**, *342*, 1054-1055; (c) Ackermann, L. *J. Org. Chem.* **2014**, *79*, 8948-8954; (d) Gao, K.; Yoshikai, N. *Acc. Chem. Res.* **2014**, *47*, 1208-1219; (e) Carney, J. R.; Dillon, B. R.; Thomas, S. P. *Eur. J. Org. Chem.* **2016**, *23*, 3912-3929; (f) Moselage, M.; Li, J.; Ackermann, L. *ACS Catal.* **2016**, *6*, 498-525; (g) Shang, R.; Ilies, L.; Nakamura, E. *Chem. Rev.* **2017**, *117*, 9086-9139; (h) Hu, Y. Y.; Zhou, B. W.; Wang, C. Y. *Acc. Chem. Res.* **2018**, *51*, 816-827.
- [121] Direct reduction of **3-2** with Mg under a CO atmosphere also afforded **3-4**, but in reduced yield by comparison with the route involving pre-treatment of **3-2** with CO.
- [122] Kent, M. A.; Woodall, C. H.; Haddow, M. F.; McMullin, C. L.; Pringle, P. G.; Wass, D. F. *Organometallics* **2014**, *33*, 5686-5692.

- [123] (a) Guard, L. M.; Hebden, T. J.; Linn, D. E.; Heinekey, D. M. *Organometallics* **2017**, *36*, 3104-3109; (b) Li, Y.; Krause, J. A.; Guan, H. *Organometallics* **2018**, *37*, 2147-2158.
- [124] Murugesan, S.; Stoger, B.; Carvalho, M. D.; Ferreira, L. P.; Pittenauer, E.; Allmaier, G.; Veiros, L. F.; Kirchner, K. *Organometallics* **2014**, *33*, 6132-6140.
- [125] (a) Fout, A. R.; Basuli, F.; Fan, H.; Tomaszewski, J.; Huffman, J. C.; Baik, M. H.; Mindiola, D. J. *Angew. Chem. Int. Ed.* **2006**, *45*, 3291-3295; (b) Ingleson, M. J.; Pink, M.; Fan, H.; Caulton, K. G. *Inorg. Chem.* **2007**, *46*, 10321-10334.
- [126] Keaton, R. J.; Blacquiere, J. M.; Baker, R. T. *J. Am. Chem. Soc.* **2007**, *129*, 1844-1845.
- [127] (a) Crabtree, R. H. *Chem. Rev.* **2016**, *116*, 8750-8769; (b) Connelly Robinson, S. J.; Heinekey, D. M. *Chem. Commun.* **2017**, *53*, 669-676.
- [128] (a) Hebden, T. J.; St John, A. J.; Gusev, D. G.; Kaminsky, W.; Goldberg, K. I.; Heinekey, D. M. *Angew. Chem. Int. Ed.* **2011**, *50*, 1873-1876; (b) Suess, D. L.; Tsay, C.; Peters, J. C. *J. Am. Chem. Soc.* **2012**, *134*, 14158-14164; (c) Vollmer, M. V.; Xie, J.; Lu, C. C. *J. Am. Chem. Soc.* **2017**, *139*, 6570-6573; (d) Gunderson, W. A.; Suess, D. L. M.; Fong, H.; Wang, X. P.; Hoffmann, C. M.; Cutsail, G. E.; Peters, J. C.; Hoffman, B. M. *J. Am. Chem. Soc.* **2014**, *136*, 14998-15009.
- [129] (a) Ingleson, M.; Fan, H. J.; Pink, M.; Tomaszewski, J.; Caulton, K. G. *J. Am. Chem. Soc.* **2006**, *128*, 1804-1805; (b) Ingleson, M. J.; Pink, M.; Fan, H.; Caulton, K. G. *J. Am. Chem. Soc.* **2008**, *130*, 4262-4276.
- [130] Morris, R. H. *Coord. Chem. Rev.* **2008**, *252*, 2381-2394.
- [131] (a) Desrosiers, P. J.; Cai, L. H.; Lin, Z. R.; Richards, R.; Halpern, J. *J. Am. Chem. Soc.* **1991**, *113*, 4173-4184; (b) Luo, X. L.; Howard, J. A. K.; Crabtree, R. H. *Mag. Res. Chem.* **1991**, *29*, S89-S93; (c) Heinekey, D. M.; vanRoon, M. *J. Am. Chem. Soc.* **1996**, *118*, 12134-12140.
- [132] (a) Maltby, P. A.; Schlaf, M.; Steinbeck, M.; Lough, A. J.; Morris, R. H.; Klooster, W. T.; Koetzle, T. F.; Srivastava, R. C. *J. Am. Chem. Soc.* **1996**, *118*, 5396-5407; (b) Grundemann, S.; Limbach, H. H.; Buntkowsky, G.; Sabo-Etienne, S.; Chaudret, B. *J. Phys. Chem. A* **1999**, *103*, 4752-4754; (c) Gelabert, R.; Moreno, M.; Lluch, J. M.; Lledos, A.; Pons, V.; Heinekey, D. M. *J. Am. Chem. Soc.* **2004**, *126*, 8813-8822.

- [133] (a) Meakin, P.; L., M. E.; Tebbe, F. N.; Jesson, J. P. *J. Am. Chem. Soc.* **1971**, *93*, 4701-4709; (b) Meakin, P.; Muetterties, E. L.; Jesson, J. P. *J. Am. Chem. Soc.* **1973**, *95*, 75-88; (c) Ball, G. E.; Mann, B. E. *Chem. Commun.* **1992**, *7*, 561-563; (d) Bakhmutov, V.; Burgi, T.; Burger, P.; Ruppli, U.; Berke, H. *Organometallics* **1994**, *13*, 4203-4213; (e) Gusev, D. G.; Kuhlman, R.; Rambo, J. R.; Berke, H.; Eisenstein, O.; Caulton, K. G. *J. Am. Chem. Soc.* **1995**, *117*, 281-292; (f) Gusev, D. G.; Berke, H. *Chem. Ber.* **1996**, *129*, 1143-1155; (g) Soubra, C.; Oishi, Y.; Albright, T. A.; Fujimoto, H. *Inorg. Chem.* **2001**, *40*, 620-627; (h) Schott, D.; Sleight, C. J.; Lowe, J. P.; Duckett, S. B.; Mawby, R. J.; Partridge, M. G. *Inorg. Chem.* **2002**, *41*, 2960-2970.
- [134] Possible η^2 -SiH-Co species can also be implicated in the mechanism for Co-H exchange in **3-5**. Unfortunately, Si-H coupling constants for **3-5** in the range of -80 - 80°C were not able to be measured. ^1H - ^{29}Si HMBC experiments revealed ^{29}Si NMR shifts of 54.9 ppm (80°C), 54.7 ppm (27°C), and 56.0 ppm (-80°C ; only one resonance observed) for **3-5**. A conceptually related example involving H_2 addition across a Co-boryl linkage has been reported by Peters: T.-P. Lin, J. C. Peters, *J. Am. Chem. Soc.* **2013**, *135*, 15310-15313. For an example of a η^1 -SiH-Co^{II} species involving a bis(phosphino)silane, see reference 24d.
- [135] (a) Li, S. H.; Hall, M. B. *Organometallics* **1999**, *18*, 5682-5687; (b) Adams, J. J.; Arulsamy, N.; Roddick, D. M. *Organometallics* **2011**, *30*, 697-708.
- [136] (a) Lin, T. P.; Peters, J. C. *J. Am. Chem. Soc.* **2013**, *135*, 15310-15313; (b) Friedfeld, M. R.; Shevlin, M.; Margulieux, G. W.; Campeau, L. C.; Chirik, P. J. *J. Am. Chem. Soc.* **2016**, *138*, 3314-3324.
- [137] (a) Punniyamurthy, T.; Velusamy, S.; Iqbal, J. *Chem. Rev.* **2005**, *105*, 2329-2363; (b) *Organometallic Oxidation Catalysis* (Eds.: Meyer, F.; Limberg, C.), Springer-Verlag, Berlin, **2007**.
- [138] (a) Bailey, C. L.; Drago, R. S. *Coord. Chem. Rev.* **1987**, *79*, 321-332; (b) Simándi, L. I., Catalytic oxidations using cobalt(II) complexes. In *Advances in Catalytic Activation of Dioxygen by Metal Complexes*, Simándi, L. I., Ed. Springer: Boston, 2003; pp 265-328.
- [139] (a) Niederhoffer, E. C.; Timmons, J. H.; Martell, A. E. *Chem. Rev.* **1984**, *84*, 137-203; (b) Jones, R. D.; Summerville, D. A.; Basolo, F. *Chem. Rev.* **1979**, *79*, 139-179; (c) Busch, D. H.; Alcock, N. W. *Chem. Rev.* **1994**, *94*, 585-623; (d) Smith, T. D.; Pilbrow, J. R. *Coord. Chem. Rev.* **1981**, *39*, 295-383.

- [140] (a) Fiedler, A. T.; Fischer, A. A. *J. Biol. Inorg. Chem.* **2017**, *22*, 407-424; (b) Hu, X. L.; Castro-Rodriguez, I.; Meyer, K. *J. Am. Chem. Soc.* **2004**, *126*, 13464-13473; (c) Egan, J. W.; Haggerty, B. S.; Rheingold, A. L.; Sendlinger, S. C.; Theopold, K. H. *J. Am. Chem. Soc.* **1990**, *112*, 2445-2446; (d) Reinaud, O. M.; Yap, G. P. A.; Rheingold, A. L.; Theopold, K. H. *Angew. Chem. Int. Ed.* **1995**, *34*, 2051-2052; (e) Reinaud, O. M.; Theopold, K. H. *J. Am. Chem. Soc.* **1994**, *116*, 6979-6980; (f) Hikichi, S.; Akita, M.; Moro-Oka, Y. *Coord. Chem. Rev.* **2000**, *198*, 61-87; (g) Dai, X. L.; Kapoor, P.; Warren, T. H. *J. Am. Chem. Soc.* **2004**, *126*, 4798-4799; (h) Jones, C.; Schulten, C.; Rose, R. P.; Stasch, A.; Aldridge, S.; Woodul, W. D.; Murray, K. S.; Moubaraki, B.; Brynda, M.; La Macchia, G.; Gagliardi, L. *Angew. Chem. Int. Ed.* **2009**, *48*, 7406-7410; (i) Larsen, P. L.; Parolin, T. J.; Powell, D. R.; Hendrich, M. P.; Borovik, A. S. *Angew. Chem. Int. Ed.* **2003**, *42*, 85-89.
- [141] (a) Schmidt, D. D.; Yoke, J. T. *J. Am. Chem. Soc.* **1971**, *93*, 637-647; (b) Heinze, K.; Huttner, G.; Zsolnai, L. *Chem. Ber.* **1997**, *130*, 1393-1403; (c) Betley, T. A.; Peters, J. C. *Inorg. Chem.* **2003**, *42*, 5074-5084; (d) Jenkins, D. M.; Di Bilio, A. J.; Allen, M. J.; Betley, T. A.; Peters, J. C. *J. Am. Chem. Soc.* **2002**, *124*, 15336-15350; (e) Fessler, M.; Eller, S.; Bachmann, C.; Gutmann, R.; Trettenbrein, B.; Kopacka, H.; Mueller, T.; Brueggeller, P. *Dalton Trans.* **2009**, *8*, 1383-1395.
- [142] Kim, J.; Park, K.; Lee, Y. *Inorg. Chim. Act.* **2017**, *460*, 55-62.
- [143] Korshin, E. E.; Leitus, G.; Shimon, L. J.; Konstantinovski, L.; Milstein, D. *Inorg. Chem.* **2008**, *47*, 7177-7189.
- [144] Lee, Y.; Seomoon, D.; Kim, S.; Han, H.; Chang, S.; Lee, P. H. *J. Org. Chem.* **2004**, *69*, 1741-1743.
- [145] Stobart, S. R.; Zhou, X.; Cea-Olivares, R.; Toscano, A. *Organometallics* **2001**, *20*, 4766-4768.
- [146] (a) Jeon, M.; Han, J.; Park, J. *ACS Catal.* **2012**, *2*, 1539-1549; (b) Matthews, S. L.; Pons, V.; Heinekey, D. M. *Inorg. Chem.* **2006**, *45*, 6453-6459; (c) Peterson, E.; Khalimon, A. Y.; Sirnionescu, R.; Kuzmina, L. G.; Howard, J. A. K.; Nikonov, G. I. *J. Am. Chem. Soc.* **2009**, *131*, 908-909; (d) Calimano, E.; Tilley, T. D. *Organometallics* **2010**, *29*, 1680-1692.
- [147] Garcia-Camprubi, A.; Martin, M.; Sola, E. *Inorg. Chem.* **2010**, *49*, 10649-10657.
- [148] (a) Safa, M.; Jennings, M. C.; Puddephatt, R. J. *Chem. Commun.* **2010**, *46*, 2811-2813; (b) Safa, M.; Jennings, M. C.; Puddephatt, R. J. *Organometallics* **2012**, *31*, 3539-3550.

- [149] (a) Holze, P.; Corona, T.; Frank, N.; Braun-Cula, B.; Herwig, C.; Company, A.; Limberg, C. *Angew. Chem. Int. Ed.* **2017**, *129*, 2347-2351; (b) Grapperhaus, C. A.; Darensbourg, M. Y. *Acc. Chem. Res.* **1998**, *31*, 451-459; (c) Kieber-Emmons, M.; Riordan, C. G. *Acc. Chem. Res.* **2007**, *40*, 618-625; (d) Otsuka, S.; Nakamura, A.; Tatsuno, Y. *J. Am. Chem. Soc.* **1969**, *91*, 6994-6999.
- [150] (a) Gall, R. S.; Rogers, J. F.; Schaefer, W. P.; Christoph, G. G. *J. Am. Chem. Soc.* **1976**, *98*, 5135-5144; (b) Schaefer, W. P.; Marsh, R. E. *J. Am. Chem. Soc.* **1966**, *88*, 178-179.
- [151] Poverenov, E.; Efremenko, I.; Frenkel, A. I.; Ben-David, Y.; Shimon, L. J. W.; Leitun, G.; Konstantinovski, L.; Martin, J. M. L.; Milstein, D. *Nature* **2008**, *455*, 1093-1096.
- [152] (a) Verat, A. Y.; Fan, H.; Pink, M.; Chen, Y. S.; Caulton, K. G. *Chem. Eur. J.* **2008**, *14*, 7680-7686; (b) Tsvetkov, N. P.; Andino, J. G.; Fan, H.; Verat, A. Y.; Caulton, K. G. *Dalton Trans.* **2013**, *42*, 6745-6755.
- [153] LaPierre, E. A.; Clapson, M. L.; Piers, W. E.; Maron, L.; Spasyuk, D. M.; Gendy, C. *Inorg. Chem.* **2018**, *57*, 495-506.
- [154] (a) Ray, K.; Heims, F.; Pfaff, F. F. *Eur. J. Inorg. Chem.* **2013**, *22-23*, 3784-3807; (b) Wang, B.; Lee, Y. M.; Tcho, W. Y.; Tussupbayev, S.; Kim, S. T.; Kim, Y.; Seo, M. S.; Cho, K. B.; Dede, Y.; Keegan, B. C.; Ogura, T.; Kim, S. H.; Ohta, T.; Baik, M. H.; Ray, K.; Shearer, J.; Nam, W. *Nat. Commun.* **2017**, *8*, 14839; (c) Nguyen, A. I.; Hadt, R. G.; Solomon, E. I.; Tilley, T. D. *Chem. Sci.* **2014**, *5*, 2874-2878.
- [155] Aresta, M., Ed. *Carbon Dioxide as Chemical Feedstock*; Wiley-VCH: Weinheim, Germany, **2010**.
- [156] (a) Braunstein, P.; Matt, D.; Nobel, D. *Chem. Rev.* **1988**, *88*, 747-764; (b) Leitner, W. *Angew. Chem. Int. Ed.* **1995**, *34*, 2207-2221; (c) Jessop, P. G.; Ikariya, T.; Noyori, R. *Chem. Rev.* **1995**, *95*, 259-272; (d) Sakakura, T.; Choi, J.-C.; Yasuda, H. *Chem. Rev.* **2007**, *107*, 2365-2387; (e) Cokoja, M.; Bruckmeier, C.; Rieger, B.; Herrmann, W. A.; Kuhn, F. E. *Angew. Chem. Int. Ed.* **2011**, *50*, 8510-8537.
- [157] Chong, C. C.; Kinjo, R. *ACS Catal.* **2015**, *5*, 3238-3259.
- [158] Shintani, R.; Nozaki, K. *Organometallics* **2013**, *32*, 2459-2462.
- [159] (a) Sgro, M. J.; Stephan, D. W. *Angew. Chem. Int. Ed.* **2012**, *51*, 11343-11345; (b) Anker, M. D.; Arrowsmith, M.; Bellham, P.; Hill, M. S.; Kociok-Köhn, G.; Liptrot, D. J.; Mahon, M. F.; Weetman, C. *Chem. Sci.* **2014**, *5*, 2826-2830; (c) Wang, T.; Stephan, D. W. *Chem. Commun.* **2014**, *50*, 7007-7010; (d) Pal, R.; Groy, T. L.; Trovitch, R. J. *Inorg. Chem.* **2015**, *54*, 7506-7515.

- [160] (a) Bontemps, S.; Vendier, L.; Sabo-Etienne, S. *Angew. Chem. Int. Ed.* **2012**, *51*, 1671-1674; (b) Bontemps, S.; Sabo-Etienne, S. *Angew. Chem. Int. Ed.* **2013**, *52*, 10253-10255; (c) Bontemps, S.; Vendier, L.; Sabo-Etienne, S. *J. Am. Chem. Soc.* **2014**, *136*, 4419-4425; (d) Jin, G.; Werncke, C. G.; Escudie, Y.; Sabo-Etienne, S.; Bontemps, S. *J. Am. Chem. Soc.* **2015**, *137*, 9563-9566.
- [161] (a) Matsuo, T.; Kawaguchi, H. *J. Am. Chem. Soc.* **2006**, *128*, 12362-12363; (b) Berkefeld, A.; Piers, W. E.; Parvez, M. *J. Am. Chem. Soc.* **2010**, *132*, 10660-10661; (c) Berkefeld, A.; Piers, W. E.; Parvez, M.; Castro, L.; Maron, L.; Eisenstein, O. *Chem. Sci.* **2013**, *4*, 2152; (d) Lu, Z.; Hausmann, H.; Becker, S.; Wegner, H. A. *J. Am. Chem. Soc.* **2015**, *137*, 5332-5335.
- [162] (a) Wang, Z. C.; Dietl, N.; Kretschmer, R.; Ma, J. B.; Weiske, T.; Schlangen, M.; Schwarz, H. *Angew. Chem. Int. Ed.* **2012**, *51*, 3703-3707; (b) Heim, L. E.; Konnerth, H.; Pechtl, M. H. G. *Green Chem.* **2017**, *19*, 2347-2355.
- [163] Murphy, L. J.; Hollenhorst, H.; McDonald, R.; Ferguson, M.; Lumsden, M. D.; Turculet, L. *Organometallics* **2017**, *36*, 3709-3720.
- [164] Wassenaar, J.; Reek, J. N. *Dalton Trans.* **2007**, *34*, 3750-3753.
- [165] (a) Tanaka, R.; Yamashita, M.; Nozaki, K. *J. Am. Chem. Soc.* **2009**, *131*, 14168-14169; (b) Fong, H.; Peters, J. C. *Inorg. Chem.* **2015**, *54*, 5124-5135.
- [166] Miller, A. J.; Heinekey, D. M.; Mayer, J. M.; Goldberg, K. I. *Angew. Chem. Int. Ed.* **2013**, *52*, 3981-3984.
- [167] Kozminski, W.; Nanz, D. *J. Mag. Res.* **1997**, *124*, 383-392.
- [168] Payet, E.; Auffrant, A.; Le Goff, X. F.; Floch, P. L. *J. Organomet. Chem.* **2010**, *695*, 1499-1506.
- [169] Zhou, S.; Junge, K.; Addis, D.; Das, S.; Beller, M. *Angew. Chem. Int. Ed.* **2009**, *48*, 9507-9510.
- [170] Papa, V.; Cabrero-Antonino, J. R.; Alberico, E.; Spanneberg, A.; Junge, K.; Junge, H.; Beller, M. *Chem. Sci.* **2017**, *8*, 3576-3585.
- [171] Simmons, B. J.; Hoffmann, M.; Hwang, J.; Jackl, M. K.; Garg, N. K. *Org. Lett.* **2017**, *19*, 1910-1913.
- [172] Das, S.; Join, B.; Junge, K.; Beller, M. *Chem. Commun.* **2012**, *48*, 2683-2685.
- [173] (a) Das, S.; Addis, D.; Zhou, S.; Junge, K.; Beller, M. *J. Am. Chem. Soc.* **2010**, *132*, 1770-1771; (b) Das, S.; Addis, D.; Junge, K.; Beller, M. *Chem. Eur. J.* **2011**, *17*, 12186-12192; (c) Kovalenko, O. O.; Volkov, A.; Adolfsson, H. *Org. Lett.* **2015**, *17*, 446-449.

- [174] (a) Bézier, D.; Venkanna, G. T.; Sortais, J.-B.; Darcel, C. *ChemCatChem* **2011**, *3*, 1747-1750; (b) Volkov, A.; Buitrago, E.; Adolfsson, H. *Eur. J. Org. Chem.* **2013**, *2013*, 2066-2070; (c) Sunada, Y.; Kawakami, H.; Imaoka, T.; Motoyama, Y.; Nagashima, H. *Angew. Chem. Int. Ed.* **2009**, *48*, 9511-9514; (d) Tsutsumi, H.; Sunada, Y.; Nagashima, H. *Chem. Commun.* **2011**, *47*, 6581-6583; (e) Das, S.; Wendt, B.; Moller, K.; Junge, K.; Beller, M. *Angew. Chem. Int. Ed.* **2012**, *51*, 1662-1666.
- [175] (a) Aluri, B. R.; Kindermann, M. K.; Jones, P. G.; Heinicke, J. *Inorg. Chem.* **2008**, *47*, 6900-6912; (b) Wheaton, C. A.; Bow, J.-P. J.; Stradiotto, M. *Organometallics* **2013**, *32*, 6148-6161.
- [176] Hein, N. M.; Suzuki, T.; Ogawa, T.; Fryzuk, M. D. *Dalton Trans.* **2016**, *45*, 14697-14708.
- [177] (a) Wolf, R.; Schnoekelborg, E.-M. *Chem. Commun.* **2010**, *46*, 2832-2834; (b) Schnoekelborg, E.-M.; Khusniyarov, M. M.; de Bruin, B.; Hartl, F.; Langer, T.; Eul, M.; Schulz, S.; Poettgen, R.; Wolf, R. *Inorg. Chem.* **2012**, *51*, 6719-6730.
- [178] Bart, S. C.; Hawrelka, E. J.; Schmisser, A. K.; Lobkovsky, E.; Chirik, P. J. *Organometallics* **2004**, *23*, 237-246.
- [179] Klein, H.-F.; Beck, R.; Flörke, U.; Haupt, H.-J. *Eur. J. Inorg. Chem.* **2003**, 240-248.
- [180] (a) Igarashi, M.; Fuchikami, T. *Tetrahedron Lett.* **2001**, *42*, 1945-1947; (b) Das, S.; Zhou, S.; Addis, D.; Enthaler, S.; Junge, K.; Beller, M. *Top. Catal.* **2010**, *53*, 979-984.
- [181] (a) Hanada, S.; Tsutsumi, E.; Motoyama, Y.; Nagashima, H. *J. Am. Chem. Soc.* **2009**, *2009*, 15032-15040; (b) Hanada, S.; Ishida, T.; Motoyama, Y.; Nagashima, H. *J. Org. Chem.* **2007**, *72*, 7551-7559.
- [182] Kameo, H.; Kawamoto, T.; Sakaki, S.; Bourissou, D.; Nakazawa, H. *Chem. Eur. J.* **2016**, *22*, 2370-2375.
- [183] Kameo, H.; Ikeda, K.; Sakaki, S.; Takemoto, S.; Nakazawa, H.; Matsuzaka, H. *Dalton Trans.* **2016**, *45*, 7570-7580.
- [184] Sun, J.; Lu, R. S.; Bau, R.; Yang, G. K. *Organometallics* **1994**, *13*, 1317-1325.
- [185] (a) Komuro, T.; Okawara, S.; Furuyama, K.; Tobita, H. *Chem. Lett.* **2012**, *41*, 774-776; (b) Valyaev, D. A.; Wei, D.; Elangovan, S.; Cavailles, M.; Dorcet, V.; Sortais, J.-B.; Darcel, C.; Lukan, N. *Organometallics* **2016**, *35*, 4090-4098.
- [186] Price, J. S.; Emslie, D. J. H.; Britten, J. F. *Angew. Chem. Int. Ed.* **2017**, *56*, 6223-6227.

Appendix A: Crystallographic Experimental Details

Table A1. Crystallographic experimental details for **2-Br**.

| | |
|--|--|
| <i>A. Crystal Data</i> | |
| formula | C ₃₇ H ₅₅ BrFeP ₂ Si |
| formula weight | 725.60 |
| crystal dimensions (mm) | 0.32 × 0.09 × 0.07 |
| crystal system | monoclinic |
| space group | <i>P</i> 2 ₁ / <i>n</i> (an alternate setting of <i>P</i> 2 ₁ / <i>c</i> [No. 14]) |
| unit cell parameters ^a | |
| <i>a</i> (Å) | 9.1762(2) |
| <i>b</i> (Å) | 37.6544(8) |
| <i>c</i> (Å) | 11.2992(2) |
| β (deg) | 112.6803(11) |
| <i>V</i> (Å ³) | 3602.24(13) |
| <i>Z</i> | 4 |
| ρ _{calcd} (g cm ⁻³) | 1.338 |
| μ (mm ⁻¹) | 5.984 |
| <i>B. Data Collection and Refinement Conditions</i> | |
| diffractometer | Bruker D8/APEX II CCD ^b |
| radiation (λ [Å]) | Cu Kα (1.54178) (microfocus source) |
| temperature (°C) | -100 |
| scan type | ω and φ scans (1.0°) (10 s exposures) |
| data collection 2θ limit (deg) | 148.38 |
| total data collected | 109525 (-11 ≤ <i>h</i> ≤ 11, -45 ≤ <i>k</i> ≤ 46, -14 ≤ <i>l</i> ≤ 13) |
| independent reflections | 7358 (<i>R</i> _{int} = 0.0911) |
| number of observed reflections (<i>NO</i>) | 6086 [<i>F</i> _o ² ≥ 2σ(<i>F</i> _o ²)] |
| structure solution method | Patterson/structure expansion (<i>DIRDIF</i> - <i>2008</i> ^c) |
| refinement method | full-matrix least-squares on <i>F</i> ² (<i>SHELXL</i> - <i>2014</i> ^d) |
| absorption correction method | multi-scan (<i>TWINABS</i>) |
| range of transmission factors | 0.7488–0.3897 |
| data/restraints/parameters | 7358 / 0 / 430 |
| goodness-of-fit (<i>S</i>) ^e [all data] | 1.052 |
| final <i>R</i> indices ^f | |
| <i>R</i> ₁ [<i>F</i> _o ² ≥ 2σ(<i>F</i> _o ²)] | 0.0497 |
| <i>wR</i> ₂ [all data] | 0.1235 |
| largest difference peak and hole | 0.500 and -0.448 e Å ⁻³ |

(continued)

Table A1. Crystallographic experimental details for **2-Br** (continued).

^aObtained from least-squares refinement of 9924 reflections with $4.70^\circ < 2\theta < 146.82^\circ$.

^bPrograms for diffractometer operation, data collection, data reduction and absorption correction were those supplied by Bruker. The crystal used for data collection was found to display non-merohedral twinning. Both components of the twin were indexed with the program *CELL_NOW* (Bruker AXS Inc., Madison, WI, 2004). The second twin component can be related to the first component by 3.8° rotation about the $[1 \ 1/5 \ -1/2]$ axis in real space and about the $[3/8 \ 1 \ -3/8]$ axis in reciprocal space. Integrated intensities for the reflections from the two components were written into a *SHELXL-2014* HKLF 5 reflection file with the data integration program *SAINT* (version 8.34A), using all reflection data (exactly overlapped, partially overlapped and non-overlapped). The refined value of the twin fraction (*SHELXL-2014* BASF parameter) was 0.387(2).

^cBeurskens, P. T.; Beurskens, G.; de Gelder, R.; Smits, J. M. M.; Garcia-Granda, S.; Gould, R. O. (2008). The *DIRDIF-2008* program system. Crystallography Laboratory, Radboud University Nijmegen, The Netherlands.

^dSheldrick, G. M. *Acta Crystallogr.* **2015**, *C71*, 3–8.

^e $S = [\sum w(F_o^2 - F_c^2)^2 / (n - p)]^{1/2}$ (n = number of data; p = number of parameters varied; $w = [\sigma^2(F_o^2) + (0.0600P)^2 + 1.9473P]^{-1}$ where $P = [\text{Max}(F_o^2, 0) + 2F_c^2]/3$).

^f $R_1 = \sum ||F_o| - |F_c|| / \sum |F_o|$; $wR_2 = [\sum w(F_o^2 - F_c^2)^2 / \sum w(F_o^4)]^{1/2}$.

Table A2. Crystallographic experimental details for **2-Cl**.

| | |
|--|---|
| <i>A. Crystal Data</i> | |
| formula | C ₃₉ H ₆₀ Cl ₂ FeO _{0.50} P ₂ Si |
| formula weight | 753.65 |
| crystal dimensions (mm) | 0.33 × 0.24 × 0.18 |
| crystal system | monoclinic |
| space group | <i>I</i> 2/ <i>a</i> (an alternate setting of <i>C</i> 2/ <i>c</i> [No. 15]) |
| unit cell parameters ^a | |
| <i>a</i> (Å) | 19.1796 (9) |
| <i>b</i> (Å) | 15.2238 (7) |
| <i>c</i> (Å) | 29.0757 (14) |
| β (deg) | 93.5781 (6) |
| <i>V</i> (Å ³) | 8473.2 (7) |
| <i>Z</i> | 8 |
| ρ_{calcd} (g cm ⁻³) | 1.182 |
| μ (mm ⁻¹) | 0.612 |
| <i>B. Data Collection and Refinement Conditions</i> | |
| diffractometer | Bruker PLATFORM/APEX II CCD ^b |
| radiation (λ [Å]) | graphite-monochromated Mo K α (0.71073) |
| temperature (°C) | -80 |
| scan type | ω scans (0.3°) (15 s exposures) |
| data collection 2θ limit (deg) | 54.05 |
| total data collected | 34395 ($-24 \leq h \leq 24$, $-19 \leq k \leq 19$, $-36 \leq l \leq 36$) |
| independent reflections | 9026 ($R_{\text{int}} = 0.0342$) |
| number of observed reflections (<i>NO</i>) | 7379 [$F_o^2 \geq 2\sigma(F_o^2)$] |
| structure solution method | intrinsic phasing (<i>SHELXT-2014</i> ^c) |
| refinement method | full-matrix least-squares on F^2 (<i>SHELXL-2014</i> ^{d,e}) |
| absorption correction method | Gaussian integration (face-indexed) |
| range of transmission factors | 0.9548–0.8969 |
| data/restraints/parameters | 9026 / 0 / 389 |
| goodness-of-fit (<i>S</i>) ^f [all data] | 1.041 |
| final <i>R</i> indices ^g | |
| R_1 [$F_o^2 \geq 2\sigma(F_o^2)$] | 0.0411 |
| wR_2 [all data] | 0.1164 |
| largest difference peak and hole | 0.523 and -0.321 e Å ⁻³ |

^aObtained from least-squares refinement of 9897 reflections with $4.34^\circ < 2\theta < 52.54^\circ$.

^bPrograms for diffractometer operation, data collection, data reduction and absorption correction were those supplied by Bruker.

(continued)

Table A2. Crystallographic experimental details for **2-Cl** (continued)

^cSheldrick, G. M. *Acta Crystallogr.* **2015**, *A71*, 3–8. (*SHELXT-2014*)

^dSheldrick, G. M. *Acta Crystallogr.* **2015**, *C71*, 3–8. (*SHELXL-2014*)

^eAttempts to refine peaks of residual electron density as disordered or partial-occupancy solvent diethylether oxygen or carbon atoms were unsuccessful. The data were corrected for disordered electron density through use of the SQUEEZE procedure as implemented in *PLATON* (Spek, A. L. *Acta Crystallogr.* **2015**, *C71*, 9–18. *PLATON* - a multipurpose crystallographic tool. Utrecht University, Utrecht, The Netherlands). A total solvent-accessible void volume of 1576 Å³ with a total electron count of 155 (consistent with 4 molecules of solvent diethylether, or 0.5 molecules per formula unit of the iron complex molecule) was found in the unit cell.

$$fS = [\sum w(F_o^2 - F_c^2)^2 / (n - p)]^{1/2} \quad (n = \text{number of data}; p = \text{number of parameters varied}; w = [\sigma^2(F_o^2) + (0.0606P)^2 + 6.5267P]^{-1} \text{ where } P = [\text{Max}(F_o^2, 0) + 2F_c^2] / 3).$$

$$gR_1 = \sum ||F_o| - |F_c|| / \sum |F_o|; wR_2 = [\sum w(F_o^2 - F_c^2)^2 / \sum w(F_o^4)]^{1/2}.$$

Table A3. Crystallographic experimental details for **2-Me**.*A. Crystal Data*

| | |
|---|---|
| formula | C ₃₉ H ₆₁ FeP ₂ Si |
| formula weight | 675.75 |
| crystal dimensions (mm) | 0.40 × 0.17 × 0.03 |
| crystal system | triclinic |
| space group | $P\bar{1}$ (No. 2) |
| unit cell parameters ^a | |
| <i>a</i> (Å) | 13.9353(2) |
| <i>b</i> (Å) | 16.5822(3) |
| <i>c</i> (Å) | 16.9689(3) |
| α (deg) | 106.5119(11) |
| β (deg) | 100.0125(12) |
| γ (deg) | 90.5822(11) |
| <i>V</i> (Å ³) | 3694.80(11) |
| <i>Z</i> | 4 |
| ρ_{calcd} (g cm ⁻³) | 1.215 |
| μ (mm ⁻¹) | 4.577 |

B. Data Collection and Refinement Conditions

| | |
|---|--|
| diffractometer | Bruker D8/APEX II CCD ^b |
| radiation (λ [Å]) | Cu K α (1.54178) (microfocus source) |
| temperature (°C) | -100 |
| scan type | ω and ϕ scans (1.0°) (10 s exposures) |
| data collection 2θ limit (deg) | 148.30 |
| total data collected | 90427 ($-17 \leq h \leq 17$, $-20 \leq k \leq 20$, $-21 \leq l \leq 21$) |
| independent reflections | 14034 ($R_{\text{int}} = 0.0936$) |
| number of observed reflections (<i>NO</i>) | 10195 [$F_o^2 \geq 2\sigma(F_o^2)$] |
| structure solution method | Patterson/structure expansion (<i>DIRDIF-2008</i> ^c) |
| refinement method | full-matrix least-squares on F^2 (<i>SHELXL-2014</i> ^d) |
| absorption correction method | multi-scan (<i>TWINABS</i>) |
| range of transmission factors | 0.9127–0.5665 |
| data/restraints/parameters | 14034 / 0 / 782 |
| goodness-of-fit (<i>S</i>) ^e [all data] | 1.030 |
| final <i>R</i> indices ^f | |
| <i>R</i> ₁ [$F_o^2 \geq 2\sigma(F_o^2)$] | 0.0530 |
| <i>wR</i> ₂ [all data] | 0.1353 |
| largest difference peak and hole | 0.660 and -0.642 e Å ⁻³ |

^aObtained from least-squares refinement of 9891 reflections with $5.52^\circ < 2\theta < 148.24^\circ$.
(continued)

Table A3. Crystallographic experimental details for **2-Me** (continued).

^bPrograms for diffractometer operation, data collection, data reduction and absorption correction were those supplied by Bruker. The crystal used for data collection was found to display non-merohedral twinning. Both components of the twin were indexed with the program *CELL_NOW* (Bruker AXS Inc., Madison, WI, 2004). The second twin component can be related to the first component by 180° rotation about the $[1 \ 1/4 \ 3/4]$ axis in real space and about the $[1 \ 0 \ 1]$ axis in reciprocal space. Integrated intensities for the reflections from the two components were written into a *SHELXL-2014* HKLF 5 reflection file with the data integration program *SAINT* (version 8.34A), using all reflection data (exactly overlapped, partially overlapped and non-overlapped). The refined value of the twin fraction (*SHELXL-2014* BASF parameter) was 0.4740(12).

^cBeurskens, P. T.; Beurskens, G.; de Gelder, R.; Smits, J. M. M.; Garcia-Granda, S.; Gould, R. O. (2008). The *DIRDIF-2008* program system. Crystallography Laboratory, Radboud University Nijmegen, The Netherlands.

^dSheldrick, G. M. *Acta Crystallogr.* **2015**, *C71*, 3–8.

^e $S = [\sum w(F_o^2 - F_c^2)^2 / (n - p)]^{1/2}$ (n = number of data; p = number of parameters varied; $w = [\sigma^2(F_o^2) + (0.0706P)^2 + 0.4414P]^{-1}$ where $P = [\text{Max}(F_o^2, 0) + 2F_c^2]/3$).

^f $R_1 = \sum ||F_o| - |F_c|| / \sum |F_o|$; $wR_2 = [\sum w(F_o^2 - F_c^2)^2 / \sum w(F_o^4)]^{1/2}$.

Table A4. Crystallographic experimental details for **2-PMe₃***A. Crystal Data*

| | |
|--|--|
| formula | C ₄₀ H ₆₄ ClFeP ₃ Si |
| formula weight | 757.21 |
| crystal dimensions (mm) | 0.25 × 0.14 × 0.10 |
| crystal system | monoclinic |
| space group | <i>P</i> 2 ₁ / <i>n</i> (an alternate setting of <i>P</i> 2 ₁ / <i>c</i> [No. 14]) |
| unit cell parameters ^a | |
| <i>a</i> (Å) | 18.7104(3) |
| <i>b</i> (Å) | 20.1249(3) |
| <i>c</i> (Å) | 21.7808(3) |
| β (deg) | 96.2008(6) |
| <i>V</i> (Å ³) | 8153.5(2) |
| <i>Z</i> | 8 |
| ρ _{calcd} (g cm ⁻³) | 1.234 |
| μ (mm ⁻¹) | 5.150 |

B. Data Collection and Refinement Conditions

| | |
|--|---|
| diffractometer | Bruker D8/APEX II CCD ^b |
| radiation (λ [Å]) | Cu Kα (1.54178) (microfocus source) |
| temperature (°C) | -100 |
| scan type | ω and φ scans (1.0°) (5 s exposures) |
| data collection 2θ limit (deg) | 148.22 |
| total data collected | 57453 (-23 ≤ <i>h</i> ≤ 23, -24 ≤ <i>k</i> ≤ 23, -27 ≤ <i>l</i> ≤ 27) |
| independent reflections | 16534 (<i>R</i> _{int} = 0.0327) |
| number of observed reflections (<i>NO</i>) | 14228 [<i>F</i> _o ² ≥ 2σ(<i>F</i> _o ²)] |
| structure solution method | Patterson/structure expansion (<i>DIRDIF</i> - <i>2008</i> ^c) |
| refinement method | full-matrix least-squares on <i>F</i> ² (<i>SHELXL</i> - <i>2014</i> ^d) |
| absorption correction method | Gaussian integration (face-indexed) |
| range of transmission factors | 0.6800–0.4229 |
| data/restraints/parameters | 16534 / 0 / 837 |
| goodness-of-fit (<i>S</i>) ^e [all data] | 1.051 |
| final <i>R</i> indices ^f | |
| <i>R</i> ₁ [<i>F</i> _o ² ≥ 2σ(<i>F</i> _o ²)] | 0.0387 |
| <i>wR</i> ₂ [all data] | 0.1072 |
| largest difference peak and hole | 2.084 and -0.856 e Å ⁻³ |

^aObtained from least-squares refinement of 9853 reflections with 5.92° < 2θ < 147.28°.

^bPrograms for diffractometer operation, data collection, data reduction and absorption correction were those supplied by Bruker.

(continued)

Table A4. Crystallographic experimental details for **2-PMe₃** (continued).

^cBeurskens, P. T.; Beurskens, G.; de Gelder, R.; Smits, J. M. M.; Garcia-Granda, S.; Gould, R. O. (2008). The *DIRDIF-2008* program system. Crystallography Laboratory, Radboud University Nijmegen, The Netherlands.

^dSheldrick, G. M. *Acta Crystallogr.* **2015**, *C71*, 3–8.

^e $S = [\sum w(F_o^2 - F_c^2)^2 / (n - p)]^{1/2}$ (n = number of data; p = number of parameters varied; $w = [\sigma^2(F_o^2) + (0.0502P)^2 + 6.3118P]^{-1}$ where $P = [\text{Max}(F_o^2, 0) + 2F_c^2]/3$).

^f $R_1 = \sum ||F_o| - |F_c|| / \sum |F_o|$; $wR_2 = [\sum w(F_o^2 - F_c^2)^2 / \sum w(F_o^4)]^{1/2}$.

Table A5. Crystallographic experimental details for **2-(CO)₂**.*A. Crystal Data*

| | |
|---|--|
| formula | C ₄₁ H ₆₀ ClFeO _{2.5} P ₂ Si |
| formula weight | 774.22 |
| crystal dimensions (mm) | 0.23 × 0.23 × 0.17 |
| crystal system | triclinic |
| space group | <i>P</i> $\bar{1}$ (No. 2) |
| unit cell parameters ^a | |
| <i>a</i> (Å) | 12.5495(2) |
| <i>b</i> (Å) | 18.1371(3) |
| <i>c</i> (Å) | 18.5396(3) |
| α (deg) | 70.1674(6) |
| β (deg) | 87.4571(7) |
| γ (deg) | 87.4461(7) |
| <i>V</i> (Å ³) | 3963.68(11) |
| <i>Z</i> | 4 |
| ρ_{calcd} (g cm ⁻³) | 1.297 |
| μ (mm ⁻¹) | 4.991 |
| <i>B. Data Collection and Refinement Conditions</i> | |
| diffractometer | Bruker D8/APEX II CCD ^b |
| radiation (λ [Å]) | Cu K α (1.54178) (microfocus source) |
| temperature (°C) | -100 |
| scan type | ω and ϕ scans (1.0°) (5 s exposures) |
| data collection 2θ limit (deg) | 148.26 |
| total data collected | 28521 ($-14 \leq h \leq 15$, $-22 \leq k \leq 22$, $-23 \leq l \leq 23$) |
| independent reflections | 15457 ($R_{\text{int}} = 0.0212$) |
| number of observed reflections (<i>NO</i>) | 14165 [$F_o^2 \geq 2\sigma(F_o^2)$] |
| structure solution method | intrinsic phasing (<i>SHELXT-2014^c</i>) |
| refinement method | full-matrix least-squares on F^2 (<i>SHELXL-2014^d</i>) |
| absorption correction method | Gaussian integration (face-indexed) |
| range of transmission factors | 0.6008–0.3875 |
| data/restraints/parameters | 15457 / 0 / 863 |
| goodness-of-fit (<i>S</i>) ^e [all data] | 1.047 |
| final <i>R</i> indices ^f | |
| <i>R</i> ₁ [$F_o^2 \geq 2\sigma(F_o^2)$] | 0.0288 |
| <i>wR</i> ₂ [all data] | 0.0774 |
| largest difference peak and hole | 0.554 and -0.497 e Å ⁻³ |

^aObtained from least-squares refinement of 9865 reflections with $5.90^\circ < 2\theta < 147.46^\circ$.

(continued)

Table A5. Crystallographic experimental details for **2-(CO)₂** (continued).

^bPrograms for diffractometer operation, data collection, data reduction and absorption correction were those supplied by Bruker.

^cSheldrick, G. M. *Acta Crystallogr.* **2015**, *A71*, 3–8.

^dSheldrick, G. M. *Acta Crystallogr.* **2015**, *C71*, 3–8.

^e $S = [\sum w(F_o^2 - F_c^2)^2 / (n - p)]^{1/2}$ (n = number of data; p = number of parameters varied; w = $[\sigma^2(F_o^2) + (0.0420P)^2 + 1.1292P]^{-1}$ where $P = [\text{Max}(F_o^2, 0) + 2F_c^2]/3$).

^f $R_1 = \sum ||F_o| - |F_c|| / \sum |F_o|$; $wR_2 = [\sum w(F_o^2 - F_c^2)^2 / \sum w(F_o^4)]^{1/2}$.

Table A6. Crystallographic experimental details for **2-Fe^I**.*A. Crystal Data*

| | |
|--|--|
| formula | C ₄₀ H ₆₄ FeN ₂ P ₃ Si |
| formula weight | 749.78 |
| crystal dimensions (mm) | 0.18 × 0.17 × 0.03 |
| crystal system | monoclinic |
| space group | <i>P</i> 2 ₁ / <i>n</i> (an alternate setting of <i>P</i> 2 ₁ / <i>c</i> [No. 14]) |
| unit cell parameters ^a | |
| <i>a</i> (Å) | 18.7089(3) |
| <i>b</i> (Å) | 22.2925(3) |
| <i>c</i> (Å) | 19.5923(3) |
| β (deg) | 102.9149(8) |
| <i>V</i> (Å ³) | 7964.6(2) |
| <i>Z</i> | 8 |
| ρ _{calcd} (g cm ⁻³) | 1.251 |
| μ (mm ⁻¹) | 4.680 |

B. Data Collection and Refinement Conditions

| | |
|--|---|
| diffractometer | Bruker D8/APEX II CCD ^b |
| radiation (λ [Å]) | Cu Kα (1.54178) (microfocus source) |
| temperature (°C) | -100 |
| scan type | ω and φ scans (1.0°) (5 s exposures) |
| data collection 2θ limit (deg) | 148.15 |
| total data collected | 56345 (-23 ≤ <i>h</i> ≤ 23, -27 ≤ <i>k</i> ≤ 27, -24 ≤ <i>l</i> ≤ 23) |
| independent reflections | 15954 (<i>R</i> _{int} = 0.0438) |
| number of observed reflections (<i>NO</i>) | 13549 [<i>F</i> _o ² ≥ 2σ(<i>F</i> _o ²)] |
| structure solution method | Patterson/structure expansion (<i>DIRDIF</i> - <i>2008</i> ^c) |
| refinement method | full-matrix least-squares on <i>F</i> ² (<i>SHELXL</i> - <i>2014</i> ^d) |
| absorption correction method | Gaussian integration (face-indexed) |
| range of transmission factors | 0.8569–0.5149 |
| data/restraints/parameters | 15954 / 0 / 855 |
| goodness-of-fit (<i>S</i>) ^e [all data] | 1.026 |
| final <i>R</i> indices ^f | |
| <i>R</i> ₁ [<i>F</i> _o ² ≥ 2σ(<i>F</i> _o ²)] | 0.0293 |
| <i>wR</i> ₂ [all data] | 0.0758 |
| largest difference peak and hole | 0.291 and -0.289 e Å ⁻³ |

^aObtained from least-squares refinement of 9837 reflections with 6.10° < 2θ < 147.38°.

^bPrograms for diffractometer operation, data collection, data reduction and absorption correction were those supplied by Bruker.

(continued)

Table A6. Crystallographic experimental details for **2-Fe^I** (continued).

^cBeurskens, P. T.; Beurskens, G.; de Gelder, R.; Smits, J. M. M.; Garcia-Granda, S.; Gould, R. O. (2008). The *DIRDIF-2008* program system. Crystallography Laboratory, Radboud University Nijmegen, The Netherlands.

^dSheldrick, G. M. *Acta Crystallogr.* **2015**, *C71*, 3–8.

^e $S = [\sum w(F_o^2 - F_c^2)^2 / (n - p)]^{1/2}$ (n = number of data; p = number of parameters varied; $w = [\sigma^2(F_o^2) + (0.0370P)^2 + 1.4673P]^{-1}$ where $P = [\text{Max}(F_o^2, 0) + 2F_c^2]/3$).

^f $R_1 = \sum ||F_o| - |F_c|| / \sum |F_o|$; $wR_2 = [\sum w(F_o^2 - F_c^2)^2 / \sum w(F_o^4)]^{1/2}$.

Table A7. Crystallographic experimental details for **2-H**.*A. Crystal Data*

| | |
|---|--|
| formula | C ₄₂ H ₇₀ FeO _{0.5} P ₃ Si |
| formula weight | 759.83 |
| crystal dimensions (mm) | 0.16 × 0.15 × 0.13 |
| crystal system | tetragonal |
| space group | $\bar{I}42m$ (No. 121) |
| unit cell parameters ^a | |
| <i>a</i> (Å) | 22.3593(7) |
| <i>c</i> (Å) | 17.3124(7) |
| <i>V</i> (Å ³) | 8655.1(6) |
| <i>Z</i> | 8 |
| ρ_{calcd} (g cm ⁻³) | 1.166 |
| μ (mm ⁻¹) | 4.306 |

B. Data Collection and Refinement Conditions

| | |
|---|--|
| diffractometer | Bruker D8/APEX II CCD ^b |
| radiation (λ [Å]) | Cu K α (1.54178) (microfocus source) |
| temperature (°C) | -100 |
| scan type | ω and ϕ scans (1.0°) (5 s exposures) |
| data collection 2θ limit (deg) | 148.22 |
| total data collected | 27514 ($-27 \leq h \leq 27$, $-26 \leq k \leq 22$, $-21 \leq l \leq 21$) |
| independent reflections | 4573 ($R_{\text{int}} = 0.0456$) |
| number of observed reflections (<i>NO</i>) | 4200 [$F_o^2 \geq 2\sigma(F_o^2)$] |
| structure solution method | intrinsic phasing (<i>SHELXT-2014</i> ^c) |
| refinement method | full-matrix least-squares on F^2 (<i>SHELXL-2014</i> ^{d,e}) |
| absorption correction method | Gaussian integration (face-indexed) |
| range of transmission factors | 0.7071–0.5401 |
| data/restraints/parameters | 4573 / 0 / 230 |
| Flack absolute structure parameter ^f | 0.304(8) |
| goodness-of-fit (<i>S</i>) ^g [all data] | 1.064 |
| final <i>R</i> indices ^h | |
| <i>R</i> ₁ [$F_o^2 \geq 2\sigma(F_o^2)$] | 0.0443 |
| <i>wR</i> ₂ [all data] | 0.1120 |
| largest difference peak and hole | 0.394 and -0.365 e Å ⁻³ |

^aObtained from least-squares refinement of 9935 reflections with $5.58^\circ < 2\theta < 147.74^\circ$.

^bPrograms for diffractometer operation, data collection, data reduction and absorption correction were those supplied by Bruker.

^cSheldrick, G. M. *Acta Crystallogr.* **2015**, *A71*, 3–8.

(continued)

Table A7. Crystallographic experimental details for **2-H** (continued).

^dSheldrick, G. M. *Acta Crystallogr.* **2015**, *C71*, 3–8.

^eAttempts to refine peaks of residual electron density as disordered or partial-occupancy solvent diethyl ether oxygen or carbon atoms were unsuccessful. The data were corrected for disordered electron density through use of the SQUEEZE procedure as implemented in *PLATON* (Spek, A. L. *Acta Crystallogr.* **2015**, *C71*, 9–18. *PLATON* - a multipurpose crystallographic tool. Utrecht University, Utrecht, The Netherlands). A total solvent-accessible void volume of 1146 Å³ with a total electron count of 221 (consistent with four molecules of solvent diethyl ether, or one-half solvent molecule per formula unit of the iron complex molecule) was found in the unit cell.

^fFlack, H. D. *Acta Crystallogr.* **1983**, *A39*, 876–881; Flack, H. D.; Bernardinelli, G. *Acta Crystallogr.* **1999**, *A55*, 908–915; Flack, H. D.; Bernardinelli, G. *J. Appl. Cryst.* **2000**, *33*, 1143–1148. The Flack parameter will refine to a value near zero if the structure is in the correct configuration and will refine to a value near one for the inverted configuration. The value observed herein is indicative of racemic twinning, and was accommodated during the refinement (using the *SHELXL-2014* TWIN instruction [see reference *d*]).

$gS = [\sum w(F_o^2 - F_c^2)^2 / (n - p)]^{1/2}$ (n = number of data; p = number of parameters varied; $w = [\sigma^2(F_o^2) + (0.0543P)^2 + 8.6235P]^{-1}$ where $P = [\text{Max}(F_o^2, 0) + 2F_c^2]/3$).

$^hR_1 = \sum ||F_o| - |F_c|| / \sum |F_o|$; $wR_2 = [\sum w(F_o^2 - F_c^2)^2 / \sum w(F_o^4)]^{1/2}$.

Table A8. Crystallographic experimental details for **2-H(N₂)**.*A. Crystal Data*

| | |
|---|--|
| formula | C ₄₃ H _{72.50} FeN _{0.25} O _{0.75} P ₃ Si |
| formula weight | 781.86 |
| crystal dimensions (mm) | 0.13 × 0.10 × 0.04 |
| crystal system | tetragonal |
| space group | $\bar{I}42m$ (No. 121) |
| unit cell parameters ^a | |
| <i>a</i> (Å) | 22.3415 (3) |
| <i>c</i> (Å) | 17.3144 (3) |
| <i>V</i> (Å ³) | 8642.4 (3) |
| <i>Z</i> | 8 |
| ρ_{calcd} (g cm ⁻³) | 1.202 |
| μ (mm ⁻¹) | 4.332 |

B. Data Collection and Refinement Conditions

| | |
|---|--|
| diffractometer | Bruker D8/APEX II CCD ^b |
| radiation (λ [Å]) | Cu K α (1.54178) (microfocus source) |
| temperature (°C) | -100 |
| scan type | ω and ϕ scans (1.0°) (5 s exposures) |
| data collection 2θ limit (deg) | 144.62 |
| total data collected | 28015 ($-27 \leq h \leq 27$, $-27 \leq k \leq 27$, $-20 \leq l \leq 21$) |
| independent reflections | 4439 ($R_{\text{int}} = 0.0919$) |
| number of observed reflections (<i>NO</i>) | 3471 [$F_o^2 \geq 2\sigma(F_o^2)$] |
| structure solution method | intrinsic phasing (<i>SHELXT-2014</i> ^c) |
| refinement method | full-matrix least-squares on F^2 (<i>SHELXL-2014</i> ^{d,e,f}) |
| absorption correction method | Gaussian integration (face-indexed) |
| range of transmission factors | 0.7536–0.5214 |
| data/restraints/parameters | 4439 / 0 / 239 |
| Flack absolute structure parameter ^g | 0.000(3) |
| goodness-of-fit (<i>S</i>) ^h [all data] | 1.052 |
| final <i>R</i> indices ⁱ | |
| <i>R</i> ₁ [$F_o^2 \geq 2\sigma(F_o^2)$] | 0.0513 |
| <i>wR</i> ₂ [all data] | 0.1402 |
| largest difference peak and hole | 0.470 and -0.398 e Å ⁻³ |

^aObtained from least-squares refinement of 9279 reflections with $5.60^\circ < 2\theta < 129.40^\circ$.

^bPrograms for diffractometer operation, data collection, data reduction and absorption correction were those supplied by Bruker.

(continued)

Table A8. Crystallographic experimental details for **2-H(N₂)** (continued).

^cSheldrick, G. M. *Acta Crystallogr.* **2015**, *A71*, 3–8. (*SHELXT-2014*)

^dSheldrick, G. M. *Acta Crystallogr.* **2015**, *C71*, 3–8. (*SHELXL-2014*)

^eAttempts to refine peaks of residual electron density as disordered or partial-occupancy solvent diethylether oxygen or carbon atoms were unsuccessful. The data were corrected for disordered electron density through use of the SQUEEZE procedure as implemented in *PLATON* (Spek, A. L. *Acta Crystallogr.* **2015**, *C71*, 9–18. *PLATON* - a multipurpose crystallographic tool. Utrecht University, Utrecht, The Netherlands). A total solvent-accessible void volume of 1150 Å³ with a total electron count of 258 (consistent with 6 molecules of solvent diethylether, or 0.75 molecules per formula unit of the iron complex molecule) was found in the unit cell.

^fThe data were tested for merohedral twinning using the TwinRotMat procedure as implemented in *PLATON* (Spek, A. L. *Acta Crystallogr.* **1990**, *A46*, C34; Spek, A. L. *J. Appl. Cryst.* **2003**, *36*, 7–13. *PLATON* - a multipurpose crystallographic tool. Utrecht University, Utrecht, The Netherlands). The second twin component can be related to the first component by twofold rotation about the [1 1 0] axis (twin law [0 1 0 1 0 0 0 -1]). The refined value of the twin fraction (*SHELXL-2014* BASF parameter) was 0.453(10).

^gFlack, H. D. *Acta Crystallogr.* **1983**, *A39*, 876–881; Flack, H. D.; Bernardinelli, G. *Acta Crystallogr.* **1999**, *A55*, 908–915; Flack, H. D.; Bernardinelli, G. *J. Appl. Cryst.* **2000**, *33*, 1143–1148. The Flack parameter will refine to a value near zero if the structure is in the correct configuration and will refine to a value near one for the inverted configuration.

^h $S = [\sum w(F_o^2 - F_c^2)^2 / (n - p)]^{1/2}$ (n = number of data; p = number of parameters varied; $w = [\sigma^2(F_o^2) + (0.0772P)^2 + 1.4548P]^{-1}$ where $P = [\text{Max}(F_o^2, 0) + 2F_c^2]/3$).

ⁱ $R_1 = \sum ||F_o| - |F_c|| / \sum |F_o|$; $wR_2 = [\sum w(F_o^2 - F_c^2)^2 / \sum w(F_o^4)]^{1/2}$.

Table A9. Crystallographic experimental details for **2-H₃**.*A. Crystal Data*

| | |
|-----------------------------------|--|
| formula | C _{43.75} H ₇₆ FeP ₃ Si |
| formula weight | 778.89 |
| crystal dimensions (mm) | 0.19 × 0.15 × 0.09 |
| crystal system | orthorhombic |
| space group | <i>P</i> 2 ₁ 2 ₁ 2 ₁ (No. 19) |
| unit cell parameters ^a | |
| <i>a</i> (Å) | 17.2963(3) |
| <i>b</i> (Å) | 22.3472(3) |
| <i>c</i> (Å) | 22.3309(4) |
| <i>V</i> (Å ³) | 8631.4(2) |
| <i>Z</i> | 8 |

| | |
|---|-------|
| ρ_{calcd} (g cm ⁻³) | 1.199 |
|---|-------|

| | |
|---------------------------|-------|
| μ (mm ⁻¹) | 4.318 |
|---------------------------|-------|

B. Data Collection and Refinement Conditions

| | |
|---|---|
| diffractometer | Bruker D8/APEX II CCD ^b |
| radiation (λ [Å]) | Cu K α (1.54178) (microfocus source) |
| temperature (°C) | -100 |
| scan type | ω and ϕ scans (1.0°) (5 s exposures) |
| data collection 2θ limit (deg) | 144.95 |
| total data collected | 371977 ($-21 \leq h \leq 21$, $-27 \leq k \leq 27$, $-24 \leq l \leq 26$) |
| independent reflections | 16978 ($R_{\text{int}} = 0.0955$) |
| number of observed reflections (<i>NO</i>) | 16803 [$F_o^2 \geq 2\sigma(F_o^2)$] |
| structure solution method | intrinsic phasing (<i>SHELXT-2014</i> ^c) |
| refinement method | full-matrix least-squares on F^2 (<i>SHELXL-2014</i> ^{d,e}) |
| absorption correction method | Gaussian integration (face-indexed) |
| range of transmission factors | 0.7137–0.5341 |
| data/restraints/parameters | 16978 / 0 / 846 |
| Flack absolute structure parameter ^f | not determined |
| goodness-of-fit (<i>S</i>) ^g [all data] | 1.044 |
| final <i>R</i> indices ^h | |
| <i>R</i> ₁ [$F_o^2 \geq 2\sigma(F_o^2)$] | 0.0247 |
| <i>wR</i> ₂ [all data] | 0.0639 |
| largest difference peak and hole | 0.241 and -0.314 e Å ⁻³ |

^aObtained from least-squares refinement of 9820 reflections with $5.60^\circ < 2\theta < 143.92^\circ$.

^bPrograms for diffractometer operation, data collection, data reduction and absorption correction were those supplied by Bruker.

(continued)

Table A9. Crystallographic experimental details for **2-H₃** (continued).

^cSheldrick, G. M. *Acta Crystallogr.* **2015**, *A71*, 3–8. (*SHELXT-2014*)

^dSheldrick, G. M. *Acta Crystallogr.* **2015**, *C71*, 3–8. (*SHELXL-2014*)

^eAttempts to refine peaks of residual electron density as disordered or partial-occupancy solvent pentane carbon atoms were unsuccessful. The data were corrected for disordered electron density through use of the SQUEEZE procedure as implemented in *PLATON* (Spek, A. L. *Acta Crystallogr.* **2015**, *C71*, 9–18. *PLATON* - a multipurpose crystallographic tool. Utrecht University, Utrecht, The Netherlands). A total solvent-accessible void volume of 1200 Å³ with a total electron count of 254 (consistent with 6 molecules of solvent pentane, or 0.75 molecules per formula unit of the iron complex) was found in the unit cell.

^eThe data were tested for nonmerohedral twinning using the TwinRotMat procedure as implemented in *PLATON* (Spek, A. L. *Acta Crystallogr.* **1990**, *A46*, C34; Spek, A. L. *J. Appl. Cryst.* **2003**, *36*, 7–13. *PLATON* - a multipurpose crystallographic tool. Utrecht University, Utrecht, The Netherlands). The second twin component can be related to the first component by twofold rotation about the [0 1 -1] axis (twin law [-1 0 0 0 0 -1 0 -1 0]). Furthermore, the data also exhibited racemic (inversion) twinning. The refined value of the twin fractions (*SHELXL-2014* BASF parameter) were 0.128(2), 0.386(2), and 0.155(2).

^fFlack, H. D. *Acta Crystallogr.* **1983**, *A39*, 876–881; Flack, H. D.; Bernardinelli, G. *Acta Crystallogr.* **1999**, *A55*, 908–915; Flack, H. D.; Bernardinelli, G. *J. Appl. Cryst.* **2000**, *33*, 1143–1148. The Flack parameter cannot be determined as twinning by inversion was present.

$gS = [\sum w(F_o^2 - F_c^2)^2 / (n - p)]^{1/2}$ (n = number of data; p = number of parameters varied; w = $[\sigma^2(F_o^2) + (0.0362P)^2 + 0.8295P]^{-1}$ where $P = [\text{Max}(F_o^2, 0) + 2F_c^2]/3$).

$^hR_1 = \sum ||F_o| - |F_c|| / \sum |F_o|$; $wR_2 = [\sum w(F_o^2 - F_c^2)^2 / \sum w(F_o^4)]^{1/2}$.

Table A10. Crystallographic experimental details for **2-py(N₂)**.*A. Crystal Data*

| | |
|--|--|
| formula | C ₅₀ H ₈₁ FeN ₃ O ₂ P ₂ Si |
| formula weight | 902.05 |
| crystal dimensions (mm) | 0.37 × 0.27 × 0.25 |
| crystal system | monoclinic |
| space group | <i>P</i> 2 ₁ / <i>n</i> (an alternate setting of <i>P</i> 2 ₁ / <i>c</i> [No. 14]) |
| unit cell parameters ^a | |
| <i>a</i> (Å) | 12.6106(2) |
| <i>b</i> (Å) | 17.8279(3) |
| <i>c</i> (Å) | 23.0687(4) |
| β (deg) | 100.3855(10) |
| <i>V</i> (Å ³) | 5101.35(15) |
| <i>Z</i> | 4 |
| ρ _{calcd} (g cm ⁻³) | 1.175 |
| μ (mm ⁻¹) | 3.482 |

B. Data Collection and Refinement Conditions

| | |
|--|--|
| diffractometer | Bruker D8/APEX II CCD ^b |
| radiation (λ [Å]) | Cu Kα (1.54178) (microfocus source) |
| temperature (°C) | -100 |
| scan type | ω and φ scans (1.0°) (5 s exposures) |
| data collection 2θ limit (deg) | 144.89 |
| total data collected | 35050 (-15 ≤ <i>h</i> ≤ 15, -22 ≤ <i>k</i> ≤ 22, -28 ≤ <i>l</i> ≤ 28) |
| independent reflections | 9706 (<i>R</i> _{int} = 0.0303) |
| number of observed reflections (<i>NO</i>) | 9175 [<i>F</i> _o ² ≥ 2σ(<i>F</i> _o ²)] |
| structure solution method | intrinsic phasing (<i>SHELXT-2014</i> ^c) |
| refinement method | full-matrix least-squares on <i>F</i> ² (<i>SHELXL-2016</i> ^{d,e}) |
| absorption correction method | Gaussian integration (face-indexed) |
| range of transmission factors | 0.6114–0.4275 |
| data/restraints/parameters | 9706 / 0 / 449 |
| goodness-of-fit (<i>S</i>) ^f [all data] | 1.021 |
| final <i>R</i> indices ^g | |
| <i>R</i> ₁ [<i>F</i> _o ² ≥ 2σ(<i>F</i> _o ²)] | 0.0279 |
| <i>wR</i> ₂ [all data] | 0.0748 |
| largest difference peak and hole | 0.319 and -0.221 e Å ⁻³ |

^aObtained from least-squares refinement of 9810 reflections with 6.30° < 2θ < 144.40°.

^bPrograms for diffractometer operation, data collection, data reduction and absorption correction were those supplied by Bruker.

(continued)

Table A10. Crystallographic experimental details for **2-py(N₂)** (continued).

^cSheldrick, G. M. *Acta Crystallogr.* **2015**, *A71*, 3–8. (*SHELXT-2014*)

^dSheldrick, G. M. *Acta Crystallogr.* **2015**, *C71*, 3–8. (*SHELXL-2016*)

^eAttempts to refine peaks of residual electron density as disordered or partial-occupancy solvent diethylether oxygen or carbon atoms were unsuccessful. The data were corrected for disordered electron density through use of the SQUEEZE procedure as implemented in *PLATON* (Spek, A. L. *Acta Crystallogr.* **2015**, *C71*, 9–18. *PLATON* - a multipurpose crystallographic tool. Utrecht University, Utrecht, The Netherlands). A total solvent-accessible void volume of 1504 Å³ with a total electron count of 314 (consistent with 8 molecules of solvent diethylether, or 2 molecules per formula unit of the iron compound) was found in the unit cell.

$$fS = [\sum w(F_o^2 - F_c^2)^2 / (n - p)]^{1/2} \quad (n = \text{number of data}; p = \text{number of parameters varied}; w = [\sigma^2(F_o^2) + (0.0423P)^2 + 1.1354P]^{-1} \text{ where } P = [\text{Max}(F_o^2, 0) + 2F_c^2] / 3).$$

$$gR_1 = \sum ||F_o| - |F_c|| / \sum |F_o|; wR_2 = [\sum w(F_o^2 - F_c^2)^2 / \sum w(F_o^4)]^{1/2}.$$

Table A11. Crystallographic experimental details for 2-(N₂)₂.

| | |
|--|--|
| <i>A. Crystal Data</i> | |
| formula | C ₃₇ H ₅₆ FeN ₄ P ₂ Si |
| formula weight | 702.73 |
| crystal dimensions (mm) | 0.32 × 0.30 × 0.16 |
| crystal system | monoclinic |
| space group | <i>P</i> 2 ₁ / <i>n</i> (an alternate setting of <i>P</i> 2 ₁ / <i>c</i> [No. 14]) |
| unit cell parameters ^a | |
| <i>a</i> (Å) | 12.4181(4) |
| <i>b</i> (Å) | 23.2868(7) |
| <i>c</i> (Å) | 13.0781(4) |
| β (deg) | 98.6048(16) |
| <i>V</i> (Å ³) | 3739.3(2) |
| <i>Z</i> | 4 |
| ρ_{calcd} (g cm ⁻³) | 1.248 |
| μ (mm ⁻¹) | 4.577 |
| <i>B. Data Collection and Refinement Conditions</i> | |
| diffractometer | Bruker D8/APEX II CCD ^b |
| radiation (λ [Å]) | Cu K α (1.54178) (microfocus source) |
| temperature (°C) | -100 |
| scan type | ω and ϕ scans (1.0°) (5 s exposures) |
| data collection 2θ limit (deg) | 147.95 |
| total data collected | 26695 ($-15 \leq h \leq 15$, $-29 \leq k \leq 28$, $-16 \leq l \leq 16$) |
| independent reflections | 7539 ($R_{\text{int}} = 0.0291$) |
| number of observed reflections (<i>NO</i>) | 7303 [$F_o^2 \geq 2\sigma(F_o^2)$] |
| structure solution method | intrinsic phasing (<i>SHELXT-2014</i> ^c) |
| refinement method | full-matrix least-squares on F^2 (<i>SHELXL-2016</i> ^d) |
| absorption correction method | Gaussian integration (face-indexed) |
| range of transmission factors | 0.5752–0.3463 |
| data/restraints/parameters | 7539 / 0 / 411 |
| goodness-of-fit (<i>S</i>) ^e [all data] | 1.056 |
| final <i>R</i> indices ^f | |
| R_1 [$F_o^2 \geq 2\sigma(F_o^2)$] | 0.0270 |
| wR_2 [all data] | 0.0739 |
| largest difference peak and hole | 0.296 and -0.416 e Å ⁻³ |

^aObtained from least-squares refinement of 9750 reflections with $7.60^\circ < 2\theta < 147.84^\circ$.

^bPrograms for diffractometer operation, data collection, data reduction and absorption correction were those supplied by Bruker.

(continued)

Table A11. Crystallographic experimental details for **2-(N₂)₂** (continued).

^cSheldrick, G. M. *Acta Crystallogr.* **2015**, *A71*, 3–8. (*SHELXT-2014*)

^dSheldrick, G. M. *Acta Crystallogr.* **2015**, *C71*, 3–8. (*SHELXL-2016*)

^e $S = [\sum w(F_o^2 - F_c^2)^2 / (n - p)]^{1/2}$ (n = number of data; p = number of parameters varied; w

= $[\sigma^2(F_o^2) + (0.0472P)^2 + 0.7271P]^{-1}$ where $P = [\text{Max}(F_o^2, 0) + 2F_c^2]/3$).

^f $R_1 = \sum ||F_o| - |F_c|| / \sum |F_o|$; $wR_2 = [\sum w(F_o^2 - F_c^2)^2 / \sum w(F_o^4)]^{1/2}$.

Table A12. Crystallographic experimental details for **3-4**.

| | |
|--|--|
| <i>A. Crystal Data</i> | |
| formula | C ₃₉ H ₅₅ CoO ₂ P ₂ Si |
| formula weight | 704.79 |
| crystal dimensions (mm) | 0.24 × 0.14 × 0.06 |
| crystal system | monoclinic |
| space group | <i>P</i> 2 ₁ / <i>n</i> (an alternate setting of <i>P</i> 2 ₁ / <i>c</i> [No. 14]) |
| unit cell parameters ^a | |
| <i>a</i> (Å) | 10.3839 (3) |
| <i>b</i> (Å) | 18.2717 (6) |
| <i>c</i> (Å) | 19.5134 (6) |
| β (deg) | 100.3498 (19) |
| <i>V</i> (Å ³) | 3642.1 (2) |
| <i>Z</i> | 4 |
| ρ_{calcd} (g cm ⁻³) | 1.285 |
| μ (mm ⁻¹) | 5.083 |
| <i>B. Data Collection and Refinement Conditions</i> | |
| diffractometer | Bruker D8/APEX II CCD ^b |
| radiation (λ [Å]) | Cu K α (1.54178) (microfocus source) |
| temperature (°C) | -100 |
| scan type | ω and ϕ scans (1.0°) (5 s exposures) |
| data collection 2θ limit (deg) | 144.58 |
| total data collected | 21046 ($-12 \leq h \leq 12$, $-22 \leq k \leq 22$, $-24 \leq l \leq 24$) |
| independent reflections | 6978 ($R_{\text{int}} = 0.0358$) |
| number of observed reflections (<i>NO</i>) | 6136 [$F_o^2 \geq 2\sigma(F_o^2)$] |
| structure solution method | intrinsic phasing (<i>SHELXT-2014</i> ^c) |
| refinement method | full-matrix least-squares on F^2 (<i>SHELXL-2014</i> ^d) |
| absorption correction method | Gaussian integration (face-indexed) |
| range of transmission factors | 0.8302–0.4291 |
| data/restraints/parameters | 6978 / 0 / 407 |
| goodness-of-fit (<i>S</i>) ^e [all data] | 1.129 |
| final <i>R</i> indices ^f | |
| R_1 [$F_o^2 \geq 2\sigma(F_o^2)$] | 0.0321 |
| wR_2 [all data] | 0.0870 |
| largest difference peak and hole | 0.287 and -0.355 e Å ⁻³ |

^aObtained from least-squares refinement of 9899 reflections with $6.68^\circ < 2\theta < 144.12^\circ$.

^bPrograms for diffractometer operation, data collection, data reduction and absorption correction were those supplied by Bruker.

(continued)

Table A12. Crystallographic experimental details for **3-4** (continued).

^cSheldrick, G. M. *Acta Crystallogr.* **2015**, *A71*, 3–8. (*SHELXT-2014*)

^dSheldrick, G. M. *Acta Crystallogr.* **2015**, *C71*, 3–8. (*SHELXL-2014*)

^e $S = [\sum w(F_o^2 - F_c^2)^2 / (n - p)]^{1/2}$ (n = number of data; p = number of parameters varied; w

= $[\sigma^2(F_o^2) + (0.0466P)^2 + 0.1458P]^{-1}$ where $P = [\text{Max}(F_o^2, 0) + 2F_c^2]/3$).

^f $R_1 = \sum ||F_o| - |F_c|| / \sum |F_o|$; $wR_2 = [\sum w(F_o^2 - F_c^2)^2 / \sum w(F_o^4)]^{1/2}$.

Table A13. Crystallographic experimental details for **3-6**.

| | |
|--|--|
| <i>A. Crystal Data</i> | |
| formula | C ₄₆ H ₆₄ CoIO ₂ P ₂ Si |
| formula weight | 924.83 |
| crystal dimensions (mm) | 0.36 × 0.11 × 0.09 |
| crystal system | monoclinic |
| space group | <i>P</i> 2 ₁ / <i>n</i> (an alternate setting of <i>P</i> 2 ₁ / <i>c</i> [No. 14]) |
| unit cell parameters ^a | |
| <i>a</i> (Å) | 9.7518 (4) |
| <i>b</i> (Å) | 16.8145 (6) |
| <i>c</i> (Å) | 28.0253 (11) |
| β (deg) | 97.8027 (5) |
| <i>V</i> (Å ³) | 4552.8 (3) |
| <i>Z</i> | 4 |
| ρ_{calcd} (g cm ⁻³) | 1.349 |
| μ (mm ⁻¹) | 1.186 |
| <i>B. Data Collection and Refinement Conditions</i> | |
| diffractometer | Bruker D8/APEX II CCD ^b |
| radiation (λ [Å]) | graphite-monochromated Mo K α (0.71073) |
| temperature (°C) | -100 |
| scan type | ω scans (0.3°) (15 s exposures) |
| data collection 2θ limit (deg) | 56.59 |
| total data collected | 42340 ($-12 \leq h \leq 12$, $-22 \leq k \leq 22$, $-37 \leq l \leq 36$) |
| independent reflections | 11114 ($R_{\text{int}} = 0.0372$) |
| number of observed reflections (<i>NO</i>) | 8874 [$F_0^2 \geq 2\sigma(F_0^2)$] |
| structure solution method | Patterson/structure expansion (<i>DIRDIF-2008</i> ^c) |
| refinement method | full-matrix least-squares on F^2 (<i>SHELXL-2014</i> ^d) |
| absorption correction method | Gaussian integration (face-indexed) |
| range of transmission factors | 0.9376–0.7341 |
| data/restraints/parameters | 11114 / 36 ^e / 560 |
| goodness-of-fit (<i>S</i>) ^f [all data] | 1.040 |
| final <i>R</i> indices ^g | |
| R_1 [$F_0^2 \geq 2\sigma(F_0^2)$] | 0.0316 |
| wR_2 [all data] | 0.0797 |
| largest difference peak and hole | 0.729 and -0.372 e Å ⁻³ |

^aObtained from least-squares refinement of 9975 reflections with $4.64^\circ < 2\theta < 50.80^\circ$.

^bPrograms for diffractometer operation, data collection, data reduction and absorption correction were those supplied by Bruker.

(continued)

Table A13. Crystallographic experimental details for **3-6** (continued).

^cBeurskens, P. T.; Beurskens, G.; de Gelder, R.; Smits, J. M. M.; Garcia-Granda, S.; Gould, R. O. (2008). The *DIRDIF-2008* program system. Crystallography Laboratory, Radboud University Nijmegen, The Netherlands.

^dSheldrick, G. M. *Acta Crystallogr.* **2015**, *C71*, 3–8.

^eBond distances and 1,3-distances within the disordered solvent benzene molecules were restrained to idealized values of 1.39(1) Å and 2.40(1) Å, respectively, during refinement.

$$fS = [\sum w(F_o^2 - F_c^2)^2 / (n - p)]^{1/2} \quad (n = \text{number of data}; p = \text{number of parameters varied}; w = [\sigma^2(F_o^2) + (0.0350P)^2 + 2.1268P]^{-1} \text{ where } P = [\text{Max}(F_o^2, 0) + 2F_c^2] / 3).$$

$$gR_1 = \sum ||F_o| - |F_c|| / \sum |F_o|; wR_2 = [\sum w(F_o^2 - F_c^2)^2 / \sum w(F_o^4)]^{1/2}.$$

Table A14. Crystallographic experimental details for **3-7**.

| | |
|---|--|
| <i>A. Crystal Data</i> | |
| formula | C ₃₇ H ₅₅ CoIOP ₂ Si |
| formula weight | 791.67 |
| crystal dimensions (mm) | 0.28 × 0.16 × 0.11 |
| crystal system | triclinic |
| space group | <i>P</i> $\bar{1}$ (No. 2) |
| unit cell parameters ^a | |
| <i>a</i> (Å) | 11.9135 (3) |
| <i>b</i> (Å) | 17.1817 (4) |
| <i>c</i> (Å) | 18.6108 (5) |
| α (deg) | 88.7237 (5) |
| β (deg) | 85.8540 (5) |
| γ (deg) | 79.3489 (5) |
| <i>V</i> (Å ³) | 3733.94 (16) |
| <i>Z</i> | 4 |
| ρ_{calcd} (g cm ⁻³) | 1.408 |
| μ (mm ⁻¹) | 1.431 |
| <i>B. Data Collection and Refinement Conditions</i> | |
| diffractometer | Bruker D8/APEX II CCD ^b |
| radiation (λ [Å]) | graphite-monochromated Mo K α (0.71073) |
| temperature (°C) | -100 |
| scan type | ω scans (0.3°) (10 s exposures) |
| data collection 2θ limit (deg) | 56.62 |
| total data collected | 36371 ($-15 \leq h \leq 15$, $-22 \leq k \leq 22$, $-24 \leq l \leq 24$) |
| independent reflections | 18522 ($R_{\text{int}} = 0.0295$) |
| number of observed reflections (<i>NO</i>) | 14856 [$F_o^2 \geq 2\sigma(F_o^2)$] |
| structure solution method | Patterson/structure expansion (<i>DIRDIF-2008</i> ^c) |
| refinement method | full-matrix least-squares on F^2 (<i>SHELXL-2014</i> ^d) |
| absorption correction method | Gaussian integration (face-indexed) |
| range of transmission factors | 0.9348–0.7843 |
| data/restraints/parameters | 18522 / 0 / 777 |
| goodness-of-fit (<i>S</i>) ^e [all data] | 1.028 |
| final <i>R</i> indices ^f | |
| <i>R</i> ₁ [$F_o^2 \geq 2\sigma(F_o^2)$] | 0.0345 |
| <i>wR</i> ₂ [all data] | 0.0866 |
| largest difference peak and hole | 1.115 and -0.793 e Å ⁻³ |

^aObtained from least-squares refinement of 7020 reflections with $4.56^\circ < 2\theta < 45.12^\circ$.
(continued)

Table A14. Crystallographic experimental details for **3-7** (continued).

^bPrograms for diffractometer operation, data collection, data reduction and absorption correction were those supplied by Bruker.

^cBeurskens, P. T.; Beurskens, G.; de Gelder, R.; Smits, J. M. M.; Garcia-Granda, S.; Gould, R. O. (2008). The *DIRDIF-2008* program system. Crystallography Laboratory, Radboud University Nijmegen, The Netherlands.

^dSheldrick, G. M. *Acta Crystallogr.* **2015**, *C71*, 3–8.

^e $S = [\sum w(F_o^2 - F_c^2)^2 / (n - p)]^{1/2}$ (n = number of data; p = number of parameters varied; $w = [\sigma^2(F_o^2) + (0.0284P)^2 + 1.7489P]^{-1}$ where $P = [\text{Max}(F_o^2, 0) + 2F_c^2]/3$).

^f $R_1 = \sum ||F_o| - |F_c|| / \sum |F_o|$; $wR_2 = [\sum w(F_o^2 - F_c^2)^2 / \sum w(F_o^4)]^{1/2}$.

Table A15. Crystallographic experimental details for **4-NiCl**.

| | |
|--|--|
| <i>A. Crystal Data</i> | |
| formula | C ₃₅ H ₅₅ ClN ₂ NiOP ₂ Si |
| formula weight | 704.00 |
| crystal dimensions (mm) | 0.47 × 0.39 × 0.27 |
| crystal system | monoclinic |
| space group | <i>P</i> 2 ₁ / <i>c</i> (No. 14) |
| unit cell parameters ^a | |
| <i>a</i> (Å) | 17.1028 (4) |
| <i>b</i> (Å) | 13.1686 (3) |
| <i>c</i> (Å) | 17.1776 (4) |
| β (deg) | 104.7070 (9) |
| <i>V</i> (Å ³) | 3741.99 (15) |
| <i>Z</i> | 4 |
| ρ_{calcd} (g cm ⁻³) | 1.250 |
| μ (mm ⁻¹) | 2.733 |
| <i>B. Data Collection and Refinement Conditions</i> | |
| diffractometer | Bruker D8/APEX II CCD ^b |
| radiation (λ [Å]) | Cu K α (1.54178) (microfocus source) |
| temperature (°C) | -100 |
| scan type | ω and ϕ scans (1.0°) (5 s exposures) |
| data collection 2θ limit (deg) | 147.92 |
| total data collected | 26226 ($-21 \leq h \leq 21$, $-16 \leq k \leq 16$, $-20 \leq l \leq 21$) |
| independent reflections | 7482 ($R_{\text{int}} = 0.0232$) |
| number of observed reflections (<i>NO</i>) | 7300 [$F_0^2 \geq 2\sigma(F_0^2)$] |
| structure solution method | Patterson/structure expansion (<i>DIRDIF-2008</i> ^c) |
| refinement method | full-matrix least-squares on F^2 (<i>SHELXL-2014</i> ^d) |
| absorption correction method | Gaussian integration (face-indexed) |
| range of transmission factors | 0.6716–0.4380 |
| data/restraints/parameters | 7482 / 0 / 391 |
| goodness-of-fit (<i>S</i>) ^e [all data] | 1.039 |
| final <i>R</i> indices ^f | |
| R_1 [$F_0^2 \geq 2\sigma(F_0^2)$] | 0.0354 |
| wR_2 [all data] | 0.0948 |
| largest difference peak and hole | 0.880 and -0.544 e Å ⁻³ |

^aObtained from least-squares refinement of 9893 reflections with $5.34^\circ < 2\theta < 147.52^\circ$.

^bPrograms for diffractometer operation, data collection, data reduction and absorption correction were those supplied by Bruker.

(continued)

Table A15. Crystallographic experimental details for **4-NiCl** (continued).

^cBeurskens, P. T.; Beurskens, G.; de Gelder, R.; Smits, J. M. M.; Garcia-Granda, S.; Gould, R. O. (2008). The *DIRDIF-2008* program system. Crystallography Laboratory, Radboud University Nijmegen, The Netherlands.

^dSheldrick, G. M. *Acta Crystallogr.* **2015**, *C71*, 3–8.

^e $S = [\sum w(F_o^2 - F_c^2)^2 / (n - p)]^{1/2}$ (n = number of data; p = number of parameters varied; $w = [\sigma^2(F_o^2) + (0.0472P)^2 + 3.2771P]^{-1}$ where $P = [\text{Max}(F_o^2, 0) + 2F_c^2]/3$).

^f $R_1 = \sum ||F_o| - |F_c|| / \sum |F_o|$; $wR_2 = [\sum w(F_o^2 - F_c^2)^2 / \sum w(F_o^4)]^{1/2}$.

Table A16. Crystallographic experimental details for **4-PdCl**.

| | |
|--|--|
| <i>A. Crystal Data</i> | |
| formula | C ₃₁ H ₄₅ ClN ₂ P ₂ PdSi |
| formula weight | 677.57 |
| crystal dimensions (mm) | 0.25 × 0.24 × 0.22 |
| crystal system | monoclinic |
| space group | <i>P</i> 2 ₁ / <i>c</i> (No. 14) |
| unit cell parameters ^a | |
| <i>a</i> (Å) | 15.3906 (5) |
| <i>b</i> (Å) | 14.5668 (5) |
| <i>c</i> (Å) | 15.3008 (5) |
| β (deg) | 111.2473 (4) |
| <i>V</i> (Å ³) | 3197.14 (18) |
| <i>Z</i> | 4 |
| ρ_{calcd} (g cm ⁻³) | 1.408 |
| μ (mm ⁻¹) | 0.825 |
| <i>B. Data Collection and Refinement Conditions</i> | |
| diffractometer | Bruker PLATFORM/APEX II CCD ^b |
| radiation (λ [Å]) | graphite-monochromated Mo K α (0.71073) |
| temperature (°C) | -100 |
| scan type | ω scans (0.3°) (15 s exposures) |
| data collection 2θ limit (deg) | 56.77 |
| total data collected | 29806 ($-20 \leq h \leq 20$, $-19 \leq k \leq 19$, $-20 \leq l \leq 19$) |
| independent reflections | 7965 ($R_{\text{int}} = 0.0242$) |
| number of observed reflections (<i>NO</i>) | 7053 [$F_o^2 \geq 2\sigma(F_o^2)$] |
| structure solution method | Patterson/structure expansion (<i>DIRDIF-2008</i> ^c) |
| refinement method | full-matrix least-squares on F^2 (<i>SHELXL-2014</i> ^d) |
| absorption correction method | Gaussian integration (face-indexed) |
| range of transmission factors | 0.9220–0.8527 |
| data/restraints/parameters | 7965 / 0 / 346 |
| goodness-of-fit (<i>S</i>) ^e [all data] | 1.047 |
| final <i>R</i> indices ^f | |
| R_1 [$F_o^2 \geq 2\sigma(F_o^2)$] | 0.0257 |
| wR_2 [all data] | 0.0699 |
| largest difference peak and hole | 0.589 and -0.374 e Å ⁻³ |

^aObtained from least-squares refinement of 9882 reflections with $5.38^\circ < 2\theta < 56.40^\circ$.

^bPrograms for diffractometer operation, data collection, data reduction and absorption correction were those supplied by Bruker.

(continued)

Table A16. Crystallographic experimental details for **4-PdCl** (continued).

^cBeurskens, P. T.; Beurskens, G.; de Gelder, R.; Smits, J. M. M.; Garcia-Granda, S.; Gould, R. O. (2008). The *DIRDIF-2008* program system. Crystallography Laboratory, Radboud University Nijmegen, The Netherlands.

^dSheldrick, G. M. *Acta Crystallogr.* **2015**, *C71*, 3–8.

^e $S = [\sum w(F_o^2 - F_c^2)^2 / (n - p)]^{1/2}$ (n = number of data; p = number of parameters varied; $w = [\sigma^2(F_o^2) + (0.0359P)^2 + 1.5096P]^{-1}$ where $P = [\text{Max}(F_o^2, 0) + 2F_c^2]/3$).

^f $R_1 = \sum ||F_o| - |F_c|| / \sum |F_o|$; $wR_2 = [\sum w(F_o^2 - F_c^2)^2 / \sum w(F_o^4)]^{1/2}$.

Table A17. Crystallographic experimental details for **4-PtCl**.

| | |
|--|--|
| <i>A. Crystal Data</i> | |
| formula | C ₃₅ H ₅₅ ClN ₂ OP ₂ PtSi |
| formula weight | 840.38 |
| crystal dimensions (mm) | 0.25 × 0.13 × 0.09 |
| crystal system | monoclinic |
| space group | <i>P</i> 2 ₁ / <i>c</i> (No. 14) |
| unit cell parameters ^a | |
| <i>a</i> (Å) | 17.576 (5) |
| <i>b</i> (Å) | 13.194 (4) |
| <i>c</i> (Å) | 17.187 (5) |
| β (deg) | 106.857 (4) |
| <i>V</i> (Å ³) | 3814.3 (17) |
| <i>Z</i> | 4 |
| ρ_{calcd} (g cm ⁻³) | 1.463 |
| μ (mm ⁻¹) | 3.892 |
| <i>B. Data Collection and Refinement Conditions</i> | |
| diffractometer | Bruker PLATFORM/APEX II CCD ^b |
| radiation (λ [Å]) | graphite-monochromated Mo K α (0.71073) |
| temperature (°C) | -80 |
| scan type | ω scans (0.3°) (15 s exposures) |
| data collection 2θ limit (deg) | 52.85 |
| total data collected | 51766 ($-21 \leq h \leq 21$, $-16 \leq k \leq 16$, $-21 \leq l \leq 21$) |
| independent reflections | 7756 ($R_{\text{int}} = 0.1338$) |
| number of observed reflections (<i>NO</i>) | 5950 [$F_o^2 \geq 2\sigma(F_o^2)$] |
| structure solution method | Patterson/structure expansion (<i>DIRDIF-2008</i> ^c) |
| refinement method | full-matrix least-squares on F^2 (<i>SHELXL-2014</i> ^d) |
| absorption correction method | multi-scan (<i>TWINABS</i>) |
| range of transmission factors | 0.5944–0.4420 |
| data/restraints/parameters | 7756 / 16 ^e / 377 |
| goodness-of-fit (<i>S</i>) ^f [all data] | 1.109 |
| final <i>R</i> indices ^g | |
| R_1 [$F_o^2 \geq 2\sigma(F_o^2)$] | 0.0681 |
| wR_2 [all data] | 0.1697 |
| largest difference peak and hole | 2.161 and -2.422 e Å ⁻³ |

^aObtained from least-squares refinement of 9947 reflections with $4.84^\circ < 2\theta < 48.40^\circ$.

(continued)

Table A17. Crystallographic experimental details for **4-PtCl** (continued).

^bPrograms for diffractometer operation, data collection, data reduction and absorption correction were those supplied by Bruker. The crystal used for data collection was found to display non-merohedral twinning. Both components of the twin were indexed with the program *CELL_NOW* (Bruker AXS Inc., Madison, WI, 2004). The second twin component can be related to the first component by 180° rotation about the [0 1 0] axis in both real space and reciprocal space. Integrated intensities for the reflections from the two components were written into a *SHELXL-2014* HKLF 5 reflection file with the data integration program *SAINTE* (version 8.34A), using all reflection data (exactly overlapped, partially overlapped and non-overlapped). The refined value of the twin fraction (*SHELXL-2014* BASF parameter) was 0.3(5).

^cBeurskens, P. T.; Beurskens, G.; de Gelder, R.; Smits, J. M. M.; Garcia-Granda, S.; Gould, R. O. (2008). The *DIRDIF-2008* program system. Crystallography Laboratory, Radboud University Nijmegen, The Netherlands.

^dSheldrick, G. M. *Acta Crystallogr.* **2015**, *C71*, 3–8.

^eThe following pairs of distances were constrained to be equal (within 0.01 Å) during refinement: d(P1–C31A) = d(P1–C31B); d(P2–C44A) = d(P2–C44B). The following constraints were applied to distances within the disordered solvent diethyl ether molecule: d(O1SA–C1SA) = d(O1SA–C3SA) = d(O1SB–C1SB) = d(O1SB–C3SB) = 1.45(1) Å; d(C1SA–C2SA) = d(C3SA–C4SA) = d(C1SB–C2SB) = d(C3SB–C4SB) = 1.52(1) Å; d(O1SA···C2SA) = d(O1SA···C4SA) = d(O1SB···C2SB) = d(O1SB···C4SB) = 2.42(1) Å; d(C1SA···C3SA) = d(C1SB···C3SB) = 2.35(1) Å.

$fS = [\sum w(F_o^2 - F_c^2)^2 / (n - p)]^{1/2}$ (n = number of data; p = number of parameters varied; $w = [\sigma^2(F_o^2) + (0.0501P)^2 + 59.3734P]^{-1}$ where $P = [\text{Max}(F_o^2, 0) + 2F_c^2]/3$).

$gR_1 = \sum ||F_o| - |F_c|| / \sum |F_o|$; $wR_2 = [\sum w(F_o^2 - F_c^2)^2 / \sum w(F_o^4)]^{1/2}$.

Table A18. Crystallographic experimental details for **4-NiH·DMAP**.*A. Crystal Data*

| | |
|--|--|
| formula | C ₄₁ H _{63.50} N ₄ NiO _{0.75} P ₂ Si |
| formula weight | 773.19 |
| crystal dimensions (mm) | 0.32 × 0.25 × 0.11 |
| crystal system | monoclinic |
| space group | <i>P</i> 2 ₁ / <i>n</i> (an alternate setting of <i>P</i> 2 ₁ / <i>c</i> [No. 14]) |
| unit cell parameters ^a | |
| <i>a</i> (Å) | 18.8950 (7) |
| <i>b</i> (Å) | 23.2217 (8) |
| <i>c</i> (Å) | 19.6141 (7) |
| β (deg) | 101.4421 (6) |
| <i>V</i> (Å ³) | 8435.1 (5) |
| <i>Z</i> | 8 |
| ρ _{calcd} (g cm ⁻³) | 1.218 |
| μ (mm ⁻¹) | 0.599 |

B. Data Collection and Refinement Conditions

| | |
|--|--|
| diffractometer | Bruker D8/APEX II CCD ^b |
| radiation (λ [Å]) | graphite-monochromated Mo Kα (0.71073) |
| temperature (°C) | -100 |
| scan type | ω scans (0.3°) (20 s exposures) |
| data collection 2θ limit (deg) | 52.80 |
| total data collected | 273531 (-23 ≤ h ≤ 23, -29 ≤ k ≤ 29, - |
| 24 ≤ l ≤ 24) | |
| independent reflections | 17475 (<i>R</i> _{int} = 0.0731) |
| number of observed reflections (<i>NO</i>) | 13784 [<i>F</i> _o ² ≥ 2σ(<i>F</i> _o ²)] |
| structure solution method | intrinsic phasing (<i>SHELXT-2014</i> ^c) |
| refinement method | full-matrix least-squares on <i>F</i> ² (<i>SHELXL-2014</i> ^d) |
| absorption correction method | multi-scan (<i>TWINABS</i>) |
| range of transmission factors | 0.7453–0.6886 |
| data/restraints/parameters | 17475 / 7 ^e / 933 |
| goodness-of-fit (<i>S</i>) ^f [all data] | 1.009 |
| final <i>R</i> indices ^g | |
| <i>R</i> ₁ [<i>F</i> _o ² ≥ 2σ(<i>F</i> _o ²)] | 0.0439 |
| <i>wR</i> ₂ [all data] | 0.1056 |
| largest difference peak and hole | 0.913 and -0.404 e Å ⁻³ |

^aObtained from least-squares refinement of 9949 reflections with 4.44° < 2θ < 48.46°.

(continued)

Table A18. Crystallographic experimental details for **4-NiH·DMAP** (continued).

^bPrograms for diffractometer operation, data collection, data reduction and absorption correction were those supplied by Bruker. The crystal used for data collection was found to display non-merohedral twinning. Both components of the twin were indexed with the program *CELL_NOW* (Bruker AXS Inc., Madison, WI, 2004). The second twin component can be related to the first component by 180° rotation about the [0.205 0 1] axis in real space and about the [0 0 1] axis in reciprocal space. Integrated intensities for the reflections from the two components were written into a *SHELXL-2014* HKLF 5 reflection file with the data integration program *SAINT* (version 8.34A), using all reflection data (exactly overlapped, partially overlapped and non-overlapped). The refined value of the twin fraction (*SHELXL-2014* BASF parameter) was 0.1137(4).

^cSheldrick, G. M. *Acta Crystallogr.* **2015**, *A71*, 3–8. (*SHELXT-2014*)

^dSheldrick, G. M. *Acta Crystallogr.* **2015**, *C71*, 3–8. (*SHELXL-2014*)

^eThe partially-occupied and inversion-disordered solvent diethylether molecule (O2S, C5S, C6S, C7S, C8S) was restrained to have the same approximate geometry as the well-behaved one by use of the *SHELXL SAME* instruction.

$$fS = [\sum w(F_o^2 - F_c^2)^2 / (n - p)]^{1/2} \quad (n = \text{number of data}; p = \text{number of parameters varied}; w = [\sigma^2(F_o^2) + (0.0493P)^2 + 5.1793P]^{-1} \text{ where } P = [\text{Max}(F_o^2, 0) + 2F_c^2] / 3).$$

$$gR_1 = \sum ||F_o| - |F_c|| / \sum |F_o|; wR_2 = [\sum w(F_o^2 - F_c^2)^2 / \sum w(F_o^4)]^{1/2}.$$

Table A19. Crystallographic experimental details for **4-NiH·PMe₃-B**.

| | |
|--|--|
| <i>A. Crystal Data</i> | |
| formula | C ₄₁ H ₆₃ N ₂ NiP ₃ Si |
| formula weight | 763.64 |
| crystal dimensions (mm) | 0.23 × 0.17 × 0.13 |
| crystal system | monoclinic |
| space group | <i>P</i> 2 ₁ / <i>c</i> (No. 14) |
| unit cell parameters ^a | |
| <i>a</i> (Å) | 17.6347 (3) |
| <i>b</i> (Å) | 13.1652 (2) |
| <i>c</i> (Å) | 18.6399 (3) |
| β (deg) | 109.6247 (10) |
| <i>V</i> (Å ³) | 4076.15 (12) |
| <i>Z</i> | 4 |
| ρ_{calcd} (g cm ⁻³) | 1.244 |
| μ (mm ⁻¹) | 2.301 |
| <i>B. Data Collection and Refinement Conditions</i> | |
| diffractometer | Bruker D8/APEX II CCD ^b |
| radiation (λ [Å]) | Cu K α (1.54178) (microfocus source) |
| temperature (°C) | -100 |
| scan type | ω and ϕ scans (1.0°) (5 s exposures) |
| data collection 2θ limit (deg) | 144.77 |
| total data collected | 27960 ($-21 \leq h \leq 21$, $-16 \leq k \leq 16$, $-23 \leq l \leq 23$) |
| independent reflections | 7939 ($R_{\text{int}} = 0.0279$) |
| number of observed reflections (<i>NO</i>) | 7340 [$F_o^2 \geq 2\sigma(F_o^2)$] |
| structure solution method | intrinsic phasing (<i>SHELXT-2014</i> ^c) |
| refinement method | full-matrix least-squares on F^2 (<i>SHELXL-2014</i> ^d) |
| absorption correction method | Gaussian integration (face-indexed) |
| range of transmission factors | 0.8076–0.6264 |
| data/restraints/parameters | 7939 / 0 / 444 |
| goodness-of-fit (<i>S</i>) ^e [all data] | 1.041 |
| final <i>R</i> indices ^f | |
| R_1 [$F_o^2 \geq 2\sigma(F_o^2)$] | 0.0355 |
| wR_2 [all data] | 0.0971 |
| largest difference peak and hole | 0.722 and -0.377 e Å ⁻³ |

^aObtained from least-squares refinement of 9726 reflections with $8.40^\circ < 2\theta < 144.60^\circ$.

^bPrograms for diffractometer operation, data collection, data reduction and absorption correction were those supplied by Bruker.

(continued)

Table A19. Crystallographic experimental details for **4-NiH·PMe₃-B** (continued).

^cSheldrick, G. M. *Acta Crystallogr.* **2015**, *A71*, 3–8. (*SHELXT-2014*)

^dSheldrick, G. M. *Acta Crystallogr.* **2015**, *C71*, 3–8. (*SHELXL-2014*)

^e $S = [\sum w(F_o^2 - F_c^2)^2 / (n - p)]^{1/2}$ (n = number of data; p = number of parameters varied; w

= $[\sigma^2(F_o^2) + (0.0477P)^2 + 3.2330P]^{-1}$ where $P = [\text{Max}(F_o^2, 0) + 2F_c^2]/3$).

^f $R_1 = \sum ||F_o| - |F_c|| / \sum |F_o|$; $wR_2 = [\sum w(F_o^2 - F_c^2)^2 / \sum w(F_o^4)]^{1/2}$.

Table A20. Crystallographic experimental details for **4-PtH·PMe₃**.

| | |
|---|--|
| <i>A. Crystal Data</i> | |
| formula | C ₃₄ H ₅₅ N ₂ P ₃ PtSi |
| formula weight | 807.89 |
| crystal dimensions (mm) | 0.37 × 0.21 × 0.20 |
| crystal system | triclinic |
| space group | <i>P</i> $\bar{1}$ (No. 2) |
| unit cell parameters ^a | |
| <i>a</i> (Å) | 9.9582 (4) |
| <i>b</i> (Å) | 10.4020 (4) |
| <i>c</i> (Å) | 18.4471 (7) |
| α (deg) | 77.5676 (4) |
| β (deg) | 76.2985 (4) |
| γ (deg) | 89.4415 (4) |
| <i>V</i> (Å ³) | 1811.22 (12) |
| <i>Z</i> | 2 |
| ρ_{calcd} (g cm ⁻³) | 1.481 |
| μ (mm ⁻¹) | 4.064 |
| <i>B. Data Collection and Refinement Conditions</i> | |
| diffractometer | Bruker PLATFORM/APEX II CCD ^b |
| radiation (λ [Å]) | graphite-monochromated Mo K α (0.71073) |
| temperature (°C) | -100 |
| scan type | ω scans (0.3°) (15 s exposures) |
| data collection 2θ limit (deg) | 56.79 |
| total data collected | 17173 ($-13 \leq h \leq 13$, $-13 \leq k \leq 13$, $-24 \leq l \leq 24$) |
| independent reflections | 8854 ($R_{\text{int}} = 0.0167$) |
| number of observed reflections (<i>NO</i>) | 8273 [$F_o^2 \geq 2\sigma(F_o^2)$] |
| structure solution method | intrinsic phasing (<i>SHELXT-2014</i> ^c) |
| refinement method | full-matrix least-squares on F^2 (<i>SHELXL-2014</i> ^d) |
| absorption correction method | Gaussian integration (face-indexed) |
| range of transmission factors | 0.6208–0.3513 |
| data/restraints/parameters | 8854 / 0 / 380 |
| goodness-of-fit (<i>S</i>) ^e [all data] | 1.065 |
| final <i>R</i> indices ^f | |
| <i>R</i> ₁ [$F_o^2 \geq 2\sigma(F_o^2)$] | 0.0215 |
| <i>wR</i> ₂ [all data] | 0.0541 |
| largest difference peak and hole | 2.825 and -0.424 e Å ⁻³ |

^aObtained from least-squares refinement of 9916 reflections with $4.66^\circ < 2\theta < 56.78^\circ$.

(continued)

Table A20. Crystallographic experimental details for **4-PtH·PMe₃** (continued).

^bPrograms for diffractometer operation, data collection, data reduction and absorption correction were those supplied by Bruker.

^cSheldrick, G. M. *Acta Crystallogr.* **2015**, *A71*, 3–8.

^dSheldrick, G. M. *Acta Crystallogr.* **2015**, *C71*, 3–8.

^e $S = [\sum w(F_o^2 - F_c^2)^2 / (n - p)]^{1/2}$ (n = number of data; p = number of parameters varied; w = $[\sigma^2(F_o^2) + (0.0304P)^2 + 0.4035P]^{-1}$ where $P = [\text{Max}(F_o^2, 0) + 2F_c^2]/3$).

^f $R_1 = \sum ||F_o| - |F_c|| / \sum |F_o|$; $wR_2 = [\sum w(F_o^2 - F_c^2)^2 / \sum w(F_o^4)]^{1/2}$.

Table A21. Crystallographic experimental details for **5-1**.*A. Crystal Data*

| | |
|--|--|
| formula | C ₃₅ H ₄₈ BrFeN ₂ P |
| formula weight | 663.48 |
| crystal dimensions (mm) | 0.31 × 0.07 × 0.06 |
| crystal system | monoclinic |
| space group | <i>P</i> 2 ₁ / <i>n</i> (an alternate setting of <i>P</i> 2 ₁ / <i>c</i> [No. 14]) |
| unit cell parameters ^a | |
| <i>a</i> (Å) | 9.72928(15) |
| <i>b</i> (Å) | 17.6622(3) |
| <i>c</i> (Å) | 19.4543(3) |
| β (deg) | 94.8892(9) |
| <i>V</i> (Å ³) | 3330.87(9) |
| <i>Z</i> | 4 |
| ρ _{calcd} (g cm ⁻³) | 1.323 |
| μ (mm ⁻¹) | 5.669 |

B. Data Collection and Refinement Conditions

| | |
|--|--|
| diffractometer | Bruker D8/APEX II CCD ^b |
| radiation (λ [Å]) | Cu Kα (1.54178) (microfocus source) |
| temperature (°C) | -100 |
| scan type | ω and φ scans (1.0°) (5-5-15 s exposures) ^c |
| data collection 2θ limit (deg) | 147.96 |
| total data collected | 22605 (-12 ≤ <i>h</i> ≤ 12, -22 ≤ <i>k</i> ≤ 21, -24 ≤ <i>l</i> ≤ 24) |
| independent reflections | 6725 (<i>R</i> _{int} = 0.0459) |
| number of observed reflections (<i>NO</i>) | 5816 [<i>F</i> _o ² ≥ 2σ(<i>F</i> _o ²)] |
| structure solution method | intrinsic phasing (<i>SHELXT-2014</i> ^d) |
| refinement method | full-matrix least-squares on <i>F</i> ² (<i>SHELXL-2014</i> ^e) |
| absorption correction method | Gaussian integration (face-indexed) |
| range of transmission factors | 0.8067–0.4611 |
| data/restraints/parameters | 6725 / 0 / 361 |
| goodness-of-fit (<i>S</i>) ^f [all data] | 1.064 |
| final <i>R</i> indices ^g | |
| <i>R</i> ₁ [<i>F</i> _o ² ≥ 2σ(<i>F</i> _o ²)] | 0.0306 |
| <i>wR</i> ₂ [all data] | 0.0820 |
| largest difference peak and hole | 0.331 and -0.568 e Å ⁻³ |

^aObtained from least-squares refinement of 9758 reflections with 6.78° < 2θ < 147.58°.

^bPrograms for diffractometer operation, data collection, data reduction and absorption correction were those supplied by Bruker.

(continued)

Table A21. Crystallographic experimental details for **5-1** (continued).

^cData were collected with the detector set at three different positions. Low-angle (detector $2\theta = -33^\circ$) and medium-angle (detector $2\theta = 75^\circ$) data frames were collected using a scan time of 5 s, and high-angle (detector $2\theta = 117^\circ$) frames using a scan time of 15 s.

^dSheldrick, G. M. *Acta Crystallogr.* **2015**, *A71*, 3–8.

^eSheldrick, G. M. *Acta Crystallogr.* **2015**, *C71*, 3–8.

^f $S = [\sum w(F_o^2 - F_c^2)^2 / (n - p)]^{1/2}$ (n = number of data; p = number of parameters varied; $w = [\sigma^2(F_o^2) + (0.0427P)^2 + 0.0996P]^{-1}$ where $P = [\text{Max}(F_o^2, 0) + 2F_c^2]/3$).

^g $R_1 = \sum ||F_o| - |F_c|| / \sum |F_o|$; $wR_2 = [\sum w(F_o^2 - F_c^2)^2 / \sum w(F_o^4)]^{1/2}$.

Table A22. Crystallographic experimental details for **5-2**.*A. Crystal Data*

| | |
|---|--|
| formula | C ₃₆ H ₆₁ FeN ₂ PSi ₂ |
| formula weight | 664.86 |
| crystal dimensions (mm) | 0.29 × 0.24 × 0.21 |
| crystal system | triclinic |
| space group | <i>P</i> $\bar{1}$ (No. 2) |
| unit cell parameters ^a | |
| <i>a</i> (Å) | 10.6970(6) |
| <i>b</i> (Å) | 11.3411(7) |
| <i>c</i> (Å) | 16.9178(10) |
| α (deg) | 94.596(4) |
| β (deg) | 99.042(3) |
| γ (deg) | 105.326(4) |
| <i>V</i> (Å ³) | 1938.8(2) |
| <i>Z</i> | 2 |
| ρ_{calcd} (g cm ⁻³) | 1.139 |
| μ (mm ⁻¹) | 4.275 |
| <i>B. Data Collection and Refinement Conditions</i> | |
| diffractometer | Bruker D8/APEX II CCD ^b |
| radiation (λ [Å]) | Cu K α (1.54178) (microfocus source) |
| temperature (°C) | -100 |
| scan type | ω and ϕ scans (1.0°) (5-5-10 s exposures) ^c |
| data collection 2θ limit (deg) | 148.18 |
| total data collected | 13446 ($-13 \leq h \leq 13$, $-14 \leq k \leq 13$, $-20 \leq l \leq 20$) |
| independent reflections | 7528 ($R_{\text{int}} = 0.0384$) |
| number of observed reflections (<i>NO</i>) | 6225 [$F_o^2 \geq 2\sigma(F_o^2)$] |
| structure solution method | Patterson/structure expansion (<i>DIRDIF-2008</i> ^d) |
| refinement method | full-matrix least-squares on F^2 (<i>SHELXL-2014</i> ^e) |
| absorption correction method | Gaussian integration (face-indexed) |
| range of transmission factors | 0.5817–0.3473 |
| data/restraints/parameters | 7528 / 12 ^f / 409 |
| goodness-of-fit (<i>S</i>) ^g [all data] | 1.101 |
| final <i>R</i> indices ^h | |
| <i>R</i> ₁ [$F_o^2 \geq 2\sigma(F_o^2)$] | 0.0495 |
| <i>wR</i> ₂ [all data] | 0.1464 |
| largest difference peak and hole | 0.640 and -0.748 e Å ⁻³ |

^aObtained from least-squares refinement of 9853 reflections with $5.34^\circ < 2\theta < 147.52^\circ$.
(continued)

Table A22. Crystallographic experimental details for **5-2** (continued).

^bPrograms for diffractometer operation, data collection, data reduction and absorption correction were those supplied by Bruker.

^cData were collected with the detector set at three different positions. Low-angle (detector $2\theta = -33^\circ$) and medium-angle (detector $2\theta = 75^\circ$) frames were collected using a scan time of 5 s, and high-angle (detector $2\theta = 117^\circ$) frames using a scan time of 10 s.

^dBeurskens, P. T.; Beurskens, G.; de Gelder, R.; Smits, J. M. M.; Garcia-Granda, S.; Gould, R. O. (2008). The *DIRDIF-2008* program system. Crystallography Laboratory, Radboud University Nijmegen, The Netherlands.

^eSheldrick, G. M. *Acta Crystallogr.* **2015**, *C71*, 3–8.

^fCorresponding distances within the conformers of the disordered cyclohexyl group were constrained to be equal (within 0.03 Å) during refinement: $d(\text{C11A-C12A}) = d(\text{C11B-C12B})$; $d(\text{C11A-C16A}) = d(\text{C11B-C16B})$; $d(\text{C12A-C13A}) = d(\text{C12B-C13B})$; $d(\text{C13A-C14A}) = d(\text{C13B-C14B})$; $d(\text{C14A-C15A}) = d(\text{C14B-C15B})$; $d(\text{C15A-C16A}) = d(\text{C15B-C16B})$; $d(\text{C11A}\cdots\text{C13A}) = d(\text{C11B}\cdots\text{C13B})$; $d(\text{C11A}\cdots\text{C15A}) = d(\text{C11B}\cdots\text{C15B})$; $d(\text{C12A}\cdots\text{C14A}) = d(\text{C12B}\cdots\text{C14B})$; $d(\text{C12A}\cdots\text{C16A}) = d(\text{C12B}\cdots\text{C16B})$; $d(\text{C13A}\cdots\text{C15A}) = d(\text{C13B}\cdots\text{C15B})$; $d(\text{C14A}\cdots\text{C16A}) = d(\text{C14B}\cdots\text{C16B})$.

$gS = [\sum w(F_o^2 - F_c^2)^2 / (n - p)]^{1/2}$ (n = number of data; p = number of parameters varied; $w = [\sigma^2(F_o^2) + (0.0890P)^2]^{-1}$ where $P = [\text{Max}(F_o^2, 0) + 2F_c^2]/3$).

$^hR_1 = \sum \|F_o\| - |F_c| / \sum \|F_o\|$; $wR_2 = [\sum w(F_o^2 - F_c^2)^2 / \sum w(F_o^4)]^{1/2}$.

Table A23. Crystallographic experimental details for **5-8**.

| | |
|---|--|
| <i>A. Crystal Data</i> | |
| formula | C ₃₉ H ₅₉ FeN ₂ PSi |
| formula weight | 670.79 |
| crystal dimensions (mm) | 0.34 × 0.13 × 0.08 |
| crystal system | triclinic |
| space group | <i>P</i> $\bar{1}$ (No. 2) |
| unit cell parameters ^a | |
| <i>a</i> (Å) | 10.0874(14) |
| <i>b</i> (Å) | 12.5644(17) |
| <i>c</i> (Å) | 17.029(2) |
| α (deg) | 96.7695(18) |
| β (deg) | 101.6157(17) |
| γ (deg) | 112.4657(16) |
| <i>V</i> (Å ³) | 1907.8(5) |
| <i>Z</i> | 2 |
| ρ_{calcd} (g cm ⁻³) | 1.168 |
| μ (mm ⁻¹) | 0.496 |
| <i>B. Data Collection and Refinement Conditions</i> | |
| diffractometer | Bruker PLATFORM/APEX II CCD ^b |
| radiation (λ [Å]) | graphite-monochromated Mo K α (0.71073) |
| temperature (°C) | -80 |
| scan type | ω scans (0.3°) (20 s exposures) |
| data collection 2θ limit (deg) | 54.86 |
| total data collected | 17071 ($-13 \leq h \leq 13$, $-16 \leq k \leq 16$, $-22 \leq l \leq 22$) |
| independent reflections | 8660 ($R_{\text{int}} = 0.0553$) |
| number of observed reflections (<i>NO</i>) | 5632 [$F_o^2 \geq 2\sigma(F_o^2)$] |
| structure solution method | Patterson/structure expansion (<i>DIRDIF-2008</i> ^c) |
| refinement method | full-matrix least-squares on F^2 (<i>SHELXL-2014</i> ^d) |
| absorption correction method | Gaussian integration (face-indexed) |
| range of transmission factors | 1.0000–0.8196 |
| data/restraints/parameters | 8660 / 0 / 400 |
| goodness-of-fit (<i>S</i>) ^e [all data] | 0.992 |
| final <i>R</i> indices ^f | |
| <i>R</i> ₁ [$F_o^2 \geq 2\sigma(F_o^2)$] | 0.0539 |
| <i>wR</i> ₂ [all data] | 0.1506 |
| largest difference peak and hole | 0.542 and -0.616 e Å ⁻³ |

^aObtained from least-squares refinement of 5448 reflections with $4.46^\circ < 2\theta < 51.24^\circ$.
(continued)

Table A23. Crystallographic experimental details for **5-8** (continued).

^bPrograms for diffractometer operation, data collection, data reduction and absorption correction were those supplied by Bruker.

^cBeurskens, P. T.; Beurskens, G.; de Gelder, R.; Smits, J. M. M.; Garcia-Granda, S.; Gould, R. O. (2008). The *DIRDIF-2008* program system. Crystallography Laboratory, Radboud University Nijmegen, The Netherlands.

^dSheldrick, G. M. *Acta Crystallogr.* **2015**, *C71*, 3–8.

^e $S = [\sum w(F_o^2 - F_c^2)^2 / (n - p)]^{1/2}$ (n = number of data; p = number of parameters varied; $w = [\sigma^2(F_o^2) + (0.0754P)^2]^{-1}$ where $P = [\text{Max}(F_o^2, 0) + 2F_c^2]/3$).

^f $R_1 = \sum ||F_o| - |F_c|| / \sum |F_o|$; $wR_2 = [\sum w(F_o^2 - F_c^2)^2 / \sum w(F_o^4)]^{1/2}$.

Appendix B: Selected NMR Spectra of Reported Compounds

Selected Spectra of Compounds Reported in Chapter 2

Figure B1. ^1H NMR spectrum (benzene- d_6 , 300 MHz) of 2-Cl.

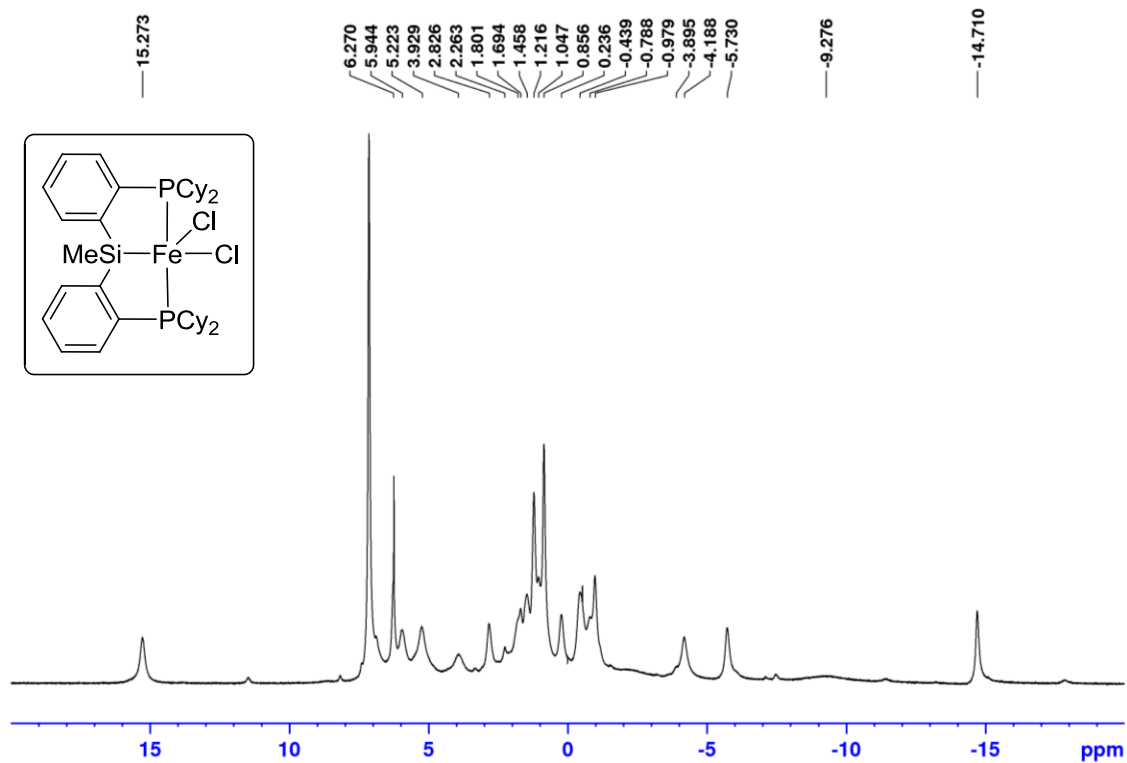


Figure B2. ^1H NMR spectrum (benzene- d_6 , 300 MHz) of **2-PMe₃**.

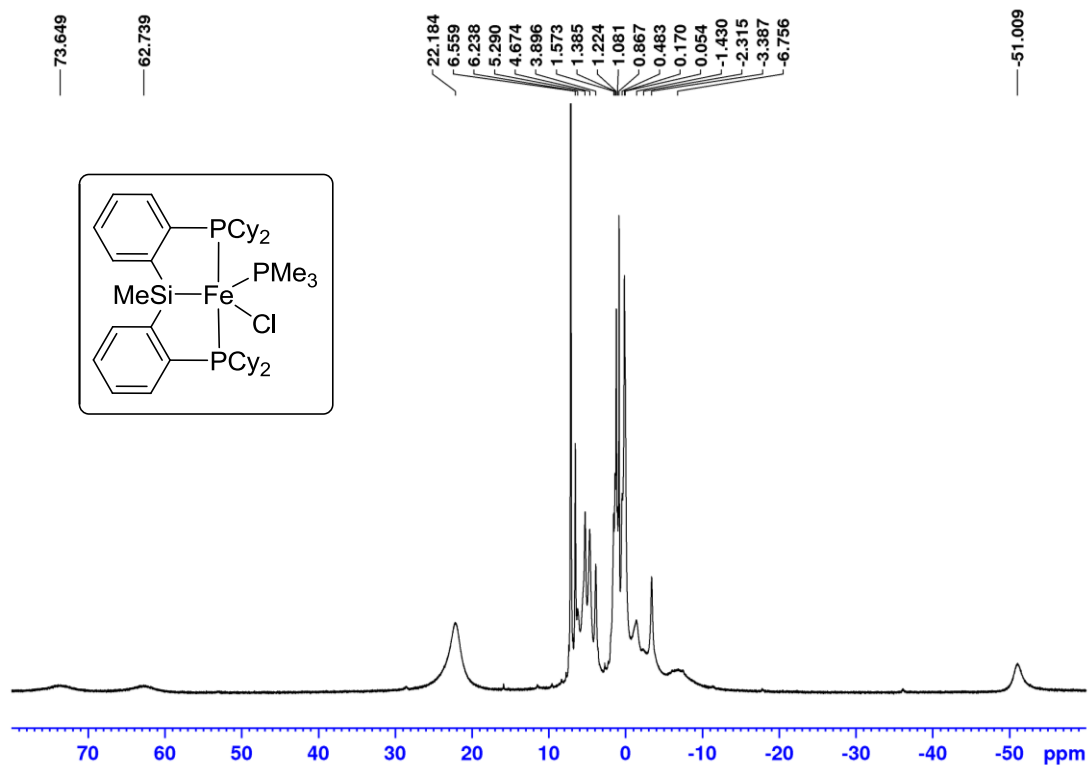


Figure B3. ^1H NMR spectrum (benzene- d_6 , 300 MHz) of **2-py**.

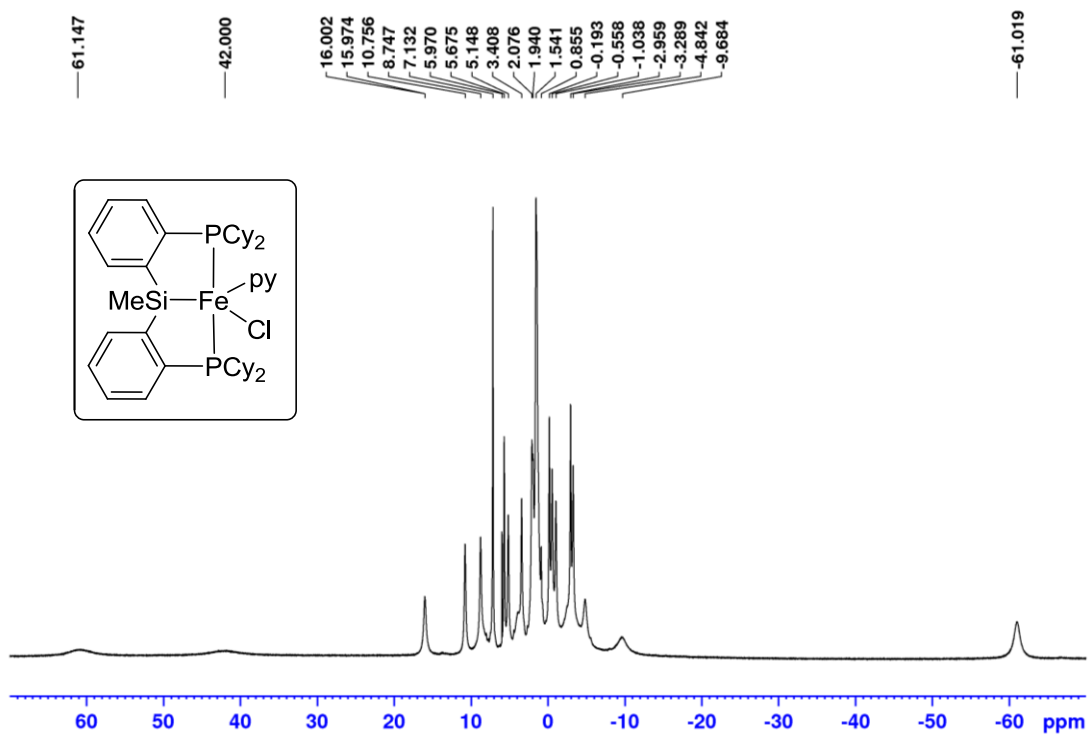


Figure B4. (A) ^1H NMR spectrum (benzene- d_6 , 300 MHz) of **2-(CO)₂**. (B) $^{31}\text{P}\{^1\text{H}\}$ NMR spectrum (benzene- d_6 , 121.5 MHz) of **2-(CO)₂**.

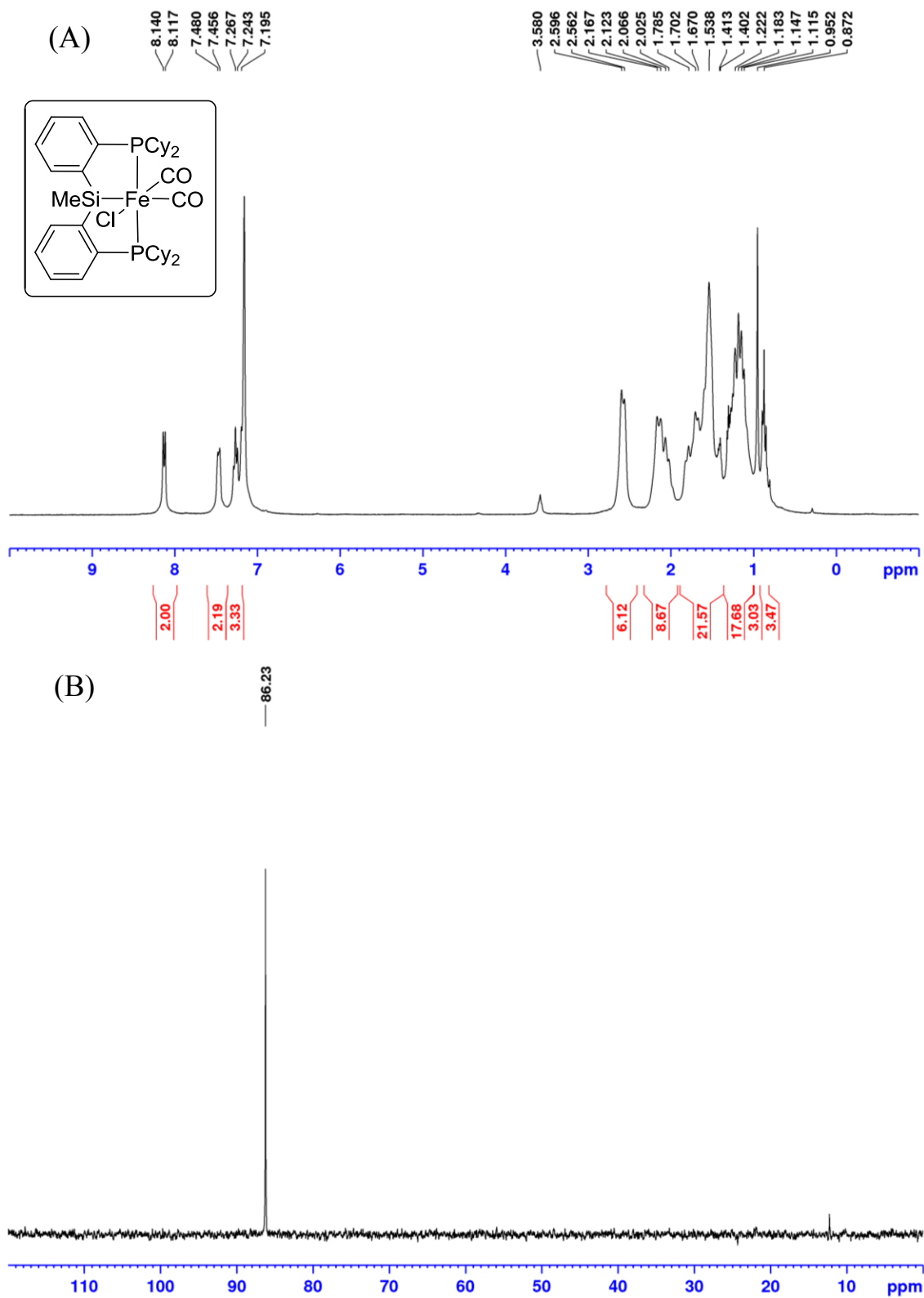


Figure B5. ^1H NMR spectrum (benzene- d_6 , 300 MHz) of **2-Fe^I**.

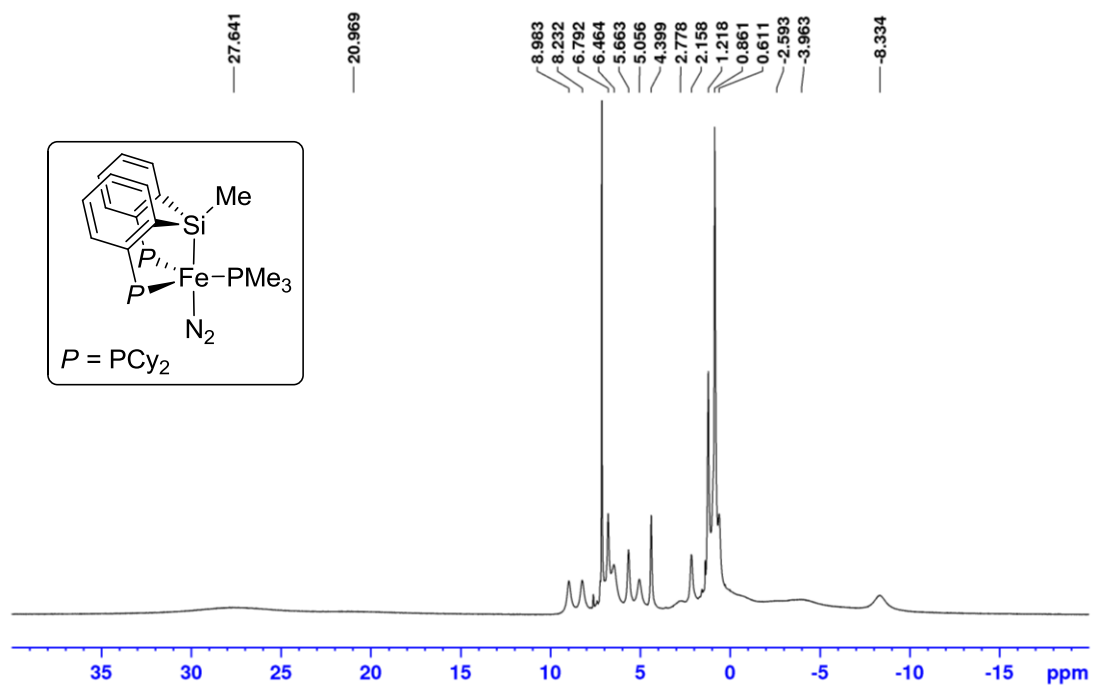


Figure B6. (A) ^1H NMR spectrum (cyclohexane- d_{12} , 300 MHz) of 2-Fe^0 . (B) $^{31}\text{P}\{^1\text{H}\}$ NMR spectrum (benzene- d_6 , 121.5 MHz) of 2-Fe^0 .

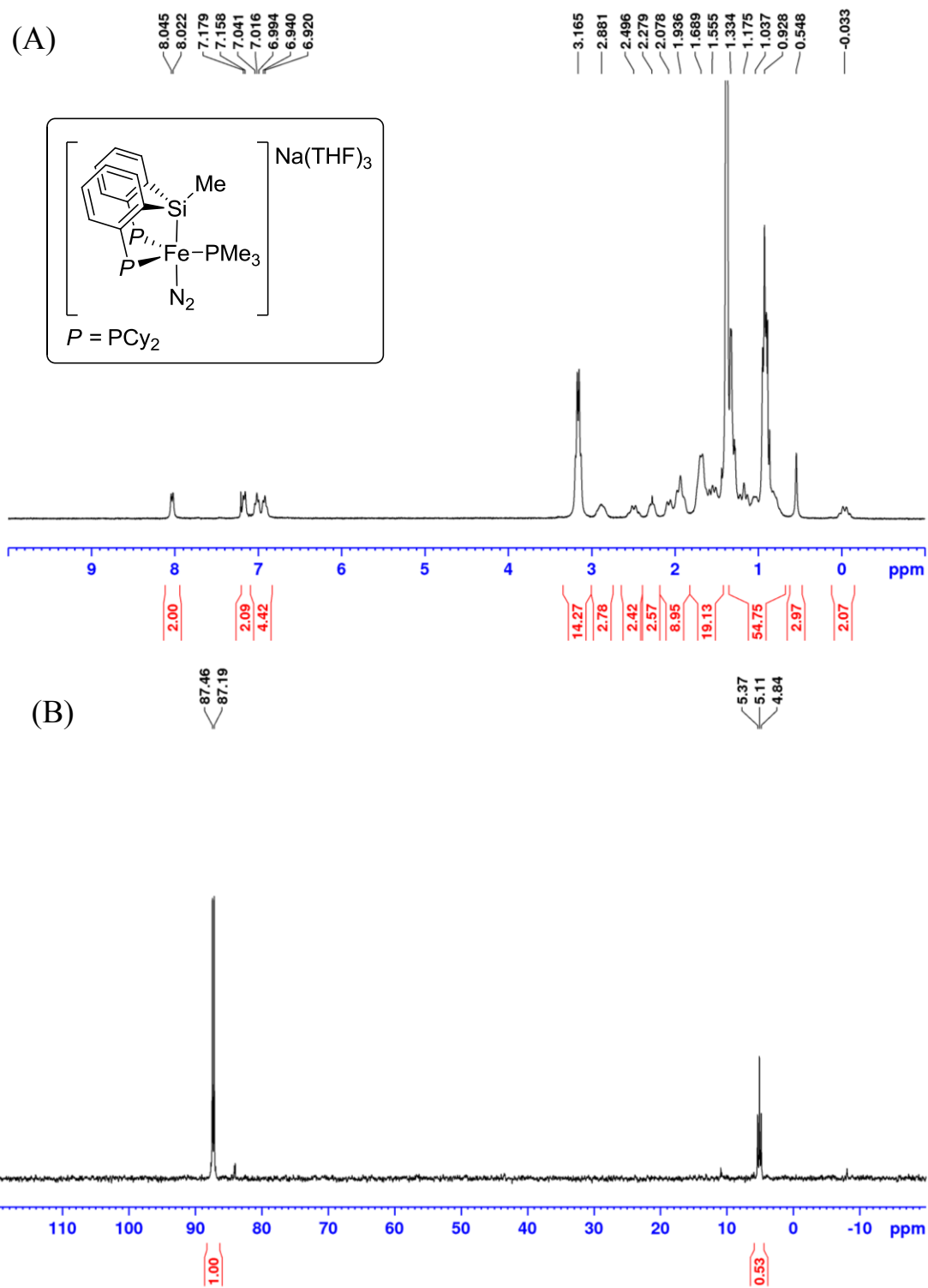


Figure B7. (A) ^1H NMR spectrum (benzene- d_6 , 500 MHz) of **2-H**. (B) $^{31}\text{P}\{^1\text{H}\}$ NMR spectrum (benzene- d_6 , 121.5 MHz) of **2-H**.

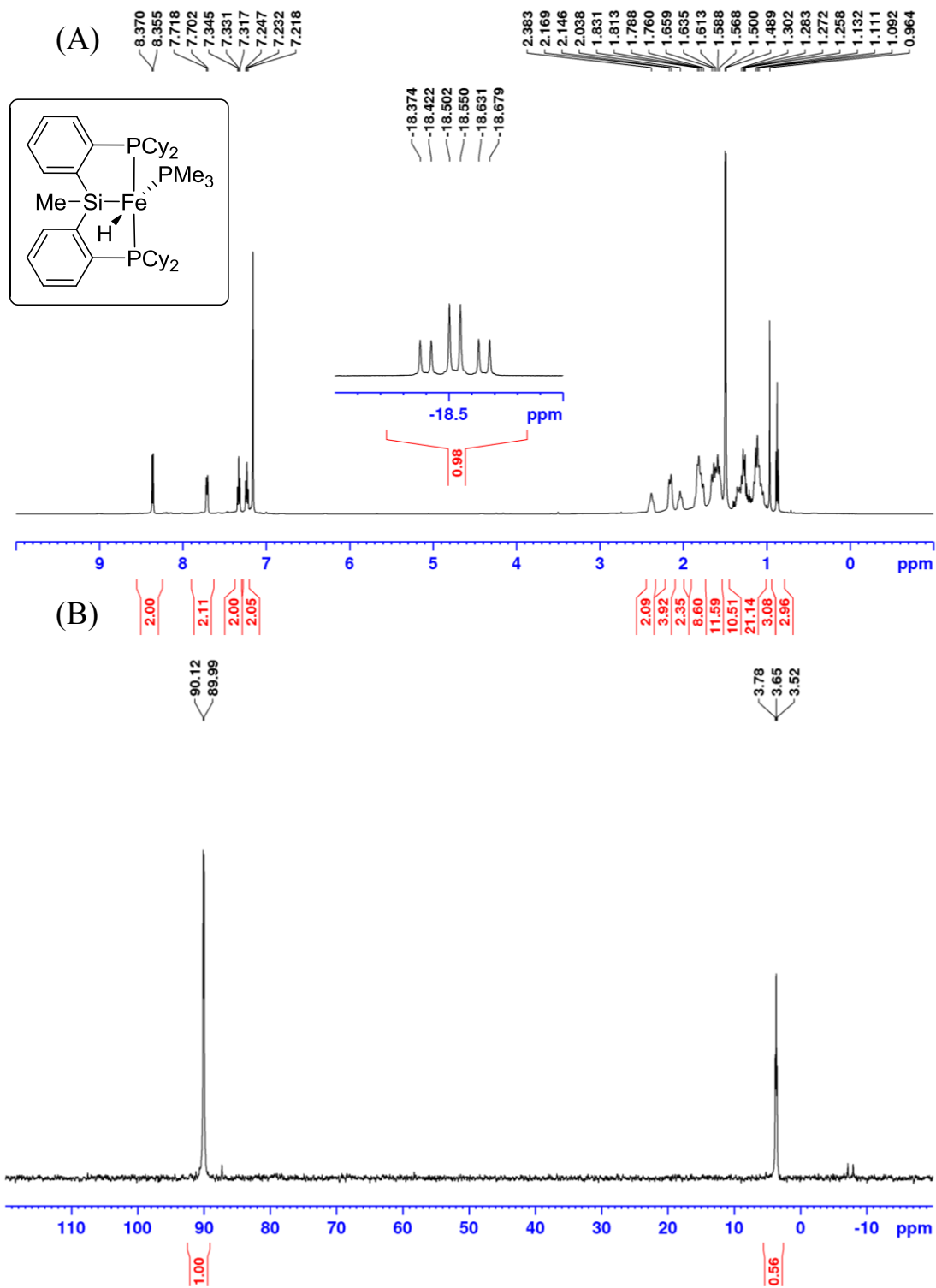


Figure B8. (A) ^1H NMR spectrum (toluene- d_8 , 300 MHz) of **2-H₃**. (B) $^{31}\text{P}\{^1\text{H}\}$ NMR spectrum (toluene- d_8 , 121.5 MHz) of **2-H₃**.

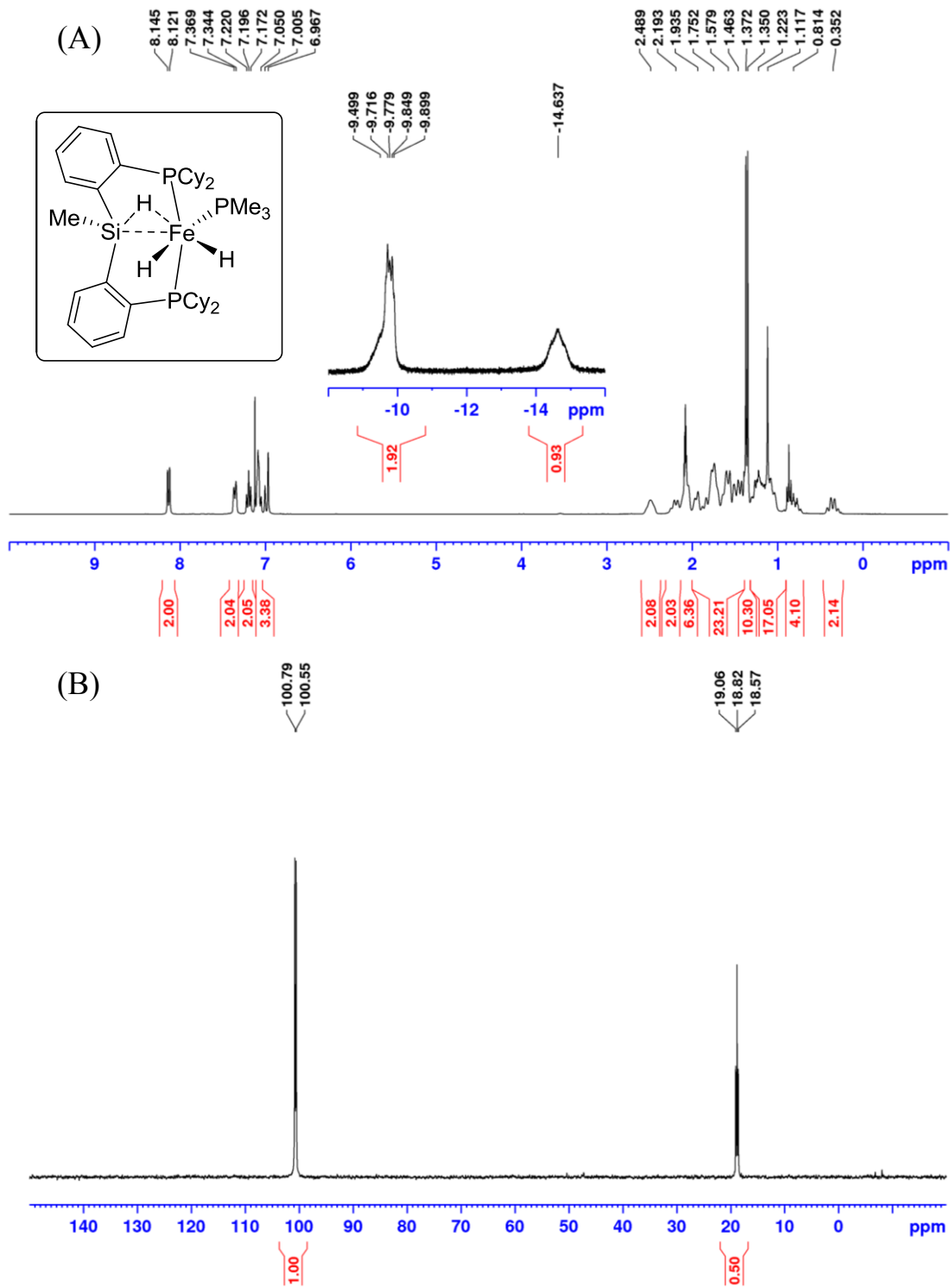


Figure B9. (A) ^1H NMR spectrum (toluene- d_8 , 253 K, 300 MHz) of **2-H₃**. (B) ^1H NMR spectrum (toluene- d_8 , 353 K, 500 MHz) of **2-H₃**.

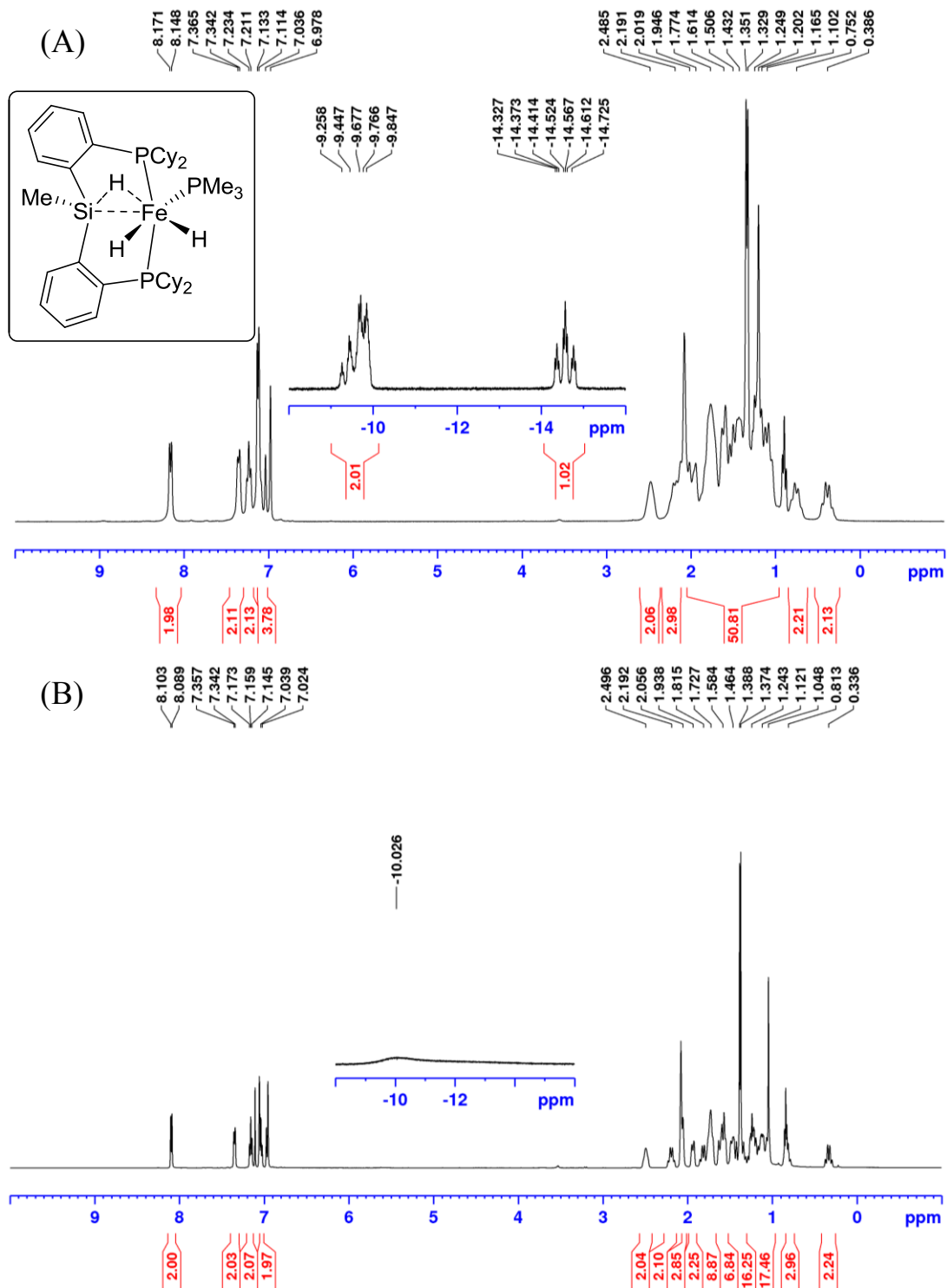


Figure B10. (A) ^1H NMR spectrum (benzene- d_6 , 300 MHz) of **2-py(N₂)**. (B) $^{31}\text{P}\{^1\text{H}\}$ NMR spectrum (benzene- d_6 , 121.5 MHz) of **2-py(N₂)**.

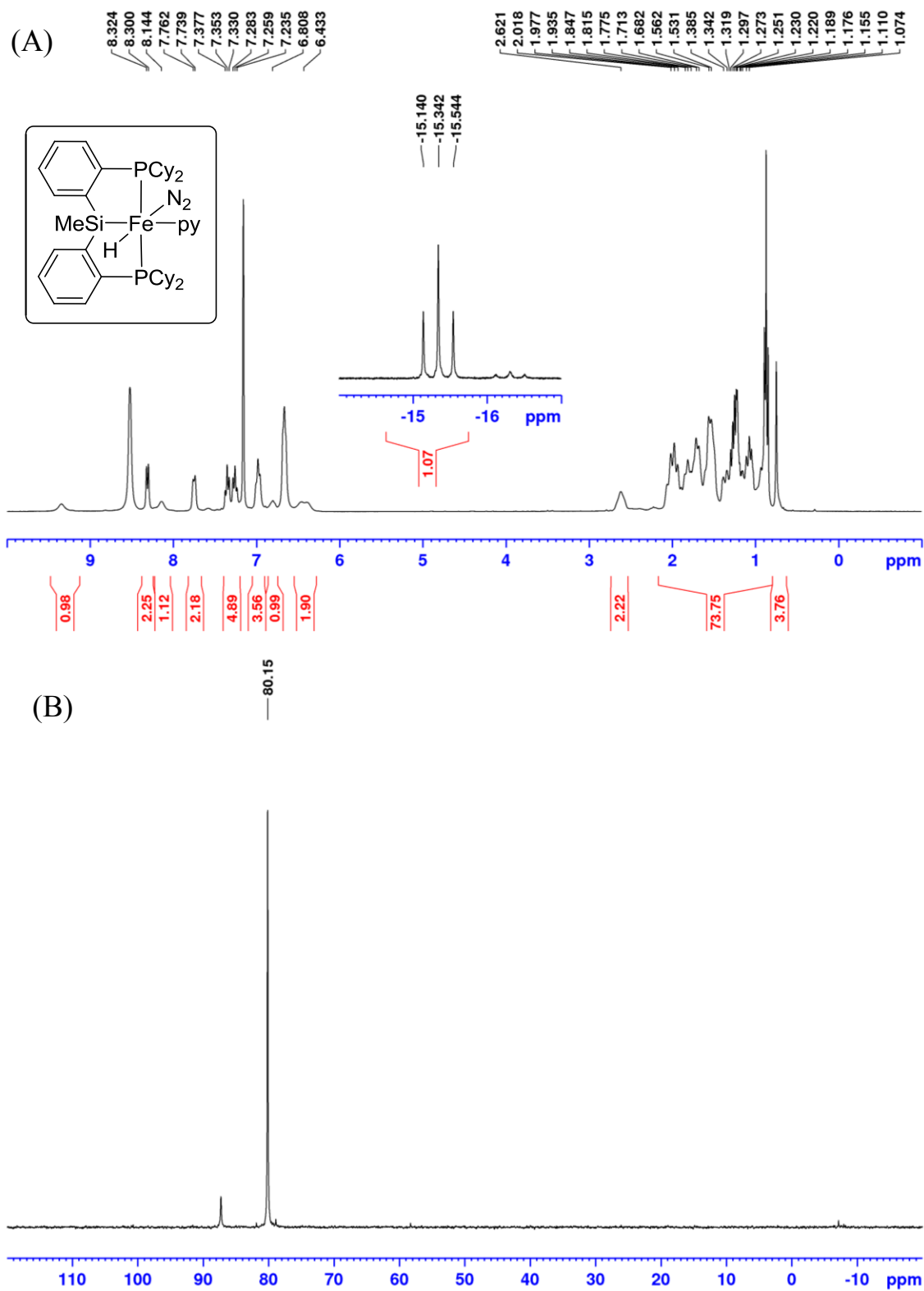
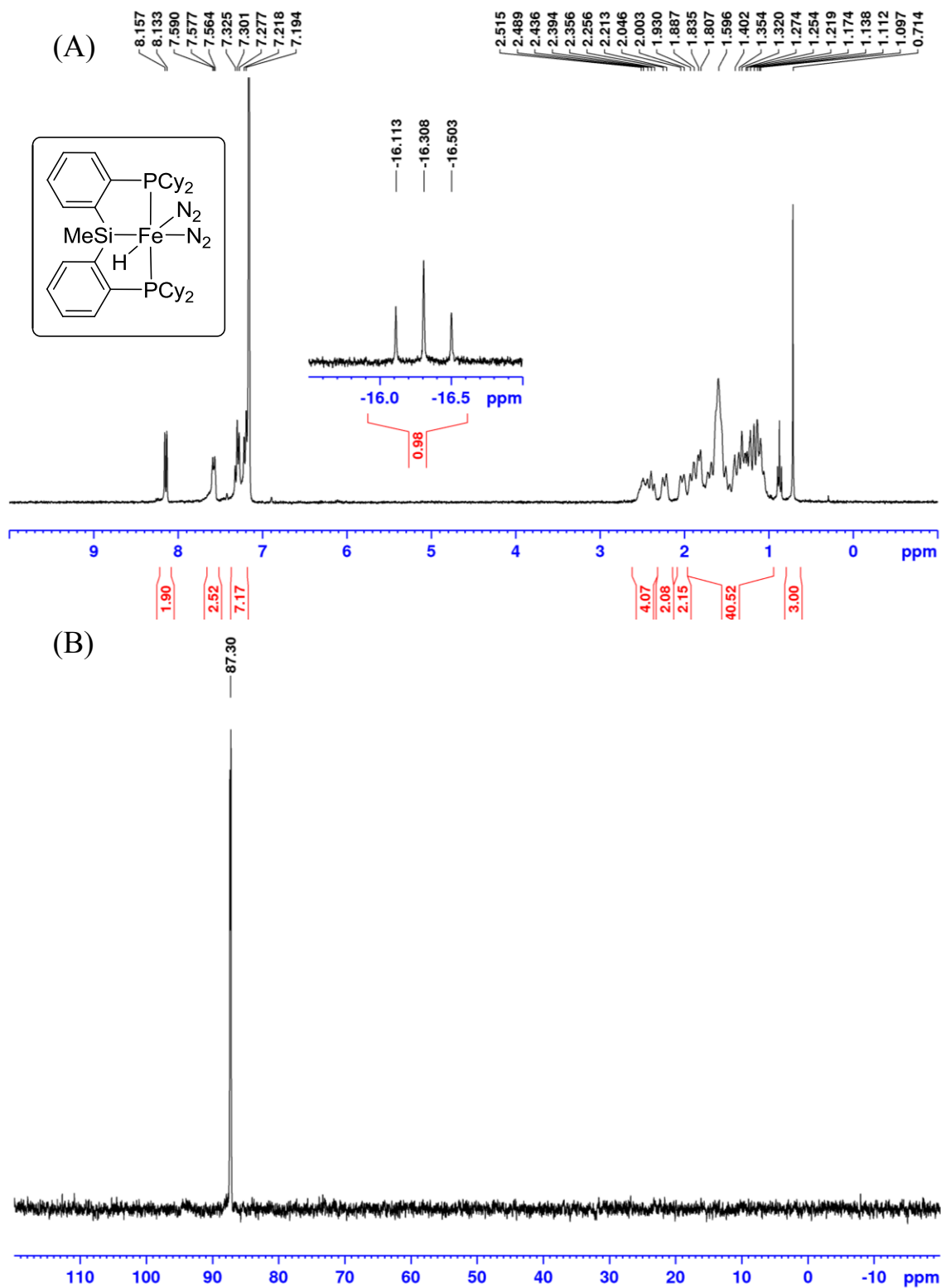


Figure B11. (A) ^1H NMR spectrum (benzene- d_6 , 300 MHz) of $2\text{-(N}_2\text{)}_2$. (B) $^{31}\text{P}\{^1\text{H}\}$ NMR spectrum (benzene- d_6 , 202.5 MHz) of $2\text{-(N}_2\text{)}_2$.



Selected NMR Spectra of Catalytic Hydrogenations Reported in Chapter 2

Figure B12. ^1H NMR spectrum (benzene- d_6 , 300 MHz) of hydrogenation of 1-octene (5 mol% catalyst, RT, 1 atm H_2 , 18 h)

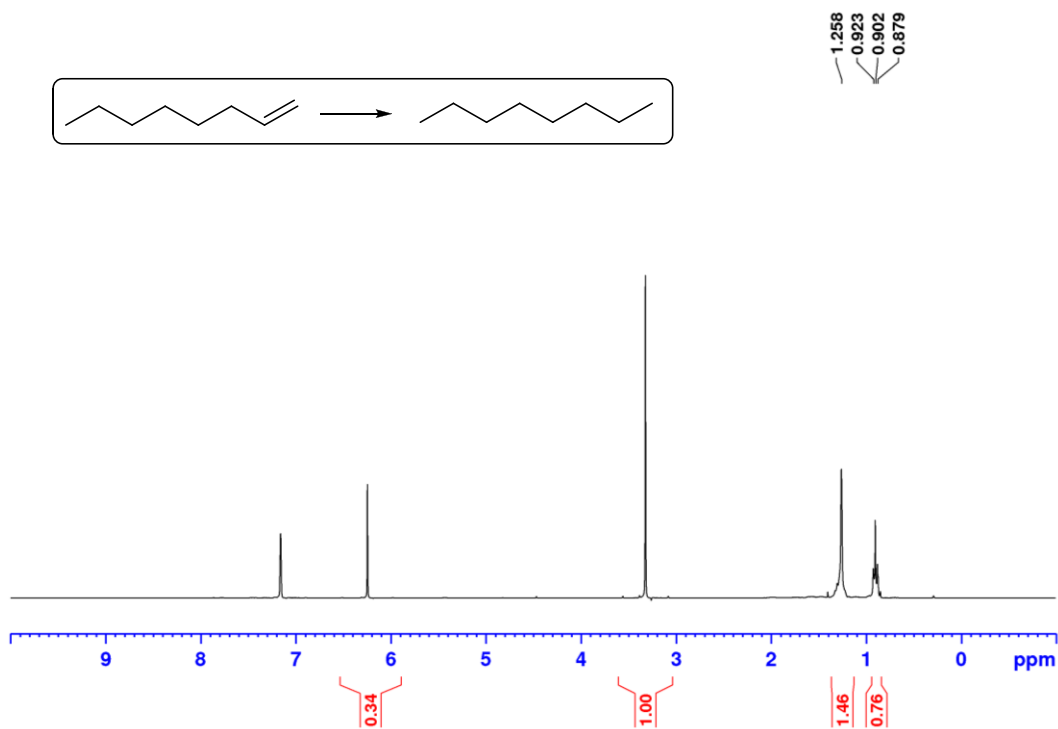


Figure B13. ^1H NMR spectrum (benzene- d_6 , 300 MHz) of hydrogenation of 1-octene (5 mol% catalyst, RT, 10 atm H_2 , 4 h).

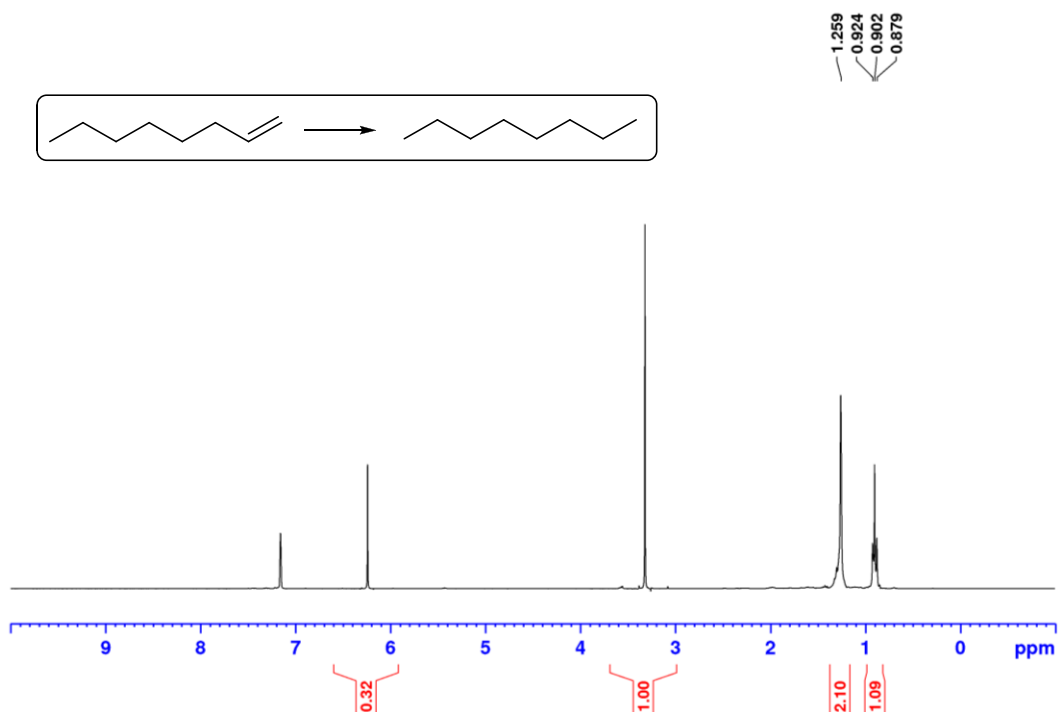


Figure B14. ^1H NMR spectrum (benzene- d_6 , 500 MHz) of hydrogenation of 1-octene (0.5 mol% catalyst, 65 °C, 10 atm H_2 , 4 h).

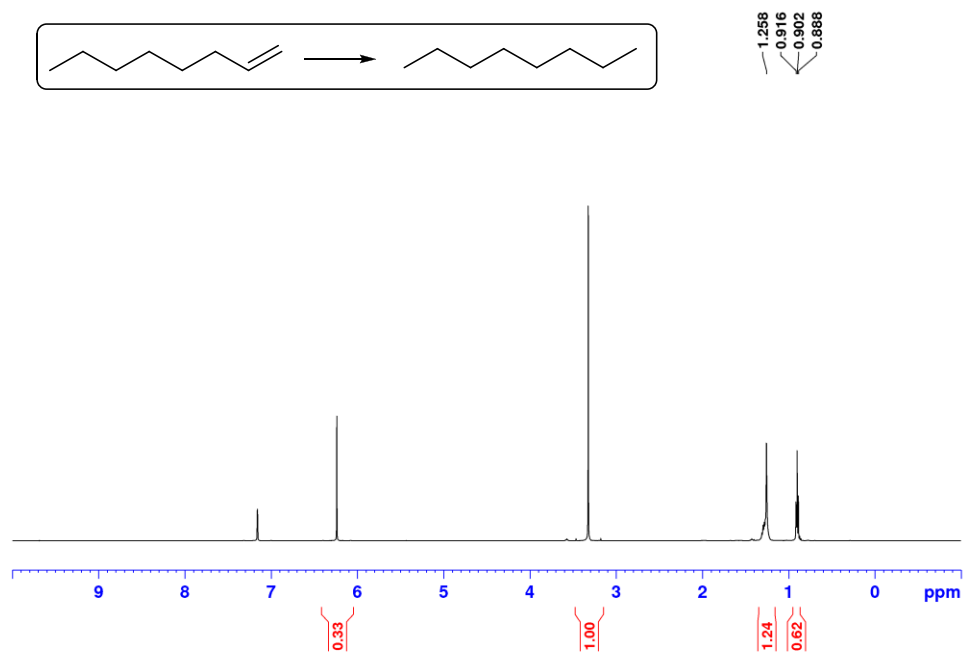


Figure B15. ^1H NMR spectrum (benzene- d_6 , 500 MHz) of hydrogenation of 1-octene (5 mol% catalyst, 65 °C, 10 atm H_2 , 4 h).

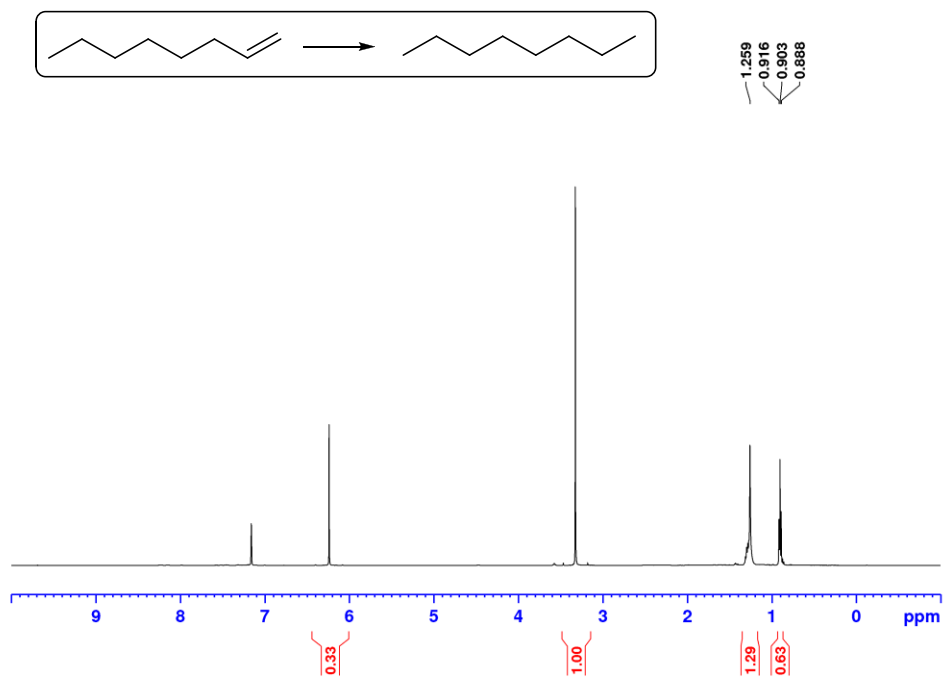


Figure B16. ^1H NMR spectrum (benzene- d_6 , 300 MHz) of hydrogenation of 1-octene (5 mol% catalyst, 65 °C, 1 atm H_2 , 4 h).

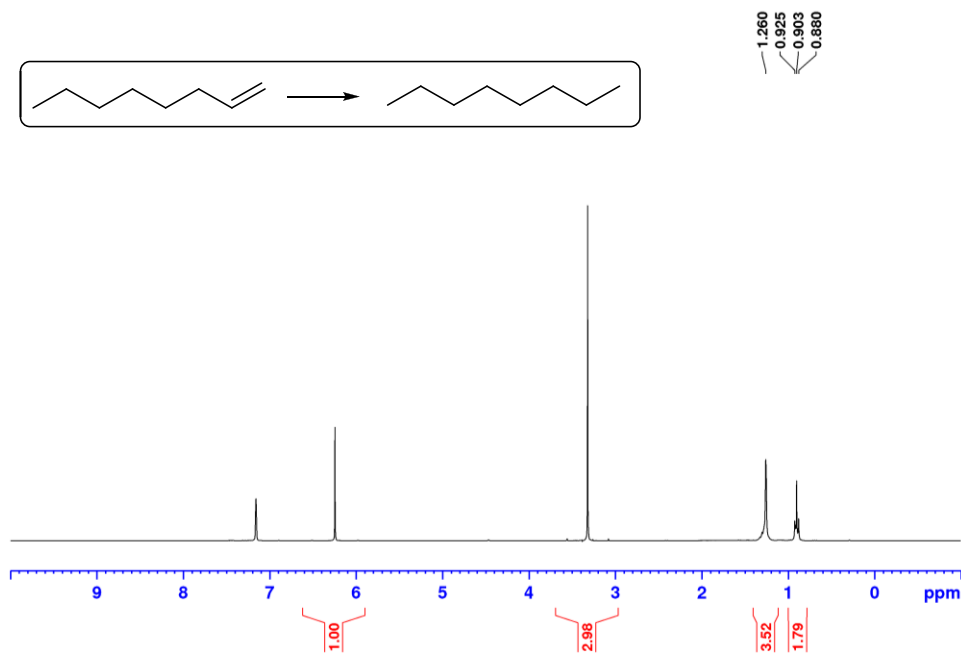


Figure B17. ^1H NMR spectrum (benzene- d_6 , 300 MHz) of hydrogenation of *cis*-4-octene (5 mol% catalyst, 65 °C, 10 atm H_2 , 4 h).

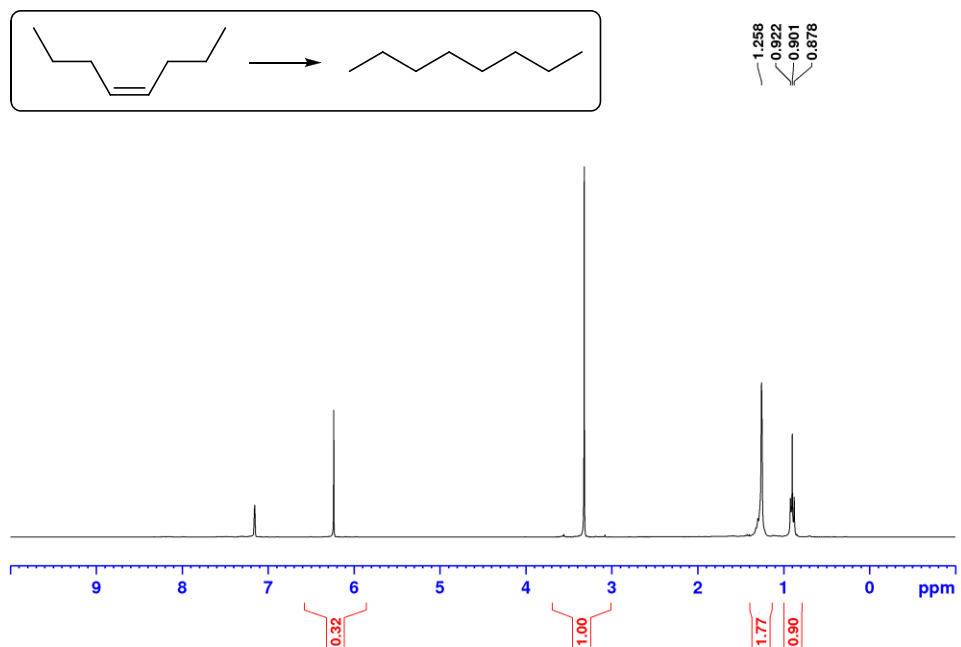


Figure B18. ^1H NMR spectrum (benzene- d_6 , 300 MHz) of hydrogenation of *trans*-4-octene (5 mol% catalyst, 65 °C, 10 atm H_2 , 4 h).

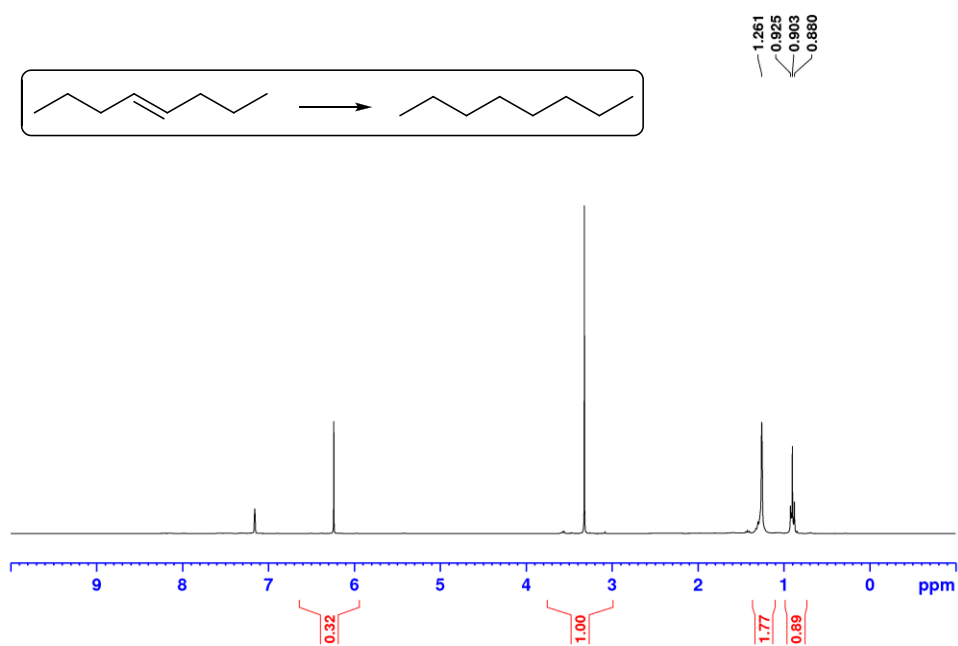


Figure B19. ^1H NMR spectrum (benzene- d_6 , 300 MHz) of hydrogenation of 4-vinylcyclohexene (5 mol% catalyst, 65 °C, 10 atm H_2 , 4 h).

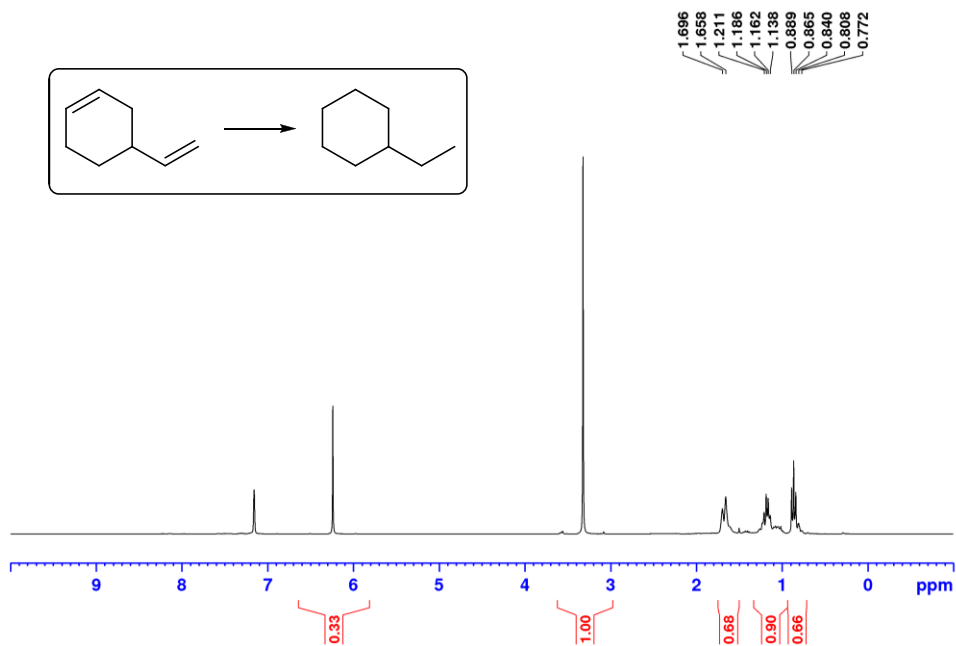


Figure B20. ^1H NMR spectrum (benzene- d_6 , 300 MHz) of hydrogenation of 4-vinylcyclohexene (5 mol% catalyst, RT, 10 atm H_2 , 4 h).

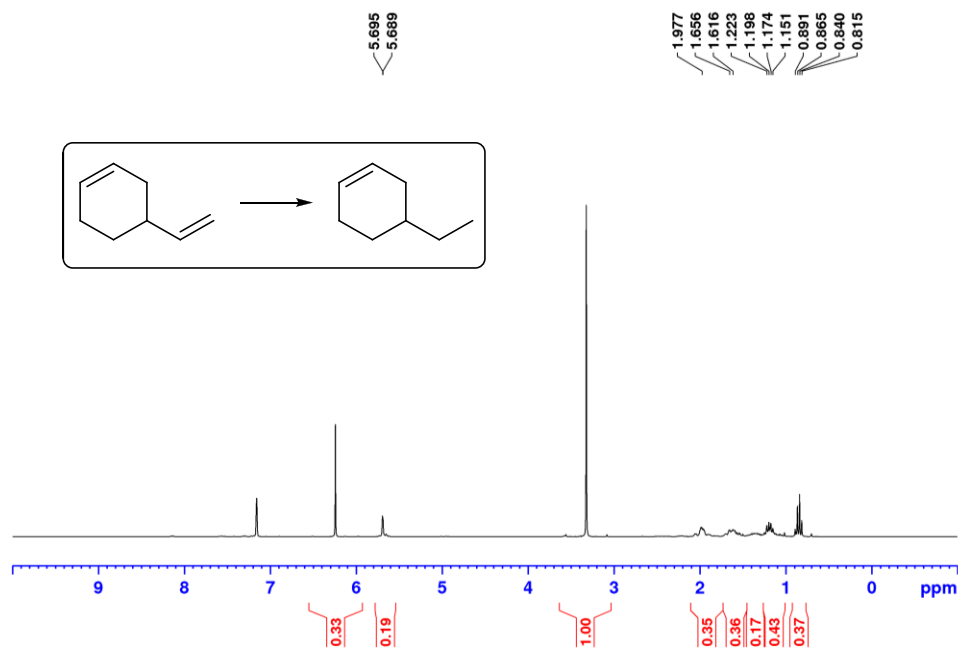


Figure B21. ^1H NMR spectrum (benzene- d_6 , 300 MHz) of hydrogenation of ethylidenecyclohexane (5 mol% catalyst, 65 $^\circ\text{C}$, 10 atm H_2 , 4 h).

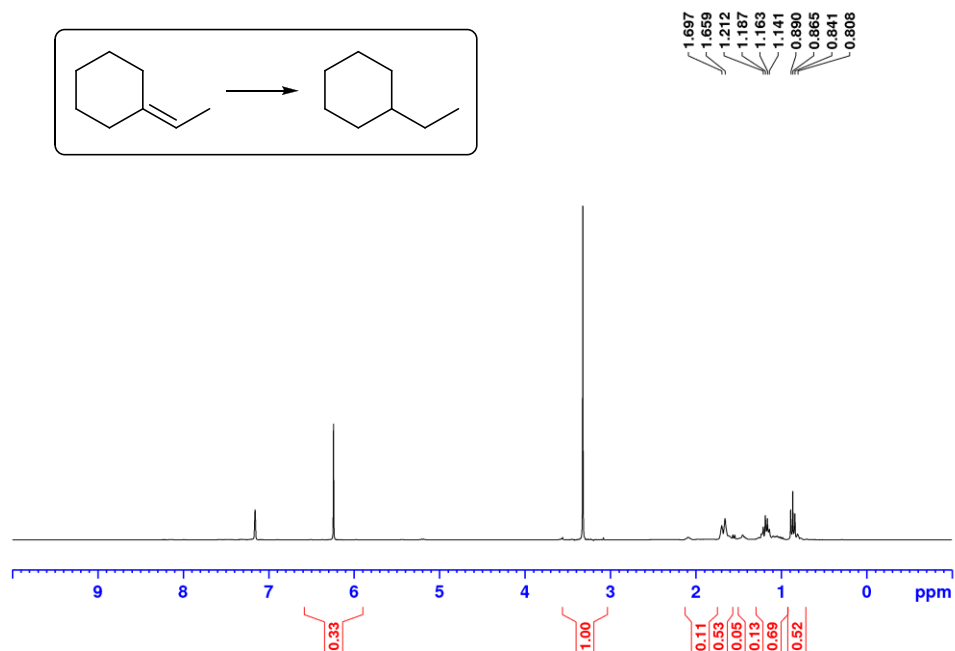


Figure B22. ^1H NMR spectrum (benzene- d_6 , 300 MHz) of hydrogenation of α -methylstyrene (5 mol% catalyst, 65 °C, 10 atm H_2 , 4 h).

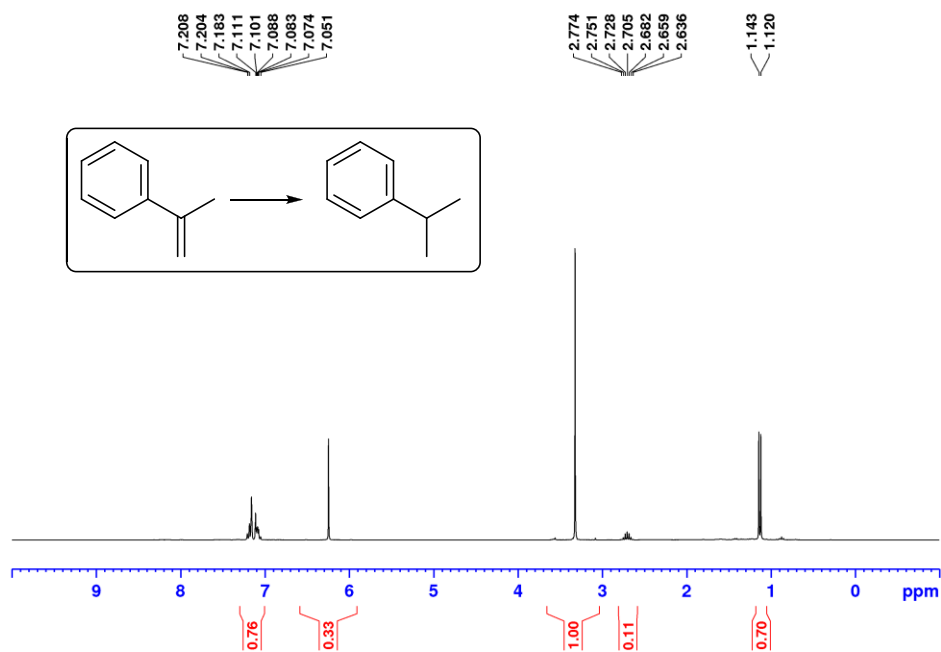


Figure B23. ^1H NMR spectrum (benzene- d_6 , 300 MHz) of hydrogenation of *cis*-stilbene (5 mol% catalyst, 65 °C, 10 atm H_2 , 4 h).

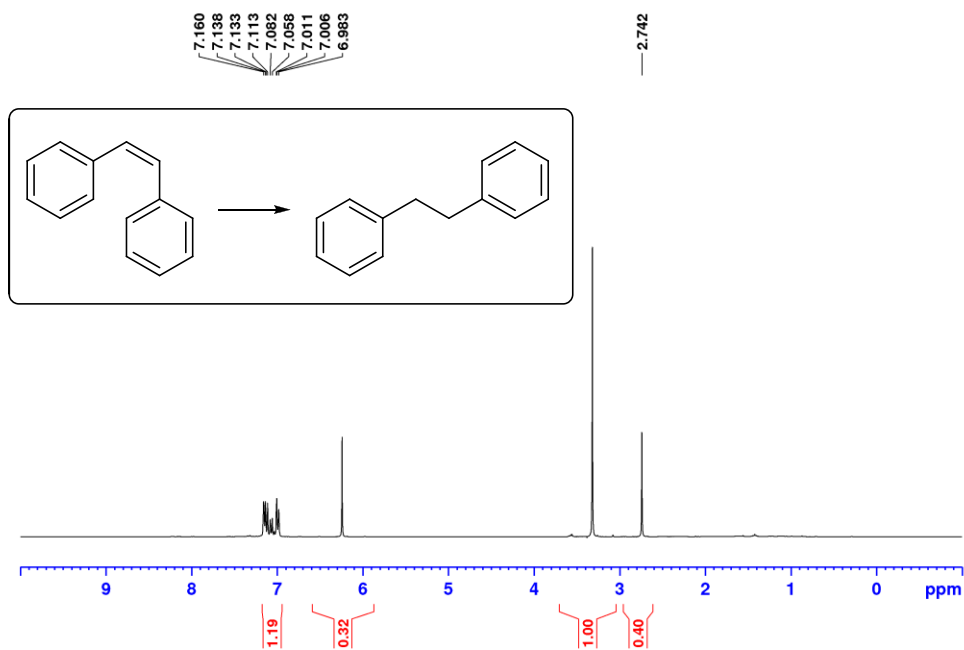


Figure B24. ^1H NMR spectrum (benzene- d_6 , 300 MHz) of hydrogenation of diphenylacetylene (5 mol% catalyst, 65 °C, 10 atm H_2 , 4 h).

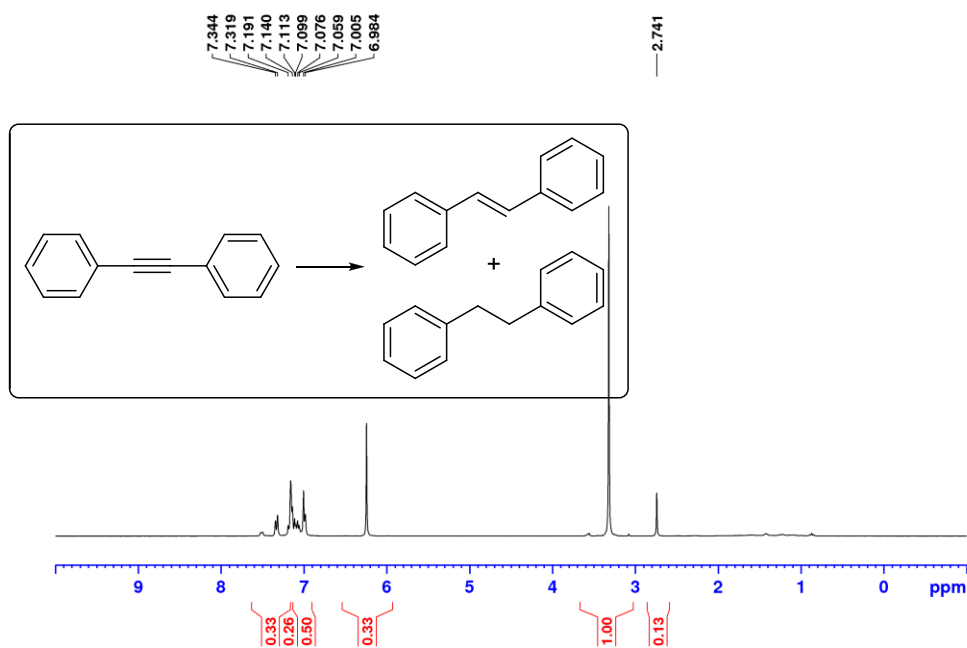


Figure B25. ^1H NMR spectrum (toluene- d_8 , 300 MHz) of hydrogenation of diphenylacetylene (5 mol% catalyst, 90 °C, 10 atm H_2 , 6 h).

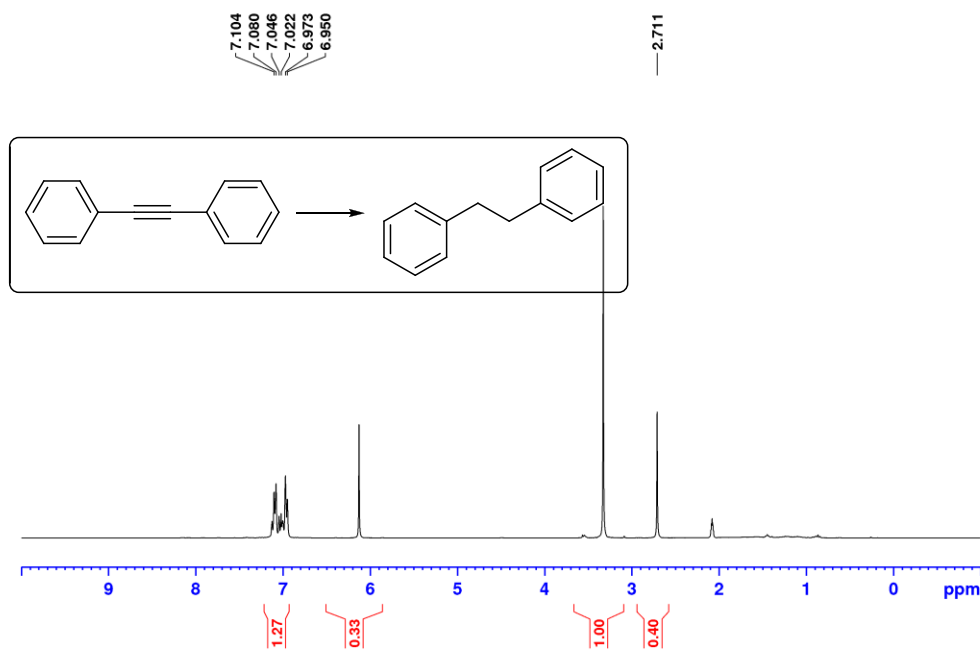


Figure B26. ^1H NMR spectrum (benzene- d_6 , 300 MHz) of hydrogenation of 5-hexen-2-one (5 mol% catalyst, 65 °C, 10 atm H_2 , 4 h).

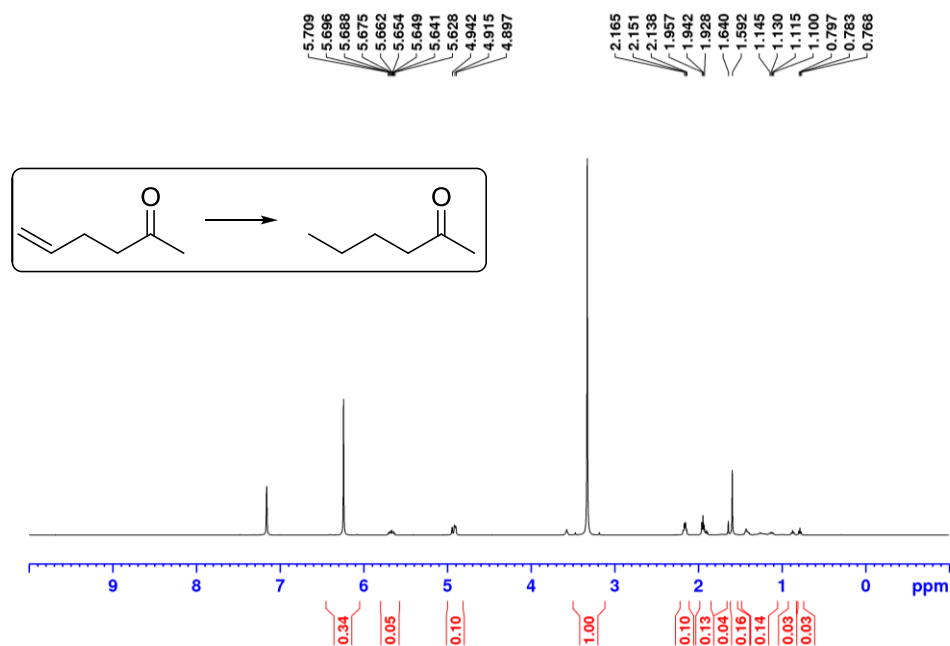


Figure B27. ^1H NMR spectrum (benzene- d_6 , 300 MHz) of hydrogenation of allyl butyl ether (5 mol% catalyst, 65 °C, 10 atm H_2 , 4 h).

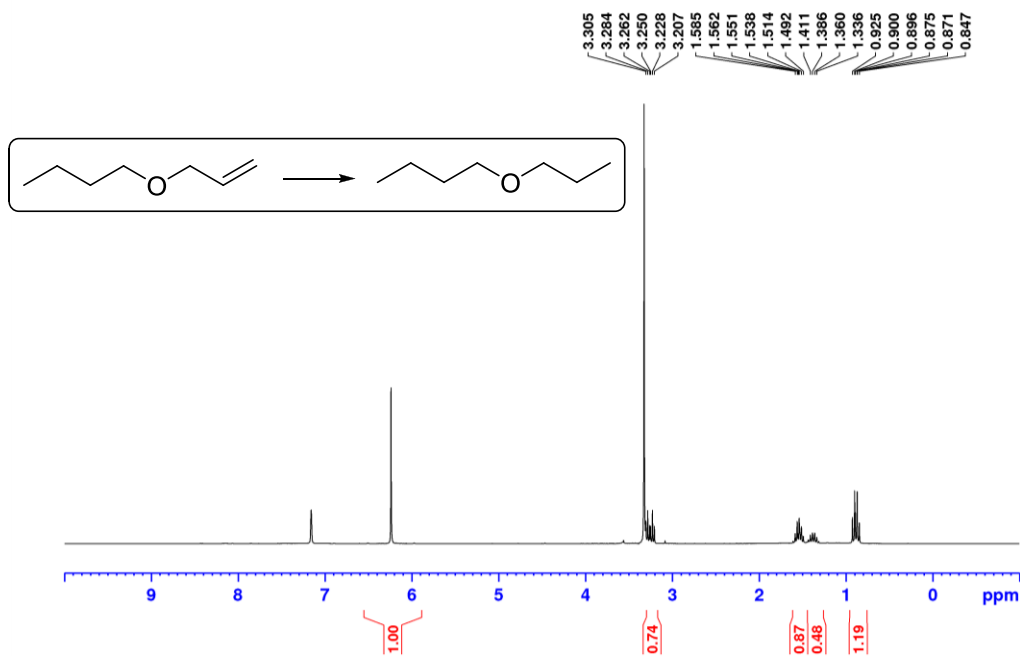


Figure B28. ^1H NMR spectrum (benzene- d_6 , 300 MHz) of hydrogenation of allyl phenyl ether (5 mol% catalyst, 65 °C, 10 atm H_2 , 4 h).

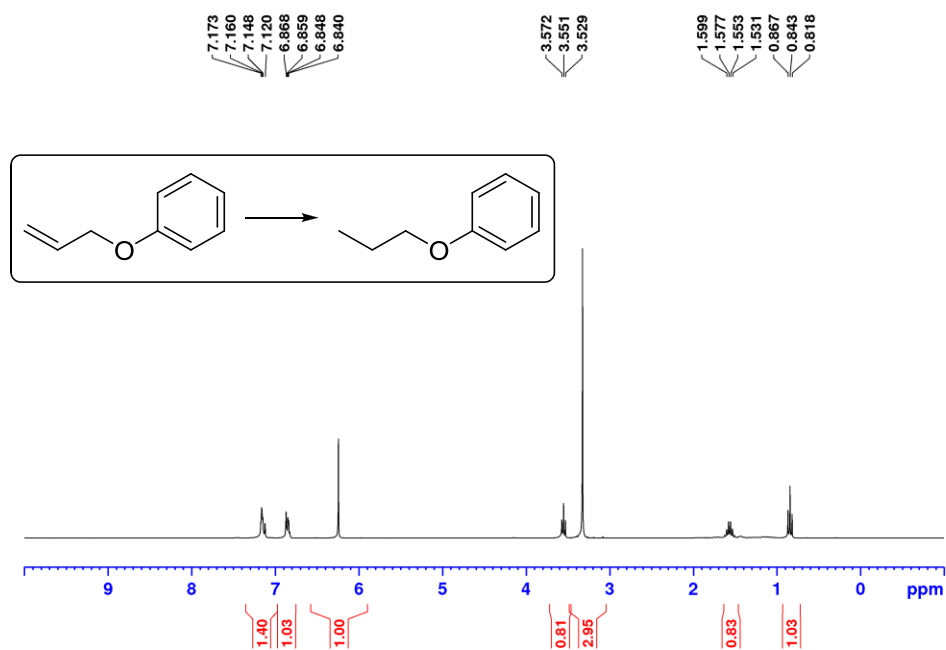


Figure B29. ^1H NMR spectrum (benzene- d_6 , 300 MHz) of hydrogenation of ethyl crotonate (5 mol% catalyst, 65 °C, 10 atm H_2 , 4 h).

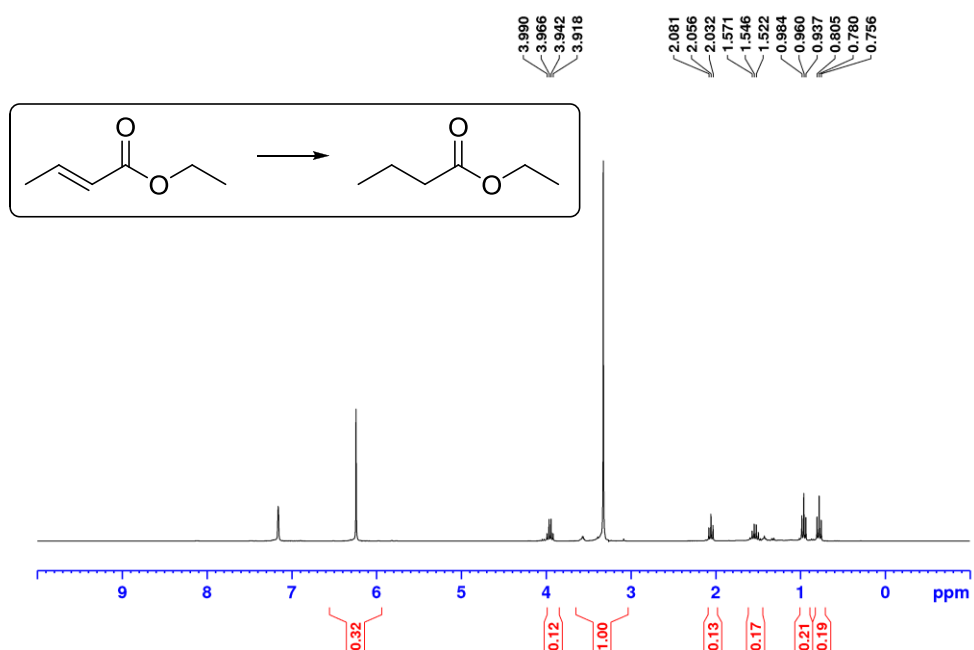


Figure B30. ^1H NMR spectrum (benzene- d_6 , 300 MHz) of hydrogenation of *trans*-4-octene catalyzed by **2-H₃** (5 mol% catalyst, 65 °C, 10 atm H₂, 4 h).

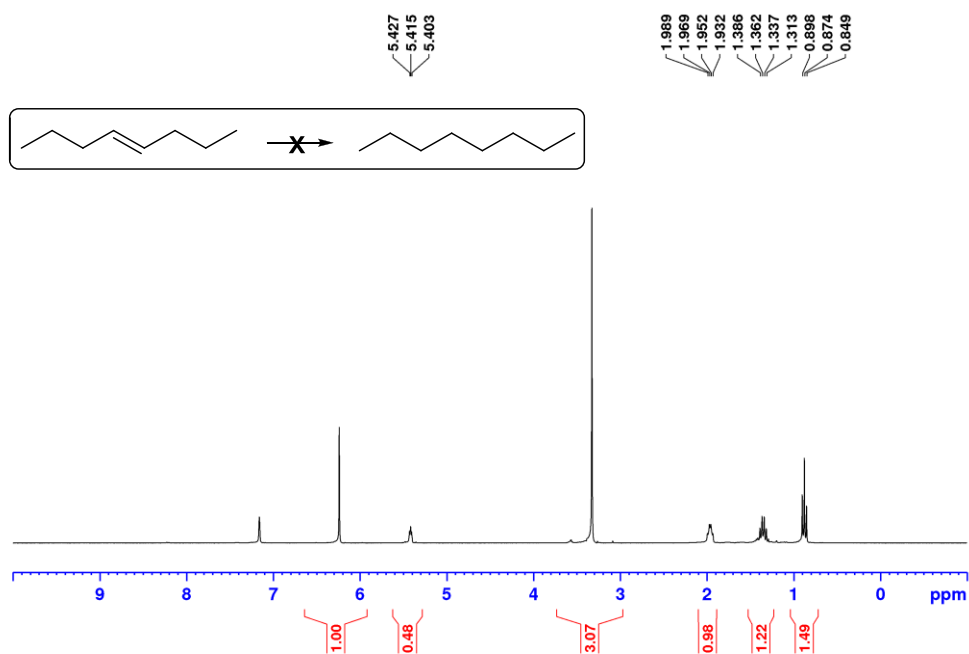
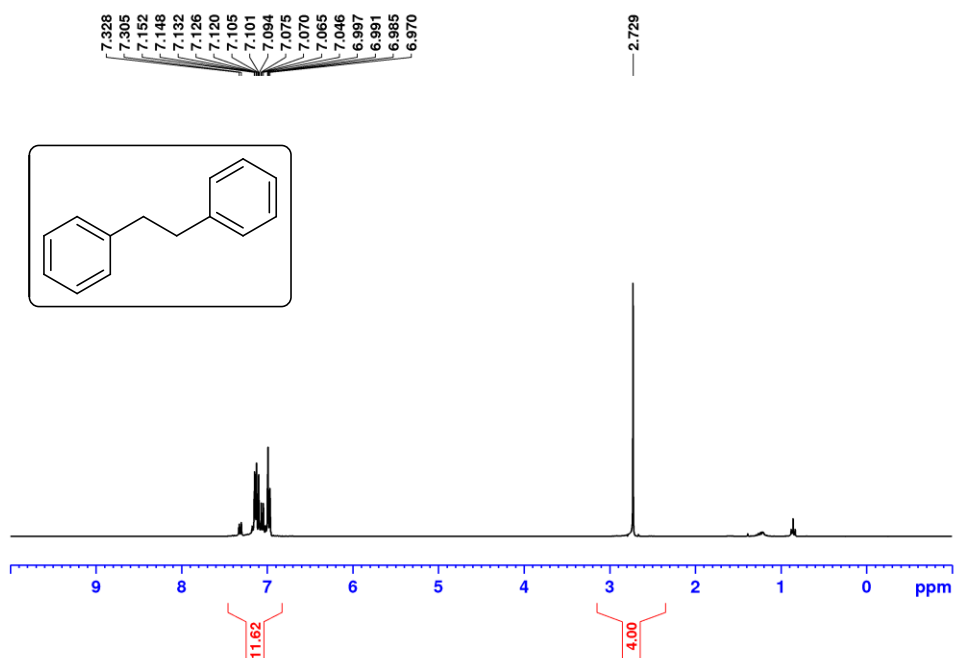


Figure B31. ^1H NMR spectrum (benzene- d_6 , 300 MHz) of isolated bibenzyl from hydrogenation of *cis*-stilbene.



Selected Spectra of Compounds Reported in Chapter 3

Figure B32. (A) ^1H NMR spectrum (benzene- d_6 , 300 MHz) of **3-3**. (B) $^{31}\text{P}\{^1\text{H}\}$ NMR spectrum (benzene- d_6 , 121.5 MHz) of **3-3**.

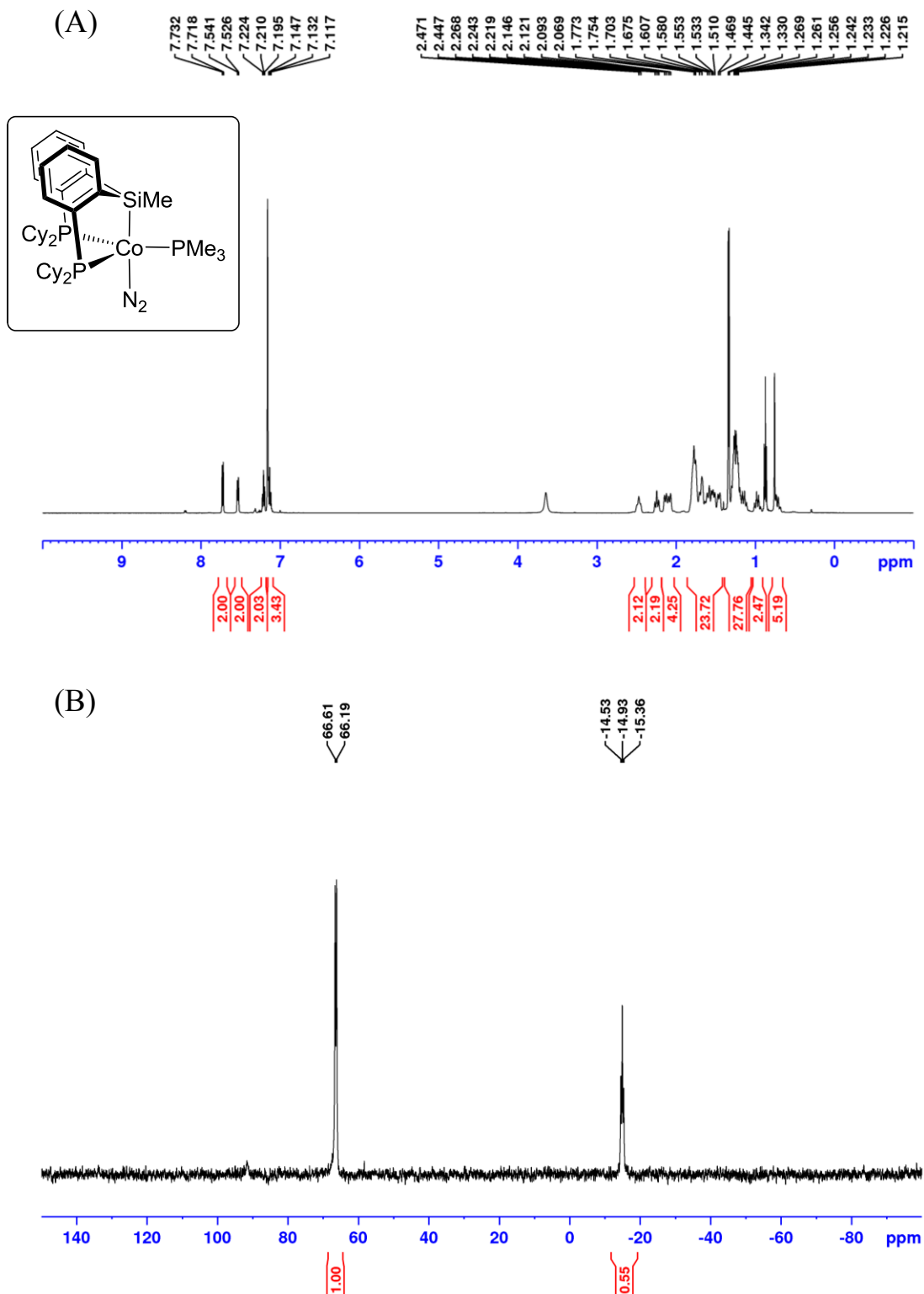


Figure B34. (A) ^1H NMR spectrum (benzene- d_6 , 300 MHz) of **3-5**. (B) $^{31}\text{P}\{^1\text{H}\}$ NMR spectrum (benzene- d_6 , 121.5 MHz) of **3-5**.

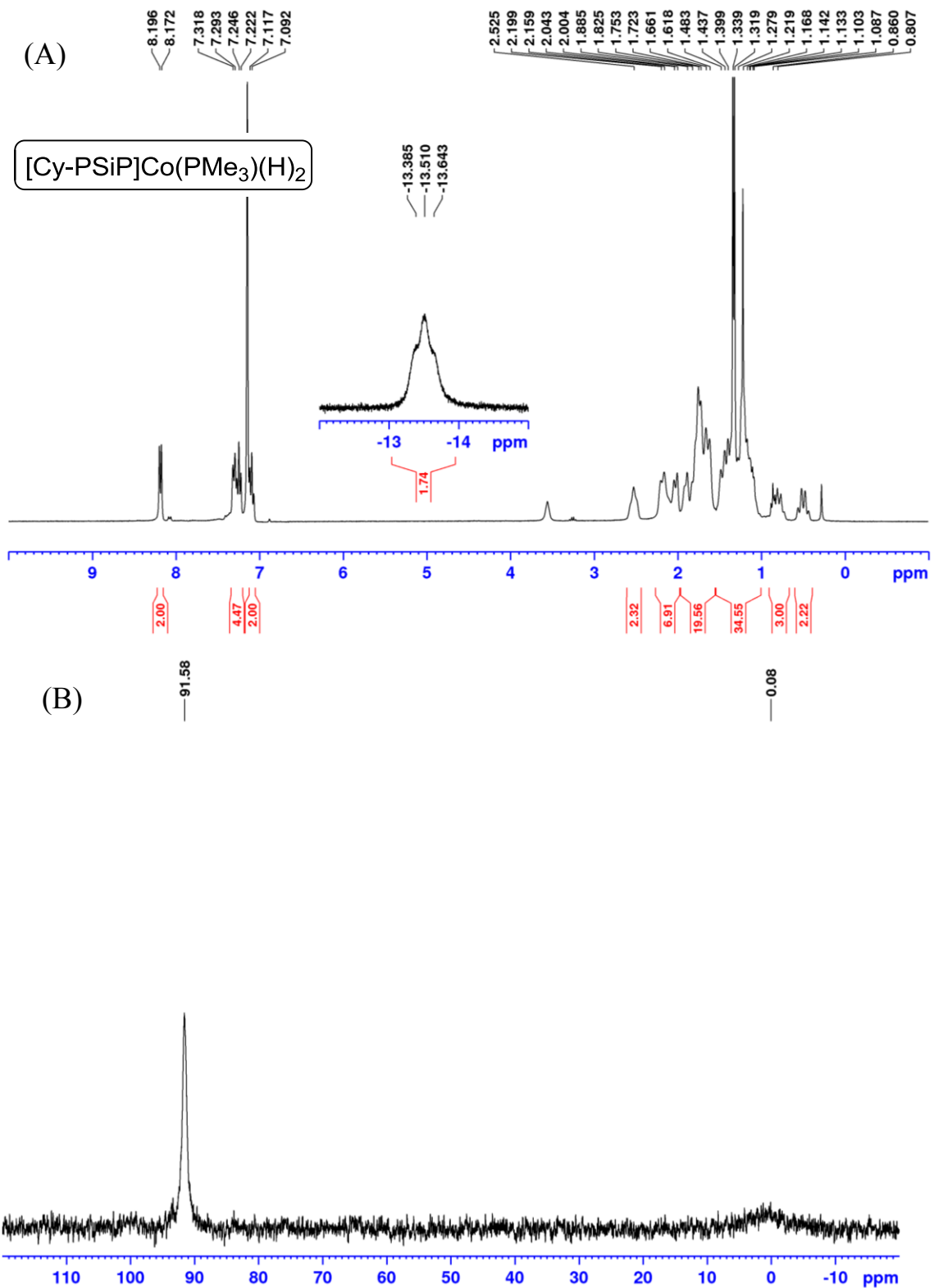


Figure B35. $^{31}\text{P}\{^1\text{H}\}$ NMR spectra (toluene- d_8 , 121.5 MHz) of **3-5** at (A) 80 °C and (B) -80 °C; (C) Variable temperature $^{31}\text{P}\{^1\text{H}\}$ NMR spectra (toluene- d_8 , 121.5 MHz) of **3-5**.

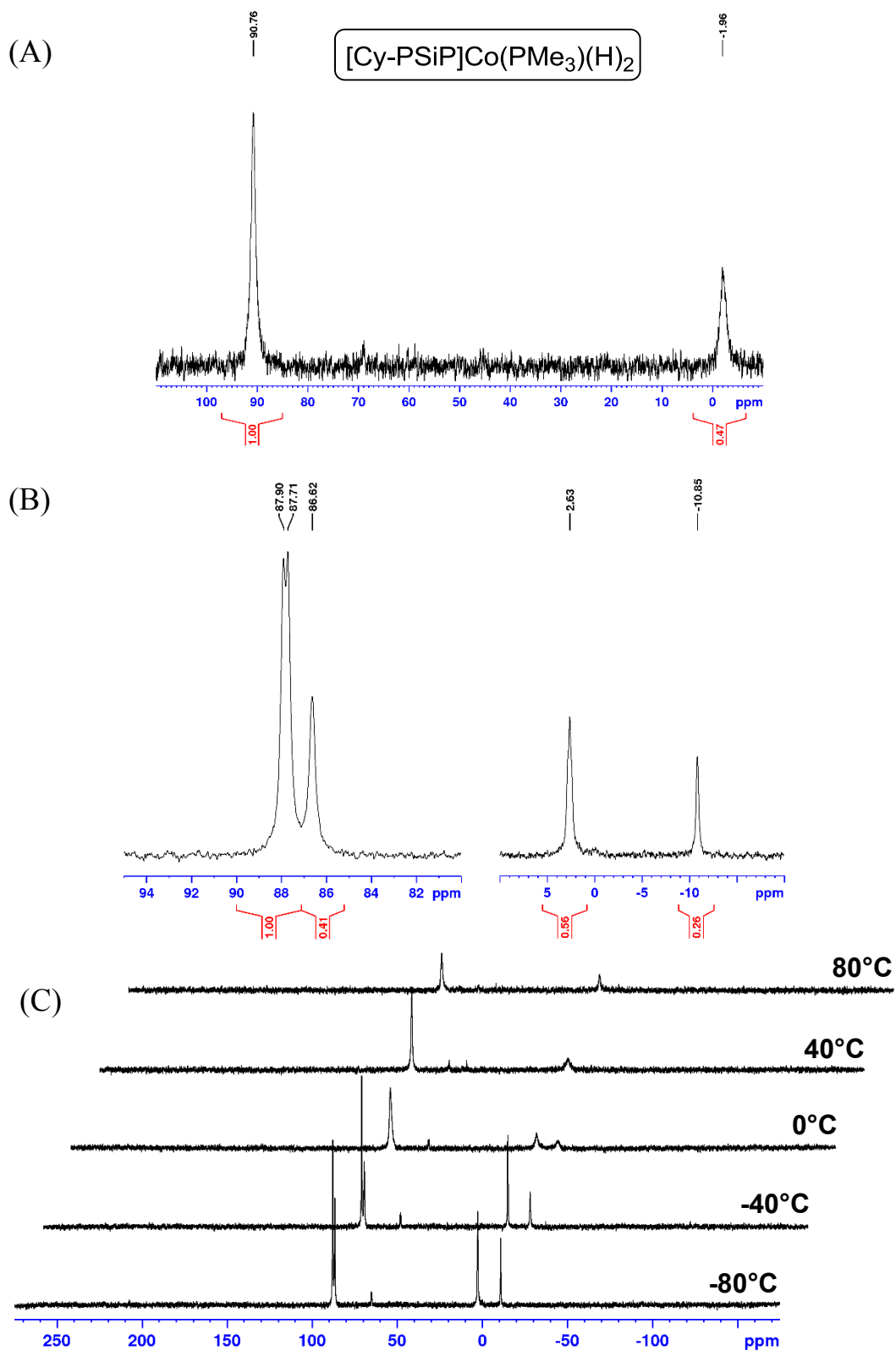


Figure B36. (A) Partial (hydride region) variable temperature ^1H NMR spectra (toluene- d_8 , 300 MHz) of **3-5**; (B) ^1H and (C) $^1\text{H}\{^{31}\text{P}\}$ NMR spectra (hydride region; toluene- d_8 , 300 MHz) of **3-5** at -80°C .

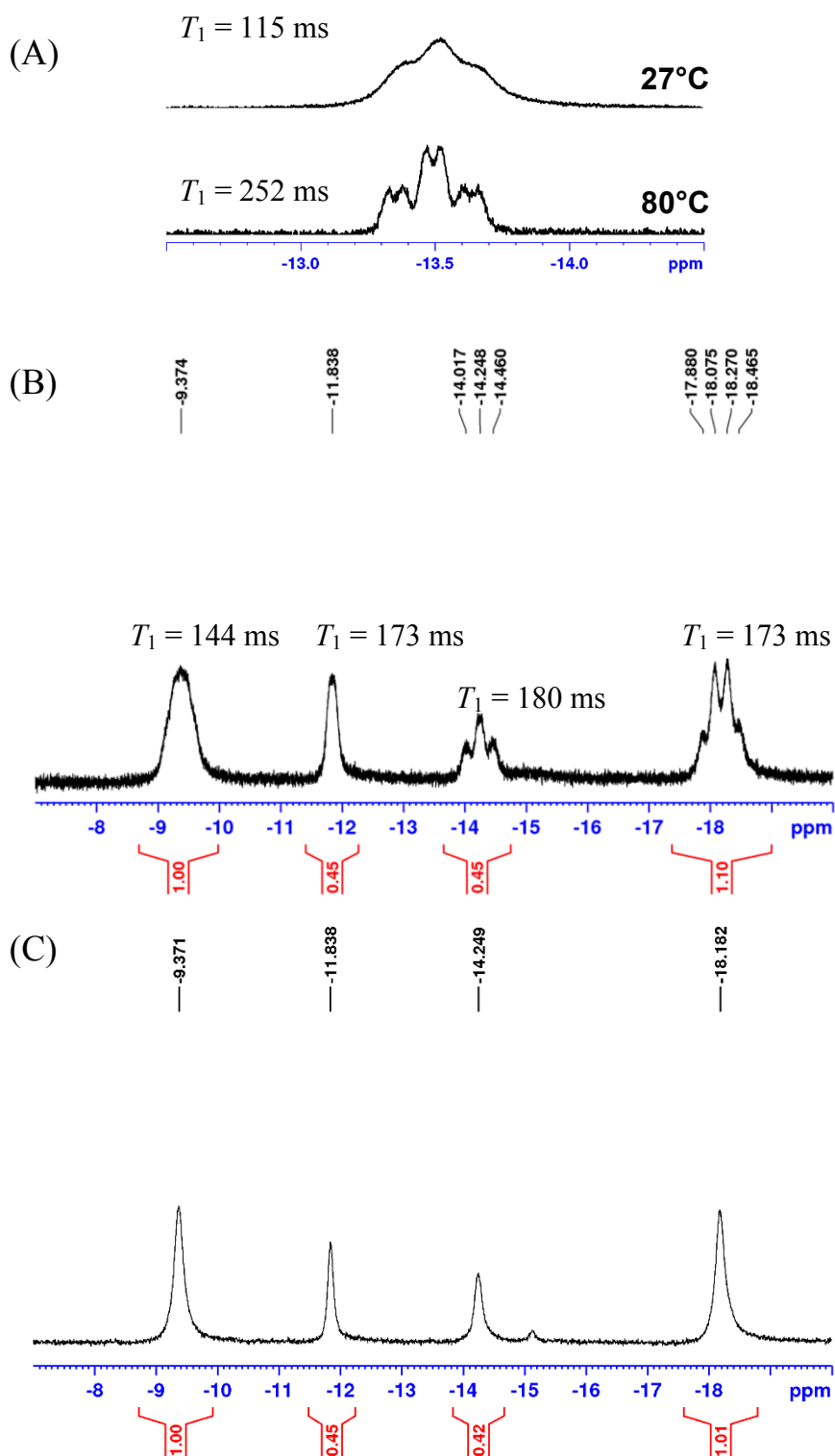


Figure B37. ^1H NMR spectrum (benzene- d_6 , 300 MHz) of **3-6**.

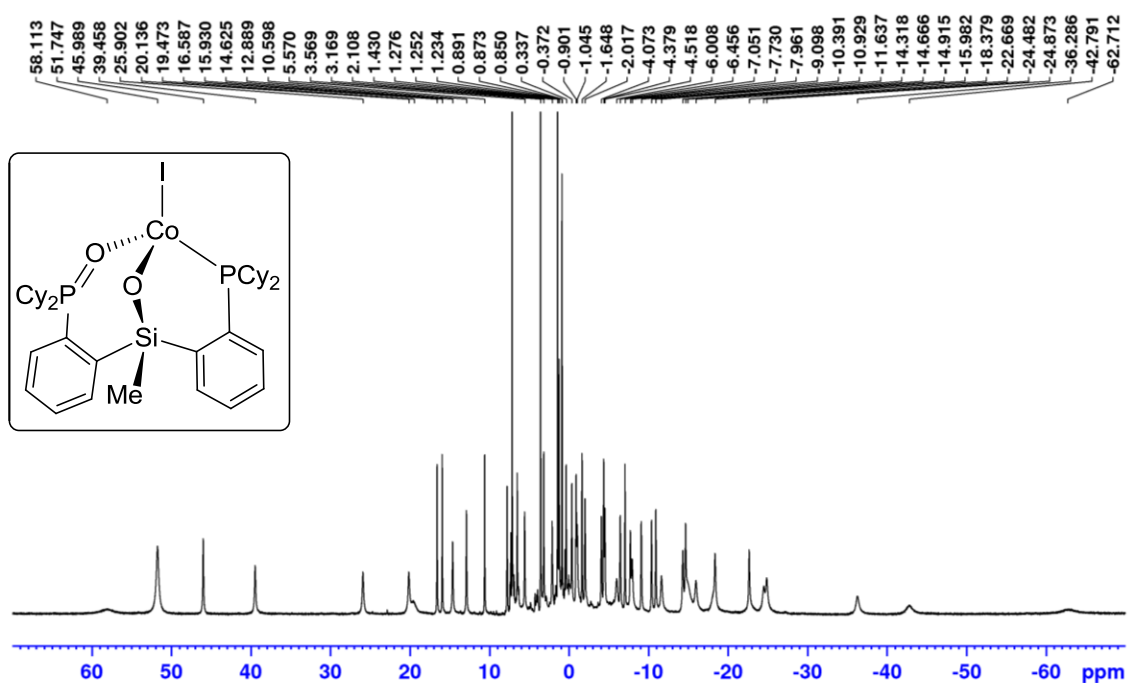
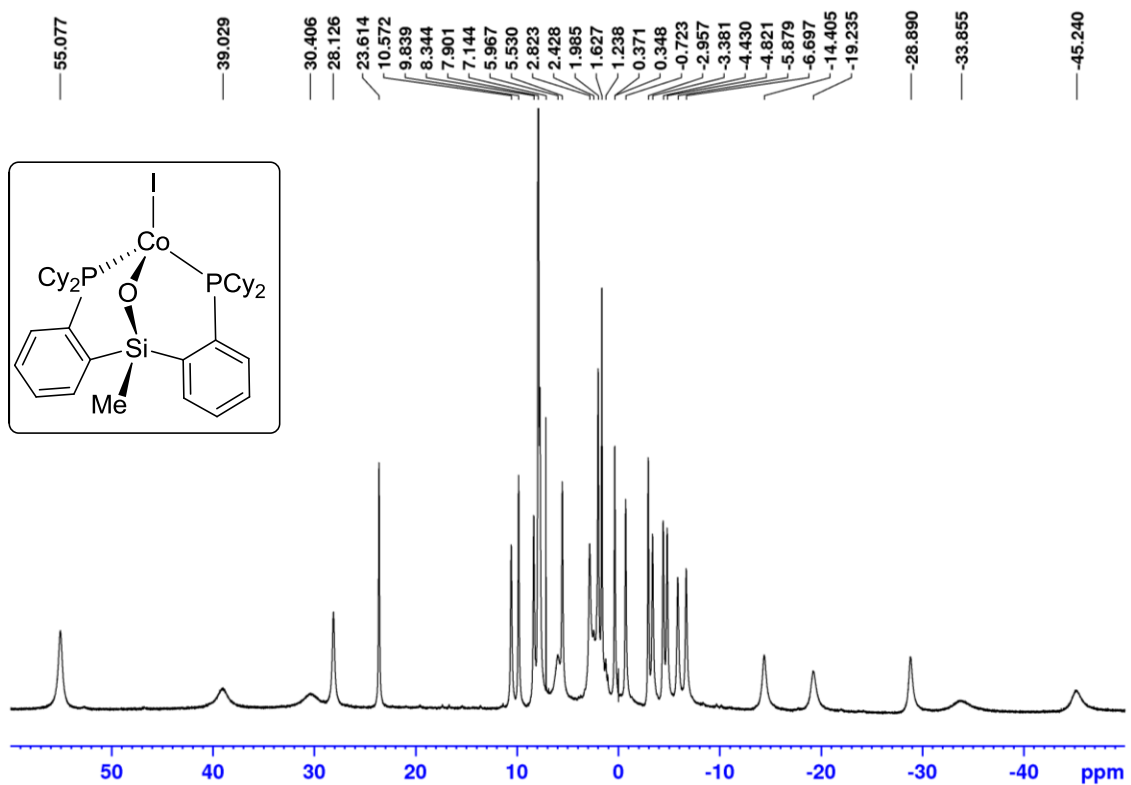


Figure B38. ^1H NMR spectrum (benzene- d_6 , 300 MHz) of **3-7**.



Selected Spectra of Compounds Reported in Chapter 4

Figure B39. (A) ^1H NMR (300 MHz, benzene- d_6) of (*i*-Pr-PSi^HP)H. (B) $^{31}\text{P}\{^1\text{H}\}$ NMR (121.5 MHz, benzene- d_6) of (*i*-Pr-PSi^HP)H.

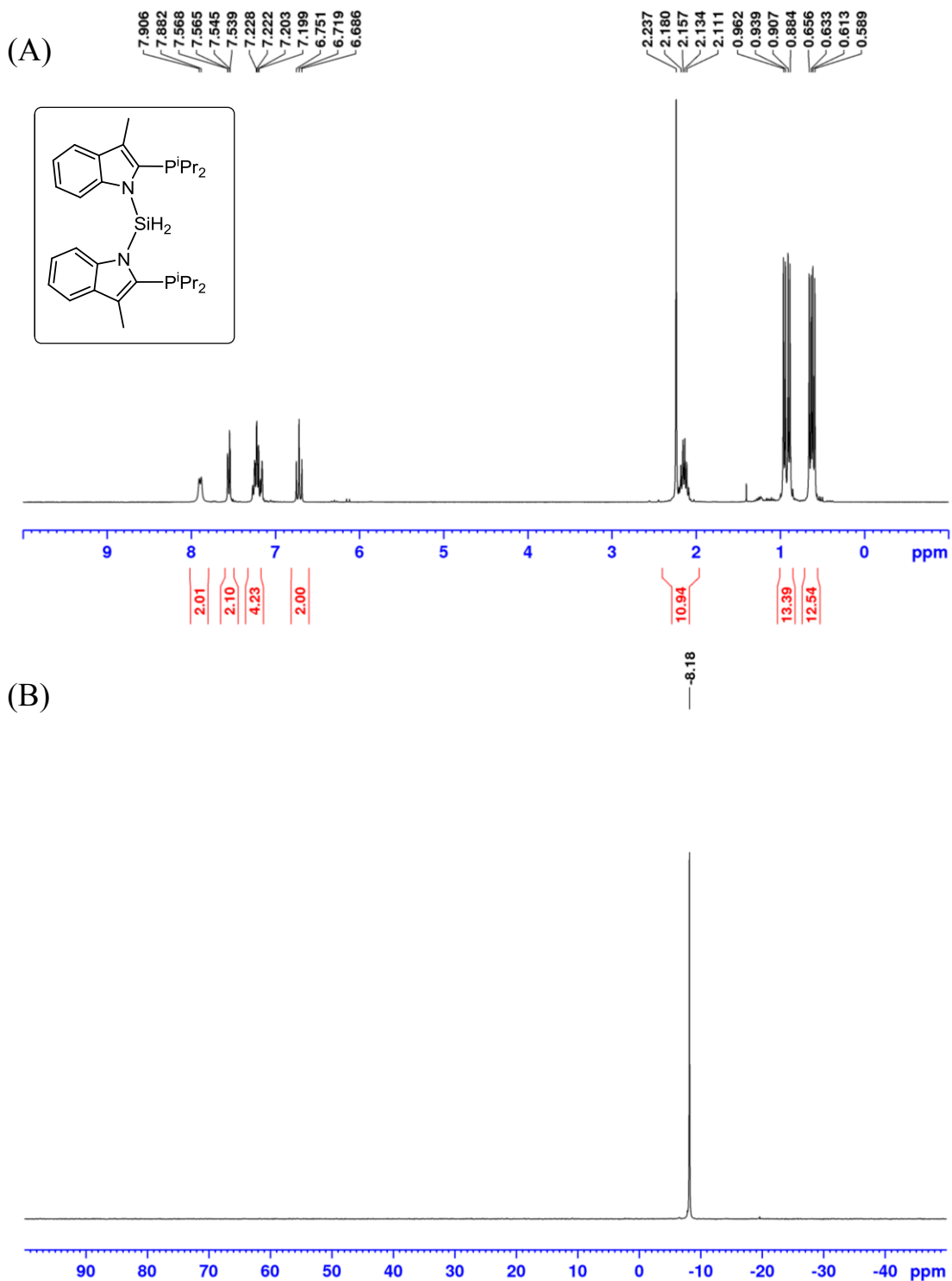


Figure B40. (A) ^1H NMR spectrum (benzene- d_6 , 300 MHz) of **4-NiCl**. (B) $^{31}\text{P}\{^1\text{H}\}$ NMR spectra (benzene- d_6 , 121.5 MHz) of **4-NiCl**.

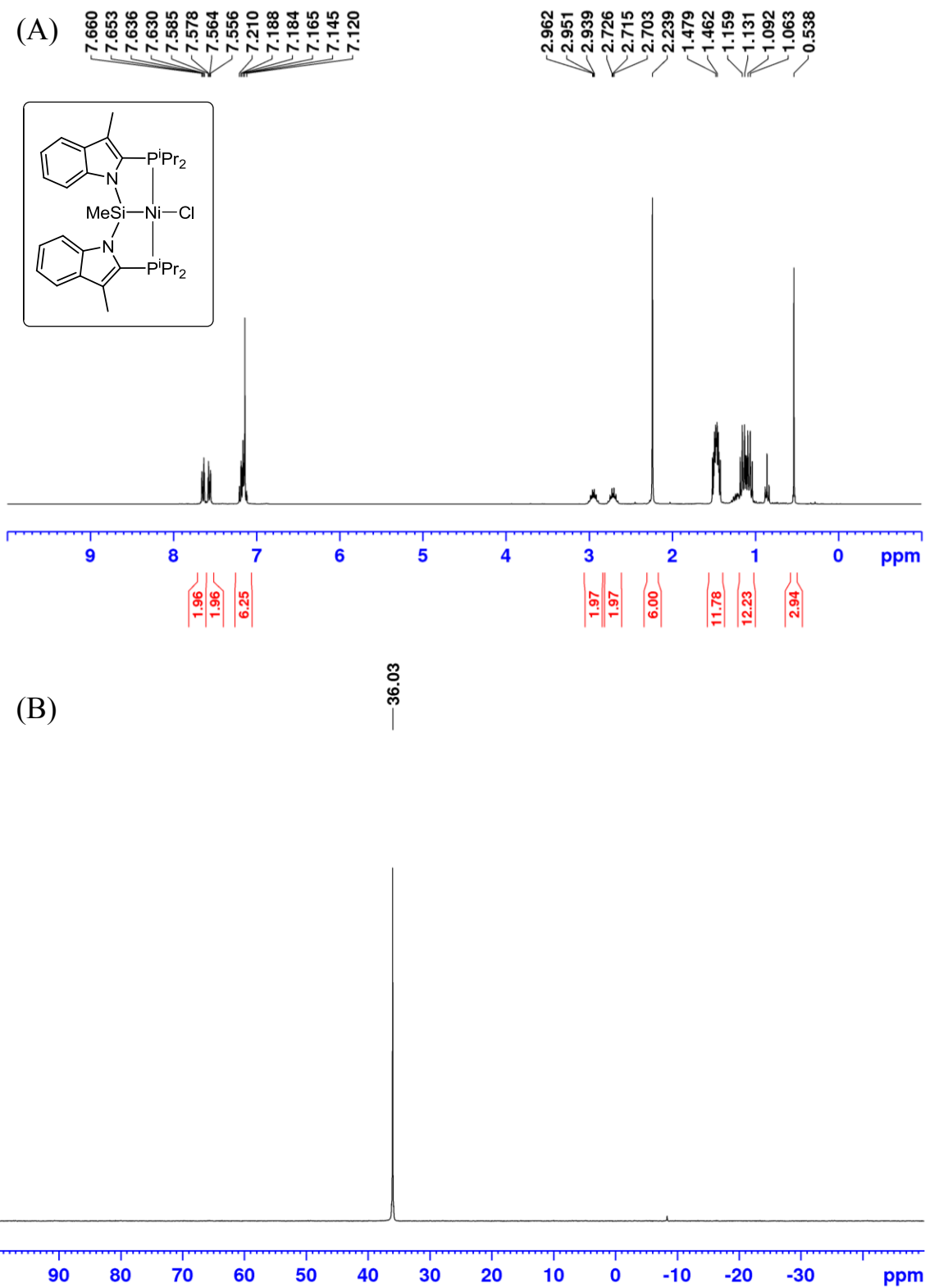


Figure B41. (A) ^1H NMR spectrum (benzene- d_6 , 300 MHz) of **4-PdCl**. (B) $^{31}\text{P}\{^1\text{H}\}$ NMR spectra (benzene- d_6 , 121.5 MHz) of **4-PdCl**.

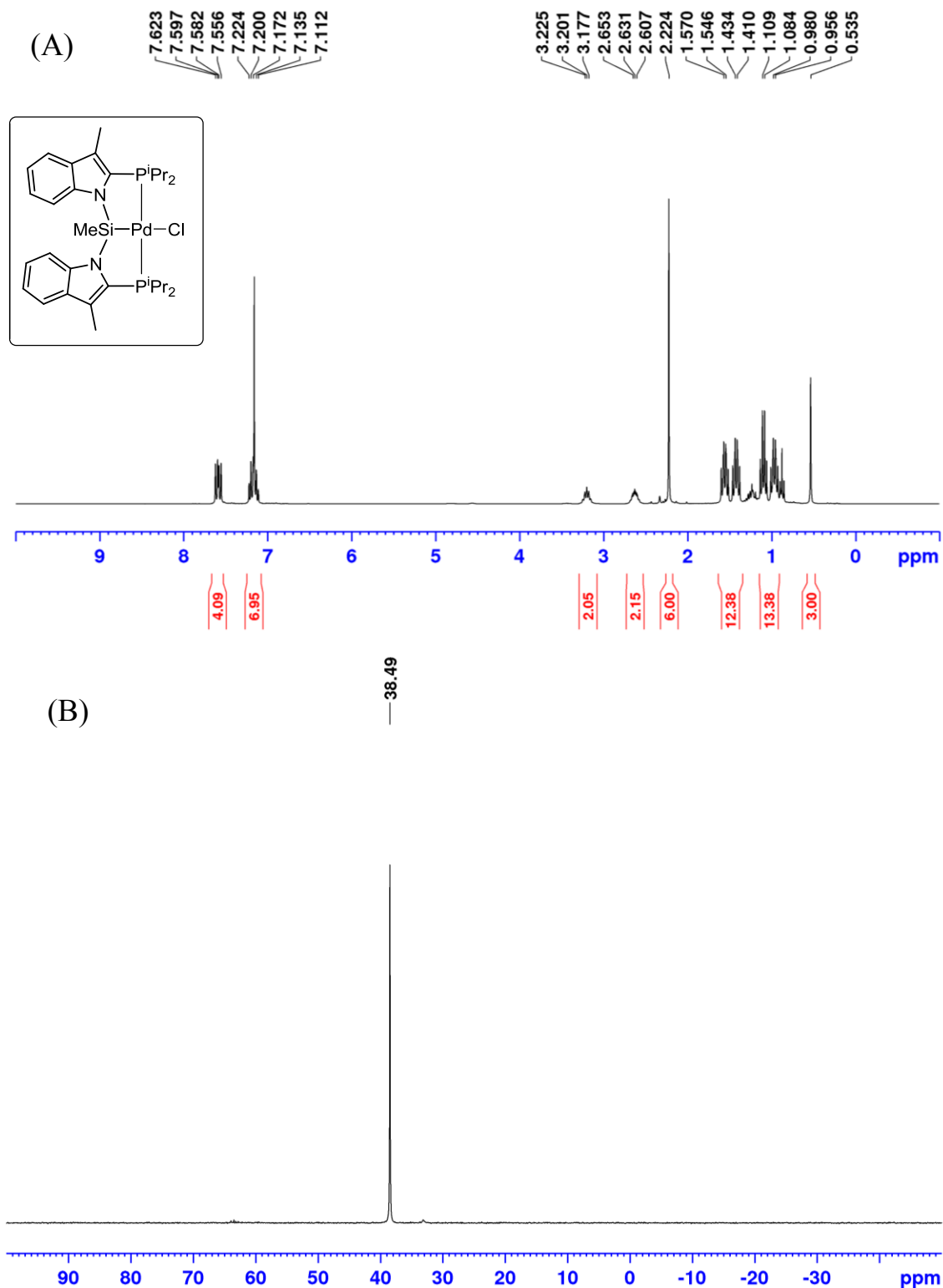


Figure B42. (A) ^1H NMR spectrum (benzene- d_6 , 300 MHz) of **4-PdCl'**. (B) $^{31}\text{P}\{^1\text{H}\}$ NMR (benzene- d_6 , 121.5 MHz) of **4-PdCl'**.

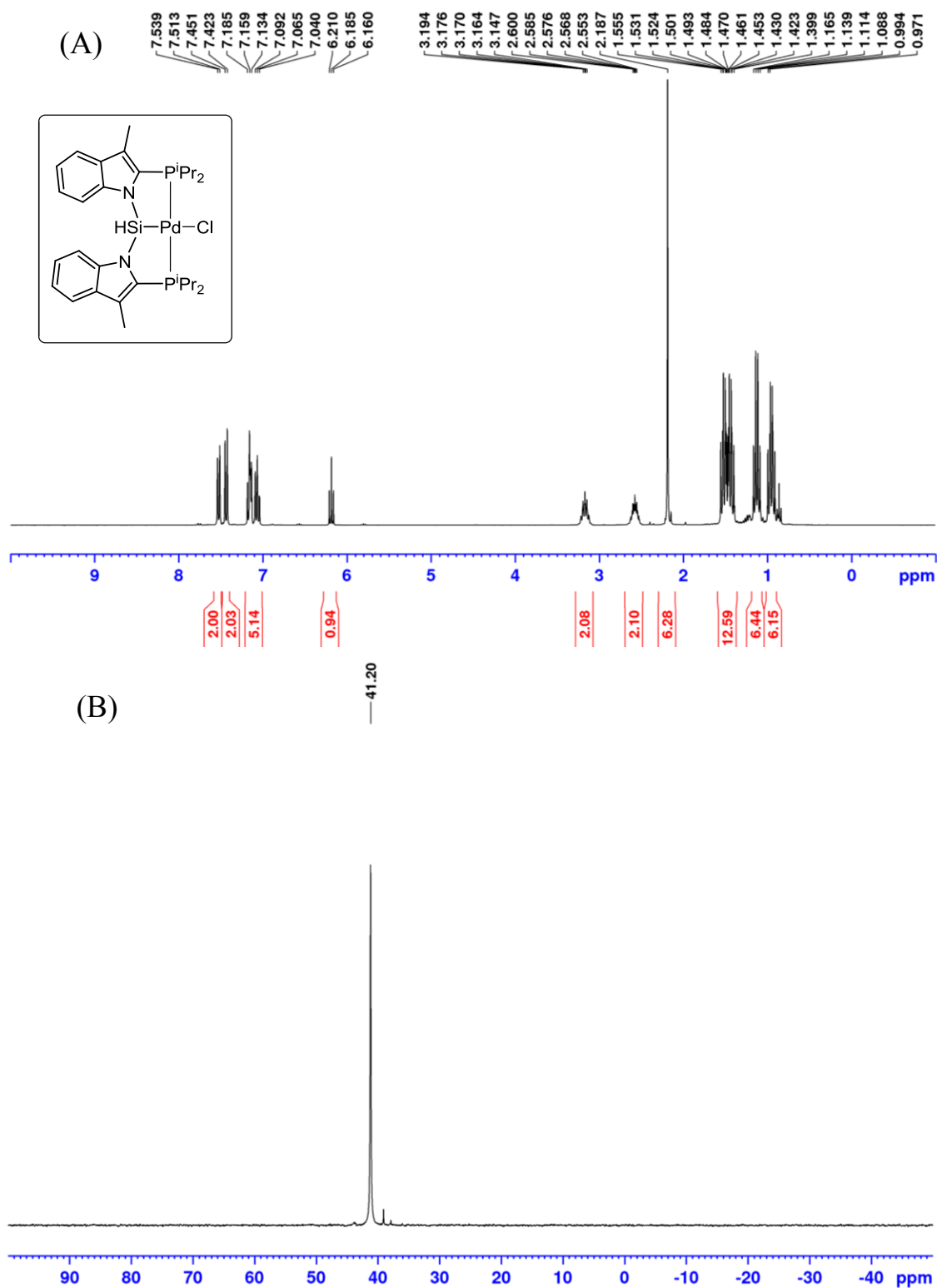


Figure B43. (A) ^1H NMR spectrum (benzene- d_6 , 300 MHz) of **4-PtCl**. (B) $^{31}\text{P}\{^1\text{H}\}$ NMR spectrum (benzene- d_6 , 300 MHz) of **4-PtCl**.

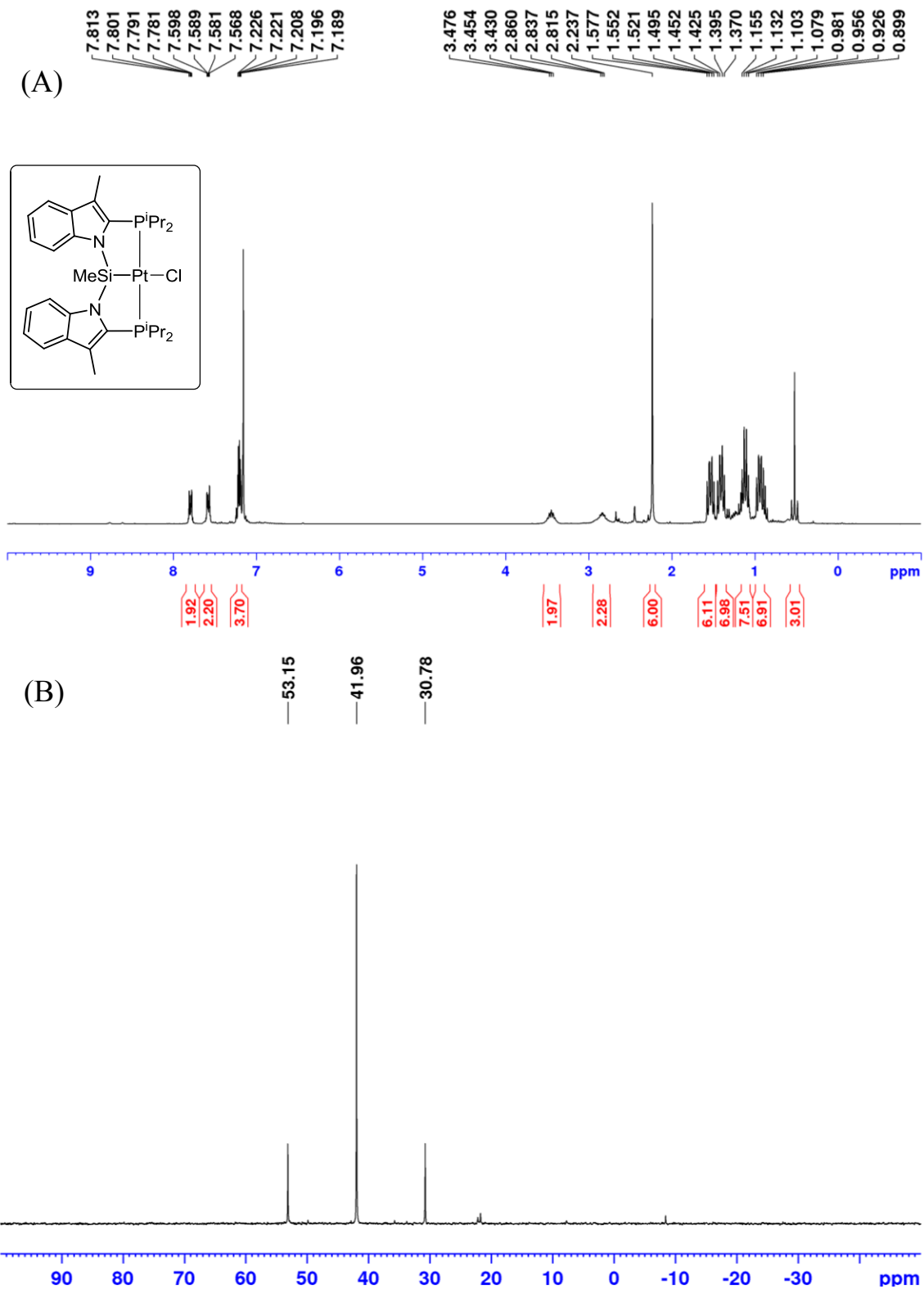


Figure B44. (A) ^1H NMR spectrum (benzene- d_6 , 500 MHz) of **4-PtCl'**. (B) $^{31}\text{P}\{^1\text{H}\}$ NMR spectrum (benzene- d_6 , 202.5 MHz) of **4-PtCl'**.

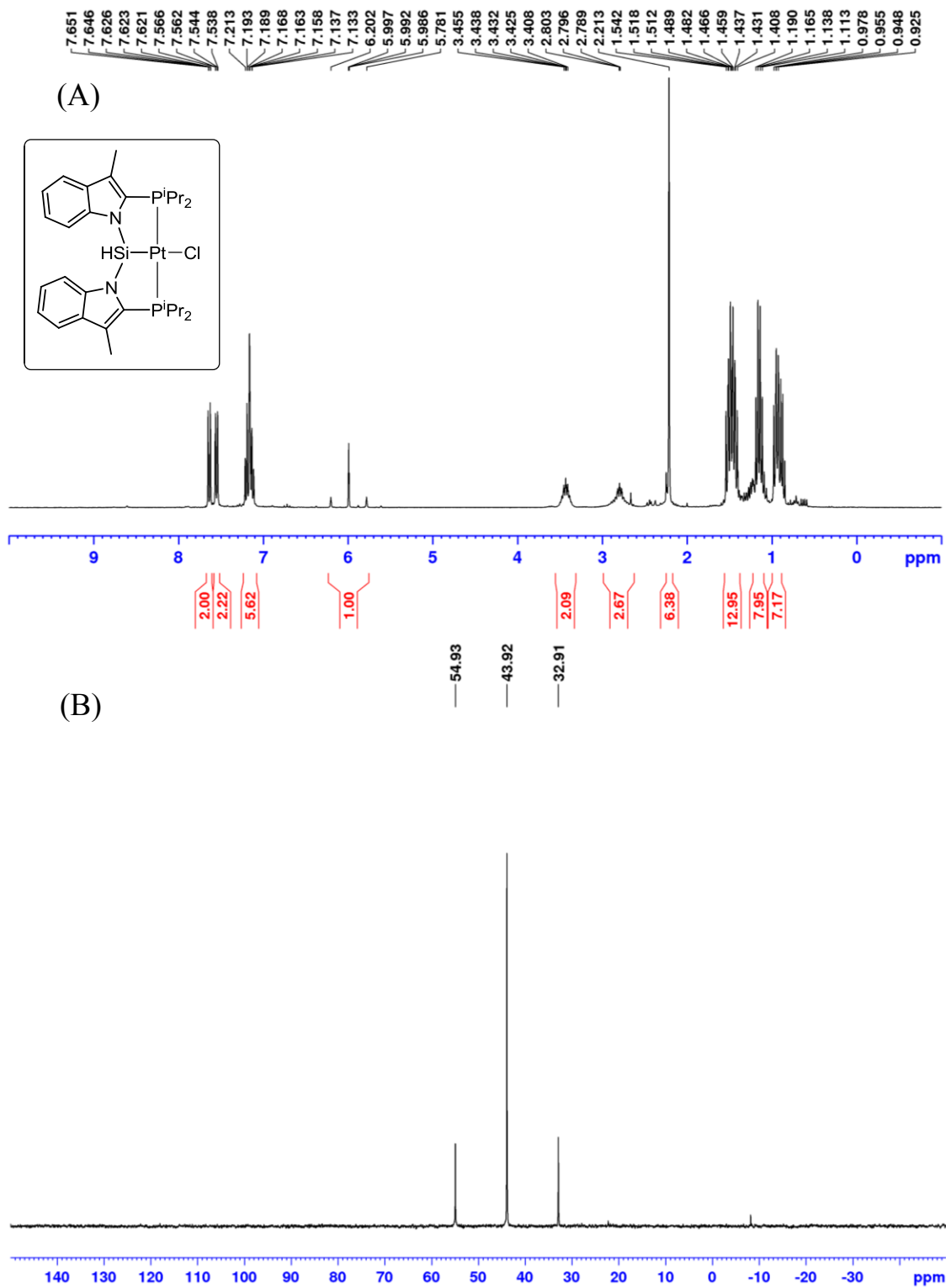


Figure B45. (A) ^1H NMR spectrum (toluene- d_8 , 500 MHz) of **4-PtH'**. (B) $^{31}\text{P}\{^1\text{H}\}$ NMR spectrum (toluene- d_8 , 202.5 MHz) of **4-PtH'**.

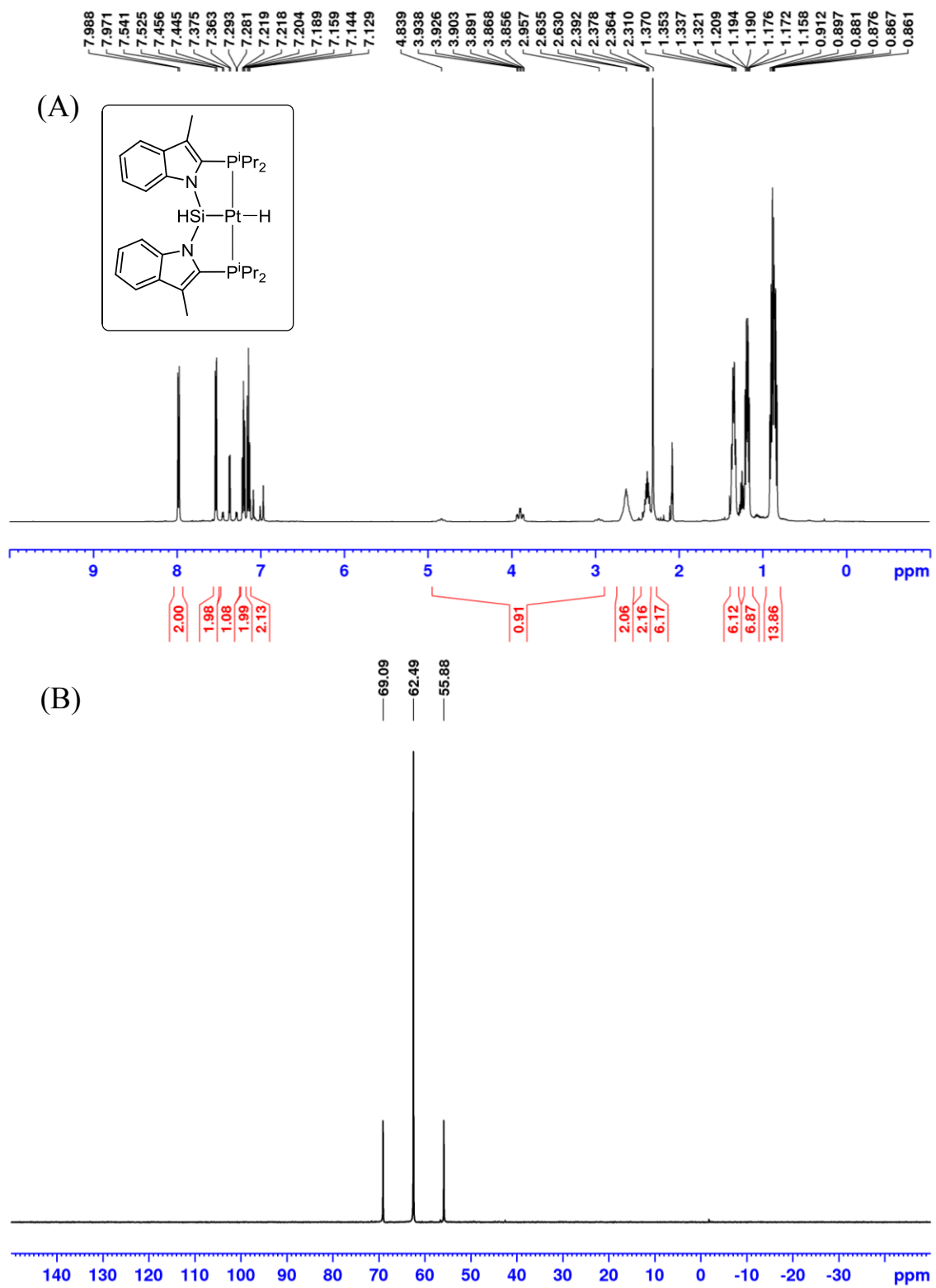


Figure B46. (A) ^1H NMR spectrum (benzene- d_6 , 300 MHz) of **4-Ni(C₃H₅)**. (B) $^{31}\text{P}\{^1\text{H}\}$ NMR spectrum (benzene- d_6 , 121.5 MHz) of **4-Ni(C₃H₅)**.

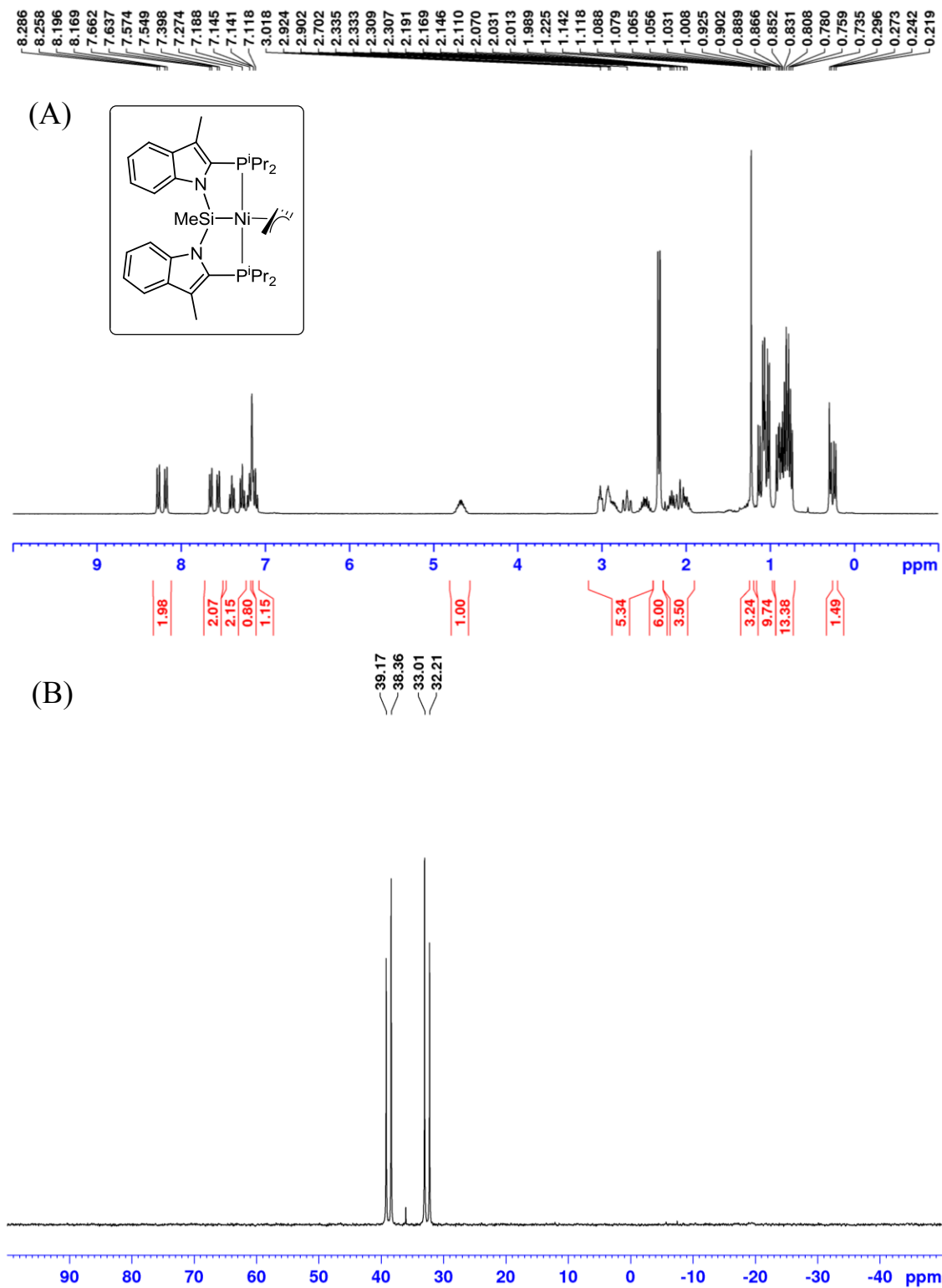


Figure B47. (A) ^1H NMR spectrum (benzene- d_6 , 500 MHz) of 4-NiHDMP. (B) $^{31}\text{P}\{^1\text{H}\}$ NMR spectrum (benzene- d_6 , 202.5 MHz) of 4-NiHDMP.

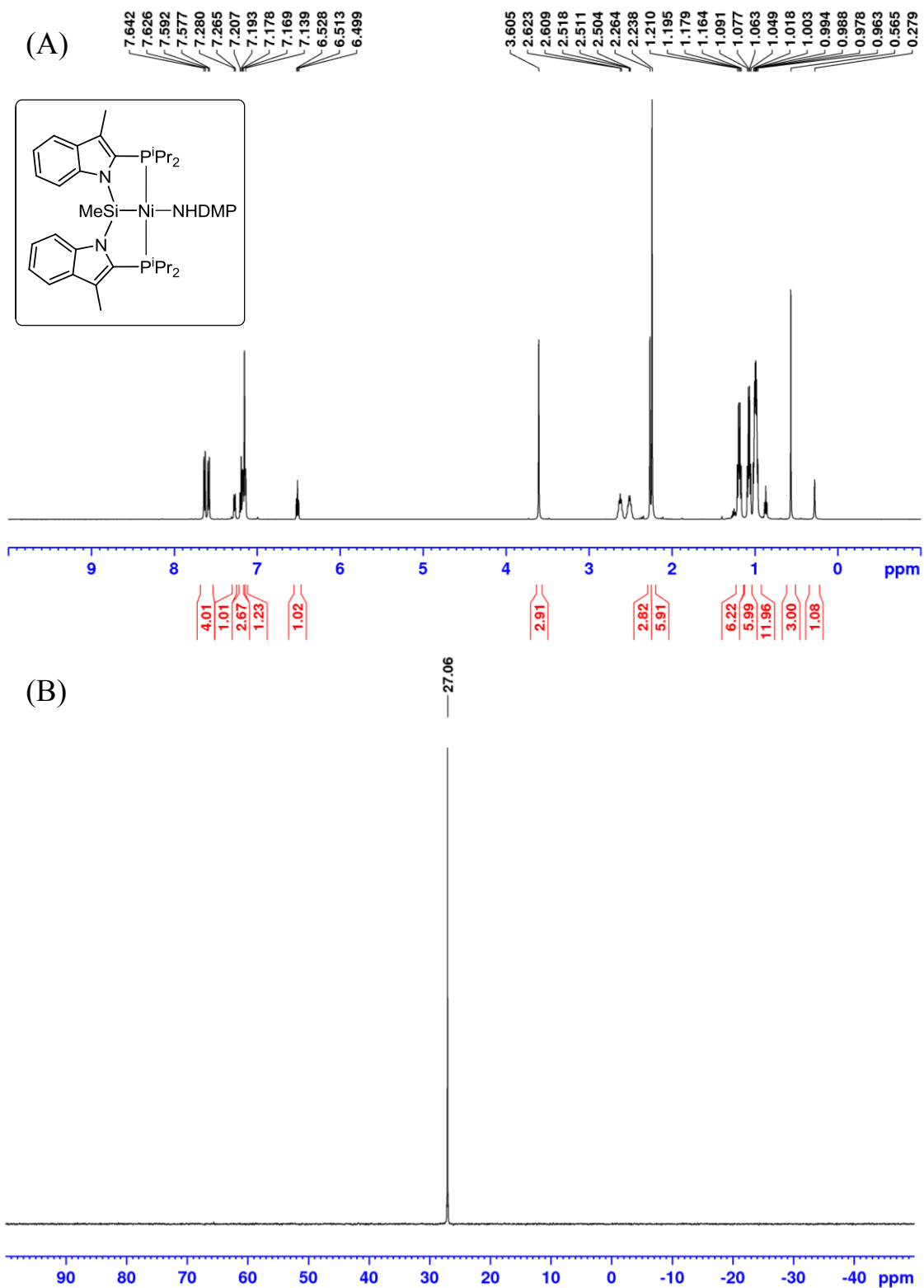


Figure B48. (A) ^1H NMR spectrum (benzene- d_6 , 500 MHz) of **4-NiOTf**. (B) $^{31}\text{P}\{^1\text{H}\}$ NMR spectrum (benzene- d_6 , 202.5 MHz) of **4-NiOTf**.

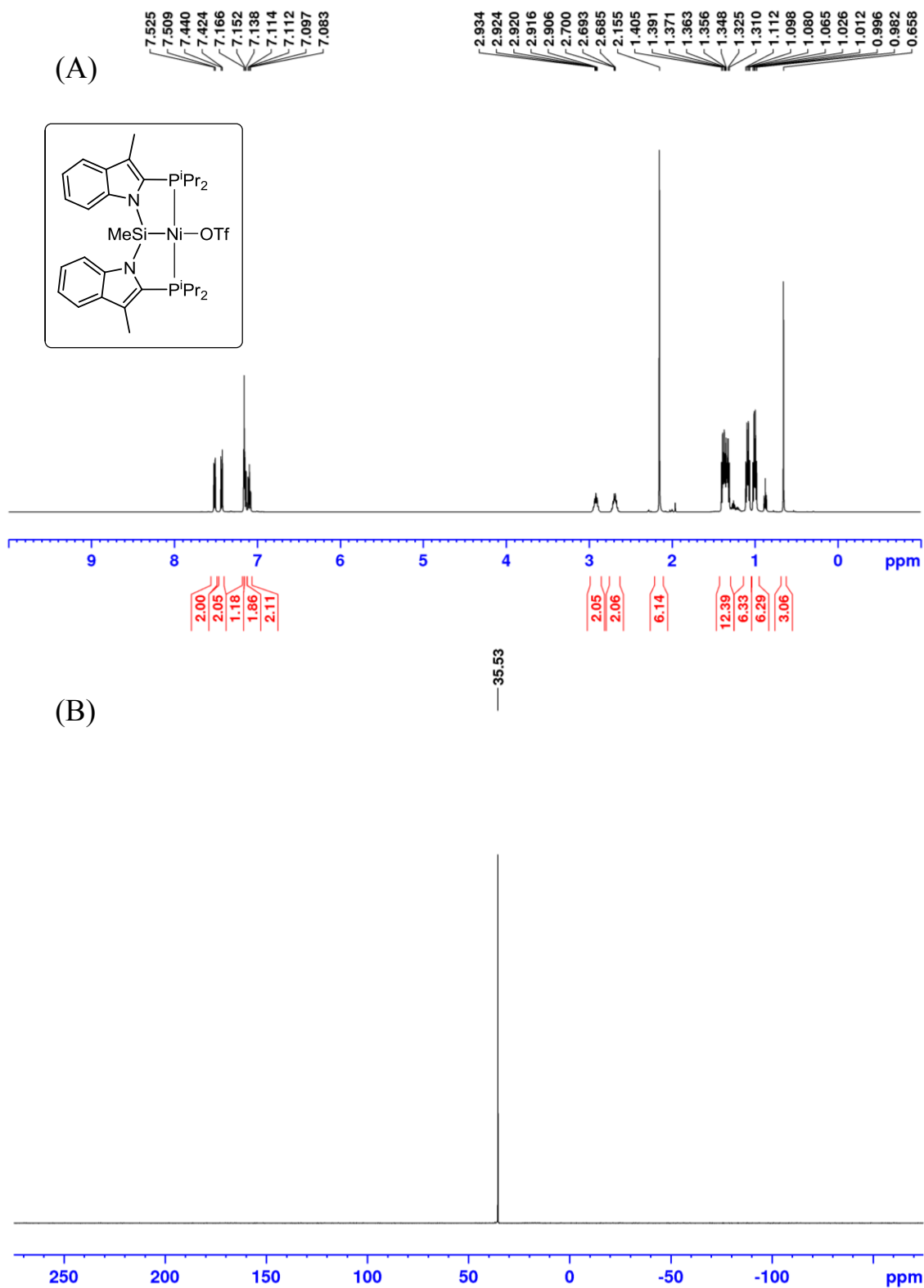


Figure B49. (A) ^1H NMR spectrum (benzene- d_6 , 300 MHz) of **4-NiH**. (B) $^{31}\text{P}\{^1\text{H}\}$ NMR spectrum (benzene- d_6 , 121.5 MHz) of **4-NiH**.

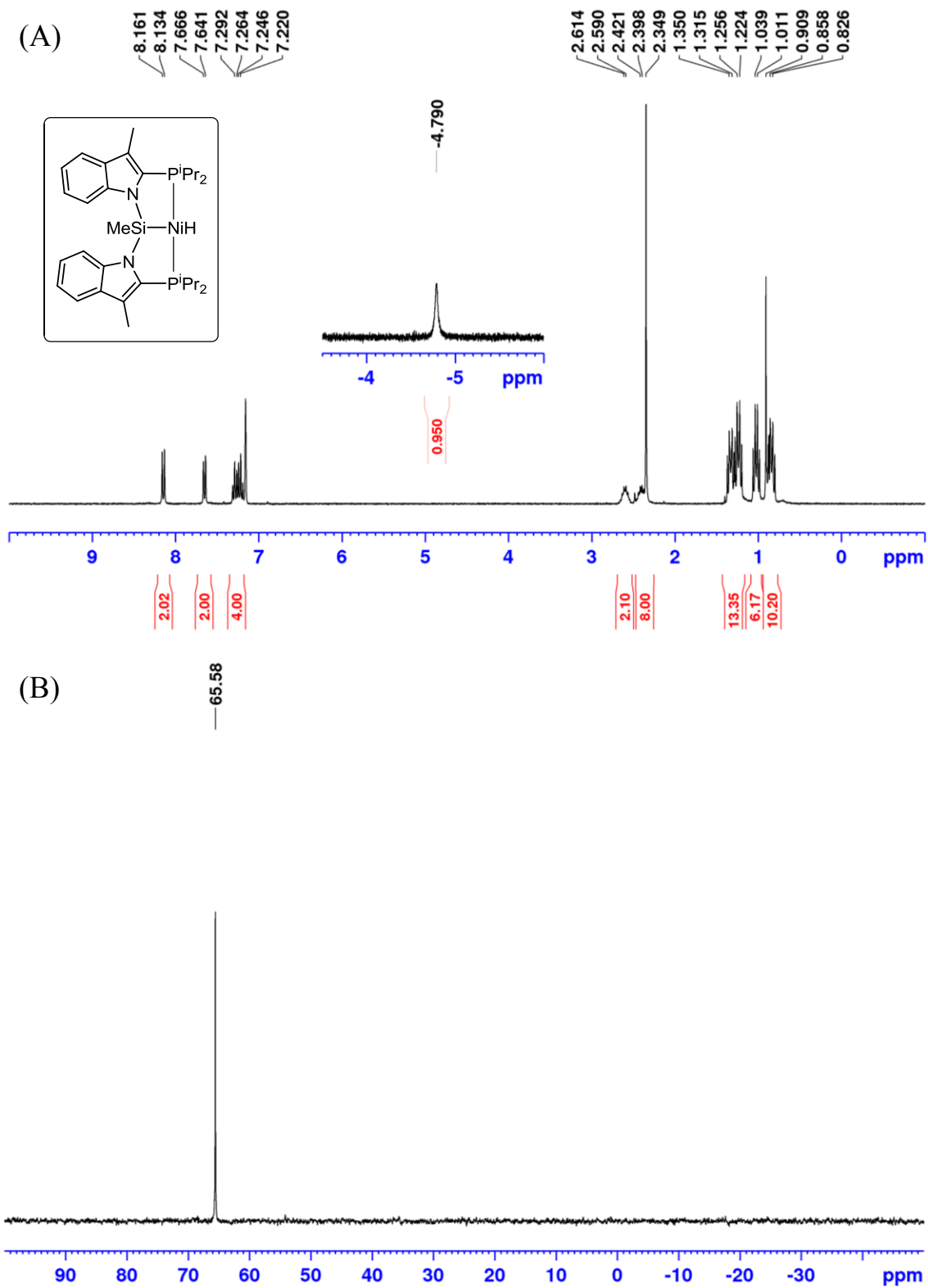


Figure B50. (A) ^1H NMR spectrum (benzene- d_6 , 300 MHz) of **4-PdH**. (B) $^{31}\text{P}\{^1\text{H}\}$ NMR spectra (benzene- d_6 , 121.5 MHz) of **4-PdH**.

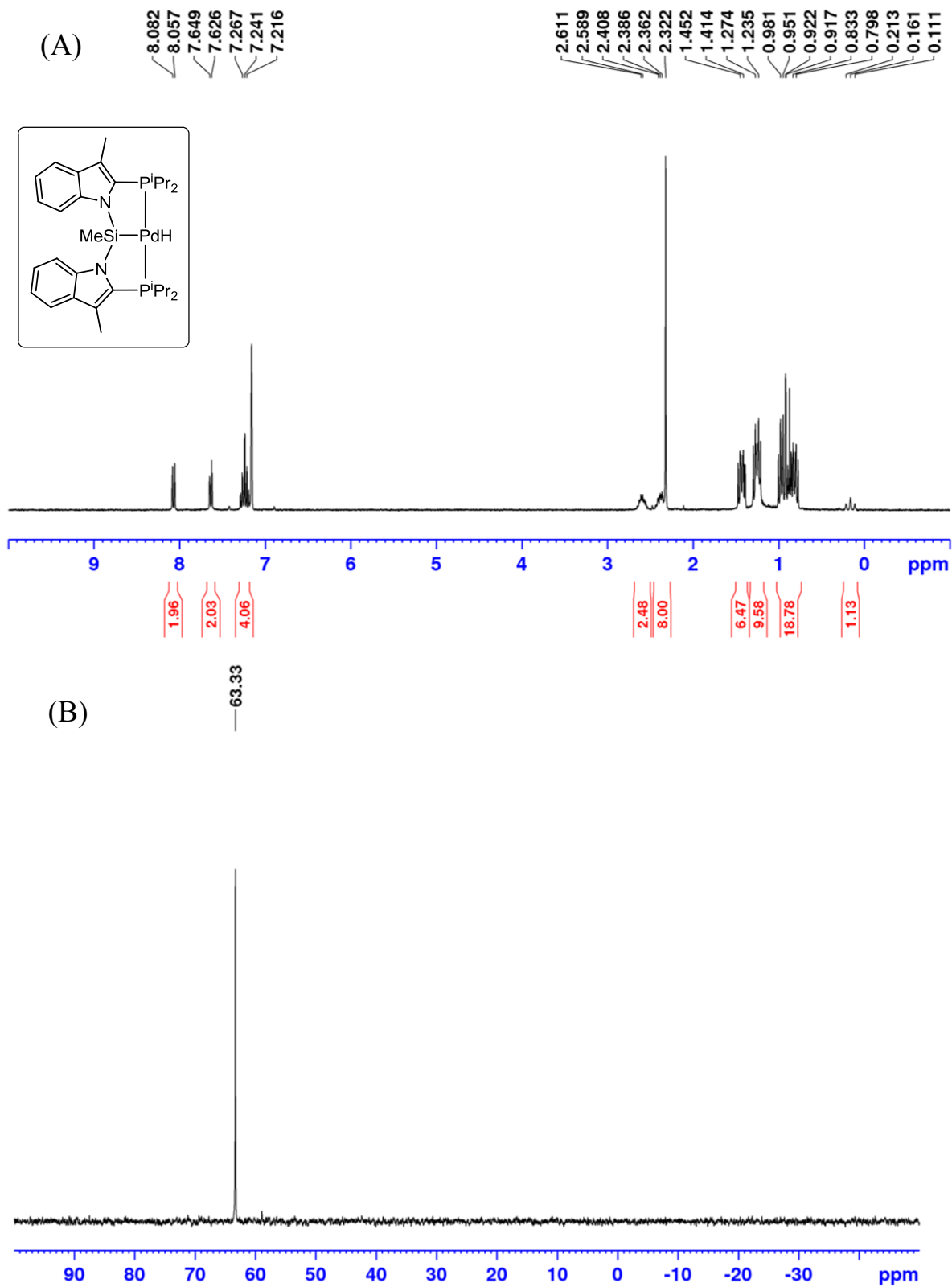


Figure B51. (A) ^1H NMR spectrum (benzene- d_6 , 300 MHz) of **4-PtH**. (B) $^{31}\text{P}\{^1\text{H}\}$ NMR spectrum (benzene- d_6 , 121.5 MHz) of **4-PtH**.

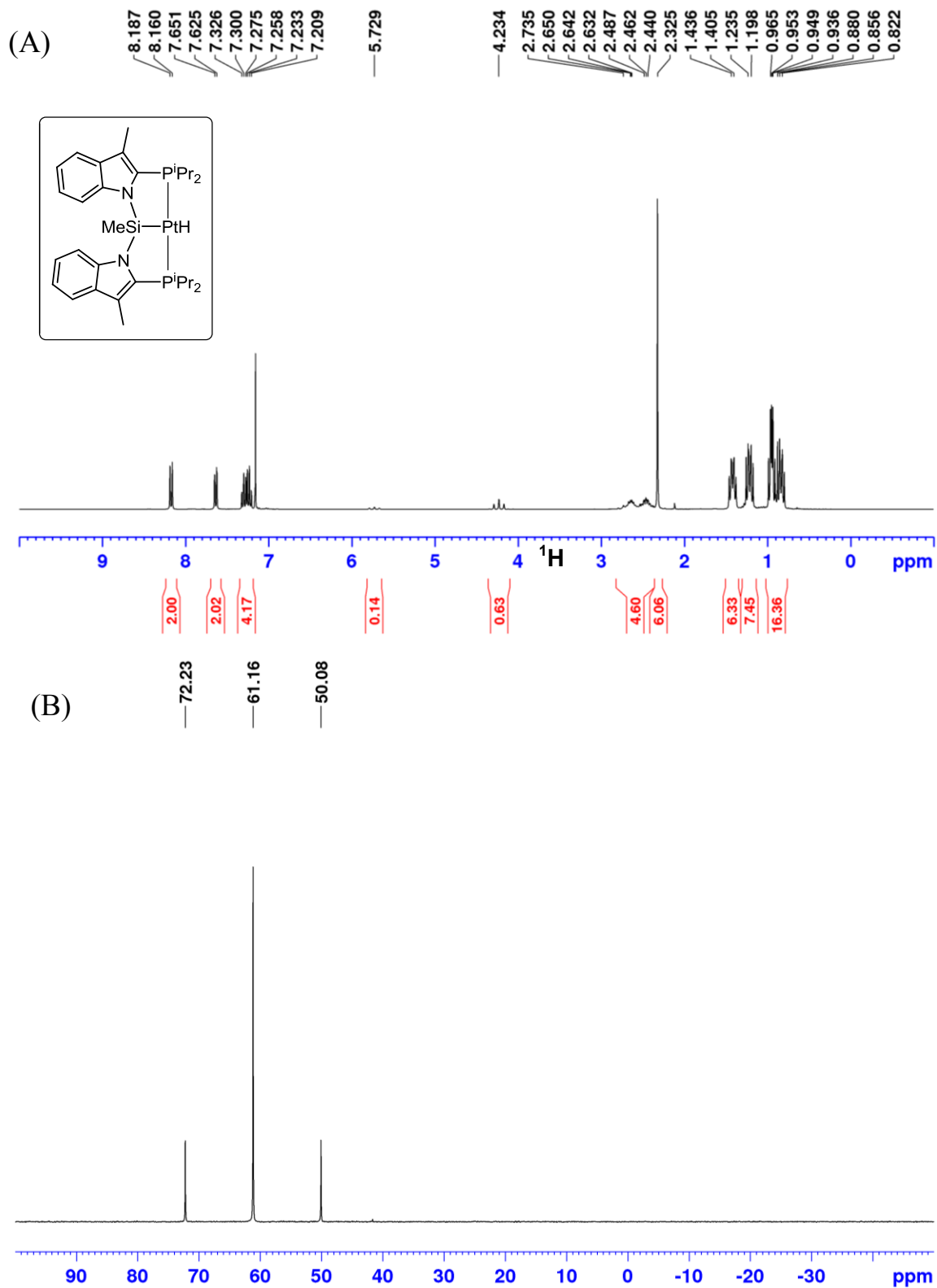


Figure B52. (A) ^1H NMR spectrum (benzene- d_6 , 300 MHz) of **4-NiH·DMAP**. (B) $^{31}\text{P}\{^1\text{H}\}$ NMR spectrum (benzene- d_6 , 121.5 MHz) of **4-NiH·DMAP**.

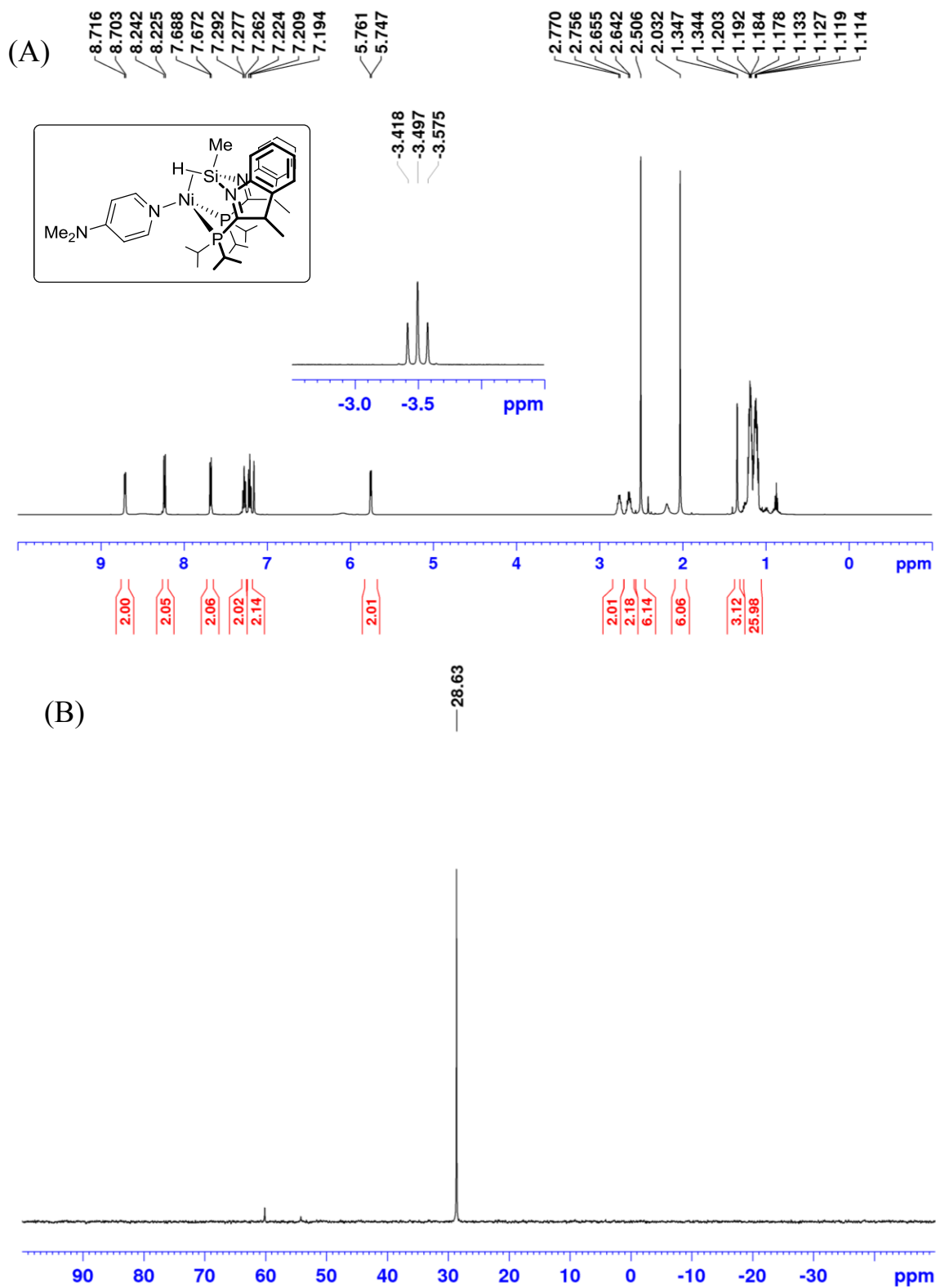


Figure B53. (A) ^1H NMR (benzene- d_6 , 500 MHz) and (B) $^{31}\text{P}\{^1\text{H}\}$ NMR spectra (benzene- d_6 , 202.5 MHz) of a mixture of **4-NiH·PMe₃-A** (major) and **4-NiH·PMe₃-B** (minor).

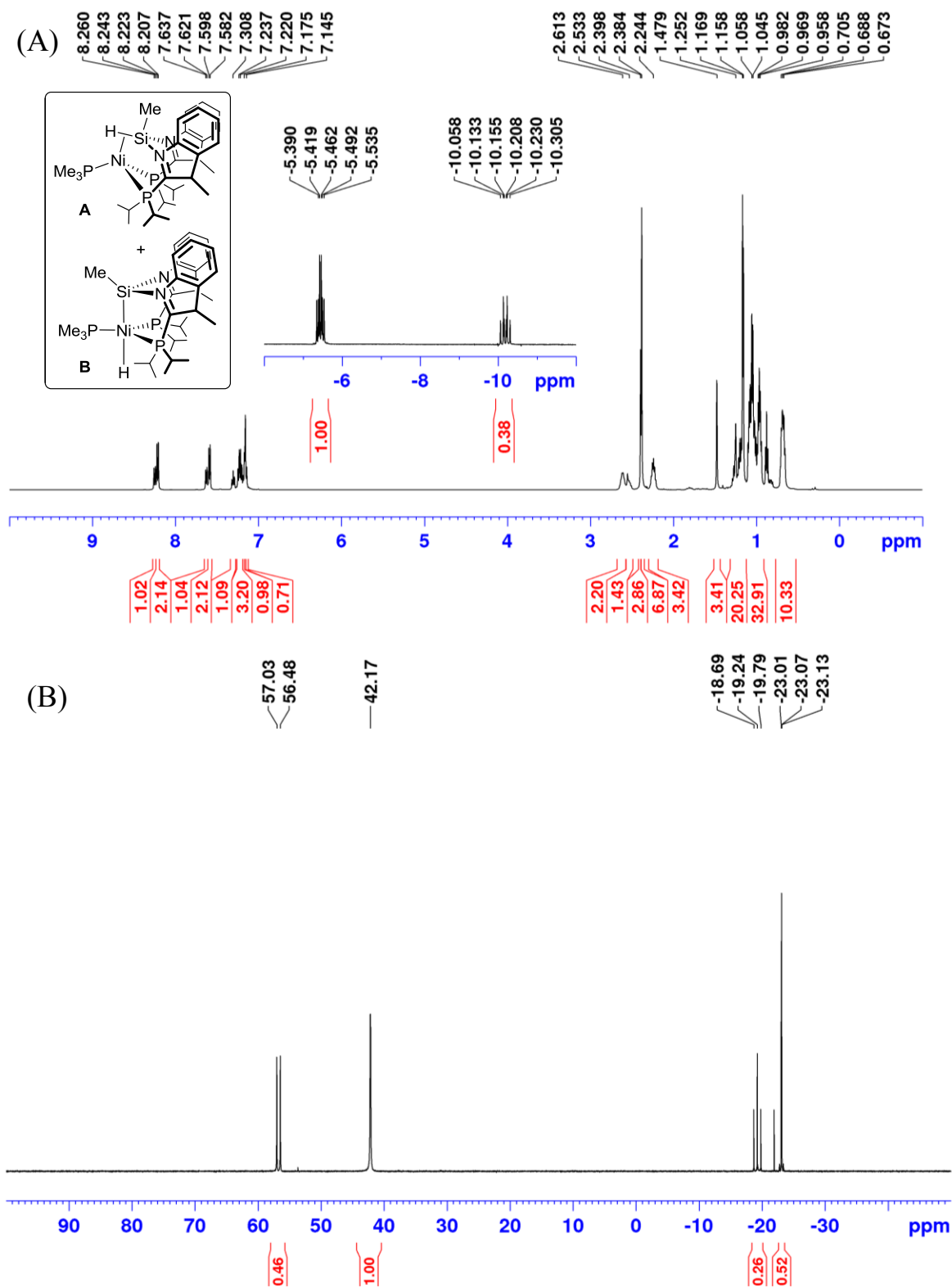


Figure B54. (A) ^1H NMR spectrum (benzene- d_6 , 500 MHz) of $4\text{-PtH}\cdot\text{PMe}_3$. $^{31}\text{P}\{^1\text{H}\}$ NMR spectrum (benzene- d_6 , 202.5 MHz) of $4\text{-PtH}\cdot\text{PMe}_3$.

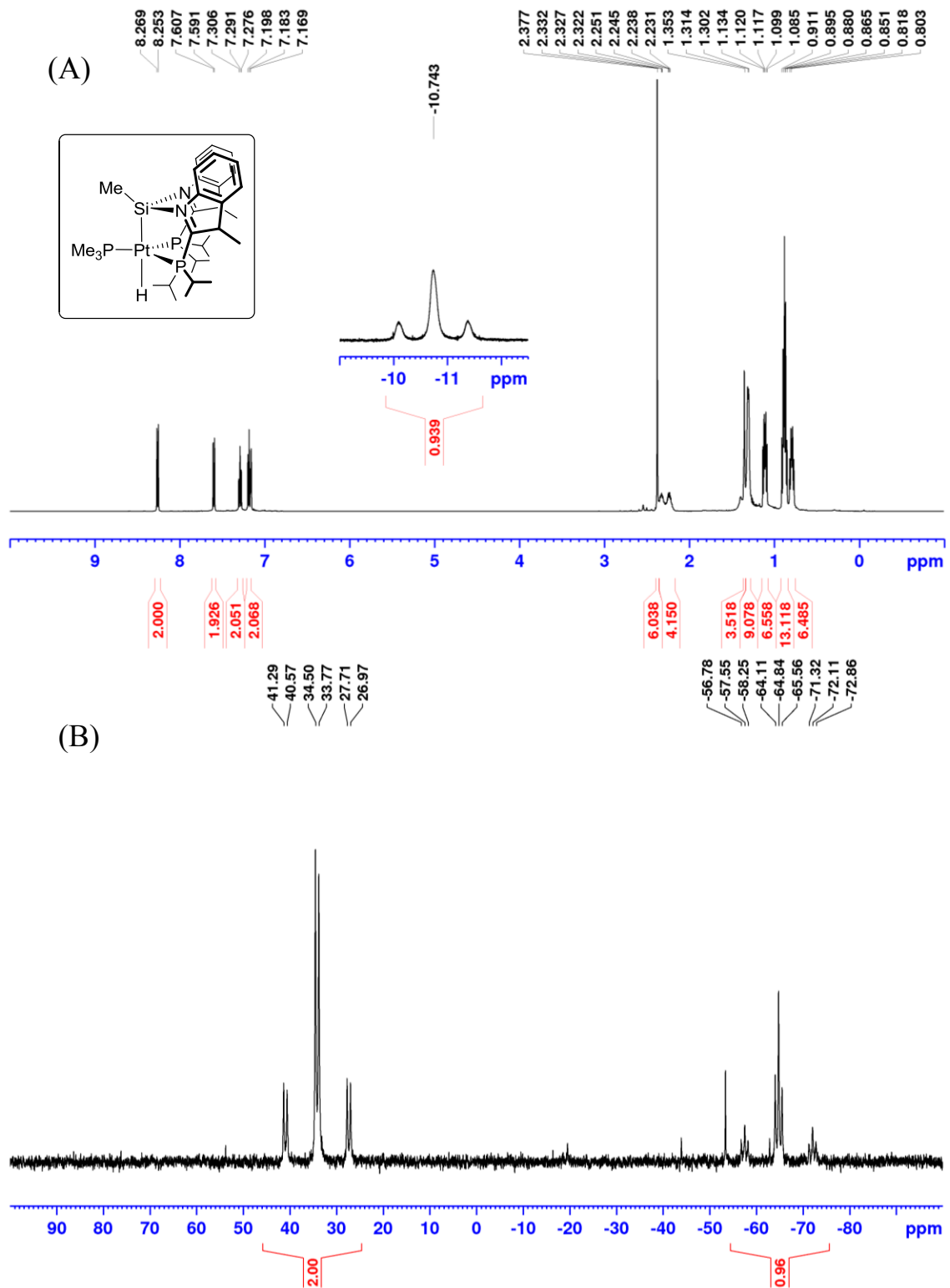


Figure B55. (A) ^1H NMR spectrum (benzene- d_6 , 300 MHz) of **4-NiHCO₂** (B) $^{31}\text{P}\{^1\text{H}\}$ NMR spectrum (benzene- d_6 , 121.5 MHz) of **4-NiHCO₂**.

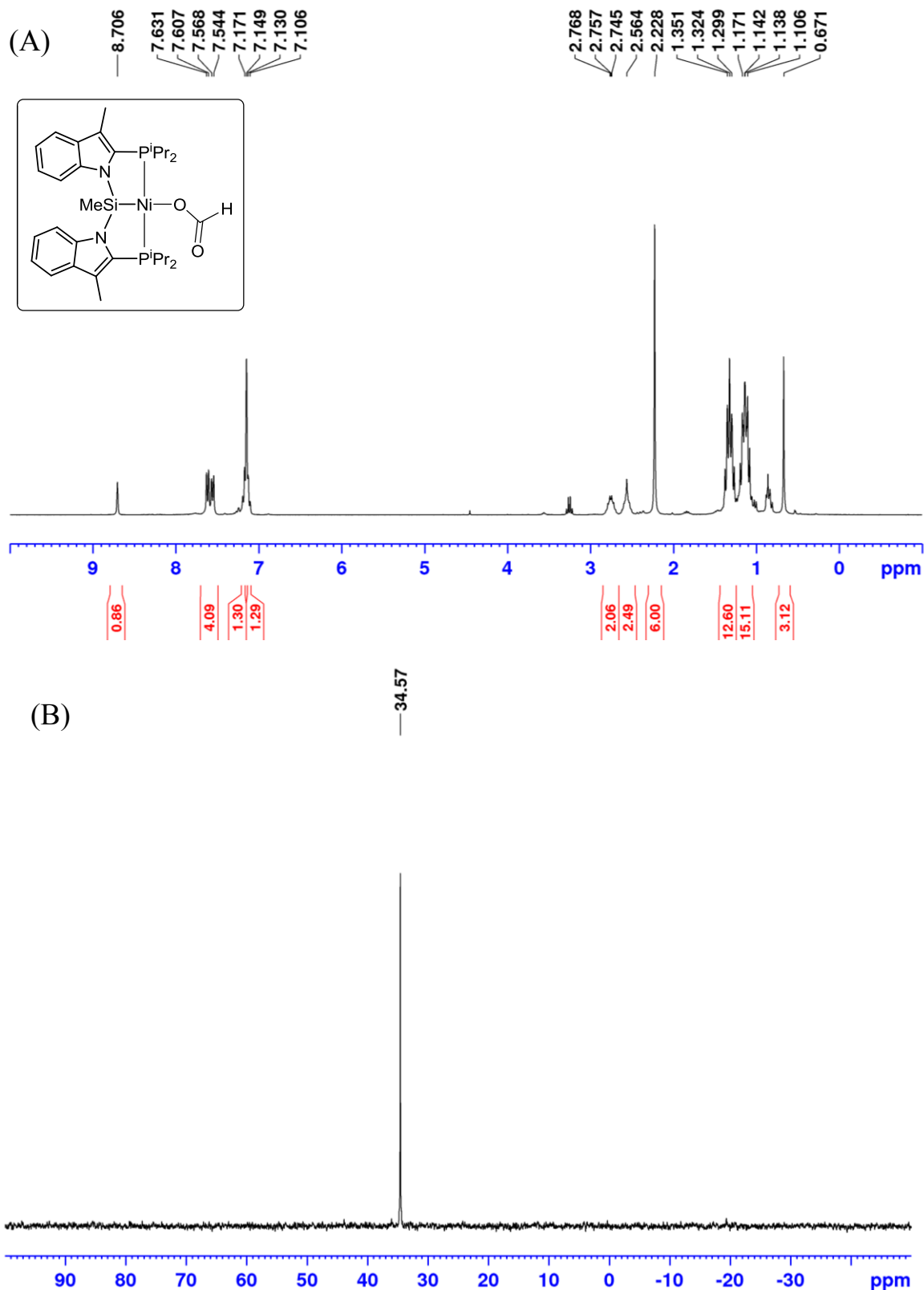


Figure B56. (A) ^1H NMR spectrum (benzene- d_6 , 300 MHz) of **4-PdHCO₂**. (B) $^{31}\text{P}\{^1\text{H}\}$ NMR spectrum (benzene- d_6 , 121.5 MHz) of **4-PdHCO₂**.

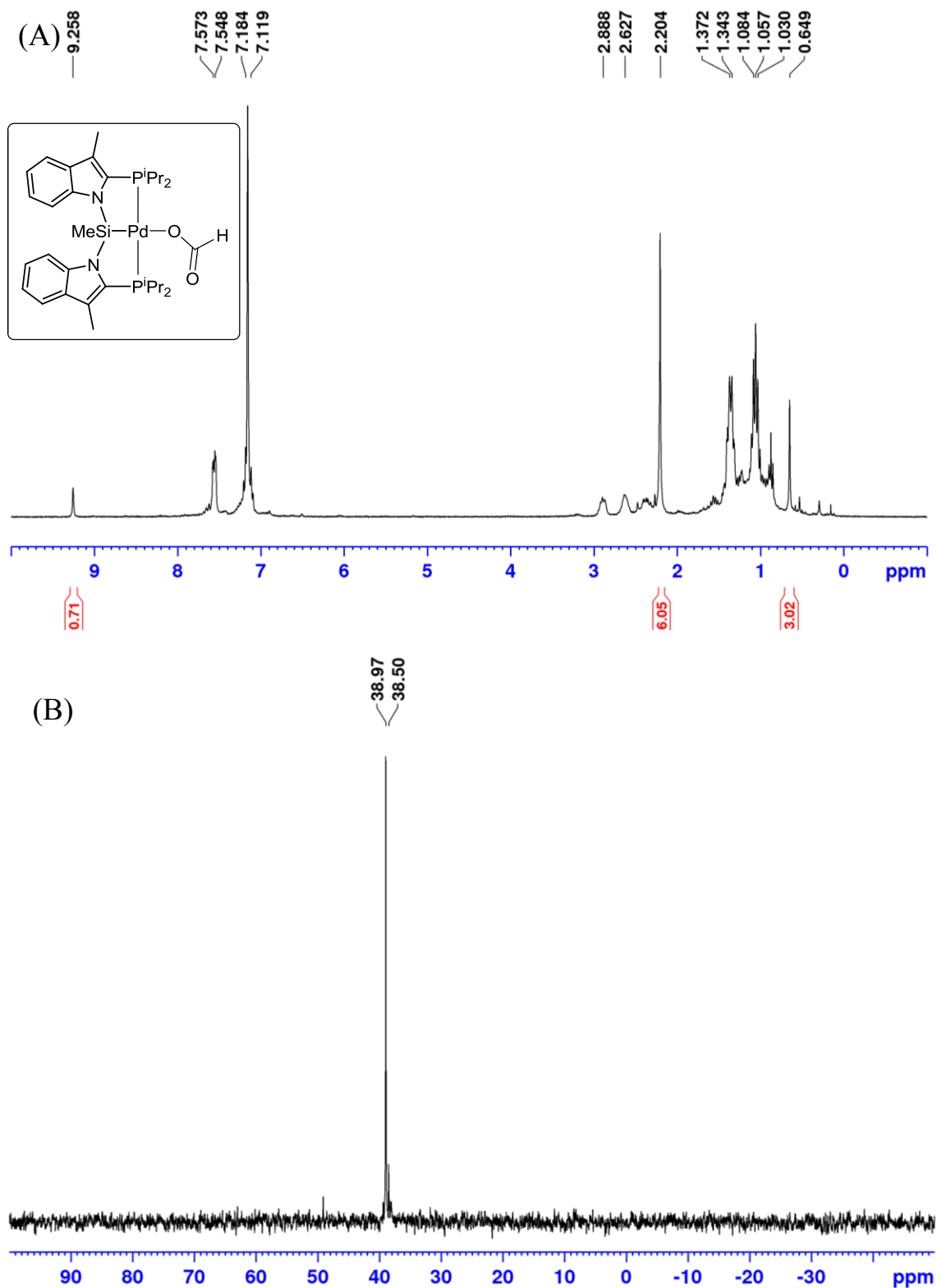


Figure B57. (A) ^1H NMR spectrum (benzene- d_6 , 500 MHz) of isolated $(\text{PinBO})_2\text{CH}_2$ (B) $^{13}\text{C}\{^1\text{H}\}$ NMR spectrum (benzene- d_6 , 125.8 MHz) of isolated $(\text{PinBO})_2\text{CH}_2$.

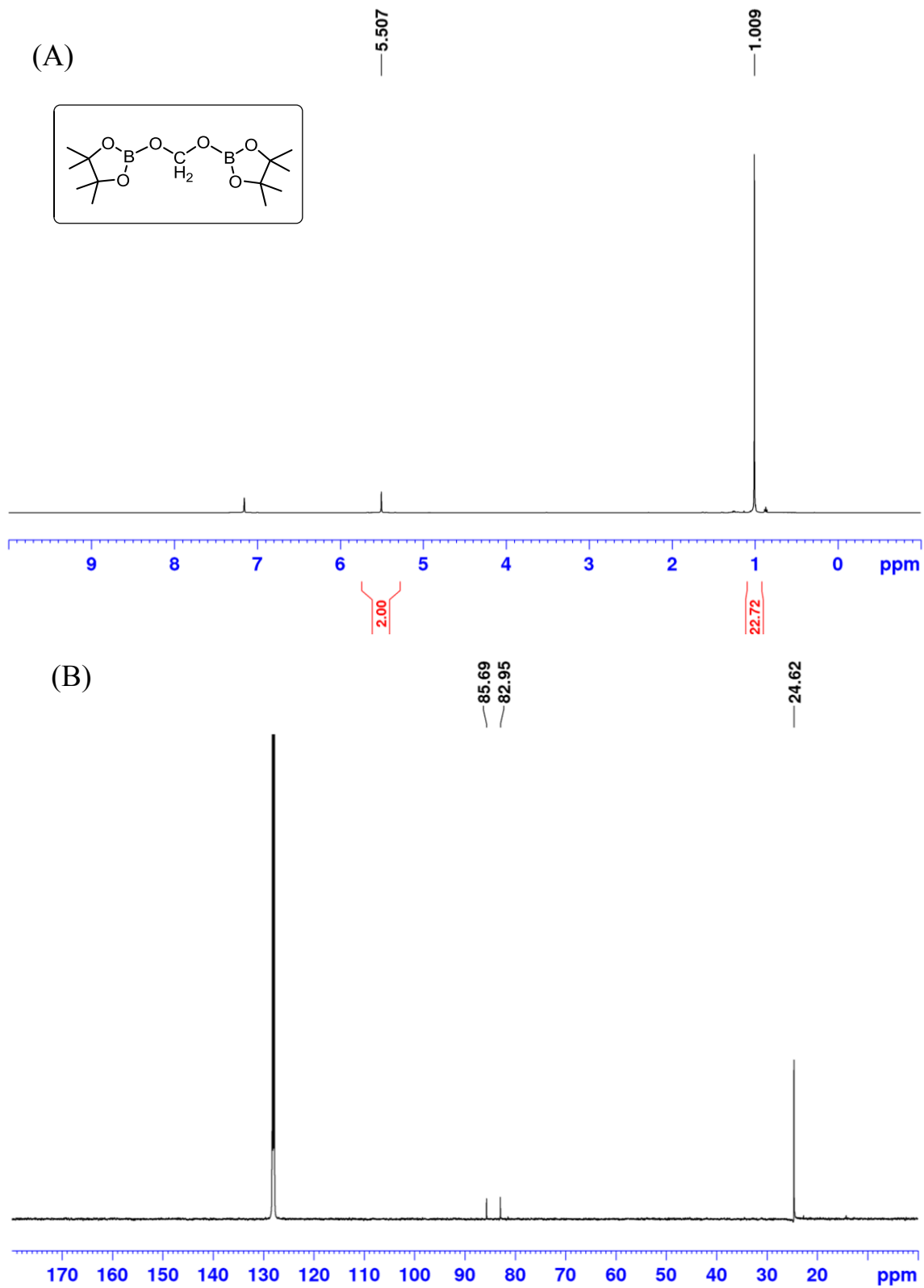


Figure B58. ^{11}B NMR spectrum (benzene- d_6 , 160.5 MHz) of isolated $(\text{PinBO})_2\text{CH}_2$.

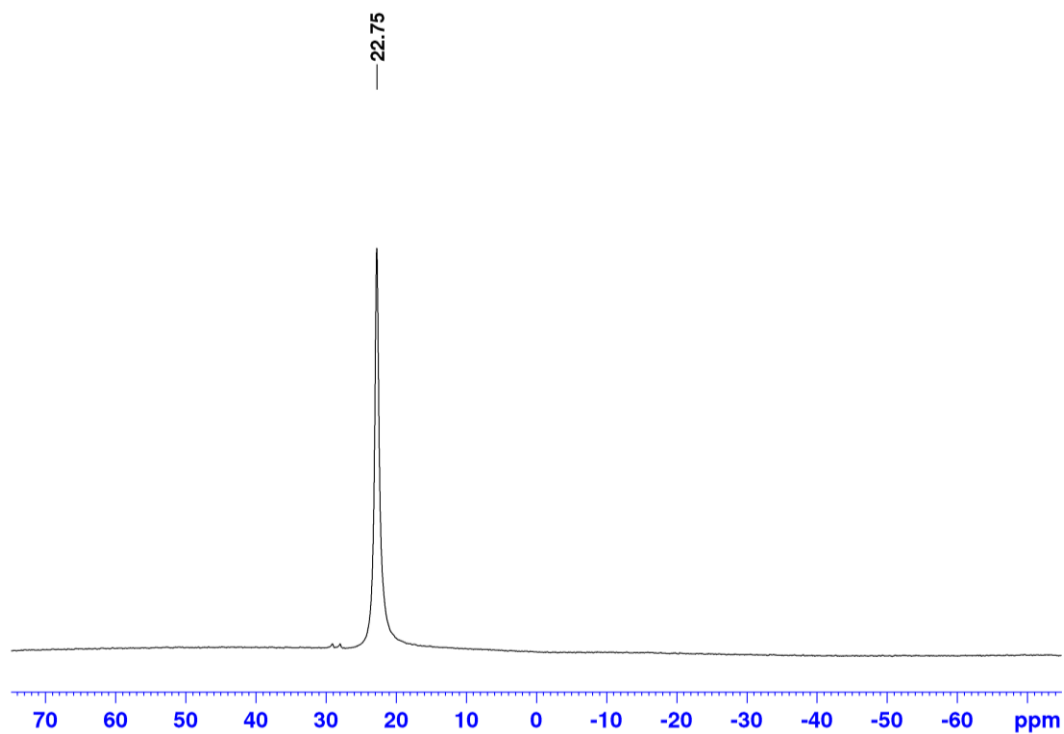


Figure B59. ^1H NMR spectrum (benzene- d_6 , 300 MHz) of $\text{CH}_2=\text{N}(2,6\text{-}^i\text{Pr}_2\text{C}_6\text{H}_3)$, generated *in situ* by treatment of $(\text{PinBO})_2\text{CH}_2$ with $\text{H}_2\text{N}(2,6\text{-}^i\text{Pr}_2\text{C}_6\text{H}_3)$.

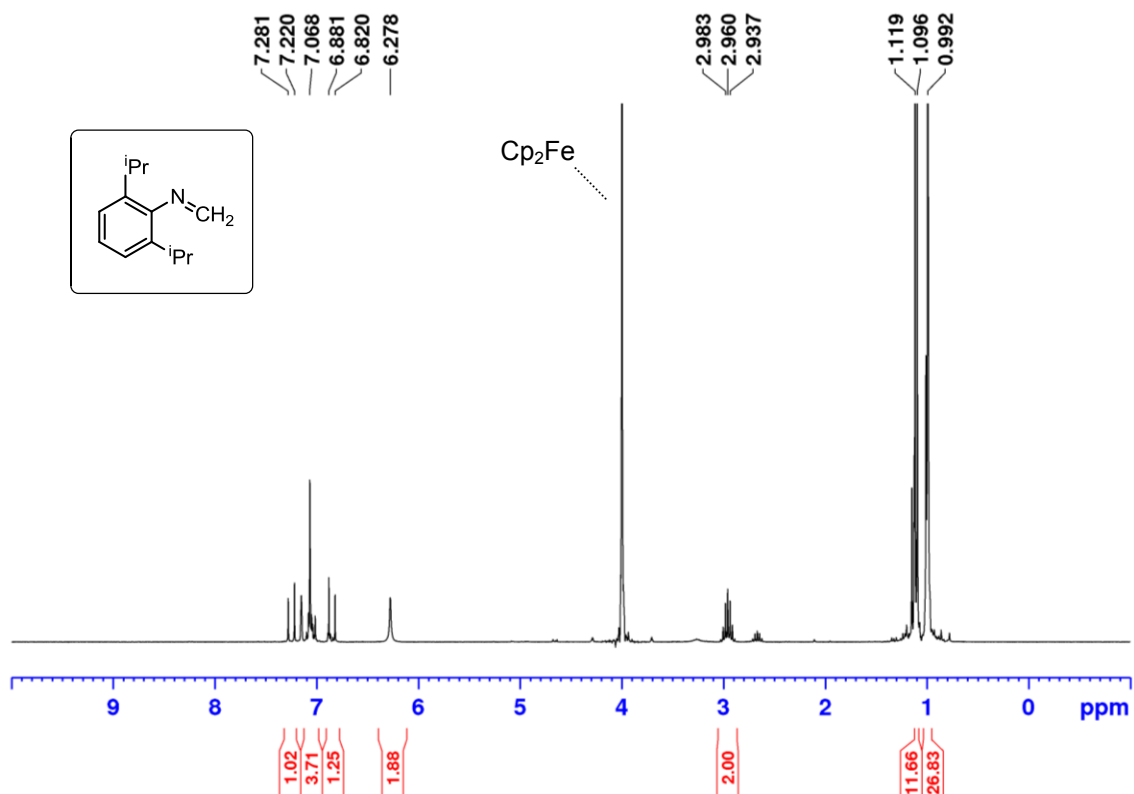


Figure B60. ^1H NMR spectrum (benzene- d_6 , 300 MHz) of $[\text{Ph}(\text{Me})\text{N}]_2\text{CH}_2$, generated *in situ* by treatment of $(\text{PinBO})_2\text{CH}_2$ with HMeNPh .

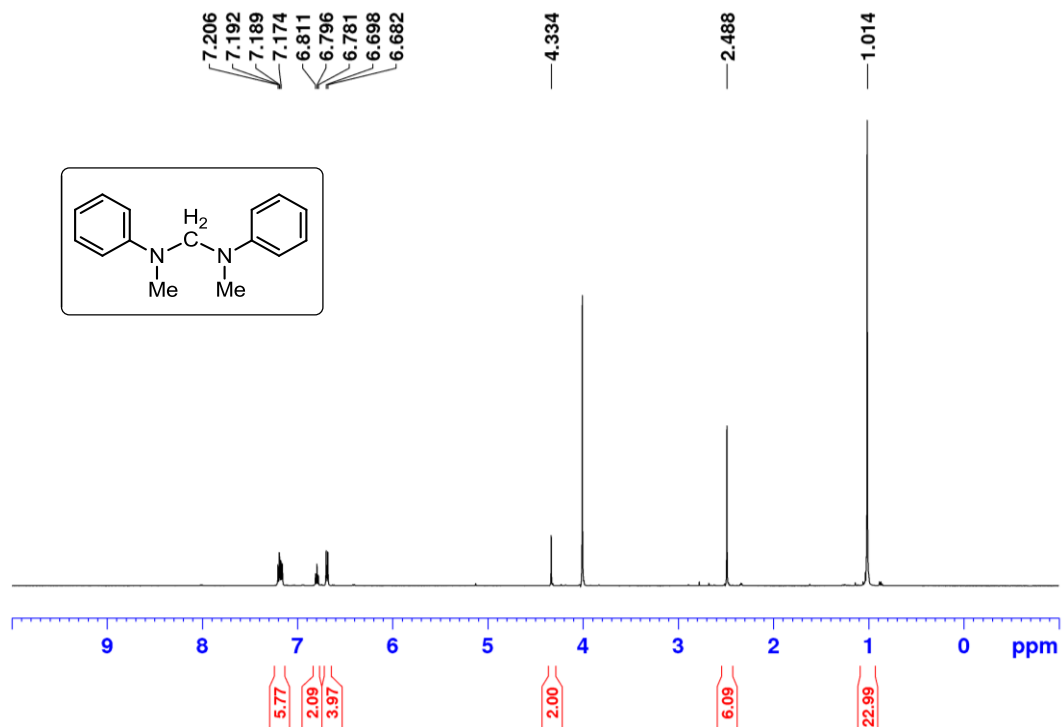


Figure B61. ^1H NMR spectrum (benzene- d_6 , 300 MHz) of $\text{PinBOCH}_2\text{PPh}_2$, generated *in situ* by treatment of $(\text{PinBO})_2\text{CH}_2$ with HPPh_2 .

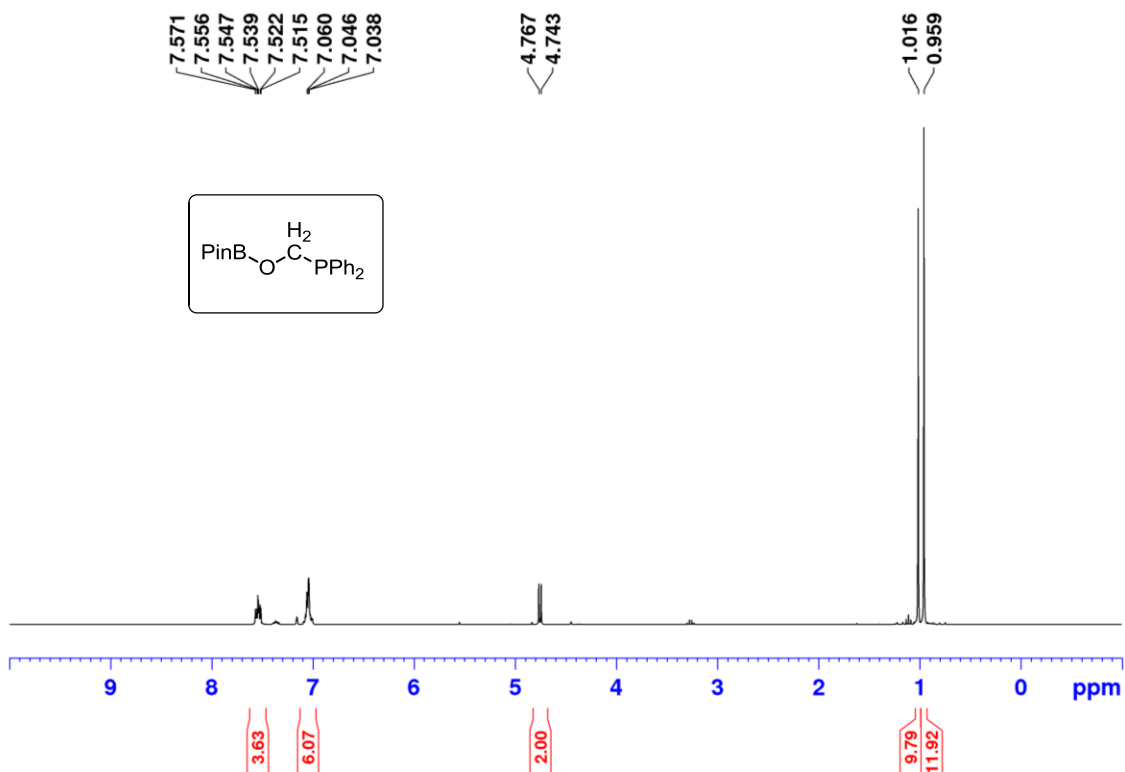


Figure B62. (A) $^{13}\text{C}\{^1\text{H}\}$ NMR (benzene- d_6 , 125.8 MHz) and (B) $^{31}\text{P}\{^1\text{H}\}$ NMR spectra (benzene- d_6 , 121.5 MHz) of PinBOCH $_2$ PPh $_2$, generated *in situ* by treatment of (PinBO) $_2$ CH $_2$ with HPPh $_2$.

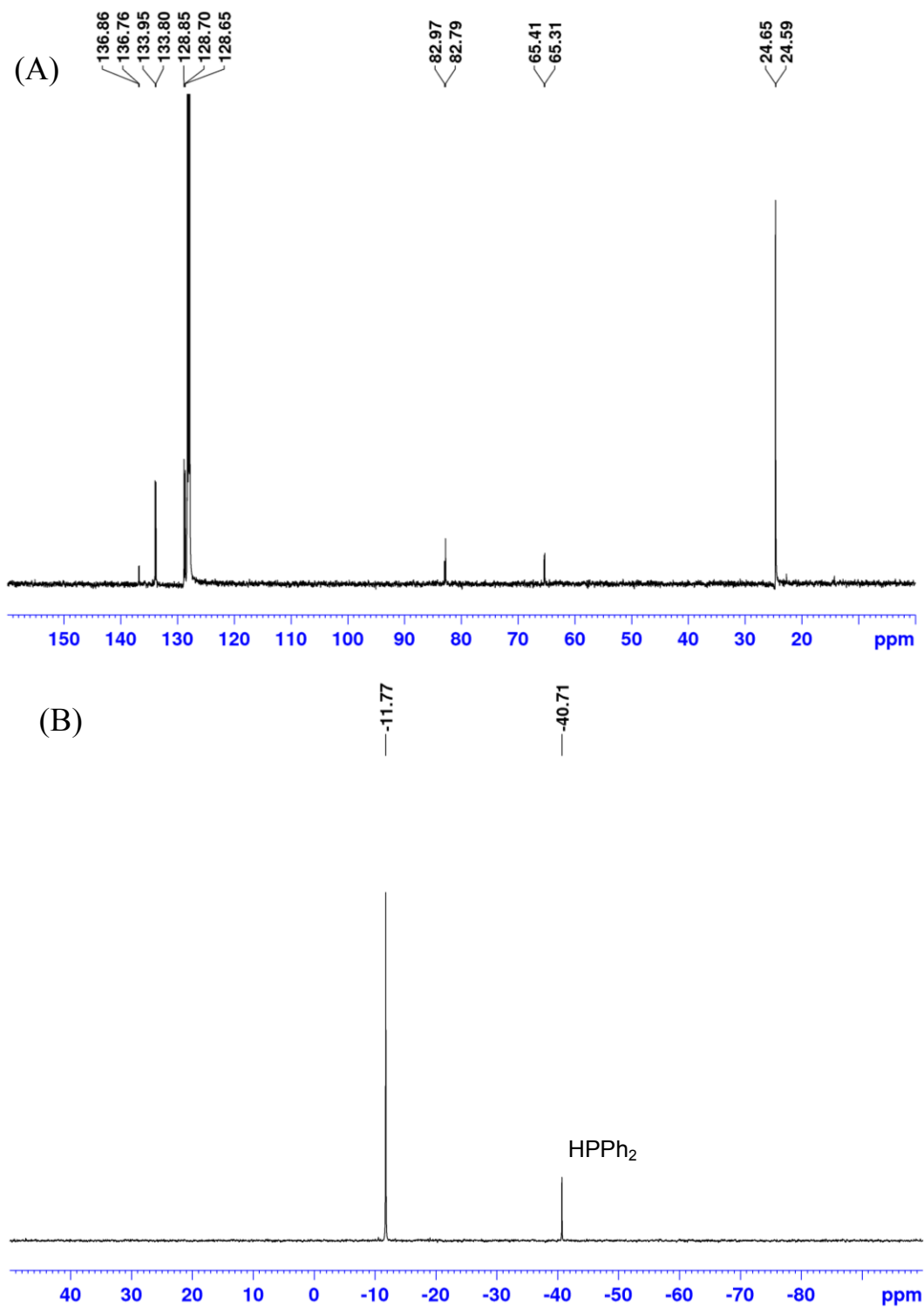
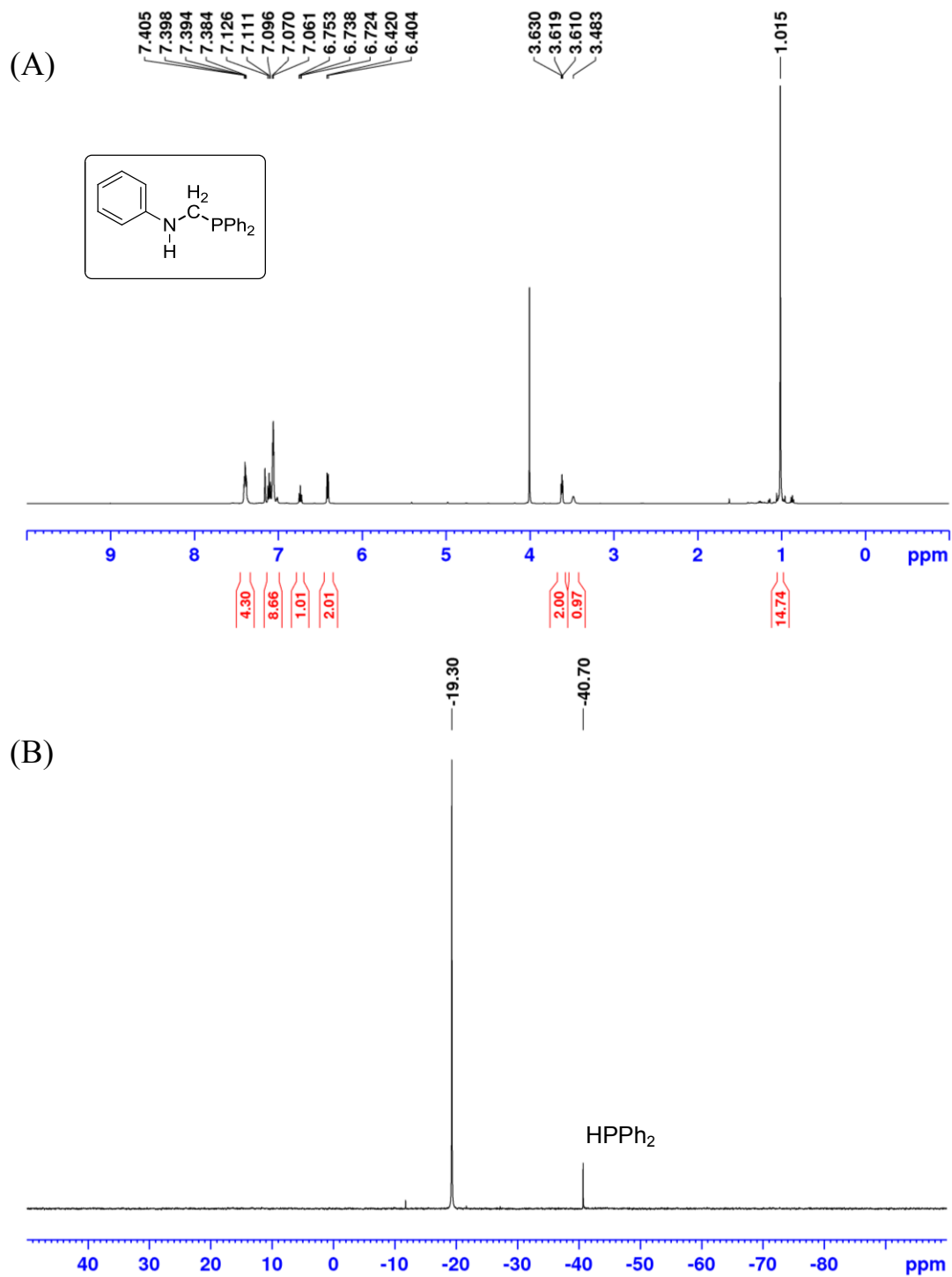


Figure B63. (A) ^1H NMR (benzene- d_6 , 500 MHz) and (B) $^{31}\text{P}\{^1\text{H}\}$ NMR spectra (benzene- d_6 , 202.5 MHz) of $\text{Ph}(\text{H})\text{NCH}_2\text{PPh}_2$, generated *in situ* from $(\text{PinBO})_2\text{CH}_2$.



Selected Spectra of Compounds Reported in Chapter 5

Figure B64. (A) ^1H NMR spectrum (benzene- d_6 , 500 MHz) of (P,N)H. (B) $^{31}\text{P}\{^1\text{H}\}$ NMR spectrum (benzene- d_6 , 202.5 MHz) of (P,N)H.

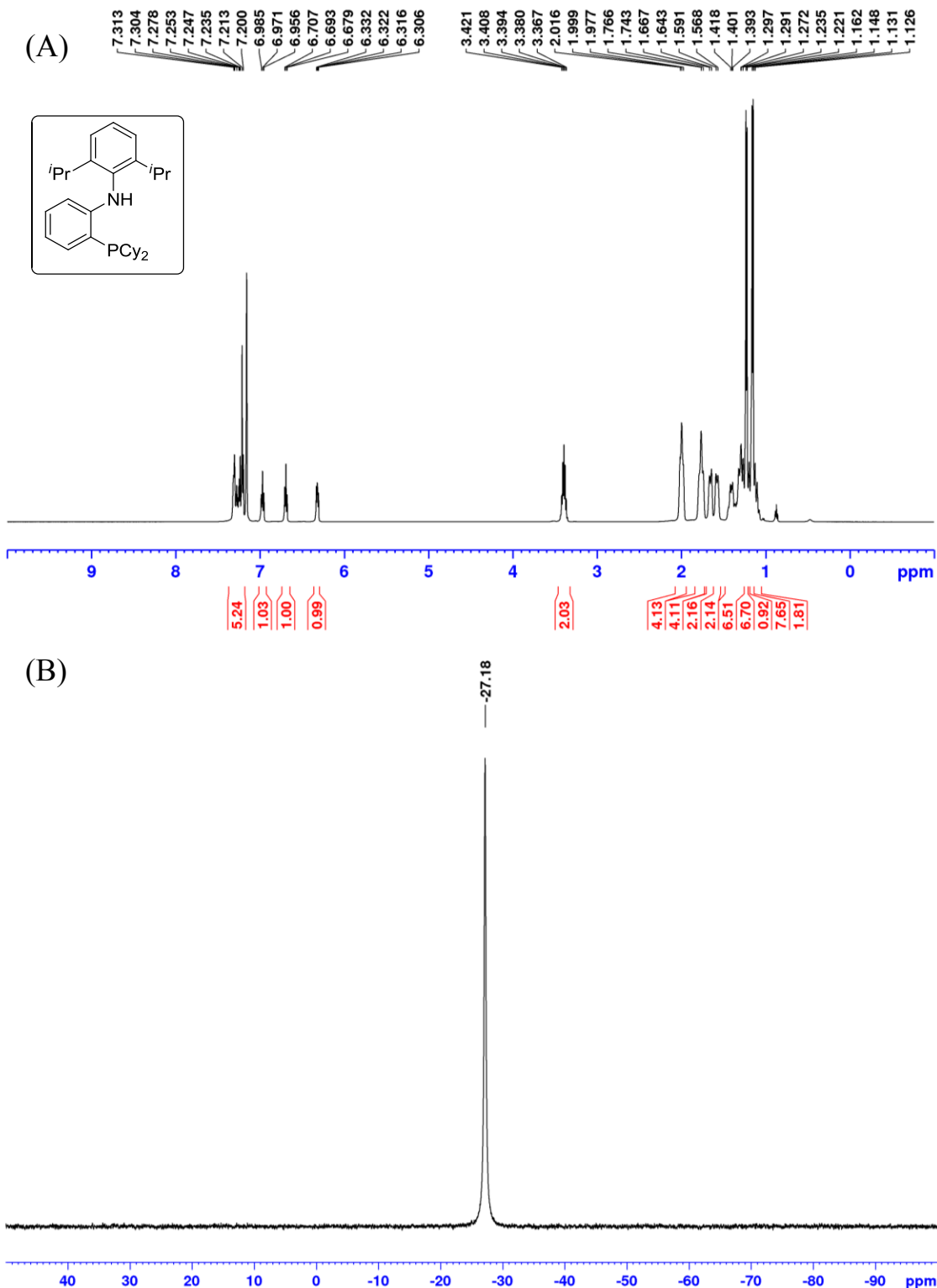


Figure B65. ^1H NMR spectrum (benzene- d_6 , 300 MHz) of **5-FeCl**.

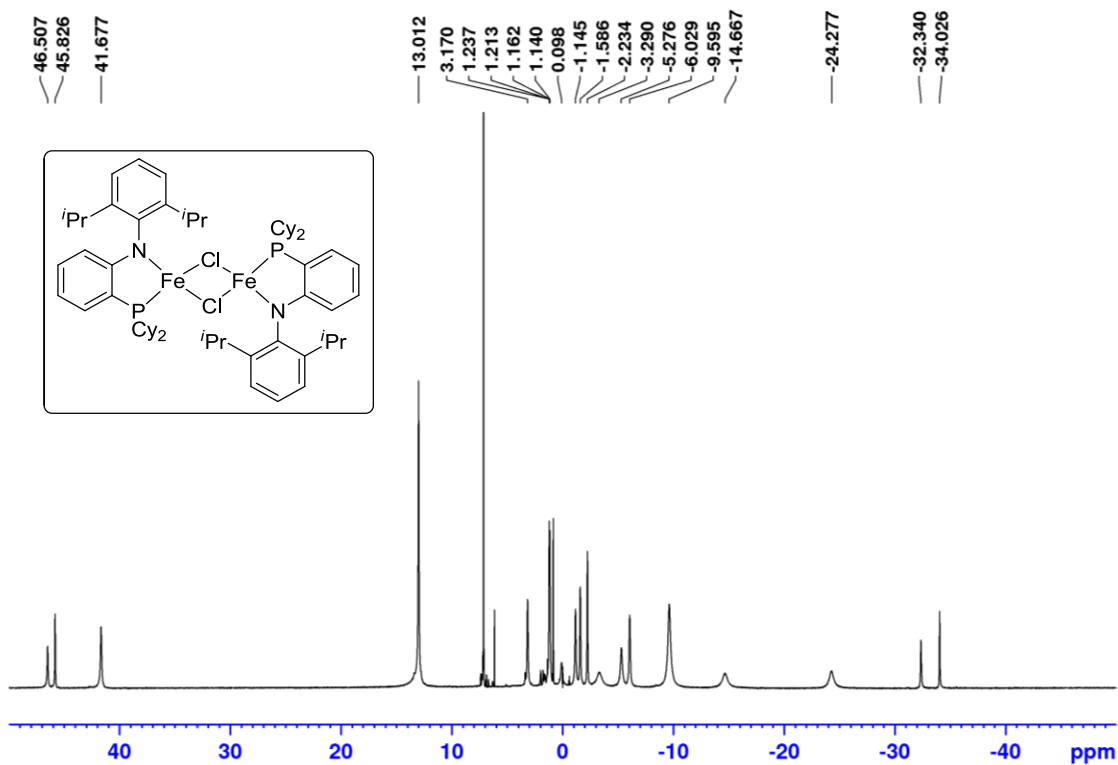


Figure B66. ^1H NMR spectrum (benzene- d_6 , 300 MHz) of **5-FeBr**.

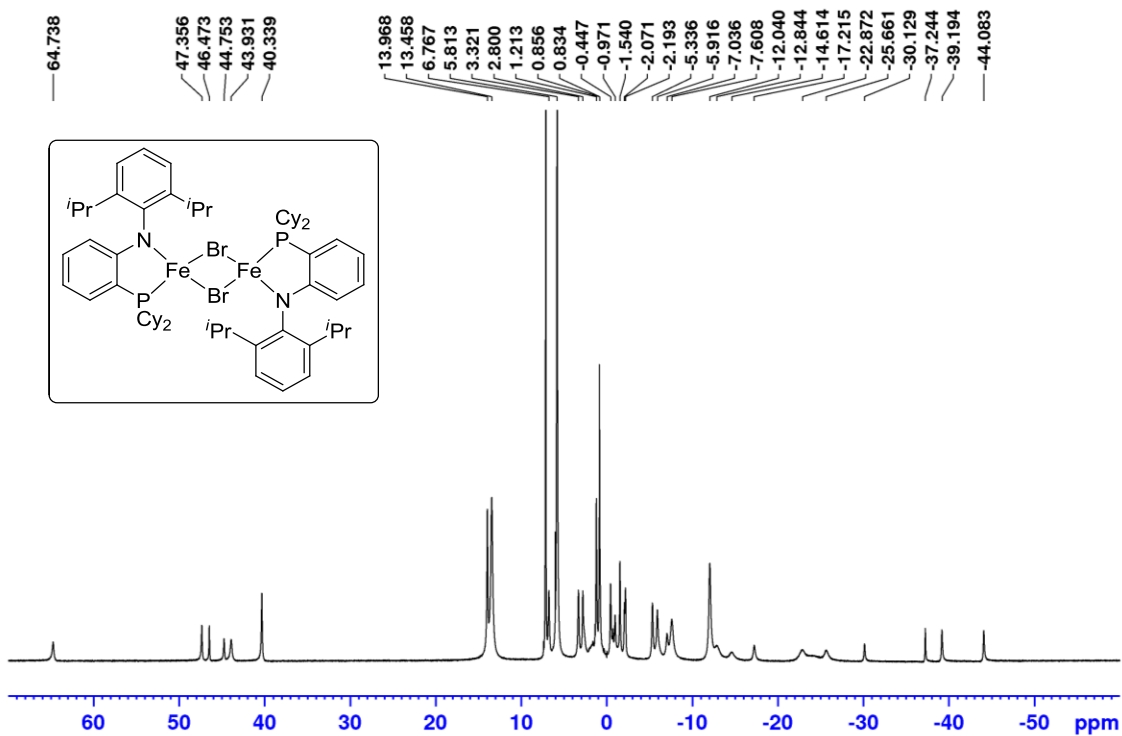


Figure B67. ^1H NMR spectrum (benzene- d_6 , 300 MHz) of **5-1**.

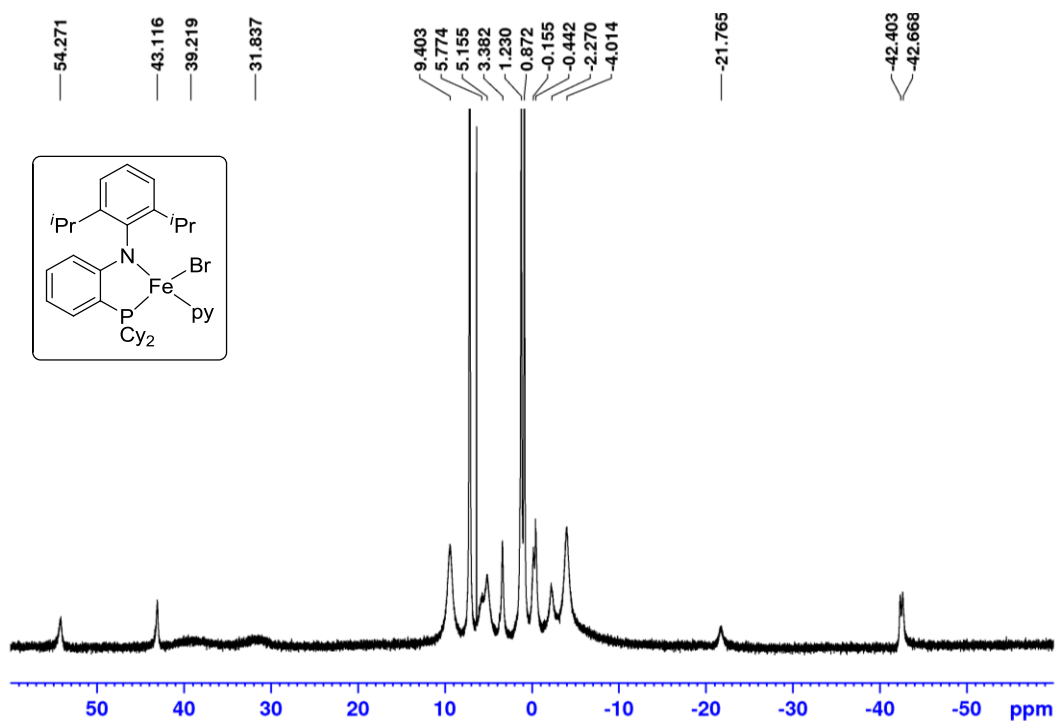


Figure B68. ^1H NMR spectrum (benzene- d_6 , 300 MHz) of **5-2**.

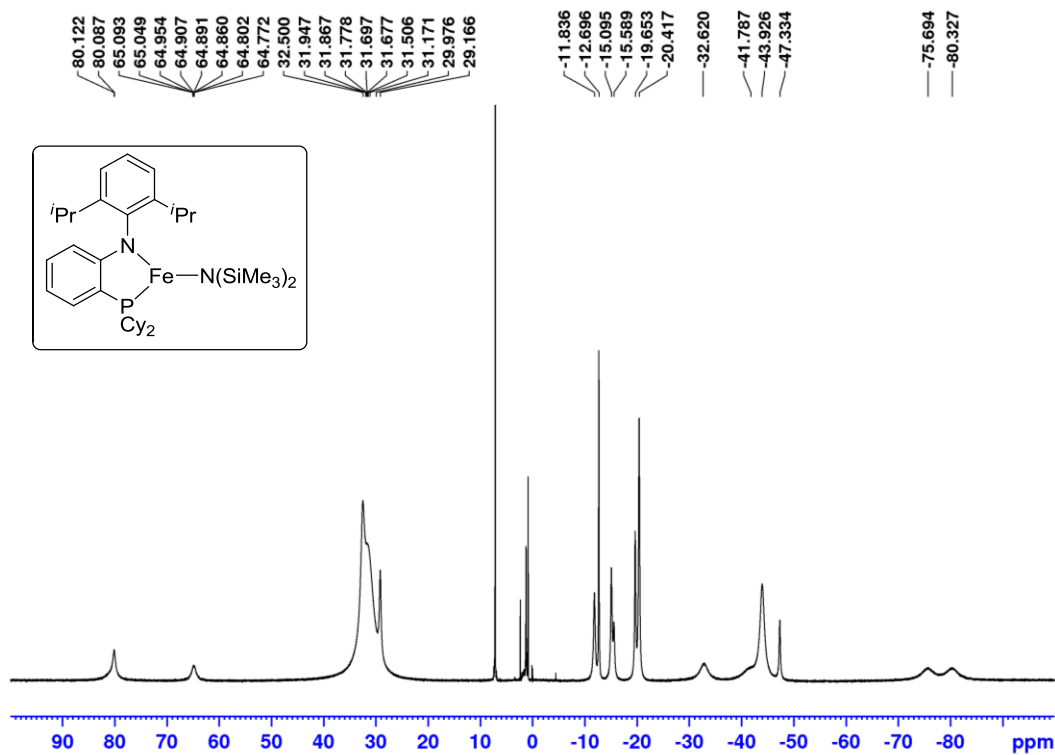


Figure B69. ^1H NMR spectrum (benzene- d_6 , 300 MHz) of **5-5**.

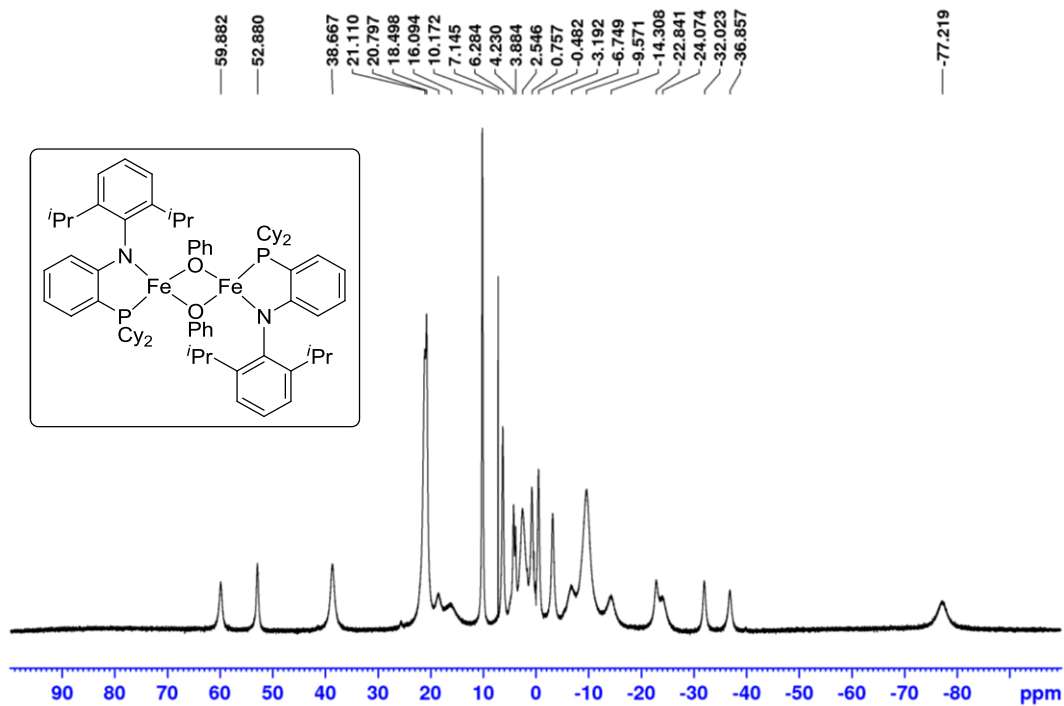


Figure B70. ^1H NMR spectrum (benzene- d_6 , 300 MHz) of **5-8**.

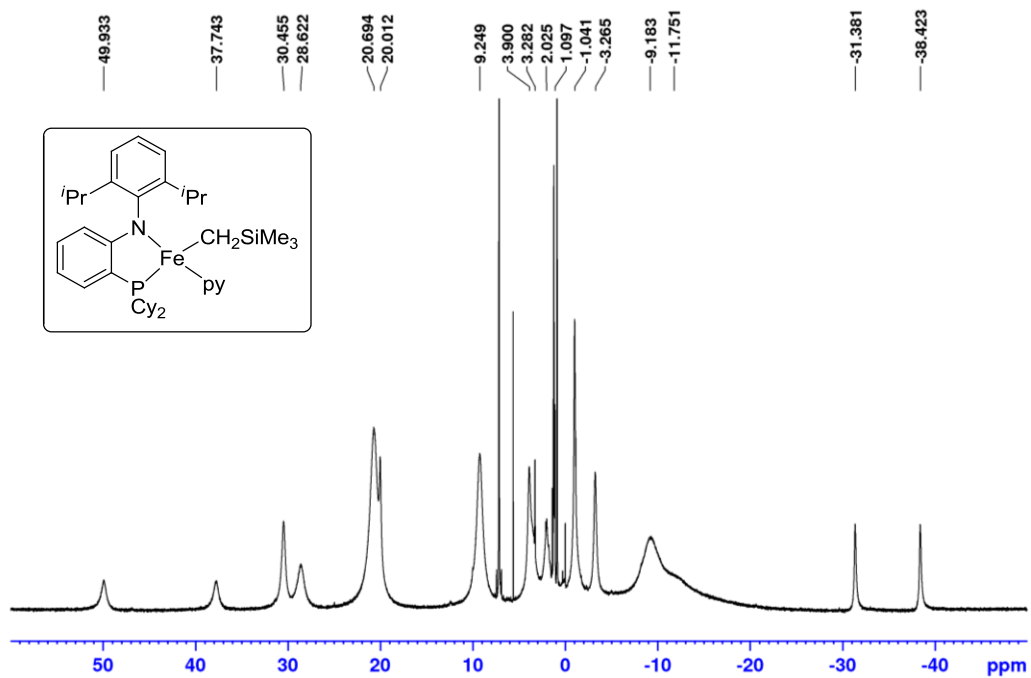
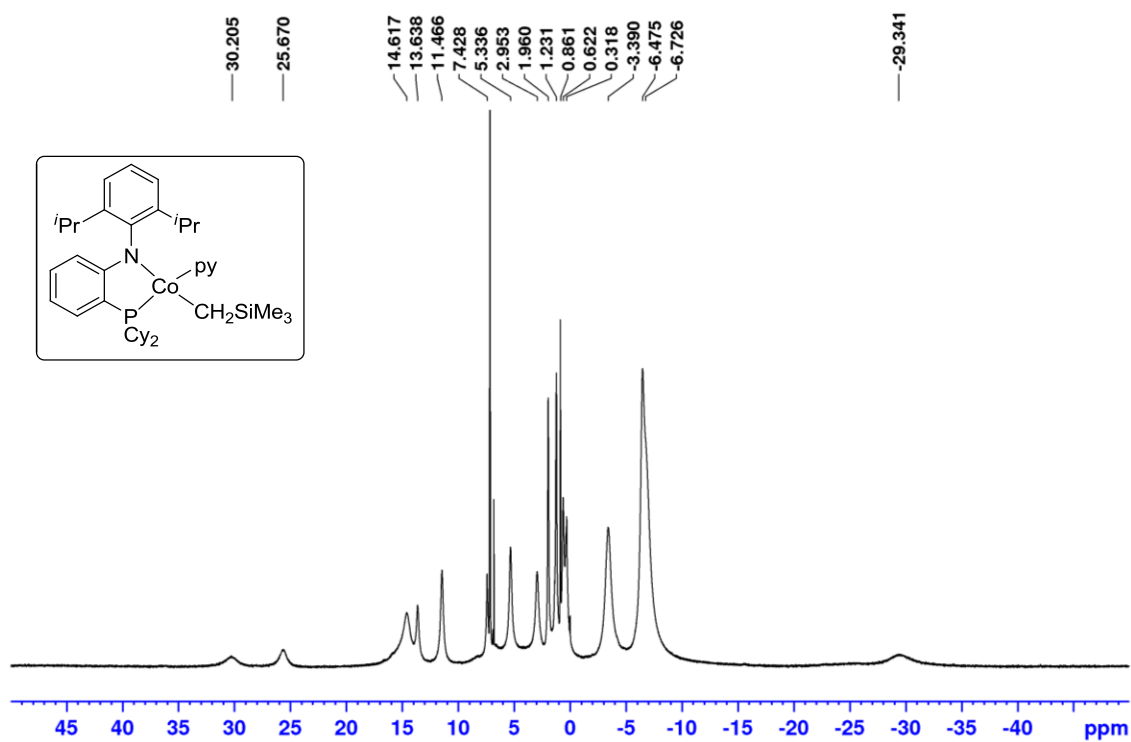


Figure B71. ^1H NMR spectrum (benzene- d_6 , 300 MHz) of **5-9**.



Appendix C: Copyright Agreements

6/20/2018

Rightslink® by Copyright Clearance Center



RightsLink®

Home

Create Account

Help



ACS Publications
Most Trusted. Most Cited. Most Read.

Title: Selective Ni-Catalyzed Hydroboration of CO₂ to the Formaldehyde Level Enabled by New PSIP Ligation
Author: Luke J. Murphy, Helia Hollenhorst, Robert McDonald, et al
Publication: Organometallics
Publisher: American Chemical Society
Date: Oct 1, 2017

Copyright © 2017, American Chemical Society

LOGIN

If you're a [copyright.com](#) user, you can login to RightsLink using your [copyright.com](#) credentials. Already a [RightsLink user](#) or want to [learn more?](#)

PERMISSION/LICENSE IS GRANTED FOR YOUR ORDER AT NO CHARGE

This type of permission/license, instead of the standard Terms & Conditions, is sent to you because no fee is being charged for your order. Please note the following:

- Permission is granted for your request in both print and electronic formats, and translations.
- If figures and/or tables were requested, they may be adapted or used in part.
- Please print this page for your records and send a copy of it to your publisher/graduate school.
- Appropriate credit for the requested material should be given as follows: "Reprinted (adapted) with permission from (COMPLETE REFERENCE CITATION). Copyright (YEAR) American Chemical Society." Insert appropriate information in place of the capitalized words.
- One-time permission is granted only for the use specified in your request. No additional uses are granted (such as derivative works or other editions). For any other uses, please submit a new request.

BACK

CLOSE WINDOW

Copyright © 2018 [Copyright Clearance Center, Inc.](#) All Rights Reserved. [Privacy statement](#). [Terms and Conditions](#). Comments? We would like to hear from you. E-mail us at customercare@copyright.com